Durham University

Durham E-Theses

Magma Chemical Evolution in the Lesser Antilles Arc Crust: Insights from Plutonic Xenoliths

JOSHUA ROBERT BROWN

How to cite:

BROWN, JOSHUA ROBERT (2023) Magma Chemical Evolution in the Lesser Antilles Arc Crust: Insights from Plutonic Xenoliths. Doctoral thesis, Durham University.

Use policy

The full-text may be used and/or reproduced, and given to third parties in any format or medium, without prior permission or charge, for personal research or study, educational, or not-for-profit purposes provided that:

- a full bibliographic reference is made to the original source
- a https://etheses.durham.ac.uk/id/eprint/14810/ is made to the metadata record in Durham E-Theses
- the full-text is not changed in any way

The full-text must not be sold in any format or medium without the formal permission of the copyright holders.

Please consult the full Durham E-Theses policy for further details.

Academic Support Office, The Palatine Centre, Durham University, Stockton Road, Durham, DH1 3LE
e-mail: e-theses.admin@durham.ac.uk Tel: +44 0191 334 6107
https://etheses.durham.ac.uk

Magma Chemical Evolution in the Lesser Antilles Arc Crust: Insights from Plutonic Xenoliths

Joshua Robert Brown

This thesis is submitted in partial fulfilment of the requirements for the degree of Doctor of Philosophy at Durham University

Department of Earth Sciences

December 2022

Abstract

Magmas generated beneath volcanic arcs at subduction zones must traverse the crust of the overriding plate, via "magma plumbing systems" prior to eruption. Magma plumbing systems are predominantly composed of crystal mush, where low volumes of melt are distributed throughout higher volumes of crystals. To understand processes controlling the chemical compositions of arc lavas, it is essential to constrain how magmas are chemically modified within mushy plumbing systems during storage and transit through the upper plate crust. Arc lavas often carry fragments of crystal mush, known as plutonic xenoliths, to the surface, which can be used to study the influence of crustal processes on arc magma chemical compositions.

This thesis investigates plutonic xenoliths from the islands of Martinique and St Vincent in the active intra-oceanic Lesser Antilles arc. These samples are used to determine whether the majority of the trace element and isotopic variation in Lesser Antilles arc lavas can be produced by crustal processes. Strontium isotopic compositions of plagioclase, in plutonic xenoliths derived from different crustal depths, are used to demonstrate that isotopic variation and highly radiogenic isotopic compositions observed in Martinique lavas are acquired via assimilation of upper crustal sediments. Textural features and mineral trace element compositions in St Vincent plutonic xenoliths record polybaric fractional crystallization and melt-mush reaction processes. These two processes control magma chemical evolution in mushes beneath the island and consequently influence the trace element compositions of St Vincent lavas.

These findings suggest that majority of trace element and radiogenic isotopic variation in Lesser Antilles arc lavas is generated within mushy magma plumbing systems in the arc crust. An important wider implication is that contributions from crustal processes must be well constrained before using trace element and isotopic compositions of arc lavas to assess subduction recycling processes and mantle source heterogeneity.

Declaration

I declare that this thesis, which I submit for the degree of Doctor of Philosophy at Durham University, is my own work and that no part of the material offered has previously been submitted by me for a degree in this or any other University.

Joshua Brown, 2022

© The copyright of this thesis rests with the author. No quotation from it should be published without the author's prior written consent and information derived from it should be acknowledged.

Contents

Abstract……...iii

Declaration…….....iv

Contents……v

List of Figures……xii

List of Tables……..xx

Acknowledgements…….xxiii

Chapter 1 – Introduction……1

1.1 – Thesis overview……1

1.2 - Trans-crustal, mush dominated magma plumbing systems…..……3

1.3 - Plutonic xenoliths – a tool for studying magma plumbing systems in active volcanic arcs…..……6

1.4 - The Lesser Antilles Arc……11

1.4.1 - Tectonic evolution of the Lesser Antilles arc……....11

1.4.2 - The arc crust and subducting slab……....13

1.4.3 - Along arc variations in lava geochemistry……....14

1.4.4 - Plutonic xenoliths in the LAA……...16

1.4.5 - Martinique and St Vincent……..……...18

1.5 - This study - investigation of plutonic xenoliths from Martinique and St Vincent……22

Chapter 2 – Analytical Methods…….……...25

2.1 - Procedures for determination of plagioclase Sr isotopic compositions……..26

2.1.1 - Micromilling preparation and procedure……26
2.1.2 - Strontium separation via ion chromatography procedure……..27
2.1.2.1 - Preparation of materials……..27
2.1.2.2 - Sample digestion……..28
2.1.2.3 - Strontium separation via ion chromatography……..28
2.1.3 - Determination of Sr isotopic composition……....28
2.1.3.1 - Post chromatography concentration checks via MC-ICP-MS……..28
2.1.3.2 - Thermal ionization mass spectrometry (TIMS)……30
2.1.4 - Data quality assessment……...…33
2.1.4.1 - Blank measurement……..33
2.1.4.2 - Isotope reference materials……34

2.2 - Procedures for determination of plutonic xenolith whole rock Sr-Nd-Pb isotopic compositions…….....37

2.2.1 - Sample digestion and Sr-Nd-Pb separation……..…37
2.2.2 - Measurement of Sr-Nd-Pb isotopic compositions via MC-ICP-MS……38
2.2.2.1 - Sr isotope analysis……38
2.2.2.2 - Nd isotope analysis……39
2.2.2.3 - Pb isotope analysis……40

2.3 - Age correction required for Sr isotopic data?.....42

2.3.1 - Plutonic xenoliths……42
2.3.2 - Lava…….…….....42

2.4 - Electron Microscopy…….....43

2.4.1 - Element mapping procedure……..……...44
2.4.2 - Mineral major element abundances……44
2.4.3 - Mineral phase and quantitative molar element ratio maps……...…...47

2.5 - LA-ICP-MS……48

2.5.1 - Instrument and parameters……...48
2.5.2 - Protocol for laser ablation analyses……..…....49
2.5.2.1 - Set up of analysis locations……49
2.5.2.2 - Set up of ICP-MS……49

2.5.3 - Data processing using Iolite……..51
2.5.4 - Reporting of measurement uncertainty……....53
2.5.5 - Testing effect of ablation time on measurement uncertainty……...55
2.5.6 - Details of St Vincent plutonic xenolith sample trace element analyses……....56

Chapter 3 - Plutonic xenolith petrography……...……61

3.1 - Martinique plutonic xenoliths……...61

3.1.1 - Petrographic descriptions of cumulate plutonic xenoliths……...64
3.1.2 - Petrographic descriptions of non-cumulate gabbro plutonic xenoliths…....68
3.1.3 - Petrographic description of Martinique lava……....73

3.2 - St Vincent plutonic xenoliths……....77

3.2.1 - Brief petrographic descriptions of St Vincent plutonic xenolith types……77
3.2.2 - Detailed petrographic descriptions of St Vincent plutonic xenoliths analysed in Chapter 5……....86

Chapter 4 - Isotopic compositions of plagioclase from plutonic xenoliths reveal crustal assimilation below Martinique, Lesser Antilles arc……...…….101

4.1 - Introduction……102

4.2 - Materials and Methods……106

4.2.1 - Sample Suite……...106
4.2.2 - Sampling and analytical techniques……..107
4.2.2.1 - Plutonic xenolith sample selection……..107
4.2.2.2 – Micro-milling ……108
4.2.2.3 - Chemical separation and measurement……108
4.2.2.4 - Whole rock Sr-Nd-Pb isotopes……109

4.3 - Results……..109

4.3.1 - Petrography……109
4.3.1.1 - Petrography and classification of xenoliths……109
4.3.1.2 - How representative are selected plagioclase?……110
4.3.2 - Geochemical Results……112
4.3.2.1 - Martinique cumulate plagioclase……113
4.3.2.2 - Martinique non-cumulate gabbro plagioclase……113
4.3.2.3 - Martinique andesitic lava plagioclase……114
4.3.2.4 - St Vincent cumulate plagioclase……114
4.3.2.5 - Martinique plutonic xenolith whole rock data……118

4.4 – Discussion……118

4.4.1 - Potential sediment sources……118
4.4.1.1 - Subducting slab……120
4.4.1.2 - Arc crust……121
4.4.2 - Cumulate isotopic compositions support crustal assimilation of sediments.123
4.4.3 - Inferences about assimilation from isotopic heterogeneity of shallow non-cumulate gabbros and lavas……124
4.4.4 - Quantifying the addition of sedimentary components……126
4.4.4.1 - AFC modelling end members and parameters……126
4.4.4.2 - Modelling and quantifying crustal assimilation……128
4.4.5 - Sediment addition to the mantle source?……131
4.4.6 - Wider significance……133

4.5 - Conclusions……134

Appendix 4.1 – Assimilation-Fractional Crystallization (AFC) modelling……136

A4.1 - Assimilation-Fractional crystallization (AFC) models……136

A4.2 - Quantifying crustal assimilation……137

Chapter 5 – Fractional crystallization and melt-mush reaction processes in the mushy plumbing system beneath St Vincent, Lesser Antilles arc……..……..…….....…….141

5.1 - Introduction……..142

5.2 - Analytical Methods……..……..……....145

5.2.1 - Chemical mapping of thin sections……145

5.2.2 - LA-ICP-MS analyses of clinopyroxene and amphibole……146

5.3 - Key petrographic features of plutonic xenoliths……147

5.3.1 - Sample selection……..147

5.3.2 - Key petrographic features of selected samples……....149

5.4 - Results…….……..156

5.4.1 - Mineral molar element ratios……..156

5.4.2 - Trace element chemistry of clinopyroxene and amphibole……165

5.4.2.1 - Clinopyroxene……165

5.4.2.2 - Amphibole……169

5.5 - Discussion……..……170

5.5.1 - Interpretation of plutonic xenolith textures……..170

5.5.1.1 - Olivine gabbro and Ol-CPX gabbro textures……170

5.5.1.2 - Banded Hbl-Ol gabbro textures……171

5.5.1.3 - Poikilitic Hbl-Ol gabbro textures……172

5.5.2 - Approach to modelling fractional crystallization and reactive melt flow…175

5.5.2.1 - Fractional Crystallization (FC) models……185

5.5.2.2 - Assimilation-Fractional Crystallization (AFC) models……194

5.5.2.3 - Calculation of modelled trends……197

5.5.2.4 - Limitations of modelling approach……197

5.5.3 - Interpretation of geochemical modelling and petrogenetic models……...198

5.5.3.1 - Are olivine gabbros products of polybaric fractional crystallization?.....198

5.5.3.2 - Do crystal populations in the poikilitic Hbl-Ol gabbro record both fractional crystallization and reactive melt flow?.....200

5.5.3.3 - Does the banded Hbl-Ol gabbro record reactive melt flow?.....214
5.5.3.4 - Summary……221
5.5.4 - Model for St Vincent magma plumbing system……222
5.5.5 - Limitations of using plutonic xenoliths for interpreting the scales of mush processes……224
5.5.6 - Implications for interpreting the trace element compositions of arc lavas…228

5.6 - Conclusions……..……233

Chapter 5 Appendices……..…….....…….235

Appendix 5.1 - Pressure-Temperature-melt H_2O conditions of St Vincent plutonic xenolith crystallization……235

A5.1.1 - Olivine gabbro and Ol-CPX gabbro……236
A5.1.2 - Banded Hbl-Ol gabbro……236
A5.1.3 - Poikilitic Hbl-Ol Gabbro……..237

Appendix 5.2 - Table of D Values/partition coefficients……239

Appendix 5.3 - Alternative FC models……242
A5.3.1 - Alternative "OL GABBRO POLYBARIC FC" model……242
A5.3.2 - Alternative FC model for poikilitic Hbl-Ol gabbro high Mg# CPX……242
A5.3.3 - Alternative FC model for poikilitic Hbl-Ol gabbro low Mg# CPX and amphibole……...244
A5.3.4 - "POIKILITIC GABBRO POLYBARIC FC" model for Nb……246
A5.3.5 - Single step FC models for poikilitic Hbl-Ol gabbro low Mg# CPX and amphibole using evolved initial melts……....248

Appendix 5.4 - St Vincent plutonic xenolith clinopyroxene and amphibole trace element data……249

Chapter 6 - Synthesis and Conclusions……..…….....…….265

6.1 - Plutonic xenoliths as a tool for investigating crustal magmatic processes...265

6.2 - Crustal magmatic processes in the Lesser Antilles arc……..266

6.2.1 - Crustal assimilation in the Lesser Antilles arc……267
6.2.1.1 - Crustal assimilation in the northern Lesser Antilles arc?.....267
6.2.1.2 - Crustal assimilation in the southern Lesser Antilles arc?.....268
6.2.2 - Fractional crystallization in the Lesser Antilles arc……270
6.2.3 - Melt-mush reaction in the Lesser Antilles arc……272
6.2.4 - Can trace element and isotopic variation in Lesser Antilles arc lavas be generated by crustal processes alone?.....273

6.3 - General model for southern Lesser Antilles magma plumbing systems…..274

6.4 - Wider implications for understanding subduction zone processes……..…277

6.5 - Conclusions……..279

6.5.1 - Key conclusions from Chapter 4……279
6.5.2 - Key conclusions from Chapter 5……279
6.5.3 - Key conclusions from Chapter 6……280

6.6 - Future research……280
6.6.1 - Future studies of plutonic xenoliths in the Lesser Antilles arc……281
6.6.2 - Future studies of plutonic xenoliths in other arcs……283

Appendix 1 - St Lucia and St Vincent Fieldwork, March 2019.....….287

A1.1 - Fieldwork description and rationale……287

A1.2 - Sample details……288

St Lucia……294

St Vincent……..…302

References……..…320

List of Figures

Chapter 1

1.1 - Schematic of conceptual models for magma plumbing systems……4
1.2 - Map of the active Lesser Antilles arc and subduction zone……..10
1.3 - Model for the tectonic evolution of the Lesser Antilles arc…….....12
1.4 - Plots showing radiogenic isotopic variation in Lesser Antilles arc lavas……..15
1.5 - Geological map of Martinique…….....20
1.6 - Geological map of St Vincent……..21

Chapter 2

2.1 - Flowchart outlining micro-milling procedure……..27
2.2 - Flowchart outlining Sr separation procedure.……...29
2.3 - Major element variation in clinopyroxene and amphibole from St Vincent plutonic xenoliths measured by EDS, compared with data from the literature measured by EPMA……...……...47
2.4 - Schematic of LA-ICP-MS analytical set-up.……49
2.5 - Screenshot showing the "baselines" stage of data processing in the Iolite software…….……..……...…52
2.6 - Screenshot showing the "samples" stage of data processing in the Iolite software.……...……53
2.7 - Deviation from accepted values for measurements of BHVO-2G glass standard calibrated using different NIST glass standards..…….54
2.8 - Deviation from accepted values for measurements of BHVO-2G and BCR-2G glass standards using different ablation times..……55
2.9 - Comparison of 2SD (%) values for a range of elements measured during ablation of BHVO-2G and BCR-2G using different ablation times..……..……..56
2.10 - Literature compilation of MgO vs CaO for Lesser Antilles arc plutonic xenolith clinopyroxene and amphibole……...……..58
2.11 - Plot illustrating uncertainty on measured trace element compositions due to variation in Ca wt % in clinopyroxene and amphibole …….…...59

Chapter 3

3.1 - Mineral modal abundances of Martinique plutonic xenoliths and lava investigated for plagioclase Sr isotopic compositions in Chapter 4……. ..……..62
3.2 - Sample MQ48 thin section image……65
3.3 - Images of typical plagioclase from MQ48……..……65
3.4 - Sample MQ1 thin section image……..……66
3.5 - Image of zoned plagioclase from MQ1……...……66
3.6 - Sample MQ59 thin section image……..……..67
3.7 - Sample VS36 thin section image……..68
3.8 - Sample MQ6 thin section image……..69
3.9 - Images of zoned plagioclase from MQ6……...71
3.10 - BSE image and chemical maps of zoned plagioclase from MQ6……71
3.11 - Sample MQ35 thin section image……..72
3.12 - Images of zoned plagioclase from MQ35……...……72
3.13 - BSE image and chemical maps of zoned plagioclase from MQ35……..73
3.14 - Sample M8321 thin section image……...……..74
3.15 - Images of plagioclase textures from M8321……...……76
3.16 - BSE image and chemical maps of reverse zoned plagioclase from M8321……76
3.17 - BSE image and chemical maps of normal zoned plagioclase from M8321……76
3.18 - BSE image and chemical maps of normal and reverse zoned plagioclase from M8321……..77
3.19 - Images of troctolite samples VS518, VS534 and VS548……79
3.20 - Images of troctolite samples VS553 and VS563……..……...80
3.21 - Images of olivine gabbro samples VS506, VS527 and VS532……...81
3.22 - Images of olivine gabbro samples VS552, VS564 and VS569……...82
3.23 - Images of hornblende-olivine gabbro samples VS551 and VS572. ……...83
3.24 - Image of hornblende gabbro sample VS566…...…….....….84
3.25 - Image of gabbronorite samples VS507, VS508 and VS520 …….……85
3.26 - Mineral modal abundances of St Vincent plutonic xenoliths investigated for clinopyroxene and amphibole trace element compositions in Chapter 5……. .……86
3.27 - Sample VS527/"olivine gabbro" thin section image……..88
3.28 - Sample VS527/"olivine gabbro" mineral phase map……89
3.29 - Sample VS532/"OL-CPX gabbro" thin section image..……...……..90
3.30 - Sample VS532/"OL-CPX gabbro" mineral phase map..……90
3.31 - Sample VS551/"banded Hbl-Ol gabbro" thin section image..……92

3.32 - Sample VS551/"banded Hbl-Ol gabbro" mineral phase map..……...92
3.33 - Images of amphibole overgrowing clinopyroxene rims and inclusion rich plagioclase in VS551/"banded Hbl-Ol gabbro"……...93
3.34 - Sample VS572/"poikilitic Hbl-Ol gabbro" thin section image..…….95
3.35 - Sample VS572/"poikilitic Hbl-Ol gabbro" mineral phase map..……95
3.36 - Element map of VS572/"poikilitic Hbl-Ol gabbro" highlighting apatite.……...96
3.37 - Images of plagioclase zoning patterns in VS572/"poikilitic Hbl-Ol gabbro"….97
3.38 - Images of poikilitic orthopyroxene enclosing embayed olivine in VS572/"poikilitic Hbl-Ol gabbro" ……...……98
3.39 - Images of textural relationships between poikilitic amphibole and clinopyroxene/olivine in VS572/"poikilitic Hbl-Ol gabbro"……...……...99
3.40 - Images of interstitial apatite in VS572/"poikilitic Hbl-Ol gabbro"…….....100

Chapter 4

4.1 - Map showing tectonic setting of the Lesser Antilles arc and surrounding arc systems in Central-South America……..……..…….…….....103
4.2 - $^{87}Sr/^{86}Sr$ vs $^{207}Pb/^{204}Pb$ of lavas from the Lesser Antilles arc, compared to nearby arcs from Central-South America…….…….…….....104
4.3 - Along arc variation in $^{87}Sr/^{86}Sr$ of Lesser Antilles arc lavas……....105
4.4 - Images of zoned and unzoned plagioclase in Martinique plutonic xenoliths....111
4.5 - $^{87}Sr/^{86}Sr$ of individual plagioclase in cumulates, and core and rim zones of plagioclase in non-cumulate gabbros, compared with the whole rock $^{87}Sr/^{86}Sr$ range of Martinique lavas……114
4.6 - Details of $^{87}Sr/^{86}Sr$ variation in cumulate and non-cumulate gabbro plagioclase…....…….115
4.7 - Details of $^{87}Sr/^{86}Sr$ variation in lava sample M8321…….116
4.8 - Sr-Nd-Pb isotopic compositions of Martinique lavas, plutonic xenoliths, potential equivalents to subducted sediments (Site 543, Site 144, Barbados) and sediments from the Orinoco and Amazon rivers…….…….119
4.9 - Radiogenic isotopic compositions of DSDP Site 543 and DSDP Site 144 sediments, compared with isotopic compositions of Martinique lavas……120
4.10 - Sr-Nd-Pb isotopic compositions of Martinique lavas, plutonic xenoliths and end members used in AFC modelling …….…….129

4.11 - Sr-Nd-Pb isotopic compositions of Martinique lavas and plutonic xenoliths compared with AFC models …….…….130
4.12 - $^{87}Sr/^{86}Sr$ of cumulate plagioclase compared with single component mixing lines between depleted mantle and potential subducted sediment end members. …….132

A4.1 - Calculated curves of ρ vs r for $^{87}Sr/^{86}Sr$, $^{143}Nd/^{144}Nd$, $^{206}Pb/^{204}Pb$, $^{207}Pb/^{204}Pb$, and $^{208}Pb/^{204}Pb$, for an AFC process involving the "Hypothetical crust" end member……..139
A4.2 - Calculated curves of ρ vs r for $^{87}Sr/^{86}Sr$, $^{143}Nd/^{144}Nd$, $^{206}Pb/^{204}Pb$, $^{207}Pb/^{204}Pb$, and $^{208}Pb/^{204}Pb$, for an AFC process involving the "Hypothetical crust 2" end member……..139

Chapter 5

5.1 - Sampling locations of plutonic xenoliths superimposed on the geological map of St Vincent……..148
5.2 - Olivine gabbro and Ol-CPX gabbro thin section images……..150
5.3 - Banded Hbl-Ol gabbro and poikilitic Hbl-Ol gabbro thin section images…..151
5.4 - Examples of well equilibrated crystal boundaries in the Ol-CPX gabbro and possible infiltration of host lava at the margins of the olivine gabbro.....……..…..152
5.5 - Thin section images showing textural features of the olivine absent band in the banded Hbl-Ol gabbro……..…..153
5.6 - Thin section images showing amphibole-clinopyroxene textural relationships in the banded Hbl-Ol gabbro matrix…….…..154
5.7 - Thin section images showing textural features of the poikilitic Hbl-Ol gabbro.....…….……..…..155
5.8 - Histograms showing the range of olivine Fo contents in St Vincent plutonic xenoliths……..…….……..…..157
5.9 - Histograms showing the range of clinopyroxene Mg# contents in St Vincent plutonic xenoliths……...…….……..…..158
5.10 - Histograms showing the range of plagioclase An contents in St Vincent plutonic xenoliths……...……..…….……...160
5.11 - Histograms showing the range of Mg# in St Vincent plutonic xenolith amphibole

and orthopyroxene……...…….…….……...161
5.12 - Quantitative Mg# in clinopyroxene thin section maps for olivine gabbro and Ol-CPX gabbro……..……...…….…….……...162
5.13 - Quantitative Mg# in clinopyroxene and An in plagioclase thin section maps for banded Hbl-Ol gabbro …...…….…….…….……...163
5.14 - Quantitative Mg# in clinopyroxene thin section map for poikilitic Hbl-Ol gabbro……....163
5.15 - Quantitative An in plagioclase thin section map for poikilitic Hbl-Ol gabbro……....164
5.16 - Trace element variation in St Vincent plutonic xenolith clinopyroxene……..……....166
5.17 - Primitive mantle normalized rare earth element patterns for St Vincent plutonic xenolith clinopyroxene……..……....168
5.18 - Trace element variation in St Vincent plutonic xenolith amphibole…….…….....168
5.19 - Primitive mantle normalized rare earth element patterns for St Vincent plutonic xenolith amphibole……..……..……....169
5.20 - Thin section images showing examples of ragged, irregular clinopyroxene-amphibole contacts from the poikilitic Hbl-Ol gabbro……..173
5.21 - Schematics illustrating the concepts of zone refining and Assimilation-Fractional Crystallization, used to model the process of reactive melt flow in previous literature……...……..177
5.22 - Schematic illustrating the FC and AFC models applied to the crystal populations in each St Vincent plutonic xenolith sample……..……..182
5.23 - Schematic illustrating the “OL GABBRO POLYBARIC FC” model……..187
5.24 - Schematic illustrating the first step only of the “OL GABBRO POLYBARIC FC” model……..189
5.25 - Schematic illustrating the “POIKILITIC GABBRO POLYBARIC FC” model……..….191
5.26 - Schematic illustrating the “OL GABBRO POLYBARIC FC” model with additional “BANDED GABBRO” step…….……193
5.27 - Schematic illustrating the “BASALTIC ANDESITE AFC, ANDESITE AFC” and “ANDESITE AFC 2” models……..196
5.28 - Primitive mantle normalized rare earth element patterns of clinopyroxene from

the banded Hbl-Ol gabbro matrix, olivine gabbro and Ol-CPX gabbro compared with the results of the “OL GABBRO POLYBARIC FC” model……..200
5.29 - Primitive mantle normalized rare earth element patterns of poikilitic Hbl-Ol gabbro high Mg# CPX compared with the results of the first step of the “OL GABBRO POLYBARIC FC” model……..201
5.30 - Primitive mantle normalized rare earth element patterns of poikilitic Hbl-Ol gabbro low Mg# CPX and amphibole compared with the results of the “POIKILITIC GABBRO POLYBARIC FC” model……..203
5.31 - Primitive mantle normalized rare earth element patterns of poikilitic Hbl-Ol gabbro low Mg# CPX and amphibole compared with the results of the “BASALTIC ANDESITE AFC” and “ANDESITE AFC” models……..207
5.32 - Primitive mantle normalized rare earth element patterns of poikilitic Hbl-Ol gabbro low Mg# CPX and amphibole compared with the results of the “ANDESITE AFC 2” model……....207
5.33 - Schematic illustrating the sequence of processes involved in the petrogenesis of the poikilitic Hbl-Ol gabbro……..……....212
5.34 - Primitive mantle normalized rare earth element patterns of amphibole and clinopyroxene from the olivine absent band in the banded Hbl-Ol gabbro, compared with the results of the “BANDED GABBRO” FC and AFC models……..……..……....216
5.35 - Primitive mantle normalized rare earth element compositions of melts in equilibrium with clinopyroxene and amphibole from the banded Hbl-Ol gabbro matrix…….218
5.36 - Schematics illustrating possible scenarios for formation of the olivine absent band in the banded Hbl-Ol gabbro.…….220
5.37 - Schematic of the envisaged magma plumbing system beneath St Vincent.….223
5.38 - Schematic illustrating how the typically small size of plutonic xenoliths affects the likelihood of these samples preserving melt-mush reaction textures.….227
5.39 - Primitive mantle normalized rare earth element compositions of melts in equilibrium with St Vincent plutonic xenolith clinopyroxene and amphibole, compared with rare earth element compositions of St Vincent lavas (whole-rock) and melt inclusions……...231

A5.1 - Variation in partition coefficients from different source publications for

clinopyroxene and amphibole at a melt SiO_2 content of 59 wt %.……...241
A5.2 - Primitive mantle normalized REE patterns of clinopyroxene from the Ol-CPX gabbro and banded Hbl-Ol gabbro matrix compared with the results of the "alternative OL GABBRO POLYBARIC FC" model……...……...243
A5.3 - Primitive mantle normalized REE patterns of the high Mg# CPX population from the poikilitic Hbl-Ol gabbro compared with the results of the first step of the "OL GABBRO POLYBARIC FC" model using an alternative initial melt composition…….……...……...244
A5.4 - Primitive mantle normalized REE patterns of poikilitic Hbl-Ol gabbro low Mg# CPX and amphibole compared with the results of the "POIKILTIC GABBRO POLYBARIC FC" model using an alternative initial melt composition……...…….…...245
A5.5 - Nb concentrations in amphibole at each step of the "POIKILITIC GABBRO POLYBARIC FC" model, compared with the Nb compositional range of poikilitic Hbl-Ol gabbro amphibole.…….246
A5.6 - Ce, Nd and Dy contents of poikilitic Hbl-Ol gabbro low Mg# CPX and amphibole compared with the results of the "BASALTIC ANDESITE FC" and "ANDESITE FC" models.…….247

Chapter 6

6.1 - Radiogenic isotopic compositions of southern Lesser Antilles arc lavas compared with Assimilation-Fractional Crystallization models using different sediment end members.…….……..…….269
6.2 - Schematic illustrating the processes by which the chemical compositions of magmas may be modified during ascent through mushy magma plumbing systems in the southern LAA. ……..…….276

Appendix 1 – Fieldwork

Photo L1.1 - Outcrop below Fort Rodney……..……..294
Photo L1.2 - Enclave in Pre-SVC 1 basalt……..……295
Photo L3.1 - Fallen block of conglomerate from Smugglers Cove…….296
Photo L3.2 - Dyke cutting the conglomerates from Smugglers Cove……296
Photo L3.3 - Cumulates in the volcaniclastic deposits from Smugglers Cove……297

Photo L4.1 - Cumulate in Pre-SVC1 lava flow……...298
Photo L5.1 - Representative section of SVC PDC deposit…….....299
Photo L6.1 - Rock piles on the quarry site from which samples were sourced……....300
Photo L7.1 - Coastal exposure at Black Point…….302
Photo L7.2 - Lower PDC deposit. …….…….303
Photo L7.3 - Yellow-orange tuff……...…….303
Photo L7.4 - High Mg basalt….. ……...…….304
Photo L10.1 - 1902 PDC deposit exposure in Dry Rabacca valley.……....306
Photo L10.2 - Exposure at locality 10……...…….306
Photo L10.3 - Schematic log through exposed 1902 section…..……...…….306
Photo L11.1 - Exposure at Locality 11……..…….……...…….307
Photo L12.1 - Typical exposure at Owia salt pond. ……...…...…….311
Photo L12.2 - In situ cumulate at Owia salt pond ……...…...…….…….312
Photo L13.1 - The basalt cliffs at Big Sand Bay..…...……...…...…….…….313
Photo L16.1 - Exposure of the 1580 deposits on the Windward trail. ..…….…….316
Photo L17.1 - Exposure in the ravine beside the Windward trail……..…….…….317
Photo L18.1 - Large fresh lava bomb found on trail……...……..…….…….318

List of Tables

Chapter 2

2.1 - Cup configuration for cumulate plagioclase Sr isotopic analyses…….32
2.2 - Cup configuration for non-cumulate gabbro and lava plagioclase Sr isotopic analyses…….....32
2.3 - Measured total procedural blanks and column blanks throughout the period of study…….....34
2.4 - Load size, $^{87}Sr/^{86}Sr$ and 2 SE (standard error) for all NBS 987 standards run throughout the period of analyses.……...….36
2.5 - $^{87}Sr/^{86}Sr$ and 2 SE (standard error) for all BCR-2 standards run throughout the period of analyses.……...….37
2.6 - Cup configuration for whole rock Sr isotope analysis on Neptune MC-ICP-MS..…….……..…...39
2.7 - Cup configuration for whole rock Nd isotope analysis on Neptune MC-ICP-MS..…….……..…...40
2.8 - Cup configuration for whole rock Pb isotope analysis on Neptune MC-ICP-MS..…….……..…...41
2.9 - Results of calculations used to determine whether age correction is required for the plutonic xenolith and lava Sr isotopic data.……..……..43
2.10 - List of parameters that are required to be set on the laser ablation system and ICP-MS prior to carrying out analyses……...……..…...50
2.11 - Calculated 2SD % uncertainty for all elements measured during laser ablation analyses of plutonic xenolith samples.……...……..…...60

Chapter 3

3.1 - Summary of petrographic characteristics of Martinique plutonic xenoliths ……63
3.2 - Summary of petrographic characteristics of St Vincent plutonic xenoliths. ……87

Chapter 4

4.1 - $^{87}Sr/^{86}Sr$ of individual plagioclase in cumulates, and core and rim zones of plagioclase in non-cumulate gabbros and lava……...113
4.2 - Whole rock $^{87}Sr/^{86}Sr$, $^{143}Nd/^{144}Nd$, $^{206}Pb/^{204}Pb$, $^{207}Pb/^{204}Pb$, and $^{208}Pb/^{204}Pb$ of cumulates and non-cumulate gabbros…….……...117

4.3 - Sr-Nd-Pb isotopic compositions and concentrations of end members used in AFC modelling. ……..……..……...127

A4.1 - Mineral-melt partition coefficients, and calculated bulk partition coefficients (D), for Sr, Nd and Pb based on the mineral assemblage of NCG sample MQ6……137
A4.2 - Calculated isotopic ratios for the AFC model involving the "Bulk Site 543" sediment end member…….……137

Chapter 5

5.1 - Geochemical models (FC and AFC) applied to each crystal population in the St Vincent plutonic xenolith samples……..……...179
5.2 - Summary of experiments that provide the best match to each St Vincent plutonic xenolith sample mineral assemblage and compositions. ……...180
5.3 - Initial melt compositions (in µg/g) used in geochemical modelling ……..…...184
5.4 - Parameters used at each fractional crystallization step of the "OL GABBRO POLYBARIC FC" model…….....186
5.5 - Parameters used at each fractional crystallization step of the "POIKILITIC GABBRO POLYBARIC FC" model……...…….....191
5.6 - Parameters used for the "BASALTIC ANDESITE AFC, ANDESITE AFC and ANDESITE AFC 2" models…….……...…….....195

A5.1 - Partition coefficients used in the geochemical models outlined in section 5.5.2 of the main text……..……..……...241
A5.2 - Initial melt compositions used in alternative FC models……...242
A5.3 - Ol-CPX gabbro clinopyroxene trace element compositions, in µg/g ……...251
A5.4 - Poikilitic Hbl-Ol gabbro high Mg# CPX clinopyroxene trace element compositions, in µg/g …….……...253
A5.5 - Poikilitic Hbl-Ol gabbro low Mg# CPX clinopyroxene trace element compositions, in µg/g …….……...254
A5.6 - Banded Hbl-Ol gabbro olivine absent band clinopyroxene trace element compositions, in µg/g …….……...256
A5.7 - Banded Hbl-Ol gabbro matrix clinopyroxene trace element compositions, in µg/g …….……...258
A5.8 - Olivine gabbro clinopyroxene trace element compositions, in µg/g ……...260
A5.9 - Poikilitic Hbl-Ol gabbro amphibole trace element compositions, in µg/g. ..261

A5.10 - Banded Hbl-Ol gabbro amphibole trace element compositions, in µg/g. ..263

Appendix 1

A.1 - Sample codes, relative ages, sampling location co-ordinates and rock types for St Lucia plutonic xenolith sample set…….290
A.2 - Sample codes, relative ages, sampling location co-ordinates and rock types for St Vincent plutonic xenolith sample set…….294

Acknowledgements

I'd like to start by thanking my whole supervisory team for their support throughout this project, particularly during the challenging times of the pandemic, and for such detailed feedback on my writing which greatly improved my work. Special thanks go to Julie Prytulak for always supporting me with implementing my scientific ideas in this project, keeping me on track when I went off on tangents and for signing off so many travel requests! I'd like to thank George Cooper for being a great field assistant and driving me around the Caribbean, providing access to the Cardiff SEM to get data during lockdown, and for organizing a fantastic workshop in Trinidad to mark the end of the VoiLA project. I am grateful to Madeleine Humphreys for setting up my access to the laser, training me on the instrument during lockdowns and for sharing your expertise in petrography. Thanks also to Geoff Nowell for your patience when training me in the lab, always being on hand to solve any clean lab issues and keeping the Triton running smoothly. I would also like to acknowledge the support of Iain Neill and Colin Macpherson with manuscript writing and Chris Ottley and Alex Iveson for support with laser work.

I am very grateful to the NERC IAPETUS DTP for funding this research and granting an additional 3 month extension to offset some of the impacts of the pandemic. I would also like to thank the IAPETUS DTP for funding my memorable placement at Etna Volcano Observatory, during which I learnt a huge amount about volcano monitoring. Special thanks go to Rosanna Corsaro, Salvo Giammanco and Salvo Consoli for hosting my placement, taking me on many exciting field excursions on Etna to see lava flows and feeding me endless granita.

I am also grateful for the opportunity to have been involved in several interesting workshops discussing Caribbean volcanism with all the members of the VoiLA project. Additionally, I'd like to thank Richie Robertson and Kemron Alexander from UWI Seismic and NEMO for their assistance and advice with fieldwork in the Caribbean.

Thanks also to the members of the Durham Volcanology Group, Durham Isotope Group and my departmental colleagues for interesting weekly meetings, fun socials, quiz nights and away weekends over the last few years. I'd also like to mention my many bandmates in "The Observatories" who I've had the best time gigging with during my time in Durham. Thanks to all my musical friends in Southampton for

regular meet-ups over the last few years and especially Ben, Georgi and Bill for that amazing holiday to Iceland. Special thanks to my best mate Josh for regularly visiting me in Durham, joining me for gigs and trips abroad and for our many Skype calls spent reviewing beers during the lockdowns.

Finally, I'd like to thank my amazing family, for always supporting me with achieving my goals and for providing fun quiz and game nights and an outdoor office when I moved back home for a few months during the first lockdown.

Chapter 1 – Introduction

1.1 – Thesis overview

At volcanic arcs, formed above subduction zones, the chemical compositions of primary magmas reflect contributions from the mantle wedge and fluids and/or melts derived from oceanic crust and sediments on the subducting slab (e.g. Kelemen et al., 2003 and references therein). Primary arc magma chemical compositions may then be modified as they traverse the overriding plate prior to eruption as arc lavas, via processes including (but not limited to) fractional crystallization, assimilation of country rock lithologies, and mixing (e.g. Hildreth and Moorbath, 1988, Davidson et al., 2005, Turner and Langmuir 2015, 2022).

The chemical compositions of arc lavas are often used to study and interpret the recycling of sediments, chemical elements and volatiles at subduction zones and the chemical heterogeneity of Earth's mantle (e.g. Plank and Langmuir, 1993, Turner and Hawkesworth, 1997, Turner et al., 1999, Patino et al., 2000, Straub and Layne, 2003, Plank, 2005, Nebel et al., 2011, Bebout et al., 2014 and references therein). A key assumption for such studies is that arc lavas reflect the chemical characteristics of their mantle source regions, without significant chemical modification within the crust *en route* to the surface. Hence, it is vital to constrain the influence of crustal level processes on arc magma chemical compositions to robustly interpret the chemical consequences of broad scale subduction zone processes.

Arc magmas traverse the overriding plate via trans-crustal magma plumbing systems, which are generally accepted to be composed predominantly of crystal mushes, where low volumes of melt are distributed within larger volumes of crystals (e.g., Cashman et al., 2017, Edmonds et al., 2019, Sparks et al., 2019). Arc lavas extracted from magma plumbing systems often carry fragments of underlying crystal mushes to the surface - these mush fragments are commonly known as "plutonic xenoliths". These samples represent a direct record of crustal processes that may influence arc magma chemical compositions during passage through and storage within mush-dominated magma plumbing systems.

Plutonic xenoliths are abundant in the active intra-oceanic Lesser Antilles arc (e.g. Arculus and Wills, 1980, Melekhova et al., 2019). Lesser Antilles arc lavas also display extremely wide ranges in chemical and isotopic compositions (e.g. Davidson, 1986, Davidson et al, 1987, MacDonald et al., 2000, Bezard et al., 2014). Hence, the Lesser Antilles arc represents an ideal setting to explore the influence of crustal processes on arc lava chemical variation using plutonic xenoliths.

The overall aim of this thesis is to investigate whether the majority of the trace element and isotopic variation in Lesser Antilles arc lavas can be produced by processes within mush-dominated magma plumbing systems in the arc crust. The thesis focusses on three crustal processes by which the chemical compositions of arc magmas may be modified:

(1) Assimilation of sedimentary rocks in the arc crust (crustal assimilation) into which the magma plumbing system is emplaced.

(2) Fractional crystallization.

(3) Reactive melt flow/melt-mush reaction, which describes interactions between migrating melts and crystal mushes in magma plumbing systems.

To investigate these processes, a field campaign to the Lesser Antilles was undertaken in 2019 where an extensive suite of plutonic xenoliths was collected. Using these new samples and previously collected material, petrographic observations are combined with chemical and isotopic measurements on mineral phases to study crustal processes. The findings have broad implications for the interpretation of arc lava chemical compositions and the use of arc lavas to study subduction zone recycling and mantle heterogeneity.

The following **sections (1.2 – 1.4**) outline the concepts of trans-crustal, mush dominated magma plumbing systems and introduce the Lesser Antilles arc geological setting. **Section 1.5** provides details of the specific aims and content of the thesis chapters.

1.2 - Trans-crustal, mush dominated magma plumbing systems

For many years, understanding of volcanic processes and igneous rocks has been based on the concept of the magma chamber (**Figure 1.1, a**). In this scenario, magmas cool and crystallize in large, predominantly molten "chambers" within the crust, which can be replenished by new mantle derived melts and tapped to feed eruptions (e.g. O'Hara 1980, Blake, 1981, O'Neill and Jenner, 2012, Bohrson et al., 2014, Sparks et al., 2019). Assimilation of the wall rocks can occur at the margins of the chamber and magmas and crystals of different compositions may mix (e.g. DePaolo, 1981, Sparks et al., 1984, 2019, Turner and Campbell 1986, Bohrson et al., 2014).

More recently, it has been proposed that high melt fraction "magma chambers" or melt-rich regions beneath volcanoes may only exist for short periods on geological timescales (e.g. Paulatto et al., 2012, Sparks et al., 2019, Lucci et al., 2020). Such proposals are based on the general lack of geophysical evidence for melt rich regions beneath most active volcanic systems (e.g. Lees, 2007, Magee et al., 2018, Paulatto et al., 2022), combined with observations that crystals in lavas are often entrained in their host melts as shortly as centuries to decades before eruptions (e.g. Druitt et al., 2012, Shamloo and Till, 2019).

In contrast, a wide array of recently acquired evidence, including field evidence from exposed roots of volcanic systems, geophysical surveys of volcanic regions and petrological studies of volcanic and plutonic rocks, has led to general acceptance of an alternative model, the "trans-crustal magmatic plumbing system" (**Figure 1.1, b**). In this scenario, magmas are stored and differentiate throughout the depth of the crust, prior to extraction from the plumbing system and eruption as lavas (e.g. Cashman et al., 2017, Sparks and Cashman, 2017, Edmonds et al., 2019, Sparks et al., 2019, 2022). In contrast to magma chambers, trans-crustal plumbing systems are predominantly made up of "crystal mush", defined by Sparks et al., (2019) as "melt (and fluids) distributed in a crystalline framework".

Thermobarometry calculations based on the chemical compositions of mineral phases (for example, clinopyroxene, amphibole and plagioclase) in lavas provide evidence for the trans-crustal nature of magma plumbing systems. Crystals erupted from the same volcano or in individual eruptions typically show a wide range of crystallization pressures, extending from the upper crust to at least the mid-crust (~ 15 km depth, e.g.

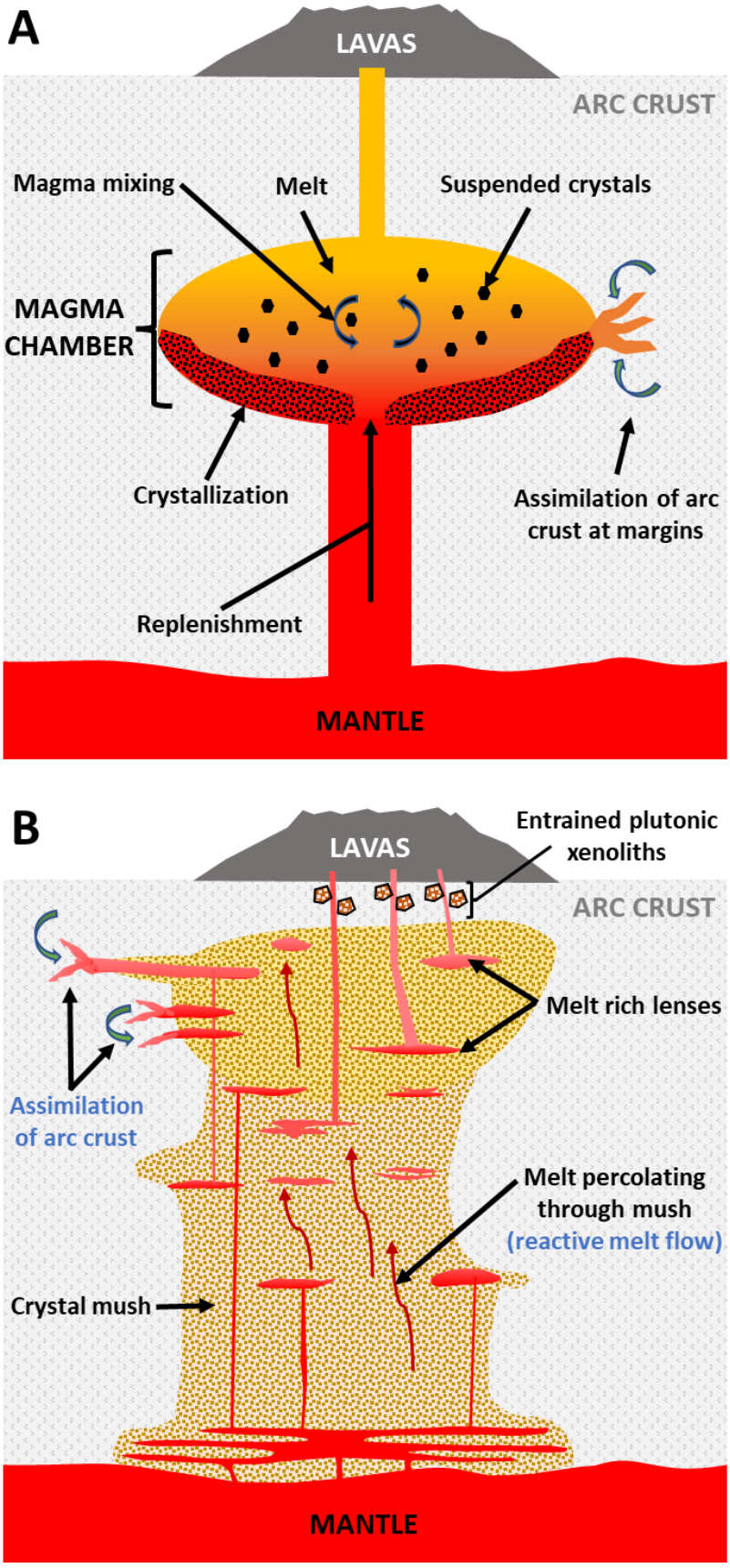

Figure 1.1: Schematic showing conceptual models for the magma plumbing systems feeding volcanoes.

A) melt dominated magma chamber. **B)** – trans-crustal, mush dominated magma plumbing system. The processes of "assimilation of arc crust" and "reactive melt flow", investigated in detail in this study, are highlighted.

Cooper and Wilson, 2014) and often to the lower crust/Moho (Edmonds et al., 2019 and references therein, Lucci et al., 2020, Giordano and Caricchi, 2022). In addition, zones within crystals may record crystallization under different pressure-temperature conditions at distinct levels of magma plumbing systems (e.g. Cashman and Blundy, 2013, Giacomoni et al., 2016).

Support from geophysical studies for mush-dominated magma plumbing systems centres around the lack of evidence for significant volumes of melt (as would be expected for a "magma chamber") in the crust beneath volcanic regions (Lees, 2007, Paulatto et al., 2010, 2022). Seismic and magnetotelluric surveys have revealed the presence of magma bodies extending throughout the crust beneath volcanic centres, with typical estimated melt fractions of ≤ 10 % (e.g. Hill et al., 2009, Huang et al., 2015, Laumonier et al., 2017, Delph et al., 2017, Magee et al., 2018) interpreted to be regions of crystal mush.

Petrological evidence for mush-dominated plumbing systems includes chemical compositions of zoned crystals in lavas that indicate crystal storage in low temperature, high crystallinity environments (crystal mushes) for long periods (thousands of years) prior to eruption (e.g. Cooper and Kent, 2014, Rubin et al., 2017). Many lavas contain significant proportions of crystals in chemical disequilibrium with their host melts (antecrysts), which are often interpreted to represent remnants of remobilized crystal mushes (e.g. Dungan and Davidson, 2004, Bachmann and Bergantz, 2006, Stamper et al., 2014, Forni et al., 2016, Humphreys et al., 2019a, Shane et al., 2019). In some cases, such crystals can be readily identified by comparison with mineral phase textures and compositions in crystal clots or plutonic xenoliths (interpreted as larger fragments of erupted mush) from the same lava/volcanic centre (e.g. Amma-Miyasaka and Nakagawa, 2002, Dungan and Davidson, 2004, Stamper et al., 2014).

An inevitable consequence of mush-dominated magma plumbing systems is that melts will interact with pre-existing crystal mushes as they traverse the arc crust. In mush-dominated systems, melt transport can occur via "porous flow" between the crystals in mushes (e.g. Solano et al., 2014, Jackson et al., 2018, Lissenberg et al., 2019), though other transport mechanisms including (but not limited to) dyking and focused

channelized flow can also operate (e.g. Lissenberg et al., 2019, Sparks et al., 2019 and references therein). Chemical disequilibrium between migrating melts and mush crystals leads to reactions, a process often referred to as "reactive melt flow" or more generally "melt-mush reaction" (e.g. Lissenberg and MacLeod, 2016, Jackson et al., 2018, Lissenberg et al., 2019), discussed in **section 1.3**.

Another consequence of mush-dominated magma plumbing systems is the idea that melt-rich bodies of eruptible magma are formed via segregation of melts from mushes (e.g. Bachmann and Bergantz, 2004, Cashman et al., 2017, Sparks et al., 2019, 2022), which can be accompanied by the entrainment of mush crystals (antecrysts). Such melt-rich, eruptible magma bodies may represent accumulations of melts and entrained crystals from different parts of mushy plumbing systems (e.g. Cashman and Edmonds, 2019, Wilson et al., 2021, Sparks et al., 2022). Hence, the chemical compositions of erupted lavas may reflect contributions from multiple melts and crystals which were formed or modified by different processes in distinct regions of mush.

1.3 - Plutonic xenoliths – a tool for studying magma plumbing systems in active volcanic arcs

In active arc settings such as the Lesser Antilles arc, the underlying mushy magma plumbing systems cannot be accessed and sampled *in situ*. Therefore, it is challenging to directly study chemical processes occurring within the arc crust. However, the erupted deposits in arcs often carry coarsely crystalline igneous rocks, variously termed "plutonic xenoliths, cumulates, nodules, intrusives", to the surface. For the remainder of this work, such samples will be referred to as **plutonic xenoliths.** These samples, typically 5-30 centimetres (but sometimes larger) in size, are interpreted to represent entrained fragments of crystal mushes (e.g. Cooper et al., 2016, 2019, Cashman et al., 2017, Melekhova et al., 2017, 2019, Holness et al., 2019, Gleeson et al., 2020) that form the dominant component of trans-crustal magma plumbing systems.

The chemical compositions of mineral phases in plutonic xenoliths are a function of pressure, temperature and the compositions of the melts from which they crystallized and hence record the chemical evolution of magmas within mushes in the crust. Plutonic xenoliths are often derived from a range of depths within magma plumbing systems, determined by thermobarometry calculations and/or comparison to products

of crystallization experiments conducted at different pressures (e.g. Chadwick et al., 2013, Barker et al., 2015, Price et al., 2016, Ziberna et al., 2017, Klaver et al., 2017, Melekhova et al., 2019). Therefore, plutonic xenoliths can record magmatic processes at different crustal levels.

Thus, plutonic xenoliths represent a valuable tool for assessing the impact of crustal processes on the chemical compositions of arc lavas extracted from mushy plumbing systems.

In this study, plutonic xenoliths are used to investigate three crustal processes.

(1) - Sediment Assimilation

As magmas are emplaced into arc crust, they can assimilate crustal lithologies, including sediments. Many arc lavas have isotopic compositions distinct from the mantle and MORB, forming arrays suggestive of mixing with sedimentary materials (e.g. Taylor, 1980, Davidson et al, 2005). However, isotopic signatures indicative of a sedimentary component in arc lavas, in isolation, do not constrain where the sediments were incorporated between mantle source and the surface (e.g. Davidson et al., 2005). Hence, there is considerable debate as to whether the sediment component in arc lavas is derived from addition of subducted sediments to the mantle source (e.g. White and Patchett, 1984, Chauvel et al., 2009, Labanieh et al., 2010, Nebel et al., 2011) or incorporated via assimilation of sediments within the upper plate crust (e.g. Hildreth and Moorbath, 1988, Gasparon and Varne, 1998, Price et al., 2005, Bezard et al., 2015b). Distinguishing between these possibilities is particularly challenging when subducting and upper plate crustal sediments have similar chemical and isotopic compositions (e.g. Vroon et al., 1993, Macpherson et al., 1998) or when the isotopic composition of the upper plate crust is poorly known (for example, in the Lesser Antilles arc, Davidson and Harmon, 1989, Smith et al., 1996 and the Vanuatu arc, Buys et al., 2014). This issue has been the subject of a long-standing debate in the Lesser Antilles arc, discussed in **section 1.4.3**.

Plutonic xenoliths from different crustal levels provide a potential means of tracking the location of sediment addition to arc magmas. For example, if isotopic compositions of plutonic xenoliths from upper crustal levels show a greater sediment influence than plutonic xenoliths from lower crustal levels, it could be inferred that magmas were contaminated by sediment assimilation within the crust. In **Chapter 4** of this thesis,

isotopic compositions of single plagioclase crystals and crystal zones within plutonic xenoliths from different crustal levels are used to determine whether isotopic variation and "crustal" isotopic signatures in lavas from the Lesser Antilles arc island of Martinique are inherited from crustal sediment assimilation or subducted sediment addition to the mantle source.

(2) - Fractional Crystallization

The chemical evolution of magmas by fractional crystallization in crustal reservoirs has long been considered an important mechanism for producing chemical variation in arc lavas (e.g. Woodhead, 1988, Heath et al., 1998, Brophy, 2008, Barker et al., 2013, Lee and Bachmann, 2014, Nandedkar et al., 2014). The hydrous nature of arc magmas influences the sequence of mineral phases that crystallize upon cooling (e.g. Gaetani et al., 1993, Grove et al., 2012). For example, experimental studies and natural rocks show that the early stages of arc magma differentiation are controlled predominantly by olivine + clinopyroxene (± spinel) crystallization (e.g. Gaetani et al., 1993, Nandedkar et al., 2014, Marxer et al., 2021), since high H_2O contents delay plagioclase crystallization to lower temperatures (e.g. Gaetani et al., 1993, Pichavant and MacDonald, 2007, Nandedkar et al., 2014). Overlap between natural arc magma/lava compositions and chemical compositions of melts formed during experiments simulating crystallization at variable pressures (e.g. Melekhova et al., 2015, Marxer et al., 2021), support the idea that fractional crystallization can operate over several stages at different pressures/crustal levels (polybaric fractional crystallization). The wide range of crystallization pressures recorded by crystals in arc lavas (e.g Lucci et al., 2020, Giordano and Caricchi, 2022) provides further evidence for polybaric fractional crystallization in arc magma plumbing systems.

Plutonic xenoliths from volcanic arcs, including many from the Lesser Antilles, often contain high An (> 80) plagioclase associated with low Fo (<80) olivine (e.g. Arculus and Wills, 1980, Beard, 1986, Tollan et al., 2012, Cooper et al., 2016, Klaver et al., 2017, Melekhova et al., 2015, 2017). These plutonic xenoliths, often determined to have crystallized at mid-upper crustal levels, are generally interpreted to record lower pressure crystallization of H_2O rich basalts which were formed by a prior, high-pressure stage of olivine and clinopyroxene crystallization (Tollan et al., 2012, Melekhova et al., 2015, Cooper et al., 2016). Olivine and clinopyroxene dominated

plutonic xenoliths interpreted to have formed during the high-pressure stage are also occasionally erupted (e.g. Stamper et al., 2014, Klaver et al., 2017). Many arc lavas display chemical signatures indicative of amphibole fractionation, such as decreasing Dy/Yb with increasing SiO_2, despite the rarity of amphibole as a phenocryst phase (e.g. Davidson et al., 2007a, Brophy, 2008, Smith, 2014). Arc plutonic xenoliths commonly contain amphibole (e.g. Smith, 2014, Cooper et al., 2016, Klaver et al., 2017, Yanagida et al., 2018, Melekhova et al., 2019), hence plutonic xenoliths can record evidence for otherwise "cryptic" fractionating assemblages that contribute to the chemical compositions of arc lavas.

In **Chapter 5**, textural observations and mineral chemistry of newly acquired plutonic xenoliths from the Lesser Antilles arc island of St Vincent are used to investigate fractional crystallization processes in a mushy arc magma plumbing system. Specifically, the effects of fractional crystallization on mineral and melt trace element compositions in the mush beneath St Vincent and the impact of this process on erupted lava trace element compositions are investigated. Plutonic xenolith mineral assemblages are compared with experimental products to determine crystallization pressures and assess evidence for polybaric fractional crystallization.

(3) - "Reactive Melt Flow"

"Reactive melt flow" or "melt-mush reactions" describe the process whereby chemical disequilibrium between migrating melts and crystal mushes with which they interact leads to reactions, which typically involve the dissolution of pre-existing mush phases and precipitation of new phases (e.g. Lissenberg and MacLeod, 2016, Hu et al., 2022). These reactions can modify the crystal textures and mineral assemblages of mushes, as well as the chemical compositions of mush crystals and migrating melts (e.g. Lissenberg and MacLeod, 2016, Jackson et al., 2018). Recent numerical modelling simulations have suggested that reactive melt flow represents the dominant mechanism controlling magma chemical evolution in mush-dominated plumbing systems (Solano et al., 2014, Jackson et al., 2018).

Reactive melt flow is commonly identified in plutonic rocks from mid-ocean ridges (equivalent to mushy plumbing systems) and arc plutonic xenoliths via textural features, such as embayed crystal boundaries indicative of dissolution (e.g. Lissenberg and MacLeod, 2016, Boulanger et al., 2021) and replacement of clinopyroxene rims

by amphibole (e.g. Smith, 2014, Cooper et al., 2016). The crystals/crystal zones formed/precipitated during reactive melt flow/melt-mush reaction processes can also show distinctive chemical characteristics, such as higher LREE/HREE ratios than would be produced by fractional crystallization (e.g. Lissenberg and MacLeod, 2016, SanFillipo et al., 2020, Boulanger et al., 2021). Since these textural and chemical indicators of reactive melt flow are preserved within the mushes modified by reactions, study of plutonic xenoliths (which directly sample crystal mushes) is essential for identifying this process in the magma plumbing systems of active arcs.

In **Chapter 5**, textural observations and trace element compositions of clinopyroxene and amphibole in newly acquired plutonic xenoliths from the Lesser Antilles arc island of St Vincent are used to investigate reactive melt flow in a mushy arc magma plumbing system. The study focuses on the impact of reactive melt flow on mineral and melt trace element compositions in the mush beneath St Vincent and the influence of this process on St Vincent lava trace element compositions.

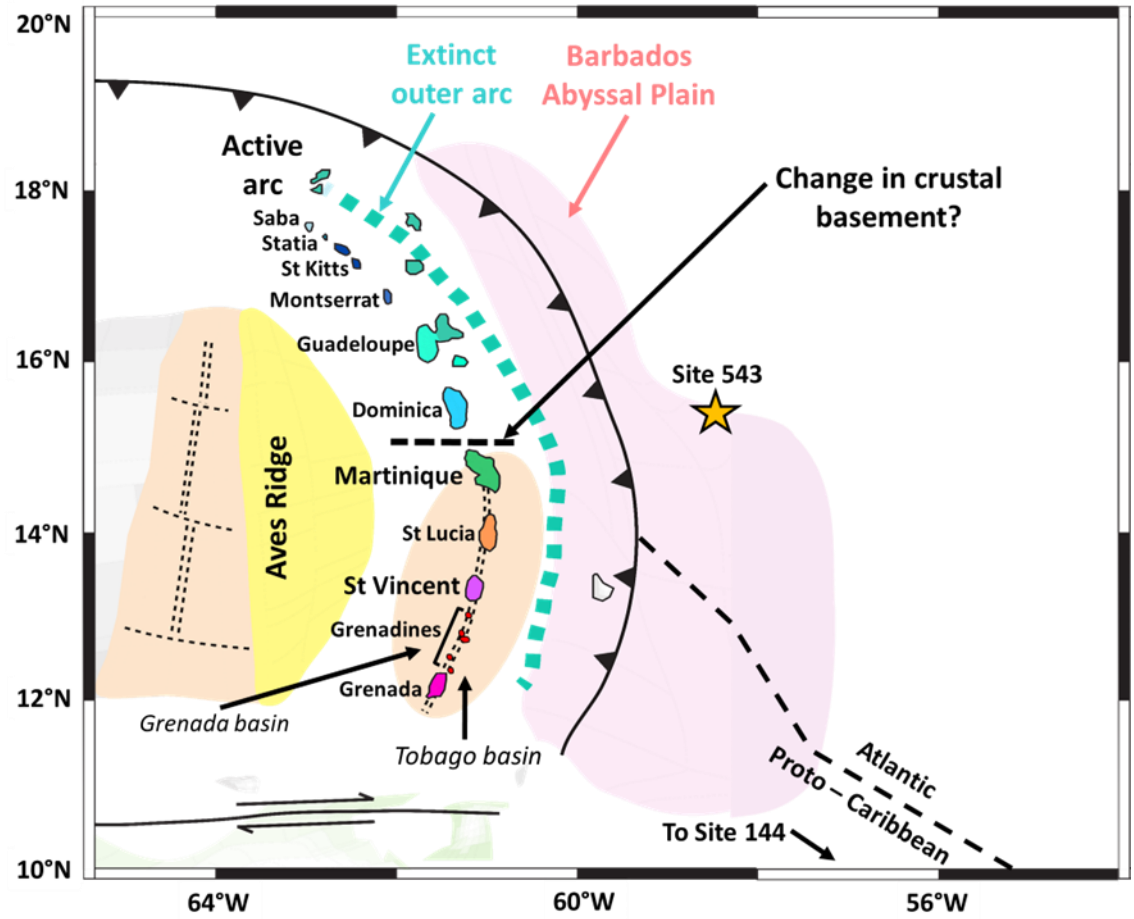

Figure 1.2: Map of the active Lesser Antilles arc and subduction zone, modified from Allen et al., (2019). Also labelled are the extinct Outer Antilles arc and key features relating to the tectonic evolution

of the arc (such as the Grenada and Tobago basins, see **Figure 1.3**). The dashed line shows the boundary between Atlantic and proto-Caribbean lithosphere on the downgoing plate (from Cooper et al., 2020, see **Section 1.4.2**). The locations of the proposed change in crustal basement along the arc and DSDP sediment core sites discussed in **Section 1.4.2** are also marked.

1.4 – The Lesser Antilles Arc

The intra-oceanic Lesser Antilles volcanic arc (LAA) (**Figure 1.2**) in the eastern Caribbean is a product of the westward subduction of Atlantic and proto-Caribbean oceanic lithosphere below the eastern margin of the Caribbean plate. The LAA is an endmember arc with slow subduction rates (2-4 cm/yr, MacDonald and Holcombe, 1978) and low magma production rates (3-5 km^3 Ma^{-1} km^{-1} of arc, MacDonald et al., 2000). The highest magma production rates occur in the central arc on the islands of Guadeloupe, Dominica and Martinique (Macdonald et al, 2000). In recent years, the LAA has been the focus of a large, multidisciplinary international research project (VoiLA – Volatiles in the Lesser Antilles, https://voilanerc.webspace.durham.ac.uk/, Goes et al., 2019). The VoiLA project involved new geophysical, geodynamic, geochemical and petrological investigations which have greatly enhanced understanding of LAA tectonic evolution (Allen et al., 2019, Braszus et al., 2021), arc crustal structure (Schlaphorst et al., 2018, Melekhova et al., 2019) and links between geological structures on the incoming plate (for example fracture zones), geophysical parameters (e.g. seismicity) and arc lava geochemistry (Cooper et al., 2020).

1.4.1 - Tectonic evolution of the Lesser Antilles arc

The tectonic evolution of the LAA remains controversial and various models have been proposed, principally based on geophysical data (e.g. Bird et al., 1999, Aitken et al., 2011). Insights from new seismic and magnetic data obtained as part of the VoiLA project, combined with existing geochronological data, were used by Allen et al., (2019) to propose an updated model for the tectonic evolution of the LAA (**Figure 1.3**).

Prior to 60 Ma, subduction at the eastern margin of the Caribbean plate produced the "Great Arc of the Caribbean" (GAC), which is preserved as part of the Aves Ridge west of the present day LAA. After 59 Ma, volcanism at the Aves Ridge ceased due to slab rollback, which caused the arc front to migrate east forming the "Outer Antilles

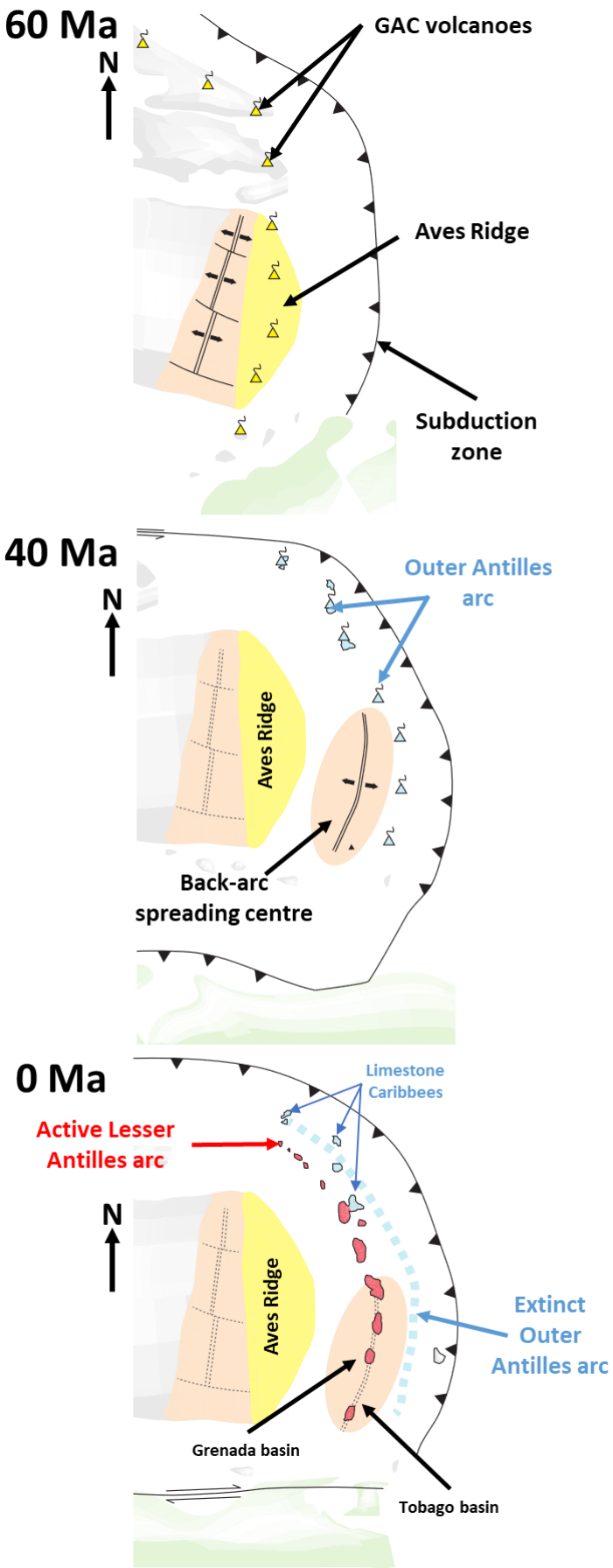

Figure 1.3: Model for the tectonic evolution of the Lesser Antilles arc, modified from Allen et al.,

(2019). Prior to 60 Ma, subduction at the eastern margin of the Caribbean plate produced the "Great Arc of the Caribbean" (GAC). After 59 Ma, GAC volcanism ceased and the arc front migrated eastward, which coincided with the opening of a back-arc spreading centre east of the abandoned GAC/Aves Ridge. The eastward arc migration ultimately led to the formation of the "Outer Antilles arc", active from 40-25 Ma. Around 25 Ma, the arc front jumped west, forming the currently active Lesser Antilles arc. The southern volcanic centres of the Lesser Antilles arc (Martinique to Grenada) were built through the oceanic crust and sediments of the back-arc basin west of the "Outer Antilles arc", creating the present day Grenada and Tobago basins.

arc". This arc migration was coincident with the opening of a back-arc basin south of the present-day location of Dominica (Allen et al., 2019, Braszus et al., 2021). The "Outer Antilles arc" was active from 40 – 25 Ma and includes the islands of the Limestone Caribbees which represent the only present-day exposures of the "Outer Antilles arc" above sea level. Around 25 Ma the arc front jumped west, forming the currently active LAA. This westward arc migration has been proposed to result from the onset of subduction of younger oceanic lithosphere, increasing the buoyancy of the subducting slab (Braszus et al., 2021). The southern volcanic centres of the LAA (Martinique to Grenada) were built through the oceanic crust and sediments of the back-arc basin located west of the "Outer Antilles arc", splitting it into the Grenada and Tobago basins (**Figure 1.3**).

1.4.2 - The arc crust and subducting slab

The complex tectonic evolution of the LAA has resulted in along-arc differences in the composition of the overriding plate crust through which the arc was built (**Figure 1.2**). Based on seismic and magnetic surveys, Allen et al., (2019) proposed that the islands north of Martinique are built upon thickened older arc crust of the Caribbean plate. Further support for this interpretation comes from the presence of subduction related basement volcanic rocks of late Jurassic to early Cretaceous age exposed on the island of La Desirade east of Guadeloupe (Neill et al., 2010). In contrast, the same seismic and magnetic data demonstrates that volcanic centres from Martinique to Grenada are built through back-arc oceanic crust and sediments (Aitken et al., 2011, Allen et al., 2019). Basalts of Eocene age (50-46 Ma) on the island of Mayreau in the Grenadines, with geochemistry suggestive of a back-arc spreading origin (White et al., 2017), are thought to represent an uplifted exposure of the oceanic crust of the Grenada and Tobago basins (Speed and Walker, 1991, Allen et al., 2019). Sediments filling the Grenada and Tobago basins were derived from the South American continent and

consist of a range of lithologies including turbidites, siltstones, limestone and shales (Aitken et al., 2011).

The age of the subducting slab varies along the length of the arc. Recent plate tectonic reconstructions (Müller et al., 2019, Braszus et al., 2021) show that the lithosphere subducted beneath the northern LAA islands was formed at the Mid-Atlantic Ridge and is up to 90 million years old (Cooper et al., 2020, **Figure 1.2**). In contrast, the lithosphere subducted beneath the southern LAA islands was formed at the proto-Caribbean mid-ocean ridge and is up to 120 million years old (Cooper et al., 2020, **Figure 1.2**). Carpentier et al., (2008) suggested that sediments from deep sea drilling programme (DSDP) Sites 543 and 144 (**Figure 1.2**) are representative of the sediments subducted in the north and south of the LAA respectively. Site 543 sediments are mostly pelagic clays whereas site 144 sediments are mostly carbonates and include a distinctive black shale unit, notable for its highly radiogenic Pb isotopic composition (Carpentier et al., 2008).

1.4.3 - Along arc variations in lava geochemistry

One of the most striking features of the LAA is the wide variation in chemical compositions of erupted lavas along the length of the arc. Previous authors (e.g. MacDonald et al., 2000) divided the arc into segments based on differences in dominant lava composition. The northern (Saba to Montserrat) and central (Guadeloupe to St Lucia) segments are dominated by andesitic lavas, along with basalts (sparse in the northern segment) and dacites. Rare rhyolitic lavas are found throughout the northern and central segments. In contrast, majority of southern segment (St Vincent to Grenada) lavas are of basalt-basaltic andesite composition, including primitive high-Mg basalts (Thirlwall and Graham, 1984, Heath et al., 1998) along with rare andesites.

Lesser Antilles lavas are notable for their broad range in trace element and isotopic compositions, which extend from MORB-like to extreme “crustal/sedimentary” values (Davidson, 1984, 1985, 1986, Davidson et al., 1987, Davidson and Harmon, 1989, Van Soest, 2000, Labanieh et al., 2010, Bezard et al., 2014). Lavas from Saba to Dominica (Northern Lesser Antilles) have a restricted range of Sr, Nd, and Pb isotopic compositions (**Figure 1.4**) similar to lavas from other intra-oceanic arcs such as the Aleutian, Mariana and South Sandwich arcs (Davidson et al., 1987). In contrast, lavas

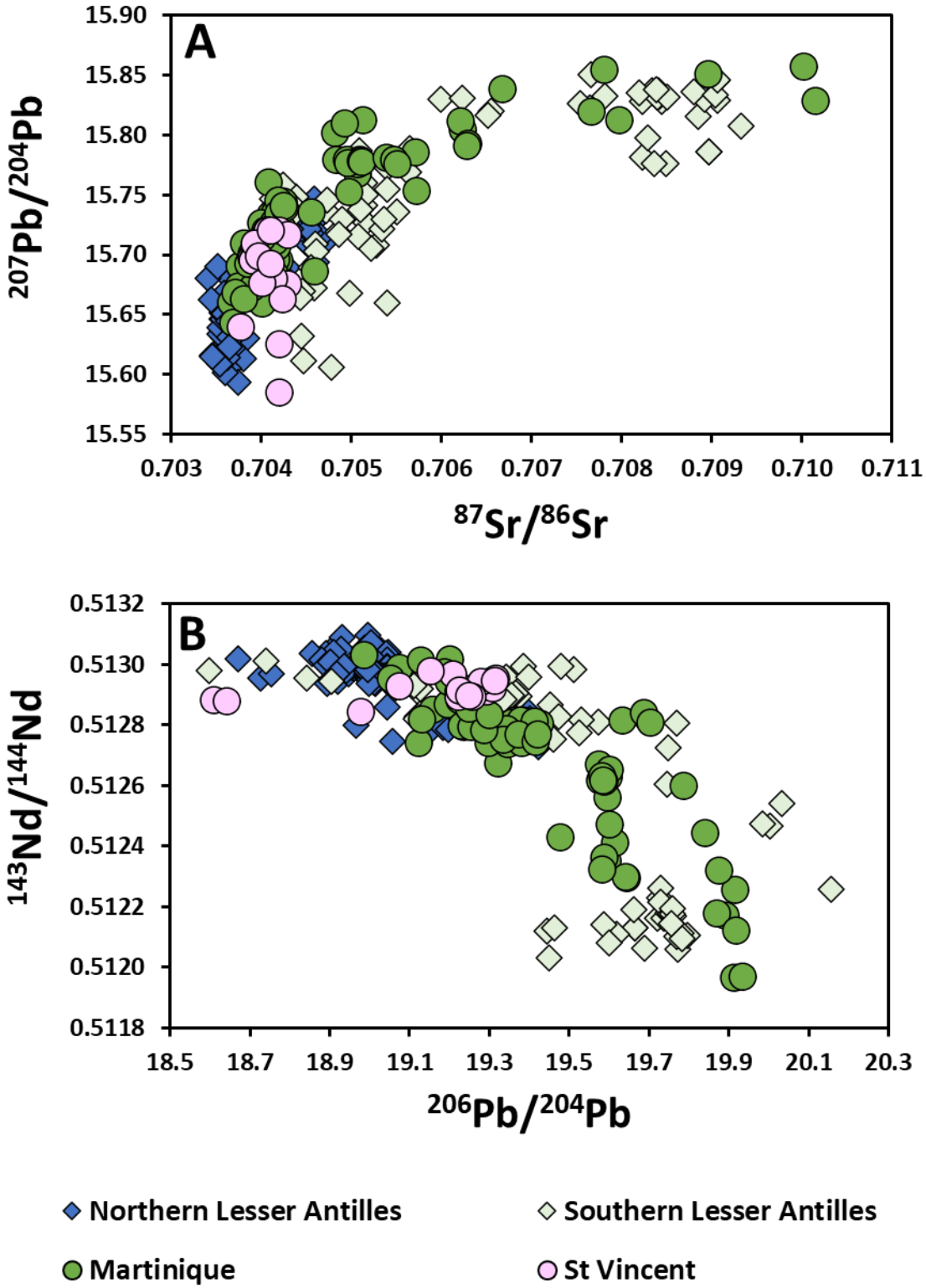

Figure 1.4: A) $^{87}Sr/^{86}Sr$ vs $^{207}Pb/^{204}Pb$ and **B)** $^{206}Pb/^{204}Pb$ vs $^{143}Nd/^{144}Nd$ for Lesser Antilles arc lavas. Northern Lesser Antilles – Saba to Dominica. Southern Lesser Antilles – Martinique to Grenada. The isotopic compositions of lavas from Martinique and St Vincent, the islands focused on in this study, are shown separately. Data sources: Northern Lesser Antilles – Van Soest et al. (2002), Lindsay et al. (2005), Toothill et al. (2007), DuFrane et al. (2009), Davidson and Wilson (2011), Cassidy et al., (2012). Southern Lesser Antilles – Thirlwall and Graham (1984), Davidson (1986), White and Dupre (1986),

Smith et al. (1996), Thirlwall et al. (1996), Turner et al. (1996), Heath et al. (1998), Labanieh et al. (2010), Huang et al. (2011), Bezard et al. (2014).

from Martinique to Grenada (Southern Lesser Antilles) show much greater isotopic heterogeneity (**Figure 1.4**), with lavas from Martinique and St Lucia spanning the entire arc compositional range (Davidson, 1986, Bezard et al., 2014). The isotopic variation and highly radiogenic, "crustal/sedimentary" signatures in the central - southern islands are typically attributed to addition of sedimentary material, though the location of sediment addition is strongly debated. Several authors favour addition of sediments to the mantle wedge from the subducting slab (White and Dupre., 1986, Carpentier et al., 2008, Labanieh et al., 2010, Labanieh et al., 2012, Hu et al., 2021), while others suggest that the sedimentary signature is derived from assimilation of sediments located within the arc crust (Davidson, 1985, Davidson, 1986, Davidson et al., 1987, Davidson and Harmon, 1989, Smith et al., 1996, Van Soest et al., 2002, Davidson and Wilson, 2011, Bezard et al., 2014).

Cooper et al., (2020) found that Boron isotope ratios of melt inclusions from LAA lavas also vary along the length of the arc, with the highest $\delta^{11}B$ values measured in the central arc (Guadeloupe, Dominica, Martinique) and St Vincent. The boron isotopic variation was attributed to variable contributions of different fluids derived from the subducting slab, with higher ^{11}B corresponding to a greater contribution of fluids from serpentine dehydration vs altered oceanic crust and sediments. Thus, some of the chemical variation in LAA lavas, for example Boron isotopes, can be related to along arc variations in the extent of hydration (where more hydrated corresponds to higher extent of serpentinization) of the subducting slab.

1.4.4 - Plutonic xenoliths in the LAA

The LAA is known for its abundant plutonic xenoliths, which have been collected and studied from almost every island. In previous studies, plutonic xenoliths have been divided into two groups – "cumulates" and "non-cumulate gabbros/plutonics/intrusives". "Cumulates" are defined as plutonic xenoliths with textures, whole rock and mineral chemistry that support an origin as a subtractive assemblage (crystals removed from a melt) (Cooper et al., 2016, 2019). "Non-cumulate gabbros" are plutonic xenoliths with chemistry and textures that represent fully solidified portions of melt, formed "without movement of crystals relative to host

melts" (Cooper et al., 2016; Cooper et al., 2019). The whole rock major element compositions of "cumulates" directly reflect their constituent minerals and do not follow liquid lines of descent defined by lavas from the same volcanic centre, whereas major element compositions of "non-cumulate gabbros" are typically close to or overlap with lavas (Cooper et al., 2016, 2019, Melekhova et al., 2017).

Plutonic xenoliths throughout the arc exhibit a wide range of textures, from adcumulates (absence of interstitial melt or crystals between primocryst phases, after Wager et al., 1960) with well equilibrated, 120° boundaries between crystals to orthocumulates (primocryst phases plus interstitial melt and/or crystals, after Wager et al., 1960) and complex poikilitic textures. Notable textural features common to plutonic xenoliths from majority of the islands include the presence of varying proportions of interstitial melt between crystals (e.g. Arculus and Wills, 1980, Tollan et al., 2012, Cooper et al., 2016, Melekhova et al., 2017) and amphibole either replacing pyroxene in a reaction relationship or occurring as an interstitial phase (e.g. Stamper et al., 2014, Cooper et al., 2016, Melekova et al., 2017, 2022, Camejo-Harry et al., 2018).

The majority of LAA plutonic xenoliths are composed of varying proportions of olivine, plagioclase, clinopyroxene, orthopyroxene, amphibole, spinel and oxides (magnetite, ilmenite), with accessory apatite, quartz and biotite. Plutonic xenoliths from individual islands often show highly variable mineralogy and represent a range of rock types. The dominant mineral phases making up plutonic xenoliths vary between islands. Plutonic xenoliths from the southern islands of Grenada and Bequia (Grenadines) are dominated by mafic minerals (olivine, clinopyroxene, amphibole) (Stamper et al, 2014, Camejo-Harry et al., 2018, Melekhova et al., 2019), whereas those from northern islands such as St Kitts, Montserrat and Guadeloupe are dominated by plagioclase (Kiddle et al., 2010, Melekhova et al., 2017, 2019). More felsic xenoliths containing quartz and biotite are mainly found on St Lucia and Guadeloupe (Melekhova et al., 2019). Orthopyroxene is rare in plutonic xenoliths from the southern islands (St Vincent, Grenadines, Grenada) compared to the rest of the arc (Tollan et al., 2012, Stamper et al., 2014, Camejo-Harry et al., 2018, Melekhova et al., 2019, 2022).

The chemical compositions of LAA plutonic xenolith mineral phases typically show a wider range, extending to more evolved compositions (e.g. lower plagioclase An, pyroxene Mg#) in "non-cumulate gabbros" compared to cumulates (e.g. Cooper et al., 2016, 2019, Melekhova et al., 2017). Compositionally zoned mineral phases are most common in "non-cumulate gabbros" (e.g. Cooper et al., 2016, 2019). A notable feature of plutonic xenoliths throughout the arc is the coexistence of high An (>80) plagioclase and low Fo (<80) olivine (e.g. Arculus and Wills, 1980, Tollan et al., 2012, Cooper et al., 2016, 2019, Ziberna et al., 2017, Camejo-Harry et al., 2018), explained by crystallization of plutonic xenoliths from melts with high H_2O contents, that were produced (from primitive high-Mg basalts) by a prior stage of olivine and clinopyroxene dominated crystallization in the lower arc crust (Tollan et al., 2012, Melekhova et al., 2015, Cooper et al., 2016, 2019). Chemical compositions of melt inclusions in plutonic xenoliths tend to show greater chemical variation than lavas from the same volcanic centre, exemplified on Statia and Bequia (Camejo-Harry et al., 2018, Cooper et al., 2019).

The magma storage conditions recorded by LAA plutonic xenoliths have been estimated via thermobarometry, comparisons with experimental products and volatile saturation pressures in melt inclusions. In general, the mineral phase assemblage and compositions in "non-cumulate gabbros" are consistent with crystallization at lower temperatures and pressures (shallower depths) than "cumulates" (e.g. Cooper et al., 2016, Melekhova et al., 2017). Melekhova et al., (2019) related the seismic velocities and densities of plutonic xenoliths from each island to seismic properties of LAA crust, to explore the structure of magma plumbing systems along the length of the arc. They concluded that the seismic properties of LAA crust are consistent with trans-crustal, mush dominated magma plumbing systems underlying each island, with erupted plutonic xenoliths sampling the mush from different crustal levels. Variations in plutonic xenolith mineral assemblages have also been attributed to local variations in melt chemistry, melt H_2O content and temperature within crystal mushes (e.g. Tollan et al., 2012, Stamper et al., 2014, Cooper et al., 2016, Camejo-Harry et al., 2018) in addition to crystallization pressure.

1.4.5 – Martinique and St Vincent

Plutonic xenoliths from the LAA islands of Martinique and St Vincent are the focus of this thesis. These islands were chosen in part because they produce lavas of contrasting chemical compositions. Andesites are common in Martinique and the compositional range spans basalt to rhyolite (Davidson, 1986, Labanieh et al., 2010), whereas St Vincent lavas are dominantly basalt-basaltic andesite, with rare andesites (Heath et al., 1998, Fedele et al., 2021). The isotopic compositions of Martinique lavas are considerably more heterogenous than St Vincent (**Figure 1.4**). Based on exposures above sea level, the islands are also of contrasting age. The oldest lavas from Martinique island have been dated at 25 Ma (Germa et al., 2011), compared to 2.74 Ma on St Vincent (Briden et al., 1979). Thus, based on erupted lavas, Martinique appears to represent an older, more chemically complex magmatic system while St Vincent represents a chemically simpler system. In addition, plutonic xenoliths from these islands have previously been subject to detailed petrological and geochemical study (Tollan et al, 2012, Cooper et al., 2016), providing key context for the investigations presented in this thesis. Full justification for the selection of Martinique and St Vincent as the focus of this study is given in **Section 1.5** and in context in **Chapters 4 and 5**.

Plutonic xenoliths from Martinique analysed in this study were sampled ex situ but are thought to have been erupted from Mt Pelee and Mt Conil (**Figure 1.5**). Plutonic xenoliths from St Vincent analysed in this study are from the Morne Garu and (mostly) La Soufriere volcanic centres (**Figure 1.6**).

A suite of Martinique plutonic xenoliths was characterized petrographically and analysed for whole rock geochemistry and major and trace element compositions of mineral phases by Cooper et al., (2016). Comparisons with experimental products suggested that the plutonic xenoliths were derived from mid-upper crustal mushes, with cumulate plutonic xenoliths derived from the mid-crust (≥ 12 km) and non-cumulate gabbros from shallower levels (6-12 km). A significant finding of the Cooper et al., (2016) study was the relationship between amphibole trace element compositions and textures. Incompatible trace element and LREE contents were lower in euhedral, early crystallizing amphibole compared to late crystallizing amphibole, which either occurs interstitially or replacing clinopyroxene (Cooper et al., 2016). The late crystallizing amphibole is interpreted to have formed via reaction of an infiltrating melt with pre-existing clinopyroxene in the mush ("reactive melt flow"). Martinique

plutonic xenoliths also contain evidence for clinopyroxene crystal cargoes in the melts from which they formed, identified by their distinct REE compositions among the clinopyroxene population analysed (Cooper et al., 2016).

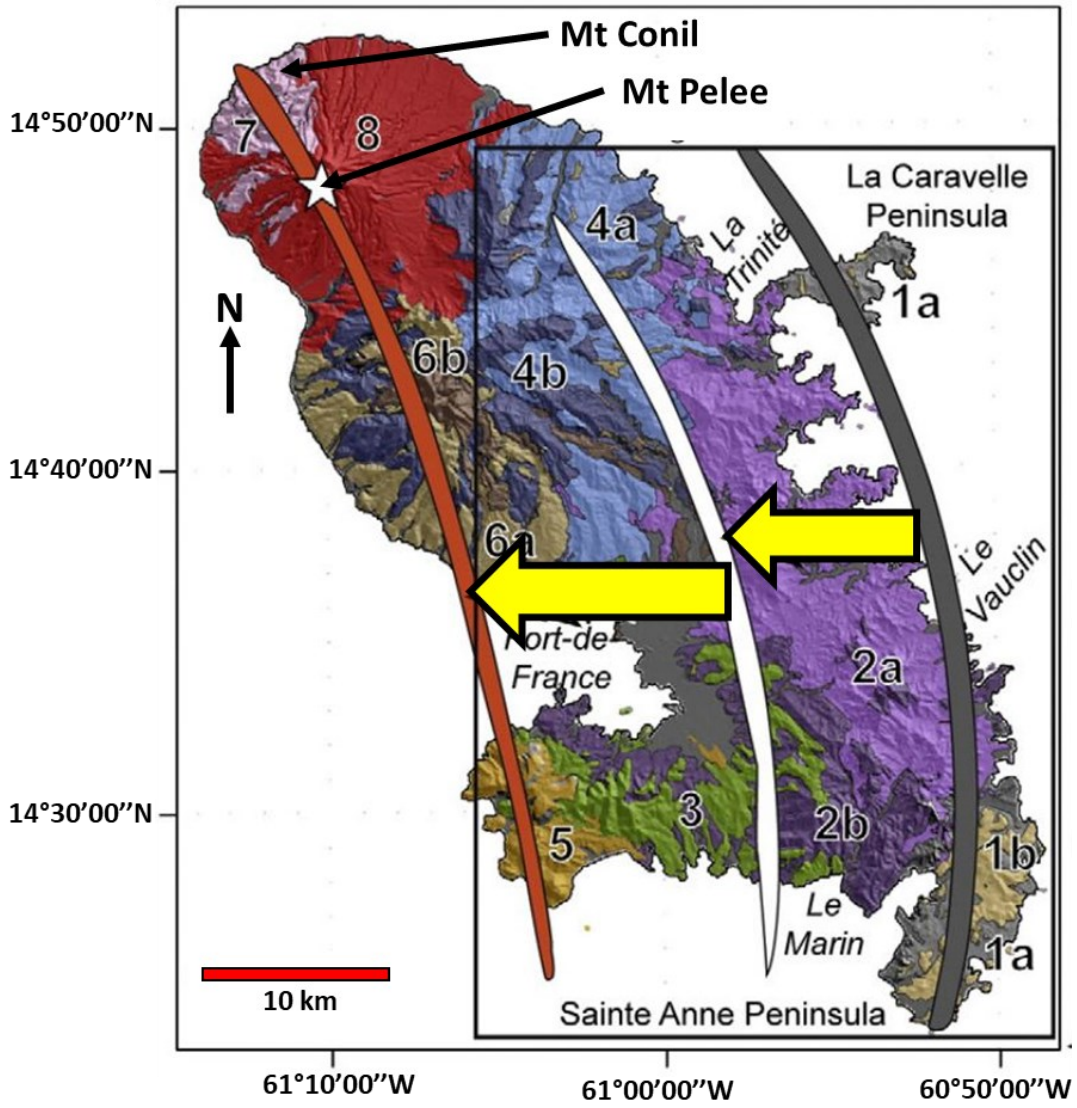

Figure 1.5: Geological map of Martinique, modified from Germa et al., (2011). The yellow arrows show the migration of volcanic centres across the island with time. The numbers (1a, 1b, 2a, etc) denote the age progression of individual volcanic centres, 1 being the oldest. The star indicates the currently active volcanic centre of Mt Pelee.

St Vincent plutonic xenoliths were analysed for mineral major element and oxygen and hydrogen isotopic compositions by Tollan et al., (2012). Melt inclusions were also studied and used to determine that the St Vincent plutonic xenoliths crystallized at ~170 MPa (~5 km depth). Oxygen and hydrogen isotopic compositions of mineral phases suggested that the magmas forming the plutonic xenoliths were unaffected by crustal assimilation. Based on the common association of high An plagioclase and low

Fo olivine, the plutonic xenoliths were interpreted as products of low pressure fractional crystallization from H_2O rich melts (as mentioned in **section 1.3** and **1.4.4**). Microxenoliths of a few millimetres in size, considered smaller equivalents to plutonic xenoliths, were reported in St Vincent scoria by Fedele et al., (2021). Microxenoliths contain similar mineral assemblages to the plutonic xenoliths studied by Tollan et al., (2012), in addition to more mafic assemblages such as wehrlites and were determined to have crystallized at greater depths (7-13 km).

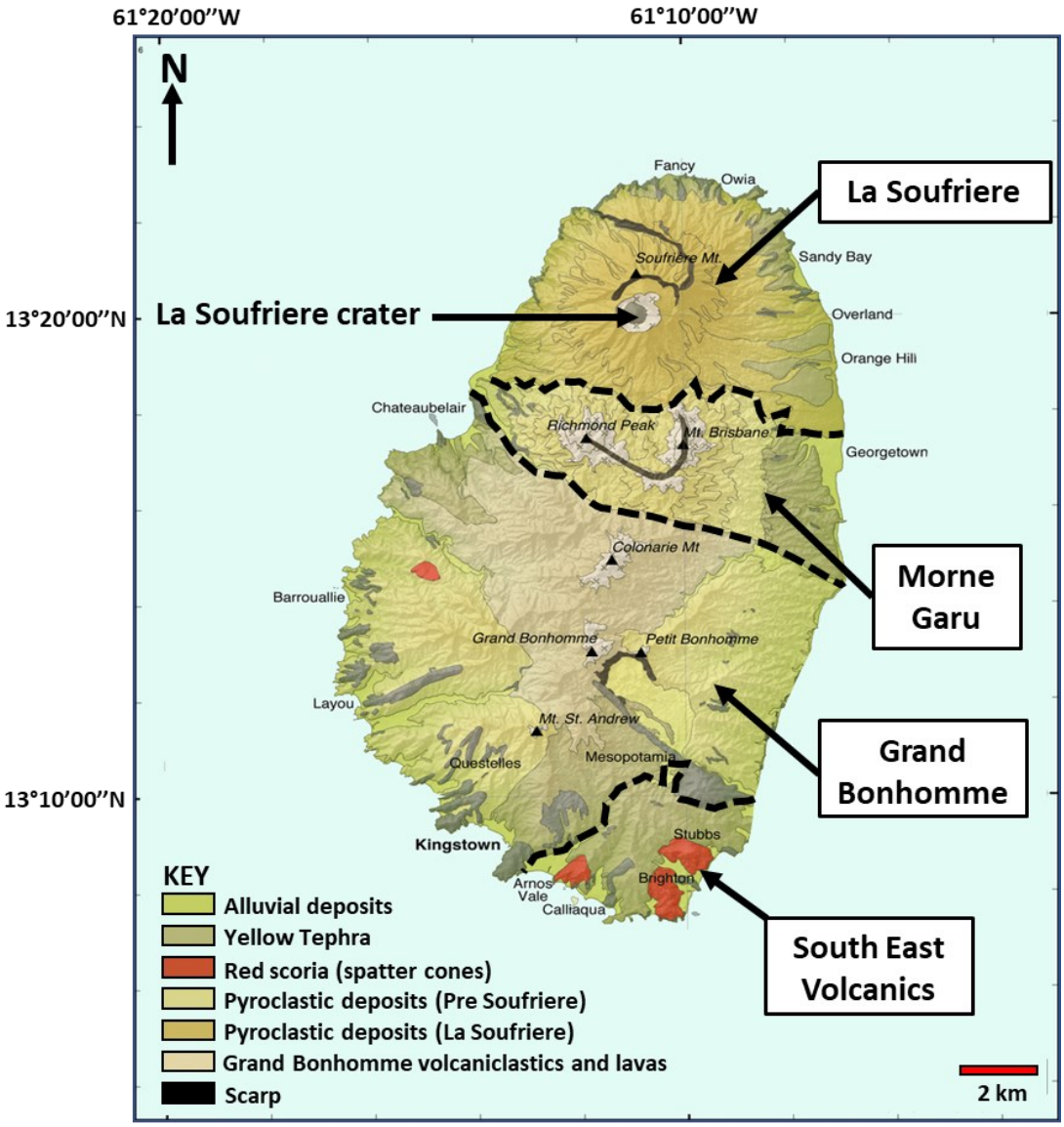

Figure 1.6: Geological map of St Vincent, modified from Robertson (2012). The dashed black lines highlight the boundaries between the four volcanic centres on St Vincent (labelled).

This previous work provides key context for the studies presented in this thesis. The petrographic and chemical characterizations of plutonic xenoliths from Martinique (Cooper et al., 2016) were used to identify plutonic xenoliths from different crustal

levels for isotopic analysis to investigate crustal sediment assimilation in **Chapter 4**. Martinique plutonic xenoliths containing evidence for reactive melt flow provided a textural and chemical dataset to compare with St Vincent plutonic xenoliths investigated for this process in **Chapter 5.** The St Vincent plutonic xenoliths studied here were newly acquired during fieldwork for this thesis. Comparison with the suite analysed by Tollan et al., (2012) identified plutonic xenoliths with textural features previously unreported from the island among the new sample set. These samples were subject to detailed study in **Chapter 5** to reveal new insights into processes in the St Vincent plumbing system.

1.5 – This study – investigation of plutonic xenoliths from Martinique and St Vincent

This thesis aims to determine whether majority of the trace element and isotopic variation in Lesser Antilles arc lavas can be produced by processes occurring within mush-dominated magma plumbing systems in the arc crust. Three crustal processes (crustal sediment assimilation, fractional crystallization, reactive melt flow) are investigated using petrographic observations and mineral chemical/isotopic compositions in plutonic xenoliths from the islands of Martinique and St Vincent. The contents of the remaining chapters are summarized below.

Chapter 2 describes the analytical techniques used to measure the chemical and isotopic compositions of mineral phases in plutonic xenoliths. **Chapter 3** presents detailed petrographic descriptions of the plutonic xenoliths from Martinique and St Vincent investigated in this study. The contents of these chapters, in particular the petrographic descriptions in **Chapter 3**, are referred back to in **Chapters 4 and 5**.

In **Chapter 4,** the origins of the isotopic variation and "crustal/sedimentary" isotopic signatures in Martinique lavas are investigated. This study aims to distinguish between competing hypotheses of addition of subducted sediments to the mantle source versus assimilation of sediments within the arc crust. To identify the location of sediment addition, Sr isotopic compositions of plagioclase within plutonic xenoliths from different levels of the Martinique magma plumbing system were analysed. This work represents the first mineral scale isotopic investigation of LAA plutonic xenoliths and provides a novel approach compared to previous studies which have argued for

subducted sediment addition or crustal assimilation based on isotopic compositions of Martinique lavas alone (e.g. Davidson, 1986, Davidson and Harmon, 1989, Labanieh et al., 2010, 2012, Davidson and Wilson, 2011, Hu et al., 2021).

Martinique represents an ideal location for this investigation because lavas from the island span the range of isotopic compositions found along the entire LAA. Hence, understanding how Martinique lavas obtain their isotopic signatures may provide insights into the roles of crustal assimilation and/or subducted sediments in producing isotopic variation in lavas throughout the LAA. This investigation also has wider implications for understanding sediment and volatile recycling at subduction zones generally. Constraining the extent to which arc lava chemical compositions have been modified by assimilation of arc crust is essential if lava compositions are to be used in calculations of sediment and volatile recycling efficiency. This chapter was published in Frontiers in Earth Science, 2021, as: Brown, J. R., Cooper, G. F., Nowell, G. M., Macpherson, C. G., Neill, I., & Prytulak, J. (2021). Isotopic compositions of plagioclase from plutonic xenoliths reveal crustal assimilation below Martinique, Lesser Antilles arc. *Frontiers in Earth Science*, *9*, 682583.

In **Chapter 5**, plutonic xenoliths from St Vincent are used as a case study to investigate magma chemical evolution processes in a mush dominated magma plumbing system from an arc setting. Specifically, this study aims to determine whether magma chemical evolution on St Vincent is controlled by fractional crystallization or reactive melt flow. St Vincent was targeted for this investigation as crustal assimilation is not considered to impact upon magma chemical compositions on the island (Heath et al., 1998, Tollan et al., 2012). This enables the effects of fractional crystallization and reactive melt flow on magma chemical compositions to be studied without additional complications from sediment assimilation. In addition, the chemical and isotopic compositions of St Vincent lavas and previously studied plutonic xenoliths support fractional crystallization as the main process controlling magma chemical evolution (Heath et al., 1998, Tollan et al., 2012, Cole et al., 2019, Fedele et al., 2021). However, Jackson et al., (2018) predicted that in mush dominated systems, reactive melt flow should represent the dominant magma chemical evolution process.

Textural observations combined with trace element analyses of clinopyroxene and amphibole in St Vincent plutonic xenoliths are used to investigate whether magma

chemical evolution in the mushy plumbing system beneath St Vincent is controlled by fractional crystallization or reactive melt flow. Specifically, this study focuses on the effects of these two processes on magma trace element compositions.

This investigation presents the first (known) analyses of trace elements in plutonic xenolith mineral phases from St Vincent and includes plutonic xenoliths exhibiting textural features not previously reported on the island, providing new insights into processes within the St Vincent magma plumbing system. The results have wider implications for understanding the processes controlling magma chemical evolution in mush-dominated magma plumbing systems in arc settings. Identifying these processes has implications for interpretation of the trace element compositions of arc lavas (and melt inclusions) and whether they can retain trace element signatures of their mantle source regions.

Chapter 6 provides a synthesis of the key findings of **Chapters 4 and 5.** The chapter starts by discussing whether the processes of crustal sediment assimilation, fractional crystallization and reactive melt flow can explain majority of the trace element and isotopic variation in LAA lavas. A typical model is proposed for how magma chemical compositions are modified on ascent through the LAA crust. Wider implications of the results of this thesis for the interpretation of arc lava chemical compositions and their use in investigations of subduction zone recycling and mantle source heterogeneity are also evaluated. Finally, ideas for future research utilising plutonic xenoliths in the LAA and other arc settings are discussed.

Appendix 1 provides details of field locations and all samples collected on a 2019 field campaign to St Lucia and St Vincent in the Lesser Antilles.

Chapter 2 – Analytical Methods

A version of part of this chapter (sections 2.1-2.3) was published as supplementary material to the following publication in Frontiers in Earth Science: Brown, J. R., Cooper, G. F., Nowell, G. M., Macpherson, C. G., Neill, I., & Prytulak, J. (2021). Isotopic compositions of plagioclase from plutonic xenoliths reveal crustal assimilation below Martinique, Lesser Antilles arc. *Frontiers in Earth Science*, *9*, 682583.

Author contributions: The work for this chapter is my own, conducted with support of my co-authors that would be usual of a supervisory team.

The plutonic xenolith whole rock Sr-Nd-Pb isotopic data presented in the above listed manuscript and Chapter 4 of this thesis were collected by supervisors Dr George Cooper and Dr Geoff Nowell. The analytical methods used to obtain this data are included in this section for completeness.

This chapter provides full details of the analytical techniques used to obtain the geochemical data presented in **Chapters 4 and 5.** Details of plutonic xenolith sample and target crystal selection for geochemical analysis are discussed in context in the relevant chapters. The contents of this chapter are referred to within the text in **Chapters 4 and 5**. **Sections 2.1-2.3** describe the analytical techniques used in the isotopic investigation of Martinique plutonic xenoliths in **Chapter 4**. **Chapter 4** presents data for the Sr isotopic compositions of individual plagioclase crystal domains from plutonic xenoliths in addition to plutonic xenolith whole-rock Sr-Nd-Pb isotopic compositions. **Sections 2.4-2.5** describe the analytical techniques used in the investigation of St Vincent plutonic xenoliths in **Chapter 5**. **Chapter 5** presents data for mineral phase molar ratios (An, Mg#, Fo) and trace element data for clinopyroxene and amphibole from St Vincent plutonic xenoliths.

2.1 - Procedures for determination of plagioclase Sr isotopic compositions

To obtain the Sr isotopic compositions of individual domains within plagioclase crystals, material was recovered from plagioclase in situ (directly from 100 µm thick sections) using a Micromill, followed by chemical separation of Sr and measurement of the $^{87}Sr/^{86}Sr$ ratio by Thermal Ionisation Mass Spectrometry (TIMS). Previous work has demonstrated that this approach can be used to obtain precise $^{87}Sr/^{86}Sr$ measurements for individual plagioclase domains (Charlier et al., 2006). Obtaining material from plagioclase in situ using a Micromill allowed targeted sampling of individual crystal zones and enabled impurities such as cracks and inclusions (that may affect the $^{87}Sr/^{86}Sr$ measurement) to be avoided.

2.1.1 - Micromilling preparation and procedure

A series of preparatory procedures were carried out prior to micro-milling, with the aim of minimising Sr blanks. Sample thin sections (100µm thickness) were first cleaned with Milli-Q (MQ) water to remove any potential debris on the surface. Squares of parafilm (previously stored immersed in MQ water) containing central holes were then adhered to the thin section under a heat lamp, with the holes centred on the target crystals and milling area. The thin section was then mounted on to the Micromill stage. Tungsten carbide dental mill bits (Komet Dental H99 104 008) were cleaned prior to use via rinsing the tips first with Teflon distilled (TD) 6 M HCl, followed by MQ water. Mill bits were then placed in a Savillex beaker and the tips immersed in MQ water. The beaker with the mill bits was then placed on a hotplate overnight at 100°C. MQ water was decanted from the beaker, followed by re-immersion of the mill tips in clean MQ water. The beaker was placed in an ultrasonic bath for 10 minutes, followed by decanting of MQ water. Finally, the mill bits were individually dried and cleaned of any remaining traces of particulate with high pressure argon gas for 5 seconds. Ar was used in preference to compressed air as the latter can contain traces of oil from the compressor.

Material was recovered from plagioclase in situ, using a New Wave Micromill. The micro-milling and sample recovery procedure closely followed Charlier et al. (2006) except that to maximize sample recovery trenches were milled rather than a series of conical holes as in the former study. Sampling trenches were 60 µm deep and of

sufficient length to yield ≥ 3 ng Sr for analysis, based on calculations of volume of material removed during milling and assuming a minimum Sr concentration of 250 µg/g (based on plagioclase Sr concentration data from Cooper et al. 2016). The procedure used to obtain sample material from each plagioclase crystal/crystal domain is described in detail in **Figure 2.1.** The same procedure was used for all samples. A new pre-cleaned mill bit was used for the sampling of each crystal/crystal domain.

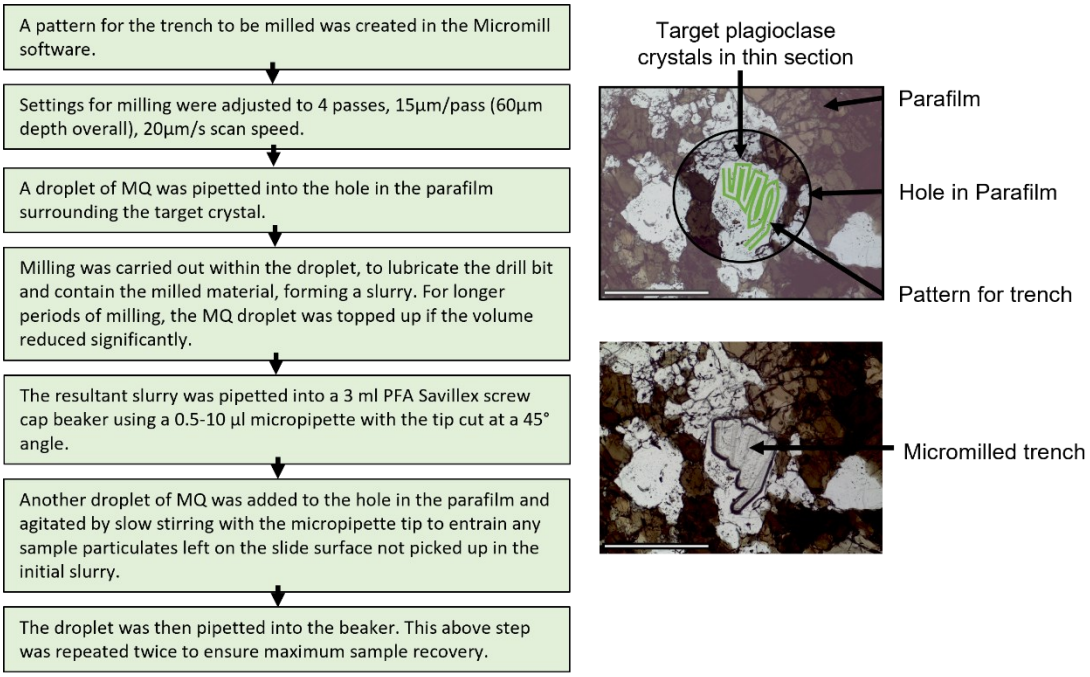

Figure 2.1: Flowchart outlining the procedure for obtaining material from a plagioclase domain via micro-milling. The images illustrate example steps in the procedure for a plagioclase from sample MQ1 (white scale bar = 1 mm). The upper image illustrates the hole in the parafilm around the target crystal, with the green line representing the pattern of the trench to be milled, as it would be plotted in the Micromill software. The lower image shows the resultant trench after micro-milling. During micro-milling, care was taken to avoid cracks and inclusions in the target crystal wherever possible. MQ = Milli-Q water.

2.1.2 - Strontium separation via ion chromatography procedure

2.1.2.1 - Preparation of materials

All sample digestion and ion chromatography procedures were carried out in a class 100 laminar flow extracted hood used solely for micro-Sr chemistry. All reagents and pre-cleaned beakers used are dedicated to micro-Sr chemistry. All reagents are Teflon

distilled (TD). The Sr-Spec resin used for Sr separation was cleaned before use using the procedure from Charlier et al. (2006), with the exception that it was carried out in a vacuum box to speed up the process. Single use, pipette tip columns, as described by Harlou et al. (2009), were used for Sr separation. The columns were pre-cleaned using the procedure outlined in Charlier et al. (2006). By carrying out these extensive pre-cleaning procedures, blank contribution from materials and reagents was minimised.

2.1.2.2 - Sample digestion

Milled material was digested using 150 µl TD 29 M HF:50 µl TD 16 M HNO_3 and refluxed overnight on a hotplate at 100 °C. The solution was then evaporated and the residue taken up in 50 µl TD 16 M HNO_3. This solution was returned to the hotplate for 90 minutes, evaporated, and redissolved in 50 µl TD 16 M HNO_3 a second time. The solution was evaporated, taken up in 400 µl TD 3 M HNO_3 and refluxed at 100 °C prior to Sr separation.

2.1.2.3 - Strontium separation via ion chromatography

Figure 2.2 illustrates the procedure to isolate Sr from the sample matrix using pipette tip micro-columns and Eichrom Sr resin. Samples were passed through the columns twice to ensure almost quantitative removal of Ca in the Sr fraction, which can inhibit the ionisation of Sr during TIMS analysis. To prepare samples for the second pass, the eluted Sr fractions were evaporated on the hotplate at 100°C, then taken up again in 400 µl TD 3 M HNO_3 and refluxed for at least 30 minutes at 100 °C. The second pass procedure was the same as in **Figure 2.2** from the post resin addition step. Columns and resin were discarded after use to maintain low blank levels.

2.1.3 - Determination of Sr isotopic composition

2.1.3.1 - Post chromatography concentration checks via MC-ICP-MS

The amount of Sr in each sample, post column chemistry, was determined prior to TIMS analysis. The rationale for these measurements was that it provided a guide to expected load size and to how well samples might run during TIMS measurement.

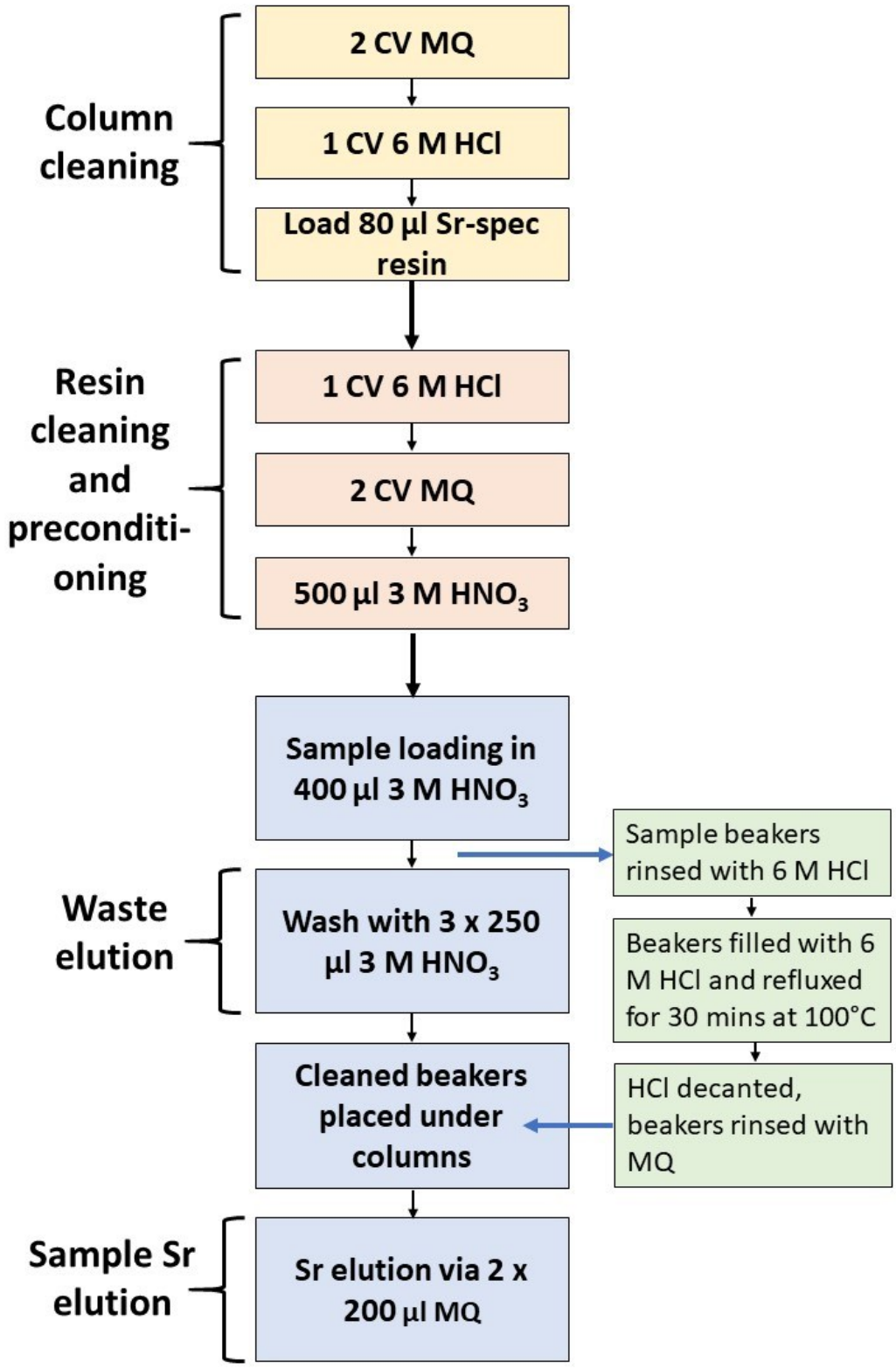

Figure 2.2: Flowchart showing steps in Sr separation procedure. CV = column volume. MQ = Milli-Q water.

To determine the mass of Sr available, a 20 µl aliquot of the Sr column fraction for each sample (5 % of the eluted 400 µl solution) was made up to 100 µl with 3 % TD HNO_3 in pre-cleaned micro centrifuge tubes. The solutions were then centrifuged and measured on a Thermo Neptune multi-collector inductively coupled plasma mass spectrometer (MC-ICP-MS). Since the concentration was only required as a guide it was determined relative to just a single 1 ng/g Sr standard solution. The ^{88}Sr beam intensity was measured for each aliquot, from which the concentration of Sr (in ng) in the eluted solution was calculated. Sample concentrations ranged from ~1-31 ng, with majority of samples > 3 ng. The remainder of the Sr column fractions were then evaporated at 100 °C in preparation for loading for Thermal Ionisation Mass Spectrometry (TIMS).

2.1.3.2 - Thermal ionization mass spectrometry (TIMS)

All micro-Sr samples were analysed for isotopic compositions at the Arthur Holmes Isotope Geology Laboratory (AHIGL), Durham University, on a Thermo Fisher Triton Plus TIMS.

Filament loading

Samples and standards were loaded on to Re filaments strung on single filament holders reserved for micro-Sr analyses. Filaments were pre-outgassed at 4.5 A for 30 minutes to remove impurities from the Re. The following procedure was used for sample loading:

First, two strips of parafilm were melted on to either end of the filament at a current of 0.9 A leaving a clear centrally positioned ~0.5–1 mm length of exposed filament. The parafilm prevents the sample/standard from spreading during dry down. The filament current was then turned off and 1 µl TaF_5 activator added to the filament in the gap between the parafilm strips. The sample was taken up in 1 µl TD 16 M HNO_3 and added to the activator droplet on the filament. Increasing the filament current to 1 A causes the sample and activator to mix by convection and ultimately dry. As the activator-sample solution dried it turned a dark purple shade, at which point the current was increased gradually to 2 A to burn off the parafilm. Finally, the current was increased to 2.2 A until the filament glowed a dull-bright red colour and was held there for approximately five seconds. The current was then turned off and filaments loaded on to a sample magazine reserved for radiogenic Sr analyses. As with the filament, the

filament side plates and shielding slit plates are also reserved for micro-Sr radiogenic Sr analyses only.

TIMS Measurement Protocol

All micro-Sr analyses were carried out during specific periods when no large samples and/or double spike Sr were being analysed on the Triton Plus. At the start of each micro-Sr analytical period the source ion lens and image slit were replaced with units dedicated for micro-Sr analysis and which are cleaned on a regular basis. Multiple NBS 987 standards, of a size approximately equivalent to, or at least encompassing that expected for the samples, were loaded on to the magazine for each run, along with a BCR-2 rock standard. Typically, the magazine was loaded into the Triton source housing at the end of day such that the source could be pumped down overnight. Source and analyser pressures were typically $<1x10^{-7}$ mbar and $\sim2x10^{-9}$ mbar at the start of each day's analysis and would increase to $\sim2x10^{-7}$ mbar and $\sim5x10^{-9}$ mbar throughout the day.

At least one analysis of the NBS 987 reference material was carried out at the start of each analytical day to assess instrument performance before starting sample analyses. Whilst the standard filament current was being increased a gain calibration was also carried out to correct for amplifier gain efficiency variations. Since amplifier gain variations are not the major source of uncertainty for Sr isotope measurements on small samples amplifier gains were only carried out once per day and amplifier rotation was not used. Following the gain calibration, a 600 s baseline measurement was carried out and used as the baseline correction for all subsequent analyses for the day.

Standard and sample filament currents were initially increased to 2200 mA, at 100 mA/minute and 50 mA/minute respectively. Once a Rb signal was observed the filament current was either held constant or increased at a slower rate to allow Rb on the filament to "burn off". If Rb was still present at 2200 mA, the current was held constant until Rb dropped below 0.1 mV. During filament heating of the initial NBS 987 standard for the day, a peak centre was carried out once the ^{86}Sr beam on the axial detector reached 20 mV. Performing a peak centre was only necessary at the start of each day due to the stability of the Triton mass calibration. Following the peak centre, or once Rb had dropped below 0.1 mV the source lenses were focused and the current turned up at 50 mA/min until an ^{88}Sr beam intensity of ~ 0.5 V was reached (typically

between 2400 and 2600 mA). For some smaller samples (< 3 ng) analyses were started at a lower ^{88}Sr beam intensity (0.3 - 0.4 V) since these samples were unlikely to run for the full number of cycles, otherwise analyses were started at 0.5 V. The source lenses were re-focused a final time before starting an analysis. Once an analysis was underway, the $^{86}Sr/^{88}Sr$ ratio was used to assess the size of the load. If $^{86}Sr/^{88}Sr$ was > 0.1200, the filament current was increased, typically at 10-30 mA/min, to improve the beam size.

Sr was analysed in static multi-collection mode using one of two cup configurations. Cumulate samples (VS36, MQ1, MQ59 and MQ48, see **Chapters 3 and 4** for details of samples/sample names) were analysed using the cup configuration shown in **Table 2.1** with ^{86}Sr in the axial detector. Each analysis comprised 20 blocks of 20 cycles, with a cycle integration time of 4 s per cycle. NCG and lava samples (MQ6, MQ35, M8321, see **Chapters 3 and 4**), for which typically < 10 ng of Sr was recovered, were analysed using the cup configuration shown in **Table 2.2** with ^{85}Rb in the axial detector. Each analysis comprised 10 blocks of 20 cycles, with a cycle integration time of 8 s per cycle. Analyses of standards used the same number of blocks, integration time and cup configuration as for samples in the corresponding run.

L3	L2	L1	C	H1	H2
^{83}Kr	^{84}Sr	^{85}Rb	^{86}Sr	^{87}Sr	^{88}Sr

Table 2.1: Cup configuration for cumulate sample analyses. ^{83}Kr is not present during TIMS analyses and L3 is not actually aligned to any isotope. It is present in the cup configuration simply as a dummy mass for when amplifier rotation is used.

L1	C	H1	H2	H3
^{84}Sr	^{85}Rb	^{86}Sr	^{87}Sr	^{88}Sr

Table 2.2: Cup configuration for NCG/lava sample analyses.

Irrespective of the cup configuration and block/integration architecture the Triton Method for Sr was written to automatically correct for mass fractionation (using an exponential law correction and a normalizing value of $^{86}Sr/^{88}Sr = 0.1194$) and Rb interference, using $^{87}Rb/^{85}Rb = 0.385707$. The measured $^{86}Sr/^{88}Sr$ ratio was monitored

throughout each analysis to assess sample fractionation. If towards the end of a run a sample became very fractionated ($^{86}Sr/^{88}Sr < 0.1180$), or fractionation became erratic (identified as significant fluctuations in measured $^{86}Sr/^{88}Sr$), the run was terminated immediately. The ^{88}Sr beam size was also monitored throughout each run, with immediate termination if beam size rapidly declined to below 0.5 V.

2.1.4 - Data quality assessment

2.1.4.1 - Blank measurement

Strontium blanks were monitored by measurement of both total procedural and column blanks throughout the period of study. A total procedural blank (TPB) is one which reflects the amount of the analyte of interest that is acquired throughout the entire sample processing protocol whereas a column blank reflects the amount of analyte acquired specifically from the column chemistry step. With micro-milling the TPB does not include the milling process because the droplet of MQ water which is used to cool the mill bit and collect the milled material as a slurry, will inevitably leach some Sr from the sample surface. Since the milling MQ water droplet is constrained to the milling area by parafilm the likelihood is any Sr leached from the sample will be isotopically similar to the milled Sr so would not be analytically resolved. Total procedural blanks replicate the sample chemistry protocol from the point of digestion through to collection of Sr from the column. In addition to the TPB at least one column blank was also collected during each session of column chemistry. To prepare blanks for analysis, solutions were dried down following the 2nd column pass and taken up in 500 µl TD 3 % HNO_3, then placed on the hotplate overnight at 80 °C to reflux.

Blanks were measured on a Thermo Neptune MC-ICP-MS. A series of standards of known concentration (1, 10, 50, 100 ppt) were used to set up a calibration for ^{88}Sr vs Sr concentration, with ^{88}Sr measured on the secondary electron multiplier (SEM). The ^{88}Sr intensity was then measured for each blank and the calibration used to calculate the Sr concentration. The sensitivity was such that 1 pg Sr yielded approximately 1500 cps. Total procedural blanks measured 5-20 pg (n = 6) and column blanks 3-50 pg (n = 9) **(Table 2.3)**, with all but one below 25 pg. Concentration checks on aliquots of

sample solutions taken after Sr separation (**Section 2.1.3.1**) indicated that majority of samples contained > 3 ng Sr, therefore blanks were typically < 1 % of sample size and any blank correction would be negligible.

TPB's		**CB's**	
Batch number	**Sr (pg)**	**Batch number**	**Sr (pg)**
433.6	10	427.6	6
448.6	6	427.8	25
454.5	20	433.12	50
454.12	11	433.14	3
467.5	7	448.8	3
476.7	5	454.7	22
		454.14	14
		467.8	4
		476.8	6

Table 2.3: Measured total procedural blanks (TPB's) and column blanks (CB's) throughout the period of study.

2.1.4.2 – Isotope reference materials

External precision and accuracy were assessed via multiple measurements (n=33) of the isotope reference material NBS 987 throughout the period of analyses, of varying load sizes from 1 to 10 ng Sr (i.e. of similar size to the samples). The average $^{87}Sr/^{86}Sr$ = 0.710259 ± 0.000031 (2σ, n=33) (**Table 2.4**) agrees well with the accepted value of $^{87}Sr/^{86}Sr$ = 0.710248 ± 0.000023 2σ (Thirlwall, 1991). Method accuracy was also assessed via 7 repeat analyses of ~10 ng Sr loads of USGS basalt rock reference material BCR-2. To avoid potential heterogeneity with the BCR-2 powder a single large digestion was made from which repeat 10 µl aliquots were taken and diluted with 390 µl TD 3 M HNO_3 prior to Sr separation. The average $^{87}Sr/^{86}Sr$ = 0.705041 ± 0.000063 (2σ, n=7) agrees within uncertainty of the value of $^{87}Sr/^{86}Sr$ = 0.705013 ± 0.000010 2σ obtained with TIMS analyses of BCR-2 by Weis et al. (2006). All measured standard values and load sizes are detailed in **Tables 2.4 and 2.5.**

Magazine number	Standard and load size	$^{87}Sr/^{86}Sr$	2 SE
213	NBS 987 5ng	0.710247	0.000007
	NBS 987 5ng	0.710245	0.000010
	NBS 987 5ng	0.710246	0.000007
	NBS 987 5ng	0.710241	0.000010
	NBS 987 5ng	0.710244	0.000008
	Magazine average (2σ)	0.710244	0.000005
217	NBS 987 10ng	0.710296	0.000016
	NBS 987 10ng	0.710245	0.000008
	NBS 987 5ng	0.710245	0.000008
	NBS 987 5ng	0.710243	0.000028
	NBS 987 5ng	0.710241	0.000008
	NBS 987 5ng	0.710274	0.000012
	Magazine average (2σ)	0.710257	0.000045
234	NBS 987 10ng	0.710267	0.000008
	NBS 987 10ng	0.710256	0.000009
	NBS 987 10ng	0.710256	0.000008
	Magazine average (2σ)	0.710260	0.000013
235	NBS 987 5ng	0.710276	0.000057
	NBS 987 5ng	0.710278	0.000008
	NBS 987 5ng	0.710265	0.000025
	NBS 987 5ng	0.710271	0.000011
	NBS 987 5ng	0.710293	0.000010
	Magazine average (2σ)	0.710277	0.000021
238	NBS 987 5ng	0.710253	0.000010
	NBS 987 5ng	0.710251	0.000009
	Magazine average (2σ)	0.710252	0.000003

246	NBS 987 5ng	0.710254	0.000007
	NBS 987 2.5ng	0.710257	0.000006
	NBS 987 2.5ng	0.710268	0.000009
	NBS 987 1ng	0.710254	0.000015
	NBS 987 2.5ng	0.710267	0.000010
	NBS 987 5ng	0.710249	0.000008
	Magazine average (2σ)	0.710258	0.000015
247	NBS 987 1ng	0.710253	0.000014
	NBS 987 1ng	0.710247	0.000013
	Magazine average (2σ)	0.710248	0.000010
250	NBS 987 1ng	0.710280	0.000016
	NBS 987 2.5ng	0.710266	0.000009
	NBS 987 2.5ng	0.710279	0.000015
	Magazine average (2σ)	0.710275	0.000015
	Overall average (2σ)	**0.710259**	**0.000031**
	1ng load average (2σ, n=4)	0.710259	0.000029
	2.5ng load average (2σ, n=6)	0.710263	0.000024
	5ng load average (2σ, n=18)	0.710256	0.000032
	10ng load average (2σ, n=5)	0.710264	0.000039

Table 2.4: Load size, $^{87}Sr/^{86}Sr$ and 2 SE (standard error) for all NBS 987 standards run throughout the period of analyses. Uncertainties for the magazine and overall averages represent 2σ (2 standard deviations).

Magazine number	**$^{87}Sr/^{86}Sr$**	**2 SE**
213	0.705017	0.000023
217	0.705010	0.000010
	0.705015	0.000012
234	0.705076	0.000020
238	0.705044	0.000027

246	0.705090	0.000017
250	0.705034	0.000007
Overall average (2 σ)	**0.705041**	**0.000063**

Table 2.5: $^{87}Sr/^{86}Sr$ and 2 SE (standard error) for all BCR-2 standards run throughout the period of analyses. All BCR-2 load sizes were ~10 ng. The uncertainty for the overall average represents 2σ (2 standard deviations) of the 7 repeat measurements of BCR-2.

2.2 - Procedures for determination of plutonic xenolith whole rock Sr-Nd-Pb isotopic compositions

2.2.1 – Sample digestion and Sr-Nd-Pb separation

Approximately 200 mg of whole rock powder was digested in 3 ml TD 29 M HF: 1 ml TD 16 M HNO_3 and refluxed at 100 °C for 24 hrs. Samples were dried and taken up in 1 ml TD 16 M HNO_3 and refluxed overnight at 120°C before being dried down. This step was repeated before samples were re-dissolved in 1 ml TD 3 M HNO_3 and transferred to micro-centrifuge tubes.

The column separation procedure for Sr-Pb-Nd involves two columns and is based on the procedures in Font et al. (2008) for the first column and Dowall. et al (2003) for the second column. The first column uses Eichrom Sr spec resin that yields a bulk matrix fraction containing the Nd, which requires an additional clean up column, and purified Sr and Pb fractions that are ready for analysis. The second cation column separates the bulk REE's from the remaining matrix and this bulk REE fraction is analysed without further processing.

The 1 ml TD 3 M HNO_3 supernatant was loaded onto micro-columns containing ~80 µl Eichrom Sr spec resin. The REE fraction, containing the Nd, was collected into the digestion beaker, along with the bulk of the sample matrix, in the first 400 µl 3 M HNO_3 eluant. After the matrix was eluted Sr was collected in 1.5 ml micro-centrifuge tubes with 400 µl MQ water. The Sr water fraction was acidified with ~18 µl TD 16 M HNO_3 to yield a 3 % HNO_3 solution ready for mass spectrometry. Finally, Pb was eluted with 250 µl 8 M HCl and collected in 3 ml Savillex PFA beakers where it was dried down and re-dissolved in 0.5 ml 3 % HNO_3 ready for analysis.

The matrix-REE fraction from the first column was dried down and re-dissolved in 1 ml TD 1 M HCl before being loaded onto Bio-rad Polyprep columns containing 2 ml of AG 50W- X8 cation resin. The remaining sample matrix was eluted with TD 1 M HCl- 1 M HF followed by TD 2.5 M HCl (Dowall et al. 2003). 10 ml of 2 M HNO_3 was then eluted to ensure removal of any remaining Ba, which can form an oxide during MC-ICP-MS that interferes on ^{146}Nd, ^{148}Nd and ^{150}Nd. Finally, the REE fraction was eluted with 14 ml TD 6 M HCl, dried down and then re-dissolved in 0.5 ml 3 % HNO_3 ready for analysis.

2.2.2 – Measurement of Sr-Nd-Pb isotopic compositions via MC-ICP-MS

All whole-rock samples were analysed for Sr-Nd-Pb isotopes at AHIGL, Durham University, on a ThermoFisher Neptune MC-ICP-MS. For all isotope analyses, samples were introduced as a 3 % HNO_3 solution using an ESI PFA50 self-aspirating nebuliser coupled to a Glass Expansion 'cinnabar' micro-cyclonic spray chamber. This combination yielded typical sensitivities at equivalent concentrations of 1 µg/g for Sr-Nd-Pb of ~60 V total Sr, 60-70 total Nd and ~90 V ppm^{-1} total Pb at an uptake rate of ~50 µl min^{-1}. Irrespective of isotope species, analyses comprised 1 block of 50 cycles with an integration time of 4 seconds per cycle, total analysis time ~3.5 minutes.

2.2.2.1 - Sr isotope analysis

Samples were analysed for Sr isotope composition during one analytical session. The cup configuration for Sr isotope analyses is given in **Table 2.6**. Samples yielded an ^{88}Sr beam size of between 17.2 and 22 V. Data were corrected for instrumental mass bias using $^{88}Sr/^{86}Sr$ ratio of 8.375209. Corrections were applied for Kr interferences on ^{84}Sr and ^{86}Sr, derived from the Ar gas supply, and for any Rb interference on ^{87}Sr, derived from the sample, by monitoring masses ^{82}Kr, ^{83}Kr and ^{85}Rb respectively. The average ^{83}Kr intensity throughout the analytical session was ~0.11 ± 0.015 mV, which is insignificant considering the Sr beam size and translates to a correction on the $^{87}Sr/^{86}Sr$ ratio of < 0.00002. The average ^{85}Rb intensity during measurement of the samples was ~ 1 mV (range: 0.05-7 mV), which equated to an average $^{87}Rb/^{86}Sr$ ratio of 0.000157 (range 0.00001-0.0011). Given the natural $^{87}Rb/^{85}Rb$ ratio and the isotope composition of each sample the Rb correction on $^{87}Sr/^{86}Sr$ amounts to between 0.000003 and 0.000320 at worst.

Given the range in $^{87}Rb/^{86}Sr$ the correction for Rb on the $^{87}Sr/^{86}Sr$ ratios is accurate and there is no correlation between corrected Sr isotopic composition of the samples and $^{87}Rb/^{86}Sr$.

L4	L3	L2	L1	Ax	H1	H2	H3
^{82}Kr	^{83}Kr	^{84}Sr	^{85}Rb	^{86}Sr	^{87}Sr		^{88}Sr

Table 2.6: Cup configuration for whole rock Sr isotope analysis on Neptune MC-ICP-MS. Isotopes in italics are monitor isotopes used for the correction of isobaric interferences from Kr and Rb on ^{84}Sr, ^{86}Sr and ^{87}Sr.

The average $^{87}Sr/^{86}Sr$ for the NBS 987 IRM during the analytical session was 0.710272 ± 0.000016 (2SD, n=11). Repeat digestions and analyses of unleached aliquots of USGS BHVO-1 basalt reference material analysed over many analytical sessions yielded an average $^{87}Sr/^{86}Sr$ ratio of 0.703475 ± 0.000022 (2SD, n=31), normalised to an NBS 987 value of 0.71024. The normalised $^{87}Sr/^{86}Sr$ ratio for BHVO-1 analysed alongside the whole rock samples was 0.703474 ± 0.000008 (2SE). These values are < 0.00001 from the value of 0.703475 ± 0.000017 (2SD, n=8) for unleached BHVO-1 reported by Weis et al. (2006), when normalised to the same 0.71024 value for NBS 987.

2.2.2.2 - Nd isotope analysis

Samples were analysed for Nd isotope composition during one analytical session. The cup configuration for Nd isotope analyses is given in **Table 2.7**. Samples yielded ^{146}Nd beam sizes of between 0.2 and 8.2 V (average 3.2 V). Instrumental mass bias was corrected for using a $^{146}Nd/^{145}Nd$ ratio of 2.079143 (equivalent to the more commonly used $^{146}Nd/^{144}Nd$ ratio of 0.7219) and an exponential law. The $^{146}Nd/^{145}Nd$ ratio is used for correcting mass bias since Nd isotopes are measured on a total REE-cut from the 2nd stage cation columns and this is the only Ce and Sm-free stable Nd isotope ratio. This approach requires a correction for isobaric interferences from Sm on ^{144}Nd, ^{148}Nd and ^{150}Nd. The correction used is based on the method of Nowell and Parrish (2001) and Nowell et al. (2008). During the analytical session the in-house Nd isotope reference material J&M was analysed multiple times as both pure solution and doped with Sm ($^{147}Sm/^{144}Nd$ ~0.15) to test the accuracy of the Sm corrections. The average

$^{147}Sm/^{144}Nd$ of the samples was 0.156, some 6 % higher than that measured on the Sm-doped standard at 0.146.

L4	L3	L2	L1	Ax	H1	H2	H3	H4
^{142}Nd	^{143}Nd	^{144}Nd	^{145}Nd	^{146}Nd	***^{147}Sm***	^{148}Nd	**^{149}Sm**	^{150}Nd

Table 2.7: Cup configuration for whole rock Nd isotope analysis on Neptune MC-ICP-MS. Isotopes in italics are monitor isotopes used for the correction of isobaric interferences from Sm on ^{144}Nd, ^{148}Nd and ^{150}Nd. Two isotope of Sm, highlighted in bold, are used to determine the Sm mass bias and correct the $^{147}Sm/^{X}Sm$, where X is 144,148 or 150, ratios prior to the interference correction.

The average $^{143}Nd/^{144}Nd$ ratio for the pure and Sm-doped J&M was 0.511112 ± 0.000009 (2SD; n=9) and 0.511114 ± 0.000012 (2SD; n=7) respectively. The overall average $^{143}Nd/^{144}Nd$ ratio for J&M was 0.511113 ± 0.000010 (2SD n=16). Cross calibration showed a J&M value of 0.511110 is equivalent to a value of 0.511862 for the more commonly used La Jolla reference material.

The accuracy of the Sm correction method for samples is also demonstrated by repeat digestions and analyses of the USGS BHVO-1 reference material, over many analytical sessions which gave an average $^{143}Nd/^{144}Nd$ ratio of 0.512983 ± 0.000010 2SD (20ppm 2RSD, n=32) after the Sm correction and when normalised to a J&M value of 0.511110. The $^{143}Nd/^{144}Nd$ ratio for the BHVO-1 analysed alongside the whole rock samples was 0.512885 ± 0.000006 2SE. These values are within 0.000012 of the TIMS ratio of 0.512986 ± 0.000009 (2SD; n=19) reported by Weis et al. (2006) when reported to the same La Jolla value, and testament to the accuracy of the Sm correction.

2.2.2.3 - Pb isotope analysis

Samples were analysed for Pb isotope composition during one analytical session. The cup configuration for Pb isotope analysis is given in **Table 2.8**. Samples yielded ^{208}Pb beams of between 10.1 and 26.9 V (average 17.1 V). Since Pb only has one stable non-radiogenic isotope (^{204}Pb), samples were spiked with Thallium in order to correct Pb isotope ratios for the effects of instrumental mass bias. Prior to isotope analysis samples were tested for Pb concentration and spiked with a Tl solution to achieve a Pb/Tl ratio of ~12, which simultaneously minimizes the low-mass abundance

sensitivity tails from ^{205}Tl onto ^{204}Pb and from ^{206}Pb onto ^{205}Tl. Since the mass bias behaviour of Pb and Tl during MC-ICP-MS are very slightly different it is necessary to optimise the ^{205}Tl/^{203}Tl ratio for Thallium in each analytical session to correct for this difference and essentially force the mass bias factor (β) for Tl to equal that for Pb ($Tl_\beta/Pb_\beta = 1$) for each of the Pb isotope ratios. This is accomplished by deriving a ^{205}Tl/^{203}Tl ratio that minimises the offset between each average Pb isotope ratio for NBS 981 in the analytical session and the corresponding accepted Pb isotope ratios for the international isotope reference material NBS981. In our case we use the Pb isotope ratios of Baker et al., (2004) as the accepted values for NBS 981. The optimised ^{205}Tl/^{203}Tl ratio is then used to correct Pb isotope ratios on unknown samples for instrumental mass bias. ^{202}Hg was monitored during each analysis to correct for the presence of ^{204}Hg in the Ar gas, using the ^{202}Hg/^{204}Hg ratio from Rosman and Taylor (1998) adjusted for instrumental mass bias using the same optimised Tl isotope ratio as used for the Pb isotopes.

L3	L2	L1	Ax	H1	H2	H3
^{202}Hg	**^{203}Tl**	^{204}Pb	**^{205}Tl**	^{206}Pb	^{207}Pb	^{208}Pb

Table 2.8: Cup configuration for whole rock Pb isotope analysis on Neptune MC-ICP-MS. Isotope in italics is used for the correction of the isobaric interference from Hg on ^{204}Pb. ^{205}Tl/^{203}Tl is used for the mass bias correction on Pb isotope ratios.

Repeat analyses of the NBS981 IRM gave the following average ^{206}Pb/^{204}Pb, ^{207}Pb/^{204}Pb, ^{208}Pb/^{204}Pb ratios after correction for instrumental mass bias using an optimised ^{205}Tl/^{203}Tl ratio of 2.38948: 16.94157 ± 0.00067, 15.49947 ± 0.00085, 36.72158 ± 0.00263 (n=10) respectively. These values are within 2, 30 and 115 ppm respectively of the accepted values of 16.9416, 15.4999, 36.7258, from Baker et al., (2004).

Analysis of an unleached aliquot of USGS reference material BHVO-1, measured alongside the samples, gave ^{206}Pb/^{204}Pb, ^{207}Pb/^{204}Pb, ^{208}Pb/^{204}Pb ratios of 18.69132 ± 0.00053, 15.57826 ± 0.00049 and 38.36291 ± 0.00155 respectively and when corrected for instrumental mass bias using the ^{205}Tl/^{203}Tl ratio of 2.38948 optimised against

NBS981. These values are within 90, 180 and 125 ppm respectively of the values reported by Weis et al. (2006) when renormalized to the same values for NBS981. Blanks for whole rock radiogenic isotope measurements run at the AHIGL are typically <50 pg for Sr and Pb and < 20 pg for Nd. The large beam sizes demonstrate that samples contained sufficiently high concentrations of Sr, Nd and Pb that blank contributions of typical size can be considered negligible.

2.3. Age correction required for Sr isotopic data?

2.3.1 - Plutonic xenoliths

Plagioclase in Martinique plutonic xenoliths have Rb/Sr ≤ 0.004 and most plutonic xenolith whole rocks have an Rb/Sr ratio < 0.01 (supplementary data of Cooper et al. 2016). To determine whether age correction of the Sr isotope data was required, calculations were carried out assuming a maximum age of 25 Ma, corresponding to the oldest volcanism in Martinique (Germa et al. 2011). A 25 Ma age correction for a sample with Rb/Sr = 0.01 (greater than almost all plutonic xenolith whole rocks and plagioclase), would shift the $^{87}Sr/^{86}Sr$ ratio by only 0.000010 (**Table 2.9**). Two plutonic xenolith samples have slightly higher whole rock Rb/Sr ratios of ~0.08, but even with this higher Rb/Sr ratio a 25 Ma age correction only results in a 0.000082 shift in the $^{87}Sr/^{86}Sr$ ratio (**Table 2.9**). Such small corrections in $^{87}Sr/^{86}Sr$ are negligible and would not affect the interpretation of the data, hence no age corrections were applied to plutonic xenolith plagioclase and whole rock Sr isotopic data.

2.3.2 - Lava

Although Rb/Sr data for plagioclase from Martinique lavas is unavailable, a reasonable approximation can be made using plagioclase from St Lucia lavas, which have Rb/Sr < 0.002 (Bezard et al. 2017, supplementary data). This suggests that the plagioclase in lava sample M8321 (see **Chapter 4**) is likely to have Rb/Sr < 0.01, which as shown in the example above and in **Table 2.9** indicates that no age correction would be required, especially given the young age of the lavas (9.2 – 8.4 Ma, see below). The Rb/Sr of the M8321 groundmass can be approximated by the whole rock value, of 0.648045 (Davidson, 1986). Since this value is significantly higher than the plutonic xenoliths, an age correction was applied to the M8321 groundmass data. The lava is from the

emergent/subaerial phase of the Intermediate arc period of volcanism on Martinique, active between 9.2 and 8.4 Ma (Germa et al. 2011). These upper and lower age limits were used to provide two age corrected $^{87}Sr/^{86}Sr$ values for each groundmass $^{87}Sr/^{86}Sr$ measurement **(Table 2.9).**

	Rb/Sr	**$^{87}Rb/^{86}Sr$**	**$^{87}Sr/^{86}Sr$ measured**	**Age (Ma)**	**Calculated initial ratio**	**Shift in $^{87}Sr/^{86}Sr$**
Plutonic xenolith	0.01	0.02893273	0.704000	25	0.703990	0.000010
	0.08	0.23146182	0.704000	25	0.703918	0.000082
M8321	0.648045	1.87543089	0.706506	9.2	0.706261	0.000245
	0.648045	1.87543089	0.706506	8.4	0.706282	0.000224
	0.648045	1.87543548	0.706531	9.2	0.706286	0.000245
	0.648045	1.87543548	0.706531	8.4	0.706307	0.000224

Table 2.9: Results of calculations used to determine whether age correction is required for the plutonic xenolith and lava Sr isotopic data. Sample M8321 groundmass measurements are age corrected to both 8.4 and 9.2 Ma, the upper and lower limits for the age of this lava. Two M8321 groundmass data points have identical measured values of $^{87}Sr/^{86}Sr = 0.706506$, hence no additional calculation is shown for the third groundmass data point.

2.4 – Electron Microscopy

Energy dispersive x-ray spectroscopy (EDS) was used to analyse the major element compositions and molar element ratios (An, Fo, Mg#) of mineral phases in the selected plutonic xenolith samples from St Vincent. Recent advances in EDS techniques (detailed in Loocke, 2016) have enabled quantitative mapping of molar element ratios across entire thin sections. Collecting quantitative data across a whole thin section has several advantages over individual spot analyses of crystals. For example, the need to choose target crystals that are fully representative of the sample is removed, since all crystals in the thin section are analysed. Variations in major element composition that are petrographically cryptic (e.g. not visible under the microscope as zoning, different

crystal colours, etc) may be revealed at the thin section scale, whereas in a dataset of spot analyses crystals with distinct compositions (but perhaps low abundance) may be missed or appear as under-represented outliers. Most importantly, mapping whole thin sections provides spatial and textural context to measured major element variation. For these reasons, quantitative whole thin section mapping was used to analyse major element compositions and element molar ratios in the plutonic xenolith samples, with the results used to guide choice of target crystals for trace element analysis.

2.4.1 - Element mapping procedure

EDS element maps of the four plutonic xenolith samples were acquired using a Zeiss Sigma HD field emission gun (FEG) SEM with two 150 mm^2 Oxford Instruments X-Max energy dispersive silicon drift detectors at Cardiff University. Prior to analysis, the thin sections were coated with a conductive layer (~ 20 nm) of carbon. The element mapping procedure was run using Oxford Instruments AZtec software. All four maps were acquired using an accelerating voltage of 20 kV, aperture size 120 µm and a working distance of 8.9 mm. The magnification was adjusted depending on the typical crystal size in thin section, with 180x used for the Ol-CPX gabbro and banded Hbl-Ol gabbro, and 190x used for the olivine gabbro and poikilitic Hbl-Ol gabbro (see **Chapters 3 and 5** for details of samples/sample names). This resulted in a pixel size of 22.90 µm for the olivine gabbro and poikilitic Hbl-Ol gabbro, and 24.17 µm for the Ol-CPX gabbro and banded Hbl-Ol gabbro. Pixel dwell time was set at 20 ms for all four sample maps. Elements that were identified during mapping were - Al, Ca, Cr, Fe, K, Mg, Mn, Na, Ni, O, P, S, Si, Ti, V. Raw X-ray maps were background corrected (via processing as TruMaps) in AZtec prior to creation of element map images.

2.4.2 - Mineral major element abundances

Major element abundances (both oxide and weight percent) were determined as spot analyses within individual crystals. For each analysis, an x-ray spectrum was acquired in the AZtec software (which is calculated from the background corrected element map). The Tru-Q function in the AZtec software was used to calculate the major element composition from each x-ray spectrum. A predefined element list, matching the major elements scanned for during typical electron microprobe (EPMA) analyses

of clinopyroxene and amphibole (e.g. Tollan et al., (2012), Cooper et al., (2016)) - O, Si, Mg, Al, Ca, Fe, Ti, Na, Mn, K, Cr - was used for the composition calculations. The Tru-Q function uses the inbuilt database of factory standardizations (based on standards measured in Oxford Instruments' factory) within the Aztec software for quantification. Totals were normalized to 100 % and outputs given in the form of both oxide and weight percent, calculated automatically by the software.

As a test of data quality obtained using the Tru-Q function in AZtec, measured compositions of clinopyroxene and amphibole were compared with EPMA data for these phases from St Vincent plutonic xenoliths (from Tollan et al., 2012) and a larger dataset from Martinique plutonic xenoliths (Cooper et al., 2016). For clinopyroxene, the Tru-Q data from the samples falls within 2 wt % of the range of St Vincent plutonic xenolith EPMA data for CaO, MgO, Al_2O_3 and SiO_2 (**Figure 2.3**). Almost all Tru-Q measurements fall within the range of compositions measured in Martinique plutonic xenolith clinopyroxene by EPMA. The few high-MgO outliers are likely to encompass real variations and represent a type of primitive clinopyroxene not present in the plutonic xenoliths studied by Tollan et al., (2012) or Cooper et al., (2016). The Tru-Q data for amphibole falls within the range of the St Vincent plutonic xenolith EPMA data for MgO but extends to lower CaO and Al_2O_3 values by a maximum of 1.5 wt %, which are within the range covered by the Martinique dataset **(Figure 2.3**). Almost all Tru-Q measurements of SiO_2 in amphibole lie outside the EPMA data fields (if excluding two outliers from the Martinique dataset), showing high SiO_2 (up to 3 wt % higher than the St Vincent EPMA range) for a given Al_2O_3. However, amphiboles with similar compositions from other LAA islands including Bequia (Camejo-Harry et al., 2018) and St Lucia (unpublished data) have been measured by EPMA. Each measured amphibole major element composition was also checked for charge balance using the formulas in the spreadsheet provided by Ridolfi et al., (2010) – all amphibole compositions passed this check. Overall, the listed checks and comparisons show that the Tru-Q major element data for clinopyroxene and amphibole generally agrees well with EPMA data from Lesser Antilles plutonic xenoliths and can be used as a reliable measurement of major element composition.

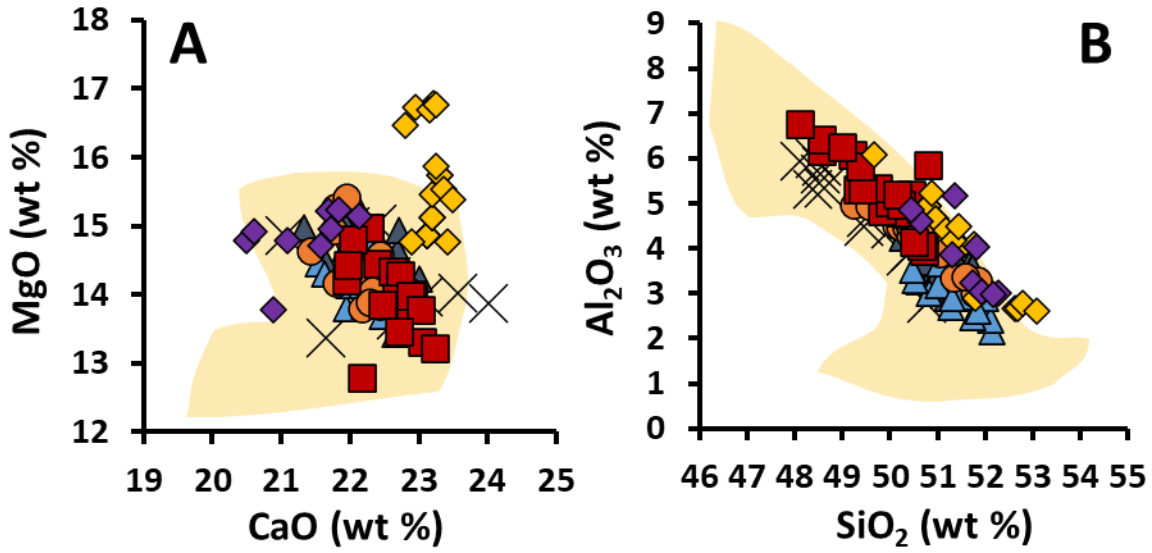

TOLLAN CPX
BANDED HBL-OL GABBRO MATRIX CPX
OLIVINE ABSENT BAND CPX
OLIVINE GABBRO CPX
OL-CPX GABBRO CPX
POIKILITIC HBL-OL GABBRO HIGH MG# CPX
POIKILITIC HBL-OL GABBRO LOW MG# CPX

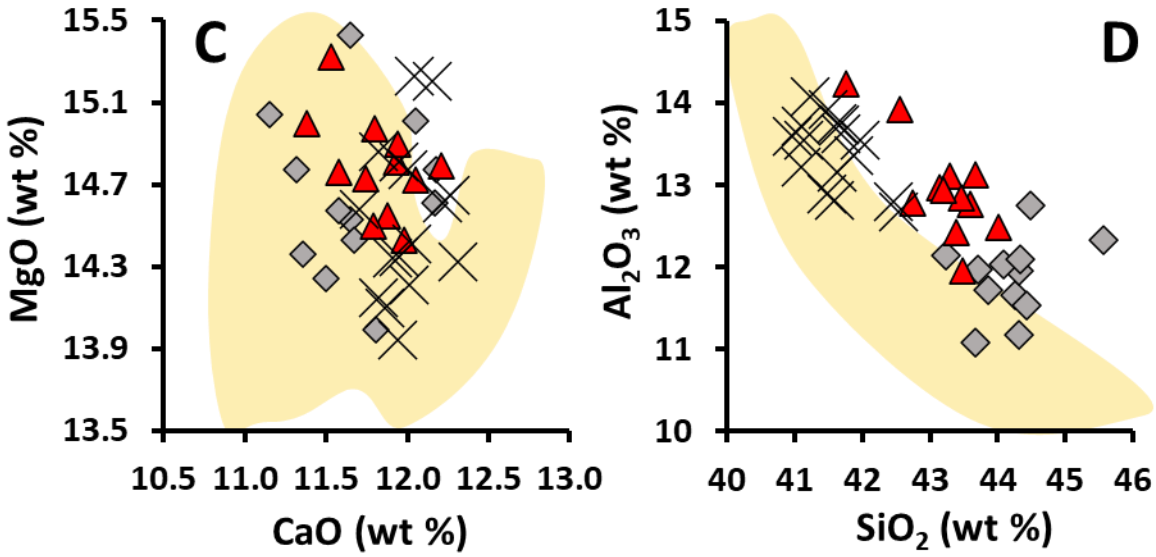

TOLLAN AMPH
POIKILITIC HBL-OL GABBRO AMPH
BANDED HBL-OL GABBRO AMPH

Figure 2.3: A) MgO vs CaO and **B)** Al_2O_3 vs SiO_2 of clinopyroxene and **C)** MgO vs CaO and **D)** Al_2O_3 vs SiO_2 of amphibole from St Vincent plutonic xenoliths analysed for trace elements in this study. See **Chapters 3 and 5** for details of plutonic xenolith samples listed in legend. All clinopyroxene and amphibole compositions were calculated using the Tru-Q function in the AZtec software from EDS x-ray maps. Data are compared with EPMA data for clinopyroxene and amphibole from St Vincent plutonic xenoliths (Tollan et al., 2012) and a larger dataset from Martinique plutonic xenoliths (Cooper et al., 2016) shown by the yellow field.

2.4.3 - Mineral phase and quantitative molar element ratio maps

The software package "QUACK", developed at Cardiff University (detailed in Loocke, 2016) was used to process the background corrected x-ray element maps generated in AZtec and produce both mineral phase and quantitative molar element ratio (e.g. plagioclase An, clinopyroxene Mg#, etc) maps. The inbuilt algorithms in the QUACK software were used to produce mineral phase maps (see **Chapter 3, section 3.2** for resulting images) based on variations in elemental composition. This process assigns a phase/mineral identity to each pixel of the map. The number of mineral phases and their distribution as defined by QUACK were verified by comparing the phase map for each sample to petrographic observations. The software displays the total number of pixels that make up the map (or a selected region of the map), as well as the number of pixels assigned to each mineral phase. These values were used to determine the mineral modal abundances of the four St Vincent plutonic xenolith samples studied (see **Chapter 3, Figure 3.26** and **Table 3.2**). For samples with a rind of the host lava present in thin section (e.g. the banded Hbl-Ol gabbro) a region of the map, excluding the host lava, was selected prior to calculation of mineral modal abundances, to ensure that calculated values were representative only of the plutonic xenolith part of the mapped thin section.

The QUACK software was used to generate quantitative molar element ratio maps for olivine Fo, plagioclase An, and Mg# for clinopyroxene, orthopyroxene and amphibole (see **Chapter 5, Figures 5.12-5.15**). Molar ratios are quantified using inbuilt correction equations, which are based on multiple linear least squares regressions of a database of reference x-ray spectra for known compositions. The regression equations relate molar ratio values calculated from x-ray intensities to known molar ratios. The choice of regression can be general, using all spectra in the database for which the chosen molar ratio was known, or mineral phase and molar ratio specific. For example, the database contains 116 reference spectra for Mg#. Of these, 40 are from measurements of

pyroxenes. Plagioclase An, olivine Fo and both clinopyroxene and orthopyroxene Mg# were quantified using the mineral specific regression equations. Amphibole Mg# was quantified using the general Mg# regression equation. In **Chapter 5**, the quantitative mineral phase molar ratio data are presented in map form (**Figures 5.12-5.15**) and as histograms (**Figures 5.8-5.11**). The histograms show the range of measured molar element ratios for mineral phases in the mapped thin sections.

Data quality of molar ratio maps produced via QUACK was rigorously tested by Loocke, 2016. They collected x-ray element maps of Astimex standards of plagioclase, diopside (clinopyroxene) and olivine, then produced molar ratio maps (plagioclase An, clinopyroxene Mg#, olivine Fo) for the standards. Histograms of each molar ratio (showing the number of pixels of the map for which a given molar ratio was calculated) were used to determine the mean molar ratio and uncertainty measured on the standards. They determined percentage error (calculated as 100 * (measured mean-accepted value)/accepted value) as 0.2 % for plagioclase An, based on 768 measurements (quantified pixels in the map of the standard). Olivine Fo percentage error was 0.216 % based on 529 measurements and clinopyroxene Mg# 0.585 % based on 761 measurements. Thus, the molar ratios of mineral standards were well reproduced by the correction equations employed by the QUACK software. The element maps in this study were acquired using the same SEM at Cardiff University (as Loocke, 2016) using near identical run conditions, therefore it is inferred that uncertainties on molar ratio measurements presented in **Chapter 5** are < 1%.

2.5 - LA-ICP-MS

Laser ablation inductively coupled plasma mass spectrometry (LA-ICP-MS) was used to analyse the trace element composition of clinopyroxene and amphibole in St Vincent plutonic xenoliths. This analytical technique was chosen due to its high spatial resolution (< 100 μm) allowing the analysis of distinct regions of individual crystals including narrow compositional zones. LA-ICP-MS also facilitates rapid acquisition of data for the concentration of multiple elements in each individual analysis, allowing co-variation of several elements to be assessed.

2.5.1 - Instrument and parameters

LA-ICP-MS analyses were carried out using a Teledyne Analyte Excite Laser Ablation System coupled to a Thermo-Scientific X-Series 2 ICP-MS at Durham University. A simple diagram of the set up is shown in **Figure 2.4**, outlining key features. Prior to analyses, several key parameters need to be set on both the laser ablation system and ICP-MS. A summary of these parameters is listed in **Table 2.10**.

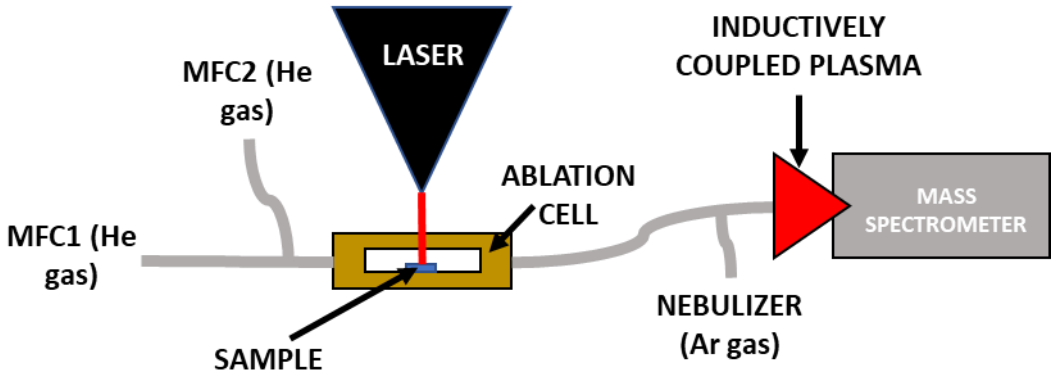

Figure 2.4: Schematic diagram showing the key components of the set up used for LA-ICP-MS analyses.

2.5.2 - Protocol for laser ablation analyses

2.5.2.1 - Set up of analysis locations

The plutonic xenolith thin sections and a polished block containing a range of reference standards (NIST 610, NIST 612, BCR-2G, BHVO-2G) were inserted into the sample holder and placed inside the ablation cell. The co-ordinates of each analysis location were saved and the laser parameters for each spot (fluence, repetition rate, shot count and spot size) set. Prior to ablation and analysis of a series of saved spots, the gas flows to the ablation cell were switched online and the amount of gas flow set for each mass flow controller.

2.5.2.2 - Set up of ICP-MS

After first igniting the plasma of the ICP-MS and preparing a series of saved spots/co-ordinates for ablation and analysis, an initial sensitivity check was carried out. Sensitivity was assessed by measuring a range of elements of different masses (Li, Mg, Ca, Sr, Ba, Pb, Th, U) during continuous ablation of the NIST 610 standard glass and

both nebuliser gas flow and sampling depth were adjusted to maximise the sensitivity. The nebuliser gas flow and sampling depth settings at which the highest number of counts was measured across the range of elements were selected for the upcoming analyses.

	Parameter	Explanation
Laser ablation system parameters	Gas flows - mass flow controllers 1 and 2 (MFC1 and MFC2)	The mass flow controllers regulate the amount of He carrier gas flowing into the ablation cell.
	Laser energy/fluence (J/cm^2)	Energy of the laser beam per unit area.
	Repetition rate (Hz)	Number of times the laser fires per second.
	Shot count and ablation duration	The total number of times the laser fires during an analysis of a single spot. The shot count divided by repetition rate gives the ablation duration (e.g. shot count 240, 8 Hz gives a 30 s ablation duration).
	Spot size and shape (µm)	The size and shape of the spot ablated by the laser during an analysis.
ICP-MS parameters	Nebuliser gas flow	The nebuliser adds Ar to the He carrier gas containing the ablated sample prior to its introduction into the ICP.
	Sampling depth	The distance into the ICP that the ablated sample is introduced (higher value = further in).
	Dwell time (ms)	The amount of time that the mass spectrometer detector spends scanning for an isotope (before moving on to an isotope of different mass) during an analysis.

Table 2.10: List of parameters that are required to be set on the laser ablation system and ICP-MS prior to carrying out analyses and explanations of what is controlled by each parameter.

A second check was then carried out using these settings that provided optimum sensitivity. For the second check, 5 repeat measurements (each lasting for 10s of ablation time) of the same elements were taken during ablation of NIST 610 using a

standard 75 µm square spot and the relative standard deviation (RSD %) assessed. This check was used to assess the stability of the signal for each element detected by the mass spectrometer, with a low RSD % indicating a stable, less "noisy" signal and repeatable analysis. The ICP-MS was deemed to be functioning optimally when RSD was < 5 % for all measured elements. If RSD for any element(s) were significantly above this threshold, the check was repeated with adjusted nebuliser gas flow and sampling depth until acceptable RSD (< 5 % for all elements) was achieved. The $^{232}Th/^{238}U$ ratio was also monitored across the five measurements of NIST 610 as a measure of elemental fractionation – a value of close to 1 was desired, indicating minimal fractionation. This sensitivity check procedure was carried out prior to any analyses at the start of every analytical day/session.

Following the sensitivity checks, the dwell time (see **Table 2.10**) was set for each element/isotope to be measured during the standard/sample analyses, with 10 ms used for most elements and 20 ms for elements likely to be present in lower abundance such as REE's. During analytical runs, a 30 s "gas blank" interval was used prior to the first ablation and between each ablation to allow washout of any material from the previous sample from the sample cell and mass spectrometer, to prevent any blending of ablated samples.

2.5.3 - Data processing using Iolite

Data processing was carried out using the software Iolite (Paton et al., 2011). **Figures 2.5 and 2.6** illustrate the steps in the data processing procedure. The first step **(Figure 2.5)** is to define the baseline regions, avoiding the periods of washout that directly follow each analysis, which generates a green spline curve used to correct the data for background interferences. The second step **(Figure 2.6)** is selection of the integration regions (region of the trace to be used to calculate the composition) for each reference material/standard, followed by the samples. Integration regions are kept a consistent length for each analysis and exclude anomalous spikes or peaks (if present) in the traces for any analysed elements **(Figure 2.6).**

Once all integration regions have been selected, the data reduction scheme in Iolite is used to convert raw counts data into concentrations for each element measured in each sample/standard analysis. The data reduction scheme is calibrated using measurements on a standard glass during the analytical sessions (known as the calibration standard)

and an internal standard. Calcium (wt %) was used as the internal standard (see **section 2.5.6**).

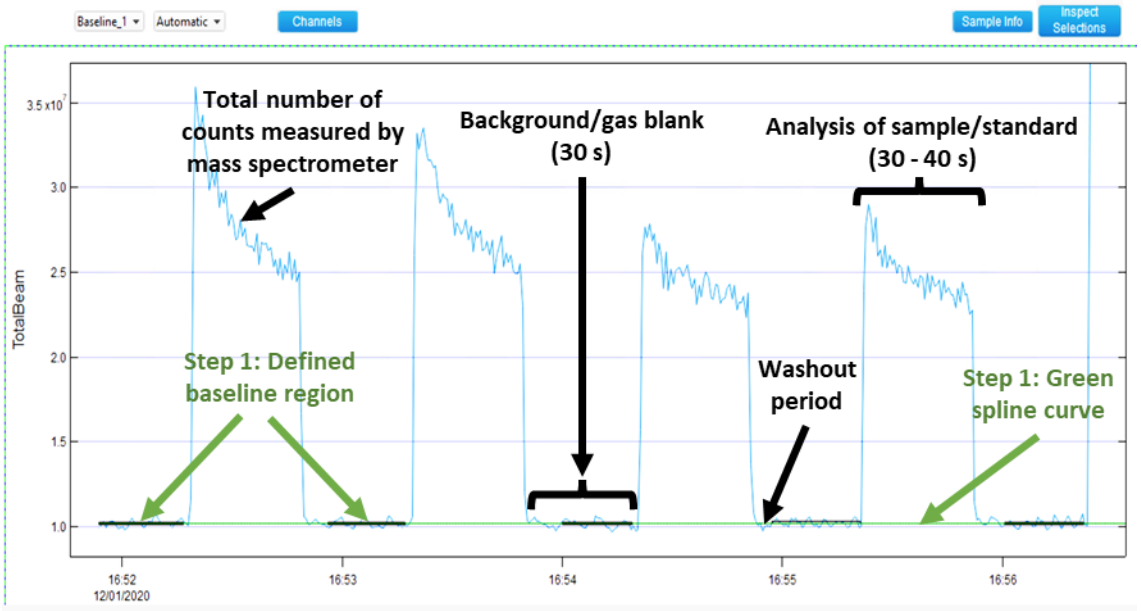

Figure 2.5: Example screenshot from the Iolite software during the "baselines" stage of data processing. Key features referred to in the text are annotated. The peaks in the blue trace show analyses of standards/samples while the troughs represent the 30 s gas blanks between each ablation (labelled).

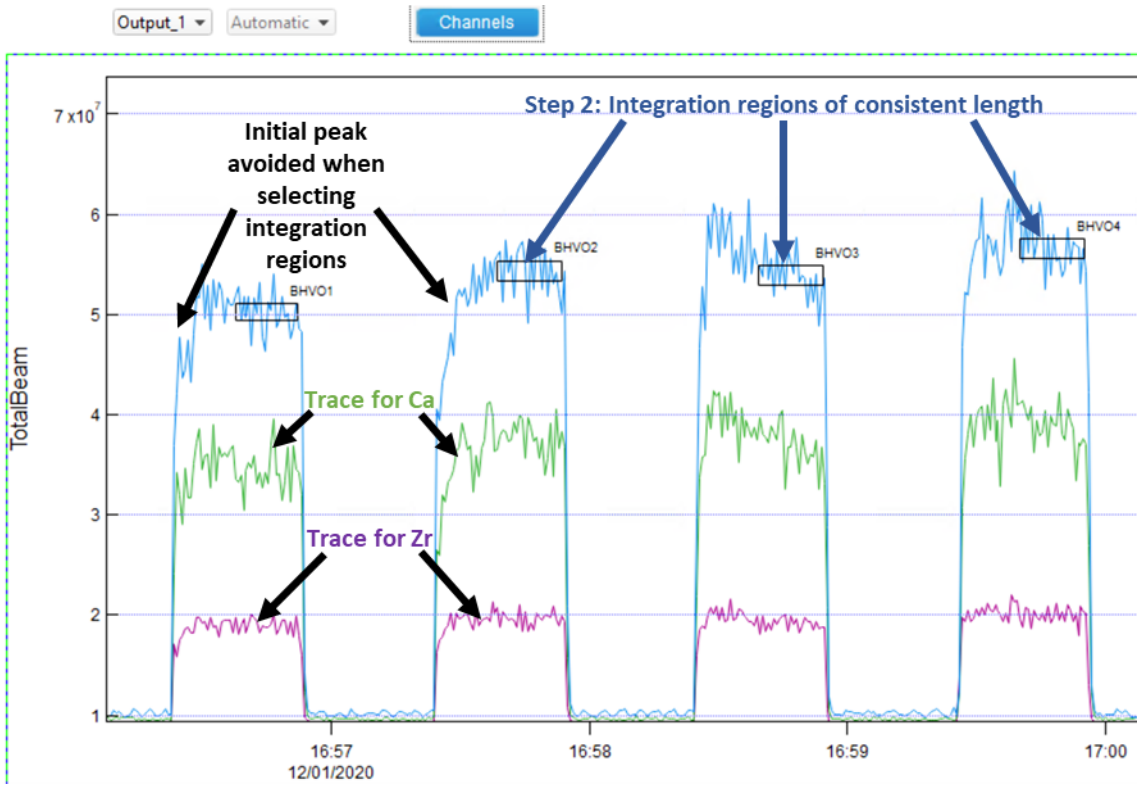

Figure 2.6: Example screenshot from the Iolite software during the "samples" stage of data processing. Key features referred to in the text are annotated. Selected integration regions cover the same part of the trace for each analysis and are kept a consistent length.

Experiments were carried out to determine the optimal reference standard glass to use as the calibration standard. The experiments showed that average measured BHVO-2G values were closer to accepted values when NIST 612 was used as the calibration standard relative to NIST 610 **(Figure 2.7).** Average BHVO-2G values showed < 15 % deviation from accepted values for most elements using NIST 612, whereas deviations of > 20 % occurred using NIST 610 for several elements including Nb, Zr and M-HREE (of particular interest in this study). Calibration using NIST 610 typically led to measured BHVO-2G values below the accepted value. The much greater difference in trace element concentrations between NIST 610 and BHVO-2G, compared to NIST 612 and BHVO-2G, may explain why NIST 610 performed less well as a calibration standard. For these reasons, NIST 612 was chosen as the calibration standard going forward for all plutonic xenolith sample analyses.

2.5.4 - Reporting of measurement uncertainty

The output from the Iolite software, of concentrations (in μg/g) of each analysed element for each sample/standard, includes an automatic calculation of the internal 2SE (standard error) on each measurement. This internal 2SE value represents uncertainty based on counting statistics. In the literature, it is more common for uncertainty on LA-ICP-MS data to be reported as a percentage value for each element, reflecting reproducibility of a secondary standard. Typically, this value is based on multiple measurements of a reference glass standard across all analytical runs and expressed as 2SD % (2 standard deviations as a percentage of the mean measured value for the standard). The 2SD % value is calculated as 2SD % = (2 SD/mean) * 100. For example, if the quoted 2SD % for La is 10 %, this is typically used to indicate that uncertainty on La measurements is ± 10 %.

In this study, either BCR-2G or BHVO-2G was used as a secondary standard (treated as an unknown) in all analytical runs. Both standards were measured across multiple runs on both analytical days on which trace element compositions in plutonic xenolith samples were measured. The calculated 2SD % uncertainty for all elements measured in mineral phases in this study is given in **section 2.5.6.** The 2SD % uncertainty on

trace element ratios (where shown in **Chapter 5**) was calculated as: 2SD (%) A/B = sqrt ((2SD % A ^2) + (2SD % B ^2)).

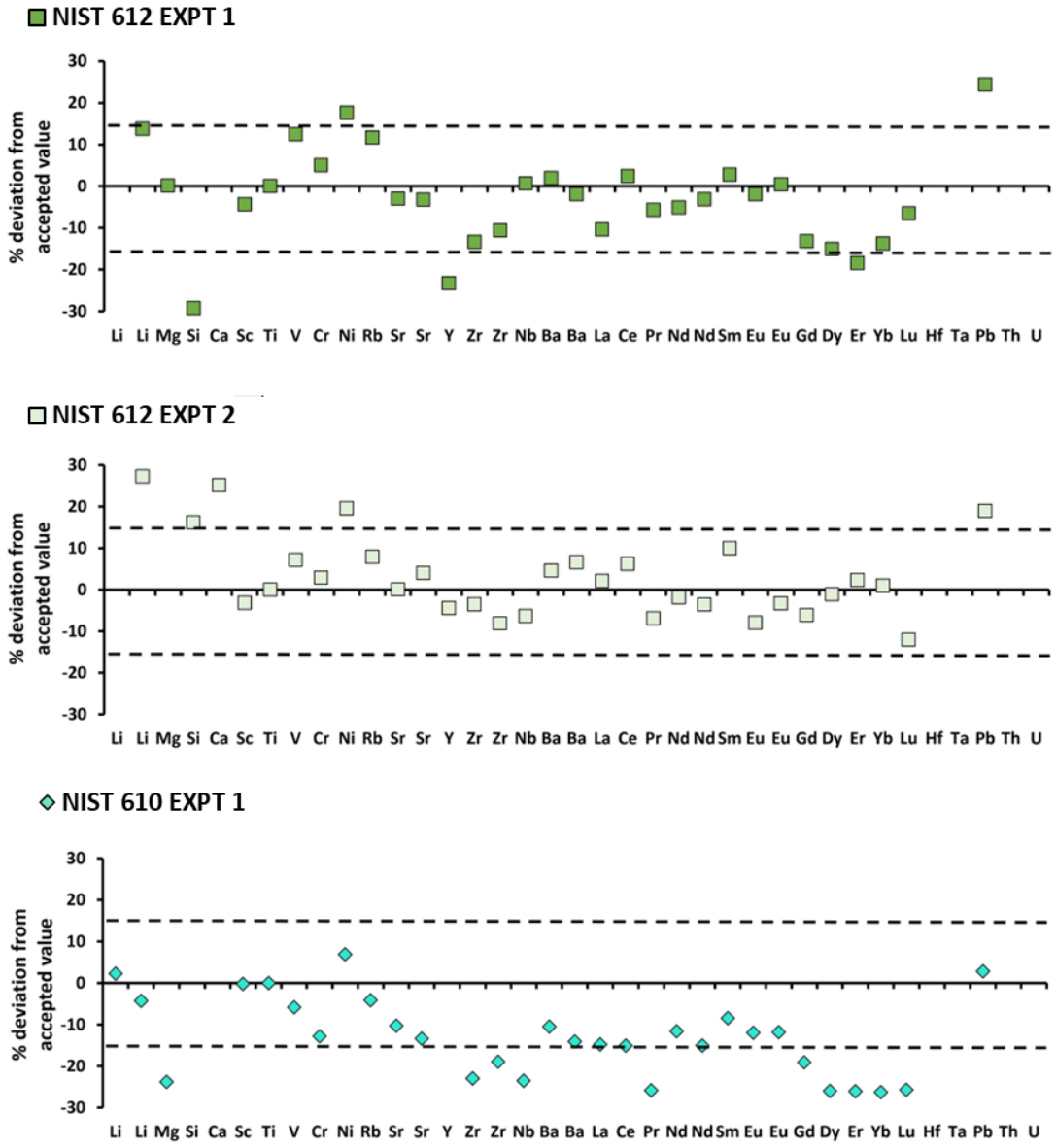

Figure 2.7: Deviation from accepted values for measurements of BHVO-2G glass standard calibrated using different NIST glass standards (NIST 610 and NIST 612). The percentage deviation from accepted value for each element was calculated as: 100 * (mean-accepted)/accepted. The mean value used in the calculation was the mean of the four BHVO-2G analyses in each experiment (NIST 612 EXPT 1 and 2, NIST 610 EXPT 1). Accepted values were taken from the GeoREM database (GeoReM - Database on geochemical, environmental and biological reference materials (gwdg.de)). Where a symbol is not visible for a given element in an experiment (e.g. Th), the deviation from accepted value is beyond the scale of the Y axis (>30 %). For some elements, two isotopes were measured to check for interferences - Li^{6} and Li^{7}, Sr^{86} and Sr^{88}, Zr^{90} and Zr^{91}, Ba^{137} and Ba^{138}, Nd^{145} and Nd^{146}, Eu^{151} and Eu^{153}. The isotope with the higher mass is to the right on the above plots. The dashed lines show a threshold of 15 %.

2.5.5 - Testing effect of ablation time on measurement uncertainty

Experiments were carried out to test the effect of ablation time on 2SD % uncertainty calculated from measurements of secondary standards. The experiments showed that deviation from accepted values was generally lower for both BHVO-2G and BCR-2G using 40 s ablation time vs 30 s **(Figure 2.8).** Calculated 2SD % values were also lower for both secondary standards using 40 s ablation time **(Figure 2.9),** below 30 % for most elements measured in contrast to much higher values (2SD % > 100 in some cases) obtained using 30 s ablation time. Following these experiments, 40 s ablation time was chosen for the plutonic xenolith sample analyses. This ablation duration balanced consistent measurements of secondary standard compositions (low 2SD %) with minimising the risk of ablating through the sample thin sections and/or into underlying crystals (not the targeted crystals) that are not visible on the thin section surface.

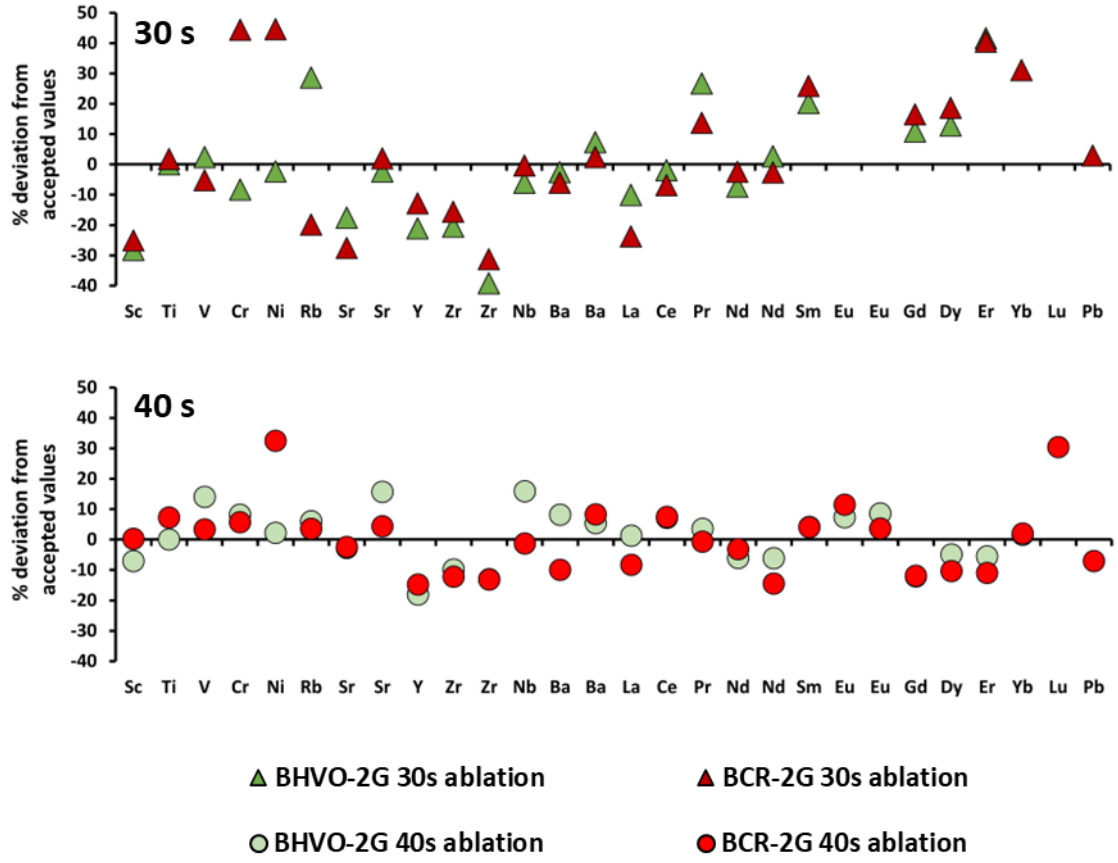

Figure 2.8: Deviation from accepted values for measurements of BHVO-2G and BCR-2G glass standards using both 30s and 40s ablation time. The percentage deviation from the accepted value for each element was calculated as: 100 * (mean-accepted)/accepted. The mean value used in the calculation was the mean of the four BHVO-2G or four BCR-2G analyses in each experiment. Accepted values were taken from the GeoREM database (GeoReM - Database on geochemical, environmental and

biological reference materials (gwdg.de)). Where a symbol is not visible for a given element in an experiment (e.g. Lu for all experiments except BCR-2G 40s ablation), the deviation from accepted value is beyond the scale of the Y axis (>50 %). For some elements, two isotopes were measured to check for interferences - Li^{6} and Li^{7}, Sr^{86} and Sr^{88}, Zr^{90} and Zr^{91}, Ba^{137} and Ba^{138}, Nd^{145} and Nd^{146}, Eu^{151} and Eu^{153}. The isotope with the higher mass is to the right on the above plots.

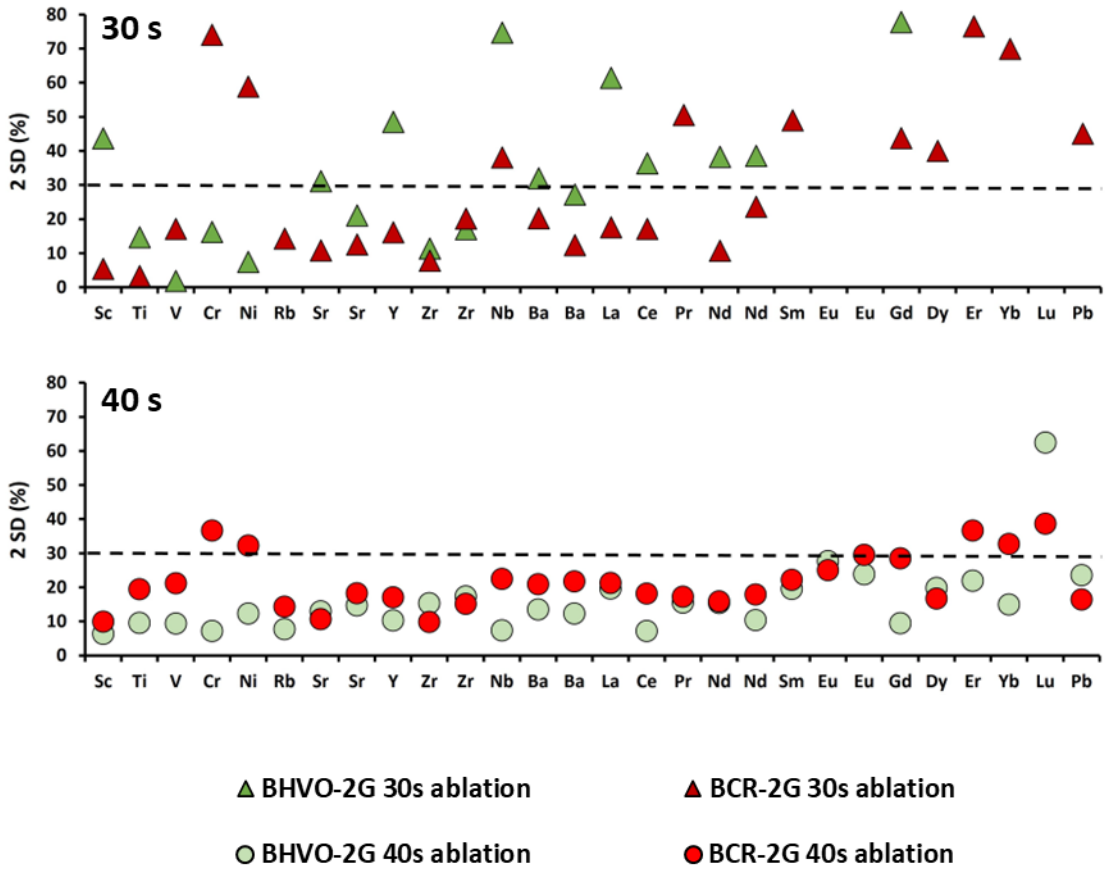

Figure 2.9: Comparison of 2SD (%) values for a range of elements measured during ablation of BHVO-2G and BCR-2G using 30s and 40s ablation time. 2SD % = (2SD/mean)*100. The 2SD and mean values used in the calculation were taken as 2SD and the mean of the four analyses of BHVO-2G or BCR-2G in each experiment. Where a symbol is not visible for a given element in an experiment (e.g. Lu for BHVO-2G 30s ablation), the 2SD % value is beyond the scale of the Y axis (>80 %). For some elements, two isotopes were measured to check for interferences - Li^{6} and Li^{7}, Sr^{86} and Sr^{88}, Zr^{90} and Zr^{91}, Ba^{137} and Ba^{138}, Nd^{145} and Nd^{146}, Eu^{151} and Eu^{153}. The isotope with the higher mass is to the right on the above plots. The dashed line shows a threshold of 30 %.

2.5.6 - Details of St Vincent plutonic xenolith sample trace element analyses

The plutonic xenolith samples were analysed over two analytical days – the Ol-CPX gabbro and poikilitic Hbl-Ol gabbro on the first day and banded Hbl-Ol gabbro and

olivine gabbro on the second day. Clinopyroxene was analysed in all samples and amphibole in the Hbl-Ol gabbros. NIST 612 was used as the calibration standard with BHVO-2G and BCR-2G measured as secondary standards (treated as unknowns). Each analytical run consisted of 16-20 individual analyses/ablations, with standard analyses bracketing the clinopyroxene and amphibole analyses. For example, the order of a typical run, in terms of samples/standards being ablated was: NIST 612 x2, BCR-2G/BHVO-2G x2, clinopyroxene/amphibole x 10, BCR-2G/BHVO-2G x2, NIST 612 x2.

The analytical runs followed the set up and measurement protocols outlined above **(sections 2.5.1 - 2.5.3).** The laser was run with a fluence of 8.09 J/cm^2, a repetition rate of 8 Hz, and a 75 µm square spot size. On the first analytical day, the gas flows were set at MFC1 = 0.7 (L/minute), MFC2 = 0.3 (L/minute), the nebuliser gas flow at 0.82 (L/minute) and the sampling depth at a value of 190. On the second analytical day, the gas flows were set at MFC1 = 0.7 (L/minute), MFC2 = 0.3 (L/minute), the nebuliser gas flow at 1 (L/minute) and the sampling depth at a value of 130. The ablation time was set at 40 s for all analyses of both samples/target crystals and standards. The following suite of elements/isotopes were measured across all analytical runs: Li^6, Li^7, Mg^{25}, Si^{29}, Ca^{43}, Ca^{44}, Sc^{45}, Ti^{47}, V^{51}, Cr^{52}, Ni^{60}, Rb^{85}, Sr^{86}, Sr^{88}, Y^{89}, Zr^{90}, Zr^{91}, Nb^{93}, Ba^{137}, Ba^{138}, La^{139}, Ce^{140}, Pr^{141}, Nd^{145}, Nd^{146}, Sm^{147}, Eu^{151}, Eu^{153}, Gd^{157}, Dy^{163}, Er^{166}, Yb^{173}, Lu^{175}, Pb^{208}, Th^{232}, U^{238}. For some elements, two isotopes were measured to check for potential interferences. A dwell time of 20 ms was used for Ti, Zr and La to U, with 10 ms used for all other elements. Poor data (significant deviation from accepted values, high 2SD %) was obtained for the secondary standards for Li, Mg and Si, (most likely due to high background counts and interferences) hence the LA-ICP-MS data for these elements is not considered further in this study.

Calcium (wt %) was used as the internal standard for data processing in Iolite. A compilation of EPMA data for Lesser Antilles plutonic xenolith clinopyroxene and amphibole is shown in **Figure 2.10.** Almost all clinopyroxene and amphibole CaO wt % data fall within a narrow range of 20.5-24.5 % for clinopyroxene and 10.5-13 % for amphibole. The EDS major element data obtained in this study from the target crystals in the St Vincent plutonic xenoliths falls within the narrow ranges listed above for CaO wt % (**Figure 2.3**). Due to the low degree of CaO wt % variation, a constant Ca wt % value was used for the data processing. A typical value of 16 wt % Ca (equivalent to

22.5 wt % CaO) was used for clinopyroxene and 8.6 wt % Ca (equivalent to 12 wt % CaO) for amphibole.

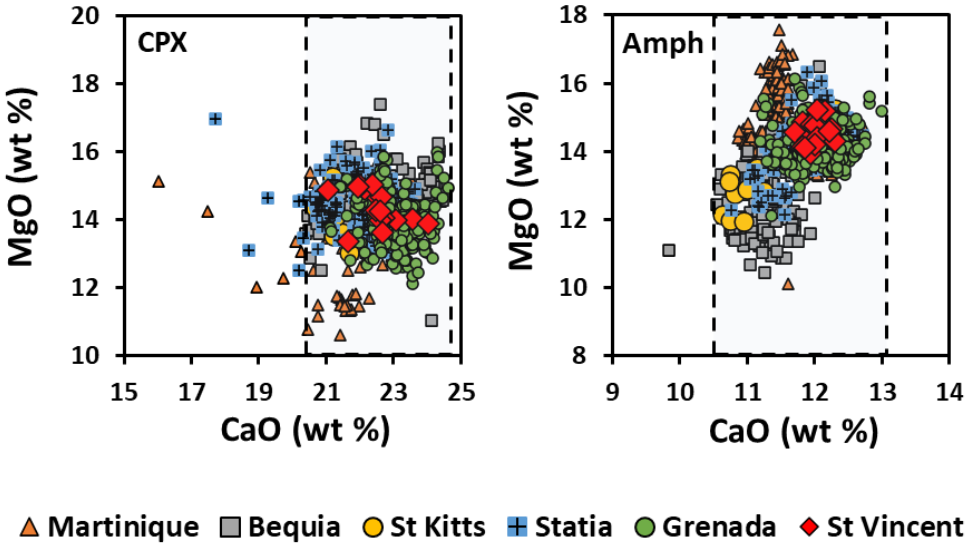

Figure 2.10: MgO vs CaO for clinopyroxene (CPX) and amphibole (Amph) in plutonic xenoliths from six islands in the LAA, measured by EPMA. The dashed lines outline the narrow range of CaO contents for majority of analyses. Data sources: Martinique – Cooper et al., (2016). Bequia – Camejo-Harry et al., (2018). St Kitts – Melekhova et al., (2017). Statia – Cooper et al., (2019). Grenada – Stamper et al., (2014). St Vincent – Tollan et al., (2012).

To investigate whether using a fixed average Ca wt % value is justified, it was tested whether variation in this value would introduce a larger analytical uncertainty than both the internal 2SE and 2SD % reproducibility on the secondary standard. Ca wt % contents were extracted from the AzTec Tru-Q data for the clinopyroxene and amphibole with the highest and lowest CaO contents. The maximum deviation from the value of 16 wt % Ca used for the data processing is 14.64 wt % Ca in the clinopyroxene with the lowest CaO, a difference of 8.5 relative %. For amphibole, the maximum difference was 7 relative % (8 wt % Ca vs 8.6). Hence, the maximum uncertainty that would be introduced to the data from variation in Ca wt % values is 8.5 %. The 2SD % reproducibility on the secondary standard is higher than 8.5 % for almost all elements measured (**Table 2.11**), while the internal 2SE on most measurements is typically around 10 %. Therefore, any uncertainty introduced by Ca wt % variation is encompassed by these greater sources of uncertainty and falls within the bounds of the error bars in the plots in **Chapter 5** where the data is reported.

Figure 2.11 illustrates this point. To assess whether uncertainty from Ca wt % variation could affect data interpretation and the ability to distinguish crystal populations, the most trace element depleted clinopyroxene compositions from **Chapter 5** were shifted up by 8.5 % and the most enriched down by 8.5 %. The shifted values fall within the bounds of the error bars (shown by the purple box), illustrating that the 2SD % uncertainty (and internal 2SE which is also typically around 10 %) represents a greater source of uncertainty than Ca wt % variation. It is also clear from the plot that the shift in values due to possible Ca wt % variation does not prevent the crystal populations being distinguished. This test justifies the use of a constant Ca wt % value for the data processing and demonstrates that this decision does not affect the interpretation of the data in **Chapter 5**.

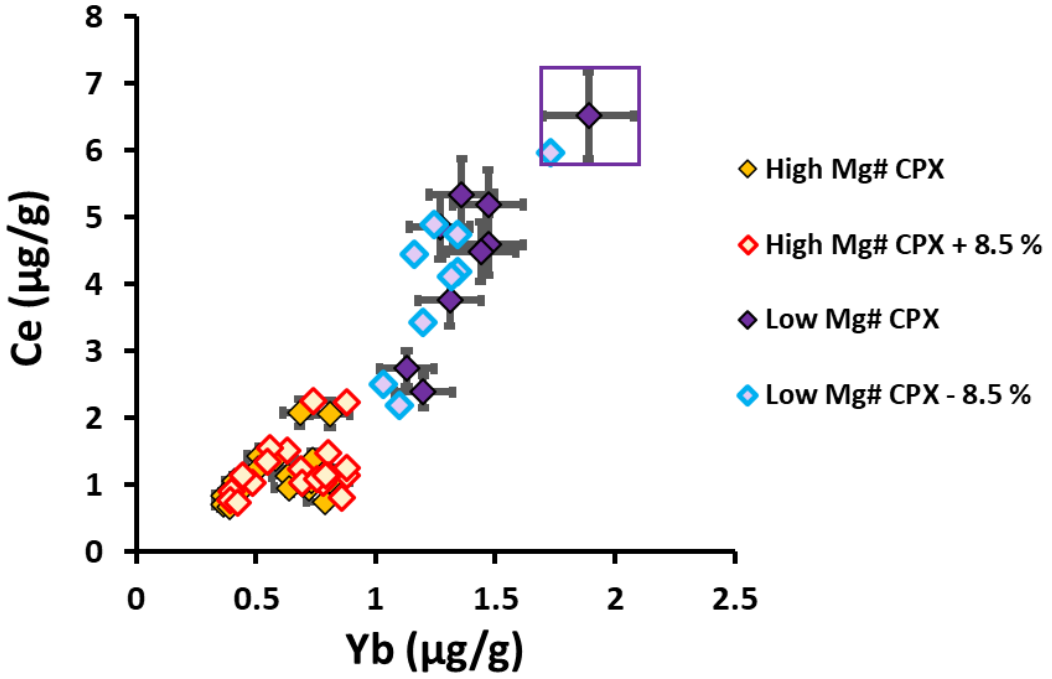

Figure 2.11: Ce vs Yb for the most trace element enriched and depleted clinopyroxene populations (low Mg# CPX and high Mg# CPX) from the plutonic xenoliths analysed in **Chapter 5**, processed using 16 wt % Ca, with error bars equivalent to 2SD % uncertainty (10 % for Ce and Yb). Also shown are the measured clinopyroxene Ce and Yb values shifted by ± 8.5 %, equivalent to the maximum uncertainty that would be introduced by Ca wt % variation.

Uncertainty on clinopyroxene and amphibole trace element data in **Chapter 5** is provided both as internal 2SE as calculated by Iolite and 2SD % for each element. The 2SD % values are based on all measurements of BCR-2G (n=32) across both analytical

days. Calculated 2SD % uncertainties are shown in **Table 2.11** and are less than 15 %, excluding Ti, Cr and Lu. Where more than one isotope of an element was measured, the isotope with the lower 2SD % uncertainty was used for the reported clinopyroxene and amphibole data in **Chapter 5.**

Element	2SD (%)	Element	2SD (%)
Sc	5.72	Ce	9.64
Ti	21.95	Pr	10.85
V	12.06	Nd^{145}	10.99
Cr	15.96	Nd^{146}	8.42
Ni	12.91	Sm	8.18
Rb	10.57	Eu^{151}	8.05
Sr^{86}	7.16	Eu^{153}	11.15
Sr^{88}	11.19	Gd	10.94
Y	8.89	Dy	9.08
Zr^{90}	7.88	Er	12.62
Zr^{91}	7.16	Yb	10.20
Nb	9.26	Lu	22.81
Ba^{137}	10.45	Pb	14.63
Ba^{138}	27.65	Th	9.29
La	9.98	U	13.98

Table 2.11: Calculated 2SD % uncertainty for all elements (and isotopes of elements) measured during trace element analyses of St Vincent plutonic xenolith clinopyroxene and amphibole. 2SD % uncertainty values are based on 32 measurements of BCR-2G throughout the analytical sessions. 2SD % = (2SD/mean)*100. These values represent reproducibility of BCR-2 measurements.

Chapter 3 – Plutonic xenolith petrography

A version of part of this chapter (section 3.1) was published as supplementary material to the following publication in Frontiers in Earth Science: Brown, J. R., Cooper, G. F., Nowell, G. M., Macpherson, C. G., Neill, I., & Prytulak, J. (2021). Isotopic compositions of plagioclase from plutonic xenoliths reveal crustal assimilation below Martinique, Lesser Antilles arc. *Frontiers in Earth Science*, *9*, 682583.

Author contributions: The work for this chapter is my own, conducted with support of my co-authors that would be usual of a supervisory team.

This chapter presents detailed petrographic descriptions of the plutonic xenoliths from Martinique and St Vincent for which geochemical data is presented in **Chapters 4 and 5**. Details of sampling locations and justification for the choice of samples for geochemical investigation are provided in context in the relevant chapters. The contents of this chapter are referred to within the text in **Chapters 4 and 5**.

3.1 – Martinique plutonic xenoliths

In **Chapter 4**, Sr isotopic compositions of plagioclase were analysed in five Martinique plutonic xenoliths (previously characterized petrographically by Cooper et al., 2016) and one lava. Detailed petrographic descriptions of these samples are given below. Plagioclase Sr isotopic compositions were also analysed in a single plutonic xenolith from St Vincent in **Chapter 4** (previously characterized petrographically by Tollan et al., 2012), which is described in this section with the Martinique plutonic xenoliths.

Petrographic observations on plutonic xenoliths including rock type, mineralogy, crystal size and habit, crystallization sequence and textural features are those of Cooper et al., (2016) (Martinique plutonic xenoliths) and Tollan et al, (2012) (St Vincent

plutonic xenolith VS36). Xenoliths were classified based on mineral assemblage using the scheme of Streckeisen (1976), and textural features. Modal mineralogy of each sample is shown in **Figure 3.1** and key characteristics summarized in **Table 3.1**. Electron microprobe data reported by Cooper et al., (2016) demonstrated that some Martinique plutonic xenolith plagioclase show chemical zonation. In this study, SEM analyses were used to confirm the nature of zoning and provide additional information on the spatial extent of zones in plagioclase in selected samples.

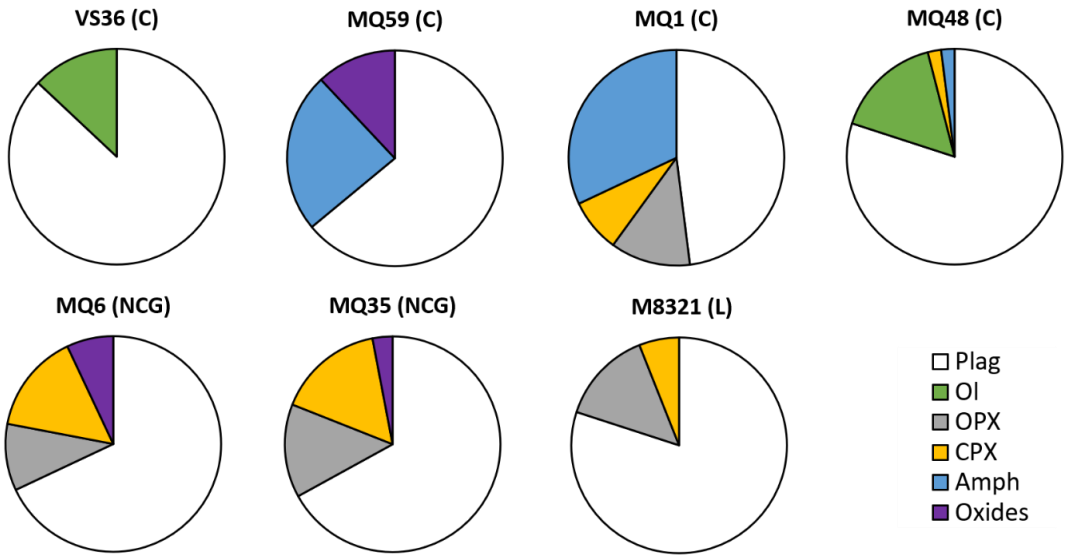

Figure 3.1: Mineral modal abundances of Martinique plutonic xenoliths (plus one St Vincent plutonic xenolith and one Martinique lava) investigated for plagioclase Sr isotopic compositions in **Chapter 4** (excluding interstitial melt). C = cumulate, NCG = non cumulate gabbro, L = lava. Modal abundances estimated by point counting on thin sections by Cooper et al., (2016) and Tollan et al., (2012). See **Table 3.1** for modal abundance percentages.

Backscattered electron (BSE) images and energy dispersive X-ray spectroscopy (EDS) data were collected using a Hitachi SU70 SEM. Prior to SEM analysis, thin sections were coated with a conductive layer of carbon. High resolution BSE images were acquired at an accelerating voltage of 15 kV and a working distance of 15 mm, using an 8 µs dwell time. Magnification was adjusted according to the size of crystal being imaged. Chemical data was collected using EDS. A linescan, showing relative changes in chemical composition along a traverse, was acquired for all identified target crystals. Linescans were acquired over 100 s, using 100 points per line of 1.2 micron size, and a dwell time of 32 microseconds per point. If both the BSE image and linescan confirmed zoning in a target crystal, a chemical map was made to show spatial extent

of the zoning. Chemical maps were acquired over 800 s, using a grid of 1200 x 900 points of 1.2 micron size and a dwell time of 256 microseconds per point.

Sample code	*Classification*	*Mineral assemblage*	*Texture*	*Plagioclase An content*	*Temperature (°C)*	*Pressure (kbar)*	*No. of Pl analysed*
MQ48 (C)	Troctolite	Pl (80 %) Ol (16 %) CPX (2 %) Amph (2 %)	Orthocumulate		1050-1150	≤ 4	4
MQ1 (C)	Hornblende Gabbronorite	Pl (48 %) Amph (32 %) OPX (12 %) CPX (8 %)	Adcumulate	83-96	790-1052	≤ 4	3
MQ59 (C)	Hornblende Gabbro	Pl (64 %) Amph (24 %) Ox (12 %)	Orthocumulate	92-95	865-1083	≤ 4	5
VS36 (C)	Olivine gabbro	Pl (87 %) Ol (13 %)	Orthocumulate	92-95	967-1210	1.7	5
MQ6 (NCG)	Gabbronorite	Pl (68 %) CPX (15 %) OPX (10 %) Ox (7 %)	Non-cumulate	Cores = 57-89 Rims = 56-60	894-909	≤ 4 (~2)	4
MQ35 (NCG)	Gabbronorite	Pl (67 %) CPX (16 %) OPX (14 %) Ox (3 %)	Non-cumulate				3
M8321 (L)	Two-pyroxene Andesite	Pl (80 %) OPX (14 %) CPX (6 %).	Porphyritic lava				3

Table 3.1: Summary of petrographic characteristics of Martinique plutonic xenoliths (plus one St

Vincent plutonic xenolith and one Martinique lava)**.** Cumulate and NCG classification, assemblage, texture, and plagioclase An contents, temperature and pressure estimates (where available) from Melekhova et al., (2019), Cooper et al., (2016), and Tollan et al., (2012).

The SEM EDS data was obtained without calibration standards and does not reflect a true measurement of chemical composition. The data simply shows changes in the **relative** abundance of calcium and sodium within plagioclase, hence was used only to identify and constrain the spatial extent of more calcic/sodic zones.

It should be noted that sample thin sections were 100 µm thick, hence in XPL images, plagioclase shows higher birefringence colours than would be observed in standard 30 µm thin sections. The Sr isotopic composition of each analysed plagioclase (from **Chapter 4**) is shown in the box next to the relevant crystal in the thin section images. Petrographic descriptions of the wider suite of Martinique plutonic xenoliths for which whole rock Sr-Nd-Pb isotopic data is presented in **Chapter 4** can be found in Cooper et al., (2016).

3.1.1 - Petrographic descriptions of cumulate plutonic xenoliths

MQ48 – Troctolite (Figure 3.2)

Mostly subhedral plagioclase (typically ≥ 2 mm) dominates, present alongside 0.5-2.5 mm subhedral olivine and minor hornblende and clinopyroxene. The crystallization sequence is olivine -> plagioclase -> hornblende/clinopyroxene. The sample has an orthocumulate texture with sporadic pockets of dark grey vesicular interstitial melt (approximately 1 % of the rock) between crystals. Two plagioclase size populations exist: those > 2 mm that form the main cumulate framework, along with < 2 mm interstitial crystals. Hornblende and clinopyroxene are also interstitial phases. Plagioclase are unzoned expect for < 10 µm normally zoned rims in contact with interstitial melt (**Figure 3.3, b**). Some plagioclase in contact with interstitial melt have small embayments **(Figure 3.3, a).**

MQ1 – Hornblende gabbronorite (Figure 3.4)

The mineral assemblage is dominated by subhedral to anhedral plagioclase (0.5 – 5 mm) and hornblende (≤ 1 mm), along with orthopyroxene and clinopyroxene (0.5-2.5 mm). The crystallization sequence is plagioclase/hornblende -> orthopyroxene -> clinopyroxene. The majority of the sample displays an adcumulate texture with some

areas displaying a granoblastic texture. Plagioclase are either unzoned (approximately 35 %) or have normally zoned rims, as shown by microprobe data of Cooper et al., 2016 and SEM analyses (this study). SEM linescan traverses show normally zoned rims of 30-50 µm width **(Figure 3.5),** narrower than can be targeted by micromilling. Inclusion trails (consisting of melt inclusions and Fe-oxides) are present in some larger plagioclase. Inclusions were carefully avoided during micromilling.

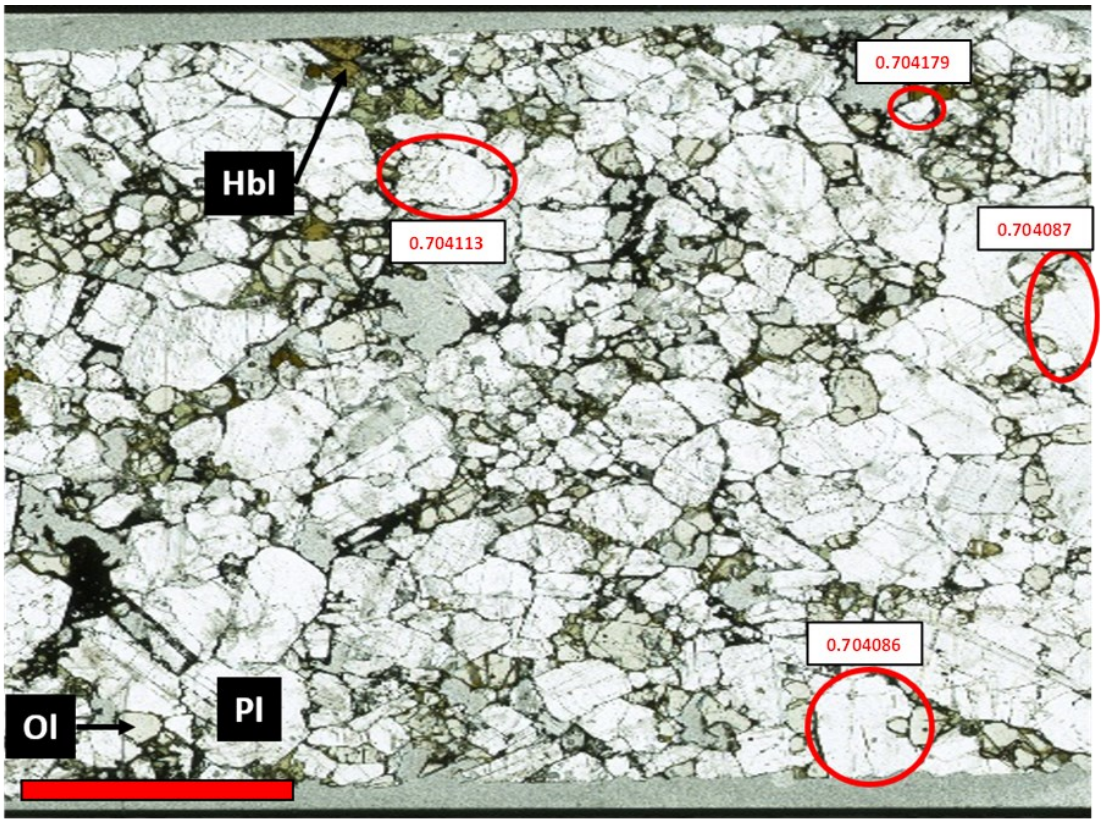

Figure 3.2: MQ48 thin section (PPL) with analysed plagioclase circled. Red scale bar = 5 mm. Section thickness = 100 µm.

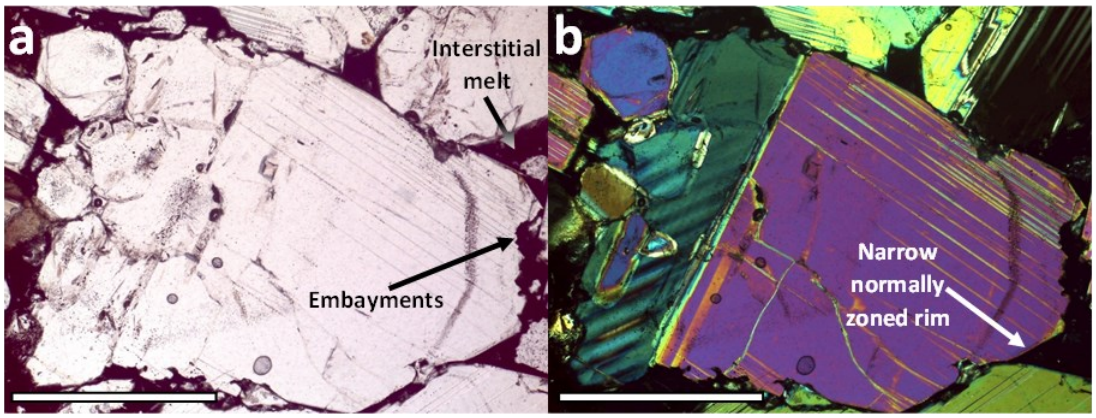

Figure 3.3: A) PPL and **B)** XPL images of a typical plagioclase from MQ48. Key features including small embayments and a narrow rim where the crystal contacts the interstitial melt are labelled. White

scale bar = 1 mm. Unusually high birefringence colours in b) are due to the 100 µm thickness of the section.

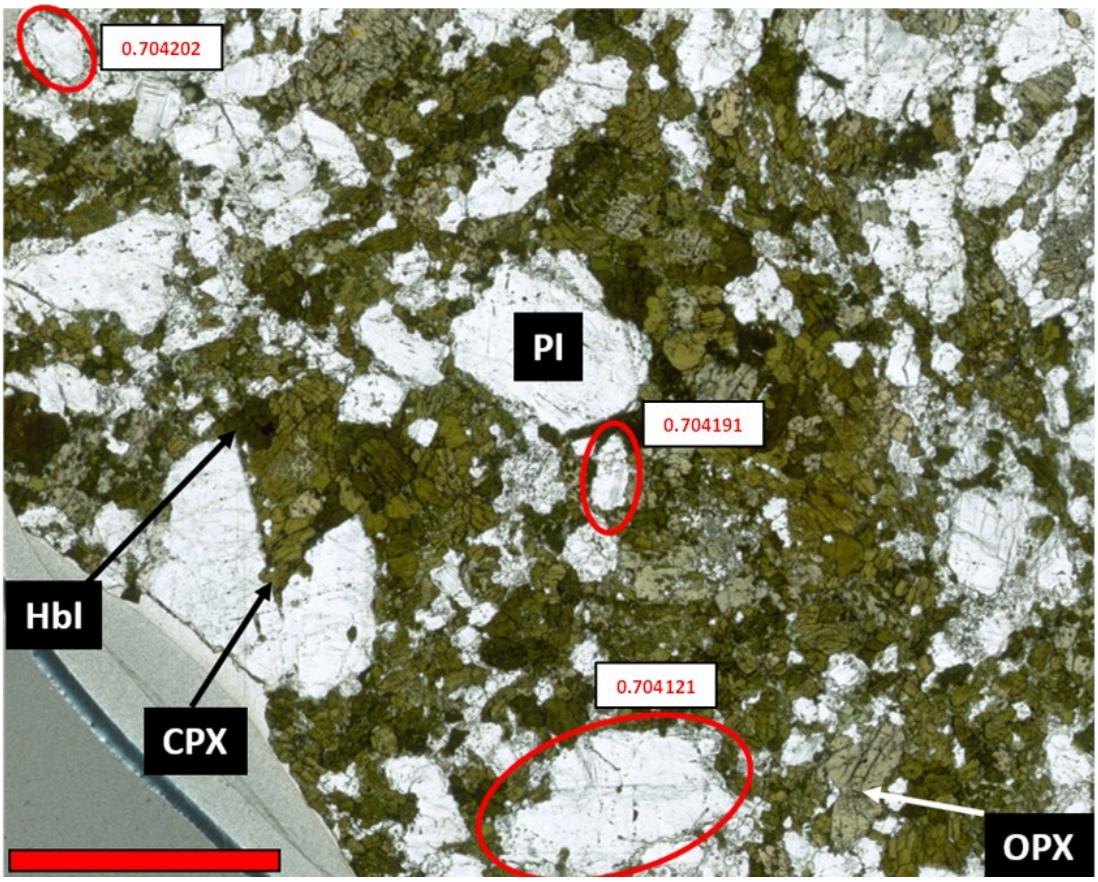

Figure 3.4: MQ1 thin section (PPL) with analysed plagioclase circled. Red scale bar = 5 mm. Section thickness = 100 µm.

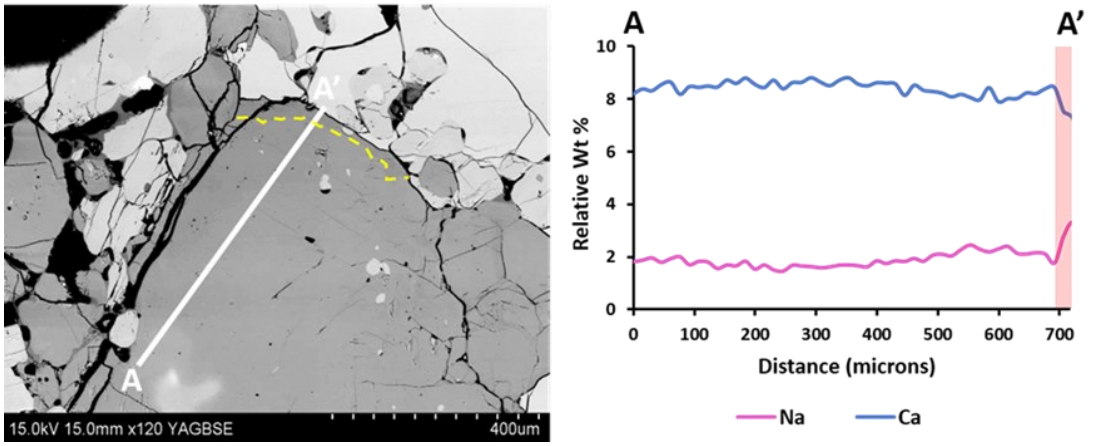

Figure 3.5: BSE image of example zoned plagioclase with location of linescan traverse marked (line A-A'), along with data from linescan traverse, showing relative wt % Na and Ca. Note the significant relative decrease in Ca and increase in Na at the rim (red band) indicating normal zoning. Extent of zoned rim of crystal marked by yellow dashed line.

MQ59 – Hornblende gabbro (Figure 3.6)

Plagioclase, mostly subhedral (1-5 mm), is modally dominant, alongside poikilitic subhedral amphibole (2-5 mm) containing < 0.5 mm plagioclase inclusions, and minor oxides. The crystallization sequence is oxides -> hornblende/plagioclase. The sample has an orthocumulate texture with approximately 15 % dark grey, highly vesicular interstitial melt. Plagioclase are unzoned except for when in contact with the interstitial melt, where < 10 µm normally zoned rims are observed. Plagioclase in contact with interstitial melt often have small embayments.

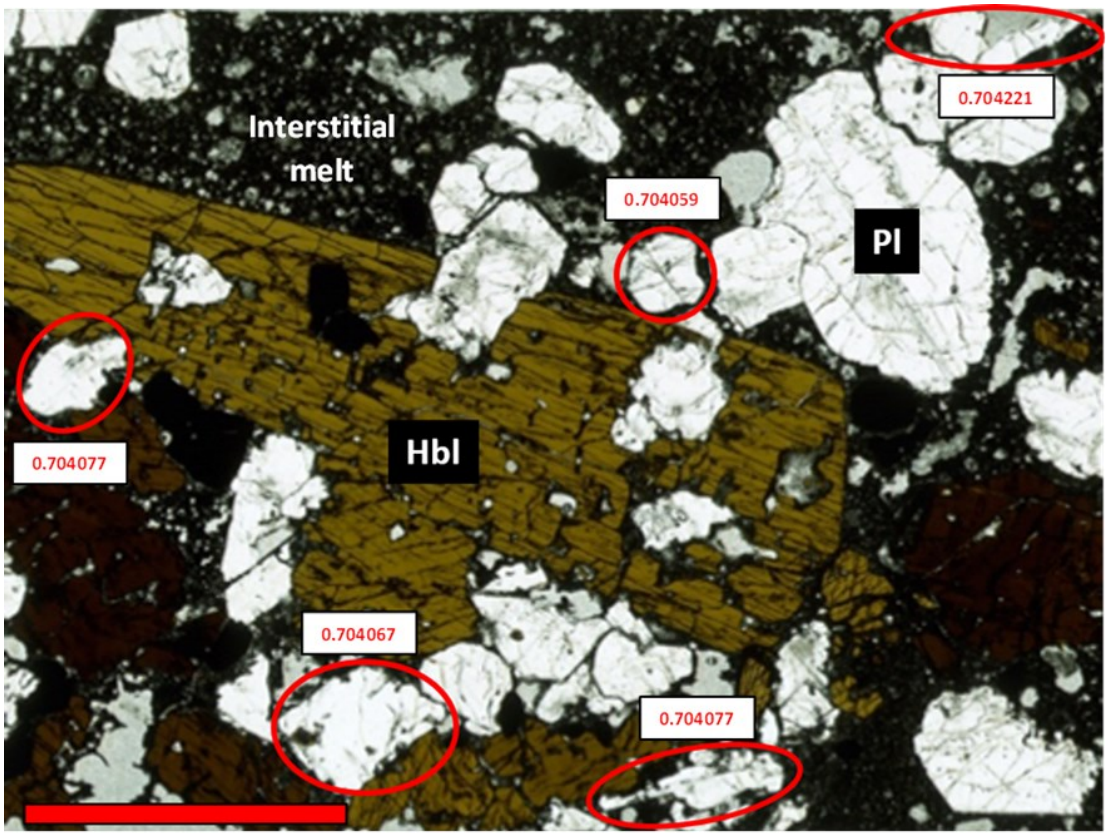

Figure 3.6: MQ59 thin section (PPL) with analysed plagioclase circled. Red scale bar = 5 mm. Section thickness = 100 µm.

VS36 – Olivine gabbro (Figure 3.7)

Majority of the rock consists of 0.5-2 mm subhedral to euhedral plagioclase, with sparse 0.5-2 mm subhedral olivine which precedes plagioclase in the crystallization sequence. The sample has an orthocumulate texture with approximately 35 % dark grey, highly vesicular interstitial melt. Plagioclase are unzoned except for < 10 µm rims in contact with interstitial melt.

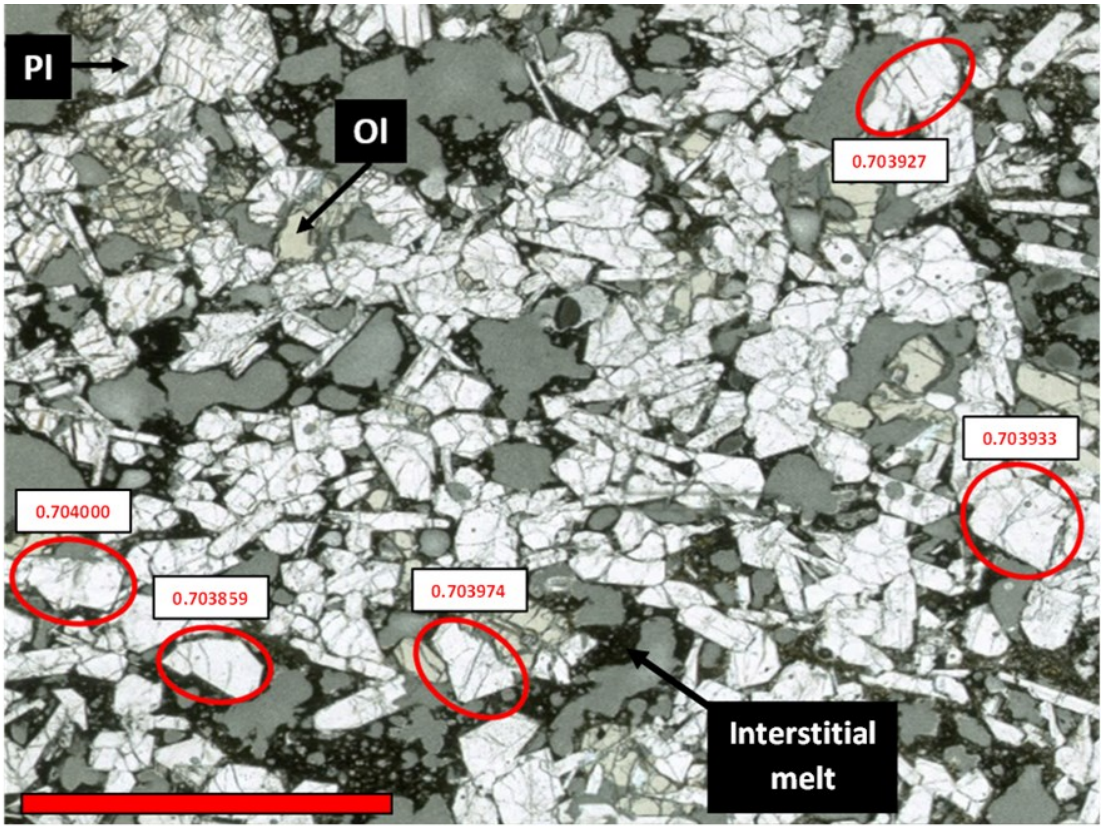

Figure 3.7: VS36 thin section (PPL) with analysed plagioclase circled. Red scale bar = 5 mm. Section thickness = 100 µm.

3.1.2 – Petrographic descriptions of non-cumulate gabbro plutonic xenoliths

MQ6 – Gabbronorite (Figure 3.8)

Subhedral plagioclase (0.5-2.5 mm) is modally dominant, followed in abundance by anhedral to subhedral 0.5-4 mm clinopyroxene and orthopyroxene, with minor oxides. The crystallization sequence is plagioclase -> oxides -> orthopyroxene/clinopyroxene. Some regions of the sample show granoblastic texture. Approximately 50 % of plagioclase are normally zoned (see **Figure 3.9, b** and chemical maps in **Figure 3.10, a-c**), with zoning typically confined to larger crystals > 1 mm. Several cores appear patchy and/or have embayments **(Figure 3.9, c)**. Almost all plagioclase contain inclusions (**Figure 3.9, a**), which in some are concentrated in trails or bands around clear cores. Inclusions are either melt or Fe-oxides, typically < 20 µm across, and were carefully avoided during micromilling.

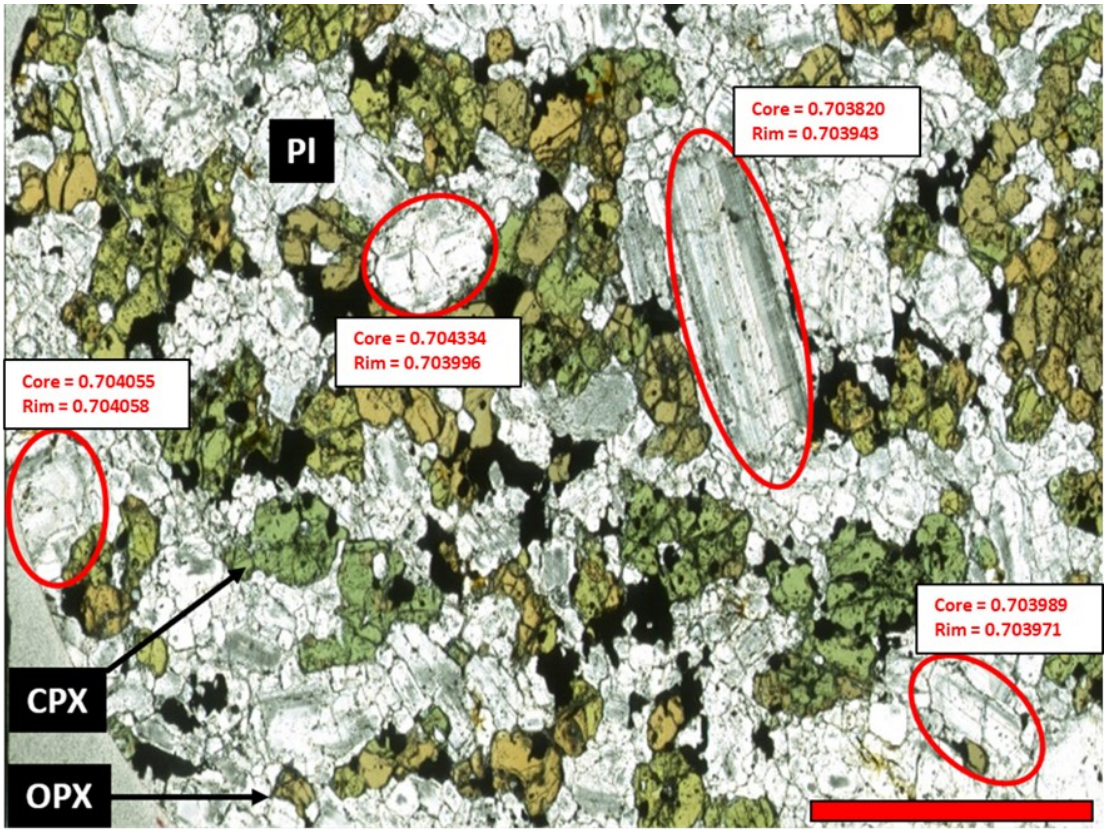

Figure 3.8: MQ6 thin section (PPL) with analysed plagioclase circled. Red scale bar = 5 mm. Section thickness = 100 µm.

MQ35 – Gabbronorite (Figure 3.11)

Plagioclase (1-5 mm), orthopyroxene (1-2 mm) and clinopyroxene (1-7 mm) are present in decreasing order of abundance, along with minor oxides. Most plagioclase are subhedral and pyroxenes subhedral to anhedral. The crystallization sequence is plagioclase -> oxides -> orthopyroxene/clinopyroxene. Some regions of the sample show granoblastic texture. Approximately 40 % of plagioclase are normally zoned ((see **Figure 3.12, a** and chemical maps in **Figure 3.13, a-c**), with zoning typically confined to larger crystals > 2 mm. Several cores appear patchy and/or have embayments **(Figure 3.12, b).** In contrast to MQ6, most plagioclase contain only sparse inclusions of melt and Fe-oxides, with a few displaying trails or inclusion rich bands. Several plagioclase have fuzzy overgrowths towards the rim. MQ35 shows some alignment of crystals defined by elongate plagioclase and occasional bent plagioclase twins are present, indicating minor compression or deformation.

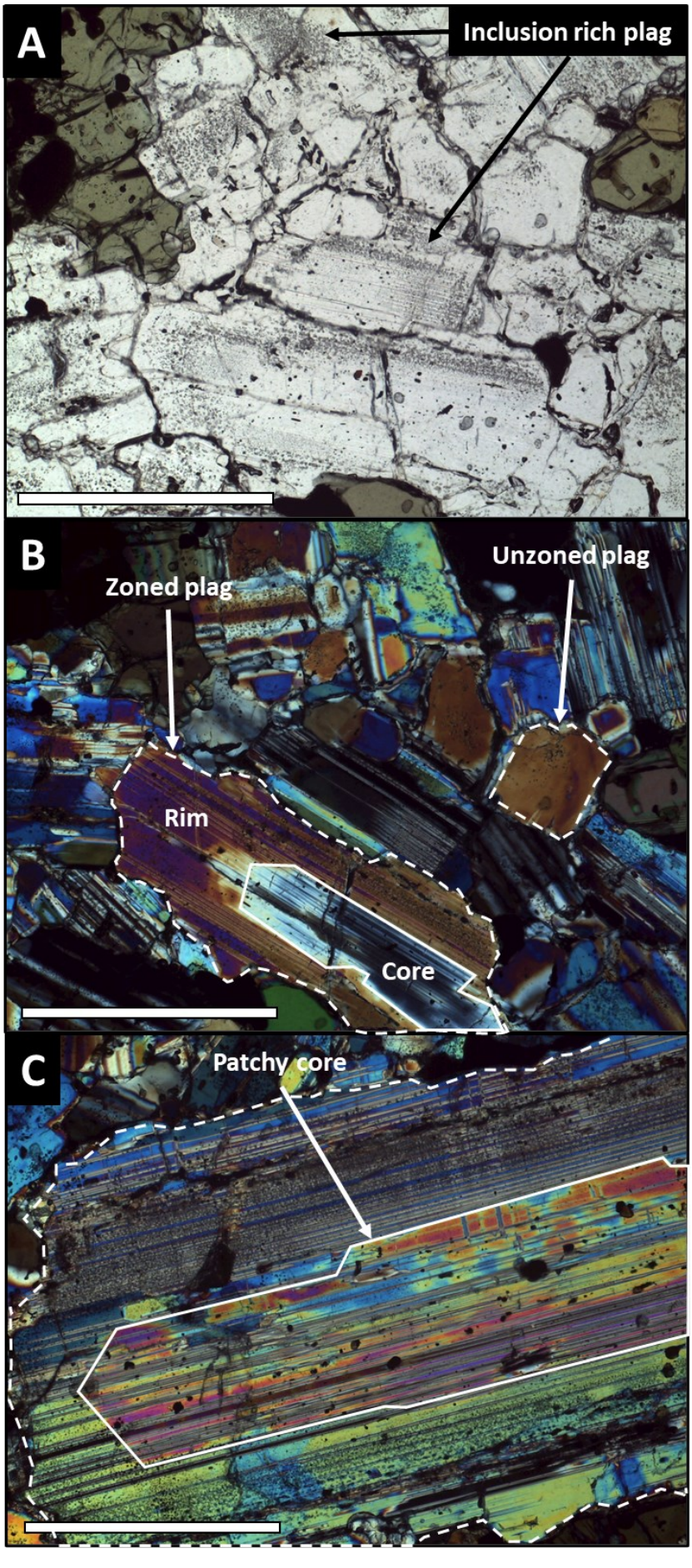
A
Inclusion rich plag
B
Zoned plag
Unzoned plag
Rim
Core
C
Patchy core

Figure 3.9: A) PPL image of MQ6, highlighting inclusions in plagioclase. **B)** XPL image of MQ6, highlighting typical examples of zoned and unzoned plagioclase. **C)** Example of zoned plagioclase (outlined with dashes) with patchy core (3rd order pink birefringence). White scale bar = 1 mm. Unusually high birefringence colours in **B)** and **C)** are due to the 100 µm thickness of the section.

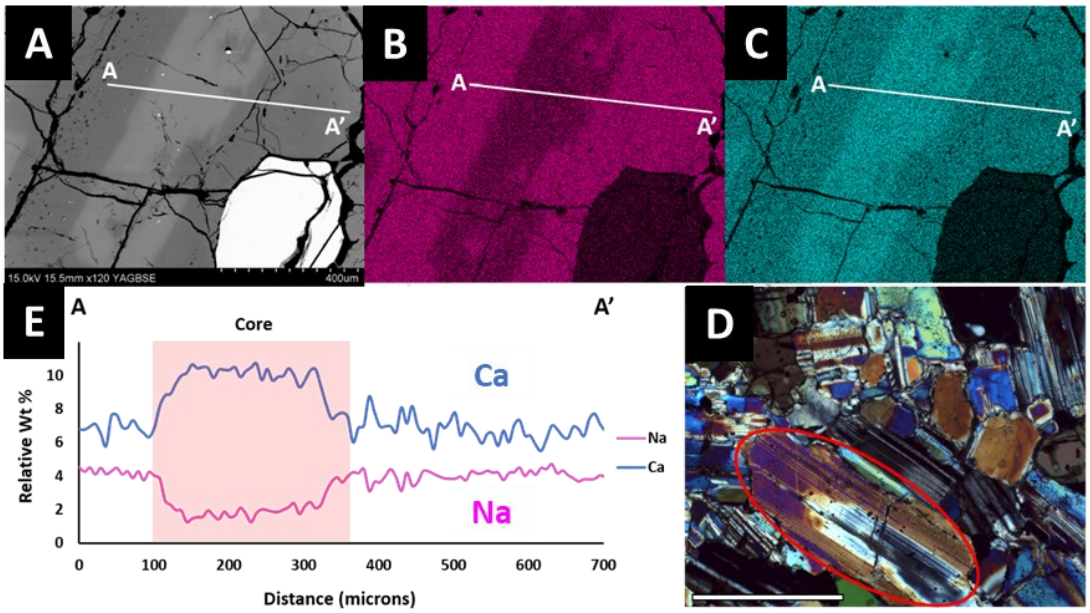

Figure 3.10: A) BSE image of zoned plagioclase with location of linescan traverse marked (line A-A'). **B)** and **C)** Chemical maps for Na and Ca respectively. Areas of the crystal with a relatively higher concentration of the element being mapped show up brighter. This shows the extent of the high Ca, low Na core and low Ca, high Na rim (normal zoning). **D)** XPL image of the analysed plagioclase (circled). White scale bar = 1 mm. Section thickness = 100 µm. **E)** Data from linescan traverse, showing relative wt % Na and Ca. Note the significant increase in Ca and decrease in Na across the core (red band) confirming normal zoning.

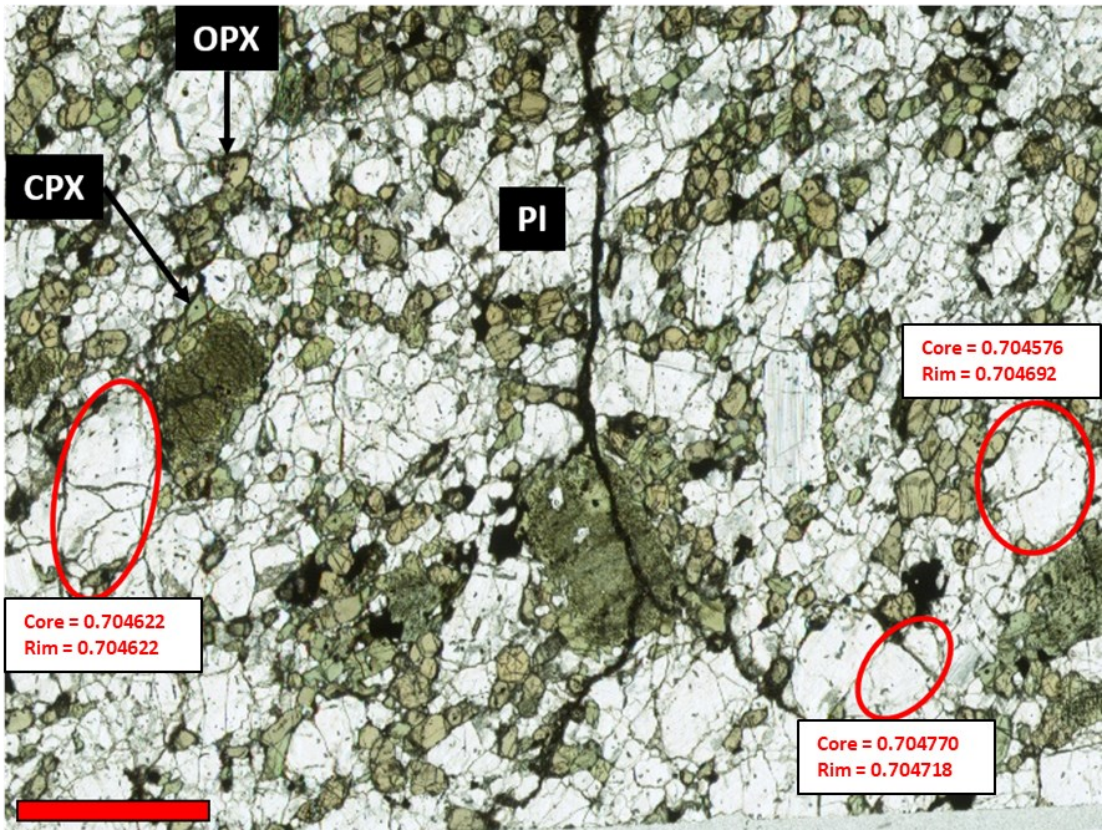

Figure 3.11: MQ35 thin section (PPL) with analysed plagioclase circled. Red scale bar = 5 mm. Section thickness = 100 µm.

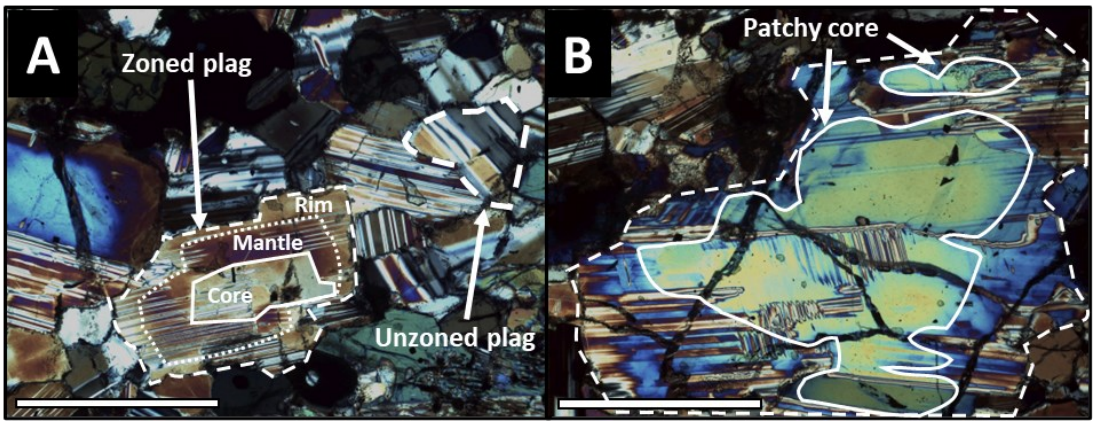

Figure 3.12: A) XPL image of MQ35, highlighting typical examples of zoned and unzoned plagioclase. **B)** Example of zoned plagioclase (outlined with dashes) with patchy core (outlined). White scale bar = 1 mm. Unusually high birefringence colours are due to the 100 µm thickness of the section.

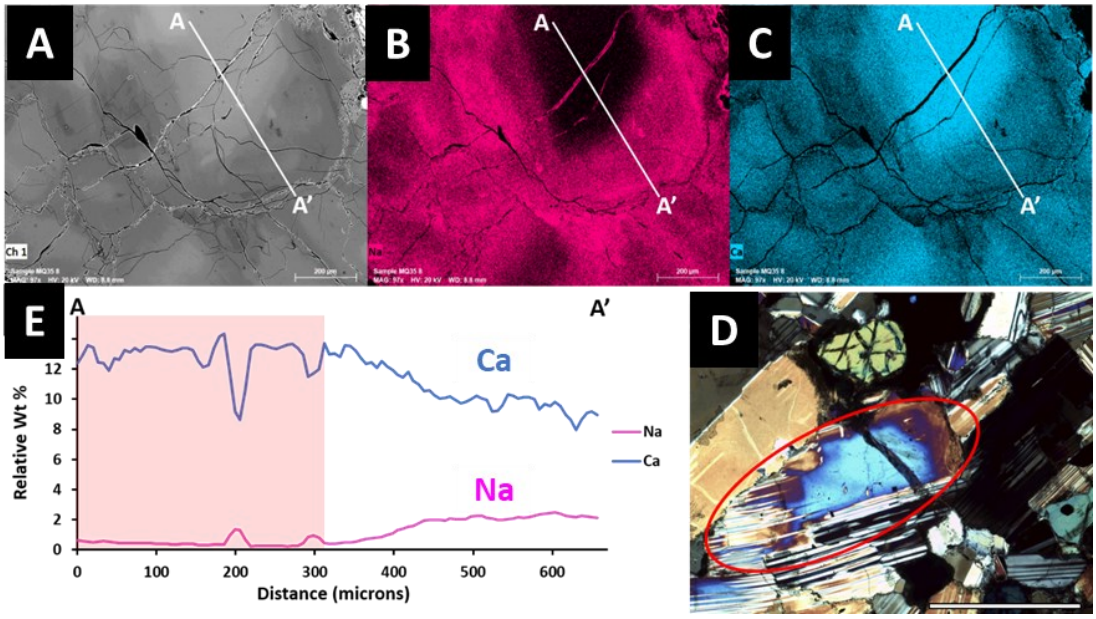

Figure 3.13: A) BSE image of zoned plagioclase with location of linescan traverse marked (line A-A'). **B)** and **C)** Chemical maps for Na and Ca respectively. Areas of the crystal with a relatively higher concentration of the element being mapped show up brighter. This shows the extent of the high Ca, low Na core and low Ca, high Na rim (normal zoning). **D)** XPL image of the analysed plagioclase (circled). White scale bar = 1 mm. Section thickness = 100 µm. **E)** Data from linescan traverse, showing relative wt % Na and Ca. Note the significant increase in Ca and decrease in Na across the core (red band) confirming normal zoning.

3.1.3 – Petrographic description of Martinique lava

M8321 - Two pyroxene andesite (Figure 3.14)

Porphyritic lava with approximately equal proportions of groundmass and crystals. Groundmass is dark brown with abundant plagioclase microlites. The subhedral to euhedral crystal assemblage consists of plagioclase (80 %, 0.5-3.5 mm), followed in abundance by orthopyroxene (14 %) and clinopyroxene (6 %) (0.5-2 mm) and minor oxides. Three different populations of plagioclase can be identified based on textural characteristics. The most common (approx. 70 %) have sieve textured cores with clear, inclusion free rims **(Figure 3.15, a).** Most cores are heavily sieved with some containing more sparse melt inclusions. The second most common type (approx. 20 %) have clear cores surrounded by sieved (melt) inclusion rich rims **(Figure 3.15, b).** In some cases, a narrow inclusion free rim is present outside the sieved area. The final type (approx. 10 %) are clear with minimal inclusions **(Figure 3.15, c).** Zoning in

plagioclase is complex and variable **(Figures 3.16-18).** SEM analysis indicates both normal and reverse zoning, with the sodic cores in reverse zoned crystals displaying rounded edges. The calcic rims of these crystals show fine scale oscillatory zoning **(see Figure 3.16, a).** Normal and reverse zoning sometimes exist in the same crystal, where patchy calcic cores are surrounded by a sodic mantle and a rim zone with calcic overgrowths **(Figure 3.18)**.

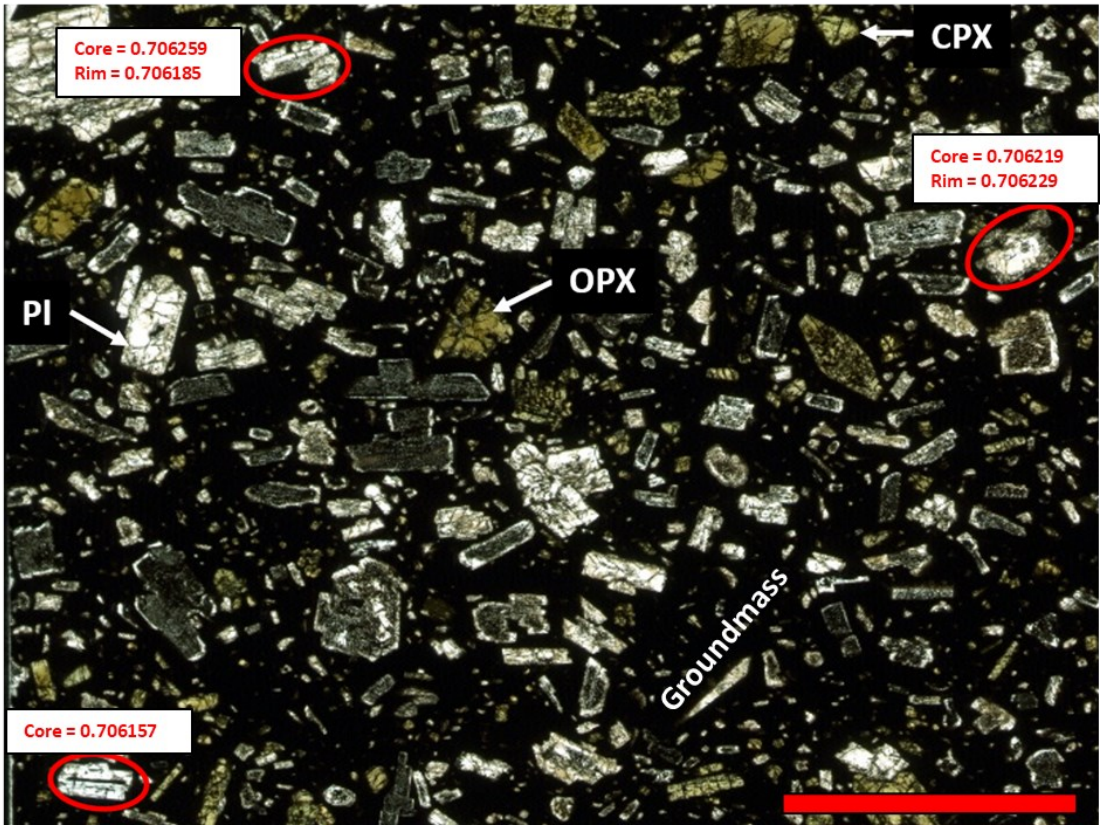

Figure 3.14: M8321 thin section (PPL) with analysed plagioclase circled. Red scale bar = 5 mm. Section thickness = 100 µm.

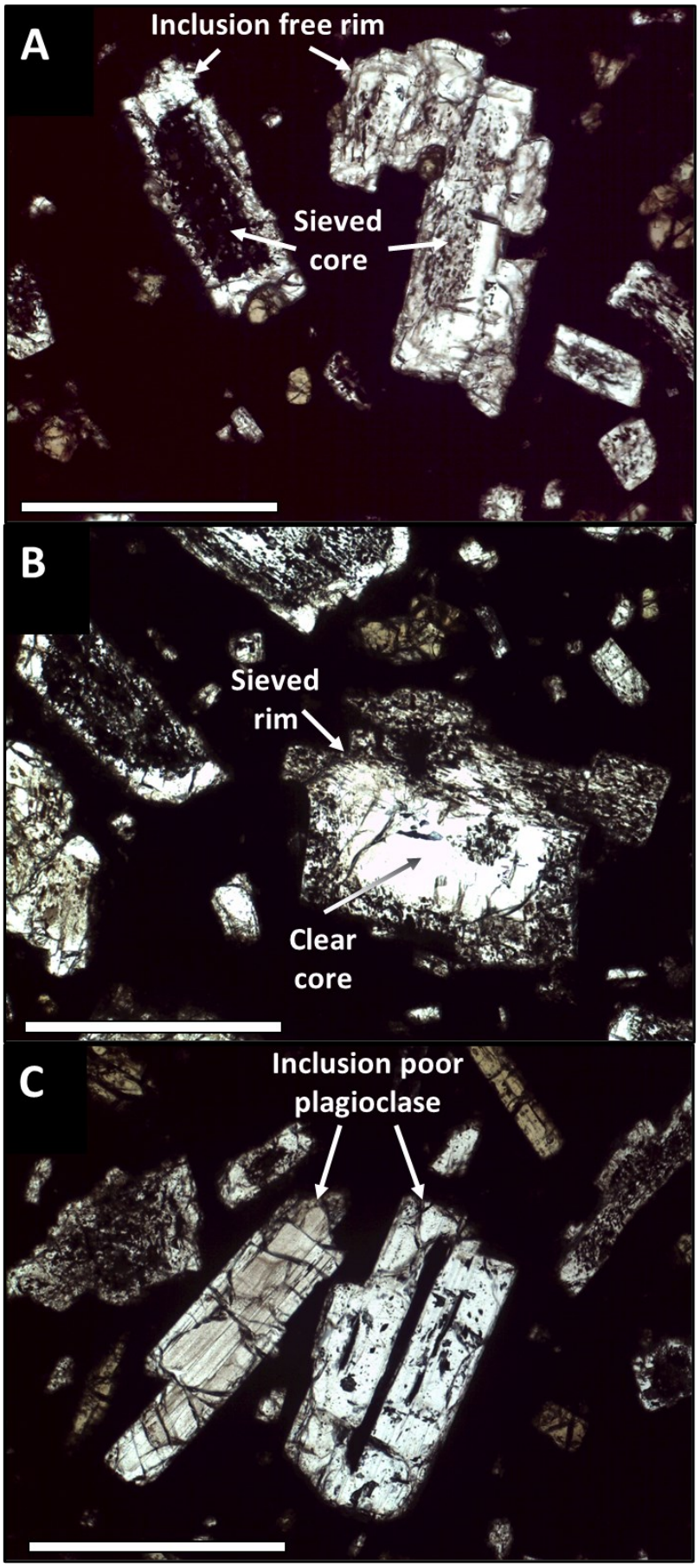
A
Inclusion free rim
Sieved
core
B
Sieved
rim
Clear
core
C
Inclusion poor
plagioclase

Figure 3.15: PPL images of plagioclase from M8321, representing typical examples of plagioclase textures in the sample. **A)** Sieved (melt inclusion rich) core, melt inclusion free rim. **B)** Clear (melt inclusion free) core, sieved rim. **C)** Melt inclusion poor.

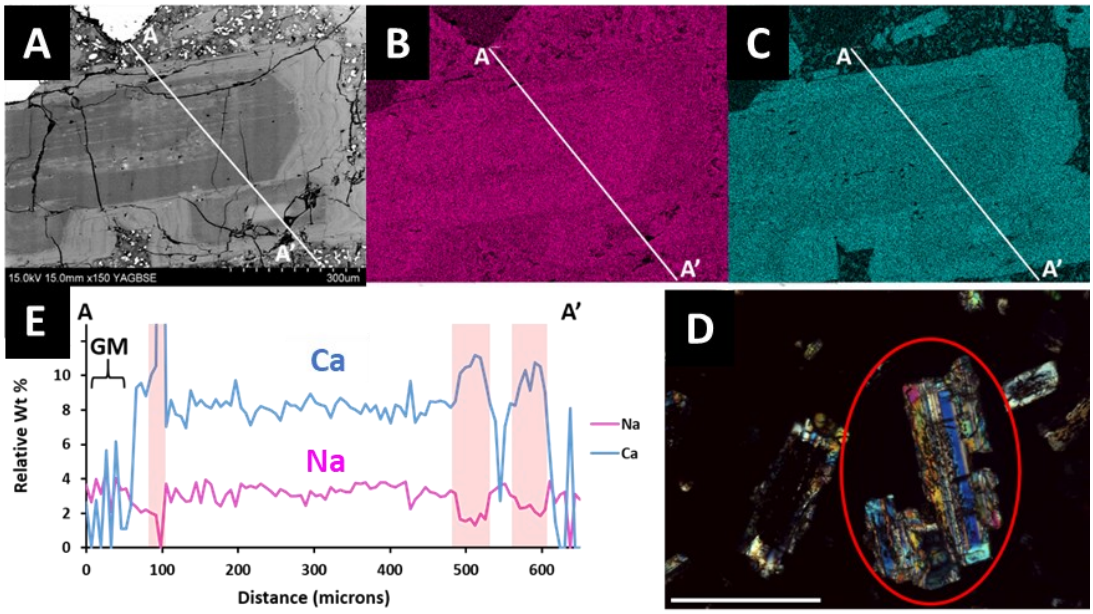

Figure 3.16: A) BSE image of zoned plagioclase with location of linescan traverse marked (line A-A'). **B)** and **C)** Chemical maps for Na and Ca respectively, showing a high Na, low Ca core and low Na, high Ca rim (reverse zoning). **D)** XPL image of the analysed plagioclase (circled). White scale bar = 1 mm. Section thickness = 100 µm. **E)** Data from linescan traverse, showing relative wt % Na and Ca. Note the significant increase in Ca and decrease in Na across the rim (red bands) confirming reverse zoning. The fluctuations from 0 – 60 microns represent data from the groundmass surrounding the crystal (labelled GM).

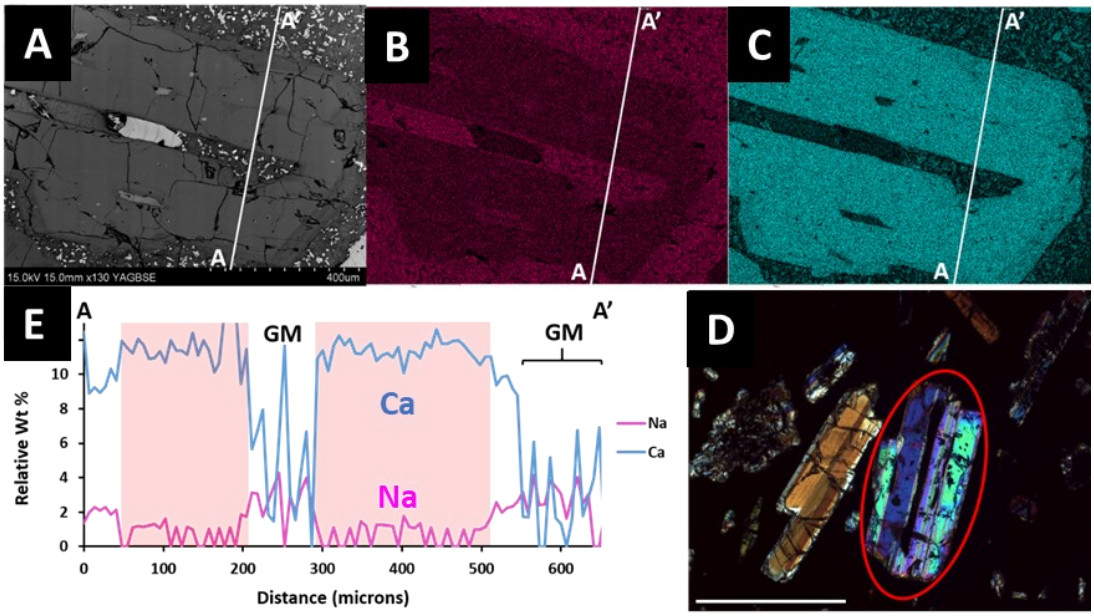

Figure 3.17: A) BSE image of zoned plagioclase with location of linescan traverse marked (line A-A'). **B)** and **C)** Chemical maps for Na and Ca respectively, showing a high Ca, low Na core and low Ca, high

Na rim (normal zoning). **D)** XPL image of the analysed plagioclase (circled). White scale bar = 1 mm. Section thickness = 100 µm. **E)** Data from linescan traverse, showing relative wt % Na and Ca. Note the significant increase in Ca and decrease in Na across the core (red band) confirming normal zoning. The fluctuations from approximately 550 - 650 microns and in the centre (approx. 220-280 microns) represent data from the groundmass (labelled GM).

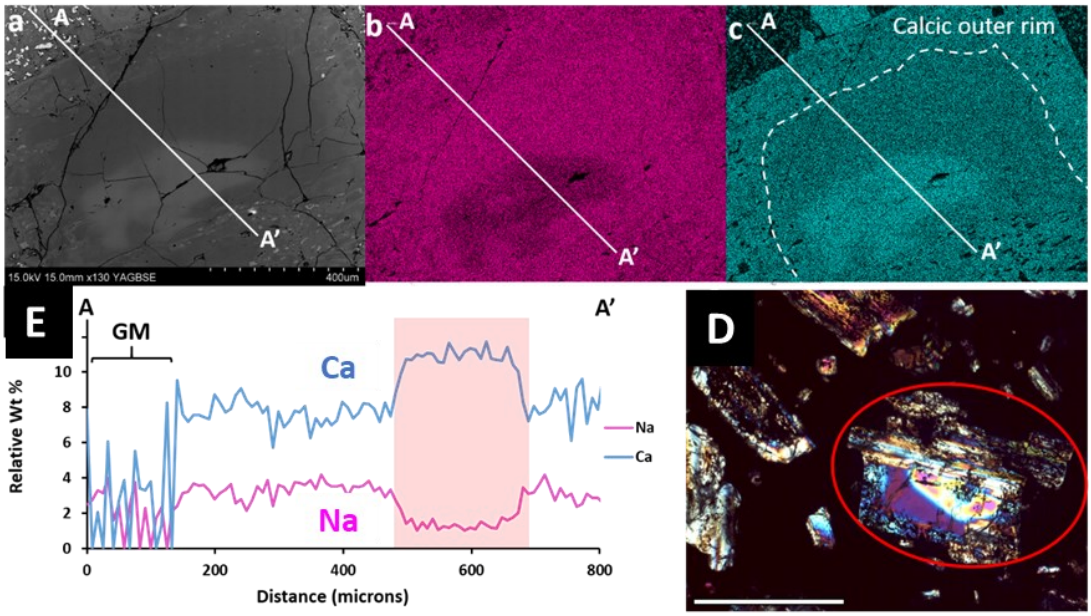

Figure 3.18: A) BSE image of zoned plagioclase with location of linescan traverse marked (line A-A'). **B)** and **C)** Chemical maps for Na and Ca respectively, showing a high Ca, low Na core surrounded by a low Ca, high Na rim (normal zoning). Another high Ca zone is present at the edge of the crystal (reverse zoning). The chemical map and BSE image indicate that this takes the form of high Ca overgrowths. **D)** XPL image of the analysed plagioclase (circled). White scale bar = 1 mm. Section thickness = 100 µm. **E)** Data from linescan traverse, showing relative wt % Na and Ca. Note the significant increase in Ca and decrease in Na across the core (red band) confirming normal zoning. The fluctuations from approximately 0-140 microns represent data from the groundmass (labelled GM).

3.2 - St Vincent plutonic xenoliths

3.2.1 – Brief petrographic descriptions of St Vincent plutonic xenolith types

Over 100 plutonic xenolith samples were collected on a 2019 field campaign to St Vincent (see **Appendix 1**). Initially, 17 of these samples, with variable appearance and mineralogy observed in hand specimen, were chosen for making into thin sections. These 17 samples were assessed petrographically, prior to selection of samples for detailed study in the investigation presented in **Chapter 5**. The plutonic xenoliths were classified using the scheme of Streckeisen (1976), based on visual observations of their

mineralogy. The plutonic xenolith types include troctolites (5 of 17 samples), olivine gabbros (6 samples), hornblende-olivine gabbros (2 samples), hornblende gabbros (1 sample) and gabbronorites (3 samples). Brief petrographic descriptions of each plutonic xenolith type are provided below, along with images of all 17 thin sections.

Troctolites (VS518, VS534, VS548, VS553, VS563) – Figures 3.19 and 3.20

Troctolites consist of olivine and plagioclase, with variable crystal sizes within and between samples which often exceed 2 mm. Textures are either orthocumulate (estimated > 5 % interstitial melt or crystals) or mesocumulate (estimated < 5 % interstitial melt or crystals). A typical feature is the presence of thin films of melt lining most crystal boundaries. Samples VS534 and VS553 contain pockets of vesiculated interstitial melt.

Olivine Gabbros (VS506, VS527, VS532, VS552, VS564, VS569) - Figures 3.21 and 3.22

Olivine gabbros consist of olivine, plagioclase, clinopyroxene ± magnetite. Crystal sizes are typically 1-2 mm. The samples have adcumulate (interstitial melt or crystals absent or estimated < 1 % of sample) or mesocumulate (estimated < 5 % interstitial melt or crystals) textures and well equilibrated, 120° crystal boundaries between primocryst (olivine, plagioclase, clinopyroxene) phases are common. Thin melts films line some crystal boundaries. Clinopyroxene occurs as an interstitial phase in samples VS527 and VS564. Samples VS506 and VS569 appear to have been influenced by alteration. Detailed descriptions of two olivine gabbro samples studied in **Chapter 5** are provided in **section 3.2.2**.

Hornblende-Olivine Gabbros (VS551, VS572) - Figure 3.23

Hornblende-olivine gabbros consist of olivine, plagioclase, clinopyroxene, amphibole, magnetite, ± orthopyroxene ± apatite, with variable crystal sizes from < 0.5 - > 5 mm. Textural and crystal size variation is observed within samples. Amphibole is typically found overgrowing or replacing the rims of clinopyroxene and/or olivine. Detailed descriptions of these two samples, which are studied in **Chapter 5,** are provided in section **3.2.2**.

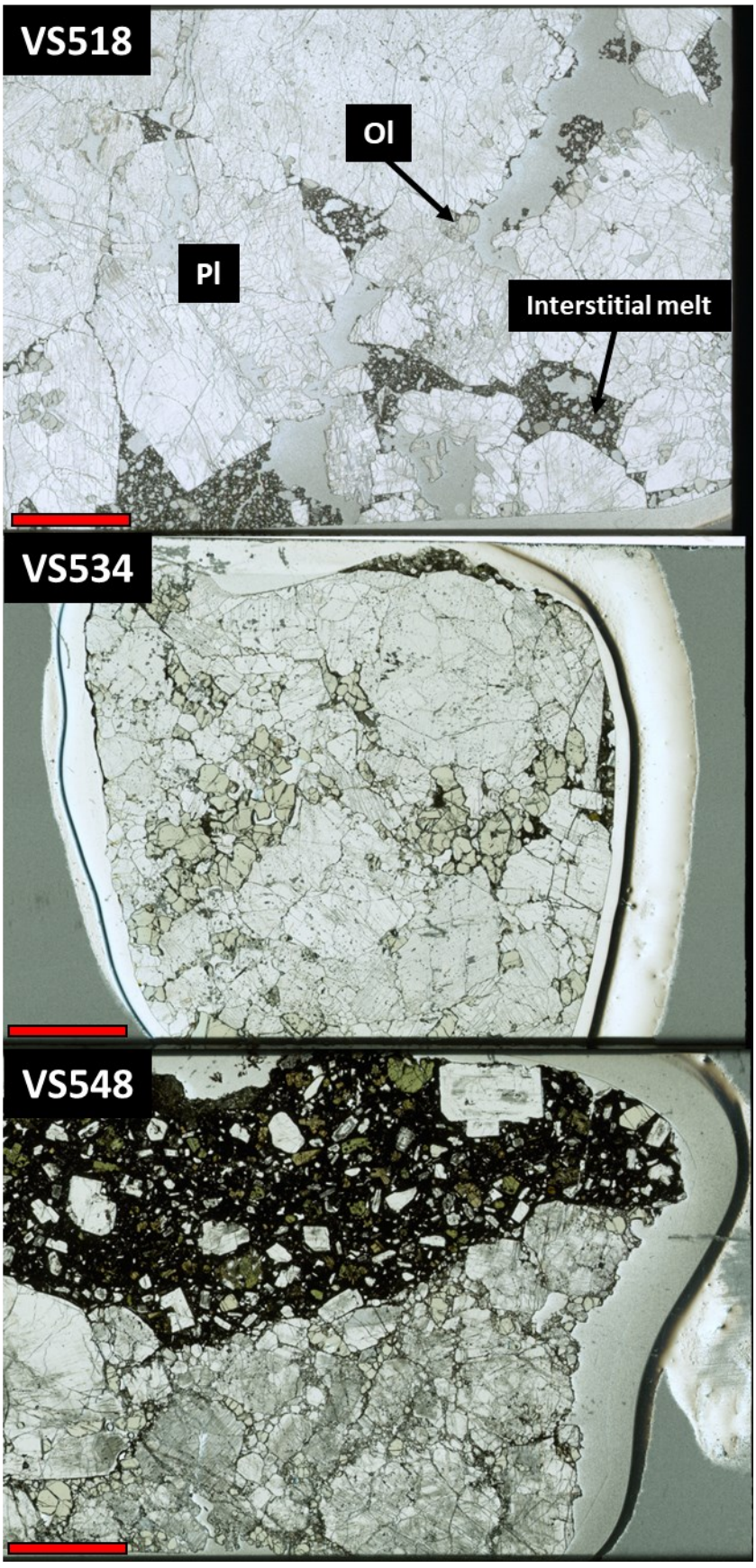

Figure 3.19: Troctolite samples VS518, VS534 and VS548. Red scale bar = 5 mm.

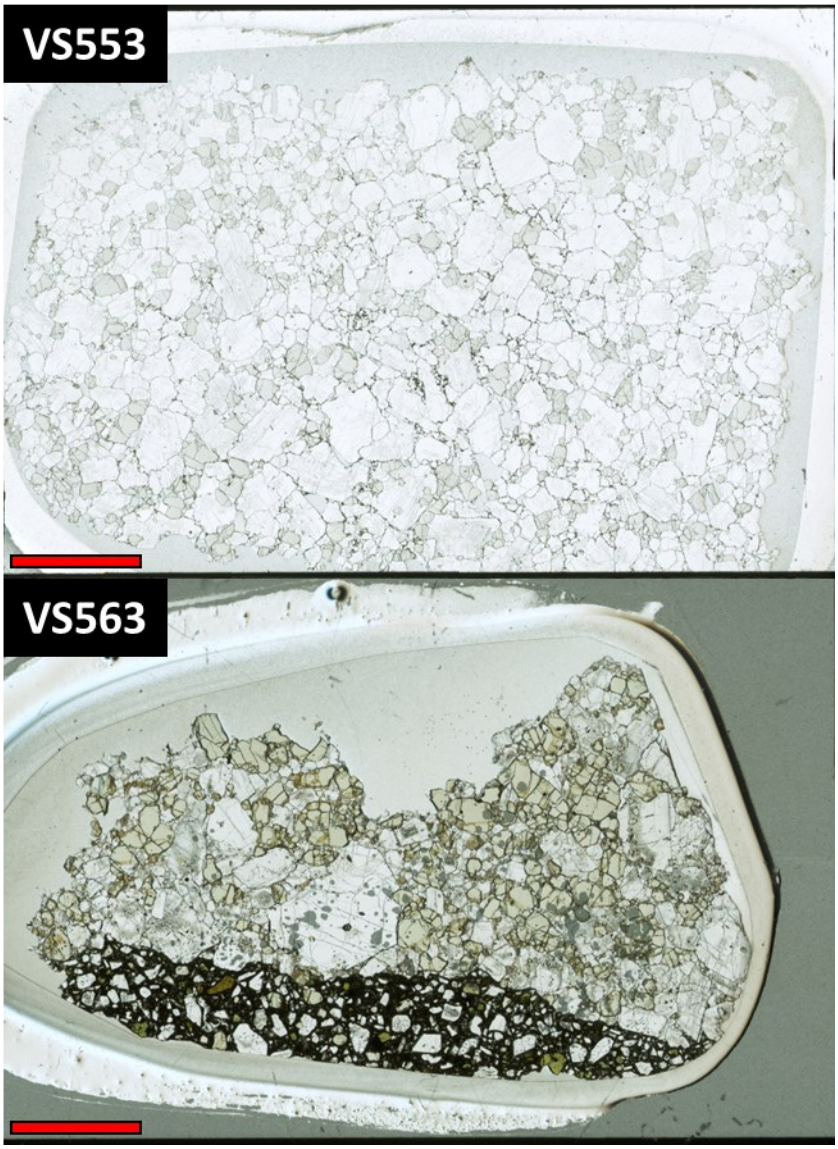

Figure 3.20: Troctolite samples VS553 and VS563. Red scale bar = 5 mm.

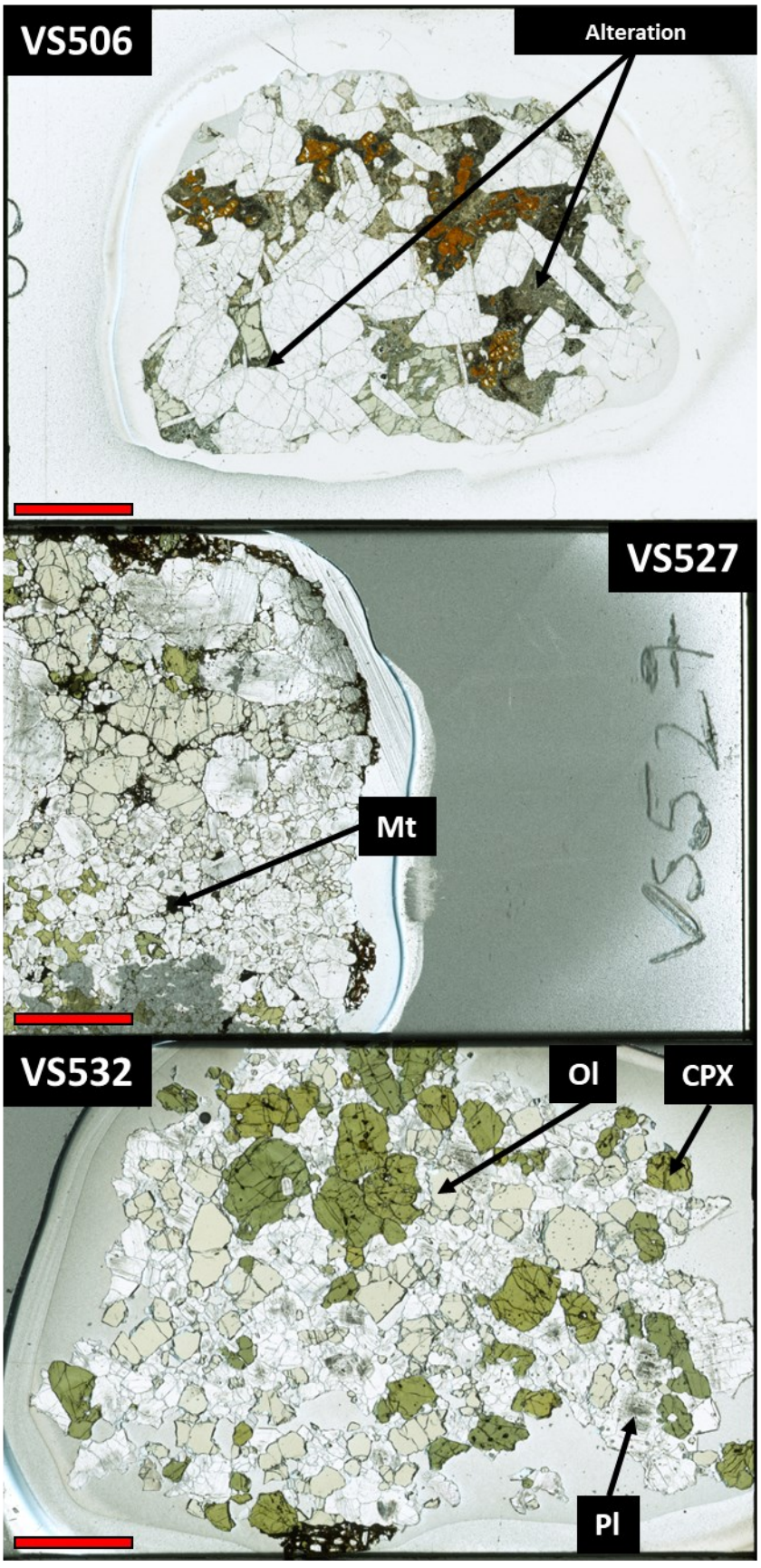

Figure 3.21: Olivine gabbro samples VS506, VS527 and VS532. Red scale bar = 5 mm.

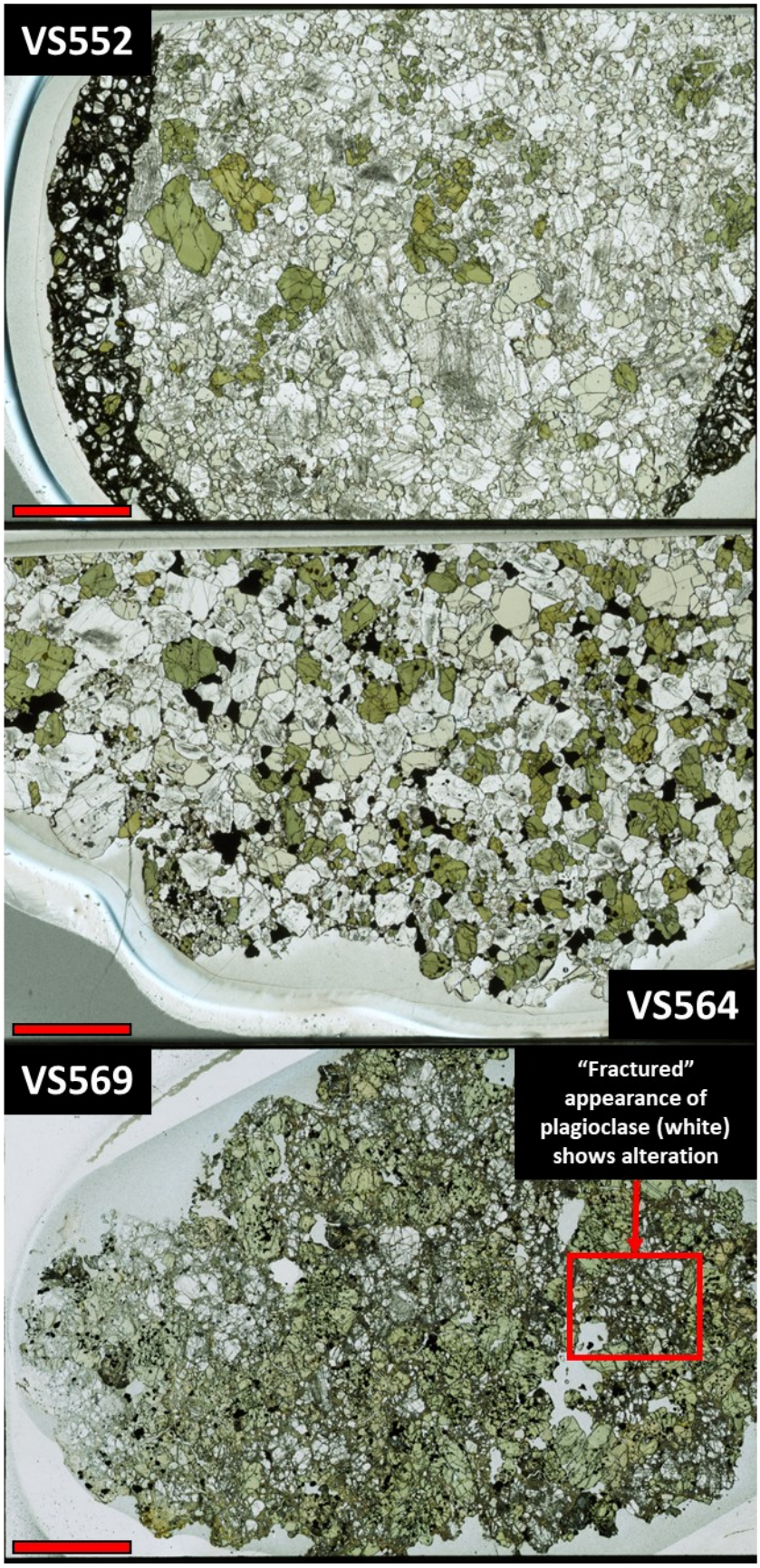

Figure 3.22: Olivine gabbro samples VS552, VS564 and VS569. Red scale bar = 5 mm.

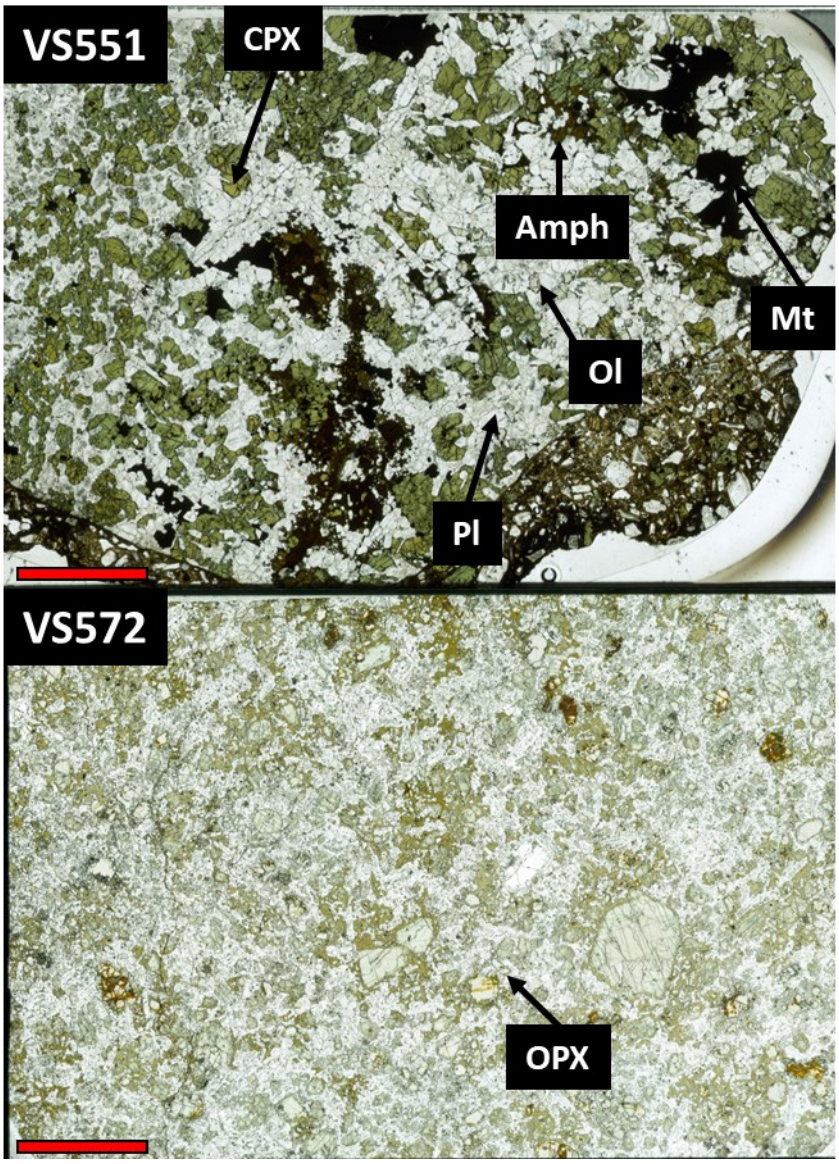

Figure 3.23: Hornblende-olivine gabbro samples VS551 and VS572. Red scale bar = 5 mm.

Hornblende Gabbro (VS566) - Figure 3.24

The hornblende gabbro consists of plagioclase, amphibole, olivine and oxides with sparse orthopyroxene and clinopyroxene. The sample is affected by alteration which hinders observation of crystal sizes and the relationships between mineral phases. A number of large, > 2 mm amphibole, which appear to have been euhedral prior to alteration, are present.

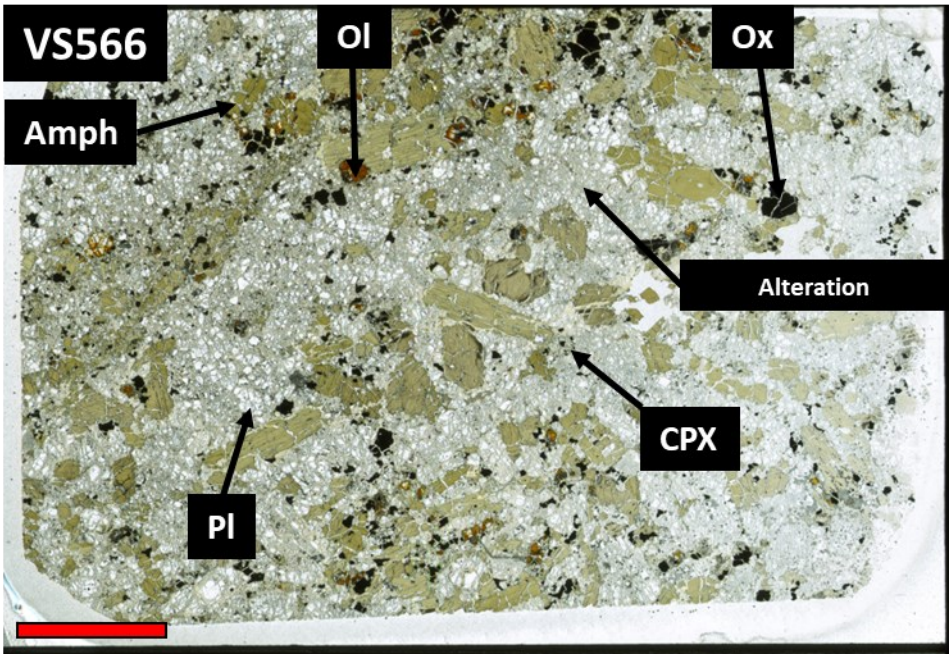

Figure 3.24: Hornblende gabbro sample VS566. Red scale bar = 5 mm.

Gabbronorites (VS507, VS508, VS520) - Figure 3.25

Gabbronorites consist of plagioclase, clinopyroxene, orthopyroxene, oxides ± olivine (altered to iddingsite), typically < 1 mm in size. Variable textures are observed – VS508 shows an adcumulate texture, while VS507 shows an orthocumulate texture with abundant brown glass between crystals. Sample VS520 shows apparent vesiculation between crystals.

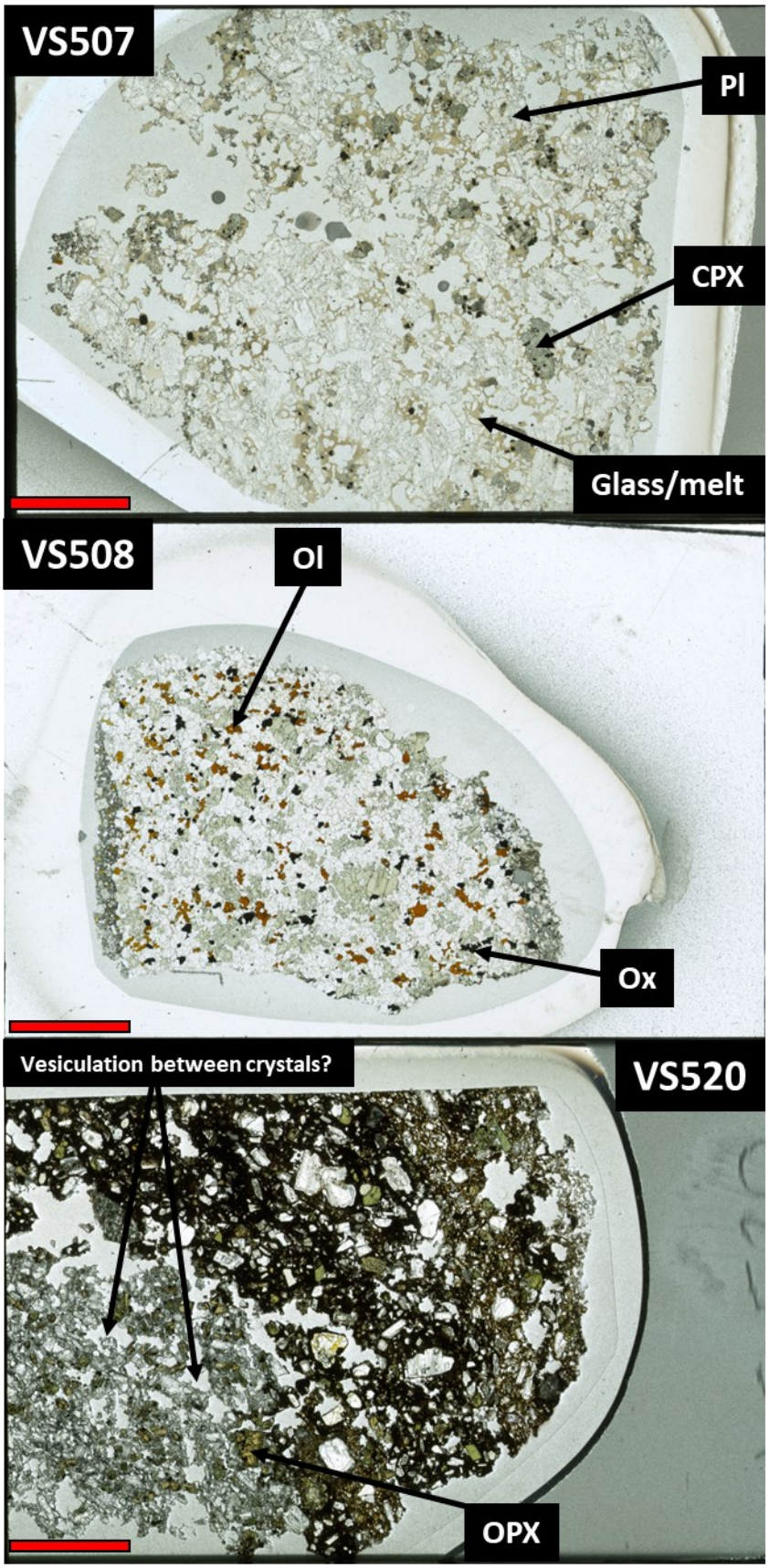

Figure 3.25: Gabbronorite samples VS507, VS508 and VS520. Red scale bar = 5 mm.

3.2.2 – Detailed petrographic descriptions of St Vincent plutonic xenoliths analysed in Chapter 5

In **Chapter 5**, four plutonic xenoliths (VS527, VS532, VS551, VS572), including two olivine gabbros and two hornblende-olivine gabbros were selected for detailed study. The other samples shown above were not studied further but serve as a reference for the range of mineral assemblages and textural features typically found in St Vincent plutonic xenoliths.

Major elements/molar element ratios of mineral phases and trace element compositions of clinopyroxene and amphibole were analysed in the four selected plutonic xenoliths. This section provides detailed petrographic descriptions of these four samples, which are referred back to in **Chapter 5**. Interpretation of the petrographic features is given in context in **Chapter 5** and is not provided here.

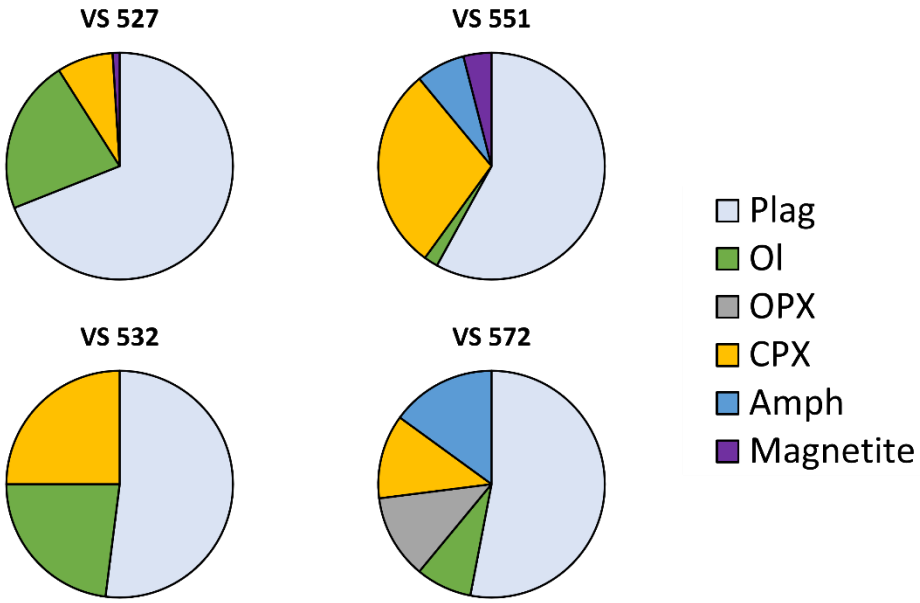

Figure 3.26: Modal proportions of mineral phases in the four St Vincent plutonic xenolith samples studied in detail in **Chapter 5**. Percentages for each mineral phase are listed in **Table 3.2**. Modal abundances were determined from mineral phase maps generated by the QUACK software **(see Chapter 2).**

Mineral modal abundances for the four St Vincent plutonic xenoliths are presented in **Figure 3.26**, with key characteristics listed in **Table 3.2**. The crystallization sequence for each plutonic xenolith was determined by textural inspection and supporting information from chemical and molar element ratio maps where required (**see Chapter**

5). For each plutonic xenolith sample, a figure showing the whole analysed thin section is provided as an overview, along with a mineral phase map to clearly illustrate the distribution of the main mineral phases. The thin sections of samples VS527 and VS551 include a rind of host lava. However, in this study (**Chapter 5**) the focus is entirely on the plutonic xenoliths, hence the petrographic characteristics of the lava rinds are not described here.

Sample	Classification	Mineral assemblage	Texture	Plag An	Ol Fo	CPX Mg#	OPX Mg#	Amph Mg#
VS527 (Olivine gabbro)	Olivine Gabbro	Plag (69 %), Ol (22 %), CPX (8 %), Mt (1 %)	Mesocumulate	89-98	76-79	70-80		
VS532 (Ol-CPX gabbro)	Olivine Gabbro	Plag (52 %), Ol (23 %), CPX (25 %)	Adcumulate	90-100	77-80	72-81		
VS551 (banded Hbl-Ol gabbro)	Hornblende-Olivine Gabbro	Plag (58 %), Ol (2 %), CPX (29 %), Mt (4 %), Amph (7 %)	Adcumulate	85-97	72-76	69-80		62-70
VS572 (poikilitic Hbl-Ol gabbro)	Hornblende-Olivine Gabbro	Plag (53 %), Ol (8 %), CPX (12 %), OPX (12 %), Amph (15 %) (plus minor accessory oxides, apatite and sulfides)	Non-cumulate gabbro	60-90	70-76	70-90	72-75	65-70

Table 3.2: Summary of key petrographic characteristics of the four St Vincent plutonic xenolith samples studied in detail in **Chapter 5**.

VS527 – Olivine Gabbro (Figures 3.27 and 3.28)

The mineral assemblage is dominated by plagioclase (0.5 - > 5 mm), followed in abundance by olivine (0.5 - > 5 mm), along with clinopyroxene (0.3-3 mm) and magnetite (0.1-0.6 mm). The crystallization sequence is olivine -> plagioclase -> clinopyroxene -> magnetite. The sample has a mesocumulate texture with remnants of vesicular brown glass between many of the crystals, giving some crystal boundaries a curved or jagged appearance **(Figure 2).** A clear spatial variation in crystal size is present, with one half of the thin section containing larger, typically > 2 mm crystals and the other typically < 2 mm crystals. Plagioclase and olivine are mostly subhedral and unzoned. Clinopyroxene are subhedral to anhedral and occur interstitially between plagioclase and olivine. Some clinopyroxene are unzoned while others show patchy

zoning. Magnetite is present as a minor interstitial phase. **In Chapter 5, this sample will be referred to as the "Olivine Gabbro".**

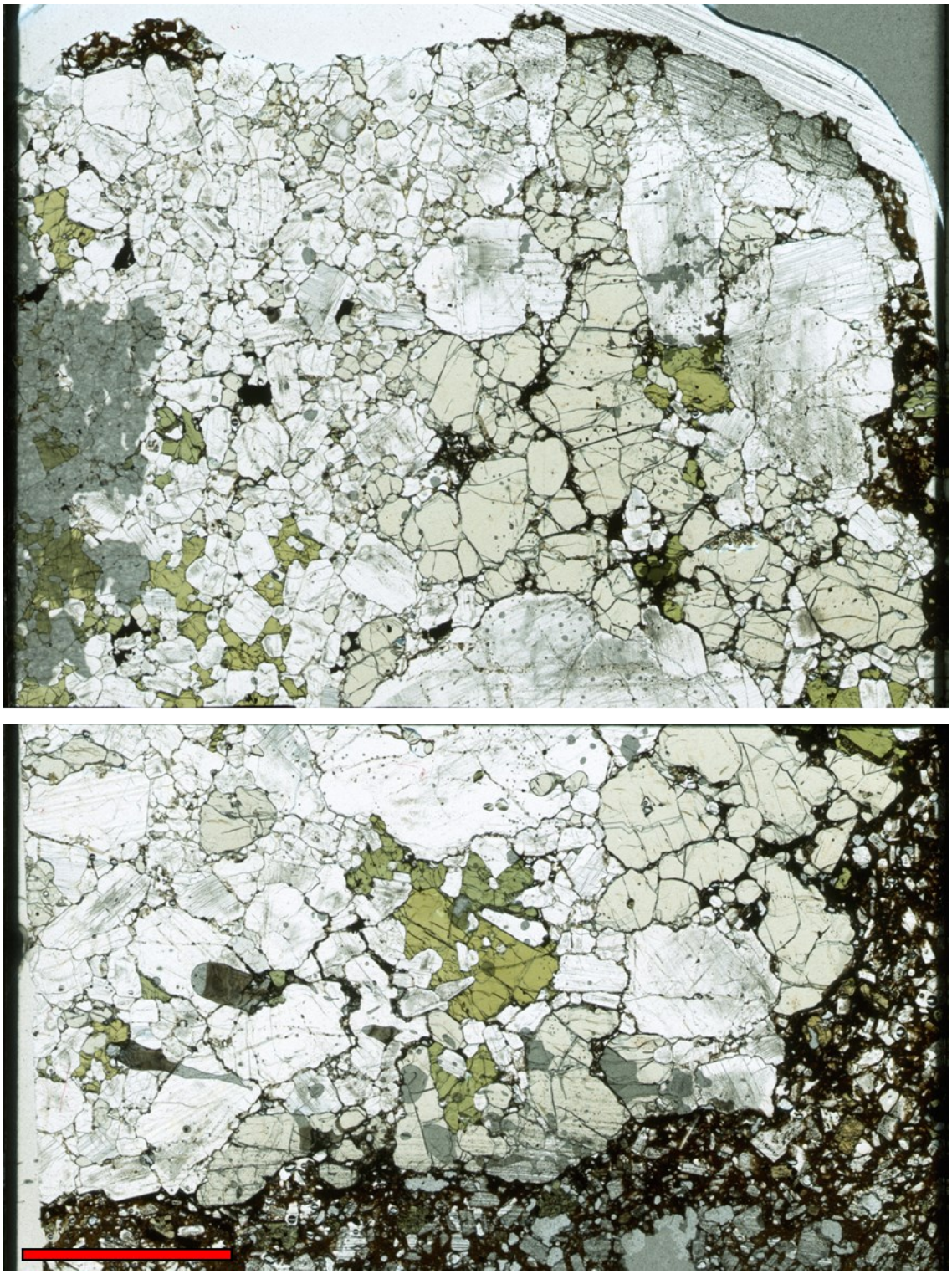

Figure 3.27: VS527/olivine gabbro thin section (PPL). Red scale bar = 5 mm. Gap between images represents a small area of the thin section that was not imaged.

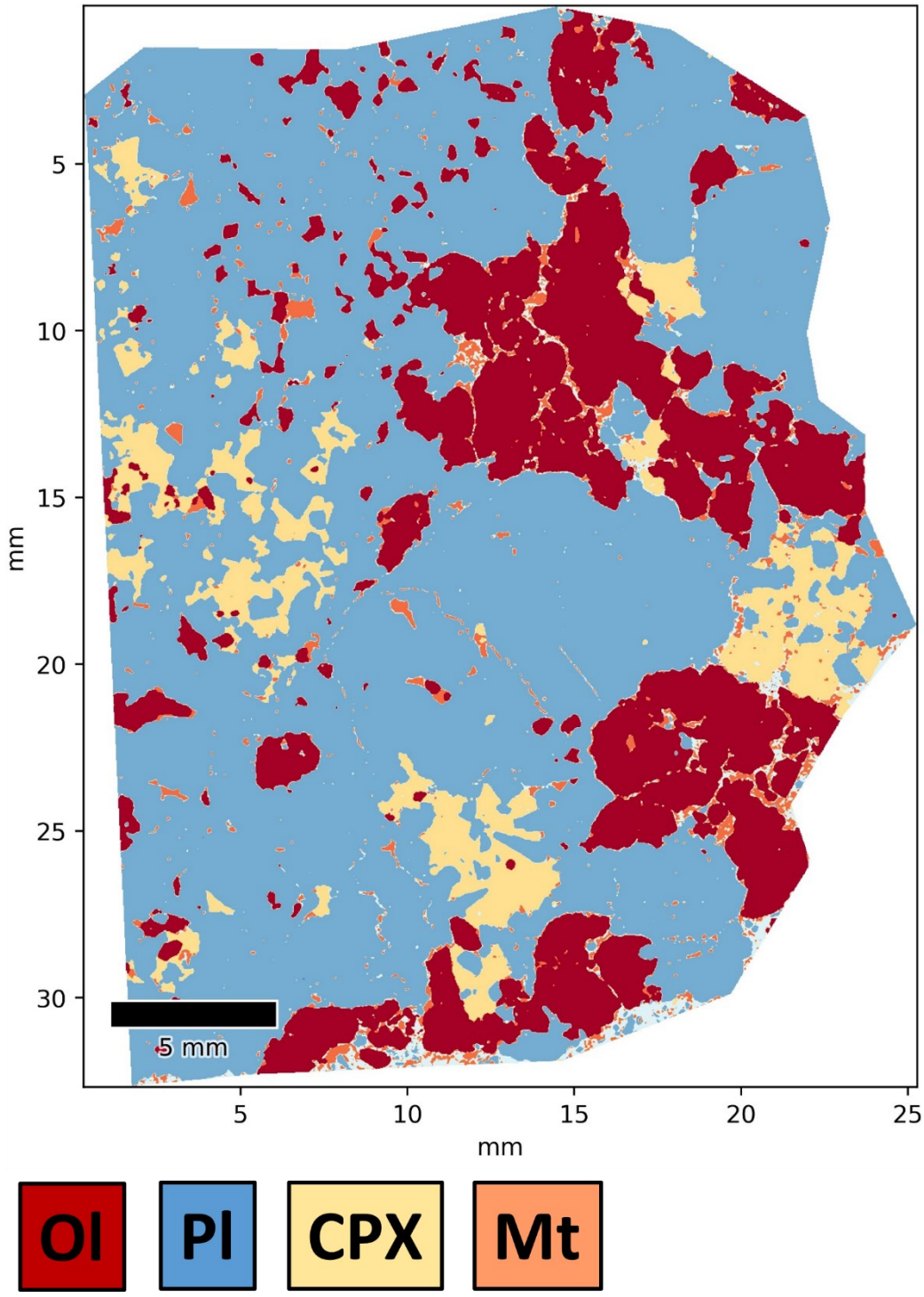

Figure 3.28: Mineral phase map of VS527/olivine gabbro showing the distribution of key phases. Map generated by the QUACK software from EDS SEM element maps. The very pale blue coloured patches represent interstitial melt.

VS532 – Olivine Gabbro (Figures 3.29 and 3.30)

Plagioclase (1-2 mm) makes up just over half of the mineral assemblage, along with olivine (<1-3 mm) and clinopyroxene (0.5-3 mm) in almost equal proportions. The

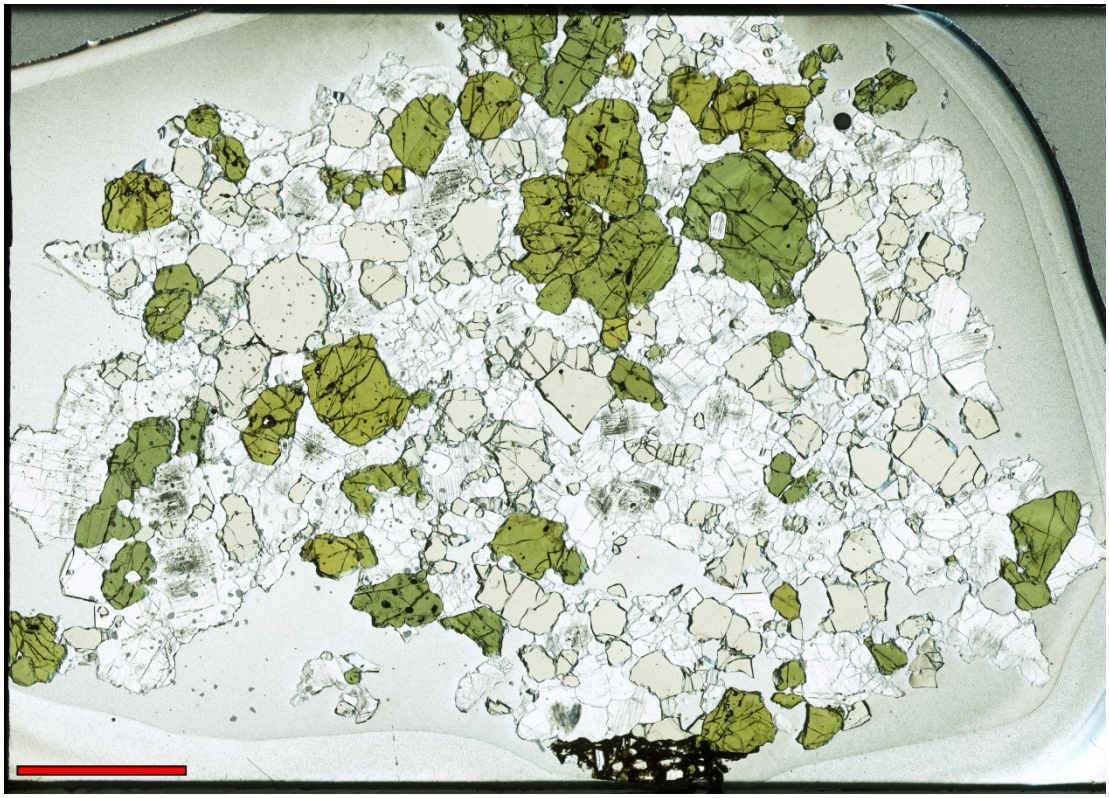

Figure 3.29: VS532/Ol-CPX gabbro thin section (PPL). Red scale bar = 5 mm.

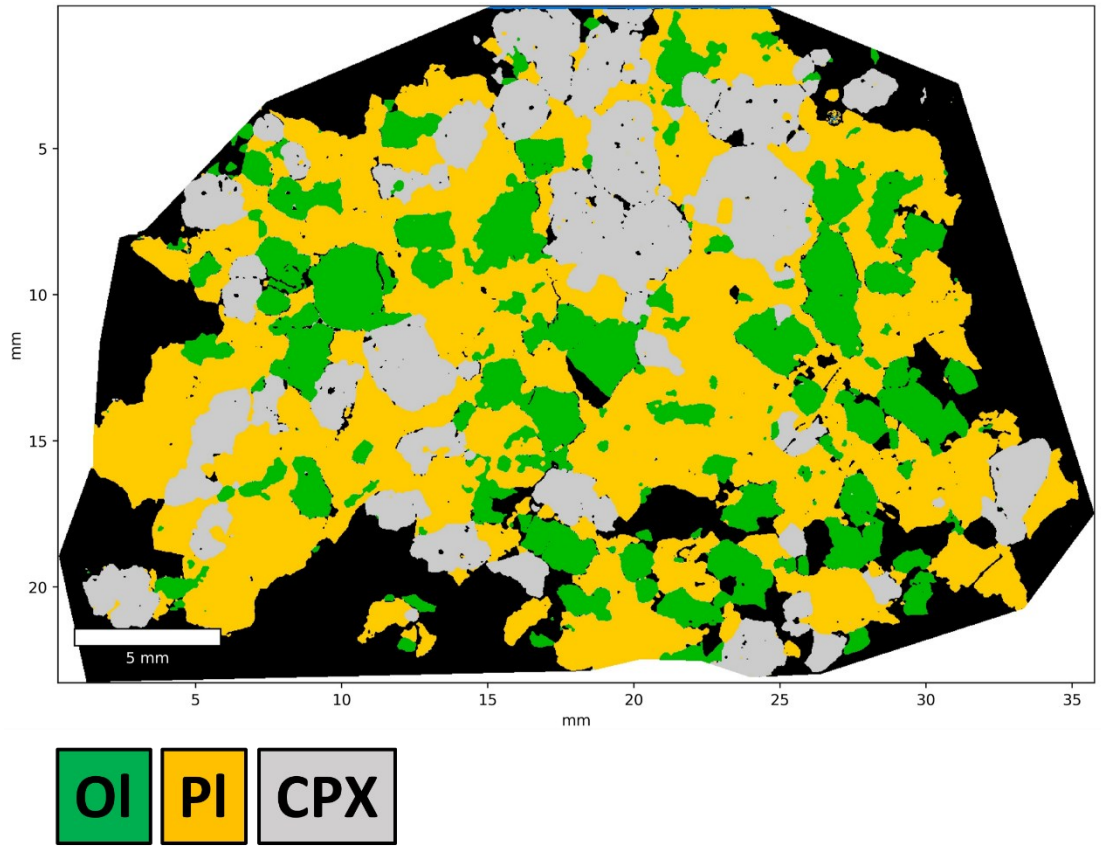

Figure 3.30: Mineral phase map of VS532/Ol-CPX gabbro showing the distribution of key phases. Map generated by the QUACK software from EDS SEM element maps.

crystallization sequence is olivine -> plagioclase -> clinopyroxene. The sample has an adcumulate texture with typically well equilibrated 120° crystal boundaries between the three primocryst (olivine, plagioclase, clinopyroxene) phases. Plagioclase and olivine are subhedral and unzoned. Clinopyroxene are mostly subhedral and some larger crystals are zoned, with one displaying faint oscillatory zoning. **In Chapter 5, this sample will be referred to as the "Ol-CPX gabbro".**

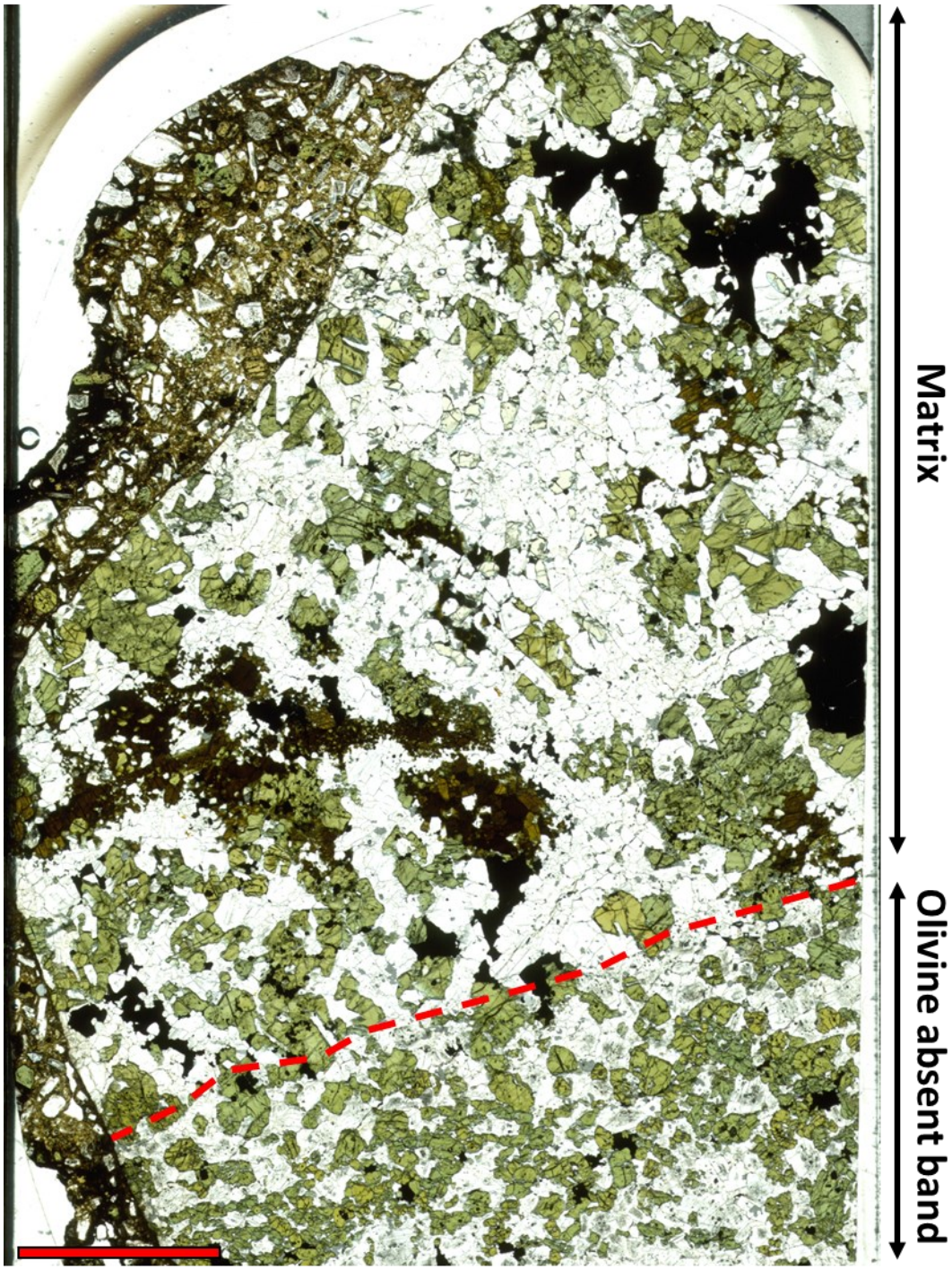

Figure 3.31: VS551/banded Hbl-Ol gabbro thin section (PPL) with olivine absent band labelled (boundary marked by red dashed line). Red scale bar = 5 mm.

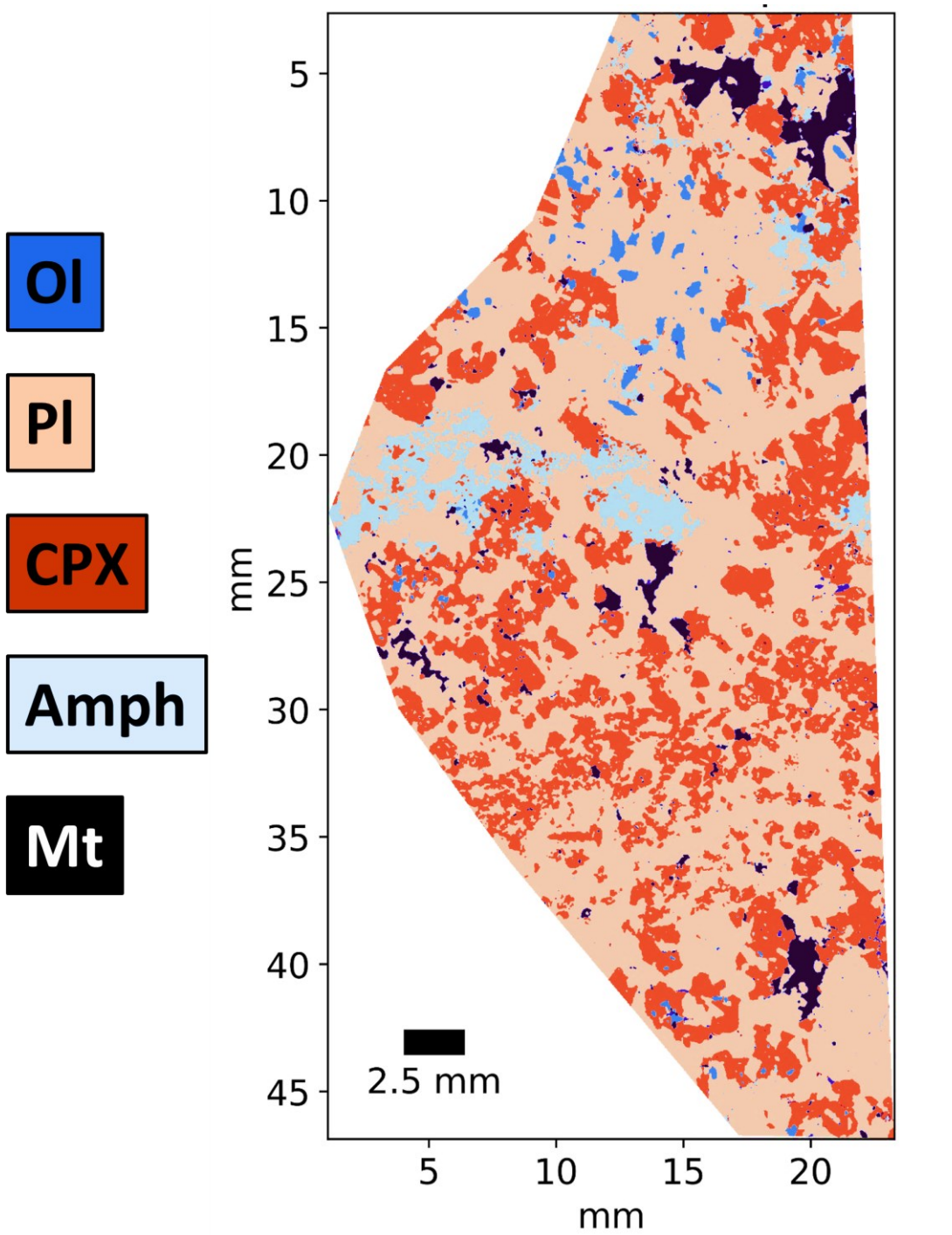

Figure 3.32: Mineral phase map of VS551/banded Hbl-Ol gabbro showing the distribution of key phases. Map generated by the QUACK software from EDS SEM element maps.

VS551 – Hornblende - Olivine Gabbro (Figures 3.31 and 3.32)

The mineral assemblage is dominated by plagioclase (0.5-1.2 mm) and clinopyroxene (0.4–2 mm), along with minor olivine (0.2-0.7 mm) and magnetite (0.2-3 mm).

Amphibole is present with a patchy distribution throughout the sample **(Figure 3.32)**. The crystallization sequence is olivine -> plagioclase -> clinopyroxene -> magnetite -> amphibole. The sample has a predominantly adcumulate texture. A key feature is the presence of a texturally and mineralogically distinct band with generally smaller crystal size, plagioclase with "fuzzy" fluid and melt inclusion rich cores and the absence of olivine relative to the sample matrix **(Figures 3.31 and 3.33).** Melt films on crystal boundaries, similar to those found in VS527, are also common within this band. This feature will be referred to hereon and in **Chapter 5** as the **olivine absent band**. Amphibole is typically found overgrowing the rims of clinopyroxene or occasionally on the rims of olivine **(Figure 3.33, a and b)** and is not present in the olivine absent band. Plagioclase and olivine are mostly subhedral and unzoned. Clinopyroxene within the olivine absent band ranges in size from 0.4-2 mm and is unzoned. Clinopyroxene throughout the rest of the sample (referred to as the "matrix" on **Figure 3.31**) is typically > 1.5 mm, mostly subhedral, with some displaying patchy zonation. Melt and fluid inclusions are common in clinopyroxene in both parts of the sample.

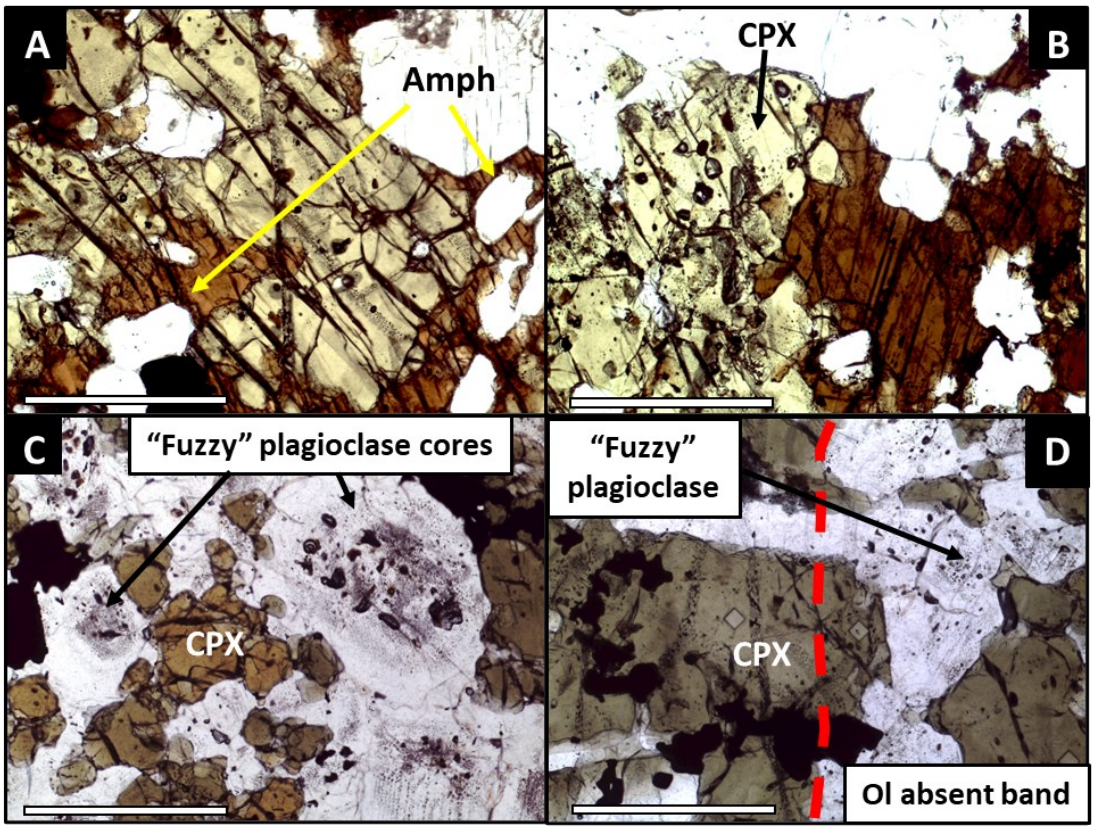

Figure 3.33: A) and **B)** PPL images of amphibole (brown) overgrowths on the rims of clinopyroxene (pale green) from VS551/banded Hbl-Ol gabbro. **C)** PPL image of plagioclase and clinopyroxene within the olivine-absent band, highlighting the "fuzzy" melt and fluid inclusion rich plagioclase cores. **D)** PPL image of the boundary between the sample matrix and olivine-absent band (red dashed line), again

highlighting "fuzzy" plagioclase within the band. The location of the boundary was determined by the quantitative compositional maps, discussed in detail in **Chapter 5**. White scale bar = 1 mm.

Magnetite occurs as either < 0.5 mm blebs overgrowing other phases (except amphibole), or larger anhedral masses (most clearly seen on the phase map, **Figure 3.32**). A few sparse magnetite crystals are present in the olivine-absent band. **In Chapter 5, this sample will be referred to as the "banded Hbl-Ol gabbro".**

VS572 – Hornblende - Olivine Gabbro (Figures 3.34 and 3.35)

Plagioclase (0.3-2.5 mm) is the most abundant mineral phase, followed by approximately equal proportions of clinopyroxene (0.3-4 mm) and orthopyroxene (0.3-1.5 mm), along with olivine (0.3-2 mm). A striking feature is the presence of poikilitic amphibole (brown) throughout the sample **(Figures 3.34 and 3.35).** Minor apatite is present, highlighted by the Phosphorus (pink) in the element map in **Figure 3.36** along with rare oxides and sulfides. The sample has a non-cumulate texture, with zoned phases, crystal sizes often < 1 mm and variable crystal boundary relationships as opposed to the well equilibrated 120° crystal boundaries typically observed in cumulates. The range of mineral phases and widespread zonation makes the crystallization sequence difficult to determine from petrographic inspection alone. The multiple phases of crystallization recorded by this sample are discussed in detail in conjunction with the chemical data obtained from this sample in **Chapter 5.**

Plagioclase is subhedral to euhedral and exhibits a wide range of sizes. Most plagioclase are zoned, with zonation occurring in both smaller (< 1 mm) and larger crystals. A complex range of zoning patterns are displayed, including simple core and rim, core-mantle-rim, patchy/relict cores and in some examples oscillatory zoning **(Figure 3.37)**. Some plagioclase contain clinopyroxene inclusions within mantle zones **(Figure 3.37, b)**. Olivine is typically anhedral-subhedral and unzoned, with some crystals showing variable degrees of alteration to iddingsite. Orthopyroxene is anhedral-subhedral, unzoned and most crystals are texturally associated with olivine **(Figure 3.35)**. Orthopyroxene typically mantles olivine crystals which have rounded edges and embayments **(Figure 3.38)**. Two size populations of clinopyroxene are present - > 1 mm mostly euhedral crystals, which are often zoned **(Figure 3.39, b)**, and ≤ 1 mm subhedral (occasionally euhedral) unzoned crystals (**Figure 3.39, d**).

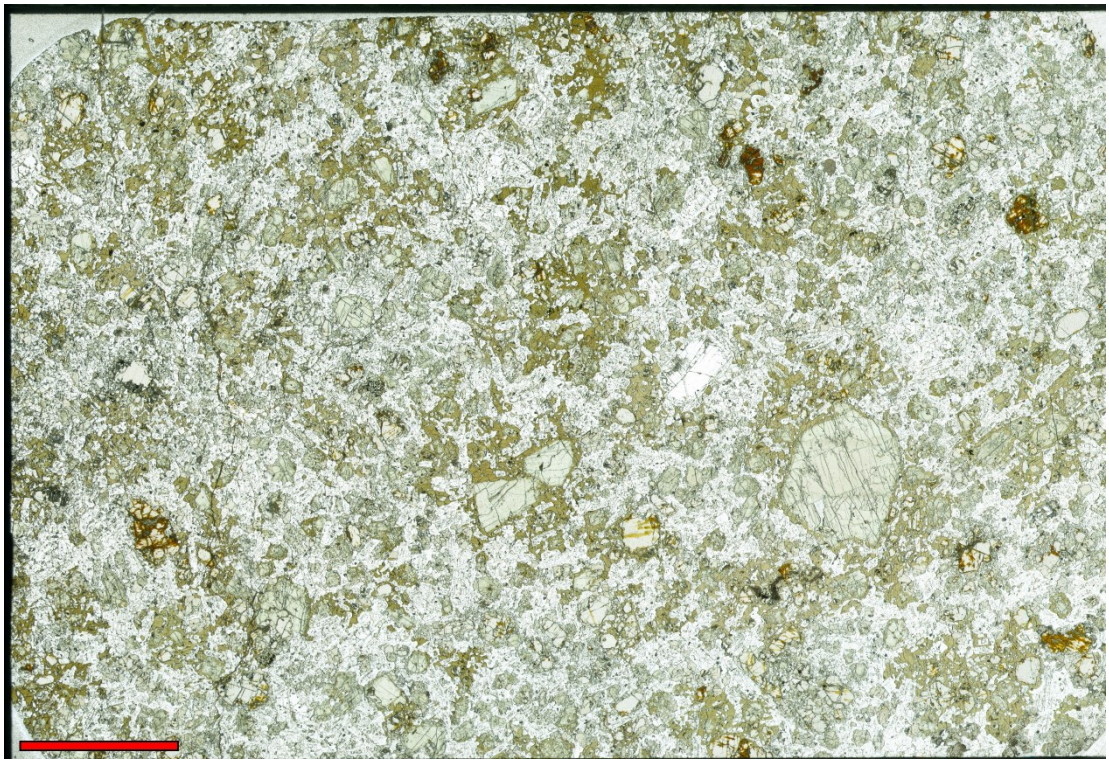

Figure 3.34: VS572/poikilitic Hbl-Ol gabbro thin section (PPL). Red scale bar = 5 mm.

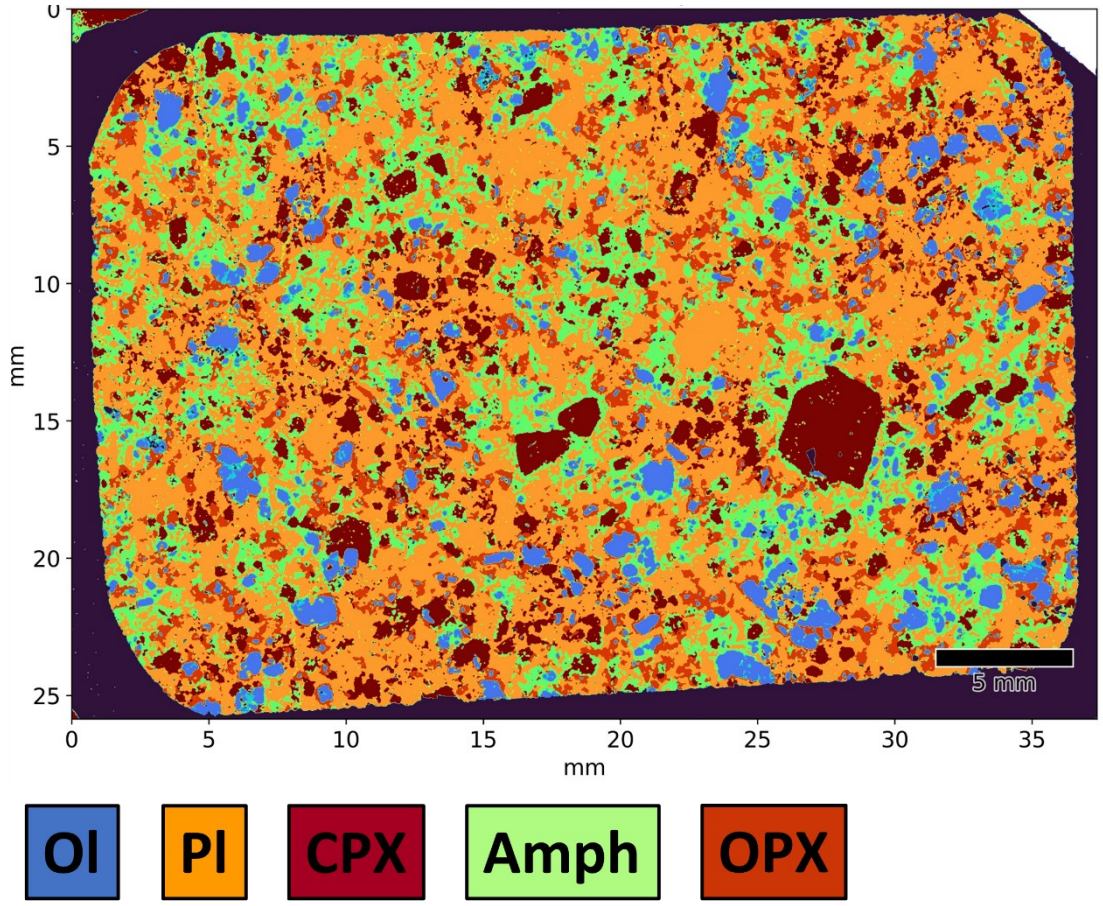

Figure 3.35: Mineral phase map of VS572/poikilitic Hbl-Ol gabbro showing the distribution of key phases. Map generated by the QUACK software from EDS SEM element maps.

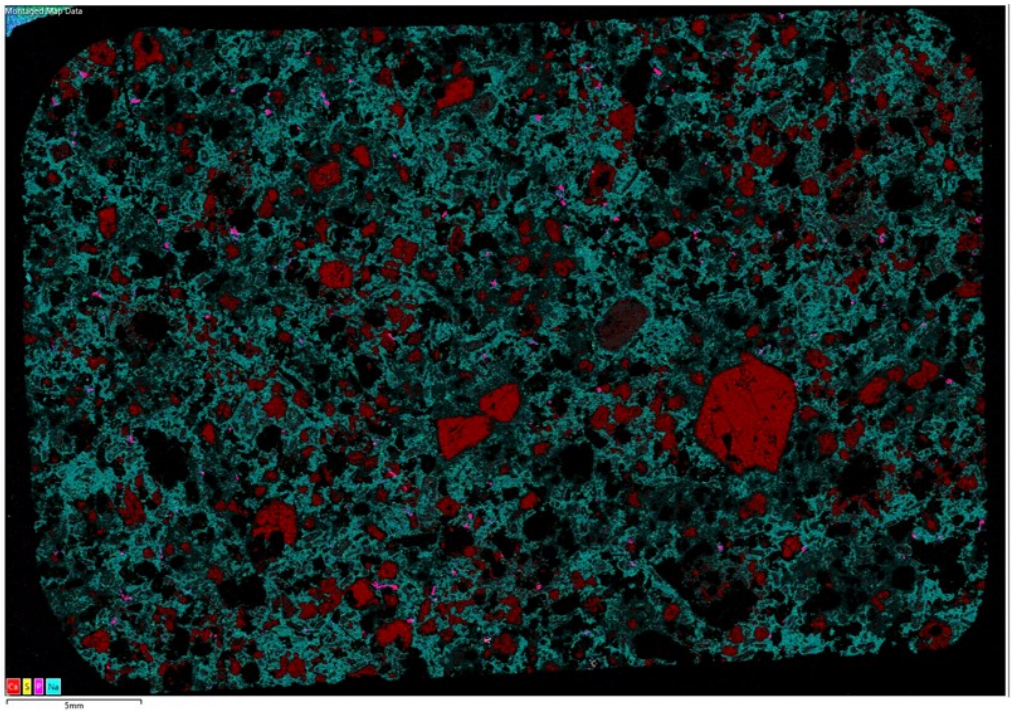

Figure 3.36: Element map of VS572/poikilitic Hbl-Ol gabbro. Ca = red, S = yellow, P = pink, Na = blue. Note the presence of apatite in the sample highlighted by the Phosphorus (pink) on the element map.

Amphibole is poikilitic, almost always unzoned and often texturally associated with clinopyroxene **(Figure 3.35)**. In several areas, a reaction relationship can be observed between clinopyroxene and adjacent amphibole, which takes the form of large poikilitic amphibole crystals replacing the rims of clinopyroxene, resulting in ragged crystal boundaries **(Figure 3.39)**. This relationship is observed between amphibole and clinopyroxene from both size populations. Poikilitic amphibole is also present around the rims of embayed olivine **(Figure 3.39, e)**. In several areas of the thin section, the poikilitic amphibole contain < 1 mm plagioclase inclusions, which do not show ragged crystal boundary junctions with the amphibole, unlike the contacts between amphibole and clinopyroxene (**Figure 3.39, f**) suggesting the plagioclase may have co-crystallized with the amphibole. Apatite is typically < 0.2 mm and present as an interstitial phase, often found at junctions between plagioclase crystals or in interstices adjacent to orthopyroxene and amphibole **(Figure 3.40)**. **In Chapter 5, this sample will be referred to as the "poikilitic Hbl-Ol gabbro".**

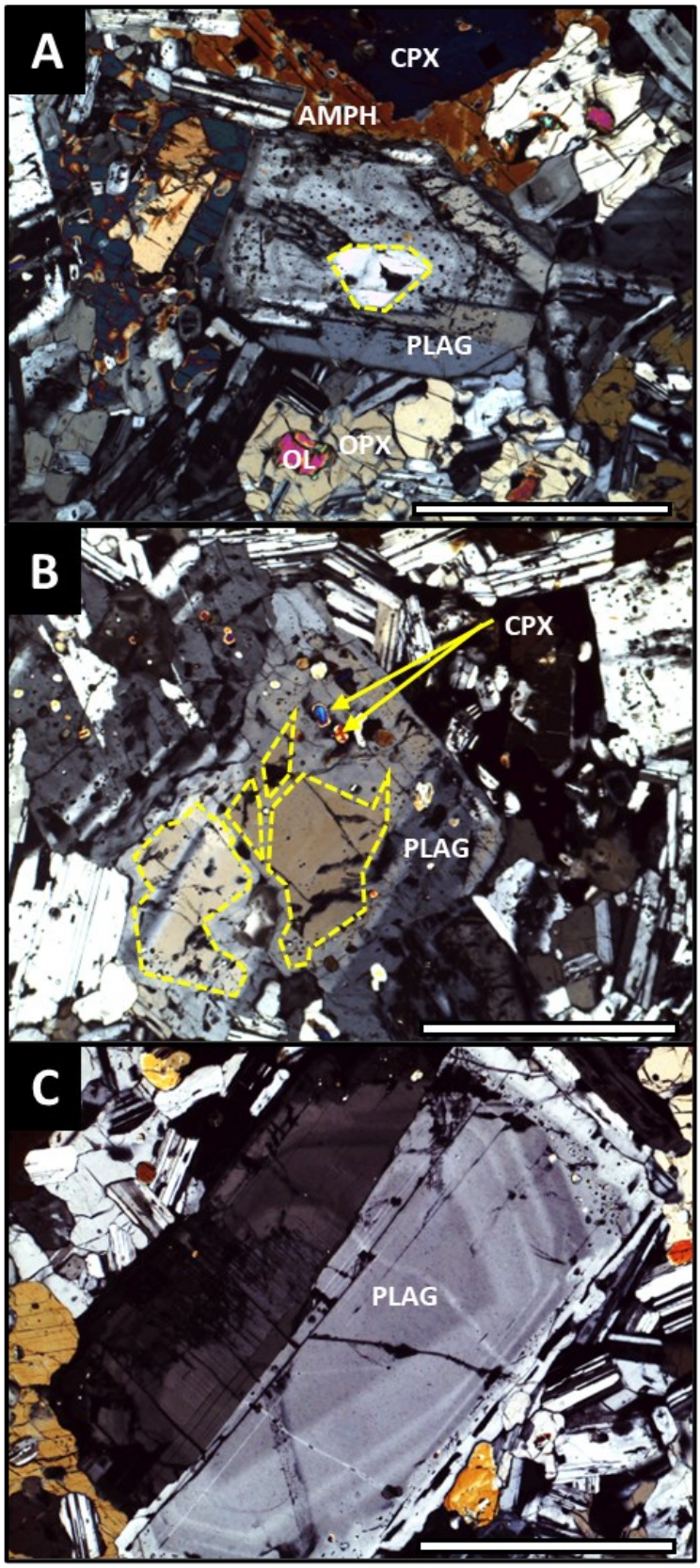

Figure 3.37: A) and **B)** Zoned plagioclase with cores outlined (dashes) from VS572/poikilitic Hbl-Ol gabbro. Correspondence with the chemical map (**Chapter 5**) shows that these cores have a high An content. Inclusions of clinopyroxene are present within a mantle zone of the plagioclase crystal in **B**. **C)** Oscillatory zoned plagioclase. White scale bar = 1 mm.

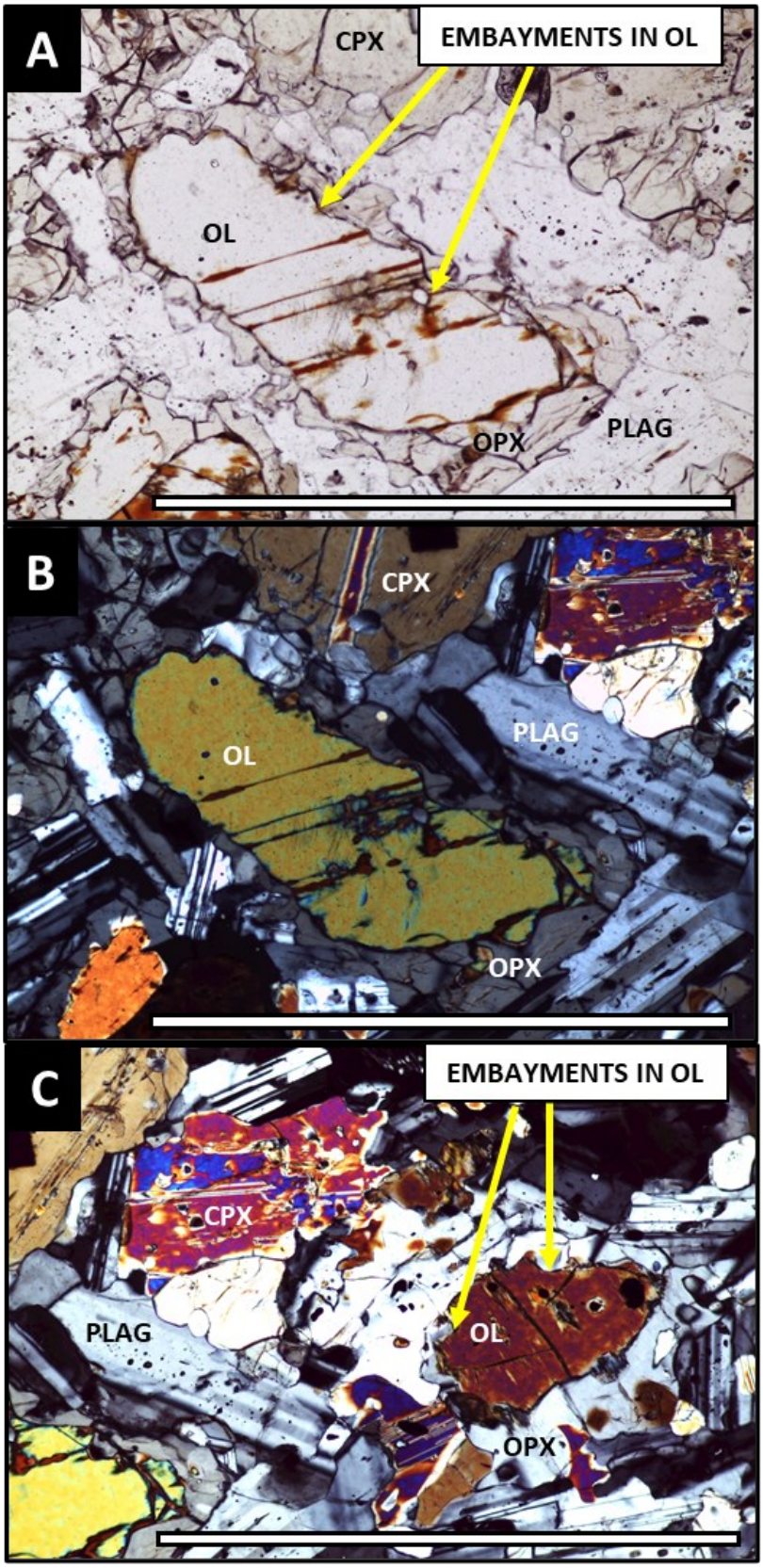

Figure 3.38: A) PPL and **B)** XPL example of poikilitic orthopyroxene surrounding embayed olivine from VS572/poikilitic Hbl-Ol gabbro. **C)** XPL example of poikilitic orthopyroxene surrounding embayed olivine. White scale bar = 1 mm.

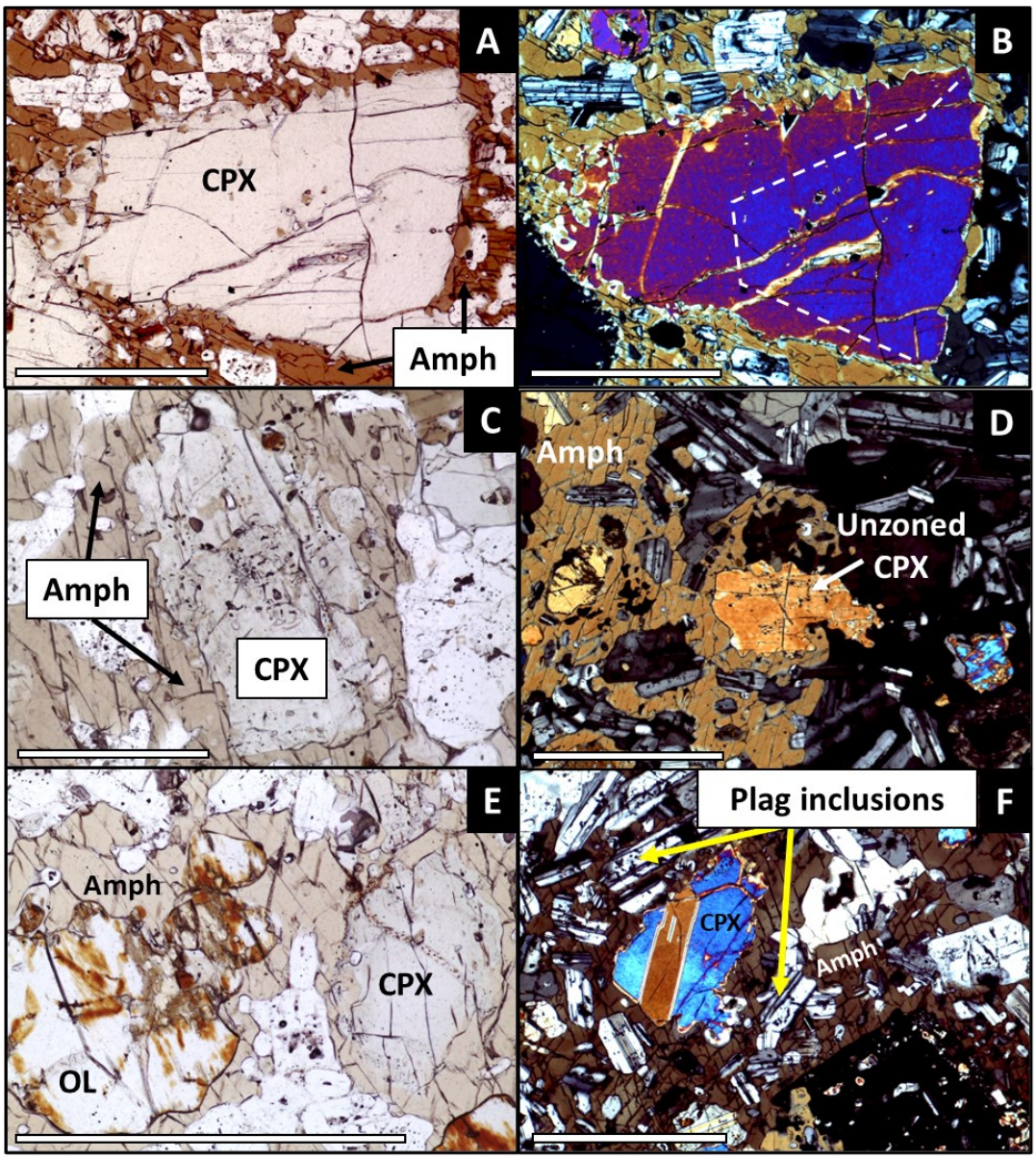

Figure 3.39: A) PPL and **B)** XPL image of zoned clinopyroxene (CPX) crystal from VS572/poikilitic Hbl-Ol gabbro with amphibole (Amph) replacing rim. The white dashed line in **B)** outlines the crystal core. **C)** PPL image of poikilitic amphibole (brown) replacing the rim of clinopyroxene from VS572/poikilitic Hbl-Ol gabbro. Note the ragged grain boundaries between clinopyroxene and amphibole in **A, B and C. D)** XPL image of unzoned clinopyroxene crystal from VS572/poikilitic Hbl-Ol gabbro, with poikilitic amphibole around part of the rim. **E)** PPL image of poikilitic amphibole (pale brown) surrounding CPX and olivine, which is variably altered to iddingsite (brown staining). **F)** Plagioclase inclusions in poikilitic amphibole. White scale bar = 1 mm.

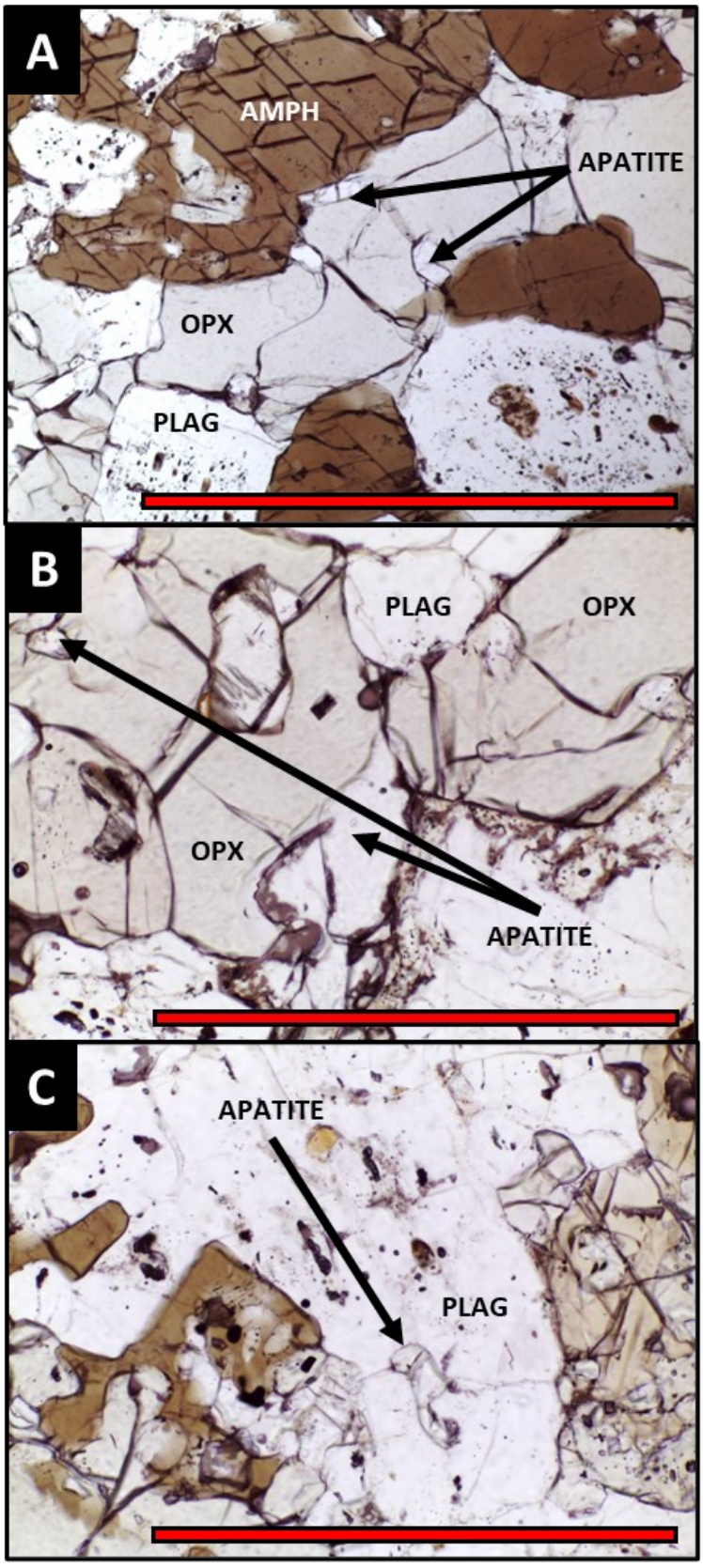

Figure 3.40: A), B) and **C)** Examples of interstitial apatite in different locations across VS572/poikilitic Hbl-Ol gabbro, in PPL. Red scale bar = 0.5 mm.

Chapter 4 - Isotopic compositions of plagioclase from plutonic xenoliths reveal crustal assimilation below Martinique, Lesser Antilles arc

A version of this chapter has been published in Frontiers in Earth Science: Brown, J. R., Cooper, G. F., Nowell, G. M., Macpherson, C. G., Neill, I., & Prytulak, J. (2021). Isotopic compositions of plagioclase from plutonic xenoliths reveal crustal assimilation below Martinique, Lesser Antilles arc. *Frontiers in Earth Science*, *9*, 682583.

Author contributions: The work for this chapter and manuscript is my own, conducted with support of my co-authors that would be usual of a supervisory team.

The plutonic xenolith whole rock data presented in this chapter were collected by supervisors Dr George Cooper and Dr Geoff Nowell. This data was interpreted as part of this work and published as part of the above listed manuscript.

Abstract

The chemical and isotopic compositions of volcanic arc lavas often show evidence for involvement of a sedimentary component during magma genesis. Determining where this sedimentary component is added to arc magmas is of vital importance for constraining the extent to which sediments and volatiles are recycled at subduction zones. Lavas from Martinique in the Lesser Antilles arc have wide ranging isotopic compositions extending to highly radiogenic values (e.g. $^{87}Sr/^{86}Sr$ up to ~0.710) that could, in principle, be explained by sediment addition to the mantle source or by crustal assimilation in the upper plate. We use Sr isotopic compositions of plagioclase from

Martinique plutonic xenoliths to provide evidence supporting the crustal assimilation hypothesis. Plagioclase from plutonic xenoliths formed in the mid-crust (~ 12 km) show a restricted range of unradiogenic Sr isotope ratios ($^{87}Sr/^{86}Sr$ = 0.7041 - 0.7042) whereas plagioclase from upper crustal plutonic xenoliths (~ 6 km) show greater intra-sample variation and more radiogenic Sr isotopic compositions up to $^{87}Sr/^{86}Sr = 0.7047$. This trend is also observed in plutonic xenolith whole rock $^{87}Sr/^{86}Sr$. Combined, these results indicate that the range of Sr isotope compositions becomes larger and more radiogenic in Martinique magmas as a result of sediment assimilation at shallow crustal levels. This is supported by Assimilation-Fractional Crystallization modelling, which shows that assimilation of chemically and isotopically heterogenous crustal sediments can produce the isotopic variation in Martinique plutonic xenoliths and lavas. Our results highlight the importance of constraining crustal contributions from the upper plate before using arc lava geochemistry to quantify sediment and volatile recycling at subduction zones and assessing potential heterogeneity of arc mantle sources.

4.1 - Introduction

The chemical and isotopic compositions of arc magmas are generally considered to reflect contributions from the mantle wedge combined with fluids and/or melts derived from subducting oceanic crust and sediments (e.g. Kelemen et al., 2003 and references therein). Many arc magmas have trace element and isotopic compositions displaced from MORB towards crustal compositions (e.g. Davidson et al., 2005), which may be explained by input from the subducting slab, or assimilation of arc crust during magma ascent and storage. Geochemical constraints upon the relative importance of slab versus upper plate contributions to arc magmas have clear implications for understanding sediment recycling at subduction zones. Trace element contents of lavas have been combined with estimates of the trace element input from subducting sediments to perform mass balance calculations to determine the extent of sediment recycling (e.g. Plank and Langmuir, 1993). However, modification of trace element concentrations in arc lavas by assimilation of crustal material can cause misleading estimates of the amount of sediment recycled into the mantle. Similar calculations have been used to assess recycling of volatiles e.g. CO_2 at subduction zones (Bebout et al.,

2014 and references therein). Assimilation of crustal sediments also modifies the volatile budget of arc magmas (e.g. Chadwick et al., 2007; Deegan et al., 2010), which in turn affects eruption explosivity, hence it is vital to constrain the relative contributions of the overlying versus subducting plate to quantify recycling in arc systems.

Lavas from the intra-oceanic Lesser Antilles arc (LAA, **Figure 4.1)** are notable for their extreme range in radiogenic isotopic compositions, extending from MORB-like signatures to highly radiogenic, "*crustal/sedimentary*" values (**Figure 4.2**; Davidson, 1985; 1986; Davidson et al., 1987; Davidson and Harmon, 1989; Van Soest, 2000; Labanieh et al., 2010; Bezard et al., 2014). Lavas show radiogenic isotopic variation both along the arc and at individual volcanic centers (**Figure 4.3).** Lavas from the island of Martinique span the whole Sr, Nd and Pb isotopic range of the arc (**Figures 4.2 and 4.3**, Nd isotopes not shown), and therefore provide an ideal suite to investigate the cause(s) of these variations.

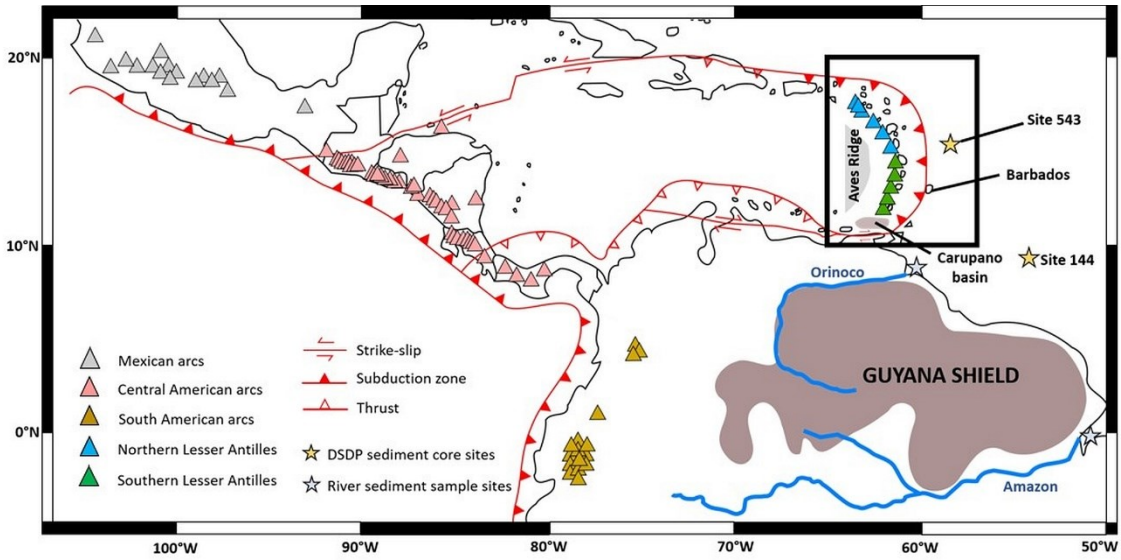

Figure 4.1: Tectonic setting of Lesser Antilles arc (outlined by black box) and nearby arcs in Central-South America. The sampling sites of sediments discussed in **section 4.4.1** are labelled. Locations of Site 543 and Site 144 from Carpentier et al. (2008). Locations for Orinoco and Amazon samples from Allegre et al. (1996), Parra et al. (1997) and Rousseau et al. (2019).

The large isotopic variation in the LAA, and in particular Martinique lavas, has been interpreted as the result of variable sediment addition (White and Dupre, 1986; Davidson et al., 1987; Carpentier et al., 2008). However, there exists significant debate as to whether the sedimentary component is (1) added to the mantle wedge from

subducting sediments (White and Dupre, 1986; Carpentier et al., 2008; Labanieh et al., 2010; 2012; Hu et al, 2021), or (2) incorporated during magma ascent and storage in the upper plate, via assimilation of unsubducted crustal sediments (Davidson, 1985, 1986; Davidson et al., 1987; Davidson and Harmon, 1989; Smith et al., 1996; Van Soest et al., 2002; Davidson and Wilson, 2011; Bezard et al., 2014).

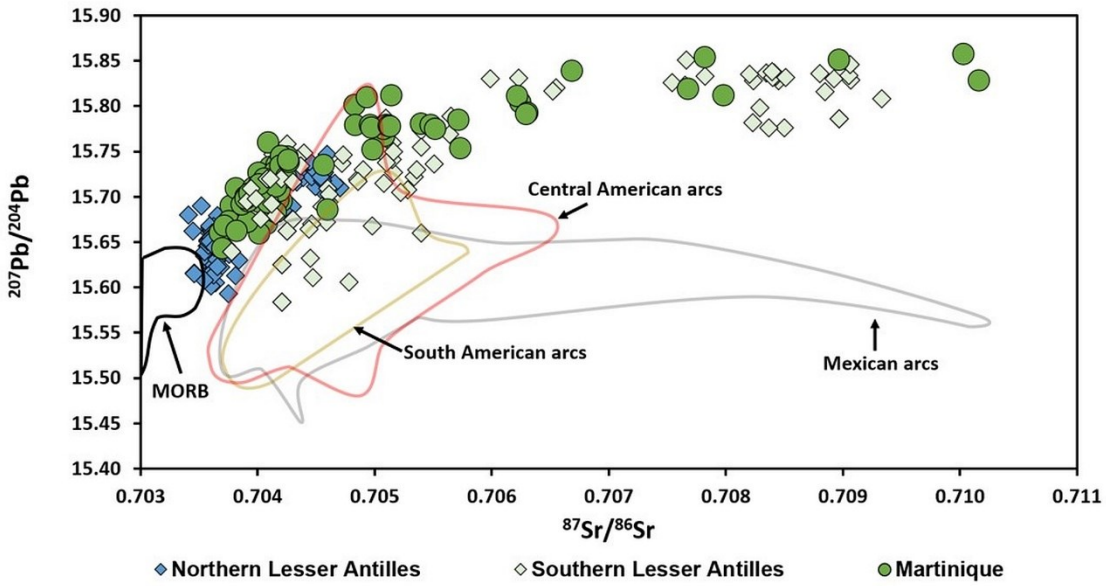

Figure 4.2: $^{87}Sr/^{86}Sr$ vs $^{207}Pb/^{204}Pb$ of lavas from the Lesser Antilles arc, compared to nearby arcs from Central-South America shown in **Figure 4.1.** For all data points, uncertainty (2 SE) is smaller than symbol size. Northern Lesser Antilles = Saba to Dominica. Southern Lesser Antilles = Martinique to Grenada (Martinique data shown separately). **Data sources:** Northern Lesser Antilles – Van Soest et al. (2002), Lindsay et al. (2005), Toothill et al. (2007), DuFrane et al. (2009), Davidson and Wilson (2011). Southern Lesser Antilles – Thirlwall and Graham (1984), Davidson (1986), White and Dupre (1986), Smith et al. (1996), Thirlwall et al. (1996), Turner et al. (1996), Heath et al. (1998), Labanieh et al. (2010), Huang et al. (2011), Bezard et al. (2014). Southern American, Central American and Mexican arc data from the Georoc database (http://georoc.mpch-mainz.gwdg.de/georoc/). MORB data from the PetDB database (www.earthchem.org/petdb) for Mid-Atlantic Ridge basalts 30° either side of the equator. Labanieh et al. (2010) found that the difference between measured and age corrected isotope ratios for the oldest lavas in the arc (~25 Ma, from Martinique) was negligible. Since majority of lavas in the LAA are much younger than 25 Ma, age correction is considered negligible by majority of authors and would not alter the trend shown.

The majority of previous studies have used whole rock radiogenic isotopic compositions of arc lavas to assess the origin of the crustal signature, but there are potential issues with this approach. Crystals formed in different parts of a magma

plumbing system record the isotopic composition of the magmas from which they grew. Whole rock compositions average the isotopic signatures of individual components e.g. crystals and groundmass, hence evidence for changes in isotopic composition of magmas during storage in the crust (recorded by the crystals) may be lost. The use of lavas may also be problematic since late stage processes such as magma mixing and/or subaerial alteration have the potential to overprint processes occurring deeper in the crust (e.g. Davidson et al., 2007b). In addition, the mid to lower crust of the upper plate is probably a key location for the differentiation of arc lavas (e.g. the 'Deep Crustal Hot Zone' of Annen et al., 2006). Finally, arc lavas travel from their mantle source through the crust before they are erupted. Even when fresh arc lava chemistry unambiguously indicates a sedimentary component, it is extremely challenging to determine where that component was incorporated.

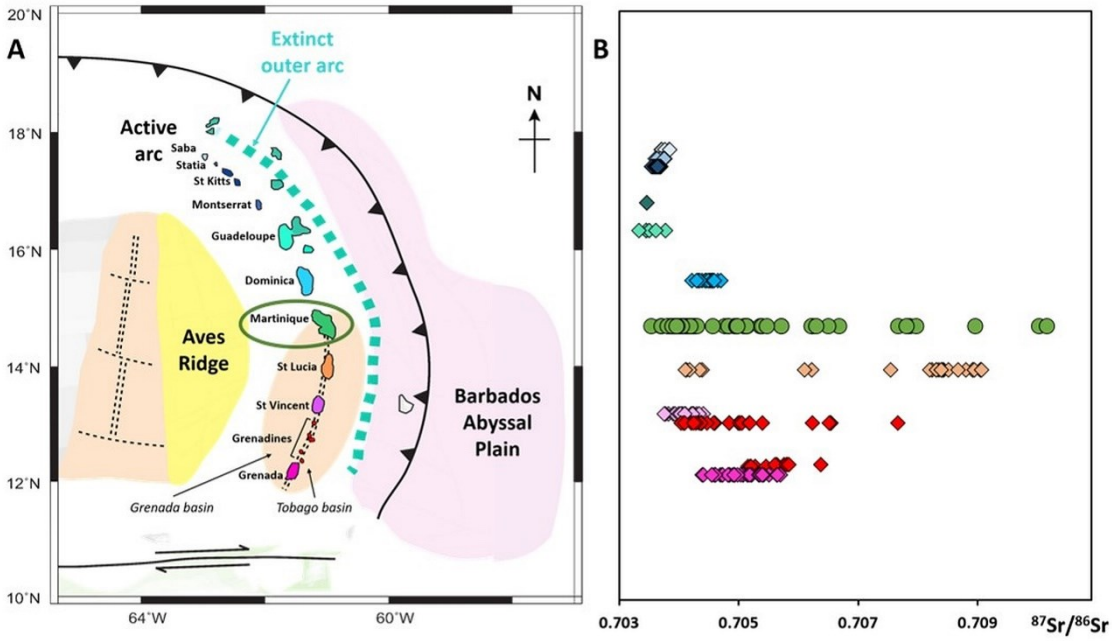

Figure 4.3: A) Map of Lesser Antilles arc (region marked by black outlined box on **Figure 4.1**) modified from Allen et al. (2019). **B)** Compilation of along arc variation in $^{87}Sr/^{86}Sr$ of lavas. For all data points, uncertainty (2 SE) is smaller than symbol size. Data sources are the same as **Figure 4.2**. Note that the same along arc trends are also observed in the Nd and Pb isotopic systems.

To overcome these ambiguities, this study explores plagioclase from plutonic xenoliths and their Sr isotopic compositions. The LAA is notable for its abundant plutonic xenoliths (e.g., Arculus and Wills, 1980; Melekhova et al. 2019), which represent deeper parts of the magmatic plumbing system. We focus on samples from Martinique due to its well-established variability in whole rock lava compositions and compare

our findings with the more isotopically restricted island of St Vincent (**Figure 4.3)**. These Martinique plutonic xenoliths record crystallization conditions at 21 to 6 km depth in the crust (Cooper et al., 2016; Melekhova et al., 2019) and, therefore, have the potential to record the isotopic composition of magmas throughout the crust.

Previous studies have employed the $^{87}Sr/^{86}Sr$ isotopic composition of plagioclase phenocrysts in erupted lavas to assess crustal assimilation at arc volcanoes (e.g. Davidson et al., 2007b; Bezard et al., 2014; Ginibre and Davidson, 2014; Waight and Tornqvist, 2018). Plagioclase is ubiquitous in Lesser Antilles plutonic xenoliths. Strontium concentrations in plagioclase are high (generally > 250 µg/g, Cooper et al., 2016), thus precise $^{87}Sr/^{86}Sr$ measurements can be achieved on microgram sized pieces extracted from crystals (Charlier et al., 2006). Here, we determine the Sr isotopic composition of crystal domains within individual plagioclase crystals in plutonic xenoliths from a range of depths in the arc crust. We aim to test whether or not the plutonic roots of Martinique already display a radiogenic Sr isotopic composition. A radiogenic composition (similar to the higher $^{87}Sr/^{86}Sr$ lavas) is expected if subducted sediments are incorporated into the mantle source, whereas less radiogenic compositions would support a dominant role for crustal contamination within the upper plate.

4.2 - Materials and Methods

4.2.1 – Sample Suite

Plutonic xenoliths were collected between 2008 and 2017 during a series of field campaigns to the Lesser Antilles. Five plutonic xenoliths from Martinique (MQ1, MQ6, MQ35, MQ48 and MQ59) and one from St Vincent (VS36) were chosen as the focus of this study. These samples form part of a wider sample set characterised in terms of petrology, mineral chemistry and whole rock major and trace elements by Cooper et al. (2016) and Tollan et al. (2012), providing key context for plagioclase isotopic analyses. We also present whole rock Sr, Nd, and Pb isotope data for 15 of the characterised Martinique plutonic xenoliths to give further context to our plagioclase Sr isotope data. Samples were collected ex situ, mostly from river beds on the flanks

of volcanic edifices. The Martinique xenoliths are inferred to be derived from eruptions of either Mt Pelee (0-126 ka) or Mt Conil (127-550 ka), the most recent phases of volcanic activity on the island (Germa et al., 2011; Cooper et al., 2016). The St Vincent xenolith is inferred to have been erupted at La Soufriere volcano (<3.6 ka, Heath et al., 1998; Tollan et al., 2012).

Samples show good textural equilibration (120° grain contacts, minor or no evidence for deformation). The relative equilibration depths of selected xenoliths were estimated by mineral geobarometry and comparison to experimental studies (Cooper et al., 2016; Melekhova et al., 2019). Calculated depths vary from 21 km to 6 km, though large uncertainty exists on these estimates (typically ~ 6 km). This suggests that the plutonic xenoliths represent portions of the magmatic plumbing system covering the middle to upper crust.

Plagioclase from Martinique lava sample M8321 ($^{87}Sr/^{86}Sr$ = 0.706246; Davidson, 1986) were also analysed for Sr isotopic composition. This is one of the most radiogenic Martinique lavas with plagioclase crystals large enough for isotopic analysis. The lava is from the emergent/subaerial phase of the Intermediate arc, dated at 9.2-8.4 Ma (Germa et al., 2011), in a period when the most radiogenic (highest $^{87}Sr/^{86}Sr$) lavas in Martinique were erupted (Davidson, 1986; Labanieh et al., 2010).

4.2.2 – Sampling and analytical techniques

Details of sample and target crystal selection, micro-milling and analytical procedures are outlined briefly below and are described in detail in **Chapter 2.** All laboratory procedures were carried out at Durham University, in the G.J. Russell Electron Microscopy Facility and the Arthur Holmes Isotope Geology Laboratory.

4.2.2.1 – Plutonic xenolith sample selection

A subset of the plutonic xenoliths characterized by Cooper et al. (2016), with a variety of mineral assemblages, were chosen for plagioclase isotopic analyses. Selected plagioclase crystals cover a range of anorthite contents **(Chapter 3, Table 3.1)**. The plutonic xenolith from St Vincent was included to compare a nearby volcanic center with restricted isotopic variation (Heath et al., 1998; **Figure 4.3**).

Optical microscopy of 100 µm thick sections was used to identify suitable plagioclase crystals for micro-milling and isotopic analysis. Potential target crystals were defined as containing minimal cracks and inclusions, and distinct core and rim zones if present. Electron backscatter imaging (BSE) and chemical mapping using a Hitachi SU70 SEM was used to confirm the presence/lack of chemical zoning (details in **Chapter 3**). BSE images and chemical maps were then assessed to identify the most suitable plagioclase domain(s) for microanalysis.

4.2.2.2 – Micro-milling

Material was recovered from plagioclase in situ, using a New Wave Micromill. The micro-milling and sample recovery procedure closely followed Charlier et al. (2006) except that to maximize sample recovery trenches were milled rather than a series of conical holes as in the former study. Sampling trenches were 60 µm deep and of sufficient length to yield ≥ 3 ng Sr for analysis, based on calculations of volume of material removed during milling and assuming a minimum Sr concentration of 250 µg/g (based on plagioclase Sr concentration data from Cooper et al. 2016). During micromilling, care was taken to avoid inclusions wherever possible.

4.2.2.3 - Chemical separation and measurement

Milled material was digested using 150 µl Teflon distilled (TD) 29 M HF:50 µl TD 16 M HNO_3 and refluxed overnight on a hotplate at 100 °C. The solution was then evaporated to incipient dryness at 100°C and the residue taken up in 50 µl TD 16 M HNO_3. This solution was returned to the hotplate for 90 minutes, evaporated, and re-dissolved in 50 µl TD 16 M HNO_3. The solution was evaporated, taken up in 400 µl TD 3 M HNO_3 and refluxed at 100 °C prior to Sr separation.

Strontium separation closely follows the procedure outlined in Charlier et al. (2006). Briefly, Sr was separated and purified via two passes through pre-cleaned Eichrom Sr spec resin. Samples were loaded on to the resin in 400 µl TD 3 M HNO_3. Matrix elements were eluted with 3 x 250 µl TD 3 M HNO_3 followed by Sr elution with 400 µl Milli-Q water. The Sr solutions were subsequently evaporated at 100 °C. All samples and standards were analysed for Sr isotope ratios on a Thermo Fisher Scientific Triton Plus Thermal Ionisation Mass Spectrometer (TIMS). Full details of the measurement protocol are given in **Chapter 2**.

External precision and accuracy were assessed via multiple measurements of NIST Sr standard NBS 987 throughout the period of analyses, of varying load sizes from 1 to 10 ng (i.e. of similar size to the samples). The average $^{87}Sr/^{86}Sr = 0.710259 \pm 0.000031$ (2σ, n=33) agrees well with the accepted value of $^{87}Sr/^{86}Sr = 0.710248 \pm 0.000023$ 2σ (Thirlwall, 1991). Method accuracy was also assessed via 7 repeat analyses of ~10 ng Sr loads of USGS reference material BCR-2. To avoid potential heterogeneity with the BCR-2 powder a single large digestion was made from which repeat 10 µl aliquots were taken and diluted with 390 µl TD 3 M HNO_3 prior to Sr separation. The average $^{87}Sr/^{86}Sr = 0.705041 \pm 0.000063$ (2σ, n=7) agrees within uncertainty of the value of $^{87}Sr/^{86}Sr = 0.705013 \pm 0.000010$ 2σ obtained with TIMS analyses of BCR-2 by Weis et al. (2006).

Total procedural blanks measured 5-20 pg (n = 6) and column blanks 3-50 pg (n = 9), with all but one below 25 pg. Concentration checks on aliquots of sample solutions taken after Sr separation indicated that majority of samples contained > 3 ng Sr, therefore blanks are typically < 1 % of sample size and any blank correction would be negligible.

4.2.2.4 – Whole rock Sr-Nd-Pb isotopes

The plutonic xenoliths analysed for major and trace element compositions by Cooper et al. (2016) were previously powdered and whole rock Sr, Nd, and Pb isotopes were determined on these powders using standard HF dissolution techniques and established column separation and measurement techniques. A more detailed description, including standard data, is found in **Chapter 2**.

4.3 - Results

4.3.1 – Petrography

4.3.1.1 – Petrography and classification of xenoliths

Plutonic xenoliths are identified as either “cumulates” or “non-cumulate gabbros” based on chemical and textural characteristics (Cooper et al., 2016). If the whole rock and mineral chemistry (and texture) are consistent with the xenolith originating as a

subtractive assemblage it is identified as a cumulate. Otherwise, xenoliths are identified as non-cumulate gabbros (NCG), indicative of origin as solidified equivalents of potentially eruptible lavas, formed "without movement of crystals relative to host melts" (Cooper et al., 2016; 2019). Based on these definitions, this study analysed the Sr isotopic composition of plagioclase in four cumulates and two NCG's. Mineral phases include plagioclase (Pl), clinopyroxene (CPX), orthopyroxene (OPX), amphibole (Hornblende, Amph/Hbl), olivine (Ol), and oxides (Ox), which is typical of Lesser Antilles plutonic xenolith assemblages (Arculus and Wills, 1980; Tollan et al., 2012; Stamper et al., 2014; Cooper et al., 2016; 2019, Melekhova et al., 2019). Xenoliths are classified based on mineral assemblage using the scheme of Streckeisen (1976), and textural features. Those in which plagioclase were analysed cover almost the full range of plutonic xenolith types from Martinique identified by Cooper et al. (2016). The single investigated lava is a two-pyroxene andesite typical of Martinique (e.g. intermediate subaerial lavas from Davidson, 1986).

A detailed petrographic description of each sample is given in **Chapter 3**. The classification and petrographic observations listed for each plutonic xenolith sample are summarised from Cooper et al. (2016) and Tollan et al. (2012), supplemented by additional details on the characteristics of plagioclase, including SEM images showing the crystals selected for isotopic analysis.

4.3.1.2 - How representative are selected plagioclase?

Plagioclase crystals were chosen primarily for their suitability for micromilling, and care was taken to ensure that selected crystals were representative of each sample. All crystals analysed from cumulates are characterised by a lack of zonation (excluding minor overgrowth rim zones too narrow to be targeted by micro-milling). Examples of typical unzoned cumulate plagioclase are shown in **Figure 4.4.** Where multiple plagioclase size populations were observed, e.g. MQ48, crystals from both populations were targeted. In NCG's, about half of the plagioclase crystals display normal zoning (examples shown in **Figure 4.4**), which provided an opportunity to assess changes in isotopic composition during their crystallization. All crystals selected from these samples display normal zoning, with both cores and rims analysed. The three plagioclase crystals selected from lava M8321 display the three different zoning

patterns (described in **Chapter 3**). In this sample cores, rims, and bulk groundmass were analysed.

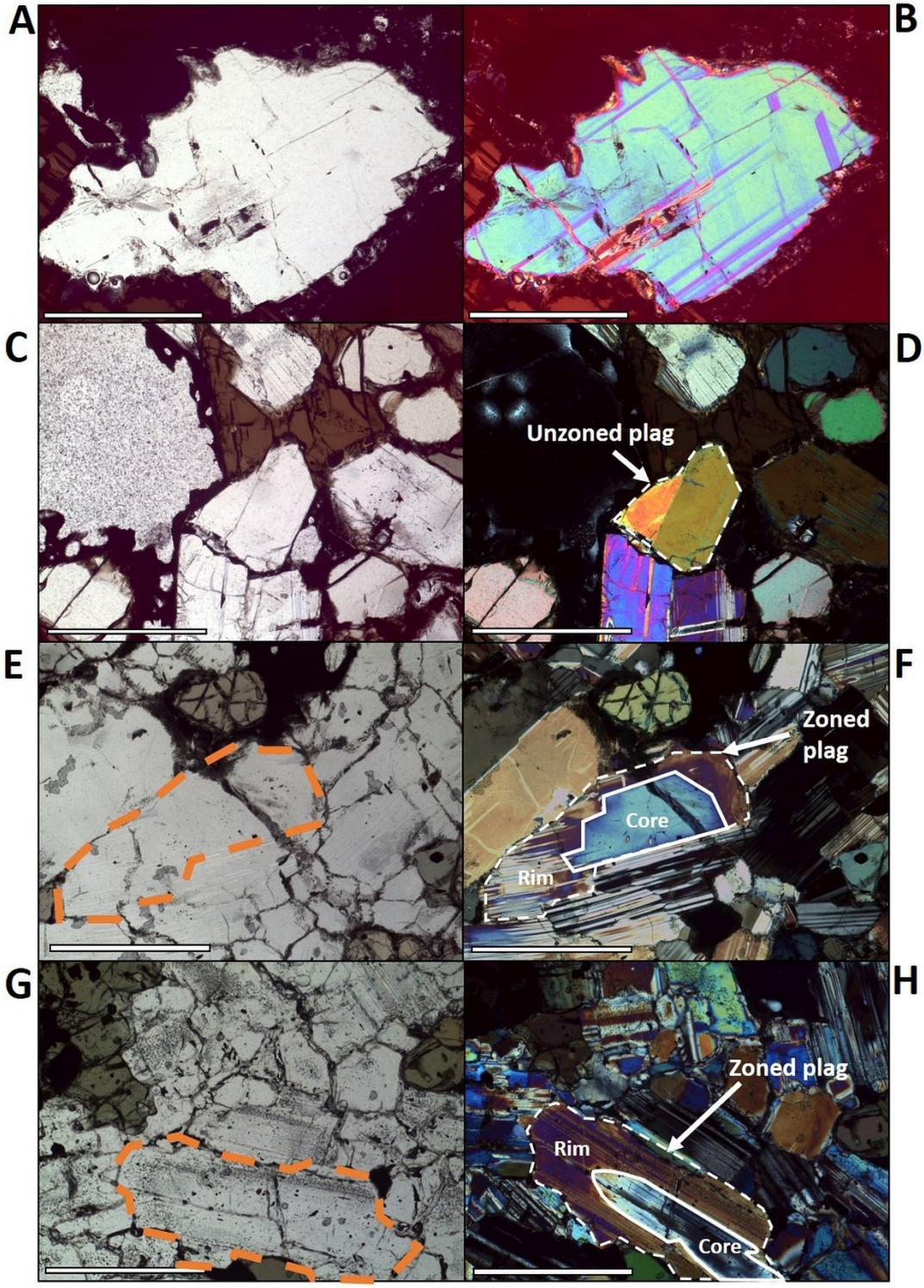

Figure 4.4: A) and **B)** Typical unzoned cumulate plagioclase from sample MQ59. **C)** and **D)** Typical unzoned cumulate plagioclase from sample MQ48. **E)** and **F)** Typical zoned plagioclase in NCG sample MQ35. **G)** and **H)** Typical zoned plagioclase in NCG sample MQ6. Orange outlines in **E)** and **G)**

highlight labelled zoned plagioclase in **F)** and **H)**. Images **A), C), E)** and **G)** in PPL, **B), D), F)** and **H)** in XPL. White scale bar = 1 mm. Unusually high birefringence colours in XPL images are due to the 100 μm thickness of the sections.

4.3.2 - Geochemical Results

Plagioclase Sr isotopic data is presented in **Table 4.1** and plutonic xenolith whole rock Sr, Nd and Pb isotopic data in **Table 4.2**. Rb/Sr ratios are very low (<0.01) in plutonic xenolith whole rock and plagioclase, and the maximum sample age is estimated at 25 Ma, hence age correction is negligible, with the exception of the M8321 groundmass data (see **Chapter 2** for age correction details).

Sample type	Sample and crystal no.	$^{87}Sr/^{86}Sr$	2 SE	Whole rock $^{87}Sr/^{86}Sr$
Cumulates	VS36 - C1	0.703974	0.000012	
	VS36 - C2	0.704000	0.000008	
	VS36 - C3	0.703927	0.000011	
	VS36 - C4	0.703859	0.000038	
	VS36 - C5	0.703933	0.000007	
	MQ1 - C1	0.704191	0.000008	
	MQ1 - C2	0.704121	0.000006	
	MQ1 - C3	0.704202	0.000013	
	MQ59 - C1	0.704067	0.000006	0.704009
	MQ59 - C2	0.704221	0.000014	
	MQ59 - C3	0.704077	0.000013	
	MQ59 - C4	0.704059	0.000009	
	MQ59 - C5	0.704077	0.000011	
	MQ48 - C1	0.704113	0.000020	0.703983
	MQ48 - C2	0.704087	0.000012	
	MQ48 - C3	0.704086	0.000024	
	MQ48 - C4	0.704179	0.000010	
NCG	MQ6 C1 Core	0.703820	0.000012	
	MQ6 C2 Core	0.704055	0.000020	
	MQ6 C3 Core	0.703989	0.000014	
	MQ6 C4 Core	0.704334	0.000030	
	MQ6 C1 Rim	0.703943	0.000022	
	MQ6 C2 Rim	0.704058	0.000014	

	MQ6 C3 Rim	0.703971	0.000012	
	MQ6 C4 Rim	0.703996	0.000014	
	MQ35 C1 Core	0.704770	0.000014	0.704562
	MQ35 C2 Core	0.704622	0.000009	
	MQ35 C3 Core	0.704576	0.000009	
	MQ35 C1 Rim	0.704718	0.000014	
	MQ35 C2 Rim	0.704622	0.000010	
	MQ35 C3 Rim	0.704692	0.000013	
Andesitic lava	M8321 C1 Core	0.706157	0.000016	0.706246
	M8321 C2 Core	0.706219	0.000014	
	M8321 C3 Core	0.706259	0.000056	
	M8321 C2 Rim	0.706229	0.000021	
	M8321 C3 Rim	0.706185	0.000028	
	M8321 GM1 9.2 Ma	0.706261	0.000007	
	M8321 GM2 9.2 Ma	0.706286	0.000005	
	M8321 GM3 9.2 Ma	0.706261	0.000012	
	M8321 GM1 8.4 Ma	0.706282	0.000007	
	M8321 GM2 8.4 Ma	0.706307	0.000005	
	M8321 GM3 8.4 Ma	0.706282	0.000012	

Table 4.1: $^{87}Sr/^{86}Sr$ of individual plagioclase in cumulates, and core and rim zones of plagioclase in NCG's and lava. Whole rock $^{87}Sr/^{86}Sr$ also shown if available. Lava whole rock value from Davidson, (1986). SE = standard error.

4.3.2.1 – Martinique cumulate plagioclase

Unzoned plagioclase from Martinique cumulates show a restricted range of unradiogenic Sr isotope ratios across all three samples ($^{87}Sr/^{86}Sr$ = 0.704059 - 0.704221) **(Figures 4.5 and 4.6).** Cumulate plagioclase $^{87}Sr/^{86}Sr$ slightly exceeds whole rock values **(Figure 4.6).**

4.3.2.2 – Martinique non-cumulate gabbro plagioclase

Plagioclase cores from both NCG samples show greater intra-sample Sr isotopic variation than those of unzoned plagioclase in cumulates **(Figures 4.5 and 4.6).** MQ6 cores show a wider range in $^{87}Sr/^{86}Sr$ (0.703820 - 0.704334) than MQ35 cores (0.704576 - 0.704770). Within samples, plagioclase rim compositions show a more

limited range in $^{87}Sr/^{86}Sr$ than cores (MQ6 = 0.703943 - 0.704058, MQ35 = 0.704622 - 0.704718) **(Figures 4.5 and 4.6).** No systematic variation in $^{87}Sr/^{86}Sr$ between core and rim is present in either sample. Notably, plagioclase in MQ35 is more radiogenic than that of cumulates. In MQ35 $^{87}Sr/^{86}Sr$ in plagioclase is equivalent to or exceeds the whole rock value **(Figure 4.6).**

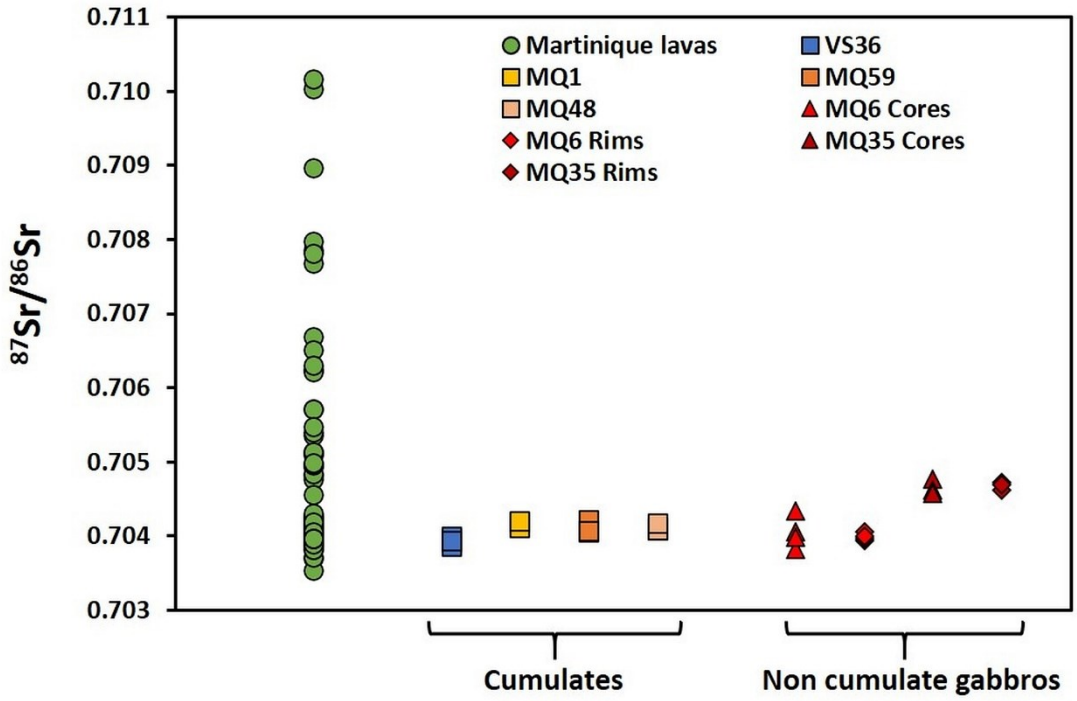

Figure 4.5: $^{87}Sr/^{86}Sr$ of individual plagioclase in cumulates, and core and rim zones of plagioclase in NCG's, compared with the whole rock $^{87}Sr/^{86}Sr$ range of Martinique lavas. Lava data from Davidson (1986) and Labanieh et al. (2010). For all data points, uncertainty (2 SE) is smaller than symbol size.

4.3.2.3 – Martinique andesitic lava plagioclase

Cores and rims in plagioclase from the andesitic lava (M8321) show a narrow range in $^{87}Sr/^{86}Sr$ (cores = 0.706157 - 0.706259, rims = 0.706185 - 0.706229), close to or within uncertainty of the whole rock value **(Figure 4.7).** Core-rim pairs have indistinguishable Sr isotopic compositions within uncertainty. Groundmass $^{87}Sr/^{86}Sr$ defines a very narrow range (0.706282 - 0.706307 corrected to 8.4 Ma, 0.706261 - 0.706286 corrected to 9.2 Ma).

4.3.2.4 – St Vincent cumulate plagioclase

Unzoned plagioclase crystals from a single St Vincent cumulate (VS36) have restricted and unradiogenic Sr isotope ratios ($^{87}Sr/^{86}Sr$ = 0.703859 – 0.704000), with slightly less radiogenic compositions than Martinique cumulate plagioclase **(Figure 4.6).**

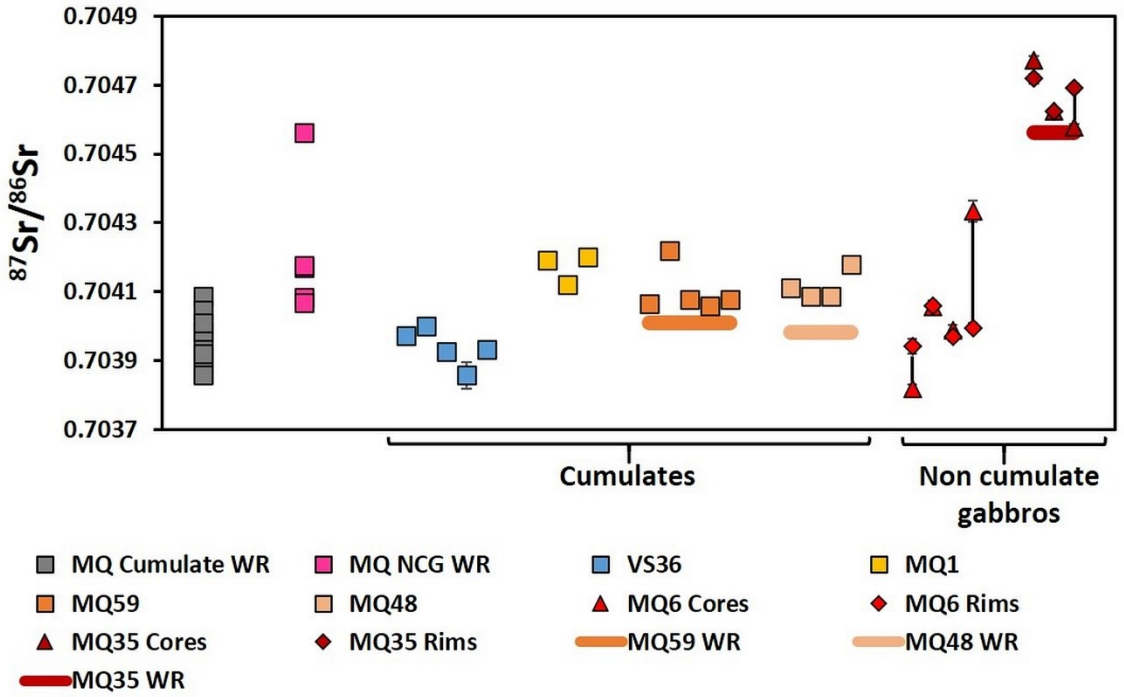

Figure 4.6: Details of $^{87}Sr/^{86}Sr$ variation in cumulate and NCG plagioclase. The whole rock $^{87}Sr/^{86}Sr$ range for Martinique cumulates and NCG's is plotted for comparison. Whole rock data for individual samples shown as coloured bars (bar width covers uncertainty). Where visible, black bars show uncertainty (2 SE), otherwise uncertainty is smaller than symbol size. Core-rim pairs are joined by tie lines.

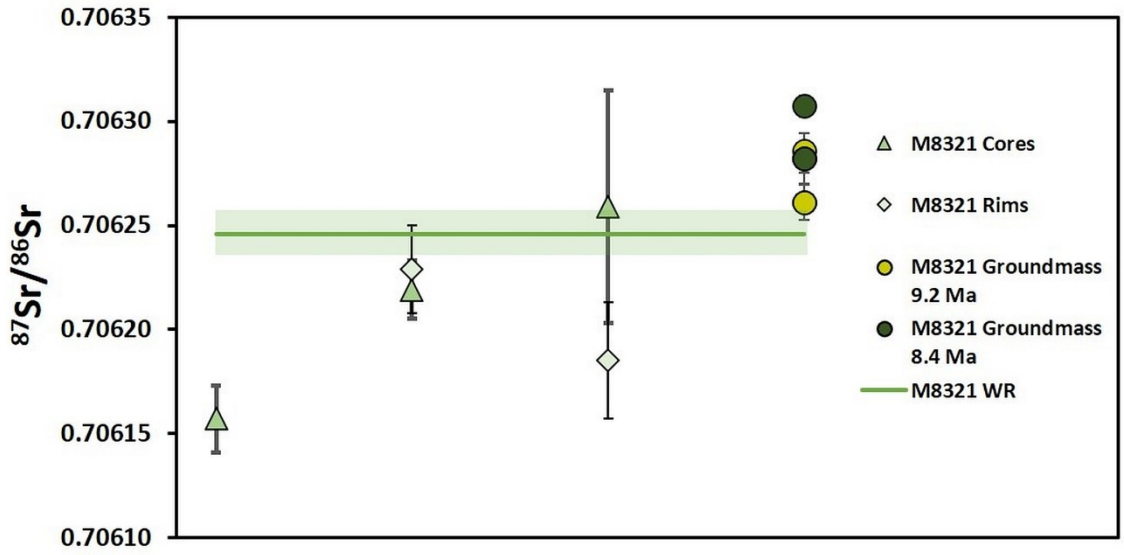

Figure 4.7: Details of $^{87}Sr/^{86}Sr$ variation in lava sample M8321. The whole rock value from Davidson (1986) is plotted for comparison. Black and grey bars (and green box around the WR value) show uncertainty (2 SE).

Sample type	Sample	$^{87}Sr/^{86}Sr$	2 SE	$^{143}Nd/^{144}Nd$	2 SE	$^{206}Pb/^{204}Pb$	2 SE	$^{207}Pb/^{204}Pb$	2 SE	$^{208}Pb/^{204}Pb$	2 SE
Cumulates	MQ44	0.703863	0.000008	0.512764	0.000031	19.21881	0.00059	15.69934	0.00074	38.97973	0.00232
	MQ48	0.703983	0.000010	0.512740	0.000049	19.16035	0.00071	15.69339	0.00070	38.91686	0.00233
	MQ42	0.703984	0.000010	0.512760	0.000032	19.15504	0.00056	15.69051	0.00052	38.91513	0.00178
	MQ61	0.703913	0.000011	0.512820	0.000023	19.20034	0.00063	15.71063	0.00054	38.98981	0.00167
	MQ43	0.704087	0.000010	0.512784	0.000016	19.30179	0.00106	15.72108	0.00110	39.06616	0.00340
	MQ28	0.703859	0.000010	0.512818	0.000029	19.15996	0.00057	15.70016	0.00058	38.92992	0.00196
	MQ10	0.703932	0.000010	0.512784	0.000015	19.15353	0.00074	15.68784	0.00074	38.91756	0.00214
	MQ12	0.704046	0.000009	0.512830	0.000007	19.91055	0.00065	15.75423	0.00059	39.04088	0.00201
	MQ30	0.703920	0.000011	0.512803	0.000018	19.11991	0.00065	15.68074	0.00064	38.88149	0.00181
	MQ59	0.704009	0.000009	0.512804	0.000020	19.21250	0.00061	15.70008	0.00068	38.97948	0.00194
NCG	MQ2	0.704171	0.000011	0.512904	0.000010	19.28292	0.00069	15.71803	0.00064	39.05094	0.00201
	MQ45	0.704178	0.000010	0.512822	0.000012	19.41224	0.00066	15.73765	0.00066	39.17373	0.00198
	MQ35	0.704562	0.000010	0.512790	0.000009	19.40569	0.00063	15.73735	0.00063	39.16694	0.00216
NCG (mushy)	MQ20	0.704083	0.000010	0.512832	0.000008	19.33140	0.00076	15.72662	0.00069	39.10648	0.00219
	MQ67	0.704069	0.000010	0.512852	0.000011	19.29855	0.00079	15.71064	0.00081	39.04603	0.00252

Table 4.2: Whole rock $^{87}Sr/^{86}Sr$, $^{143}Nd/^{144}Nd$, $^{206}Pb/^{204}Pb$, $^{207}Pb/^{204}Pb$, and $^{208}Pb/^{204}Pb$ of cumulates and NCG's. SE = standard error.

4.3.2.5 – Martinique plutonic xenolith whole rock data

Martinique cumulates show a narrow range in whole rock $^{87}Sr/^{86}Sr$ and unradiogenic compositions ($^{87}Sr/^{86}Sr$ = 0.703859 – 0.704087, **Figures 4.6 and 4.8**). NCG's show a wider range in whole rock $^{87}Sr/^{86}Sr$ and extend to slightly more radiogenic compositions ($^{87}Sr/^{86}Sr$ = 0.704069 – 0.704562, **Figures 4.6 and 4.8**).

Cumulates also show a restricted whole rock Nd isotopic range ($^{143}Nd/^{144}Nd$ = 0.512740 – 0.512830) which extends to slightly more unradiogenic compositions than NCG's ($^{143}Nd/^{144}Nd$ = 0.512790 – 0.512904) (**Figure 4.8**). Cumulate whole rock Pb isotopic compositions vary from $^{206}Pb/^{204}Pb$ = 19.11991 – 19.30179, $^{207}Pb/^{204}Pb$ = 15.68074 – 15.72108, and $^{208}Pb/^{204}Pb$ = 38.88149 – 39.06616 (**Figure 4.8**), excluding sample MQ12, which represents a clear outlier with anomalously high $^{206}Pb/^{204}Pb$ (19.91055) and $^{207}Pb/^{204}Pb$ (15.75423). NCG's show a slightly more radiogenic range in whole rock Pb isotopic compositions (**Figure 4.8**), with $^{206}Pb/^{204}Pb$ = 19.28292 – 19.41226, $^{207}Pb/^{204}Pb$ = 15.71064 – 15.73765, and $^{208}Pb/^{204}Pb$ = 39.04603 – 39.17373.

4.4 – Discussion

The new Sr isotopic data from plutonic xenoliths is used to test whether the crustal/sedimentary component in Martinique lavas is introduced from the subducting slab or upper plate crust. We first discuss the chemical characteristics of potential sediment sources on the subducting plate and in the arc crust. We then explain how the data supports the crustal sediment assimilation hypothesis. Assimilation-Fractional Crystallization modelling is used to attempt to quantify the amount of sediment addition and provide constraints on the type of sediments assimilated. Finally, the wider implications of these findings for magma genesis and subduction zone recycling processes in the LAA and other arcs are discussed.

4.4.1 – Potential sediment sources

If a sediment component is responsible for the range of isotopic compositions measured in Martinique lavas, then it must have more radiogenic Sr and Pb and less radiogenic Nd isotope compositions than the most extreme Martinique lava **(Figure 4.8a).** The lithological and chemical characteristics of the two main potential sediment sources – the slab and the arc crust - are discussed below.

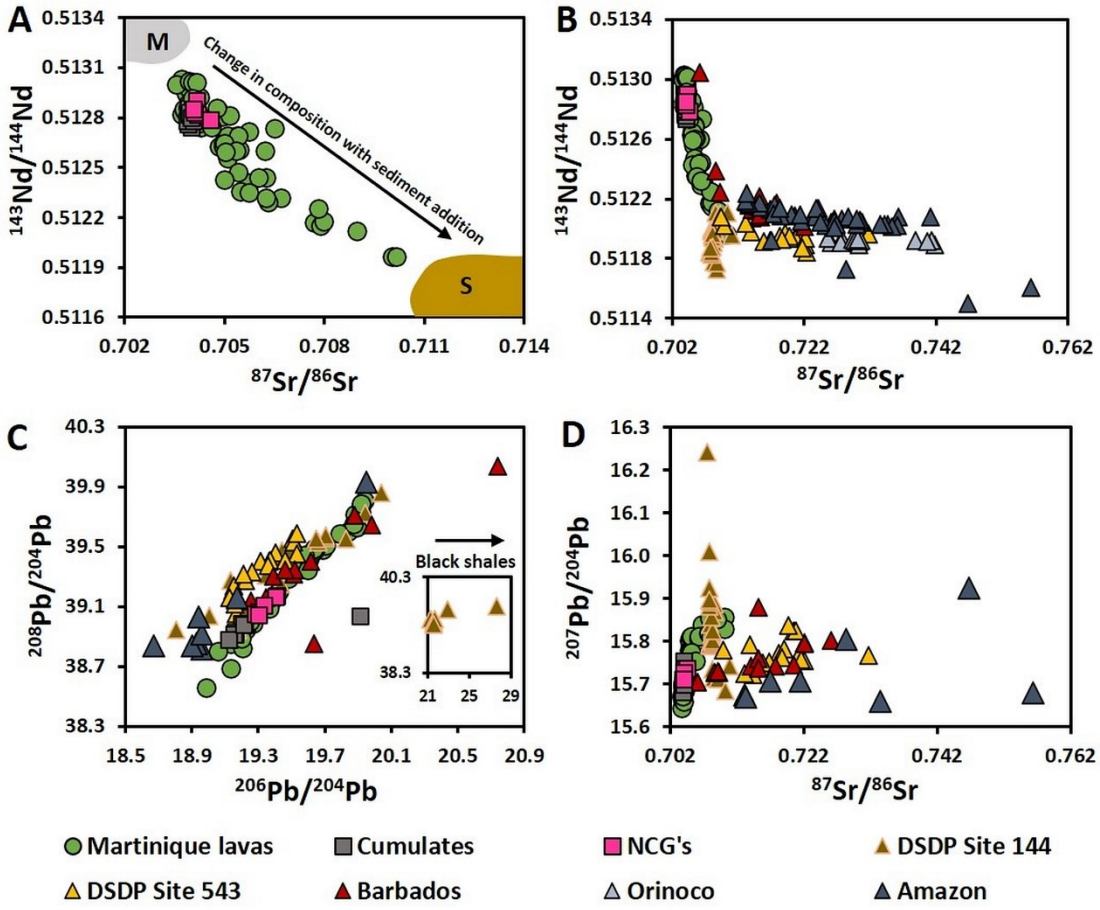

Figure 4.8: A) Whole rock $^{87}Sr/^{86}Sr$ vs $^{143}Nd/^{144}Nd$ for Martinique lavas and plutonic xenoliths (this study), with schematic fields for mantle (M) and sediment (S) end members. As shown, a suitable sediment end member is likely to have more radiogenic Sr and less radiogenic Nd than the lavas. **B), C),** and **D)** $^{87}Sr/^{86}Sr$ vs $^{143}Nd/^{144}Nd$, $^{208}Pb/^{204}Pb$ vs $^{206}Pb/^{204}Pb$, and $^{87}Sr/^{86}Sr$ vs $^{207}Pb/^{204}Pb$, respectively, for Martinique lavas and plutonic xenoliths (this study), potential equivalents to subducted sediments (Site 543, Site 144, Barbados) and sediments from the Orinoco and Amazon rivers. Inset in **C)** shows data for black shale unit of Site 144. For all data points, uncertainty (2 SE) is smaller than symbol size. **Data sources:** Martinique lavas – Davidson (1986), Labanieh et al. (2010). Site 543, Site 144 and Barbados – Carpentier et al. (2008) (2009). Amazon – Allegre et al. (1996), Parra et al. (1997), Viers et al. (2008), Rousseau et al. (2019). Orinoco - Parra et al. (1997), Rousseau et al. (2019).

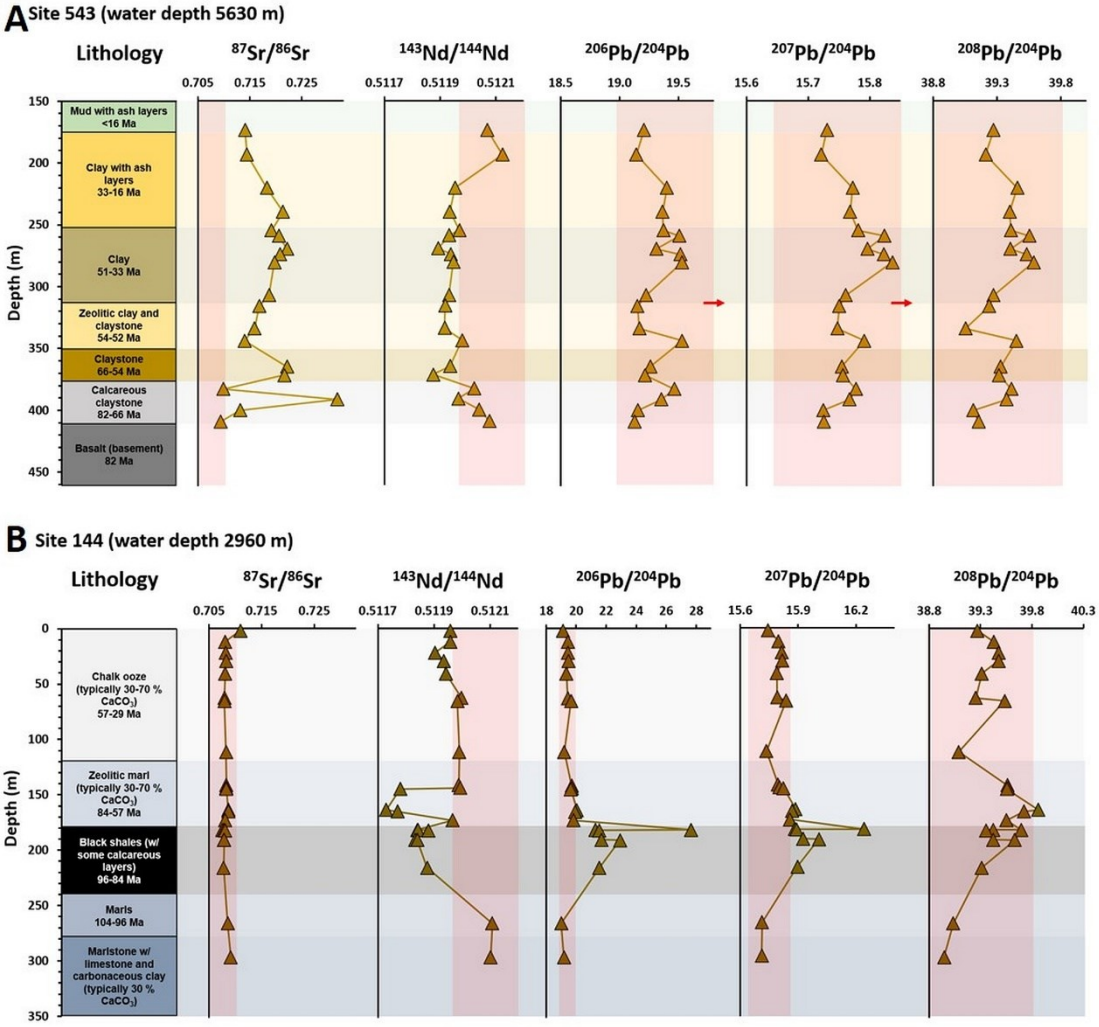

Figure 4.9: A) Radiogenic isotopic compositions of DSDP Site 543 sediments, modified from Carpentier et al. (2008). **B)** Radiogenic isotopic compositions of DSDP Site 144 sediments, modified from Carpentier et al. (2008). Pink bar indicates isotopic range of Martinique lavas (data sources as per Figure 4.8). For all data points, uncertainty (2 SE) is smaller than symbol size. Red arrows in **(A)** indicate that range of lavas exceeds the scale shown on the plot.

4.4.1.1 – Subducting slab

Potential analogues to sediments subducting below the Lesser Antilles arc (LAA) come from Deep Sea Drilling Program (DSDP) Sites 543 and 144 in the Atlantic Ocean, and Barbados (Carpentier et al., 2008; Labanieh et al., 2010, **Figure 4.1**). These sediments are probably similar to those subducted based on their location and age relative to the age of oceanic crust at the trench (Carpentier et al., 2008). Sediments at DSDP Site 543 (< 16-82 Ma) are mostly carbonate-free pelagic clays, in contrast to DSDP Site 144 sediments (29-104 Ma) which are mostly calcareous and include a distinctive black

shale unit (Carpentier et al., 2008). Sediments from both sites contain a component of South American continental material delivered by the Amazon and Orinoco rivers (**Figure 4.1**; Carpentier et al., 2008). The variation in radiogenic isotopic composition of Site 543 and Site 144 sediments with depth is presented and compared with the isotopic range of Martinique lavas in **Figure 4.9.** Both Site 543 and Site 144 contain sediments with sufficiently radiogenic Sr and unradiogenic Nd isotopic compositions to represent a viable end member for Martinique lavas, while Site 144 sediments also have adequately radiogenic Pb isotopic compositions.

Sediments from Barbados include carbonate poor terrigenous claystones and sandstones, marls and chalks, with ages between 57 and 15 Ma (Carpentier et al., 2008). They are mixtures of detrital material from South America and volcanigenic material from the LAA and surrounding arcs (Carpentier et al., 2008; 2009). The radiogenic isotopic compositions of Barbados sediments are compared with Martinique lavas in **Figure 4.8, b-d**. Carpentier et al. (2008) noted that a mixture of the most radiogenic Barbados and Site 543 compositions represents a suitable sediment end member for Martinique (and Lesser Antilles) lavas.

4.4.1.2 – Arc crust

Recent tectonic models based on seismic and magnetic data show that the arc crust below the southern LAA (Martinique to Grenada) consists of oceanic crust and sedimentary cover of the formerly contiguous Grenada and Tobago basins **(Figure 4.3)** (Aitken et al., 2011; Allen et al., 2019). Fragments of dismembered Jurassic-Palaeocene age oceanic island arc terranes may also be present in the LAA basement (Neill et al., 2013). Tectonic reconstructions suggest that the region currently occupied by the southern LAA has been a site of sediment deposition since the Eocene (Escalona and Mann, 2011), supporting the idea that the arc, active since 25 Ma (Germa et al., 2011), was built through Grenada-Tobago basin sediments. These sediments comprise the upper few km of crust, thickening away from the centers of arc magmatism, reaching total thicknesses of 13-14 km (Aitken et al., 2011).

To the best of our knowledge, sediment samples from the Grenada and Tobago basins are not available, hence the type and chemical characteristics of the sediments cannot be directly constrained. However, Aitken et al. (2011) used seismic data to identify

sedimentary lithologies in the two basins via correlation with well logs in the Carupano Basin, **(Figure 4.1)** to the south, and uplifted sediments on the Grenadine Islands considered equivalent to deep Grenada basin sediments (Speed et al., 1993). Lithologies include turbidites, pelagic siltstones and marls, limestones, and shales (Aitken et al., 2011). Similar lithologies, along with a greater shale component and minor sandstone, are present in the Carupano Basin (Ysaccis, 1997). These studies suggest that sediments in the southern LAA crust are likely to be highly heterogeneous.

Data from modern sediments derived from the same sources as Grenada-Tobago basin sediments can provide constraints on the isotopic composition of sediments in LAA crust. From the Eocene to mid-Miocene (49-11.2 Ma), Grenada-Tobago basin sediments were sourced from the South American continent (Aitken et al., 2011). Sediment derived from uplifted Andean terranes and the Guyana shield was supplied by the proto-Maracaibo and Orinoco rivers (Escalona and Mann, 2011; Xie et al., 2010; Rojas-Agramonte et al., 2017). The present-day Orinoco and Amazon rivers also drain the Andes and Guyana shield (Rojas-Agramonte et al., 2017, Rousseau et al., 2019), hence the isotopic composition of sediments from these rivers is likely to be analogous to the sediments in the LAA crust.

The Amazon and Orinoco rivers drain old cratonic material with suspended sediment and clay typically having highly radiogenic $^{87}Sr/^{86}Sr$ (0.7132 - 0.7564) and unradiogenic $^{143}Nd/^{144}Nd$ (0.5122-0.5115) (Allègre et al., 1996; Parra et al., 1997; Viers et al., 2008; Rousseau et al., 2019) **(Figure 4.8,b).** The limited Pb isotope data are typically less radiogenic than most Martinique lavas, though highly radiogenic samples ($^{206}Pb/^{204}Pb$ = 19.95, $^{207}Pb/^{204}Pb$ = 15.924, $^{208}Pb/^{204}Pb$ = 39.93) have been reported (Allègre et al., 1996) **(Figure 4.8,c, d).** Based on these data, it is plausible that sediments within LAA crust have the highly radiogenic Sr and Pb, and unradiogenic Nd isotopic compositions required to produce the isotopic variation in Martinique lavas. Since sediments at Sites 543 and 144 also include material from the Amazon and Orinoco (Carpentier et al., 2008), sediments of similar lithologies and isotopic compositions to those of the fore-arc are expected in the arc crust.

Overall, the wide range of isotopic compositions in potential equivalents to sediments in the arc crust combined with a range of potential lithologies suggests that the arc crust is chemically and isotopically heterogenous. Both recycled subducted and unsubducted

crustal sediments provide viable isotopic components in Martinique lavas specifically and lavas of the Lesser Antilles more generally. Thus, chemical characteristics of lavas alone cannot be used to distinguish whether the sediment component is incorporated by recycling into the mantle source or crustal assimilation of sediments.

4.4.2 – Cumulate isotopic compositions support crustal assimilation of sediments

Plutonic xenoliths from Martinique are considered to represent portions of an open crystal mush system (Cooper et al., 2016), which consists predominantly of cumulates in the mid-crust and NCG's in the upper crust. If the Sr isotopic variation observed in Martinique lavas is produced by varying sediment input to the mantle source (e.g., Carpentier et al., 2008, Labanieh et al., 2010), then a similar isotopic range would also be expected in mid-crustal magmas. To a first order, the unradiogenic and extremely restricted Sr isotopic range determined for individual cumulate plagioclase crystals **(Figure 4.6)** indicates that mid-crustal magmas beneath Martinique have not yet been modified significantly by sediment addition. The same logic can be applied to the wider cumulate whole rock $^{87}Sr/^{86}Sr$ data. The plagioclase and whole rock data support the hypothesis that isotopic heterogeneity and extreme radiogenic compositions of Martinique lavas are produced by assimilation of sediments at shallower crustal levels.

For comparison, plagioclase from a St Vincent cumulate also show unradiogenic Sr isotopic compositions close to those of Martinique cumulates **(Figures 4.5 and 4.6).** Tollan et al. (2012), used oxygen isotopes to show that St Vincent cumulates experienced negligible crustal contamination, suggesting that their isotopic composition should reflect the mantle source. St Vincent cumulate plagioclase have slightly lower $^{87}Sr/^{86}Sr$ than those from Martinique, suggesting that the two islands are fed by mantle sources with similar, but not identical, compositions. This conclusion was also reached by Davidson and Wilson (2011) and Bezard et al. (2015b) in studies of primitive Lesser Antilles lavas. Unlike Martinique, lavas on St Vincent do not extend to highly radiogenic isotopic compositions **(Figure 4.3)** and the impact of crustal assimilation is considered minimal (Heath et al., 1998). Since there are only subtle differences in the isotopic compositions inferred for the mantle sources of the two islands, the wider isotopic range of Martinique lavas is better explained by assimilation of crustal sediments.

4.4.3 - Inferences about assimilation from isotopic heterogeneity of shallow non-cumulate gabbros and lavas

Non-cumulate gabbros are considered plutonic equivalents of potentially eruptible lavas that crystallized within the 27 km thick Martinique crust at shallower levels than the cumulates (Cooper et al., 2016). Evidence for upper crustal crystallization comes from comparing natural mineral assemblages and compositions to those from experimental studies. These comparisons suggest crystallization of NCGs between 2 and 4 kbar (Martel et al., 1998; Cooper et al., 2016; Melekhova et al. 2019), corresponding to depths of approximately 6-12 km (vs ~12 km or greater for cumulates).

If the isotopic composition of a magma is inherited from its mantle source and subsequent evolution of that magma remains a closed system, crystals within the same rock should show minimal radiogenic isotopic variation. In contrast, intra-sample isotopic variation among crystals is characteristic of an open system, involving, for example, crustal assimilation (e.g., Baker et al., 2000). The isotopic diversity recorded by NCG plagioclase cores (particularly MQ6, **Figure 4.6**) may therefore indicate sediment assimilation during crystallization. In NCG sample MQ35, the presence of both cores and rims with significantly more radiogenic $^{87}Sr/^{86}Sr$ than cumulates again suggests that magmas can acquire more radiogenic compositions during crystal growth at shallow crustal levels.

In both NCG samples, more evolved plagioclase rims show less isotopic variation than cores and have Sr isotopic compositions within the range defined by the associated cores. We propose the following processes to explain this trend. Emplacement of new magma into the upper crust, in contact with crustal sediments, leads to sediment assimilation and crystallization of plagioclase cores. Assimilation of variable amounts of sediment, or sediments with different isotopic compositions, could produce an isotopically heterogenous magma resulting in crystallization of isotopically heterogenous plagioclase. Alternatively, isotopic variation among plagioclase cores may reflect crystallization at different times during progressive contamination of the newly emplaced magma.

Plagioclase rims may have crystallized from a more evolved, more isotopically homogenous melt that interacted with the pre-existing plagioclase cores. Other Martinique plutonic xenoliths contain evidence for percolating evolved melts (Cooper et al., 2016) and plutonic xenoliths from Statia in the northern LAA contain melt inclusions ranging in composition from basalt to rhyolite (Cooper et al., 2019). These lines of evidence suggest that it is plausible for plagioclase formed during an initial phase of crystallization (accompanied by assimilation) to interact with more evolved melts in the Martinique magma plumbing system. The fact that NCG plagioclase rims have Sr isotopic compositions within the range defined by the cores from the same sample suggests that in this scenario, the rim-forming melts were contaminated with crust to a similar extent to the core forming melts, hence were likely sourced from nearby regions of the crystal mush in the upper crust.

The most radiogenic Sr isotopic signatures in the LAA are observed in Martinique lavas. Sample M8321 represents one of the more radiogenic lavas, with a whole rock isotopic composition of $^{87}Sr/^{86}Sr = 0.706246$. Plagioclase crystals from M8321 have $^{87}Sr/^{86}Sr$ close to the whole rock value **(Figure 4.7)** and are significantly more radiogenic than NCG plagioclase (**Figure 4.6**)**.** This suggests that the magma from which they are derived had assimilated more sediment, or a more radiogenic sediment, than the magmas that crystallized the NCGs. M8321 plagioclase crystals show either normal, reverse, or both normal and reverse zoning, a feature commonly observed in Martinique lavas and interpreted as evidence for mixing shortly before eruption (Coulon et al., 1984; Bourdier et al., 1985; Gorgaud et al., 1989). The indistinguishable Sr isotopic composition of analysed core-rim pairs **(Figure 4.7)** suggests that all components involved in this mixing probably had similar Sr isotopic compositions. Plagioclase crystals show only very minor isotopic disequilibrium with the bulk groundmass and have isotopic compositions close to or within uncertainty of the whole rock value, consistent with an origin as true phenocrysts grown in the final erupted melt (or mixed melts).

If the minimal isotopic variation between plagioclase cores, rims and groundmass in M8321 was considered in isolation, then it could be argued that the radiogenic isotopic composition of this lava was inherited from the mantle source. However, by combining this observation with the isotopic data from plutonic xenoliths, we argue that shallow

level assimilation is the dominant process controlling isotopic variation in Martinique lavas. Lava M8321 is quite evolved (approx. 58 wt % SiO_2) and increasing $^{87}Sr/^{86}Sr$ generally correlates with increasing SiO_2 in Martinique lavas (Davidson, 1986; Davidson and Wilson, 2011). As discussed by Bezard et al. (2014), this would require a fortuitous process linking the extent of source contamination and magmatic differentiation for isotopic variation to be produced by subducted sediment addition alone.

4.4.4 – Quantifying the addition of sedimentary components

Previous estimates of the amount of sediment addition required to generate the radiogenic isotopic compositions of Martinique and Lesser Antilles lavas are based on Sr, Nd, Pb and oxygen isotope data and calculated using binary mixing models. These studies estimate that bulk addition of up to 20-40 % sediment in either the mantle source (Carpentier et al., 2008; Labanieh et al., 2010) or within the crust (Bezard et al., 2014; Davidson and Harmon, 1989) explains the *most extreme* Lesser Antilles lava compositions. Here we use Assimilation-Fractional Crystallization (AFC) modelling to assess whether crustal sediment assimilation can produce the Sr-Nd-Pb isotopic variation in Martinique lavas and estimate the amount of sediment assimilation required.

4.4.4.1 – AFC modelling end members and parameters

Mid-crustal cumulates from Martinique crystallize from magmas that have undergone prior olivine fractionation at depth (Cooper et al., 2016). This suggests that parental magmas to NCGs and lavas, ascending to the upper crust from the mid-crust or deeper, are likely to have higher Sr concentrations than primary mantle melts, because Sr is incompatible in olivine. Therefore, we model sediment addition to a parental magma rather than a primary mantle melt composition. The Îlet à Ramiers basalt, the least evolved lava erupted in Martinique (~ 12 % MgO, Labanieh et al., 2010), is a reasonable approximation for parental magmas ascending to the upper crust. Its Sr isotopic composition of $^{87}Sr/^{86}Sr \sim 0.7038$ is consistent with the isotopic composition of Martinique primitive magmas calculated by Davidson and Wilson (2011), and is close to the least radiogenic value measured in this study (NCG sample MQ6). Hence

the composition of the Îlet à Ramiers basalt is used here to represent magmas prior to upper crustal sediment assimilation, hereon referred to as "parental magmas".

End member	$^{87}Sr/^{86}Sr$	$^{143}Nd/^{144}Nd$	$^{206}Pb/^{204}Pb$	$^{207}Pb/^{204}Pb$	$^{208}Pb/^{204}Pb$	Sr (µg/g)	Nd (µg/g)	Pb (µg/g)
Bulk Site 543	0.71585	0.511966	19.315	15.767	39.347	110	30.6	18.7
Bulk Site 144	0.70851	0.512014	19.516	15.765	39.220	656	14.8	7.24
Bulk Barbados	0.71642	0.512122	19.674	15.765	39.456	103	23.3	13.1
Bezard 50:50 Bulk 543:144	0.71218	0.511990	19.415	15.766	39.284	383	22.7	13
Average Orinoco	0.73198	0.511920				107	31	
Most radiogenic Amazon	0.75640	0.511500	19.950	15.924	39.930	97	17	42
Least radiogenic Amazon	0.71319	0.512185	18.670	15.675	38.84	97	17	42
Most extreme Barbados	0.71531	0.512080	20.740	15.879	40.037	85	77.9	9.3
Hypothetical crust	0.71280	0.511700	20.030	15.879	39.920	110	40	15
Hypothetical crust 2	0.71280	0.511500	20.000	15.879	39.950	217	32	20
Parental magma	0.70380	0.512951	19.055	15.662	38.802	181	5.8	1.41
Depleted mantle	0.70270					9.8		

Table 4.3: Sr-Nd-Pb isotopic compositions and concentrations of end members used in AFC modelling. **Data sources:** Bulk Site 543, Bulk Site 144, Bulk Barbados, Most extreme Barbados - Carpentier et al, (2008, 2009). Bezard 50:50 Bulk 543:144 - Bezard et al, (2015b). Average Orinoco – average of samples from Parra et al, (1997) and Rousseau et al, (2019) (n=15). Most and least radiogenic Amazon – Allegre et al, (1996), Rousseau et al, (2019). Primitive magma – Îlet à Ramiers high Mg basalt from Labanieh et al, (2010), (2012). Depleted mantle – Salters and Stracke, (2004). End members in italics represent sediment/crustal end members.

End member compositions used in AFC models are given in **Table 4.3**. In **section 4.4.1.2**, we argue that LAA crustal sediments are likely to be both lithologically and chemically heterogenous, based on the best available constraints. This heterogeneity is

emphasised by the wide range of potential crustal sediment compositions shown in **Figure 4.8**. To represent a lithologically and chemically heterogenous crust, eight different potential sediment end members were considered. These include the average Sr-Nd-Pb isotopic compositions of sediments from DSDP Sites 543 and 144, and from Barbados. We also include the 50:50 mixture of bulk Site 543 and bulk Site 144 sediments that Bezard et al. (2015b) suggested were involved in St Lucia magmatism. Potential highly radiogenic crustal end members are represented by the average composition of sediments from the Orinoco (from Parra et al., 1997; Rousseau et al., 2019) and the most extreme composition from Barbados (Carpentier et al., 2008; 2009). Amazon sediments show a wide range of very radiogenic compositions (e.g. $^{87}Sr/^{86}Sr$ = 0.7132-0.7564, Allègre et al., 1996). The minimum and maximum isotopic compositions were used as additional potential crustal end members, with concentrations equal to the average of Amazon sediments (Sr and Pb from Allègre et al. (1996); Nd from Rousseau et al. (2019)). The end member compositions in **Table 4.3** are plotted relative to Martinique lavas and the isotopic range of sediments potentially equivalent to those in the arc crust in **Figure 4.10**.

The fractionating assemblage used in the AFC models was that of NCG sample MQ6 (**see Chapter 3**), which closely resembles the phenocryst assemblage of the lavas (e.g. Coulon et al., 1984; Davidson and Wilson, 2011). Bulk partition coefficients were calculated for this modal mineralogy using the mineral-melt partition coefficients listed in **Appendix 4.1.**

4.4.4.2 – Modelling and quantifying crustal assimilation

Results of AFC models, calculated using the equations of De Paolo (1981), are plotted in **Figures 4.10** and **4.11,** with details of the calculations given in **Appendix 4.1.** The value of r (rate of assimilation/rate of crystal fractionation) was set at 0.3, similar to previous AFC models for LAA lavas (e.g., Smith et al., 1996, Labanieh et al., 2010). An additional sediment end member ("Hypothetical crust" in **Table 4.3)** was also modelled in order to reproduce the most extreme (most radiogenic Sr and Pb, most unradiogenic Nd) lava compositions. This end member (plotted on **Figure 4.10**) lies within the range of potential arc crust sediment isotopic compositions identified in **section 4.4.1.2 (Figures 4.8 and 4.10)** and hence represents a reasonable approximation for an assimilant. Combined, the AFC models for the various crustal

end members cover most of the observed isotopic variation in Martinique lavas **(Figure 4.11).** This suggests that Martinique lava isotopic compositions can be explained by assimilation of crustal sediments with a range of isotopic and chemical compositions, with individual lavas having assimilated different crustal sediments.

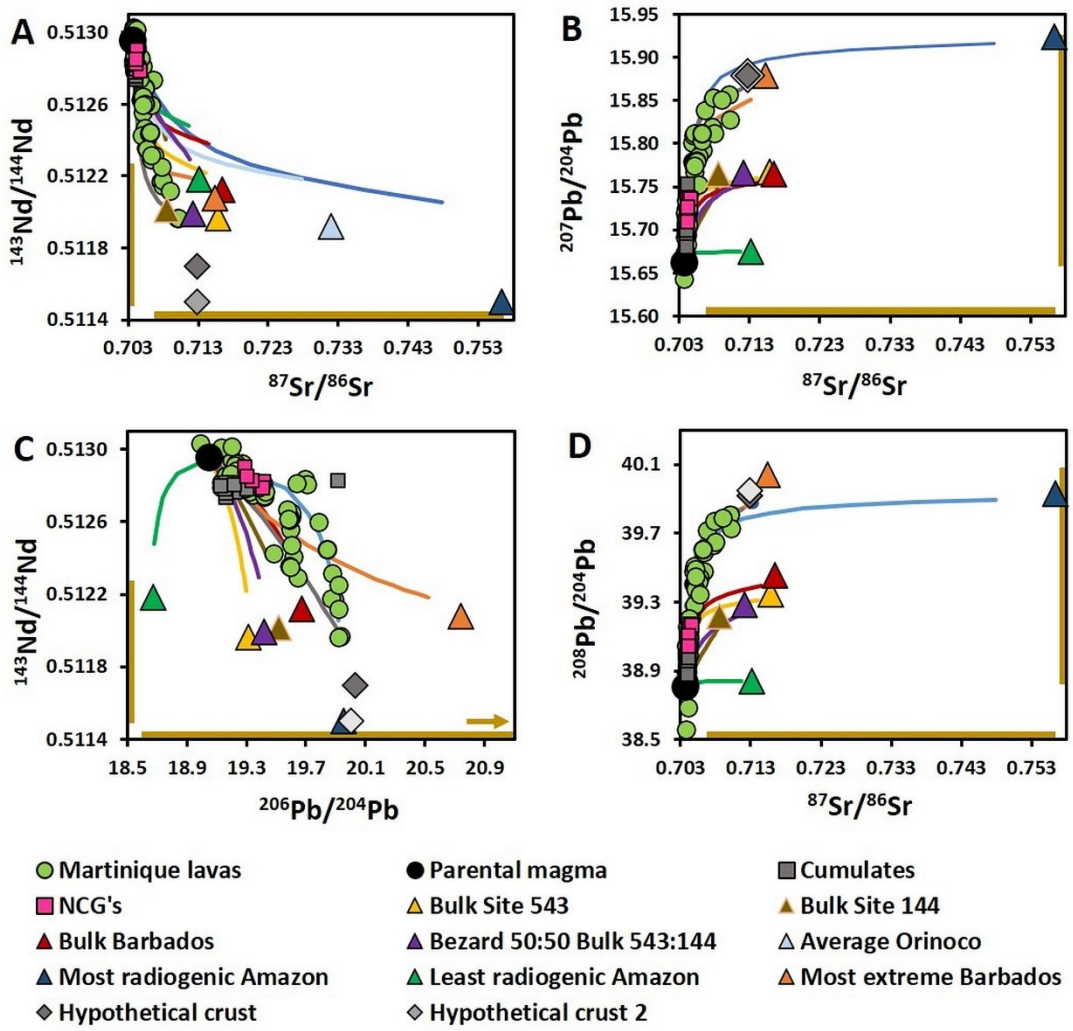

Figure 4.10: A) $^{87}Sr/^{86}Sr$ vs $^{143}Nd/^{144}Nd$, **B)** $^{87}Sr/^{86}Sr$ vs $^{207}Pb/^{204}Pb$, **C)** $^{206}Pb/^{204}Pb$ vs $^{143}Nd/^{144}Nd$ and **D)** $^{87}Sr/^{86}Sr$ vs $^{208}Pb/^{204}Pb$, for Martinique lavas, plutonic xenoliths (this study) and end members used in AFC modelling from **Table 4.3**. Data sources as per **Table 4.3** and **Figure 4.8**. For all data points, uncertainty (2 SE) is smaller than symbol size. Brown bars along axes show range of isotopic compositions of sediments potentially equivalent to those in the arc crust from **Figure 4.8**. Coloured curves correspond to AFC models for each crustal end member, shown in detail in **Figure 4.11.**

The sediment end members considered represent only a few possible assimilants, which theoretically could lie anywhere within the range of sediment compositions outlined in **Figures 4.8 and 4.10.** Since the LAA crust has yet to be directly sampled, its actual isotopic composition remains to be determined but it is possible that

sediments with more extreme isotopic compositions than those considered here could also exist within the arc crust.

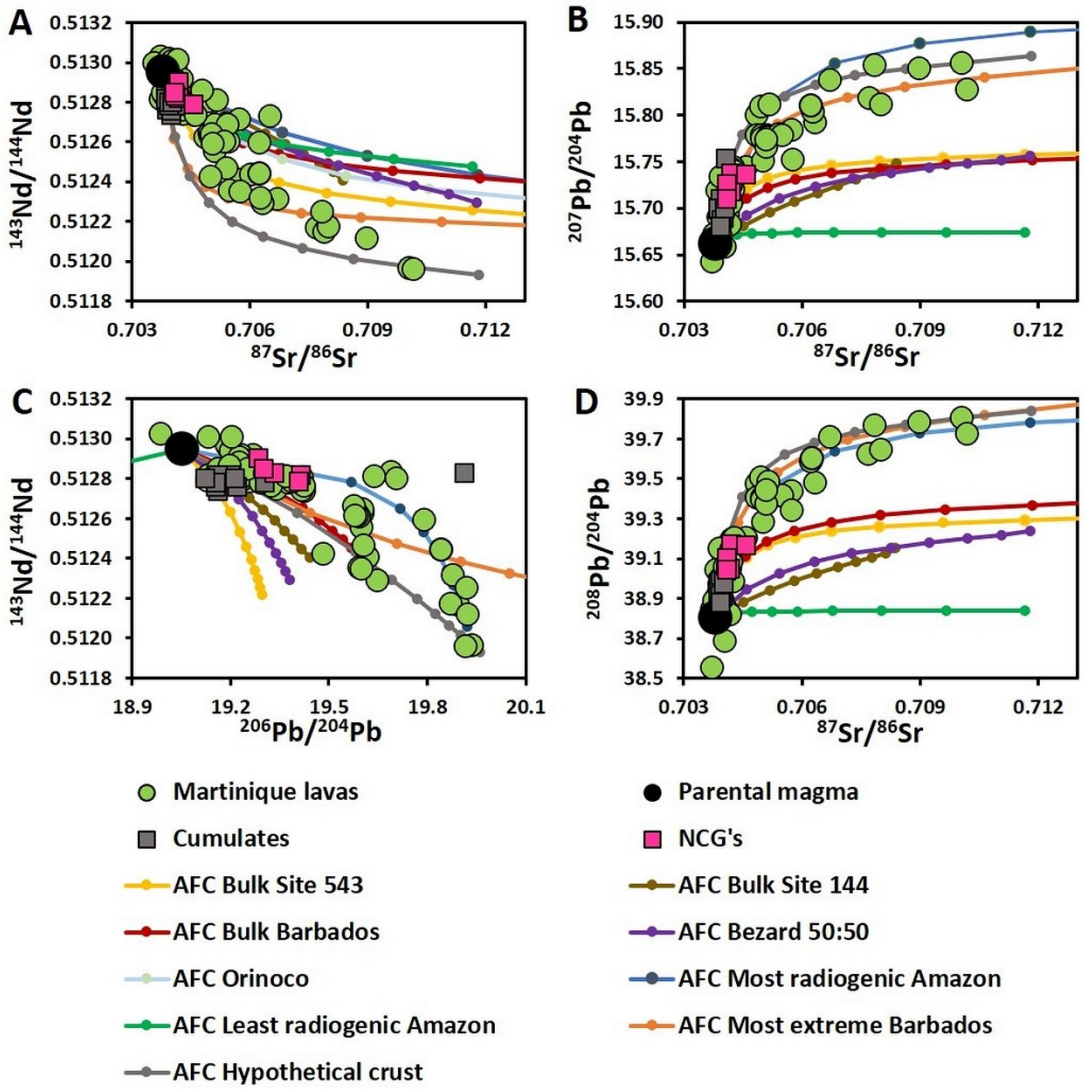

Figure 4.11: A) $^{87}Sr/^{86}Sr$ vs $^{143}Nd/^{144}Nd$, **B)** $^{87}Sr/^{86}Sr$ vs $^{207}Pb/^{204}Pb$, **C)** $^{206}Pb/^{204}Pb$ vs $^{143}Nd/^{144}Nd$ and **D)** $^{87}Sr/^{86}Sr$ vs $^{208}Pb/^{204}Pb$, for Martinique lavas and plutonic xenoliths (this study). Data sources as per **Table 4.3** and **Figure 4.8**. For all data points, uncertainty (2 SE) is smaller than symbol size. Each coloured curve corresponds to an AFC model using a different crustal end member from **Table 4.3** as the assimilant composition (see legend). Each point along the curves represents an increment of 10 % fractional crystallization, up to a maximum of 90 %. Details of AFC model calculations are given in **Appendix 4.1**.

To quantify the amount of crustal assimilation required to produce the isotopic compositions of Martinique lavas, we employed the method of Aitcheson and Forrest (1994). This method solves the AFC equations of De Paolo (1981) to determine the

crust/magma ratio ρ (mass of crust assimilated/mass of original magma), which can be converted into a proportion of crust assimilated. If the isotopic and elemental compositions of the original magma and assimilant are defined, then the crust/magma ratio can be calculated for a *lava of a given isotopic composition*. We calculated the crust/magma ratio for the Martinique lava with the most extreme isotopic composition to determine the maximum amount of crustal sediment assimilated by Martinique lavas (details of the calculation given in **Appendix 4.1**). Assimilation of 28 % sediment with the composition of the "Hypothetical crust" end member is required to produce the most extreme Martinique lava composition. To illustrate the effect of a chemically and isotopically heterogenous crust, we generated an alternative sediment end member ("Hypothetical crust 2" in **Table 4.3**) which also reproduces the isotopic composition of the most extreme Martinique lava with only 23 % assimilation (**Appendix 4.1**). This end member also has isotopic compositions within the potential range for crustal sediments shown on **Figures 4.8 and 4.10.** These results show that the amount of crustal assimilation required varies depending on the composition of crust being assimilated.

Previous estimates of the amount of sediment addition (whether to the mantle source or via crustal assimilation) required to produce the most extreme Martinique lava composition are similar to our calculated values of 23-28 %. Given the wide range of potential assimilant compositions, the proportion of crustal sediment assimilated by Martinique lavas cannot be accurately quantified. However, 28% should be treated as a maximum amount, with most lavas likely experiencing significantly less assimilation. Our new AFC modelling, combined with the constraints from plutonic xenoliths on where assimilation takes place, clearly demonstrates that isotopic variation in Martinique lavas is best explained by assimilation of isotopically and chemically heterogenous sediments in the upper crust.

4.4.5 – Sediment addition to the mantle source?

Although the evidence presented supports crustal assimilation at shallow crustal levels as the dominant process responsible for the large isotopic range and radiogenic compositions of Martinique lavas, this does not preclude the involvement of subducted sediment in generating the compositions of the parental magmas and cumulates, which are more radiogenic in terms of Sr isotopes than typical depleted mantle. As such, the

amount of subducted sediment addition to the mantle source required to produce parental magma and cumulate plagioclase Sr isotopic compositions was calculated. A binary mixing approach was used for simplicity. The average depleted mantle composition of Salters and Stracke (2004) was used as the mantle end member. Potential subducted sediment end members were represented by average compositions of DSDP Site 543, DSDP Site 144 and Barbados sediments **(Table 4.3).**

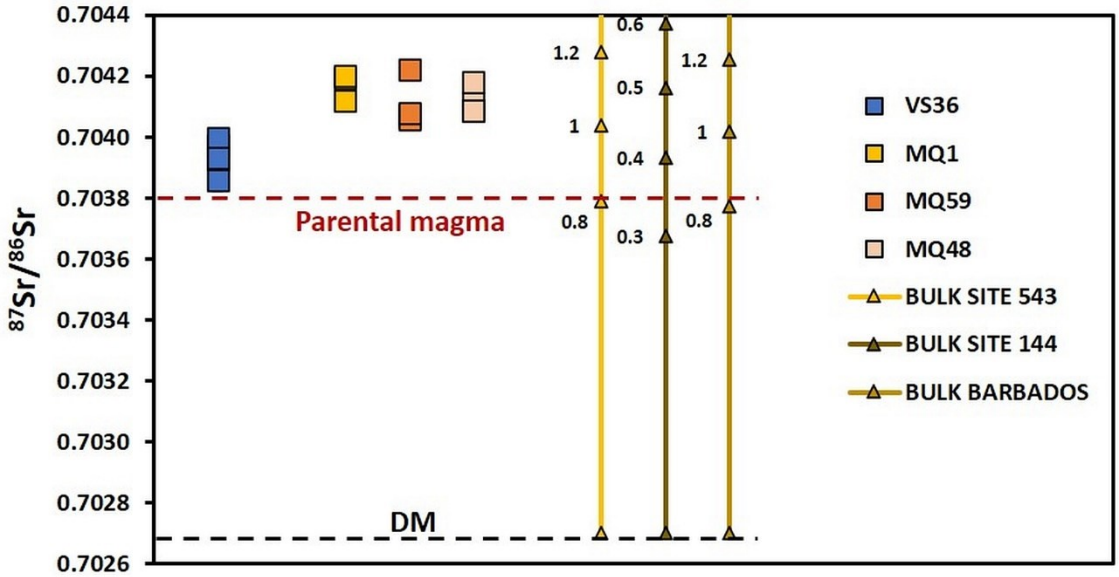

Figure 4.12: $^{87}Sr/^{86}Sr$ of cumulate plagioclase compared with single component mixing lines between depleted mantle and potential subducted sediment end members. The subducted sediment end member from **Table 4.3** corresponding to each mixing line is shown in the legend. Labelled tick marks represent percentage sediment addition to mantle source. Data sources as per **Table 4.3**. Dashed line labelled DM = depleted mantle ($^{87}Sr/^{86}Sr$ = 0.70270, from Salters and Stracke (2004)). Red dashed line shows Martinique parental magma composition ($^{87}Sr/^{86}Sr$ = 0.70380). Where visible, black bars show uncertainty (2 SE), otherwise uncertainty is smaller than symbol size.

The Sr isotopic composition of Martinique parental magmas ($^{87}Sr/^{86}Sr$ = 0.7038) allows a maximum of ~ 0.8 % bulk sediment addition to the mantle source **(Figure 4.12)**. This value agrees well with the < 1 % subducted sediment contribution to parental magmas at Mt Pelee, Martinique estimated by Davidson and Wilson (2011). Cumulate plagioclase compositions allow a maximum of 1-1.2 % bulk sediment addition to the mantle source **(Figure 4.12)**. The slightly higher $^{87}Sr/^{86}Sr$ of the cumulates relative to parental magma could be explained by minor variations in sediment input to the mantle source. Alternatively, the parental and cumulate forming magmas may have been affected by minor assimilation, either of deep sediments or

oceanic crustal material, which underlies Grenada-Tobago basin sediments (Aitken et al., 2011, Allen et al., 2019). Since the maximum sediment contribution to the parental magma is < 1 % (regardless of where sediment addition occurs), this composition can still be considered a reasonable proxy for Martinique magmas prior to upper crustal assimilation. It should be noted that the Nd and Pb isotopic compositions of the parental magma also require < 1 % sediment contribution (when modelled as above for Sr isotopic composition).

4.4.6 – Wider significance

Our study of Martinique lavas *in conjunction* with plutonic xenoliths places important spatial constraints on the location where the crustal/sedimentary isotopic signatures of Martinique lavas are introduced, which simply cannot be derived from studies of lavas alone. We have shown that the crustal/sedimentary signatures are almost entirely inherited from AFC processes taking place in the upper crust, with only a very minor role for subducted sediment in the mantle source. Application of the approach applied here may reveal a greater role for crustal assimilation than previously considered in other arc systems where lava geochemistry is currently interpreted to reflect source processes. If crustal contributions are underestimated, relative contributions from the subducting slab and mantle will be overestimated, which has major implications for quantifying element and sediment recycling at subduction zones. Improved constraints on crustal contributions could also be utilized to re-assess the composition and heterogeneity of arc mantle source regions, by correcting lava compositions for the effects of crustal assimilation.

The latest tectonic model for the evolution of the LAA (Allen et al., 2019) corroborates evidence for crustal sediment assimilation in Martinique. The model suggests that an outer arc was active east of the current arc from 40-25 Ma. A back-arc basin formed during this period, extending from the present-day location of Dominica south to Grenada. Around 22 Ma, the arc migrated west and the southern volcanic centers of the current Lesser Antilles arc (Martinique to Grenada) were subsequently built through the back-arc basin crust (oceanic crust and sediments), separating it into the Grenada and Tobago basins **(Figure 4.3).** Evidence for crustal contamination in Martinique (and other southern LAA islands) demonstrates that magma interacted with the thick sediment pile of the Grenada-Tobago basins. In other arc settings where the

tectonic evolution is less well constrained, the methods employed in this study could be used to identify shallow crustal sediment assimilation and thereby indicate the presence of sediments within the arc crust. This information could be used to infer the past locations of sedimentary basins/depocenters, which could be incorporated into tectonic models for arc development and may also indicate potential locations of hydrocarbon bearing sediments.

In an alternative scenario, isotopic studies of plutonic xenoliths from other arcs may prove a less effective means of recognizing crustal assimilation than in the LAA. The proximity of the LAA to the South American continental margin has resulted in a component of the arc crust composed of sediments which, based on available constraints, can be assumed to have highly radiogenic isotopic compositions. The contrast in isotopic compositions between crustal sediments and primitive magmas makes sediment assimilation easily detected in the LAA and may be unique among arcs. Upper plate crustal sediments elsewhere may not have such highly radiogenic or diverse compositions resulting in a less obvious geochemical signature of assimilation.

Recent studies have demonstrated that volatile fluxes from arc volcanoes (e.g. He and CO_2) contain contributions from crustal sediments (e.g. Troll et al., 2012; Yu et al., 2016; Aiuppa et al., 2017; Mason et al., 2017). Therefore, it is likely that volatile contents and compositions of magmas in volcanic arcs are modified by crustal sediment assimilation. This highlights the importance of considering and accurately quantifying volatile contributions from upper plate crust in models of volatile recycling at subduction zones. If volatiles added in the crust are mistakenly attributed to the subducted component, the contribution from the downgoing slab to arc volatile output could be significantly overestimated, resulting in misleadingly elevated volatile recycling efficiency estimates. Finally, addition of volatiles to magmas at shallow crustal levels may influence the typically explosive eruptive behaviour of LAA volcanoes, as has been suggested for other arc volcanoes e.g. Merapi (Deegan et al., 2010).

4.5. Conclusions

The Sr isotopic composition of plagioclase from plutonic xenoliths has been used to evaluate the origin of the wide isotopic range and highly radiogenic compositions of

Martinique lavas. Through this approach it has been possible to distinguish between competing hypotheses where the compositions of the lavas result from variations in subducted sediment addition to the mantle source versus assimilation of unsubducted, shallow, crustal sediments. Unzoned plagioclase crystals from mid-crustal cumulate xenoliths show restricted ranges of unradiogenic Sr isotope ratios. In contrast, cores of zoned plagioclase crystals from upper-crustal NCG xenoliths are characterized by wider intra-sample Sr isotopic ranges than cumulate plagioclase. Some NCG plagioclase crystals have both core and rim compositions with more radiogenic $^{87}Sr/^{86}Sr$ than mid-crustal cumulates. Whole rock Sr isotopic compositions follow the same pattern, with cumulates showing restricted, unradiogenic $^{87}Sr/^{86}Sr$ and NCG's extending to slightly more radiogenic values. Combined, these results support the hypothesis that Martinique magmas acquire more radiogenic compositions and isotopic diversity via assimilation of in situ sediment in the upper crust. Consistent with the best available constraints for crustal sediment composition, AFC modelling demonstrates that the isotopic variation in Martinique lavas can be produced by assimilation of chemically and isotopically heterogenous crust. The novel approach used here could be applied to other arc systems to assess the relative roles of subducted sediment and crustal contributions which in turn would have significant implications for understanding arc mantle source compositions and quantifying sediment and volatile recycling at subduction zones.

Appendix 4.1 – Assimilation-Fractional Crystallization (AFC) modelling

A4.1 - Assimilation-Fractional crystallization (AFC) models

To assess whether crustal assimilation can produce the Sr-Nd-Pb isotopic variation in Martinique lavas, we modelled AFC processes using equation 15a of DePaolo (1981). The following parameters are required for the modelling:

-Isotopic and elemental compositions of the original magma and assimilant

-The value of r (rate of assimilation/rate of crystal fractionation)

-The bulk partition coefficient, D, for the element of interest, which is dependent on the fractionating assemblage.

The NCG samples in this study record evidence for crustal assimilation and have modal mineralogy and mineral compositions similar to Martinique lavas, hence represent a reasonable approximation for the fractionating assemblage during the AFC process. We used the modal composition of NCG sample MQ6 to represent the fractionating assemblage during assimilation. Using this assemblage, the bulk partition coefficients (D) for Sr, Nd and Pb were calculated using the mineral-melt partition coefficients in **Table A4.1**. NCG oxide minerals are typically magnetite and ilmenite (Cooper et al, 2016), hence the oxide fraction of the assemblage was divided accordingly into 4 % magnetite, 3 % ilmenite.

A previous attempt to model the isotopic compositions of Martinique lavas using AFC processes (Labanieh et al, 2010) used an r value of 0.25. Our modelling differs from that of Labanieh et al, (2010) by including a much wider range of sediment end member compositions. For our modelling, we chose an r value of 0.3. Using this value makes our models similar, but not identical, to those of Labanieh et al, (2010) and allows us to investigate whether including more isotopically diverse sediment end members can successfully model the lava compositions.

Example calculated values for the AFC model on **Figure 4.11** using end members "parental magma" as the original magma composition and "Bulk Site 543" as the assimilant are shown in **Table A4.2.** Isotopic ratios were calculated in 10 %

increments of F (fraction of liquid remaining), from F = 1 to F = 0.1, which corresponds to 90 % fractional crystallization. The value of r is set at 0.3, and the D values for each element are those in **Table A4.1.**

Overall, nine AFC models were calculated, all using the "parental magma" as the original magma composition and varying the sediment end member used as the assimilant composition. All models used r = 0.3 and the D values from the table above.

Mineral	**Pl**	**OPX**	**CPX**	**Ilm**	**Mag**	
Proportion of mineral	0.68	0.10	0.15	0.03	0.04	
Mineral-melt partition coefficients						**Bulk D**
Sr	2.60	0.03	0.09	0.01	0.10	1.7888
Nd	0.17	0.30	1.00	0.01	0.01	0.2963
Pb	0.61	0.52	0.87	0.01	2.90	0.7136

Table A4.1: Mineral-melt partition coefficients, and calculated bulk partition coefficients (D), for Sr, Nd and Pb based on the mineral assemblage of NCG sample MQ6. Mineral-melt partition coefficients compiled from Rollinson, (1993), Ewart and Griffin, (1994) and Ersoy and Helvaci, (2010). Pl = plagioclase, OPX = orthopyroxene, CPX = clinopyroxene, Ilm = ilmenite, Mag = magnetite.

F	**$^{87}Sr/^{86}Sr$**	**$^{143}Nd/^{144}Nd$**	**$^{206}Pb/^{204}Pb$**	**$^{207}Pb/^{204}Pb$**	**$^{208}Pb/^{204}Pb$**
0.1	0.714091	0.512219	19.29689	15.75979	39.30911
0.2	0.711665	0.512257	19.28969	15.75689	39.29405
0.3	0.709580	0.512297	19.28212	15.75384	39.27822
0.4	0.707969	0.512342	19.27335	15.7503	39.25987
0.5	0.706754	0.512395	19.26255	15.74594	39.23726
0.6	0.705835	0.512457	19.24851	15.74027	39.20790
0.7	0.705131	0.512534	19.22915	15.73246	39.16739
0.8	0.704583	0.512633	19.20030	15.72082	39.10703
0.9	0.704149	0.512765	19.15213	15.70139	39.00626
1	0.703800	0.512951	19.05450	15.66200	38.80200

Table A4.2: Calculated isotopic ratios for the AFC model involving the "Bulk Site 543" sediment end member (**Figure 4.11**, main text). F = fraction of liquid remaining. F = 0.1 corresponds to 90 % fractional crystallization.

A4.2 - Quantifying crustal assimilation

The method of Aitcheson and Forrest (1994) can be used to solve the AFC equations of DePaolo (1981) to calculate the crust/magma ratio ρ (mass of crust assimilated/mass

of original magma), which can then be converted into a proportion of crust assimilated. Specifically, the crust/magma ratio for a lava/magma of a given isotopic composition can be calculated using equation 5 of Aitcheson and Forrest, (1994) if the isotopic and elemental compositions of the original magma and assimilant are defined.

Equation 5 of Aitcheson and Forrest, (1994):

$$\rho = (r/r-1) * \{[1 + \lambda(r + D -1)/r\gamma]^{(r-1)/(r + D - 1)} -1\}$$

$$\lambda = \text{Isotope ratio}_{\text{original magma}} - \text{Isotope ratio}_{\text{magma}} / \text{Isotope ratio}_{\text{magma}} - \text{Isotope ratio}_{\text{assimilant}}$$

$$\gamma = \text{Concentration}_{\text{assimilant}} / \text{Concentration}_{\text{original magma}}$$

D = bulk partition coefficient for element of interest

To obtain an estimate for ρ, the above equation is used to calculate ρ for different values of r (rate of assimilation/rate of crystal fractionation) for each isotopic system ($^{87}Sr/^{86}Sr$, $^{143}Nd/^{144}Nd$, $^{206}Pb/^{204}Pb$, $^{207}Pb/^{204}Pb$, $^{208}Pb/^{204}Pb$). This results in a curve for each isotopic system on a plot of r vs ρ. A point at which the curves intersect shows that the composition of the lava in question ($\text{Isotope ratio}_{\text{magma}}$) can be produced by an AFC process involving the specified end members. The value of r at the point of intersection corresponds to the value of r required for an AFC model that produces the sample composition, with the value of ρ providing an estimate of the crust/magma ratio.

To determine the proportion of crustal assimilation required to produce the most extreme Martinique lava, the process outlined above was applied, with ρ calculated for values of r = 0.1-0.9 for each isotopic system. The "parental magma" was used as the original magma, and "Hypothetical crust" as the assimilant, since the AFC models involving these end members produce the isotopic composition of the lava (see Figure 11, main text). The values of D used in the calculations for each isotopic system are those in **Table A4.1**. The calculated curves for each isotopic system are plotted on **Figure A4.1** below. The curves intersect at r = 0.32, close to the r value of 0.3 used for the AFC model involving these end members. At the point of intersection, ρ = 0.39. This estimate of the crust/magma ratio can then be converted to a proportion of crust assimilated (% crust = ρ/(1 + ρ) * 100) (Aitcheson and Forrest, 1994). For this example,

28 % assimilation of a sediment with the composition of "Hypothetical crust" produces the most extreme Martinique lava isotopic composition.

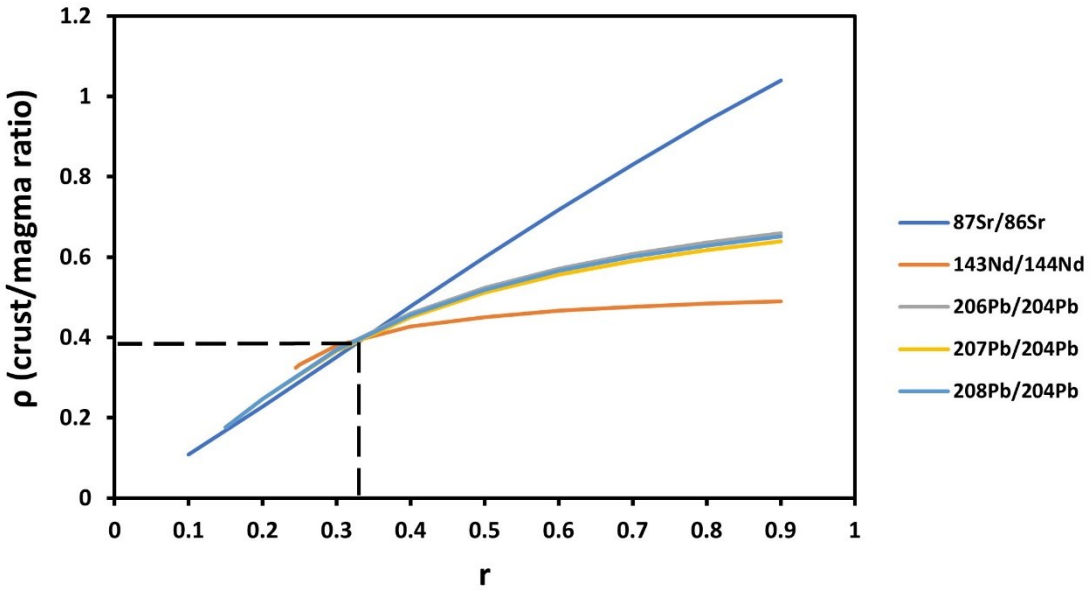

Figure A4.1: Calculated curves of ρ vs r for each isotopic system, for an AFC process involving the "Hypothetical crust" end member. The dashed lines mark the point at which all curves intersect, at r = 0.32, ρ = 0.39.

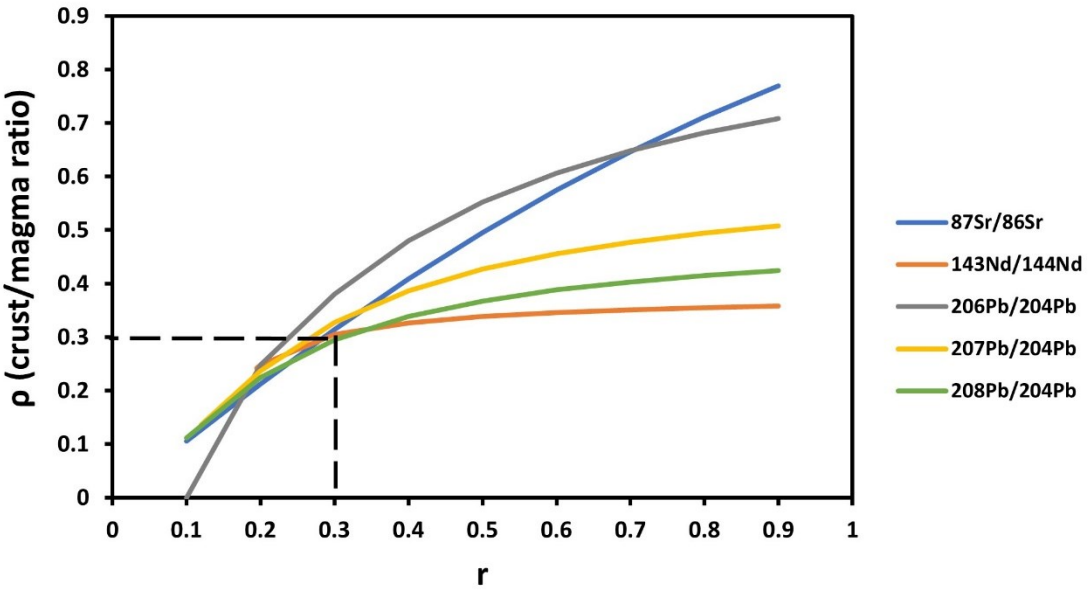

Figure A4.2: Calculated curves of ρ vs r for each isotopic system, for an AFC process involving the "Hypothetical crust 2" end member. The dashed lines mark the point around which majority of the curves intersect, at r = 0.3, ρ = 0.3.

The same procedure was carried out for an AFC process involving a different sediment end member, "Hypothetical crust 2". The calculated curves for each isotopic system in

this scenario are plotted on **Figure A4.2**, with majority intersecting at approximately r = 0.3, ρ = 0.3. This demonstrates that the most extreme Martinique lava could also be produced by only 23 % assimilation of a sediment with the composition of "Hypothetical crust 2".

Chapter 5 – Fractional crystallization and melt-mush reaction processes in the mushy plumbing system beneath St Vincent, Lesser Antilles arc

Abstract

The chemical compositions of arc magmas generated in the mantle wedge may be modified during passage through and storage within crystal mush-dominated plumbing systems prior to eruption. Plutonic xenoliths represent fragments of crystal mush brought to the surface by lavas and therefore have the potential to record processes controlling the chemical evolution of magmas within mushes. Recent studies of plutonic rocks from a variety of settings (mid-ocean ridges, arcs, ocean islands) have identified the process of reactive melt flow, where percolating melts react with pre-existing crystals in mushes. These studies suggest that reactive melt flow is an important process controlling magma chemical evolution in mush-dominated systems. Here, we use plutonic xenoliths from St Vincent, Lesser Antilles arc, where lava chemical compositions are consistent with fractional crystallization, to investigate mush processes in an active arc setting. We aim to determine whether plutonic xenoliths record fractional crystallization or reactive melt flow as the dominant process controlling magma chemical (specifically trace element) compositions in mushes beneath St Vincent.

To investigate fractional crystallization and reactive melt flow, we combine trace element compositions of clinopyroxene and amphibole with textural observations and chemical mapping of thin sections. Modelling of clinopyroxene and amphibole trace element compositions using fractional crystallization and Assimilation-Fractional Crystallization (simulating reactive melt flow) show that mineral trace element compositions in isolation do not distinguish the process by which these phases formed. This result highlights the value of textural observations for identifying melt-mush reaction processes (such as reactive melt flow) in plutonic xenoliths/crystal mushes.

Olivine gabbro plutonic xenoliths do not contain textural features indicative of disequilibrium or reaction. The mineral assemblage and clinopyroxene trace element chemistry of olivine gabbros are consistent with crystallization during the mid-upper

crustal (6-18 km depth) stages of polybaric fractional crystallization from a primitive basaltic magma. Hornblende-olivine gabbros from 6-12 km depth contain textural features indicative of melt-mush reaction. The "banded hornblende-olivine gabbro" contains a centimetre wide band with distinct texture, mineral assemblage and mineral phase compositions that replaces the surrounding (amphibole bearing) olivine gabbro matrix. The "poikilitic hornblende-olivine gabbro" contains clinopyroxene and olivine with ragged and embayed margins, indicative of dissolution during reaction, enclosed by poikilitic amphibole and orthopyroxene. The scale on which melt-mush reaction processes operate in the St Vincent plumbing system cannot be directly interpreted from the plutonic xenoliths due to their small size (< 6 cm). Comparisons with extinct plutonic systems, displaying similar textures to the plutonic xenoliths, suggests that melt-mush reaction may occur over metre-kilometre scales in the mush beneath St Vincent. Evidence for both processes in plutonic xenoliths suggests that fractional crystallization and melt-mush reaction influence magma chemical compositions in the St Vincent plumbing system.

Melts in equilibrium with clinopyroxene and amphibole from both olivine gabbros and hornblende-olivine gabbros overlap St Vincent lava trace element compositions, suggesting that both fractional crystallization and melt-mush reaction influence trace element compositions of St Vincent lavas. The contribution of melt-mush reaction is cryptic if lava trace element compositions are viewed in isolation, without context from plutonic xenoliths. Our findings imply that the impact of interactions and reactions between melts and mushes on the trace element compositions of arc lavas and melt inclusions must be carefully considered before using such data to interpret mantle source processes.

5.1 – Introduction

A growing body of evidence supports the idea that lavas erupted at arc volcanoes are derived from "trans-crustal magma plumbing systems" that extend throughout the arc crust, within which magma is stored predominantly in a mushy state (e.g. Cashman et al., 2017, Edmonds et al., 2019, Sparks et al., 2019, Paulatto et al., 2022). Interpretation of arc lava chemical compositions must take into account potential modification of the primary magma during passage through and storage within the mushy trans-crustal

magma plumbing system, via processes such as fractional crystallization, assimilation and mixing (e.g. Hildreth and Moorbath, 1988, Davidson et al., 2005, Turner and Langmuir 2015, 2022, Marxer et al., 2021).

These processes are often inferred based on the chemical compositions of arc lavas alone. However, lava chemical compositions represent an average of their components (melts and crystals) and may obscure evidence for processes which contributed to the chemical modification of magmas prior to eruption (e.g. Davidson et al., 2007b). Plutonic xenoliths, carried to the surface in erupted lavas, offer an alternative means of studying magma differentiation processes. These are typically coarse-grained igneous rocks interpreted to represent fragments of crystal mush derived from a range of depths within trans-crustal plumbing systems (e.g. Chadwick et al., 2013, Stamper et al., 2014, Cooper et al., 2016, Price et al., 2016, Melekhova et al., 2017, 2019, Camejo-Harry et al., 2018).

Melt inclusions, and the compositions of melts calculated to be in trace element equilibrium with minerals in plutonic xenoliths, commonly display wider chemical variation than lavas from the same volcanic centre (e.g. Yanagida et al., 2018, Cooper et al., 2019, Gleeson et al., 2020, Stock et al., 2020), hinting that a more complete and complex record of magmatic processes may be recorded in such materials. Plutonic xenoliths are typically either holocrystalline or "mushy" (composed of crystals with interstitial melt), which allows observation of the spatial relationships between mineral phases and interstitial melt. Such observations can provide additional information on processes in crystal mushes that cannot be obtained from equilibrium melts, melt inclusions or the chemical compositions of erupted lavas.

In particular, several recent studies of plutonic xenoliths have identified so-called "reactive melt flow", which describes the reaction of percolating melt with pre-existing crystals in a mush (e.g. Lissenberg and MacLeod, 2016, Jackson et al., 2018). Evidence for reactive melt flow is commonly based on textural features. Examples include ragged or embayed crystal boundaries or crystal cores, interpreted to have formed due to dissolution by a reactive melt (e.g. Lissenberg and MacLeod, 2016, Boulanger et al., 2021). Textural evidence in plutonic xenoliths for replacement of clinopyroxene and/or olivine by amphibole along cleavage planes or at crystal boundaries is also widely interpreted to result from reactive melt flow (e.g. Smith, 2014, Cooper et al., 2016,

Melekhova et al., 2017). Features indicative of reactive melt flow have been identified in plutonic xenoliths and equivalent plutonic rocks from arcs (e.g. Costa et al., 2002, Smith, 2014, Bouilhol et al., 2015, Cooper et al., 2016, Klaver et al., 2017, Melekhova et al., 2017, Camejo-Harry et al., 2018, Villares et al., 2022), mid-ocean ridge (MOR) settings (e.g. Lissenberg et al., 2013, Lissenberg and MacLeod, 2016, SanFillipo et al., 2020, Zhang et al., 2020, Boulanger et al., 2020, 2021, Ferrando et al., 2021) and ocean island volcanoes (Gleeson et al., 2020). Several studies of MOR plutonic rocks have suggested that reactive melt flow represents an important magma differentiation process (e.g. Lissenberg et al., 2013, Lissenberg and MacLeod, 2016, Boulanger et al., 2020, 2021, SanFillipo et al., 2020, Ferrando et al., 2021) and can exert a significant control over MORB trace element compositions (Lissenberg and MacLeod, 2016). Furthermore, based on numerical modelling, Jackson et al., (2018) suggested that reactive melt flow represents the dominant magma differentiation process in mush-dominated magma plumbing systems.

This study uses newly collected plutonic xenoliths from the island of St Vincent in the Lesser Antilles arc (LAA) (**Figure 5.1**) as a case study to investigate the processes controlling magma chemical evolution in mushy plumbing systems in an arc setting. Isotopic studies of St Vincent lavas (Heath et al., 1998) and plutonic xenoliths (Tollan et al., 2012, **Chapter 4** of this thesis) have shown that assimilation of isotopically distinct crust is negligible, hence plutonic xenoliths from this island represent an ideal means of studying magma chemical evolution within mushes in the crust without further complicating effects from crustal assimilation. Previous studies have suggested that St Vincent lava chemical compositions, including trace elements, can be explained by fractional crystallization (FC) of Ol + Sp + Cpx + Pl ± Mt, followed by Ol + Pl + Cpx ± Mt, followed by Pl + Cpx + Opx + Mt (Heath et al., 1998, Cole et al., 2019, Fedele et al., 2021). Using constraints from experimental petrology, Melekhova et al., (2015) further proposed that polybaric crystallization of a high-Mg basalt parent magma with 0.6-4.5 wt % H_2O could produce majority of the major element compositional range of lavas erupted on St Vincent. Fractionating assemblages in their experiments were dependent on melt H_2O and pressure and included Ol + Cpx + Sp, Cpx + Opx + Sp ± Hbl and Pl + Cpx + Opx + Sp. A study of mineral major element chemistry and oxygen isotopic compositions from a suite of St Vincent plutonic xenoliths supported a FC origin, at relatively shallow crustal levels (~ 5 km, based on

melt inclusion data), from a basaltic magma that had undergone a prior stage of differentiation in the lower crust (Tollan et al., 2012).

However, some St Vincent plutonic xenoliths studied here show textural features including compositional banding and replacement of clinopyroxene with amphibole, which are often interpreted as evidence for reactive melt flow (e.g. Smith, 2014, Cooper et al., 2016, Lissenberg and MacLeod, 2016, SanFillipo et al., 2020). This raises the question whether reactive melt flow could also be an important process controlling magma chemical evolution in some parts of the mushy plumbing system at St Vincent, as would be predicted based on the modelling of Jackson et al., (2018).

In this study, we aim to determine whether the textures and mineral chemistry of plutonic xenoliths are most consistent with FC or reactive melt flow as the dominant magma chemical evolution process within mushes in the St Vincent magma plumbing system. Specifically, we focus on the effects of these two processes on magma trace element compositions. We investigate these processes using trace element compositions of clinopyroxene and amphibole, which can incorporate a wide array of trace elements including REE's and HFSE's. In addition, trace element compositions of these phases have been used to investigate the effects of reactive melt flow in previous studies (e.g. Smith, 2014, Cooper et al., 2016, Lissenberg and MacLeod, 2016, SanFillipo et al., 2020). Our findings have major implications for understanding the processes controlling magma chemical evolution in mush-dominated magma plumbing systems in arc settings, and for the interpretation of arc lava trace element compositions.

5.2 - Analytical Methods

The mineral phases in St Vincent plutonic xenoliths were analysed for molar ratios (An, Mg#, etc), major elements and trace elements (clinopyroxene and amphibole). For full details of analytical methods, refer to **sections 2.4 and 2.5 of Chapter 2.** A summary of these methods is given below.

5.2.1 - Chemical mapping of thin sections

Chemical maps of whole thin sections were acquired via Energy Dispersive X-ray Spectroscopy (EDS), using a Zeiss Sigma HD field emission gun (FEG) SEM with two 150 mm^2 Oxford Instruments X-Max energy dispersive silicon drift detectors at Cardiff

University. The maps were acquired using an accelerating voltage of 20 kV, aperture size 120 µm and working distance of 8.9 mm. The magnification was adjusted depending on the typical crystal size in thin section, resulting in a pixel size of 22.9 µm or 24.17 µm. Pixel dwell time was set at 20 ms for all sample maps. Raw data were background corrected (via processing as "TruMaps") using Oxford Instruments AZtec software prior to generation of element maps.

Major element compositions of minerals were determined from individual areas within target mineral phases on the background-corrected element maps, via the Tru-Q function in AZtec **(see Chapter 2, section 2.4.2** for full details**).** The software package "QUACK", developed at Cardiff University (Loocke, 2016) was used to process the background-corrected x-ray element maps generated in AZtec and produce maps of both the distribution of mineral phases and quantitative molar element ratios (e.g. plagioclase An, clinopyroxene Mg#, olivine Fo, see **Chapter 2, section 2.4.3).**

Data quality of molar element ratio maps processed via QUACK was rigorously tested by Loocke, (2016), via analysis of plagioclase, clinopyroxene and olivine standards with known An, Mg# and Fo. Percentage error on molar ratio measurements (deviation of mean measured value from accepted value of standard, expressed as a percentage) was determined as 0.20 % for plagioclase An, 0.59 % for clinopyroxene Mg# and 0.22 % for olivine Fo.

5.2.2 - LA-ICP-MS analyses of clinopyroxene and amphibole

The trace element compositions of clinopyroxene and amphibole from St Vincent plutonic xenoliths were analysed by laser ablation inductively coupled plasma mass spectrometry (LA-ICP-MS), using a Teledyne Analyte Excite Laser Ablation System coupled to a Thermo-Scientific X-Series 2 ICP-MS at Durham University. Analyses were made on the chemically mapped thin sections over two analytical sessions. The laser was run with a fluence of 8.09 J/cm^2, a repetition rate of 8 Hz, and a 75 µm square spot size. Helium was used as the carrier gas, with Ar mixed in prior to the introduction of the sample into the mass spectrometer. Data reduction was carried out using the software Iolite (Paton et al., 2011). The NIST 612 glass standard was analysed during all runs and used as the calibration standard. The internal standard was Ca (wt %) – a constant value of 16 wt % was used for clinopyroxene and 8.6 wt % for amphibole, due to the minimal variation in CaO in LAA plutonic xenolith clinopyroxene and

amphibole **(see Chapter 2, section 2.5.6 for full details).** Uncertainty on clinopyroxene and amphibole trace element data is provided both as internal 2SE (standard error) as calculated by Iolite and 2SD % for each element. The 2SD % uncertainty values are based on measurements of the BCR-2G glass standard (n=32) across both analytical sessions and reflect reproducibility of BCR-2 measurements (**see Chapter 2, Table 2.11**). The calculated 2SD % uncertainties are less than 15 % relative, excluding Ti (22 %), Cr (16 %) and Lu (23 %).

5.3 - Key petrographic features of plutonic xenoliths

Full petrographic descriptions and accompanying images of the St Vincent plutonic xenolith samples analysed in this study are given in **Chapter 3, section 3.2.** The key petrographic features of the selected samples are summarised in this section.

5.3.1 - Sample selection

Plutonic xenolith samples were collected on a 2019 field campaign to St Vincent **(see Appendix 1).** The majority were collected in situ from deposits (pyroclastic density currents and some lavas) on the flanks of La Soufrière volcano and coastal exposures on the eastern side of the island (**Figure 5.1**). Initially, thin sections from 17 samples with variable mineralogy and appearance in hand specimen were assessed petrographically. Using the classification scheme of Streckeisen (1976), plutonic xenolith types include troctolites (5 samples), olivine gabbros (6 samples), hornblende-olivine gabbros (2 samples), hornblende gabbros (1 sample) and gabbronorites (3 samples) (see **Chapter 3, Figures 3.19-3.25** for an overview of these samples). Half the olivine gabbros (3 samples), a gabbronorite and a hornblende-olivine gabbro have adcumulate textures (no interstitial melt). Orthocumulate and mesocumulate textures, with interstitial melt lining crystal boundaries or present as small pockets, are observed in all troctolites, plus two olivine gabbro samples and two gabbronorite samples. Clinopyroxene forms a primocryst phase in olivine gabbros (5 samples), all gabbronorites and a hornblende-olivine gabbro and is also present as an interstitial phase in two olivine gabbros. Amphibole in the hornblende-olivine gabbro samples occurs interstitially and is texturally associated with clinopyroxene and/or olivine.

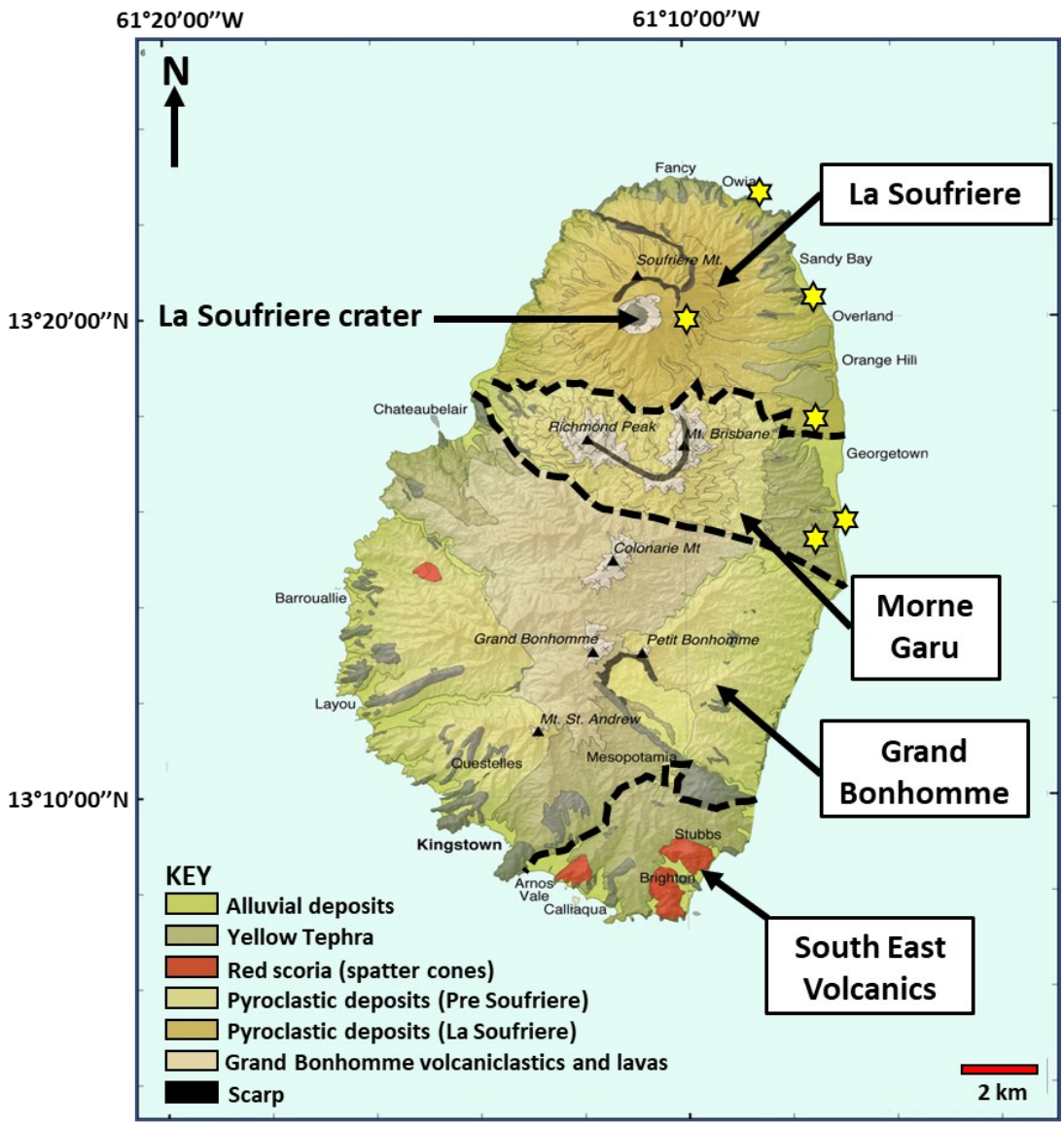

Figure 5.1: Sampling locations of plutonic xenoliths (yellow stars) superimposed on the geological map of St Vincent from Robertson (2012). See **Appendix 1** for details of St Vincent fieldwork. The dashed black lines highlight the boundaries between the four (labelled) volcanic centres on St Vincent.

Here, we investigate FC and reactive melt flow using textural observations and clinopyroxene and amphibole trace element compositions. Hence, four alteration-free clinopyroxene and/or amphibole bearing plutonic xenoliths (two olivine gabbros and two hornblende-olivine gabbros) were selected for detailed study **(section 5.3.2, Figures 5.2 and 5.3, Chapter 3, section 3.2.2**). Troctolites were not selected due to a lack of clinopyroxene and amphibole in the mineral assemblage (**Chapter 3**). Unlike clinopyroxene and amphibole, olivine and to a lesser extent plagioclase do not typically contain significant trace element concentrations and hence troctolites are less well suited to investigating the effects of mush processes on magma trace element

compositions. The hornblende gabbro was not selected for analysis due to the presence of alteration which affects amphibole in the sample (**Chapter 3, Figure 3.24**). The chosen samples are texturally distinct from each other and contain clinopyroxene in different textural relationships (found as primocrysts, interstitially, or partially overgrown/reacted) with other phases. The four selected plutonic xenoliths cover the range of clinopyroxene textural relationships observed in the wider sample suite. Gabbronorites were not analysed as these samples only contain primocryst clinopyroxene, which is represented in two of the chosen samples. Selected hornblende-olivine gabbros have distinctive textural features from the other 15 thin sections initially analysed petrographically (**Chapter 3, Figures 3.19 - 3.25**). Such features have not previously been reported in St Vincent plutonic xenoliths (Tollan et al., 2012), hence the inclusion of these samples in this study has the potential to reveal new insights into processes in the St Vincent magma plumbing system.

5.3.2 - Key petrographic features of selected samples

Olivine gabbro (VS527) - Figure 5.2, a

The mineral assemblage consists of plagioclase (69 %), olivine (22 %), clinopyroxene (8 %) and minor magnetite (1 %) with crystal size varying from 0.5-5 mm. Clinopyroxene is predominantly an interstitial phase found between primocryst plagioclase and olivine. The sample has a mesocumulate texture with films of melt lining most crystal boundaries. At the contact with the rind of host lava, the host melt appears to be infiltrating into the xenolith (**Figure 5.4**). Determining whether the melt at this contact is residual from crystallization of the plutonic xenolith phases or has infiltrated from the host lava is beyond the scope of this study. No clinopyroxene measurements were taken directly adjacent to the contact, therefore possible infiltration of host lava will not have impacted the clinopyroxene compositions analysed and is not considered further.

Ol-CPX gabbro (VS532) - Figure 5.2, b

The mineral assemblage consists of plagioclase (52 %), olivine (23 %) and clinopyroxene (25 %) with crystal size varying from 0.5-3 mm. Clinopyroxene is a primocryst phase. The sample has an adcumulate texture with typically well equilibrated, 120° crystal boundaries (**Figure 5.4**) between the three primocryst phases. No interstitial melt is present.

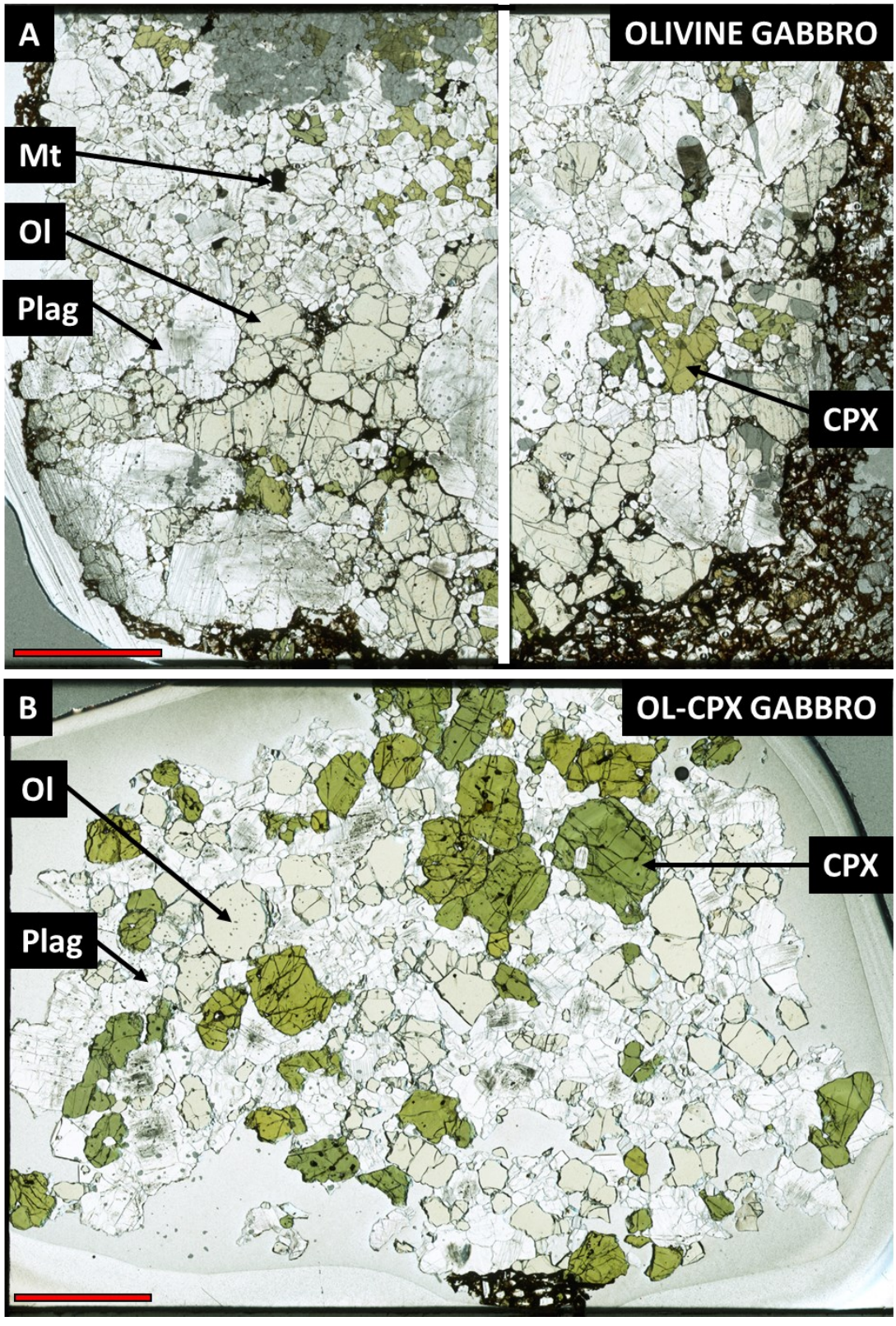

Figure 5.2: A) Olivine gabbro thin section (PPL) overview . Red scale bar = 5 mm. Gap between images represents a small area of the thin section that was not imaged. Pl = plagioclase, Ol = olivine, CPX = clinopyroxene, Mt = magnetite. **B)** Ol-CPX gabbro thin section (PPL) overview. Red scale bar = 5 mm. Pl = plagioclase, Ol = olivine, CPX = clinopyroxene.

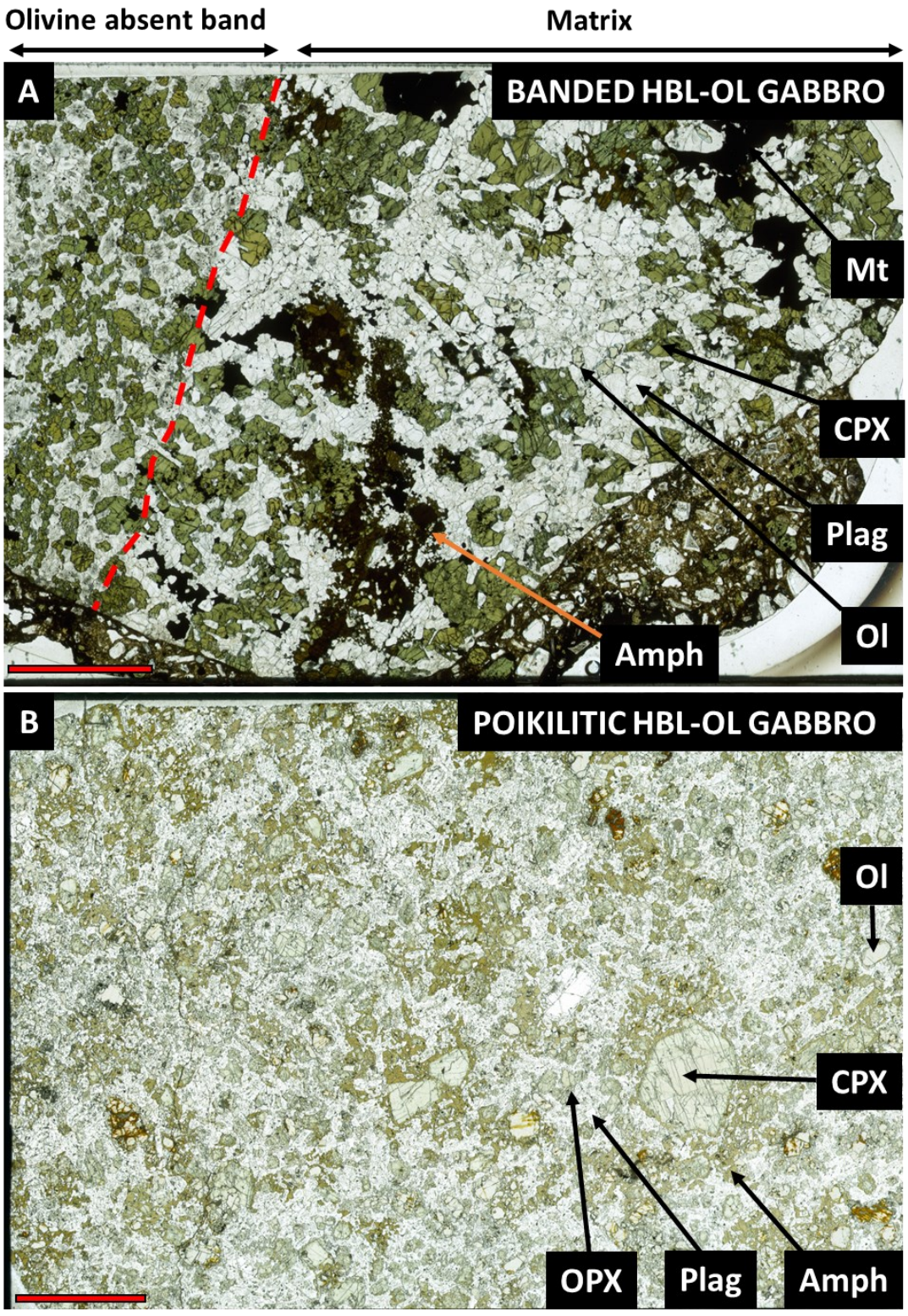

Figure 5.3: A) Banded Hbl-Ol gabbro thin section (PPL) overview with texturally distinct olivine absent band labelled (boundary marked by red dashed line). The reminder of the sample is referred to as the sample matrix. Red scale bar = 5 mm. Pl = plagioclase, Ol = olivine, CPX = clinopyroxene, Amph = amphibole, Mt = magnetite. **B)** Poikilitic Hbl-Ol gabbro thin section (PPL) overview. Red scale bar = 5 mm. Pl = plagioclase, Ol = olivine, CPX = clinopyroxene, Amph = amphibole, OPX = orthopyroxene.

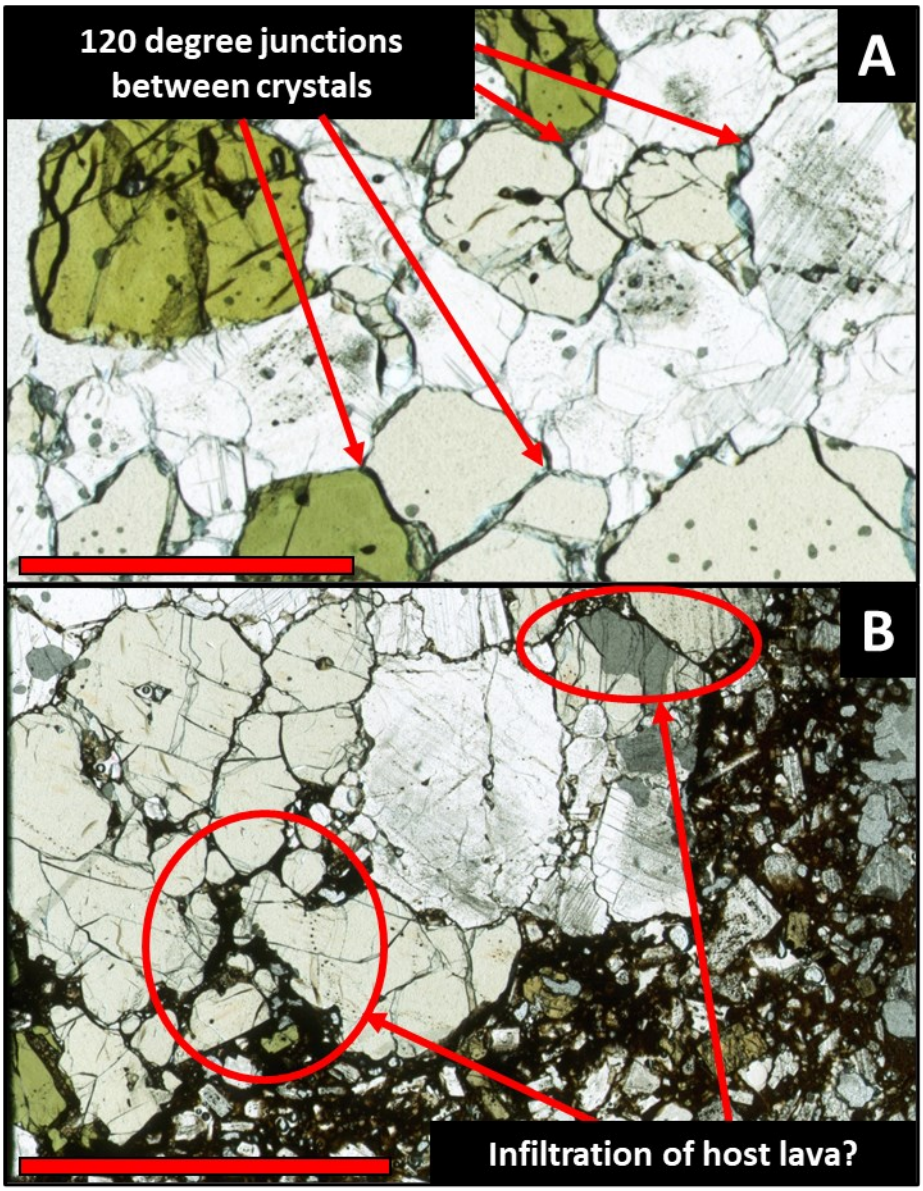

Figure 5.4: A) Example of well equilibrated crystal boundaries and 120° crystal junctions in the Ol-CPX gabbro (PPL). Red scale bar = 2.5 mm. **B)** Possible sites of infiltration of host lava into the olivine gabbro (PPL), highlighted in the red circles. Red scale bar = 5 mm.

Banded Hbl-Ol gabbro (VS551) - Figure 5.3, a

The mineral assemblage consists of plagioclase (58 %), olivine (2 %), clinopyroxene (29 %), amphibole (7 %) and magnetite (4 %) with crystal size varying from 0.2-3 mm. Clinopyroxene is a primocryst phase. Majority of the sample has an adcumulate texture with typically well equilibrated crystal boundaries and no interstitial melt. A key feature is the presence of a texturally and mineralogically distinct band, characterized by a generally smaller crystal size, inclusion rich plagioclase (**Figure 5.5**) and the absence of olivine (**Figure 5.3, a, Figure 5.5**). This feature is hereon referred to as the

"olivine absent band". The remainder of the sample outside the band is referred to as the sample "matrix" (**Figure 5.3, a**). Amphibole is distributed in patches within the sample matrix and notably only occurs outside the "olivine absent band". Amphibole is generally anhedral and typically found overgrowing the rims of clinopyroxene **(Figure 5.6).**

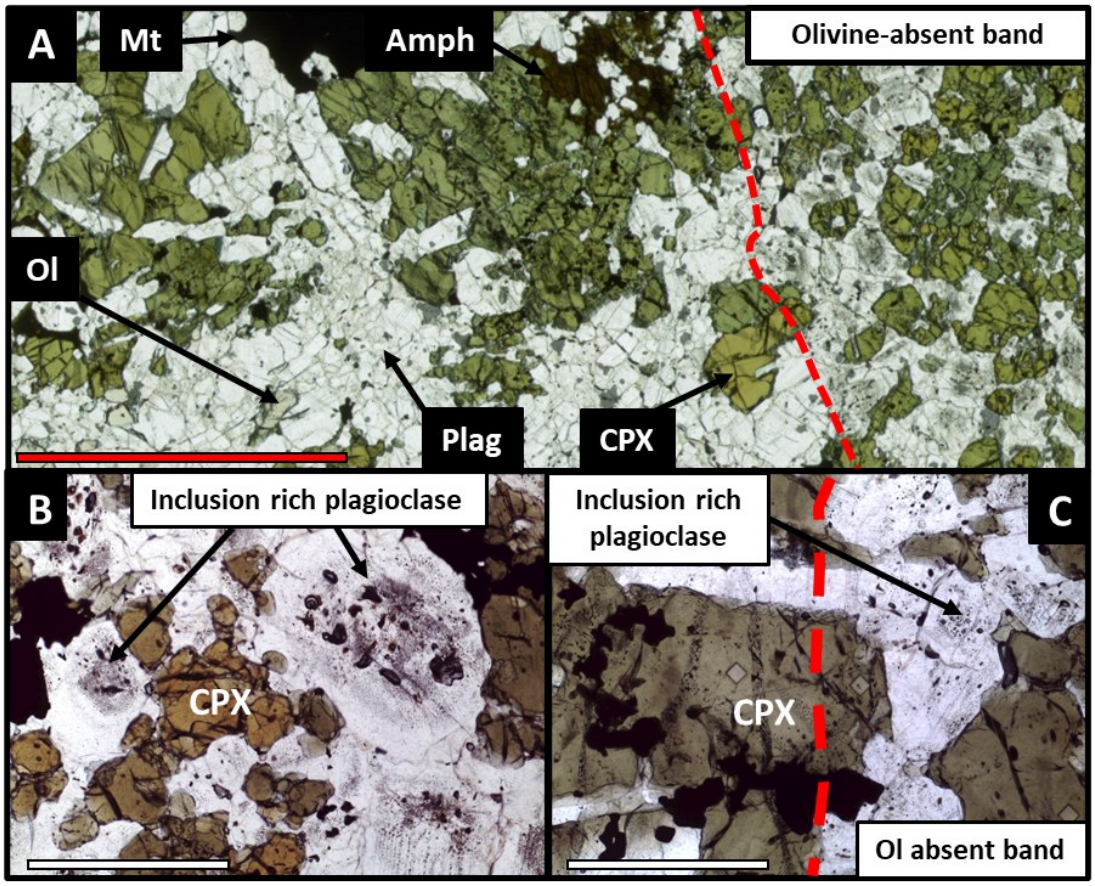

Figure 5.5: A) PPL image of the difference in textures between the banded Hbl-Ol gabbro matrix and olivine absent band. Note the abrupt transition from clear plagioclase in the matrix to inclusion rich plagioclase in the band. Also note the generally smaller clinopyroxene crystal size and absence of olivine within the band. The red dashed line marks the boundary between matrix and olivine absent band. The location of the boundary was determined by the quantitative compositional maps in **Figure 5.13**. Red scale bar = 5 mm. **B)** PPL image of plagioclase and clinopyroxene within the olivine absent band, highlighting the melt and fluid inclusion rich plagioclase. **C)** PPL image of the boundary between the sample matrix and olivine-absent band (red dashed line), again highlighting inclusion rich plagioclase within the band. The location of the boundary was determined by the quantitative compositional maps in **Figure 5.13**. White scale bar = 1 mm.

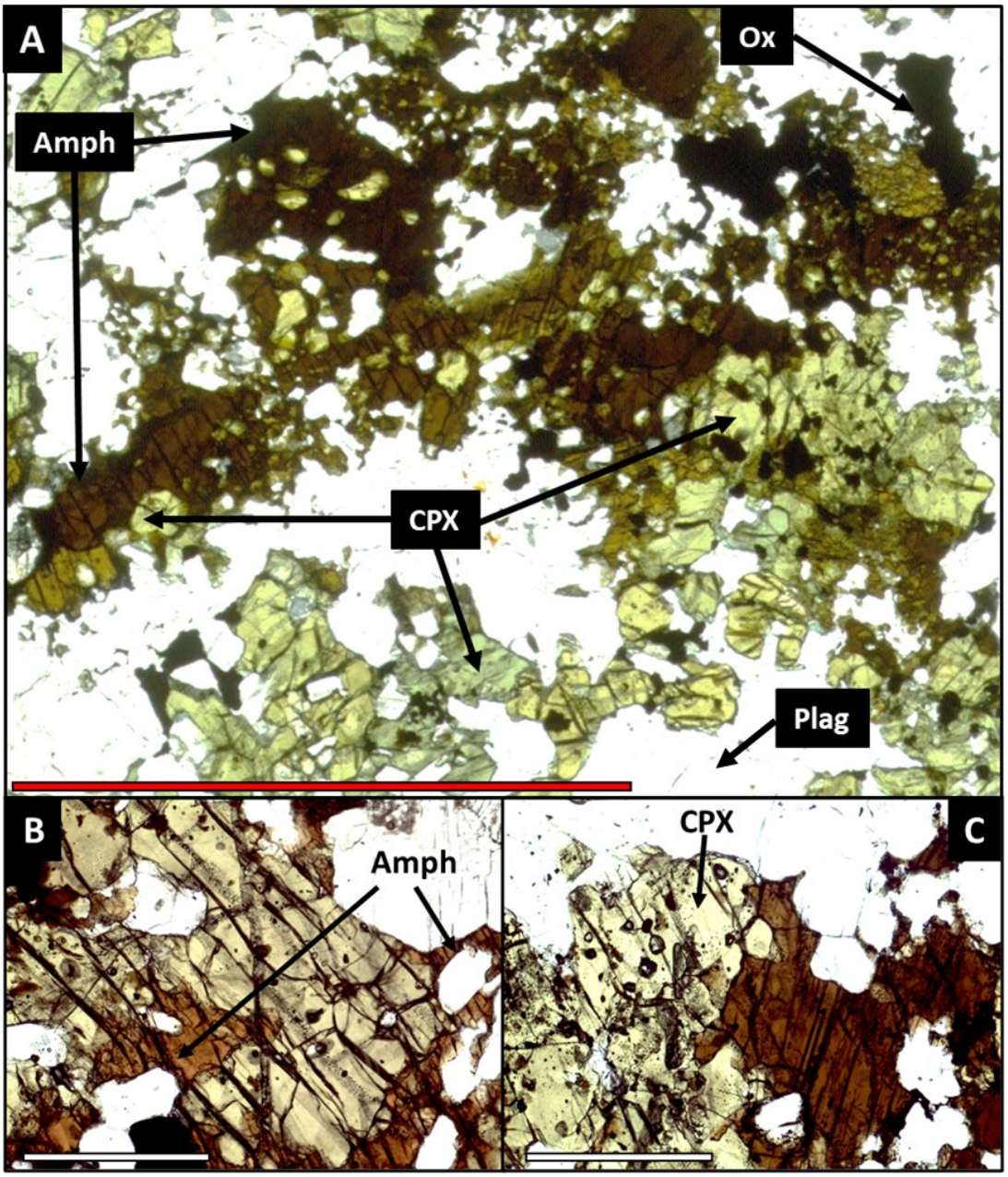

Figure 5.6: A) PPL image of cluster of amphibole (brown) overgrowing clinopyroxene (pale green) rims from the matrix of the banded Hbl-Ol gabbro. Red scale bar = 5 mm. **B)** and **C)** PPL images of amphibole overgrowths on the rims of clinopyroxene from the matrix of the banded Hbl-Ol gabbro. White scale bar = 1 mm.

Poikilitic Hbl-Ol gabbro (VS572) - Figure 5.3, b

The mineral assemblage consists of plagioclase (53 %), olivine (8 %), clinopyroxene (12 %), orthopyroxene (12 %), and amphibole (15 %) with minor interstitial apatite, oxides and very rare sulfides. Crystal size varies from 0.3-4 mm. The sample has a non-cumulate/intrusive texture with zoned plagioclase and clinopyroxene and many crystals (particularly plagioclase) < 1 mm. A key feature is the presence of poikilitic

amphibole throughout the sample, which is often found replacing the rims of clinopyroxene **(Figure 5.7, a,b,d).** Two clinopyroxene size populations (> 1 mm euhedral, < 1 mm subhedral) are present. Olivine is commonly altered to iddingsite, rounded and/or embayed and enclosed by orthopyroxene or amphibole **(Figure 5.7, c,d).** Plagioclase exhibits a wide range of zoning patterns with some crystals showing complex zonation and relict/patchy cores **(Figure 5.7, e,f).**

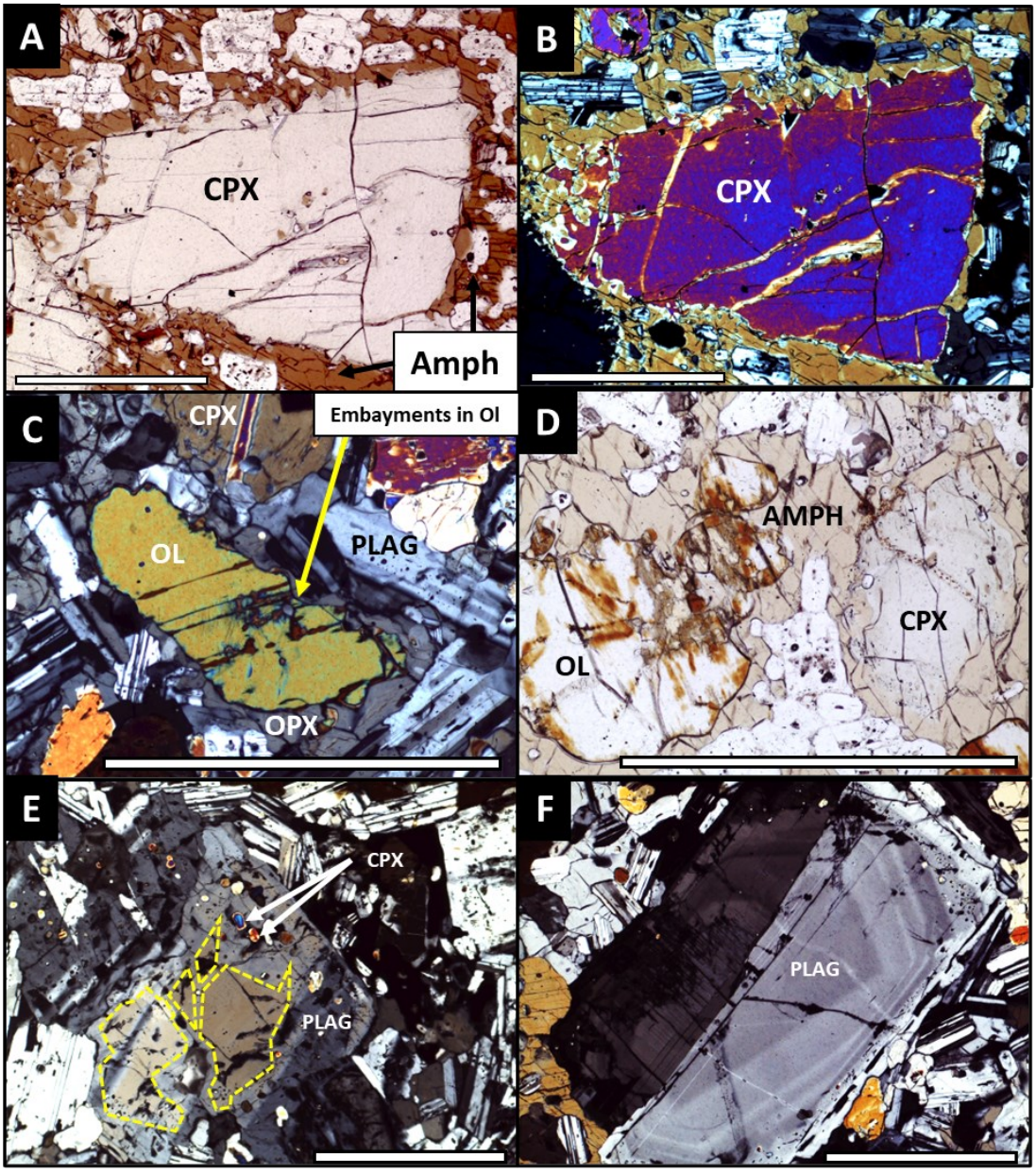

Figure 5.7: A) PPL and **B)** XPL image of zoned clinopyroxene (CPX) with poikilitic amphibole (Amph) replacing rim. Note the ragged contact between clinopyroxene and amphibole. **C)** XPL image showing example of poikilitic orthopyroxene (OPX) surrounding embayed olivine (Ol). **D)** PPL image of poikilitic amphibole surrounding both clinopyroxene and olivine. **E)** XPL image of zoned plagioclase

(plag) with relict core outlined (yellow dashes). Correspondence with the chemical map shows that this core has a high An content. Note the clinopyroxene inclusions in the crystal zone outside the relict core. **F)** PPL image of plagioclase with complex oscillatory zoning. White scale bar = 1 mm.

5.4 – Results

5.4.1 – Mineral molar element ratios

The histograms in **Figures 5.8-5.11** show the range of molar element ratios (An, Mg#, Fo) for the main mineral phases in each plutonic xenolith sample, determined from EDS-SEM quantitative molar element ratio maps. The range of olivine Fo compositions is narrow in all samples (2-4 mol %) and the average olivine Fo content differs between samples, with the most primitive olivine in the Ol-CPX gabbro **(Figure 5.8).** Overall olivine varies from Fo_{72-80}. Clinopyroxene shows a narrow range in Mg# in the olivine gabbro and Ol-CPX gabbro (~ Mg# 73-80) and a slightly broader range (Mg# 70-80) in the banded Hbl-Ol gabbro **(Figure 5.9)**. Clinopyroxene from the poikilitic Hbl-Ol gabbro show a wider range (~ Mg# 72-89) **(Figure 5.9, d**). The range in plagioclase An compositions show the same trend as clinopyroxene with olivine gabbro and Ol-CPX gabbro plagioclase displaying the narrowest range (An_{90-99}), followed by the banded Hbl-Ol gabbro plagioclase (An_{86-97}) and poikilitic Hbl-Ol gabbro plagioclase (An_{60-90}) **(Figure 5.10).** Amphibole from both Hbl-Ol gabbros have a narrow range of Mg# (~ 9 mol %) with slightly higher average Mg# (68) in the poikilitic Hbl-Ol gabbro versus the banded Hbl-Ol gabbro (Mg# 66) **(Figure 5.11).** Orthopyroxene from the poikilitic Hbl-Ol gabbro show a very narrow range of Mg# (71-76, **Figure 5.11).**

Clinopyroxene shows minor Mg# zonation in the olivine gabbro and Ol-CPX gabbro, with a patchy distribution of higher Mg# zones **(Figure 5.12)**. The clinopyroxene Mg# map for the banded Hbl-Ol gabbro shows a band of clinopyroxene with distinctly lower Mg# (70-74, **Figure 5.13, a)** which corresponds to the olivine absent, texturally distinct band within this sample. Higher Mg# (77-80) zones are seen in some of the clinopyroxene outside of the texturally distinct, olivine absent band. The plagioclase An map shows an abrupt change to lower An (86-91) plagioclase within the olivine absent band **(Figure 5.13, b)**, demonstrating that this region of the sample is both texturally and chemically distinct.

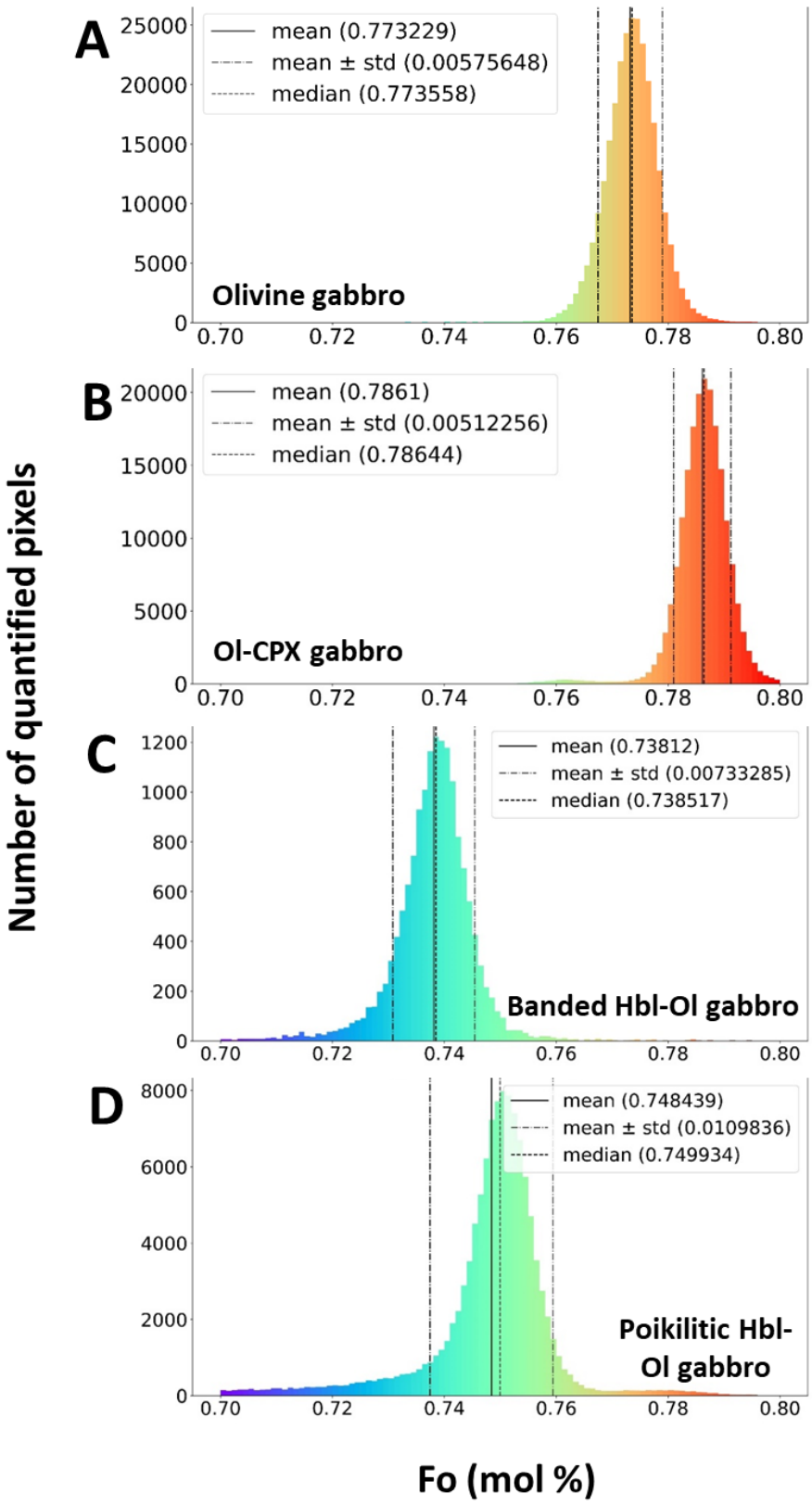

Figure 5.8: Histograms showing the range of olivine Fo contents in samples **A)** olivine gabbro **B)** Ol-CPX gabbro **C)** banded Hbl-Ol gabbro **D)** poikilitic Hbl-Ol gabbro. Histograms generated by the QUACK software (see **Chapter 2**) based on Fo contents measured via quantitative molar element ratio

mapping of thin sections. Mean, standard deviation and median values were automatically calculated by the QUACK software.

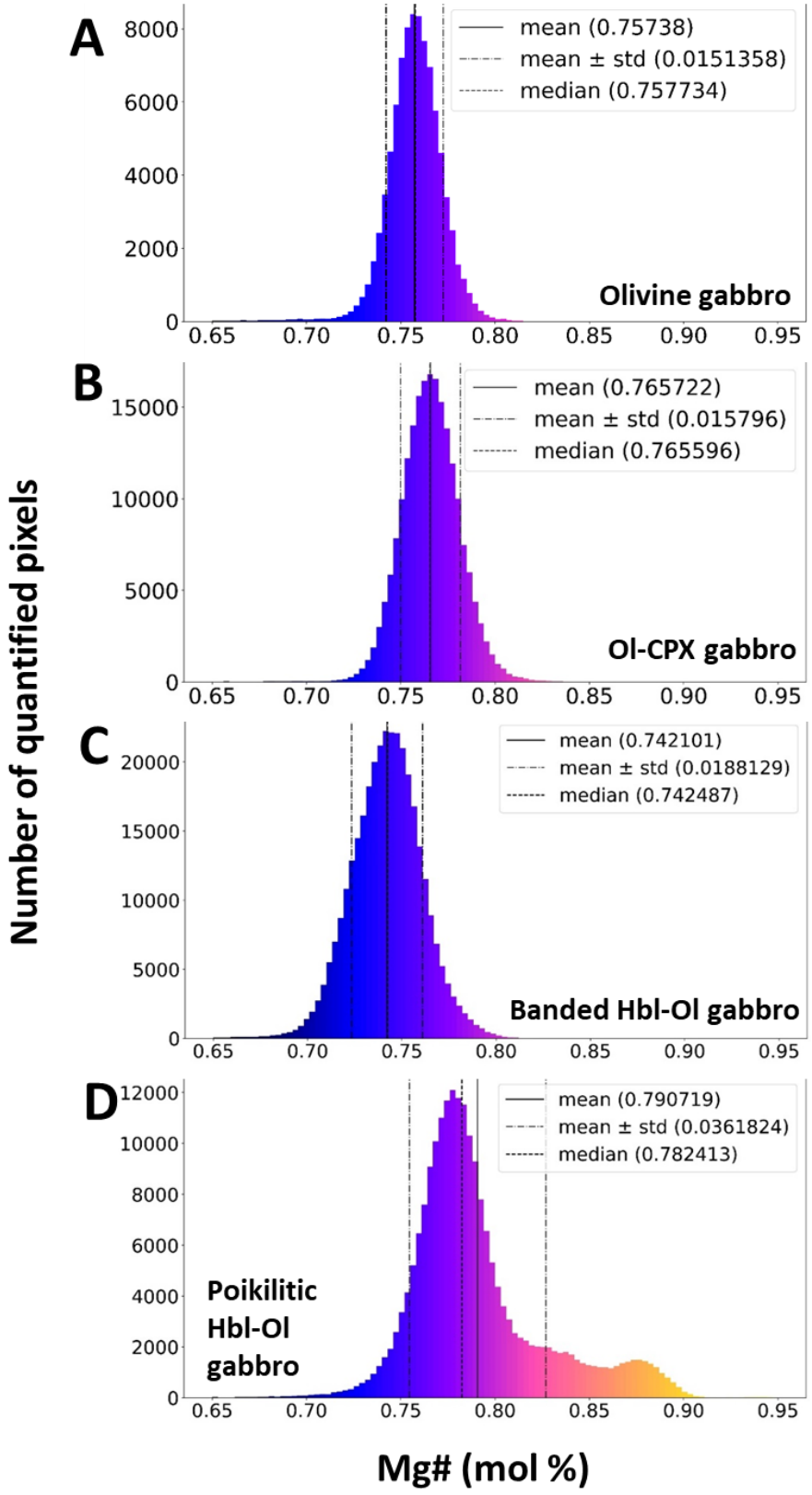

Figure 5.9: Histograms showing the range of clinopyroxene Mg# contents in samples **A)** olivine gabbro **B)** Ol-CPX gabbro **C)** banded Hbl-Ol gabbro **D)** poikilitic Hbl-Ol gabbro. Histograms generated by the

QUACK software (see **Chapter 2**) based on Mg# contents measured via quantitative molar element ratio mapping of thin sections. Mean, standard deviation and median values were automatically calculated by the QUACK software.

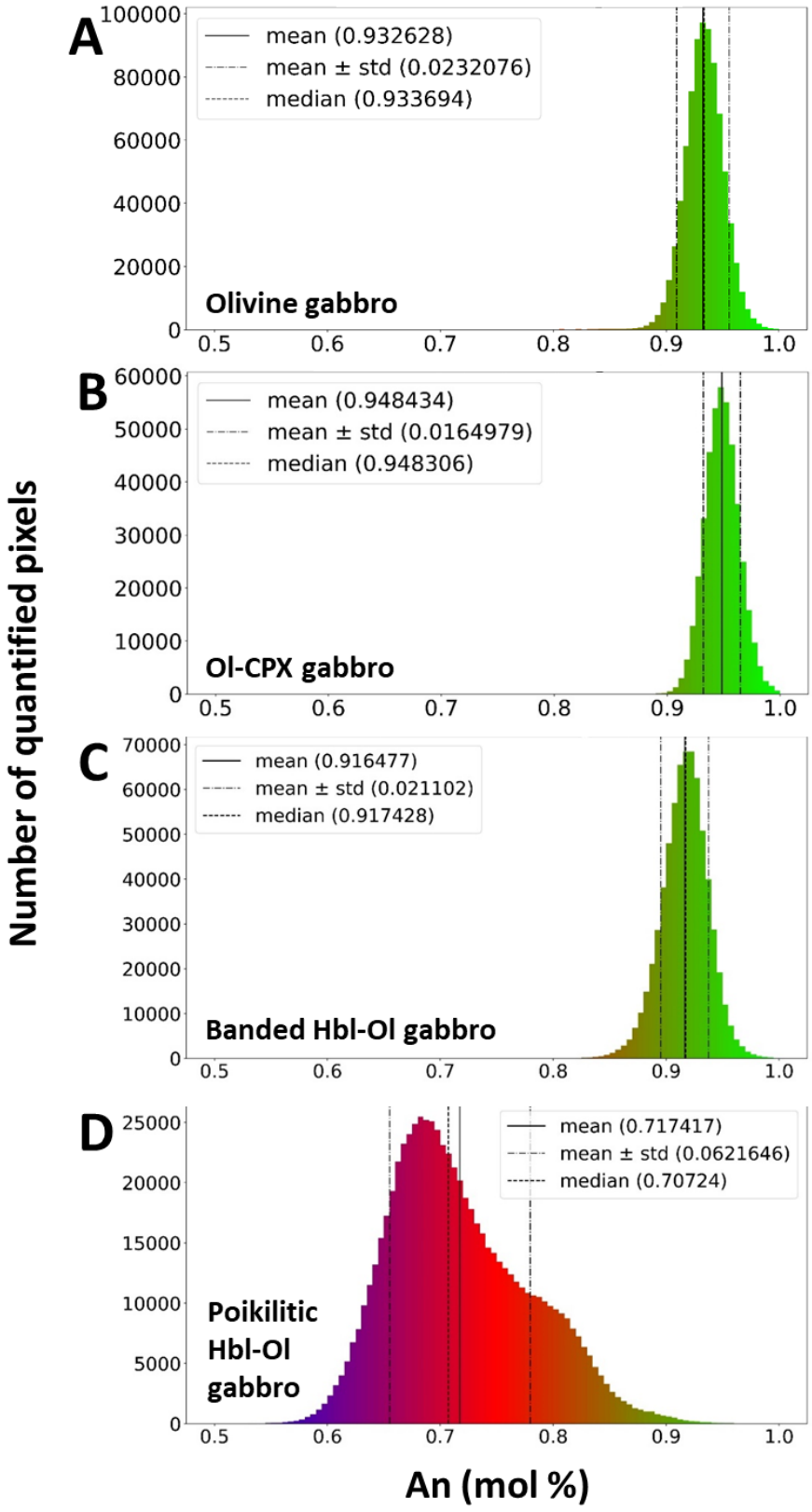

Figure 5.10: Histograms showing the range of plagioclase An contents in samples **A)** olivine gabbro **B)** Ol-CPX gabbro **C)** banded Hbl-Ol gabbro **D)** poikilitic Hbl-Ol gabbro. Histograms generated by the QUACK software (see **Chapter 2**) based on An contents measured via quantitative molar element ratio

mapping of thin sections. Mean, standard deviation and median values were automatically calculated by the QUACK software.

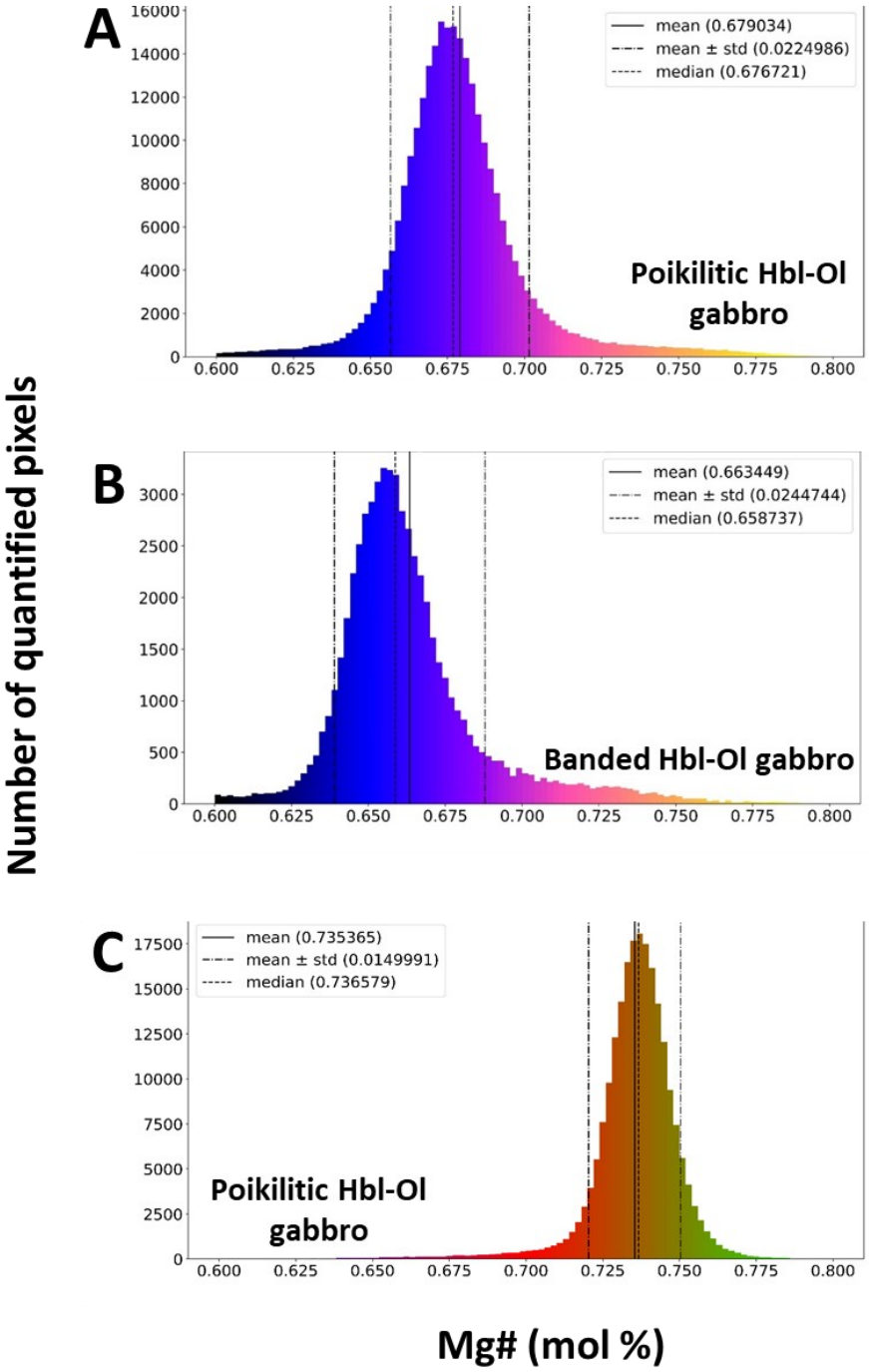

Figure 5.11: Histograms showing the range of amphibole Mg# contents in samples **A)** poikilitic Hbl-Ol gabbro **B)** banded Hbl-Ol gabbro**.** Histogram in **C)** shows range of orthopyroxene Mg# contents in poikilitic Hbl-Ol gabbro. Histograms generated by the QUACK software (see **Chapter 2**) based on Mg# contents measured via quantitative molar element ratio mapping of thin sections. Mean, standard deviation and median values were automatically calculated by the QUACK software.

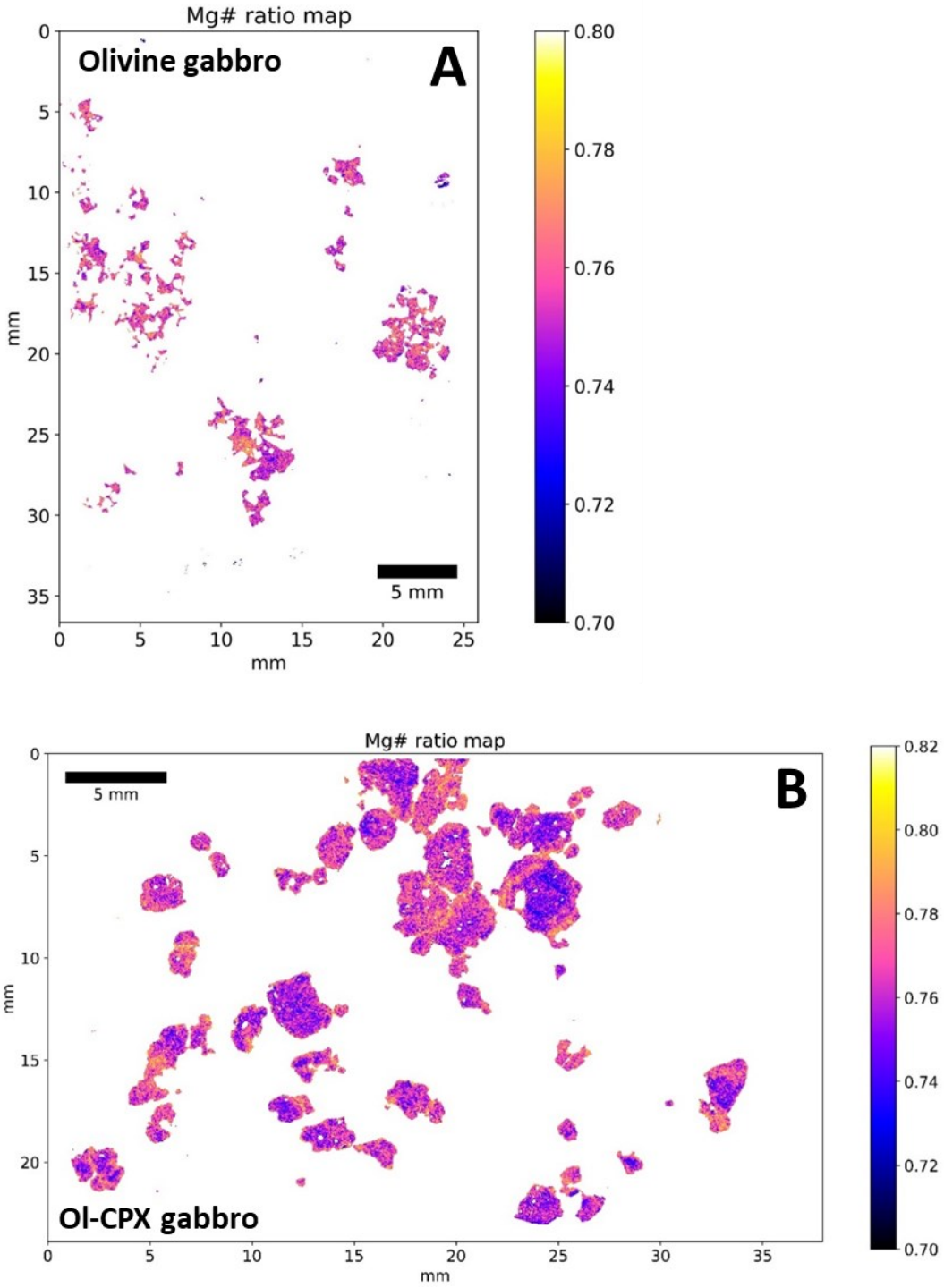

Figure 5.12: Quantitative Mg# in clinopyroxene thin section maps for **A)** olivine gabbro and **B)** Ol-CPX gabbro. Note the slight Mg# enrichment towards some crystal rims in **B)**. The thin section maps were generated by the QUACK software (see **Chapter 2**).

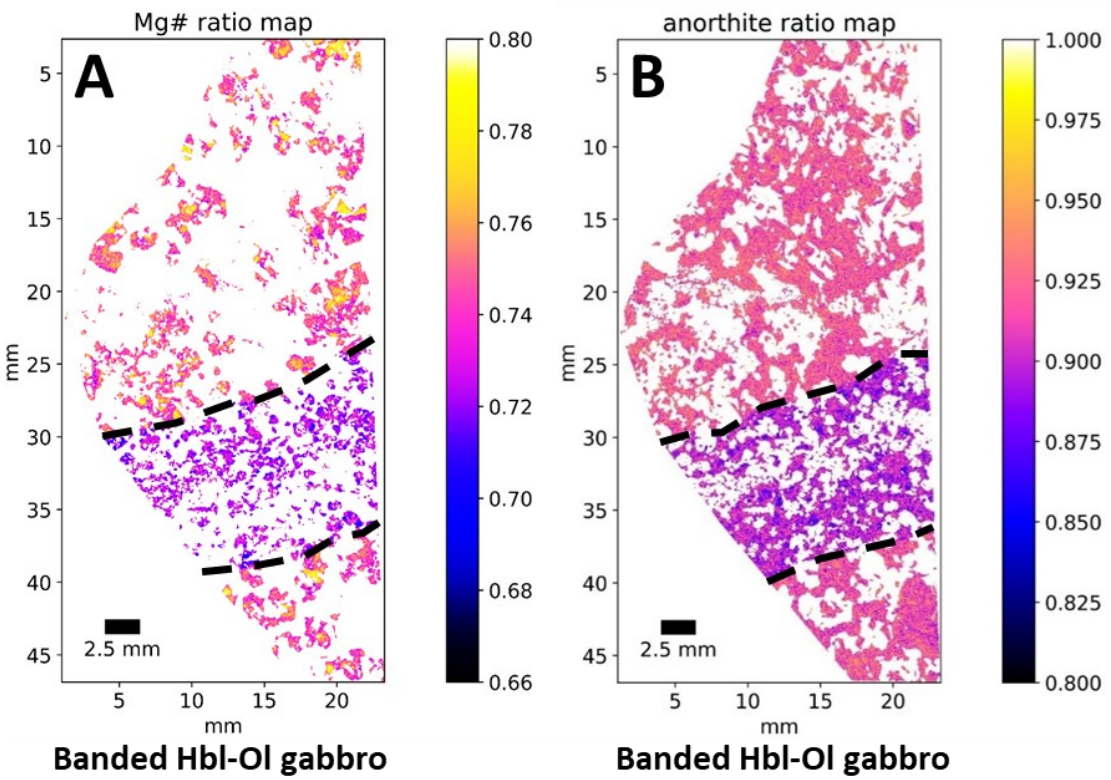

Figure 5.13: A) Quantitative Mg# in clinopyroxene thin section map and **B)** quantitative An in plagioclase thin section map for banded Hbl-Ol gabbro. The thin section maps were generated by the QUACK software (see **Chapter 2**). The dashed lines highlight the texturally distinct, olivine absent band within the sample.

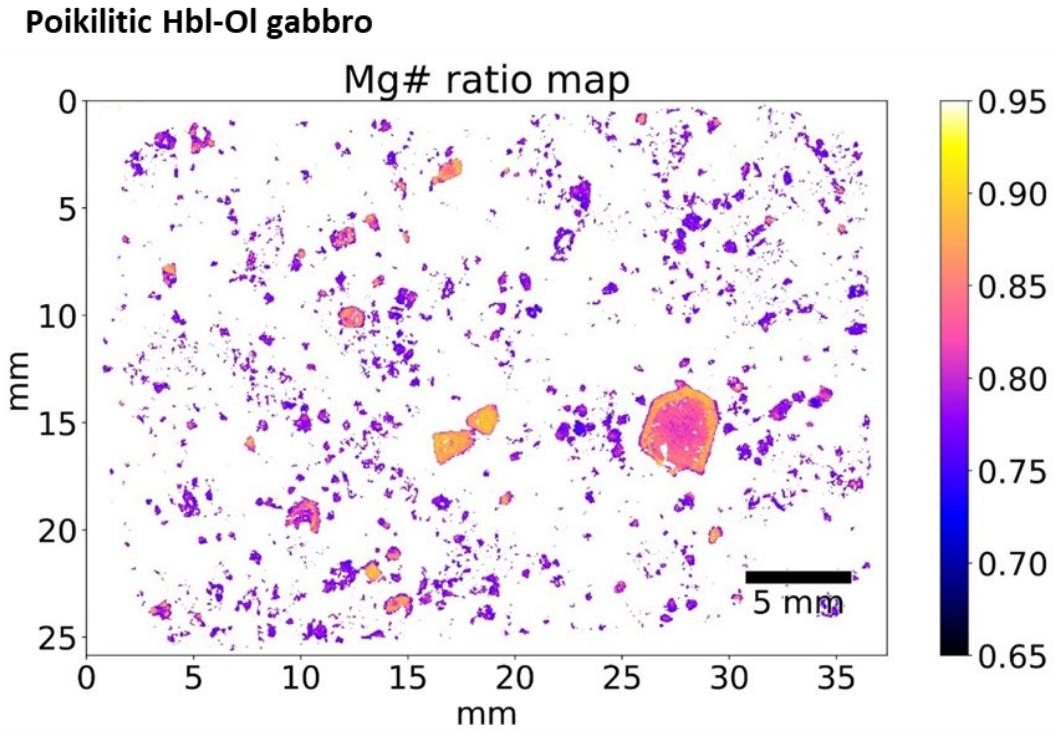

Figure 5.14: Quantitative Mg# in clinopyroxene thin section map for poikilitic Hbl-Ol gabbro. The thin section map was generated by the QUACK software (see **Chapter 2**).

The clinopyroxene Mg# map for the poikilitic Hbl-Ol gabbro **(Figure 5.14)** highlights the presence of two compositionally distinct clinopyroxene populations, which correspond to the two size populations observed in the sample. The first population includes clinopyroxene with Mg# > 80, (pink and yellow in **Figure 5.14**), which generally consists of the larger (> 1 mm) crystals in the sample. The second population (purple in **Figure 5.14**), have lower Mg# with majority in the range 75-80. These will be referred to as the "high Mg# CPX population" (Mg# > 80) and "low Mg# CPX population" (Mg# < 80) in the remainder of the text. The plagioclase An map **(Figure 5.15)** reveals the distribution of An variation in plagioclase in the poikilitic Hbl-Ol gabbro and allows three populations to be identified. Rare high An (An_{85-90}) plagioclase (yellow on **Figure 5.15**), typically found as crystal cores, are sparsely distributed throughout. The second, moderately high An (An_{75-85}) plagioclase population (orange on **Figure 5.15**) are found as mantles to high An cores, as well as discrete crystals or crystal cores. The third, lower An plagioclase (An_{60-75}) population (blue on **Figure 5.15**) form rims on (An_{75-85}) population cores or discrete lower An plagioclase crystals.

Poikilitic Hbl-Ol gabbro

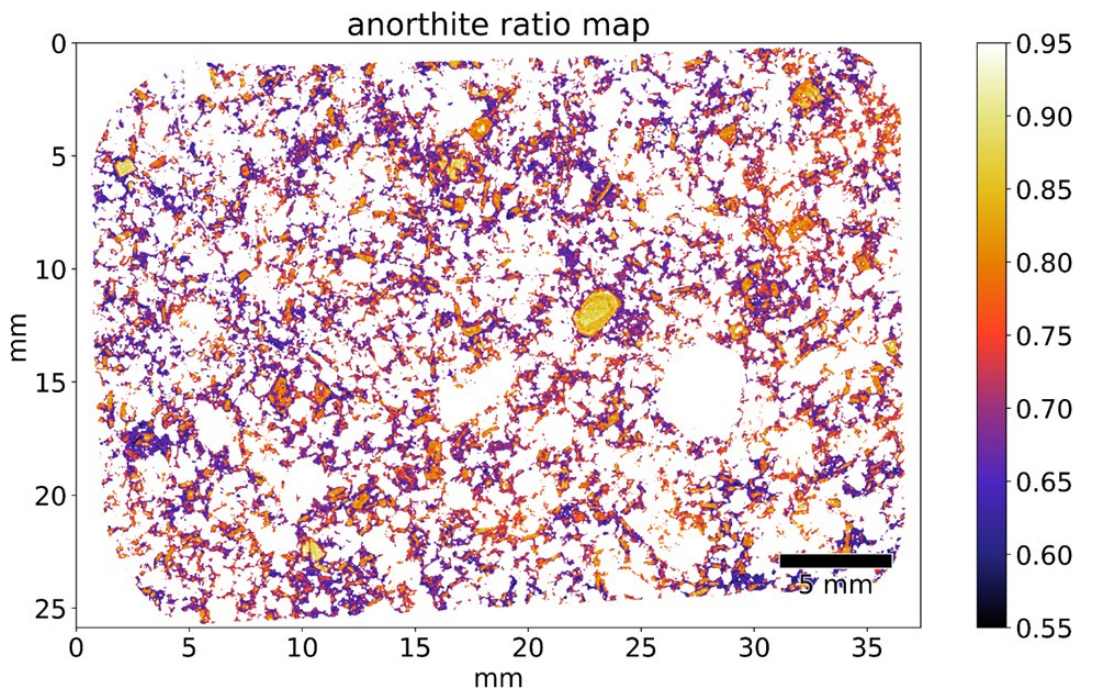

Figure 5.15: Quantitative An in plagioclase thin section map for poikilitic Hbl-Ol gabbro. The thin section map was generated by the QUACK software (see **Chapter 2**).

5.4.2 – Trace element chemistry of clinopyroxene and amphibole

Full trace element data for all measured clinopyroxene and amphibole can be found in **Appendix 5.4.**

5.4.2.1 – Clinopyroxene

The concentrations of incompatible trace elements (Zr, Y and Ce) broadly increase with decreasing Mg# **(Figure 5.16, a,b,c).** Clinopyroxene from the olivine gabbro, Ol-CPX gabbro and banded Hbl-Ol gabbro matrix have a similar range in Mg# and overlapping Zr, Y and Ce. Clinopyroxene within the olivine absent band have slightly elevated Ce relative to those from the sample matrix. The lowest incompatible trace element contents are found in the high Mg# CPX from the poikilitic Hbl-Ol gabbro, though a range of compositions is observed within this population. The low Mg# CPX from the same sample have higher Zr and Ce contents at a given Mg# compared with other samples.

Clinopyroxene Cr and Ni contents decrease with decreasing Mg# **(Figure 5.16, d,e)**, with maximum values of 3850 µg/g Cr and 185 µg/g Ni in the poikilitic Hbl-Ol gabbro high Mg# CPX and minimum values of 0.62 µg/g Cr and 1.98 µg/g Ni in the olivine absent band clinopyroxene. The poikilitic Hbl-Ol gabbro low Mg# CPX show anomalously high Ni and Cr contents at a given Mg#. Primitive mantle normalized LREE/MREE (e.g. La/Sm) and LREE/HREE (e.g. La/Yb) ratios are similar for clinopyroxene from the olivine gabbros and banded Hbl-Ol gabbro **(Figure 5.16, f).** Poikilitic Hbl-Ol gabbro clinopyroxene show more variation, with the low Mg# CPX showing significant LREE enrichment **(Figure 5.16, c,f).**

Clinopyroxene from the olivine gabbro, Ol-CPX gabbro and banded Hbl-Ol gabbro have broadly similar curved REE patterns, with low LREE, relatively flat M-HREE and small negative Eu anomalies (**Figure 5.17)**. The olivine absent band clinopyroxene have the same pattern as those from the sample matrix but are slightly more REE enriched **(Figure 5.17, b).** Most of the poikilitic Hbl-Ol gabbro high Mg# CPX have similar REE patterns to clinopyroxene from other samples, though two measurements show LREE enrichment relative to MREE/HREE **(Figure 5.17, a and Figure 5.16, f).** All high Mg# CPX have lower M-HREE contents than clinopyroxene from other samples. In contrast, poikilitic Hbl-Ol gabbro low Mg# CPX have almost flat REE

patterns indicating LREE enrichment **(Figure 5.17, a)**, with similar M-HREE contents to clinopyroxene from other samples.

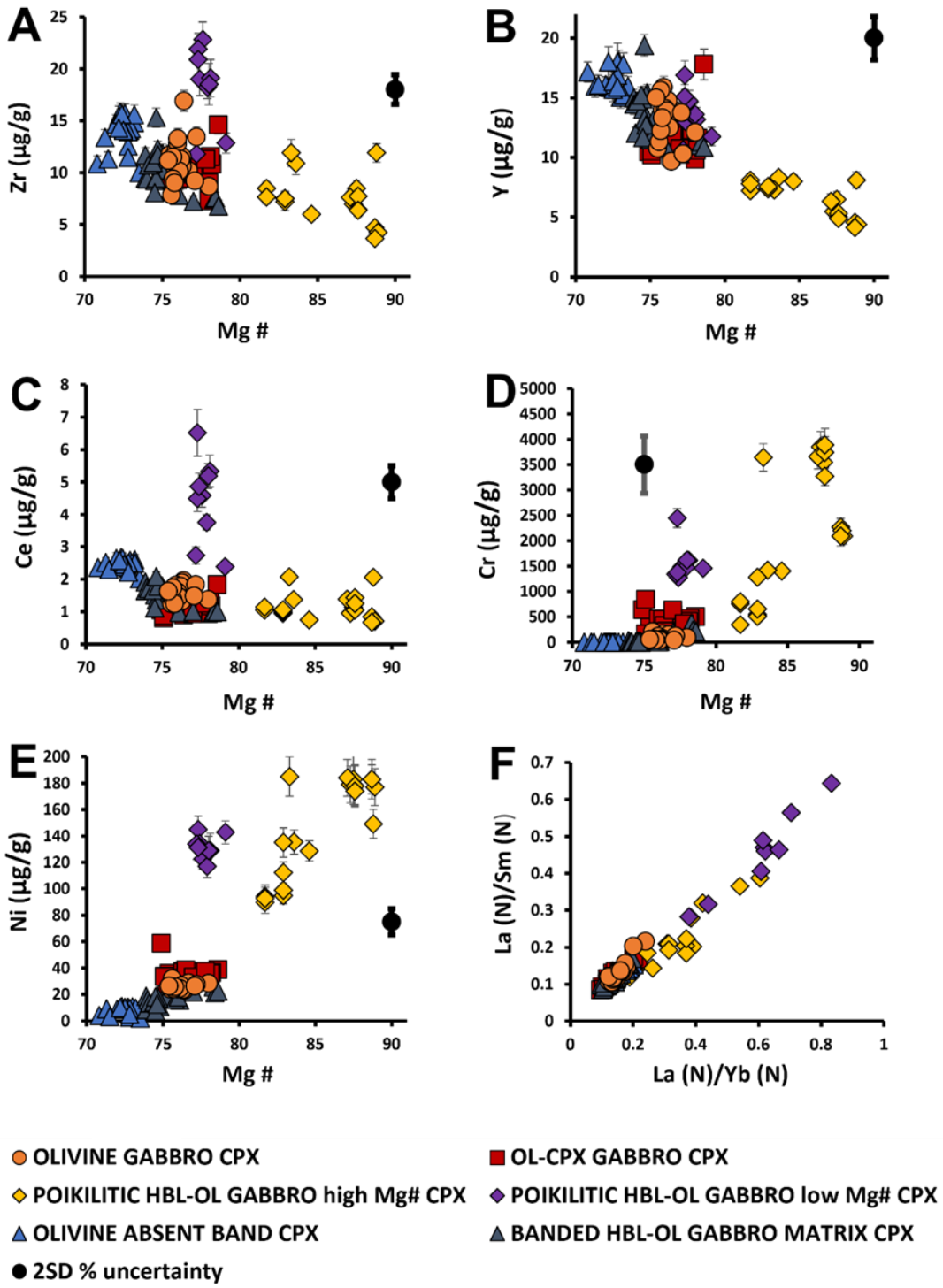

Figure 5.16: A) Zr **B)** Y **C)** Ce **D)** Cr **E)** Ni vs Mg# and **F)** La(N)/Sm(N) vs La(N)/Yb(N) for clinopyroxene from all four plutonic xenolith samples. Black bar with circle shows 2SD % uncertainty. Error bars on individual data points show internal 2SE uncertainty. Where error bars are not visible, uncertainty is smaller than symbol size.

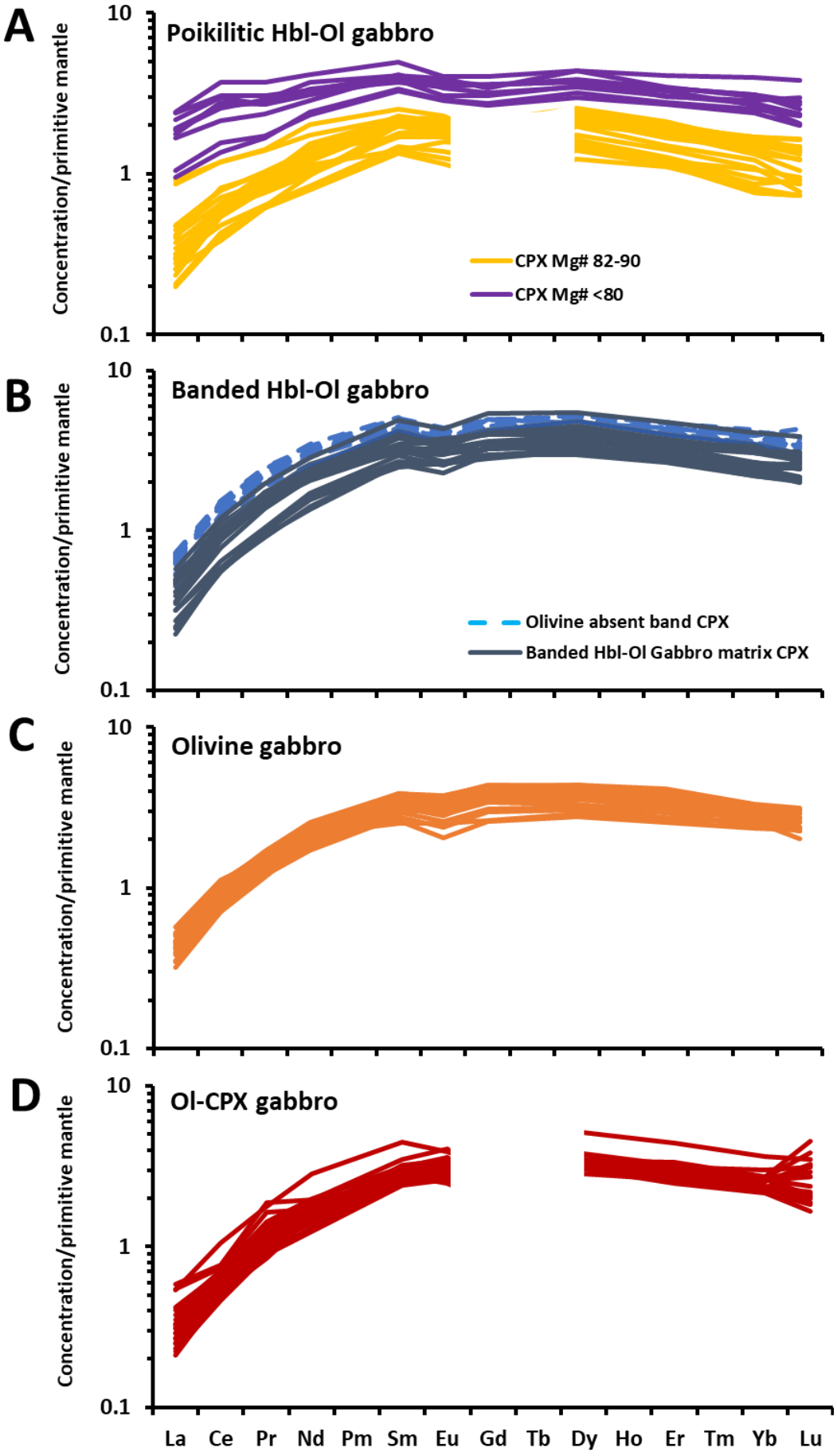
A
Poikilitic Hbl-Ol gabbro
Concentration/primitive mantle
10
1
0.1
CPX Mg# 82-90
CPX Mg# <80
B
Banded Hbl-Ol gabbro
Concentration/primitive mantle
10
1
0.1
Olivine absent band CPX
Banded Hbl-Ol Gabbro matrix CPX
C
Olivine gabbro
Concentration/primitive mantle
10
1
0.1
D
Ol-CPX gabbro
Concentration/primitive mantle
10
1
0.1
La Ce Pr Nd Pm Sm Eu Gd Tb Dy Ho Er Tm Yb Lu

Figure 5.17: Primitive mantle normalized REE patterns for clinopyroxene from **A)** poikilitic Hbl-Ol gabbro **B)** banded Hbl-Ol gabbro **C)** olivine gabbro **D)** Ol-CPX gabbro. Primitive mantle normalizing values taken from Palme and O'Neill, (2003). Data was not obtained for Gd in the poikilitic Hbl-Ol gabbro high-Mg# CPX (Mg# 82-89) and Ol-CPX gabbro.

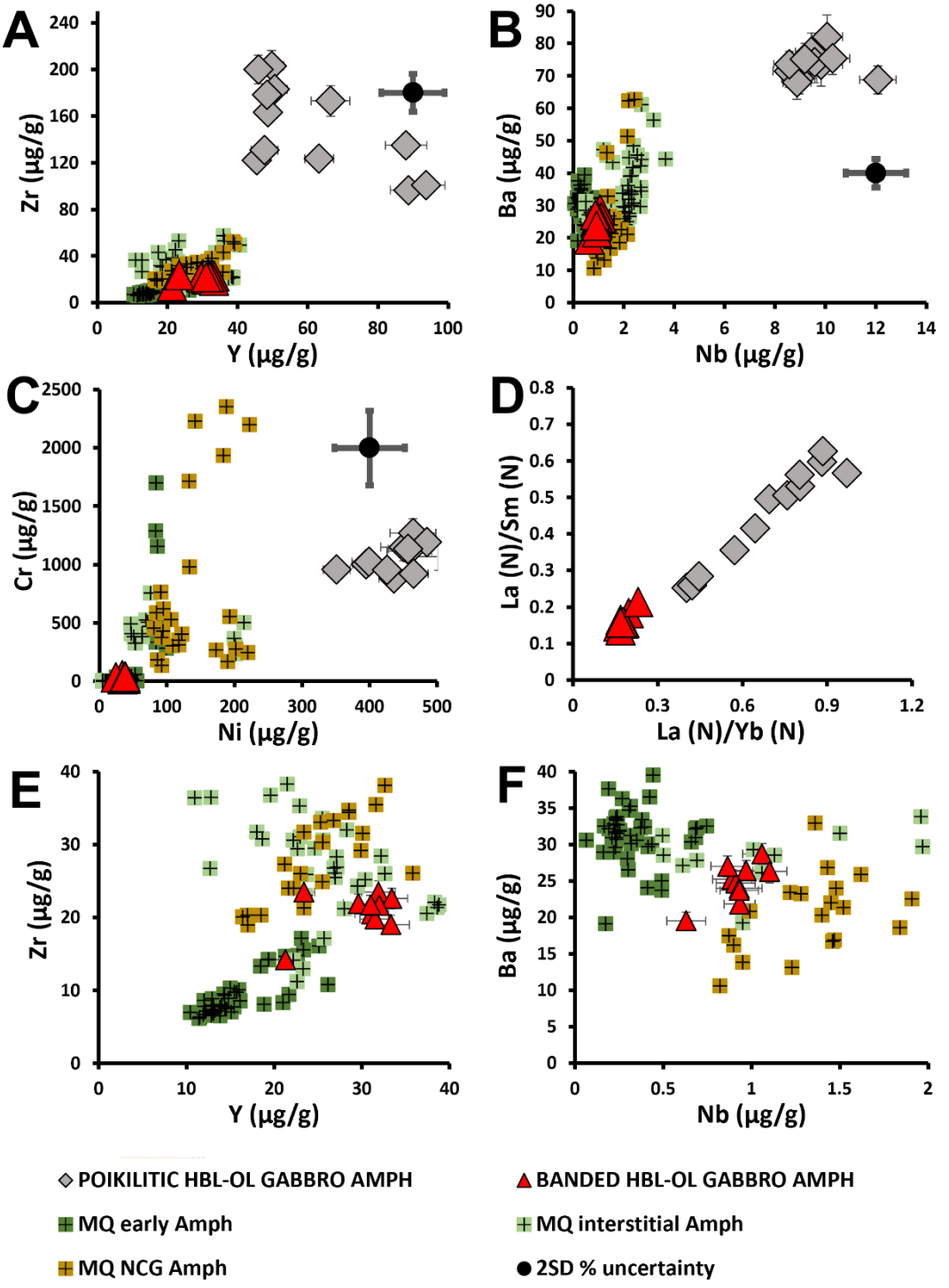

Figure 5.18: A) Zr vs Y **B)** Ba vs Nb **C)** Cr vs Ni **D)** La(N)/Sm(N) vs La(N)/Yb(N) for amphibole from the Hbl-Ol gabbros. Shown for comparison are compositions of amphibole from Martinique plutonic xenoliths with different textural characteristics (see legend). NCG = non-cumulate gabbro. **E)** and **F)**

Zoomed in versions of **A)** and **B)** respectively. Martinique (MQ) plutonic xenolith amphibole data from Cooper et al., (2016). Black bars with circle show 2SD % uncertainty. Error bars on individual data points show internal 2SE uncertainty. Where error bars are not visible, uncertainty is smaller than symbol size.

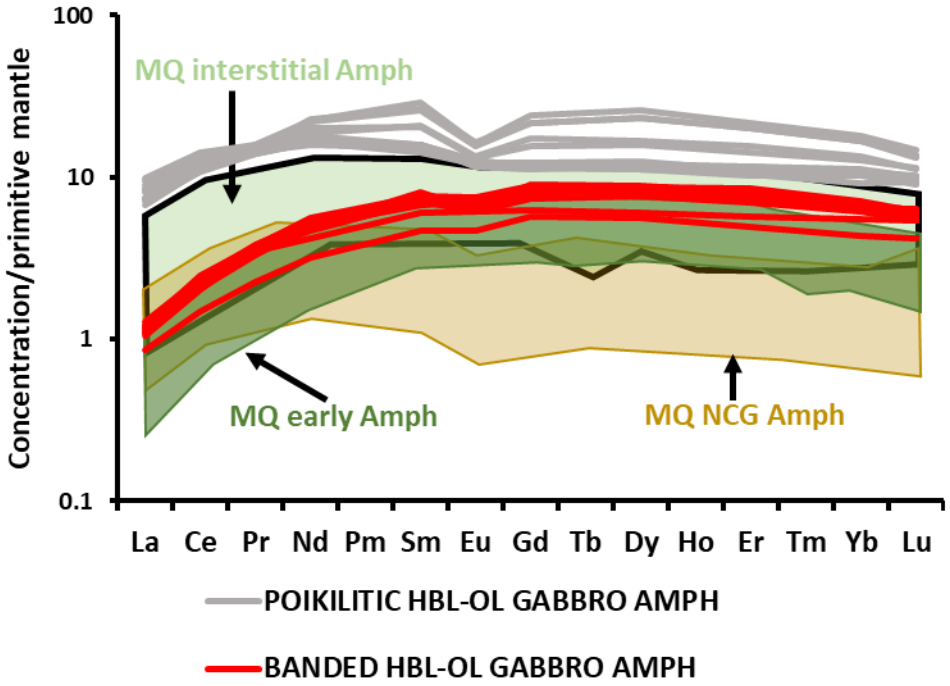

Figure 5.19: Primitive mantle normalized REE patterns for amphibole from Hbl-Ol gabbros. Shown for comparison are primitive mantle normalized REE patterns of amphibole from Martinique plutonic xenoliths with different textural characteristics (labelled shaded fields). Primitive mantle normalizing values taken from Palme and O'Neill, (2003). Martinique plutonic xenolith amphibole data from Cooper et al., (2016).

5.4.2.2 – Amphibole

Incompatible trace element contents (Zr, Y, Ba, Nb) are markedly higher and more variable in poikilitic Hbl-Ol gabbro amphibole (Y = 45-94 µg/g, Nb = 8.5-12 µg/g) relative to banded Hbl-Ol gabbro amphibole (Y = 21-33 µg/g, Nb = 0.6-1.1 µg/g) (**Figure 5.18**). Poikilitic Hbl-Ol gabbro amphibole are also enriched in the compatible elements Ni and Cr **(Figure 5.18, c)** relative to those from the banded Hbl-Ol gabbro.

The REE concentrations and patterns of the amphibole from the two samples show a similar contrast **(Figure 5.19).** Banded Hbl-Ol gabbro amphibole are depleted in LREE relative to MREE/HREE and most have a small negative Eu anomaly. In contrast, poikilitic Hbl-Ol gabbro amphibole are LREE enriched with almost flat REE patterns. Five of the analysed amphiboles from this sample are more enriched in Sm-Yb and display Eu anomalies. Compositions of amphibole with various textural characteristics

from Martinique plutonic xenoliths (Cooper et al., 2016) are shown for comparison and discussed in **section 5.5.3.3**.

5.5 – Discussion

Using textures and mineral chemistry of the plutonic xenoliths, we aim to determine to what extent magma chemical (specifically trace element) evolution in the St Vincent plumbing system is driven by fractional crystallization (FC) versus reactive melt flow. We start by interpreting the textural features of each plutonic xenolith sample (**section 5.5.1**). We then discuss our approach to modelling the effects of FC and reactive melt flow (**section 5.5.2**) on trace element compositions of melts and mineral phases, with the aim of reproducing the clinopyroxene and amphibole trace element data. In **section 5.5.3**, we discuss the results of our geochemical modelling on a sample-by-sample basis. Combining constraints from our modelling with textural observations, supported by previous thermobarometry and experimental petrology work from the literature, we interpret the processes recorded by each plutonic xenolith and propose petrogenetic models to explain the textural features and mineral phase associations. In **section 5.5.4**, we outline a model for the St Vincent magma plumbing system. We then discuss limitations of using plutonic xenoliths to determine the scales over which magma differentiation processes operate in mushy plumbing systems (**section 5.5.5**). We conclude by discussing the implications of our findings for interpreting trace element compositions of St Vincent lavas, in addition to arc lavas and melt inclusions generally (**section 5.5.6**).

5.5.1 – Interpretation of plutonic xenolith textures

To determine the processes recorded by our plutonic xenoliths, we first interpret the textural features of each sample. Evidence for reactive melt flow in plutonic rocks is often identified/interpreted via textural features, including irregular/ragged or embayed crystal boundaries/crystal cores indicative of dissolution, abrupt variations in mineral assemblage and/or textures at the hand specimen or thin section scale and reaction-relationships between mineral phases (e.g. Smith, 2014, Cooper et al., 2016, Lissenberg and MacLeod, 2016, SanFillipo et al., 2020, Boulanger et al., 2021).

5.5.1.1 – Olivine gabbro and Ol-CPX gabbro textures

Neither the olivine gabbro nor Ol-CPX gabbro contain textural features indicative of reactive melt flow as described above. The olivine, plagioclase and clinopyroxene in the Ol-CPX gabbro generally show well equilibrated, 120° crystal boundaries (**Figure 5.4**). In the olivine gabbro, thin films of interstitial melt are present between most crystal boundaries (**Figure 5.2, a**), which likely represent trapped melts residual from crystallization of the plutonic xenolith assemblage. The well equilibrated textures closely resemble St Vincent plutonic xenoliths (including other olivine gabbros) investigated by Tollan et al., (2012) which were interpreted as products of low-pressure fractional crystallization. These textural similarities and the lack of evidence for reactions or disequilibrium imply a similar origin for the Ol-CPX gabbro and olivine gabbro.

5.5.1.2 - Banded Hbl-Ol gabbro textures

In the banded Hbl-Ol gabbro, regions of the sample matrix that are free of amphibole display similar textural relationships between olivine, plagioclase and clinopyroxene to the Ol-CPX gabbro (**Figures 5.2, 5.3 and 5.5**). We suggest that the matrix of the banded Hbl-Ol gabbro was initially an olivine gabbro mush, which was subsequently modified (discussed below and in detail in **section 5.5.3.3**). Amphibole is distributed in patches throughout the sample matrix and notably is not present within the olivine absent band. Amphibole is almost always texturally associated with and overgrowing the rims of clinopyroxene (**Figure 5.6**) and occasionally olivine. This textural relationship implies that amphibole formed via a reaction between clinopyroxene and hydrous melt (e.g. Foden and Green, 1992, Smith, 2014). Near identical amphibole-clinopyroxene textural relationships have been observed in plutonic xenoliths from other LAA islands (e.g. Stamper et al., 2014, Cooper et al., 2016, Melekhova et al., 2017, Camejo-Harry et al., 2018,) and other arcs (Costa et al., 2002, Smith, 2014). In these studies, trace elements reveal that this textural relationship likely results from reactive flow of hydrous melts through clinopyroxene-bearing mushes. Alternatively, this textural relationship could be explained by an in situ peritectic reaction between clinopyroxene and evolving interstitial melt in a crystallizing mush, without input of externally derived reactive melts (e.g. Foden and Green, 1992, Laroque and Canil, 2010, Chang et al., 2021). From textural inspection alone, it is unclear whether amphibole is replacing partially dissolved clinopyroxene or simply overgrowing clinopyroxene rims and filling pore space within the mush (**Figure 5.6**), with the latter

supporting an in situ peritectic reaction origin. Therefore, the textural investigation needs to be coupled to *in-situ* geochemistry (**section 5.5.3.3)** in order to distinguish between these processes.

The olivine absent band forms an approximately one-centimetre wide, texturally (and chemically) distinct, continuous region within the banded Hbl-Ol gabbro (**Figures 5.3 and 5.13**, see also **Chapter 3**). The complete disappearance of olivine, more evolved chemistry of plagioclase and clinopyroxene, and distinctive appearance of plagioclase (with inclusion rich cores) within the band compared with the matrix (**Figure 5.5**) suggests that this feature has replaced the initial mush assemblage (the olivine gabbro matrix). Reactive melt flow provides a mechanism by which such replacement could occur. This process was invoked to explain similar centimetre wide bands, with distinct textures, mineral assemblages and mineral chemistry to the surrounding matrix, in MOR plutonic rocks (Lissenberg and MacLeod, 2016). Reactive flow of primitive melt into gabbroic crystal mush has also been proposed to explain abundant centimetre-decimetre thick bands, composed predominantly of fine grained mafic phases (olivine, clinopyroxene, oxides), within host gabbros of the Skaergaard intrusion (Namur et al., 2013).

The olivine absent band also strongly resembles a feature reported in a MOR olivine gabbro by SanFillipo et al., (2020). Their sample contained an approximately centimetre wide band with a lower modal abundance of olivine and more evolved olivine, plagioclase and clinopyroxene compositions than the surrounding olivine gabbro matrix. This feature was interpreted by SanFillipo et al., (2020) as a "reactive porous flow channel" produced by a melt percolating through and reacting with a pre-existing crystal mush. Their "reactive porous flow channel" mimics the disappearance of olivine and presence of more evolved plagioclase and clinopyroxene in the banded Hbl-Ol gabbro olivine absent band. In the banded Hbl-ol gabbro, the evidence for replacement of the initial mush with a new mineral assemblage and textural (and chemical) similarities to banded features from MOR plutonic rocks and layered intrusions implies a reactive melt flow origin for the olivine absent band.

5.5.1.3 - Poikilitic Hbl-Ol gabbro textures

The most distinctive textural feature of this sample is poikilitic amphibole, texturally associated with and replacing clinopyroxene and enclosing embayed olivine (**Figure**

5.7, a,b,d, Chapter 3, Figure 3.39). As for the banded Hbl-Ol gabbro, this textural relationship suggests that amphibole may be formed via a reaction between clinopyroxene/olivine and hydrous melt.

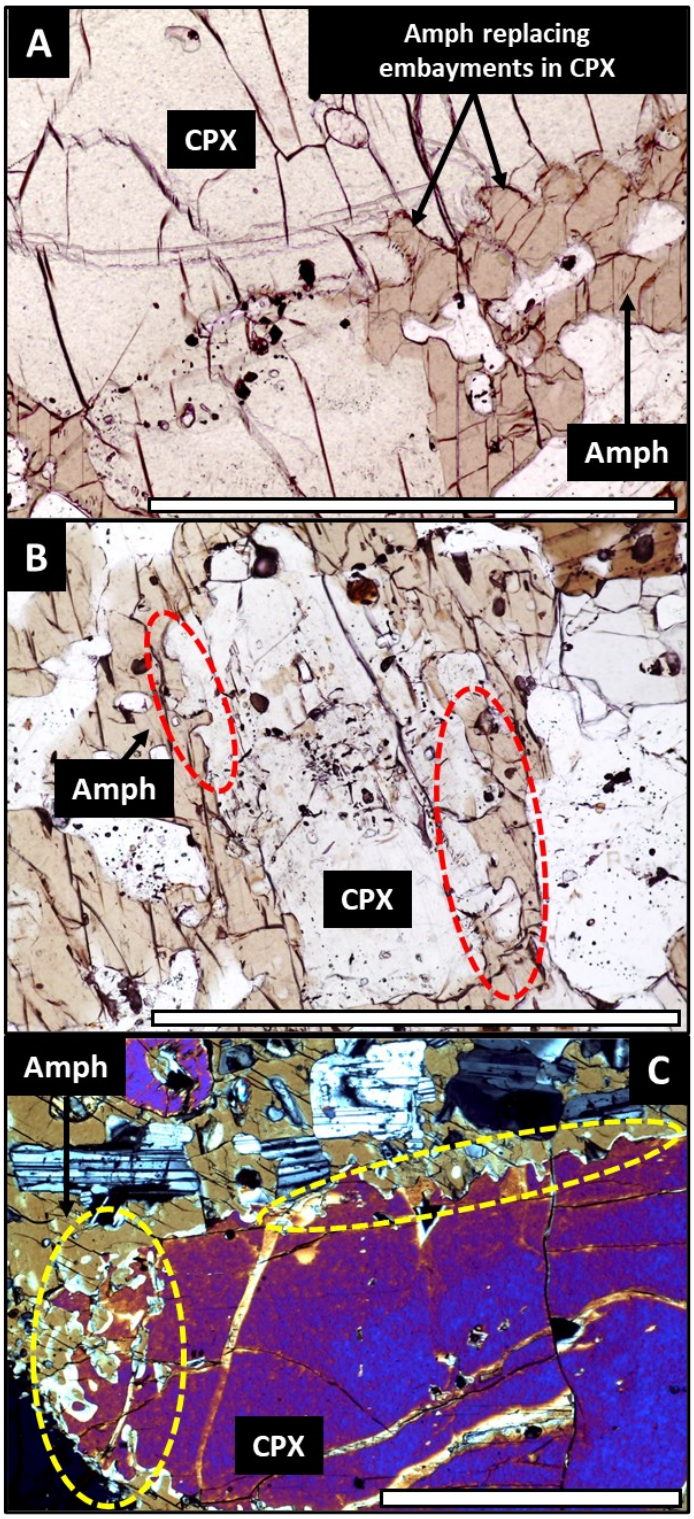

Figure 5.20: Examples of ragged, irregular clinopyroxene-amphibole contacts from the poikilitic Hbl-Ol gabbro. **A)** PPL image of poikilitic amphibole replacing rounded embayments in clinopyroxene**. B)**

PPL and **C)** XPL images of ragged, irregular clinopyroxene-amphibole contacts, highlighted by the dashed ellipses. White scale bar = 1 mm.

Similar poikilitic amphibole and amphibole-clinopyroxene/olivine textural relationships attributed to reactive melt flow are found in plutonic xenoliths from Martinique and St Kitts in the LAA (Cooper et al., 2016, Melekhova et al., 2017) and the Solomon Island arc (Smith, 2014). The ragged and irregular nature of some amphibole-clinopyroxene grain contacts is suggestive of dissolution of clinopyroxene (**Figure 5.20**). Reactive melt flow is proposed to operate via dissolution-reprecipitation reactions (e.g. Lissenberg and MacLeod, 2016, SanFillipo et al., 2020, Hu et al., 2022). Therefore, evidence for clinopyroxene dissolution implies that the poikilitic amphibole were more likely formed via reactive melt flow than an in situ peritectic reaction during closed system crystallization.

Where olivine in the poikilitic Hbl-Ol gabbro is not enclosed by amphibole, it is typically rounded/embayed and enclosed by poikilitic orthopyroxene (**Figure 5.7, c, Chapter 3, Figure 3.38**), indicative of a peritectic reaction between olivine and a more evolved (higher SiO_2) melt (e.g. Barnes et al., 2016, Kaufmann et al., 2018, Antonicelli et al., 2020). The poikilitic Hbl-Ol gabbro olivine resemble rounded and/or embayed olivine created by dissolution in experiments simulating melt-mush and melt-rock reaction (Yang et al., 2019, Wang et al., 2021). Poikilitic orthopyroxene enclosing rounded and/or embayed olivine have also been observed in plutonic rocks from layered intrusions and the lower continental crust (e.g. Barnes et al., 2016, Kaufmann et al., 2018, Antonicelli et al., 2020). In these examples, this textural relationship was attributed to reactive melt flow, supported by additional constraints such as chemical zoning patterns in poikilitic orthopyroxene and reaction zones between different mush lithologies observed in the field. Based on comparisons to experimental products and natural examples, we propose that orthopyroxene-olivine and amphibole-olivine textural relationships in the poikilitic Hbl-Ol gabbro are likely to have been produced by reactive melt flow.

The high An (85-90) plagioclase population from the poikilitic Hbl-Ol gabbro is mostly present as relict or patchy cores (**Figure 5.7, e, Figure 5.15**) with lower An plagioclase mantles or rims. Relict plagioclase cores are also preserved within texturally and chemically distinct bands interpreted to have formed via reactive melt flow in mid-ocean ridge plutonic rocks (Lissenberg and MacLeod, 2016, SanFillipo et al., 2020).

In these studies, the relict plagioclase cores are interpreted to represent remnants of the initial mush that was partially dissolved during reactive melt flow. In the melt-mush reaction experiments of Yang et al., (2019), relict high An plagioclase cores from the initial mush were preserved in newly crystallized phases (clinopyroxene) produced during the reaction. Lower An rims were also produced on some initial high An plagioclase in these experiments, resembling the poikilitic Hbl-Ol gabbro. The patchy/relict nature of high An plagioclase cores in the poikilitic Hbl-Ol gabbro and textural and chemical similarities with melt-mush reaction experimental products suggests that this crystal population may represent remnants of a precursor crystal mush, subsequently modified by reactive melt flow.

5.5.2 – Approach to modelling fractional crystallization and reactive melt flow

In this section, we outline the approach used to geochemically model FC and reactive melt flow, with the aim of reproducing the plutonic xenolith clinopyroxene and amphibole trace element data. The models focus on reproducing the REE compositions of clinopyroxene and amphibole. The REE patterns are expected to strongly discriminate between the processes modelled. Examples from mid-ocean ridge settings have shown that reactive melt flow typically leads to over-enrichment in LREE relative to HREE compared with FC (e.g. Lissenberg and MacLeod, 2016, SanFillipo et al., 2020, Boulanger et al., 2021, Ferrando et al., 2021). In magmatic systems, LREE are generally more incompatible than HREE and therefore become more concentrated in reactive melts, resulting in LREE/HREE enrichment in phases crystallizing from these melts as reaction products (Lissenberg and MacLeod, 2016). Reactive melt flow in an arc system may be more complex than at mid-ocean ridges, for example involving additional mineral phases such as amphibole, therefore our models provide a test of whether the same trend is expected in an arc system.

Fractional crystallization was modelled using the Raleigh fractionation equation, given below:

$$C_L = F^{(D-1)} * C_0 \qquad \textbf{[Eqn 5.1]}$$

where C_L = concentration of trace element in melt, C_0 = concentration of trace element in initial melt, F = fraction of melt remaining, D = bulk partition coefficient.

The geochemical consequences of reactive melt flow are commonly modelled using two different methods/equations, which describe the processes of zone refining (used by Lissenberg and MacLeod, 2016, Gleeson et al., 2020) and Assimilation-Fractional Crystallization (AFC) (DePaolo, 1981, used by SanFillipo et al., 2020, Boulanger et al., 2020, 2021, Ferrando et al., 2021). Lissenberg and MacLeod (2016) used zone refining to model the trace element enrichment from core to rim in a zoned clinopyroxene crystal (see schematic in **Figure 5.21**), which they attributed to reactive melt flow (based on over enrichment of rim incompatible trace element compositions compared with FC models). The zone refining equation from Harris (1957) was used in their study:

$$\mathbf{C_L/C_0 = (1/D - ((1/D - 1) * exp^{-DI}))} \qquad \textbf{[Eqn 5.2]}$$

where C_L = concentration of element in melt after zone refining, C_0 = concentration of element in initial melt, D = bulk partition coefficient of crystallizing assemblage and I = number of equivalent lengths of solid processed by the melt.

For example, if the value of I is assigned as 2, this means that a batch of melt of a given length (e.g. 5 cm) has reacted with double the length of solid/crystals (e.g. 10 cm). In their models, Lissenberg & MacLeod (2016) compared the enrichment factor (trace element concentration in rim/trace element concentration in core) of trace elements in a clinopyroxene crystal with the enrichments (C_L/C_0) produced by zone refining for different values of D and I. In contrast, our data consists of single points from multiple, mostly unzoned crystals distributed across the area of a thin section, so we cannot apply this method in the same way. Recent numerical modelling studies of reactive melt flow have described reactive flow as a form of "chemical" melting, acting via dissolution and precipitation of new mineral phases (Hu et al., 2022). In addition, textural evidence for mineral dissolution/replacement has been used as a key indicator of reactive melt flow in previous studies (e.g. Smith, 2014, Cooper et al., 2016, SanFillipo et al., 2020, Boulanger et al., 2021). In this scenario, it is reasonable to assume that the initial reactive melt would itself contribute some trace elements and that trace elements would be added to the reactive melt from the crystals being dissolved and replaced. However, the zone refining equation [Eqn 5.2] does not contain a term that accounts for trace element contributions from the initial mush crystals that a reactive melt interacts with.

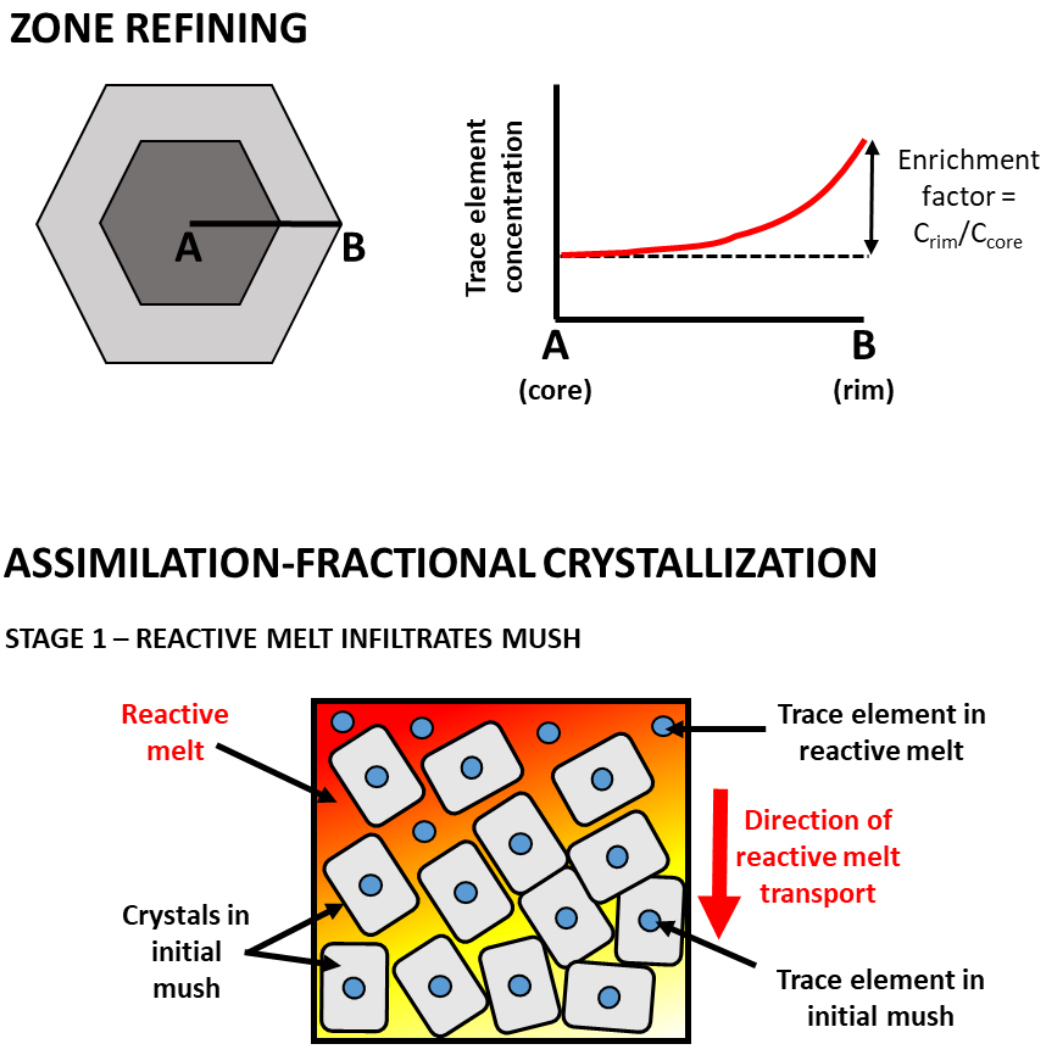

Figure 5.21: ZONE REFINING - Schematic illustrating the concept of the "enrichment factor" (trace element concentration at rim/trace element concentration at core) for a trace element in a zoned crystal, which was modelled using zone refining by Lissenberg and MacLeod, (2016). The authors considered zone refining a proxy for reactive melt flow, whereby the enrichment factor (C_L/C_0) for a given trace

element modelled by zone refining is equivalent to the core to rim enrichment in the trace element that would be produced in a zoned crystal by reactive melt flow.

ASSIMILATION-FRACTIONAL CRYSTALLIZATION - Schematic illustrating how the concept of AFC operates in a mushy magmatic system. In Stage 1, a reactive melt with an initial trace element content interacts with a crystal mush, which also contains the trace element within the crystals. In Stage 2, the crystals in the mush are partially dissolved, releasing the trace element and increasing its concentration in the melt. New crystals, enriched in trace elements, form from the modified melt.

For these reasons, we prefer AFC as a means of modelling reactive melt flow. Typically, AFC is used to model the assimilation of (usually chemically distinct) solid country rock by a magma (e.g. DePaolo, 1981, Hildreth and Moorbath, 1988, Bezard et al., 2015b). However, in the context of reactive flow in a mushy magmatic system, AFC approximates the dissolution of pre-existing crystals in the mush by an invading melt and subsequent crystallization from the modified melt, shown in the schematic in **Figure 5.21**.

The equation for AFC (6a from DePaolo (1981)) is shown below:

$$C_L = \left(F^{-Z} + \left(\frac{r}{r-1} \times \frac{C_a}{(Z \times C_0)} \times 1 - F^{-Z} \right) \right) \times C_0 \qquad \textbf{[Eqn 5.3]}$$

where C_L = concentration of trace element in melt, C_0 = concentration of trace element in initial melt, C_a = concentration of trace element in assimilant, F = fraction of melt remaining, Z = (r+D-1)/(r-1), D = bulk partition coefficient, r = rate of assimilation/rate of crystal fractionation.

Unlike zone refining, AFC explicitly takes into account trace element contributions from both the initial reactive melt and crystals in the pre-existing mush (the assimilant), as illustrated in **Figure 5.21.** Hence, we consider AFC as the most appropriate method to model reactive melt flow for our plutonic xenolith trace element data.

The magma differentiation processes (FC and reactive melt flow/AFC) modelled for each plutonic xenolith sample are listed in **Table 5.1.** Specific models were applied to each sample, based on the different mineral assemblages and textural features discussed in **section 5.5.1**. Regardless of textural evidence for reactive processes, we modelled FC for all samples, to test whether the trace element compositions of clinopyroxene and amphibole alone can be used to distinguish between a FC and

reactive melt flow origin for these phases. Where textures are indicative of reactive processes (banded Hbl-Ol gabbro and poikilitic Hbl-Ol gabbro, **section 5.5.1**) we also modelled reactive melt flow (via AFC) to test whether this process could reproduce the clinopyroxene and amphibole REE compositions.

Increasing textural complexity of samples

Sample	Crystal populations	Models applied	Model names
Ol-CPX gabbro	Cpx	FC	OL GABBRO POLYBARIC FC
Olivine gabbro	Cpx	FC	OL GABBRO POLYBARIC FC
Banded Hbl-Ol gabbro	Matrix Cpx	FC	OL GABBRO POLYBARIC FC
	Ol-absent band Cpx	FC, AFC	BANDED GABBRO
	Amphibole	FC, AFC	BANDED GABBRO
Poikilitic Hbl-Ol gabbro	High Mg# Cpx	FC	OL GABBRO POLYBARIC FC (Step 1 only)
	Low Mg# Cpx and poikilitic amphibole	FC (primitive basalt initial melt)	POIKILITIC GABBRO POLYBARIC FC
	Low Mg# Cpx and poikilitic amphibole	AFC (basaltic andesite/ andesite initial melts)	BASALTIC ANDESITE AFC, ANDESITE AFC, ANDESITE 2 AFC

Table 5.1: Table showing the geochemical models (FC and AFC) applied to each crystal population in the plutonic xenolith samples, along with the model names as referred to in the text and figures.

To provide constraints on the depths at which our plutonic xenoliths crystallized and hence where in the crust the modelled processes occur, we compared the plutonic xenolith mineral assemblages and compositions of this study with published experimental petrology results that have studied LAA and arc basalt starting materials.

Sample	Mineral assemblage and compositions	Experiment name and reference	Run conditions	Starting material and melt H_2O content	Mineral phase compositions produced in experiment	Estimated crystallization depth (km)
Olivine gabbro	Plag An 90-98 , Ol Fo 76-79, CPX Mg# 73-80 , minor Mt	L2, L4 – Pichavant et al., (2018)	975-1000 °C, 0.2 GPa	HAB, 5.9-6.3 wt % H_2O	Plag An 85-88 , Ol Fo 72.4-74 , CPX Mg# 75	6-18
		FM93, FM134 – Marxer et al., (2021)	1050 °C, 0.6 GPa	HAB, 3.73 wt % H_2O	Plag An 90, Ol Fo 76-78 , CPX Mg# 75-79	
Ol-CPX gabbro	Plag An 90-99 , Ol Fo 77-80, CPX Mg# 73-80	L2, L4 – Pichavant et al., (2018)	975-1000 °C, 0.2 GPa	HAB, 5.9-6.3 wt % H_2O	Plag An 85-88 , Ol Fo 72.4-74 , CPX Mg# 75	6-18
		FM93, FM134 – Marxer et al., (2021)	1050 °C, 0.6 GPa	HAB, 3.73 wt % H_2O	Plag An 90, Ol Fo 76-78 , CPX Mg# 75-79	
Banded Hbl-Ol gabbro	Plag An 86-97 , Ol Fo 72-76, CPX Mg# 70-80, Amph Mg# 63-72, minor Mt	HAB 7 – Pichavant et al., (2002)	1000 °C, 0.4 GPa	Basaltic andesite, 6.8 wt % H_2O	Plag An 84 , Ol Fo 69 , CPX Mg# 72, Amph Mg# 68	~12
		FM129 – Marxer et al., (2021)	990 °C, 0.4 GPa	HAB, 4.6 wt % H_2O	Plag An 87, Ol Fo 66, CPX Mg# 72, Amph Mg# 68	
Poikilitic Hbl-Ol gabbro	Plag An 60-90 , Ol Fo 72-76 , CPX Mg# 72-89, OPX Mg# 71-76, Amph Mg# 63-72, minor apatite, oxides and very rare sulfides.	BM3, BM6, BM9 – Melekhova et al., (2015)	1100-1200°C, 1 GPa	HMB, 2.3-4.5 wt % H_2O	CPX Mg# 85-87	High Mg# CPX – 21-30, other mineral phases ~6
		FM81, FM152 – Marxer et al., (2021)	1080-1110°C, 0.8 GPa	LMB, 3.0-3.5 wt % H_2O	CPX Mg# 83-85	
		L1 – Pichavant et al., (2018)	950 °C, 0.2 GPa	HAB, 5.8 wt % H_2O	OPX Mg# 73, Amph Mg# 69, Plag An 78	
		S5 – Pichavant et al., (2018)	875 °C, 0.15 GPa	Andesite, 5.1 wt % H_2O	OPX Mg# 74. CPX Mg# 76, Plag An 64	

Table 5.2: Summary of experiments that provide the best match to each plutonic xenolith sample

mineral assemblage and compositions. The conditions under which the samples formed are inferred from the experimental run conditions. See **Appendix 5.1** for detailed comparisons of samples and experimental run products and definitions of starting material compositions. Estimated crystallization depths assume 0.1 GPa = 3 km.

The run conditions of experiments that produced close matches to the plutonic xenolith assemblages and mineral chemistry are detailed in **Table 5.2** and discussed in **Appendix 5.1**. Estimated plutonic xenolith crystallization depths (based on comparison of mineral assemblages and compositions to experiments, **Table 5.2**) are shown on **Figure 5.22**, which illustrates the models applied to each plutonic xenolith sample and the approximate location in the crust at which each step of the models occurs.

The equations used to model FC and AFC have three common variables/parameters – the initial melt composition, the fractionating mineral assemblage and the partition coefficients used to calculate a bulk D value for the fractionating mineral assemblage. For the majority of the models, the modal proportions of mineral phases in the fractionating assemblage were estimated from their relative abundances in the relevant sample. For AFC/reactive melt flow models, textural observations were used to identify which mineral phases/populations from the relevant sample crystallized during the reaction. Alternatively, some models were based on experiments which reproduced the mineral phases and compositions of the plutonic xenoliths – in these models the proportions of mineral phases crystallized in the reference experiments were used as the fractionating assemblage.

An important aspect of REE partitioning is the increase of mineral-melt partition coefficients (D) with increasing melt SiO_2 (e.g. Brophy, 2008), which can be particularly significant for clinopyroxene and amphibole (e.g. Bedard, 2014, Nandedkar et al., 2016). Brophy (2008) provided equations for the prediction of a suite of REE (La, Ce, Nd, Sm, Dy, Er, Yb) partition coefficients for the mineral phases present in the St Vincent plutonic xenoliths as a function of melt SiO_2. The melt SiO_2 used for each specific model and/or step in the models is discussed in detail in the following subsections. To ensure consistency between all the models, we used the equations from Brophy (2008) to calculate REE partition coefficients for each mineral phase.

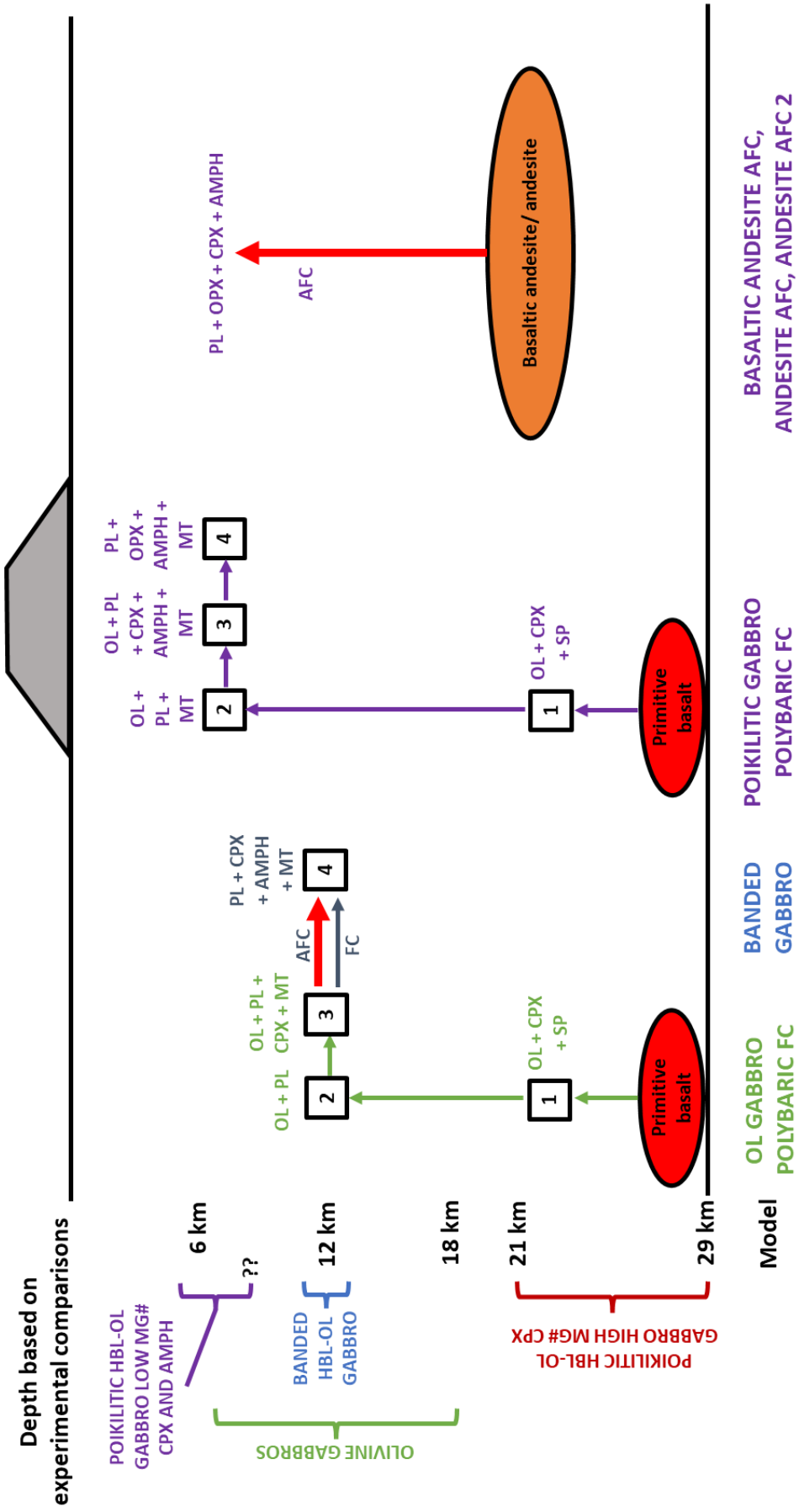

Figure 5.22: Schematic illustrating the FC and AFC models applied to the crystal populations in each

plutonic xenolith sample (**Table 5.1**). The mineral phases crystallizing at each step (e.g 1 to 3) of the models are shown. The left hand side shows estimated crystallization depths of plutonic xenoliths (or particular crystal populations) based on comparisons to experimental products at different pressures (**Appendix 5.1, Table 5.2**). The schematic shows the approximate depth within the crust at which each model step is assumed to occur.

To explore the extent to which modelled scenarios were dependent on the choice of partition coefficients, we used alternative clinopyroxene and amphibole REE partition coefficients for some additional models. Alternative partition coefficients for clinopyroxene were taken from the regressions of Bedard (2014), for "mafic terrestrial silicates", with melt SiO_2 as the input parameter. Alternative partition coefficients for amphibole were experimentally determined values from Nandedkar et al., (2016) at different melt SiO_2 values. Some of the FC models based on experiments include spinel as a fractionating phase. Brophy (2008) did not provide equations for calculation of spinel partition coefficients, therefore in all models involving spinel, D for all REE in spinel was set at 0.01 as per Mckenzie and O'Nions (1991) and used by Fedele et al., (2021) in modelling chemical evolution of St Vincent lavas. Similarly low D values for spinel were reported by Nagasawa et al., (1980) and are consistent with the typically extremely low abundances of REE in spinel (e.g. Bedini and Bodinier, 1999, Witt-Eickschen and O'Neill, 2005). The D values chosen for each mineral phase across the range of melt SiO_2 contents used in the models are listed in **Appendix 5.2**.

Several initial melt compositions were explored (**Table 5.3)**. The initial melt compositions were calculated from the mineral trace element data ("inverted") using partition coefficients (see **Table 5.3** caption).

Initial melt composition/method of calculation	Abbreviation used in other Tables	La	Ce	Nd	Sm	Dy	Er	Yb
Inverted highest Mg# Cpx (Brophy 47 % SiO_2)	Inv Cpx Bas (Br)	1.34	4.36	3.66	1.04	1.26	0.80	0.84
Inverted least enriched low Mg# Cpx (Brophy 53 % SiO_2)	Inv Cpx Bas And (Br)	5.83	14.89	8.21	2.36	2.19	1.31	1.42
Inverted least enriched low Mg# Cpx (Brophy 59 % SiO_2)	Inv Cpx And (Br)	5.33	13.47	7.27	2.05	1.82	1.07	1.13

Assimilant	La	Ce	Nd	Sm	Dy	Er	Yb
Average Martinique plutonic xenolith	2.00	4.92	4.15	1.32	1.88	1.09	1.03
Adjusted assimilant	2.00	4.92	3.50	0.65	1.60	1.09	1.30

Table 5.3: Initial melt compositions (in µg/g) used in the geochemical modelling. The "Inv CPX Bas (Br)" initial melt composition was calculated by inverting the composition of the highest Mg# clinopyroxene measured in this study (from the poikilitic Hbl-Ol gabbro) using clinopyroxene-melt partition coefficients from Brophy (2008). These partition coefficients were calculated from a melt SiO_2 input value of 47 wt %. The "Inv CPX Bas And (Br)" and "Inv CPX And (Br)" initial melt compositions

were calculated by inverting the composition of the least REE enriched measured clinopyroxene crystal from the low Mg# CPX population in the poikilitic Hbl-Ol gabbro, using clinopyroxene-melt partition coefficients from Brophy (2008), calculated using melt SiO_2 input values of 53 wt % and 59 wt %. These partition coefficients are listed in **Appendix 5.2**. The "average Martinique plutonic xenolith" assimilant composition is based on whole-rock data for Martinique plutonic xenoliths from Cooper et al., (2016). The "adjusted assimilant" was used to illustrate the effect of changing the assimilant composition for some REE within reasonable limits (within the range of compositions in Martinique plutonic xenolith WR data).

5.5.2.1 – Fractional Crystallization (FC) models

The parameters used for each of the FC models are justified in the following subsections.

Clinopyroxene in Olivine Gabbros

The textures and mineral compositions of the Ol-CPX gabbro, olivine gabbro and in the matrix of the banded Hbl-Ol Gabbro (excluding amphibole) are similar to each other and closely resemble those of previously investigated plutonic xenoliths from St Vincent (Tollan et al., 2012). Tollan et al (2012) proposed that these plutonic xenoliths were products of fractional crystallization from a high-Al basalt magma at low pressure, which was itself produced by an initial phase of high-pressure fractionation of Ol + Cpx + Sp from a primitive basaltic magma. The high-pressure (mostly > 0.7 GPa) experiments of Melekhova et al., (2015), using a primitive St Vincent basalt starting composition, failed to reproduce the mineral phase assemblages and compositions of plutonic xenoliths studied by Tollan et al., (2012), leading them to agree that these samples represent products of low-pressure stages of polybaric FC. This proposed petrogenetic scenario has yet to be investigated using trace element concentrations of mineral phases in plutonic xenoliths from St Vincent, which have not previously been reported (by Tollan et al., 2012 or others). Therefore, we modelled a polybaric FC scenario to test whether it can reproduce clinopyroxene REE compositions in the Ol-CPX gabbro, olivine gabbro and matrix of the banded Hbl-Ol gabbro.

The "OL GABBRO POLYBARIC FC" model has three fractionation steps (**Table 5.4; Figure 5.23**). Step 1 simulates fractionation in the lower crust (high pressure stage)

Fractionation Step	Melt SiO_2 at end of step	Fractionating assemblage	D values source	Initial melt composition	% crystallization at each step	Assimilant composition (AFC models only)	R (AFC models only)
1	49	Ol (55 %) Cpx (35 %) Sp (10 %)	Brophy (2008) at 49 % SiO_2	Inv CPX Bas (Br) from Table 5.3	10		
2	51	Ol (15 %) Pl (85 %)	Brophy (2008) at 51 % SiO_2	Previous step at F = 0.9 (after 10 % crystallization)	20		
3	53	Ol (17 %) Cpx (18 %) Pl (62 %) Mt (3 %)	Brophy (2008) at 53 % SiO_2	Previous step at F = 0.8 (after 20 % crystallization).	Up to 60.		
BANDED GABBRO	53	Pl (55 %) Cpx (27 %) Amph (15 %) Mt (3 %).	Brophy (2008) at 53 % SiO_2	Step 3 of OL GABBRO POLYBARIC FC model after 30 % crystallization	Up to 60.	Average Martinique plutonic xenolith (from Table 5.3)	0.4

Table 5.4: Parameters used at each fractional crystallization step of the "OL GABBRO POLYBARIC

FC" model. The parameters used in the additional "BANDED GABBRO" step, to model both FC and AFC, are also shown.

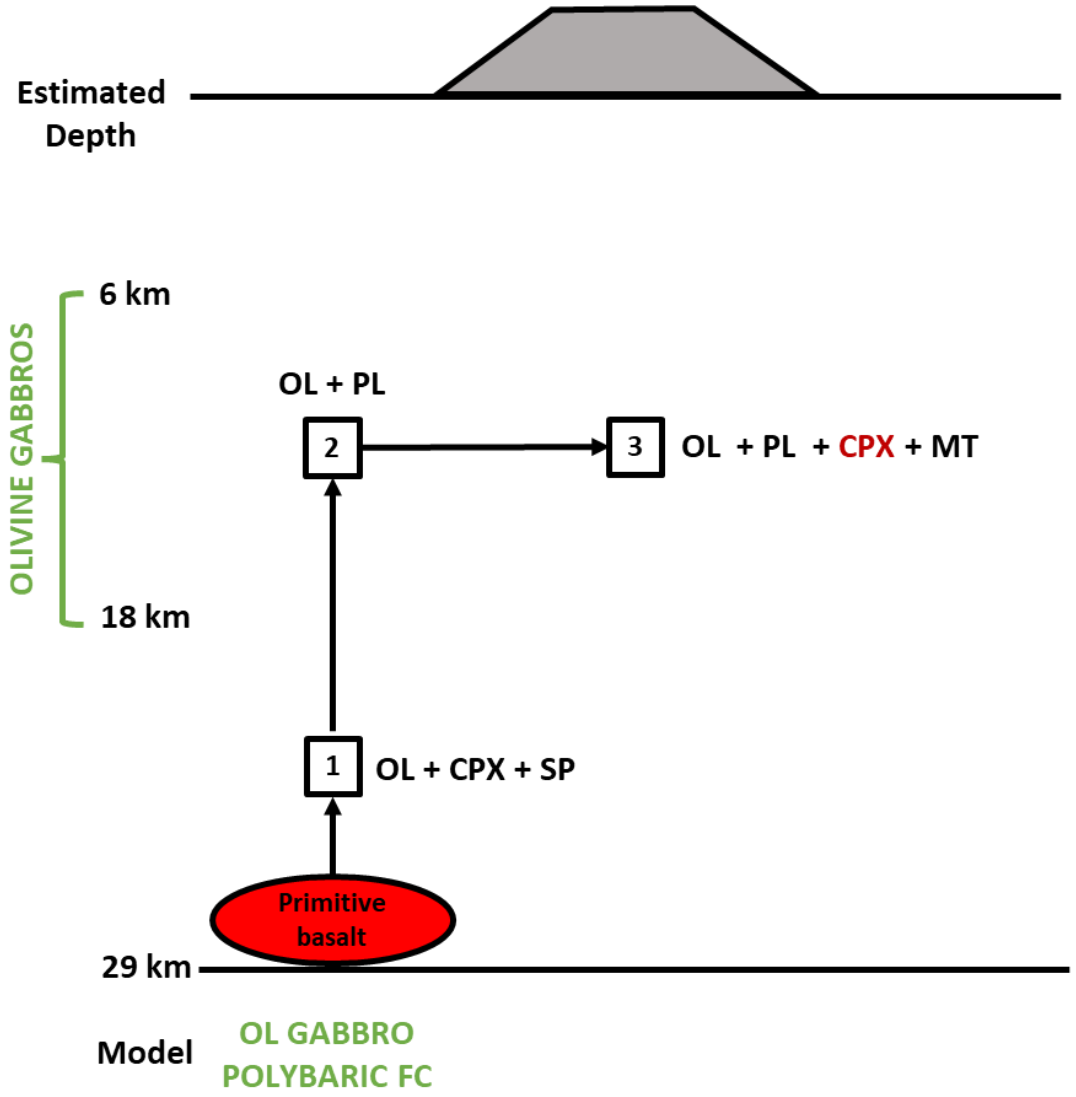

Figure 5.23: Schematic illustrating the "OL GABBRO POLYBARIC FC" model. The model was applied to the clinopyroxene in the olivine gabbro, Ol-CPX gabbro and matrix of the banded Hbl-Ol gabbro. The model assumes that these clinopyroxene formed during the third fractionation step.

from a primitive basaltic magma, while Steps 2 and 3 simulate fractionation of a troctolitic assemblage, followed by an olivine gabbro assemblage, in the mid-upper crust (low pressure stage) (**Figure 5.23**). Troctolites are common on St Vincent (Tollan et al., 2012, **Chapter 3, Appendix 1**) and this sequence is consistent with the crystallization sequence observed in the samples (Ol -> Ol + Pl -> Ol + Pl + Cpx). Modal proportions (**Table 5.4**) of fractionating phases at each step are similar to those in experiments that formed equivalent assemblages (Nandedkar et al., 2014,

Melekhova et al., 2015, Marxer et al., 2021) and natural troctolite and olivine gabbro plutonic xenolith samples from St Vincent (Tollan et al., 2012, this study).

The partition coefficients and initial melt composition used at each step of the model are listed in **Table 5.4**. The initial melt composition for the first step was calculated from the most Mg-rich clinopyroxene measured in this study using clinopyroxene-melt partition coefficients at 47 wt % SiO_2 (see **Table 5.3**), to represent a primitive basaltic magma**.** Assuming a $K_D(Fe\text{-}Mg)^{cpx/melt}$ of 0.27 ± 0.03 (Putirka, 2008), melts in equilibrium with the most Mg-rich measured clinopyroxene have Mg# 66-71, matching the most primitive St Vincent lavas with Mg# 69-71 and 47 wt % SiO_2 (Heath et al., 1998, Plank, 2005). Hence, 47 wt % SiO_2 is justifiable for the primitive basaltic magma composition.

The melt SiO_2 contents (and hence partition coefficients) used for Steps 1 and 2 reflect progressive evolution of the melt and are consistent with melt SiO_2 contents in experimental charges which crystallized the fractionating assemblages (e.g. Marxer et al., 2021). Assuming a $K_D(Fe\text{-}Mg)^{cpx/melt}$ of 0.27 ± 0.03 (Putirka, 2008), melts in equilibrium with clinopyroxene (Mg# 70-80) in these plutonic xenoliths have Mg# 36-55, in line with basaltic andesite lavas (Mg# 43-54) and glasses (Mg# 31-45) from St Vincent (Fedele et al., 2021). Hence 53 wt % SiO_2, corresponding to a basaltic andesite, was chosen as the melt SiO_2 for the final step (at which clinopyroxene corresponding to those in the sample crystallize, **Figure 5.23**).

High Mg# CPX in the Poikilitic Hbl-Ol Gabbro

Comparison to experiments and other plutonic xenoliths/lower crustal plutonic rocks (Yogodzinski and Kelemen, 2007, Bouilhol et al., 2015, Otamendi et al., 2016) suggests that the high Mg# CPX population in the poikilitic Hbl-Ol gabbro have compositions consistent with an origin via high pressure fractionation (co-crystallizing with olivine and spinel) in the lower crust (**Table 5.2, Appendix 5.1**). This scenario is covered by Step 1 of the "OL GABBRO POLYBARIC FC" model (**Figure 5.24**). To model the high Mg# CPX REE compositions, we used identical parameters to Step 1 in **Table 5.4**, with the exception that melt (and equilibrium clinopyroxene) compositions were modelled for up to 60 % fractionation of Ol + Cpx + Sp (as opposed

to only 10 % crystallization at this step in the "OL GABBRO POLYBARIC FC" model).

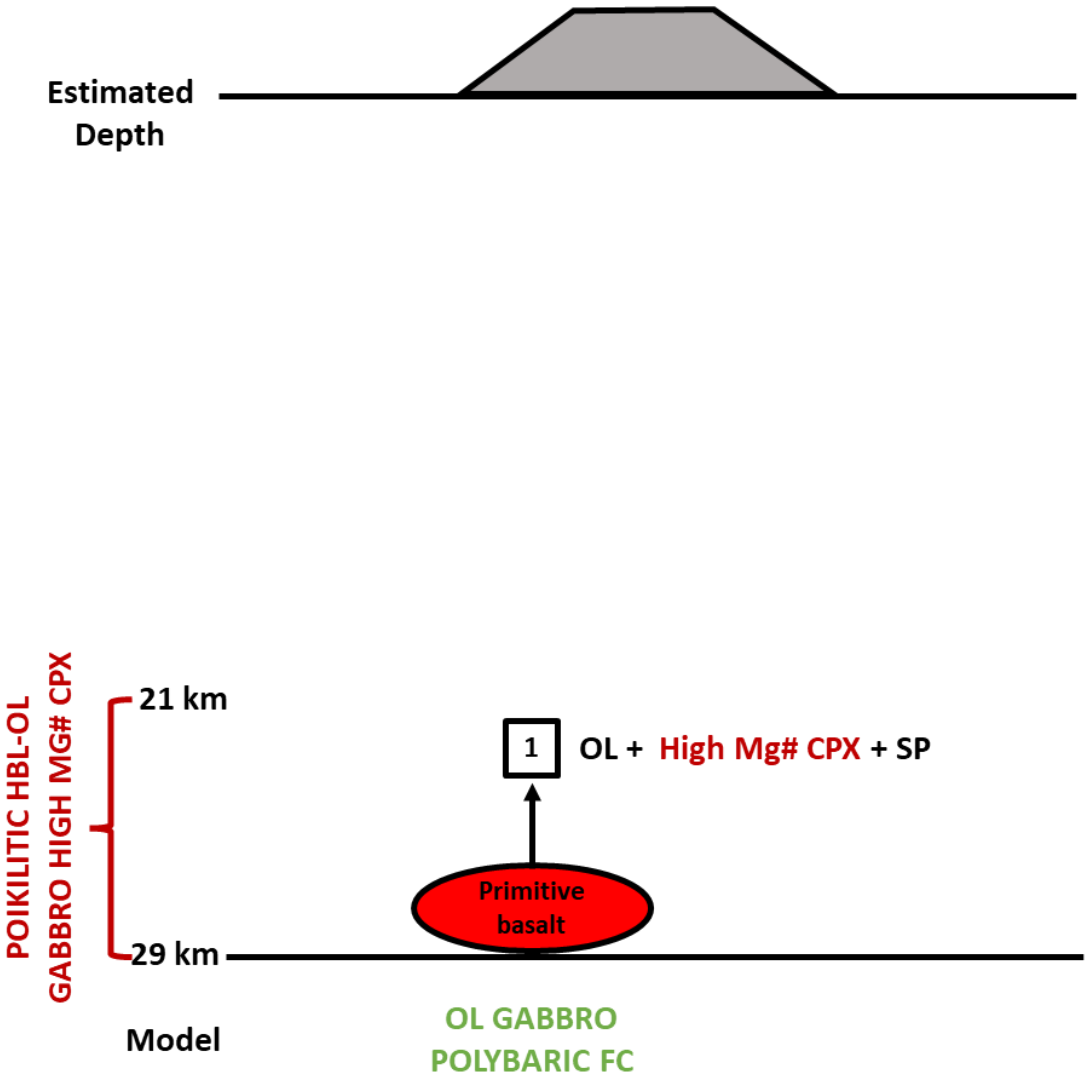

Figure 5.24: Schematic illustrating the first step only of the "OL GABBRO POLYBARIC FC" model. This single fractionation step was used to model the REE compositions of the high Mg# CPX population in the poikilitic Hbl-Ol gabbro.

Low Mg# CPX and amphibole in the Poikilitic Hbl-Ol Gabbro

The poikilitic Hbl-Ol gabbro contains the following mineral phase populations; low Fo (72-76) olivine, high Mg# (>80) CPX, low Mg# (77-79) CPX, orthopyroxene, poikilitic amphibole, three plagioclase populations (An_{85-90}, An_{75-85} and An_{60-75}) and minor interstitial apatite. The molar element ratios of majority of mineral phases in the poikilitic Hbl-Ol gabbro were best reproduced by lower pressure (~ 0.2 GPa) experiments (**Table 5.2, Appendix 5.1**). This observation suggests that the poikilitic Hbl-Ol gabbro assemblage (with exception of the high Mg# CPX, see above) could be

Fractionation step	Reference experiment name	Reference experiment temperature (°C) and pressure (GPa)	Reference experiment melt SiO_2	Fractionating assemblage	D values source	Initial melt composition	% crystallization at each step
1	BM6 (Melekhova)	1100, 1	47	Ol (42 %) + CPX (42 %) + Sp (16 %)	Brophy (2008) at 47 % SiO_2.	Inv CPX Bas (Br) from Table 5.3	24
2	L4 (Pichavant)	1000, 0.2	53	Ol (19 %) + Pl (75 %) + Mt (6%)	Brophy (2008) at 53 % SiO_2.	Previous step at F = 0.76 (after 24 % crystallization)	16
3	L2 (Pichavant)	975, 0.2	59	Ol (9%) + Cpx (1 %) + Pl (53 %) + Amph (28 %) + Mt (9 %)	Brophy (2008) at 59 % SiO_2.	Previous step at F = 0.84 (after 16 % crystallization)	43
4	L1 (Pichavant)	950, 0.2	62	Pl (52 %) + Opx (12 %) + Amph (28 %) + Mt (8 %)	Brophy (2008) at 62 % SiO_2.	Previous step at F = 0.57 (after 43 % crystallization)	61

Table 5.5: Parameters used at each fractional crystallization step of the "POIKILITIC GABBRO POLYBARIC FC" model. The four steps of the model are based on four reference experiments from Melekhova et al., (2015) and Pichavant et al., (2018), listed in the second column (see Table 2 of Melekhova et al., 2015 and Table 3 of Pichavant et al., 2018 for full details of these experiments).

produced by the low-pressure stages of polybaric FC. To test whether the REE compositions of the low Mg# CPX and amphibole could be accounted for by polybaric FC, we modified the "OL GABBRO POLYBARIC FC" model to include the additional mineral phase populations present in the poikilitic Hbl-Ol gabbro. This model is referred to as the "POIKILITIC GABBRO POLYBARIC FC" model, with the parameters used for each step listed in **Table 5.5**.

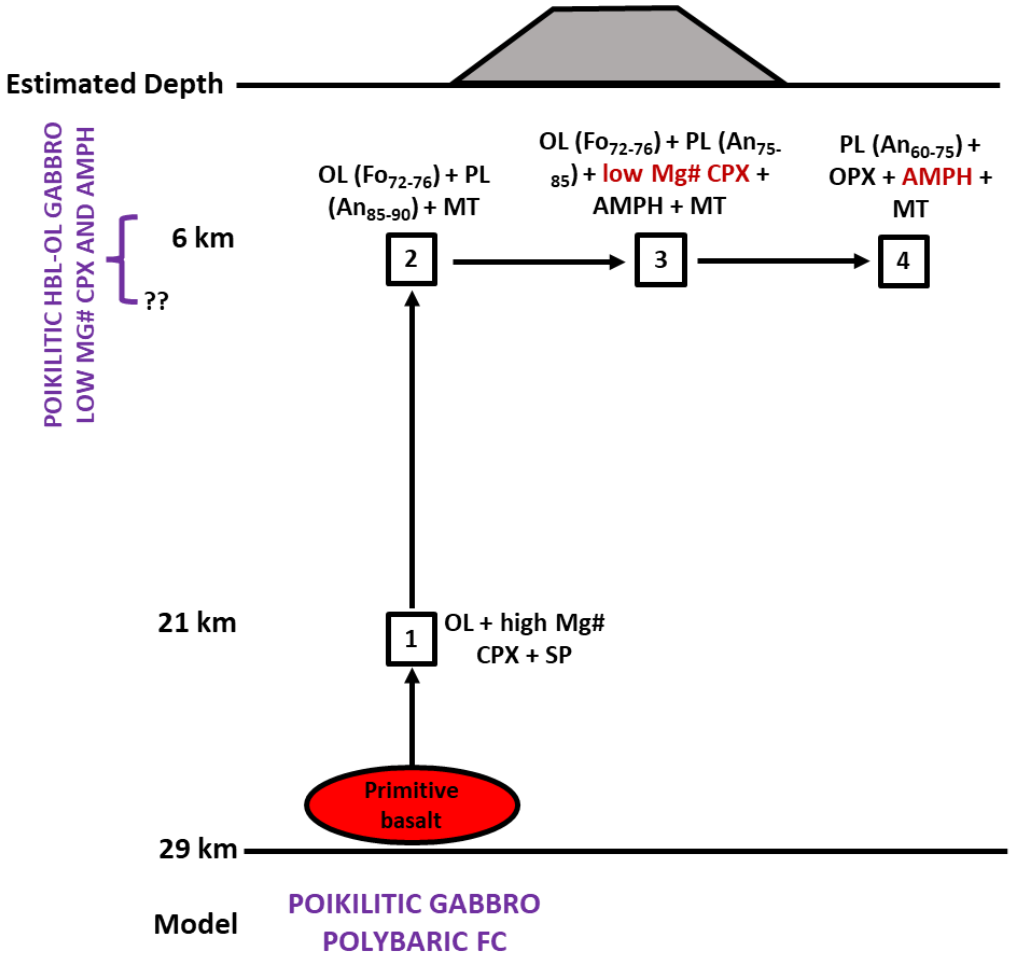

Figure 5.25: Schematic illustrating the "POIKILITIC GABBRO POLYBARIC FC" model. The model was applied to the low Mg# CPX population and amphibole in the poikilitic Hbl-Ol gabbro. The model assumes that the low Mg# CPX formed at the third fractionation step and the amphibole at the fourth fractionation step. The model was designed to represent a polybaric FC scenario by which all mineral phase populations in the sample could be formed over a series of fractionation steps.

The crystallizing assemblage at each step (**Table 5.5, Figure 5.25**) was based on the sequence of mineral phases produced with decreasing temperature in the crystallization experiments of Melekhova et al., (2015) (Step 1, high-pressure stage – 1 GPa) and Pichavant et al., (2018) (Steps 2-4, low-pressure stage – 0.2 GPa). These experiments used starting materials of a high-Mg basalt from St Vincent and high-Al basalt from Guadeloupe (northern LAA) respectively and closely reproduced the sample mineral phase assemblage and molar element ratios. The melt SiO_2 used for each step is based on the melt composition in the reference experiments. The proportions of mineral phases crystallizing at each step were taken directly from the experimental data (**Table 5.5**). The percentage/extent of crystallization at each step was taken from the percentage of crystals relative to glass formed in each reference experiment. The initial melt composition used for Step 1 was the same as the "OL GABBRO POLYBARIC FC" model.

This model was repeated using alternative cpx-melt partition coefficients from Bedard (2014) and amph-melt partition coefficients from Nandedkar et al. (2016), calculated using the listed melt SiO_2 at each step, with all other parameters identical. As an example of how the partition coefficients from different source publications vary, the difference in D values for clinopyroxene and amphibole at Step 3 of the model (partition coefficients calculated using 59 wt % SiO_2) is shown in **Appendix 5.2, Figure A5.1**.

<u>Amphibole and clinopyroxene from the olivine absent band in the banded Hbl-Ol gabbro</u>

Although textural evidence supports a reactive melt flow origin for the olivine absent band clinopyroxene and possibly amphibole (**section 5.5.1**) in the banded Hbl-Ol gabbro, we tested whether their REE compositions could be modelled by FC. This provides a test of whether the clinopyroxene and amphibole REE compositions can be used to distinguish between FC and reactive melt flow. To model FC, we added an additional step (crystallizing plagioclase + clinopyroxene + amphibole + magnetite) to the "OL GABBRO POLYBARIC FC" model (**Figure 5.26**). This scenario assumes that the olivine absent band and amphibole formed after crystallization of an initial olivine gabbro matrix assemblage. The parameters used for this additional step, referred to as "BANDED GABBRO" are listed in **Table 5.4.** Assuming a K_D(Fe-

Mg)$^{cpx/melt}$ of 0.27 ± 0.03 (Putirka, 2008), melts in equilibrium with olivine absent band clinopyroxene have Mg# 36-46, in line with St Vincent basaltic andesite glasses (Mg# 31-45, Fedele et al., 2021). Hence partition coefficients corresponding to a basaltic andesite composition (53 wt % SiO_2) were used for the additional step (**Table 5.4**).

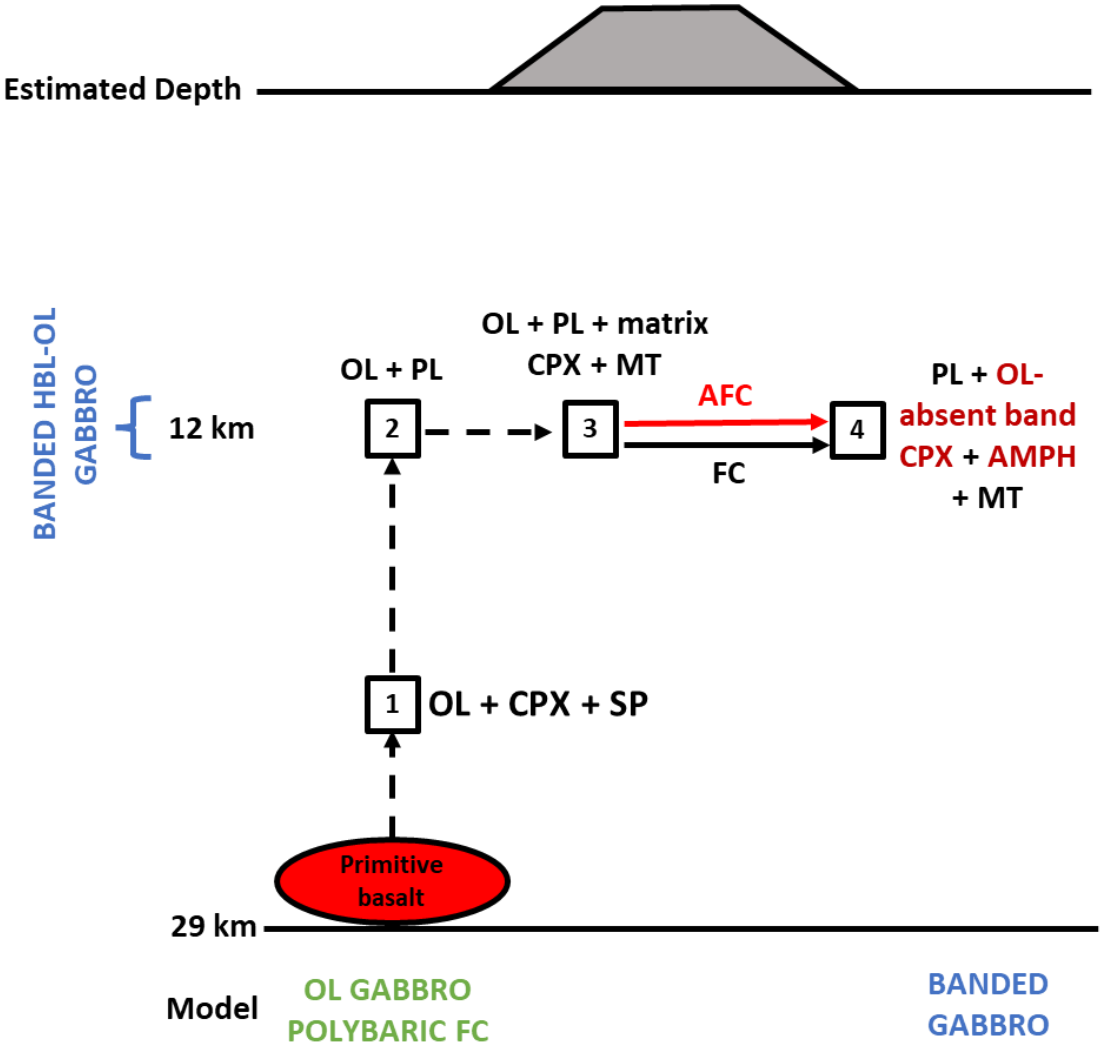

Figure 5.26: Schematic illustrating the "OL GABBRO POLYBARIC FC" model with additional "BANDED GABBRO" step. The additional "BANDED GABBRO" step (step 4) was used to model the REE compositions of the amphibole, and clinopyroxene within the olivine absent band, of the banded Hbl-Ol gabbro. The "BANDED GABBRO" step was modelled using both FC and AFC (see main text for details).

This model ("BANDED GABBRO") was repeated using alternative amph-melt partition coefficients from Nandedkar et al. (2016), with all other parameters identical. These amph-melt partition coefficients were those corresponding to 51 wt % SiO_2 from

Nandedkar et al., (2016) (see **Appendix 5.2** for values) since partition coefficients at 53 wt % SiO_2 were unavailable.

5.5.2.2 – Assimilation-Fractional Crystallization (AFC) models

The parameters used in AFC models applied to crystal populations in the banded and poikilitic Hbl-Ol gabbros are justified in the following subsections. In addition to the initial melt composition, fractionating assemblage and partition coefficients, AFC modelling requires input values for two additional parameters - the assimilant composition and the parameter r (rate of assimilation/rate of crystal fractionation). The assimilant composition was taken as the average whole rock composition of plutonic xenoliths from Martinique (Cooper et al., 2016), listed in **Table 5.3**. Various values were tested for the parameter r, with a consistently good fit to the data obtained using r = 0.4 across the REE, used in majority of models.

If reactive melt flow involves the dissolution of a mush containing REE rich phases, such as apatite (which can be highly LREE enriched) this could significantly increase the REE content of the assimilant compared to the compositions used in our models. Apatite is present in the poikilitic Hbl-Ol gabbro as a minor, interstitial phase **(see Chapter 3)** suggesting that it crystallized late (after the clinopyroxene and amphibole), as expected based on experimental data on hydrous arc basalt crystallization sequences (e.g. Nandedkar et al., 2014, Marxer et al., 2021). These observations suggest that if the low Mg# CPX and amphibole in the poikilitic Hbl-Ol gabbro were formed via reactive melt flow, apatite was not present in the initial mush assemblage prior to reaction, since it is likely to have crystallized after these phases. Hence, we do not consider an apatite bearing/highly REE enriched mush assimilant composition in our AFC models.

Biotite is also a late appearing phase, crystallizing with or after apatite, in experimental crystallization sequences (Nandedkar et al., 2014, Marxer et al., 2021). Niobium is highly compatible in biotite (e.g. D_{Nb} = 0.5-9, typically > 1, Stepanov and Hermann, 2013). Biotite has never been observed in St Vincent plutonic xenoliths and only rarely reported in LAA plutonic xenoliths generally (Arculus and Wills, 1980, Camejo-Harry et al., 2018). The lack of evidence for the presence of biotite in St Vincent plutonic xenoliths suggests that the high Nb concentrations in poikilitic Hbl-Ol gabbro

amphibole (**section 5.4.2**, discussed in **section 5.5.3.2**) are not a result of biotite dissolution.

Low Mg# CPX and amphibole in the poikilitic Hbl-Ol gabbro

Textural observations suggest that amphibole in the poikilitic Hbl-Ol gabbro may have formed via reaction between melt and clinopyroxene/olivine (**section 5.5.1**). The low Mg# CPX population show distinct LREE enrichment relative to HREE compared to clinopyroxene from other plutonic xenoliths analysed. This LREE enrichment is typical of clinopyroxene formed via reactive melt flow (e.g. Lissenberg and MacLeod, 2016, SanFillipo et al., 2020). Hence, we tested whether AFC could reproduce the REE compositions of the low Mg# CPX and amphibole. The parameters used for the three modelled AFC scenarios ("BASALTIC ANDESITE AFC, ANDESITE AFC, ANDESITE AFC 2") are listed in **Table 5.6.**

Model name	Fractionating assemblage	D values source	Initial melt composition	Assimilant composition	R
ANDESITE AFC	Pl (30 %) + Opx (15 %) + Cpx (25 %) + Amph (30 %)	Brophy (2008) at 59 % SiO_2.	Inv CPX And (Br) from Table 5.3	Average Martinique plutonic xenolith from Table 5.3	0.4
BASALTIC ANDESITE AFC	Pl (30 %) + Opx (15 %) + Cpx (25 %) + Amph (30 %)	Brophy (2008) at 53 % SiO_2.	Inv CPX Bas And (Br) from Table 5.3	Average Martinique plutonic xenolith from Table 5.3	0.4
ANDESITE AFC 2	Pl (46 %) + Opx (22 %) + Cpx (17 %) + Amph (15 %)	Brophy (2008) at 59 % SiO2.	Inv CPX And (Br) from Table 5.3	Adjusted assimilant	0.4

Table 5.6: Parameters used for the "BASALTIC ANDESITE AFC, ANDESITE AFC and ANDESITE AFC 2" models.

Textural observations also suggest that the high An plagioclase and olivine in the sample could be remnants of a precursory crystal mush assemblage, modified by reactive melt flow. We also assume that the high Mg# CPX population were introduced as a crystal cargo in the initial melt (discussed in detail in **section 5.5.3.2**). Based on these assumptions, we chose a fractionating mineral assemblage of plagioclase (representing the lower An populations) + clinopyroxene + orthopyroxene + amphibole for the AFC models (**Figure 5.27**).

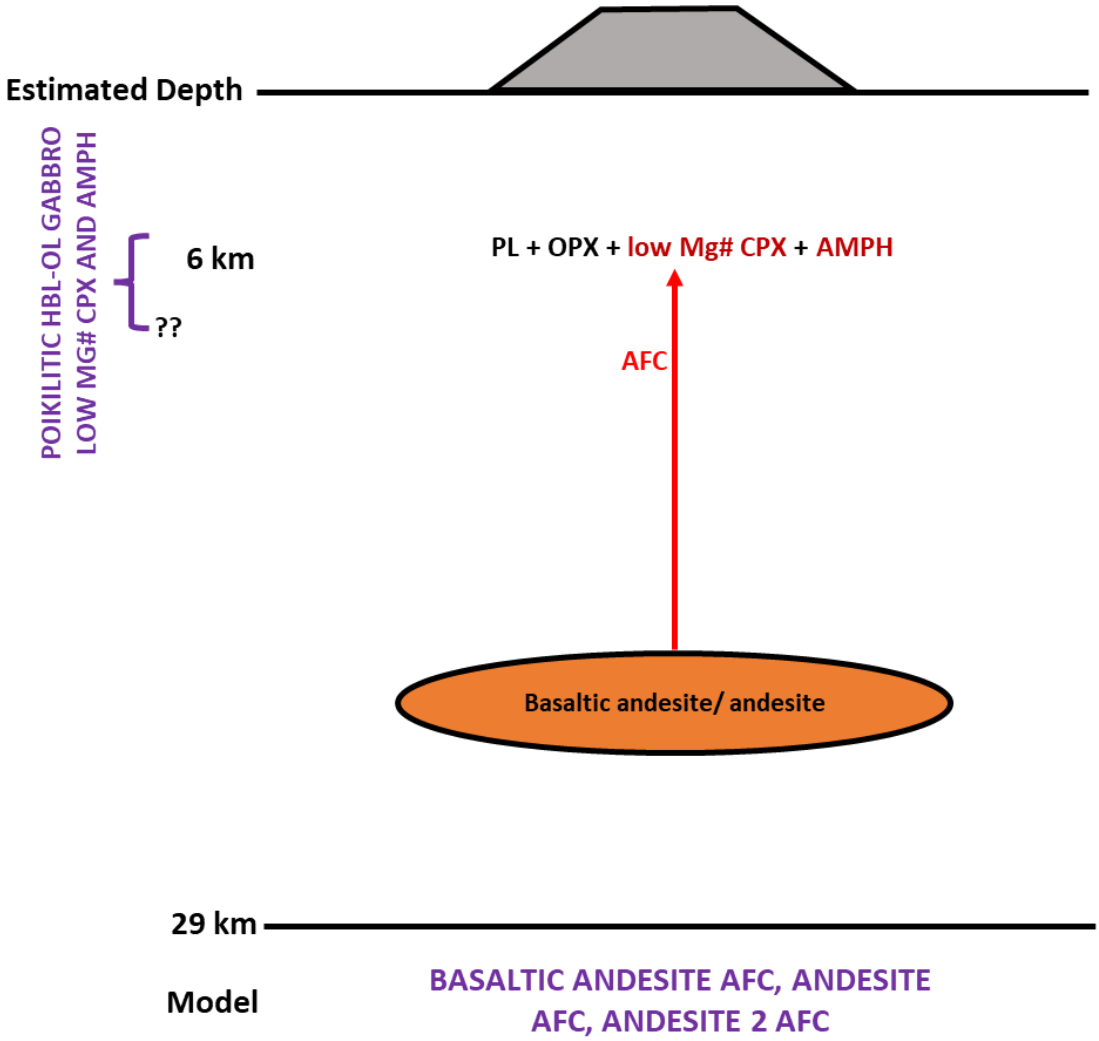

Figure 5.27: Schematic illustrating the "BASALTIC ANDESITE AFC, ANDESITE AFC" and "ANDESITE AFC 2" models. The three scenarios were used to model the REE compositions of the low Mg# CPX population and amphibole in the poikilitic Hbl-Ol gabbro via AFC.

Some experiments which best reproduced the mineral assemblage and molar element ratios of the sample used andesitic starting compositions (**Table 5.2, Appendix 5.1**). Assuming a $K_D(Fe\text{-}Mg)^{cpx/melt}$ of 0.27 ± 0.03 (Putirka, 2008) and a $K_D(Fe\text{-}Mg)^{opx/melt}$ of 0.28 ± 0.04 (Beattie, 1993), melts in equilibrium with low Mg# CPX and orthopyroxene have estimated Mg# 44-53 and Mg# 38-49 respectively, within the range of both basaltic andesite (Mg# 31-45) and andesite (Mg# 48-24) glasses from St Vincent scoria (Fedele et al., 2021). Hence, we trialled both basaltic andesite (53 wt % SiO_2) and andesite (59 wt % SiO_2) initial melt compositions (**Table 5.3**). The third model, "ANDESITE AFC 2" (**Table 5.6**) uses a modified assimilant composition (**Table 5.3**) and slightly different modal proportions of mineral phases in the

fractionating assemblage, to illustrate the effect of changing these parameters on the model outcome. The modified assimilant composition has slightly lower (maximum difference of 0.67 µg/g) Nd, Sm, Dy and slightly higher Yb than the "Average Martinique plutonic xenolith" assimilant. The modified fractionating assemblage contains higher proportions of plagioclase and orthopyroxene and lower proportions of amphibole and clinopyroxene.

Amphibole and clinopyroxene from the olivine absent band in the banded Hbl-Ol gabbro

Textural observations suggest that the olivine absent band in the banded Hbl-Ol gabbro may have formed via reactive melt flow, which may also account for the sample amphibole (**section 5.5.1**). To test this scenario, we modelled the REE compositions of the amphibole and olivine absent band clinopyroxene using AFC. The parameters used are listed in **Table 5.4** – the initial melt composition, fractionating assemblage and partition coefficients were identical to the "BANDED GABBRO" FC model. This AFC model was repeated using alternative amph-melt partition coefficients (at 51 wt % SiO_2) from Nandedkar et al. (2016), with all other parameters identical.

5.5.2.3 - Calculation of modelled trends

The results of the geochemical modelling are shown in **Section 5.5.3**. The figures in this section show compositions of clinopyroxene and amphibole in equilibrium with modelled melt compositions. The REE compositions of modelled clinopyroxene and amphibole were calculated from modelled melt compositions using the partition coefficients listed in the "D values source" column of the relevant table describing the model. For example, the composition of modelled clinopyroxene at Step 3 of the "OL GABBRO POLYBARIC FC" model was calculated using clinopyroxene-melt partition coefficients from Brophy (2008) at 53 wt % SiO_2 (**Table 5.4**). In models using alternative clinopyroxene-melt and amphibole-melt partition coefficients, these were also used to calculate the modelled clinopyroxene and amphibole compositions.

5.5.2.4 – Limitations of modelling approach

When modelling magma chemical evolution in a mushy magmatic system, it is difficult to constrain the parameters required for the FC and AFC models. We use initial melt compositions inverted from clinopyroxene compositions in our plutonic xenoliths, in

an attempt to represent the melts present within the mushy plumbing system. We prefer this to the use of whole-rock lava compositions from St Vincent which may not reflect true melt compositions due to the highly porphyritic nature of the lavas (Heath et al., 1998, Fedele et al., 2021). Nonetheless, initial melt compositions involved in the petrogenesis of the plutonic xenoliths could vary from those used in the models and are poorly constrained. Partition coefficients from different sources (e.g. Brophy (2008) and Nandedkar et al., (2016) for amphibole) can also vary significantly, as shown in **Appendix 5.2**. The proportions of fractionating phases can be estimated from the samples and/or experimental data. However, particularly when modelling reactions (simulated via AFC), there is considerable uncertainty over the proportions of mineral phases crystallizing. Whole rock REE compositions of plutonic xenoliths from Martinique and Statia in the LAA show considerable variation (e.g. Ce 1-14 µg/g, Cooper et al., 2016, 2019), illustrating the uncertainty on the assimilant composition used in the AFC models. Although the modelled FC steps and reactions simulated by AFC models can be justified, in reality these processes are likely to be more complex and/or may not proceed via the exact steps/reactions used in the models.

Some additional models, used to illustrate the effect of changing one or more parameters on the model outcomes, are presented in **Appendix 5.3**. These additional models are discussed as part of the interpretation of the modelling results in **section 5.5.3**.

5.5.3 – Interpretation of geochemical modelling and petrogenetic models

In this section, we interpret the results of the geochemical models applied to the mineral phase populations in each plutonic xenolith (**Table 5.1**). We then combine our modelling results with the textural observations outlined in **section 5.5.1** to propose petrogenetic models explaining the mineral phase associations and chemical compositions in each plutonic xenolith sample.

5.5.3.1 – Are olivine gabbros products of polybaric fractional crystallization?

The clinopyroxene REE compositions produced at step 3 of the "OL GABBRO POLYBARIC FC" model overlap the range of clinopyroxene from the olivine gabbro, Ol-CPX gabbro and banded Hbl-Ol gabbro matrix (**Figure 5.28**). The shapes of the modelled REE profiles closely match the sample clinopyroxene. The modelling results suggest that majority of the clinopyroxene REE compositional range can be produced

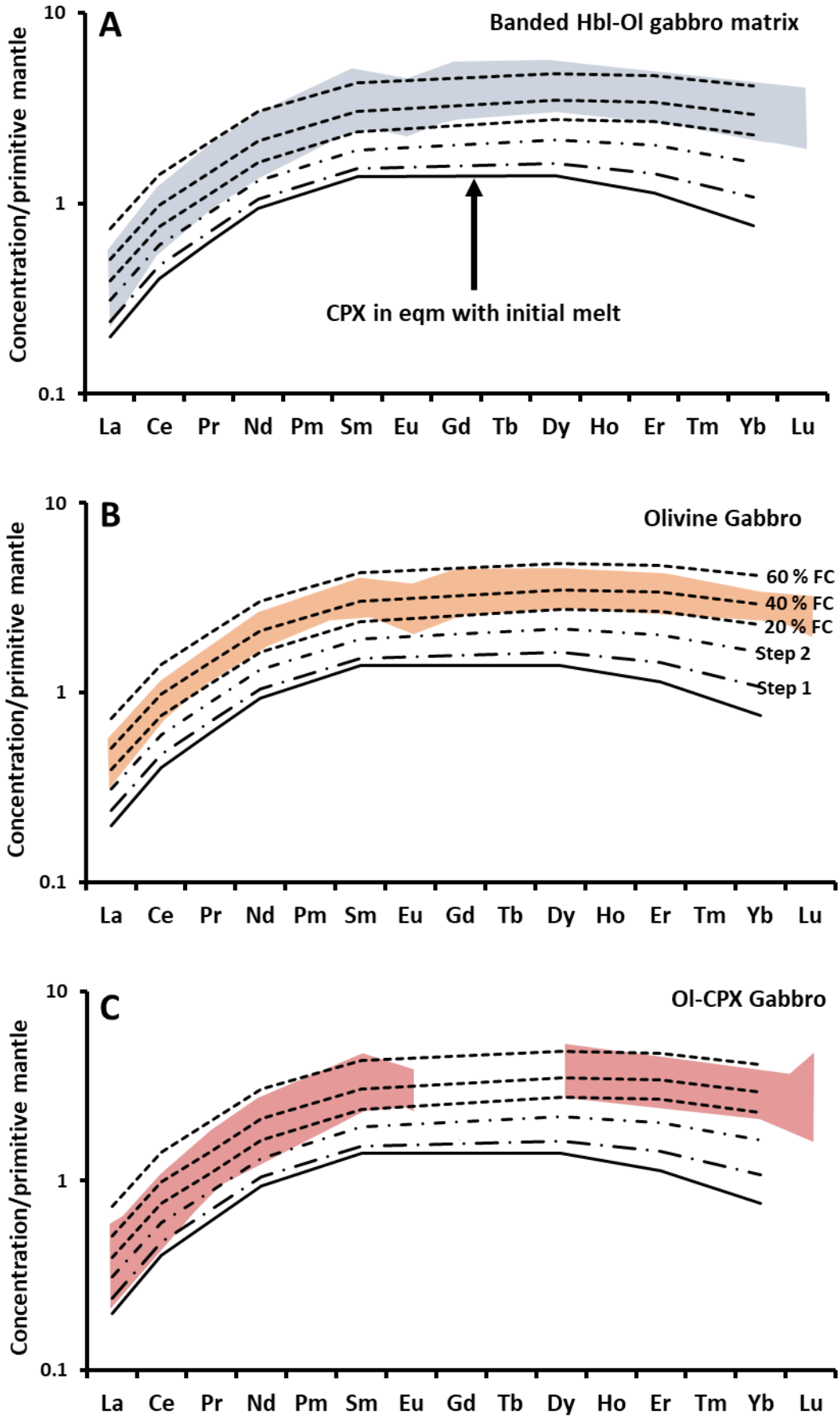
A
Banded Hbl-Ol gabbro matrix
CPX in eqm with initial melt
B
Olivine Gabbro
60 % FC
40 % FC
20 % FC
Step 2
Step 1
C
Ol-CPX Gabbro
Concentration/primitive mantle
10
1
0.1
La Ce Pr Nd Pm Sm Eu Gd Tb Dy Ho Er Tm Yb Lu

Figure 5.28: Primitive mantle normalized REE patterns of clinopyroxene from **A)** banded Hbl-Ol gabbro matrix **B)** olivine gabbro and **C)** Ol-CPX gabbro, shown by the shaded fields. The data are compared with the **clinopyroxene compositions in equilibrium with the melt (solid and black dashed lines)** at each step of the "OL GABBRO POLYBARIC FC" model. For the third step, the composition of clinopyroxene in equilibrium with the melt after 20, 40 and 60 % fractional crystallization is shown. Primitive mantle normalizing values from Palme and O'Neill (2003).

by 20-60 % fractionation of an olivine gabbro assemblage (**Figure 5.28**). It can therefore be inferred that these plutonic xenoliths are products of the mid-upper crustal stages of polybaric FC. This interpretation agrees well with comparisons to experimental studies which reproduced the mineral phase molar ratio associations of the samples at 0.6-0.2 GPa (18-6 km depth, **Table 5.2**). The association of high An plagioclase and low Fo olivine in these samples suggests crystallization from melts with high H_2O contents (e.g. Sisson and Grove, 1993, Melekhova et al., 2015). The olivine gabbro and Ol-CPX gabbro lack textural features indicative of reactive melt flow or disequilibrium (e.g. partial replacement of mineral phases, embayed crystals recording dissolution, **section 5.5.1**), suggesting that FC is the dominant magmatic process recorded by these samples. Amphibole-free regions of the banded Hbl-Ol gabbro matrix have similar textures and clinopyroxene chemistry to the olivine gabbro and Ol-CPX gabbro and are likely to have formed via the same process (discussed further in **section 5.5.3.3**).

The "OL GABBRO POLYBARIC FC" model represents one possible scenario for polybaric FC on St Vincent. However, in a natural scenario, the parameters (initial melt composition, proportions of mineral phases in the fractionating assemblage, amount of crystallization at each step, partition coefficients) could easily vary from those used in our model. A small discrepancy between the model and data can be observed for the LREE, particularly La, in the Ol-CPX gabbro and banded Hbl-Ol gabbro matrix clinopyroxene. This discrepancy can be reconciled by varying the parameters used in the model, for example the initial melt composition (at step 1), shown in **Appendix 5.3, Figure A5.2.**

5.5.3.2 – Do crystal populations in the poikilitic Hbl-Ol gabbro record both fractional crystallization and reactive melt flow?

<u>High Mg# CPX population</u>

The high Mg# CPX population in the poikilitic Hbl-Ol gabbro has distinctive geochemical features (higher Mg#, Ni and Cr, lower M-HREE and incompatible trace element concentrations) compared to the clinopyroxene from other plutonic xenolith samples. We tested whether the high Mg# CPX REE compositions could be explained by high pressure FC from a primitive basaltic magma, simulated by step 1 of the "OL GABBRO POLYBARIC FC" model. The modelled clinopyroxene REE compositions overlap with majority of the high Mg# CPX data range, excluding the most LREE enriched compositions (**Figure 5.29**).

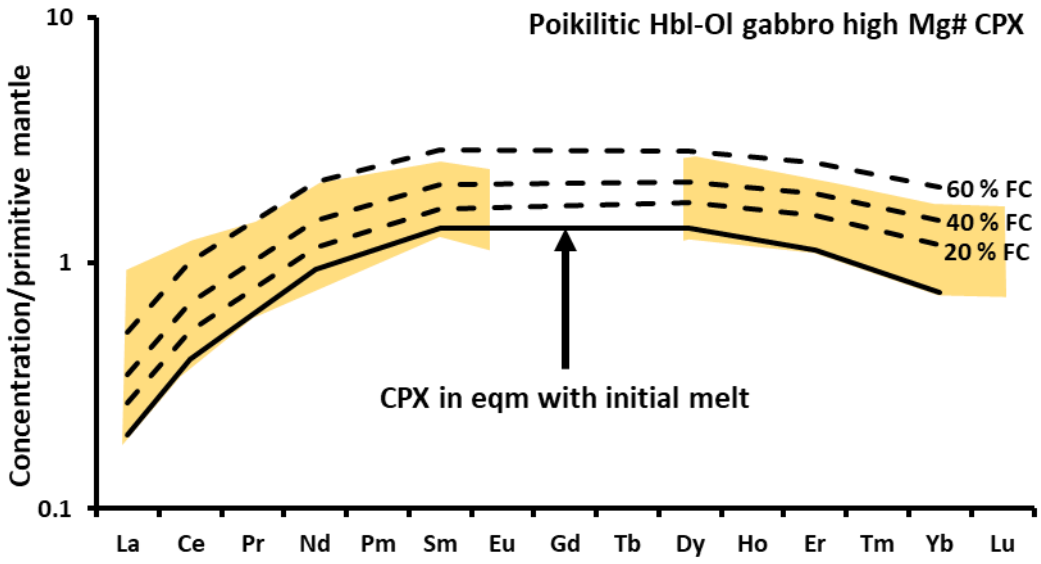

Figure 5.29: Primitive mantle normalized REE patterns of poikilitic Hbl-Ol gabbro high-Mg# CPX (yellow shaded field). The data are compared with the **clinopyroxene compositions in equilibrium with the melt (solid and black dashed lines)** after 20, 40 and 60 % fractionation of Ol + Cpx + Sp (1st step of the "OL GABBRO POLYBARIC FC" model). Primitive mantle normalizing values from Palme and O'Neill (2003).

The shape of the modelled REE profiles closely matches most of the sample clinopyroxene (again excluding the two more LREE enriched analyses, see **Figure 5.17, a)**. The model results show that majority of the REE compositional range in the high Mg# CPX can be produced by significant extents (up to 60 %) of fractionation of the high-pressure assemblage olivine + clinopyroxene + spinel from a primitive basaltic magma. These modelling results support earlier inferences on the origin of this crystal population from comparison to experimental studies (**Table 5.2, Appendix 5.1).** The REE contents of the high Mg# CPX (Ce = 0.7-2, Yb = 0.36-0.81) are similar to those of high Mg# (84-91) clinopyroxene in Aleutian arc ultramafic plutonic

xenoliths (Ce = 0.68-1.91, Yb = 0.13-0.78, Yogodzinski and Kelemen, 2007) and high Mg# (> 87) clinopyroxene in cumulates from the exposed lower crust of the Famatinian arc (Ce = 0.5-2.1, Yb = 0.4-1.3, Otamendi et al., 2016) and the Cascades (average Ce = 2.32, average Yb = 0.45, Dessimoz et al., 2012), lending further support to a lower crustal origin. We therefore infer that the high Mg# CPX record the initial, lower crustal/high pressure stage of magma differentiation on St Vincent proposed by Tollan et al., (2012) based on the association of high An plagioclase and low Fo olivine in St Vincent plutonic xenoliths.

As noted above, the first step of the "OL GABBRO POLYBARIC FC" model only represents one possible scenario for high-pressure FC beneath St Vincent. Discrepancies between model and data (for example, the failure to reproduce the most LREE enriched high Mg# CPX) could be resolved by using a different initial melt composition and/or modified fractionating assemblage and/or partition coefficients. Since the chemical compositions of the high Mg# CPX generally support a lower crustal origin, it is also possible that some of the variation in REE compositions within this population records variation in primitive magma compositions entering the base of the crust beneath St Vincent, as opposed to REE variation generated by high-pressure FC. In **Appendix 5.3**, we demonstrate that this is plausible as the high Mg# CPX with high La and Ce can be reproduced by our model using a reasonable alternative initial melt composition (**Figure A5.3** in **Appendix 5.3)**.

Low Mg# CPX and poikilitic amphibole

Despite the textural evidence for reactive processes in the poikilitic Hbl-Ol gabbro, we first tested whether the compositions of these phases could be reproduced by polybaric FC from a primitive basaltic magma, simulated by the "POIKILITIC GABBRO POLYBARIC FC" model. This approach provided a test of whether the REE compositions of the low Mg# CPX and amphibole alone can be used to distinguish whether FC or reactive melt flow formed these crystal populations.

The low Mg# CPX are considered to crystallize at step 3 of the model (**Figure 5.25**), hence the clinopyroxene composition in equilibrium with the melt after step 3 represents the most REE enriched clinopyroxene that could be formed in our polybaric FC scenario. Primitive mantle normalized REE patterns of the low Mg# CPX population and the clinopyroxene composition from step 3 of the model are compared

in **Figure 5.30, a.** The modelled clinopyroxene (green line **in Figure 5.30, a**) does not reach the LREE enriched (high La and Ce) compositions of the low Mg# CPX. Using alternative partition coefficients (orange line in **Figure 5.30, a)**, the modelled clinopyroxene better fits the low Mg# CPX REE profiles, particularly for M-HREE **(Figure 5.30, a).** However, the modelled clinopyroxene does not reach the most REE enriched low Mg# CPX compositions and the modelled La concentration is lower than any of the measured low Mg# CPX. The REE compositional range, in particular the elevated La and Ce (relative to clinopyroxene from other samples) in the low Mg# CPX population is therefore inconsistent with our polybaric FC model.

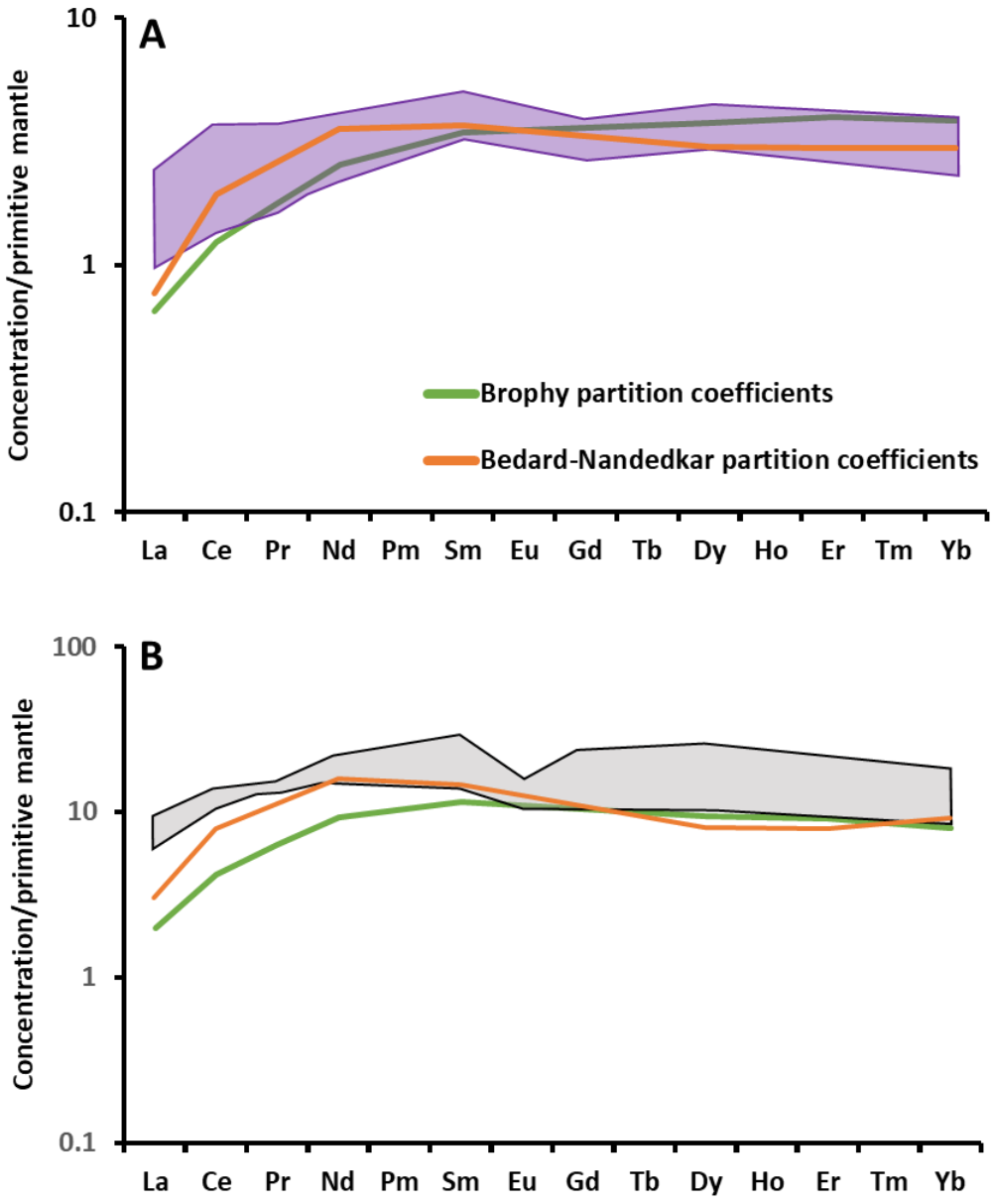

Figure 5.30: A) Primitive mantle normalized REE patterns of poikilitic Hbl-Ol gabbro low Mg# CPX (purple field) compared with the most REE enriched clinopyroxene compositions produced by the

"POIKILITIC GABBRO POLYBARIC FC" model (orange or green line depending on partition coefficients used in the model, see legend and text for details). **B)** Primitive mantle normalized REE patterns of poikilitic Hbl-Ol gabbro amphibole (grey field) compared with the most REE enriched amphibole compositions produced by the "POIKILITIC GABBRO POLYBARIC FC" model. Primitive mantle normalizing values from Palme and O'Neill (2003).

The poikilitic Hbl-Ol gabbro amphibole are considered to crystallize at step 4 of the model (**Figure 5.25**), hence the amphibole composition in equilibrium with the melt after step 4 represents the most REE enriched amphibole that could be formed in our polybaric FC scenario. Primitive mantle normalized REE patterns of the poikilitic Hbl-Ol gabbro amphibole and amphibole compositions from step 4 of the model are compared in **Figure 5.30, b.** Regardless of the partition coefficients used, the modelled amphibole composition is generally more REE depleted than the poikilitic Hbl-Ol gabbro amphibole, though for M-HREE the model almost matches the least enriched sample amphibole.

Another distinctive geochemical feature of the poikilitic Hbl-Ol gabbro amphibole is their high Nb content (8.5-12 μg/g). The "POIKILITIC GABBRO POLYBARIC FC" model was applied to Nb, using an initial melt composition of 0.15 μg/g Nb (inverted from the Nb concentration in the highest Mg# clinopyroxene in this study, assuming $^{CPX/L}D_{Nb}$ = 0.03 after Fedele et al., 2021). Partition coefficients for Nb in olivine, plagioclase, clinopyroxene, orthopyroxene, spinel and apatite were < 0.05 (with the exception of magnetite set at 1.8), with values equivalent to those used by Fedele et al., (2021) to model the chemical evolution of St Vincent lavas. Constant partition coefficients were used for these phases with melt evolution. The amphibole partition coefficient for Nb was increased with increasing melt SiO_2, with values taken from the experimental data of Nandedkar et al., (2016) (**Appendix 5.2, Table A5.1**). Amphibole Nb concentrations modelled in this way do not reach the high Nb contents observed in the poikilitic Hbl-Ol gabbro amphibole (**Appendix 5.3, Figure A5.5**).

Overall, the model results suggest that the range of REE compositions measured in the low Mg# CPX and amphibole (and high Nb in amphibole) are inconsistent with an origin via polybaric fractional crystallization from a primitive basaltic magma.

A major limitation of the "POIKILITIC GABBRO POLYBARIC FC" model is that it only represents a single possible polybaric FC scenario. In reality, polybaric FC may not proceed via the exact steps/fractionating assemblages used in the model and the

initial melt composition and partition coefficients could vary from our chosen values. In **Appendix 5.3**, we show an alternative version of the "POIKILITIC GABBRO POLYBARIC FC" model using a significantly more REE enriched initial melt composition. Using this model, a poor fit to the poikilitic Hbl-Ol gabbro low Mg# CPX data is obtained for clinopyroxene, but a relatively close fit (in line with the sample compositional range for most modelled REE, but with slightly lower La and Ce) is obtained for amphibole (**Figure A5.4** in **Appendix 5.3**). The initial melt composition used in this alternative model is from lava whole-rock data, which may not represent a realistic melt composition. However, we have shown that by varying the input parameters of initial melt composition (**Appendix 5.3**) and partition coefficients (**Figure 5.30**), significantly different results can be achieved using our "POIKILTIC GABBRO POLYBARIC FC" model. This highlights the dependence of the model result on the poorly constrained input parameters. Thus, we suggest that our modelling results do not completely rule out the possibility that the REE compositions of the low Mg# CPX and amphibole in the poikilitic Hbl-Ol gabbro could be produced by polybaric FC, although overall the results suggest that this is unlikely.

Despite the model limitations, the failure of the "POIKILITIC GABBRO POLYBARIC FC" model to reproduce the low Mg# CPX and amphibole REE compositions is consistent with textural observations that support a role for reactive melt flow (**section 5.5.1**). The results of our AFC models, simulating this scenario, are shown in **Figure 5.31**. The range of low Mg# CPX REE compositions and REE profile shapes are closely reproduced via an AFC process crystallizing up to 60 % plagioclase + clinopyroxene + orthopyroxene + amphibole, using both basaltic andesite and andesite initial melt compositions. Even after 90% crystallization, the AFC models do not reproduce the amphibole M-HREE contents using either initial melt composition, though a good match is obtained for LREE (**Figure 5.31**). The "ANDESITE AFC 2" model was used to illustrate the effect of changing the fractionating assemblage and assimilant composition (**Tables 5.3 and 5.6**). Using this model, the range of low Mg# CPX compositions were again reproduced after up to 60 % crystallization (**Figure 5.32, a**), though clinopyroxene compositions are typically slightly over-enriched in M-HREE relative to LREE in this model (emphasised by the modelled clinopyroxene after 60 % crystallization). A good fit for the amphibole data, falling in line with the sample range for all REE, was achieved using this model after 85-90 % crystallization (**Figure**

5.32, b). However, the most M-HREE enriched amphibole compositions were not reproduced by the model, even after 90 % crystallization. Our model results, using justifiable parameters, suggest that majority of the REE variation measured in the low Mg# CPX and amphibole from the poikilitic Hbl-Ol gabbro could be produced via an AFC process, akin to reactive melt flow.

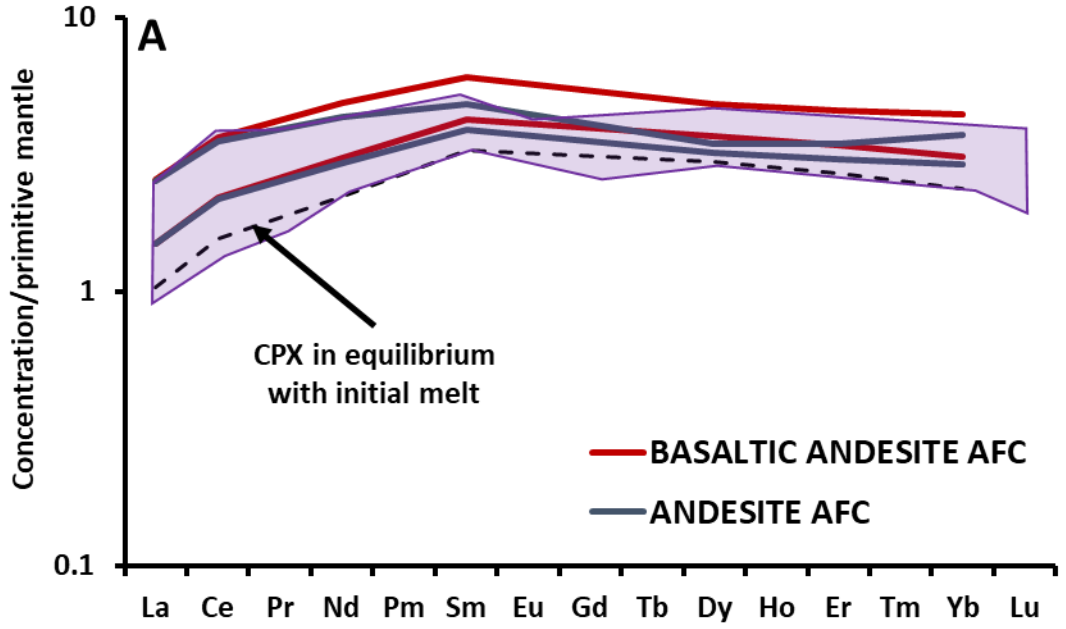

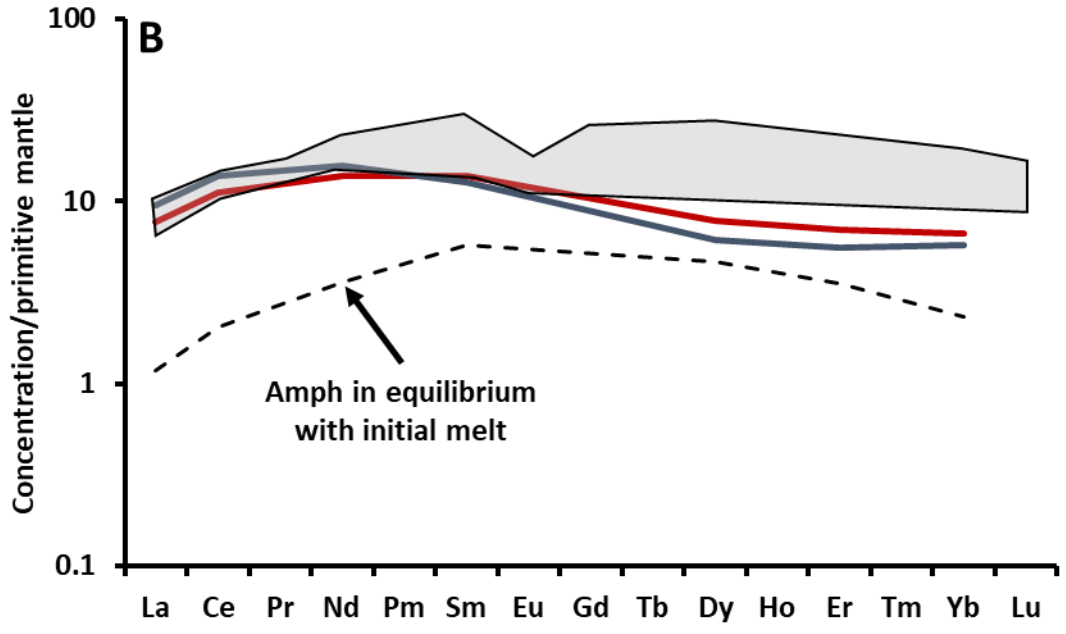

Figure 5.31: A) Primitive mantle normalized REE patterns of poikilitic Hbl-Ol gabbro low Mg# CPX (purple field). The data are compared with the **clinopyroxene compositions in equilibrium with the melt** after 30 % and 60 % crystallization during AFC, simulated by the "BASALTIC ANDESITE AFC" and "ANDESITE AFC" models. The upper of the two lines for each model represents the clinopyroxene in equilibrium with the melt after 60 % crystallization. **B)** Primitive mantle normalized REE patterns of poikilitic Hbl-Ol gabbro amphibole (grey field). The data are compared with the **amphibole composition in equilibrium with the melt** after 90 % crystallization during AFC, simulated by the "BASALTIC ANDESITE AFC" and "ANDESITE AFC" models. Primitive mantle normalizing values from Palme and O'Neill (2003).

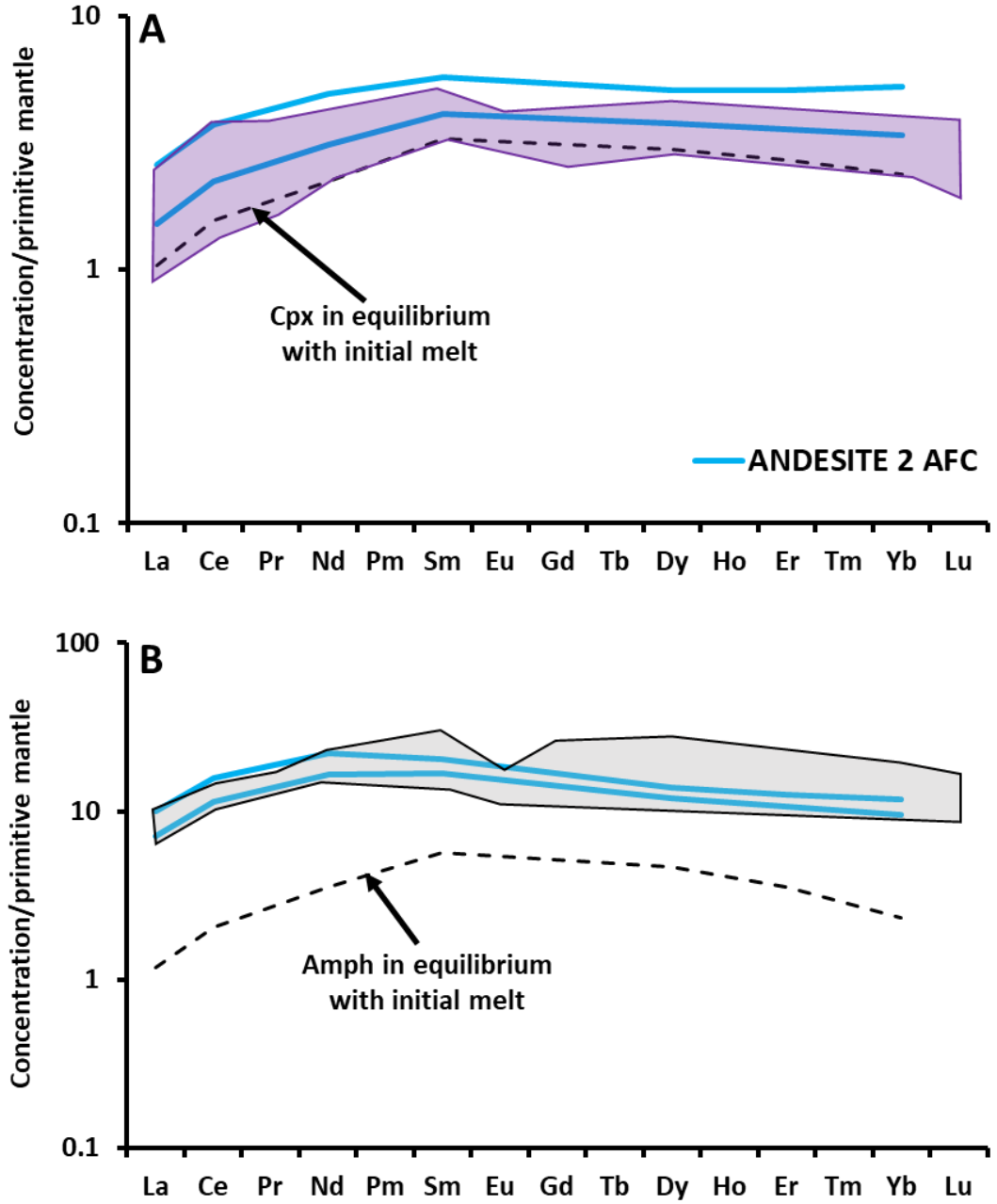

Figure 5.32: A) Primitive mantle normalized REE patterns of poikilitic Hbl-Ol gabbro low Mg# CPX (purple field). The data are compared with the **clinopyroxene compositions in equilibrium with the**

melt after 30 % and 60 % crystallization during AFC, simulated by the "ANDESITE AFC 2" model. The upper of the two lines represents the clinopyroxene in equilibrium with the melt after 60 % crystallization. **B)** Primitive mantle normalized REE patterns of poikilitic Hbl-Ol gabbro amphibole (grey field). The data are compared with the **amphibole composition in equilibrium with the melt** after 85 and 90 % crystallization during AFC, simulated by the "ANDESITE AFC 2" model. The upper of the two lines represents the amphibole in equilibrium with the melt after 90 % crystallization. Primitive mantle normalizing values from Palme and O'Neill (2003).

The "ANDESITE 2 AFC" model illustrates the effect of adjusting two of the input parameters (fractionating assemblage and assimilant composition) within reasonable limits and demonstrates that, as observed for the FC models, reproducing the sample data is strongly dependent on the chosen input parameters. The uncertainty over the values of the input parameters for the AFC model can offer an explanation as to why the full range of amphibole REE compositions was not reproduced in our specific modelled scenarios. It is also likely that the AFC equations of DePaolo (1981) may not be able to accurately simulate a complex process such as reactive melt flow and its effects on the trace element compositions of mineral phases and the reactive melt.

The demonstrated sensitivity of the FC and AFC modelling results to the highly uncertain values chosen for the input parameters implies that geochemical modelling in isolation cannot be used to distinguish confidently between the contributions of FC and AFC/reactive melt flow to the petrogenesis of the poikilitic Hbl-Ol gabbro. This observation highlights the importance of combining the clinopyroxene and amphibole trace element data with textural observations in order to constrain the processes recorded by the mineral phase populations in the poikilitic Hbl-Ol gabbro.

Petrogenetic model for poikilitic Hbl-Ol gabbro

Petrographic observations combined with chemical mapping and trace element compositions of clinopyroxene and amphibole have enabled us to identify the following mineral phase populations in the poikilitic Hbl-Ol gabbro; low Fo (72-76) olivine, high Mg# (>80) CPX, low Mg# (< 80) LREE enriched CPX, orthopyroxene, LREE enriched poikilitic amphibole, plagioclase with highly variable An (60-90) and minor interstitial apatite. The plagioclase are divided into three populations based on chemical compositions and textures - An_{85-90}, An_{75-85} and An_{60-75} (see **section 5.4.1**). A model for the petrogenesis of the poikilitic Hbl-Ol gabbro must account for the association of these chemically distinct mineral phase populations. The textural

relationships indicative of reactions between olivine and melt to form orthopyroxene/amphibole and clinopyroxene and melt to form amphibole must also be incorporated.

We propose that the complex mineral assemblage of the poikilitic Hbl-Ol gabbro could be formed via interaction between a reactive melt and pre-existing mush. In this scenario, some mineral populations derive from the pre-existing mush and others are products of reactions between melt and mush. Comparison of mineral chemistry with other St Vincent plutonic xenoliths can provide constraints on the mineral populations derived from the pre-existing mush. The low Fo content of the olivine (Fo 72-75) and a small population of high An_{85-90} plagioclase (which exist as relict/patchy cores) are similar to the olivine gabbro and Ol-CPX gabbro samples from this study and other St Vincent olivine gabbros and troctolites (Tollan et al., 2012). The high Mg# CPX population have higher Mg# (82-89) than clinopyroxene from the olivine gabbro, Ol-CPX gabbro (Mg# 73-80) and olivine gabbros studied by Tollan et al., (2012). Both the high Mg# CPX and low Mg# CPX populations have contrasting trace element chemistry to clinopyroxene in the olivine gabbro and Ol-CPX gabbro (**section 5.4.2.1**). For these reasons, we suggest that the clinopyroxene populations were not part of an initial olivine gabbro mush assemblage alongside olivine and high An plagioclase. Instead, we infer that the low Fo olivine and high An plagioclase could represent a feasible initial assemblage - a troctolite mush. The textural observations of embayed olivine (indicative of dissolution) enclosed by orthopyroxene/amphibole and sparsely distributed high-An plagioclase cores support the notion that these mineral phase populations represent remnants of a pre-existing assemblage, subsequently modified by reaction with an invading melt (e.g. Yang et al., 2019, **section 5.5.1**).

The geochemical modelling showed that the REE compositions of the majority of the low Mg# CPX and amphibole could be produced via AFC from a basaltic andesite or andesite initial melt (**Figures 5.31 and 5.32**). In addition, melts in equilibrium with low Mg# CPX and orthopyroxene in the poikilitic Hbl-Ol gabbro have Mg# corresponding to St Vincent basaltic andesite and andesite glass compositions (**section 5.5.2.2**). Therefore, we propose that the complex mineral phase assemblage of the poikilitic Hbl-Ol gabbro could result from interaction of a hydrous basaltic-andesite or andesite melt with a pre-existing troctolite mush. Tollan et al., (2012) proposed that St Vincent troctolites crystallized at approximately 5 km depth, though comparisons with

previous experimental work showed that the high An plagioclase-low Fo olivine association can be reproduced by experiments at 0.2-0.6 GPa, with 3.7-6.3 wt % H_2O (6-18 km depth, **Table 5.2**). Mineral phase compositions matching the poikilitic Hbl-Ol gabbro (excluding the high Mg# CPX) were best reproduced by experiments at 0.2 GPa (~ 6 km depth). Hence, we suggest that this interaction occurred in the mid-upper crust, possibly around 6 km depth. The high An plagioclase-low Fo olivine association suggests that the initial troctolite mush crystallized from a water rich melt (e.g. Sisson and Grove, 1993, Tollan et al., 2012, Melekhova et al., 2015).

We suggest that the chemically distinct high Mg# CPX population are introduced as a crystal cargo in the melt interacting with the initial troctolite. Above, we have suggested that the high Mg# CPX crystal population formed during a deep/early stage of magma differentiation, which is likely to have occurred in a deep crustal hot zone (e.g. Annen et al., 2006) in the lower crust beneath St Vincent (Tollan et al., 2012). Numerical modelling has indicated that evolved melts can be generated by extensive crystallization in deep crustal hot zones (e.g. Annen et al., 2006, Solano et al., 2012). Hence, the presence of the high Mg# CPX as a crystal cargo in the interacting melt can be reconciled if this melt was sourced from a deep crustal hot zone, with the clinopyroxene entrained from deep/early formed clinopyroxene ± olivine ± spinel cumulates. This idea is consistent with the proposal of Marxer et al., (2021) who suggested that ascending magmas from regions of clinopyroxene dominated differentiation in arc lower crust are likely to entrain clinopyroxene crystal cargoes. Further support for this concept comes from the presence of chemically distinct clinopyroxene cargoes in Martinique plutonic xenoliths (Cooper et al., 2016).

A deep crustal hot zone source for the interacting melt could also explain the high Ni and Cr contents of the low Mg# CPX and amphibole. Klaver et al., (2018) proposed that rhyodacite lavas with unusually high Ni and Cr (for evolved lavas) from Nysiros, Aegean arc, were formed via reaction of melts with olivine-clinopyroxene cumulates (forming amphibole) in a deep crustal hot zone. Similarly, high Ni and Cr contents in andesitic lavas and mafic enclaves from Mt Lamington, Papua New Guinea, were attributed to incorporation of olivine and Cr-spinel from mushes formed during high-pressure fractionation (Zhang et al., 2015). Similar processes could occur beneath St Vincent, with resorption of olivine-clinopyroxene-spinel bearing lower crustal

cumulates enriching ascending melts in Ni and Cr, reflected in the clinopyroxene and amphibole that crystallize from these melts at shallower levels.

We propose that the interaction between melt and pre-existing troctolite mush occurred via a "mush cannibalization" mechanism, as opposed to "reactive flow" of melt between crystals in a mush. In this scenario, a dyke carrying a high Mg# CPX crystal cargo intrudes the troctolite mush, which disaggregates into the invading body of melt (**Figure 5.33, Stage 1**). The requirement for our invading melt to transport a crystal cargo (of clinopyroxene measuring up to 4 mm across) suggests that it is unlikely to have travelled through a mush between crystal boundaries. In addition, the low overall abundance (~ 15 %) of our proposed initial (troctolite) assemblage in the final rock supports the idea that these crystals represent disaggregated mush entrained in a melt, as opposed to remnants of a mush invaded by a percolating reactive melt (which would require extensive dissolution). These arguments justify our proposed "mush cannibalization" mechanism over a more typical "reactive flow" scenario.

We next propose that the chemical contrast between the invading hydrous basaltic andesite-andesite melt and entrained disaggregated troctolite mush triggers reactions involving partial dissolution of olivine, high An plagioclase and the high Mg# CPX crystal cargo. The reactions crystallize poikilitic orthopyroxene around olivine, poikilitic amphibole around olivine and high Mg# CPX, plus plagioclase An_{75-85} and low Mg# CPX, forming a new crystal mush assemblage **(Figure 5.33, Stage 2)**. Co-crystallization of low Mg# CPX and the An_{75-85} plagioclase population is supported by the presence of small low Mg# CPX inclusions in plagioclase zones of this composition (**Figure 5.7, e, Chapter 3**).

Still to be accounted for in our petrogenetic model are poikilitic amphibole texturally associated with low Mg# CPX, the An_{60-75} plagioclase population and interstitial apatite. We propose that these phases formed after the initial interaction between invading melt and troctolite (**Figure 5.33, Stage 3**) as the newly formed (plagioclase An_{75-85} + clinopyroxene + orthopyroxene + amphibole, with remnant olivine and plagioclase An_{85-90}) mush continued to cool and crystallize. These phases (amphibole + An_{60-75} plagioclase + apatite) may represent products of late-stage crystallization of the residual melt in the newly formed mush. This interpretation is supported by experimental data on hydrous arc basalt crystallization sequences, where amphibole

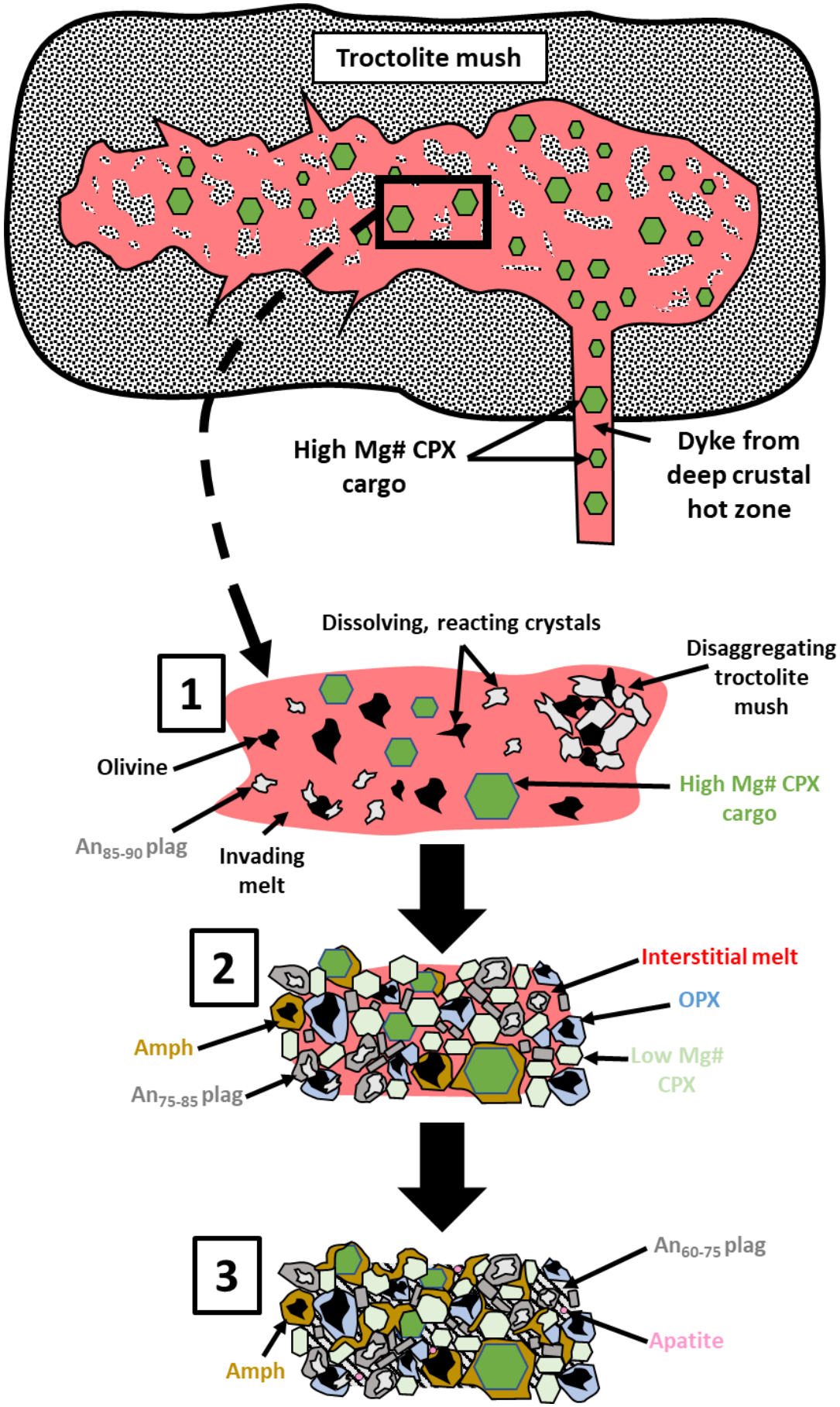

Figure 5.33: Schematic illustrating the sequence of processes involved in the petrogenesis of the

poikilitic Hbl-Ol gabbro. It should be noted that the schematic is not drawn to a given scale.

Stage 1 - A dyke carrying a crystal cargo of high Mg# CPX intrudes a troctolite mush, which disaggregates into the body of invading melt.

Stage 2 – Chemical disequilibrium between the invading melt and entrained mush triggers reactions which lead to partial dissolution of the high An_{85-90} plagioclase and olivine from the troctolite, as well as the high Mg# CPX cargo. The reactions crystallize poikilitic orthopyroxene around partially dissolved olivine and poikilitic amphibole around olivine and the high Mg# CPX. Plagioclase An_{75-85} and the low Mg# CPX population also crystallize from the melt, which has been chemically modified by reaction with the troctolite mush. A new plagioclase-orthopyroxene-clinopyroxene-amphibole mush (with remnant An_{85-90} plagioclase, olivine and high Mg# CPX) is formed.

Stage 3 - Late stage crystallization of residual evolved melts in the mush formed low An_{60-75} plagioclase, amphibole and apatite. In some pockets of the mush, local disequilibrium between residual melt and low Mg# CPX leads to some amphibole crystallization via reaction between melt and clinopyroxene.

and plagioclase co-crystallize in the lower temperature stages (typically at melt SiO_2 > 59 wt %), with apatite joining the assemblage at 62-66 wt % SiO_2 (Nandedkar et al., 2014, Marxer et al., 2021). In addition, some plagioclase inclusions in poikilitic amphibole do not show ragged grain contacts suggesting possible co-crystallization (see **Chapter 3, Figure 3.39**). Alternatively, some amphibole may have been formed at this stage via reaction between residual melts in chemical disequilibrium with low Mg# CPX.

This model for the petrogenesis of the poikilitic Hbl-Ol gabbro could be tested and refined with additional data. For example, trace element compositions of orthopyroxene and plagioclase zones of different An content could be used to refine stages 2 and 3 of the model. In this proposed scenario, the orthopyroxene and An_{75-85} plagioclase population would be expected to show LREE/HREE enrichment matching the (co-crystallizing) low Mg# CPX and amphibole. Trace element data for the high An plagioclase population could be used to test the idea that these crystals are derived from a disaggregated mush. A different, more LREE depleted profile relative to the An_{75-85} and An_{60-75} plagioclase populations, suggestive of crystallization from a more LREE depleted melt, would support the proposed model. Stable Sr isotopic compositions of plagioclase could provide further evidence for the proposed "mush cannibalization" process. Plagioclase fractionates stable Sr isotope ratios (e.g. Charlier et al., 2012), hence a process involving dissolution and crystallization of plagioclase

would be expected to generate heterogeneity in plagioclase stable Sr isotopic compositions.

5.5.3.3 – Does the banded Hbl-Ol gabbro record reactive melt flow?

Geochemical modelling of amphibole and olivine absent band clinopyroxene

We attempted to model the REE compositions of the amphibole and olivine absent band clinopyroxene in the banded Hbl-Ol gabbro using both FC and AFC ("BANDED GABBRO" model, **sections 5.5.2.1 and 5.5.2.2, Table 5.4, Figure 5.26**). This allowed us to test whether the trace element compositions of these mineral phase populations can be used to distinguish between FC and a reactive melt flow origin. The modelled FC trend can match the olivine absent band clinopyroxene data but gives a very poor fit for the amphibole data, exemplified by a plot of Ce vs Yb (**Figure 5.34, a and b**). Repeating the model using alternative amph-melt partition coefficients led to an improved fit for amphibole but a slightly less good fit for the olivine absent band clinopyroxene (**Figure 5.34, a and b**). In the alternative amph-melt partition coefficients version of the model, the range of REE compositions in the amphibole and olivine absent band clinopyroxene can be reproduced by up to 60 % fractional crystallization (of plagioclase + clinopyroxene + amphibole + magnetite) (**Figure 5.34, c and d**).

The modelled AFC trends are very similar to the FC models and the amphibole data was again only fit by the AFC model using alternative amph-melt partition coefficients (**Figure 5.34, a and b**). The REE compositional range in the olivine absent band clinopyroxene and amphibole can be produced by an AFC process after up to 50 % crystallization (**Figure 5.34, c and d**). The significant difference in model outcomes using alternative partition coefficients for amphibole once again highlights the sensitivity of the FC and AFC models to the chosen input parameters. A major assumption in the "BANDED GABBRO" FC and AFC models is the fractionating assemblage, which includes both clinopyroxene (representing the olivine absent band clinopyroxene) and amphibole. However, amphibole is not present in the olivine absent band, suggesting it may have crystallized separately from the clinopyroxene in the band – this possibility is explored further below. In this scenario, our model may not accurately simulate the FC or AFC process by which these mineral phase populations were formed. Despite these limitations, our results show that using reasonable input

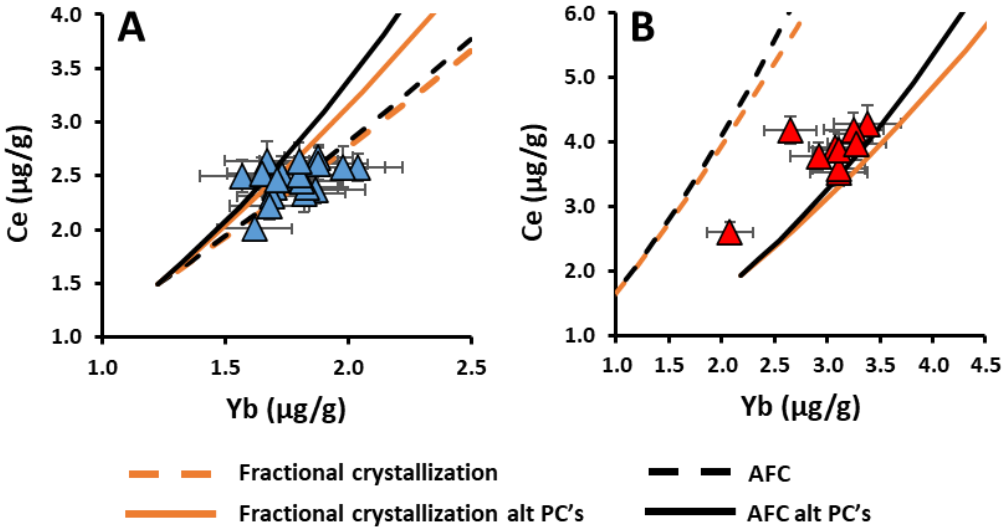
A
B
Ce (µg/g)
Yb (µg/g)
Fractional crystallization
Fractional crystallization alt PC's
AFC
AFC alt PC's

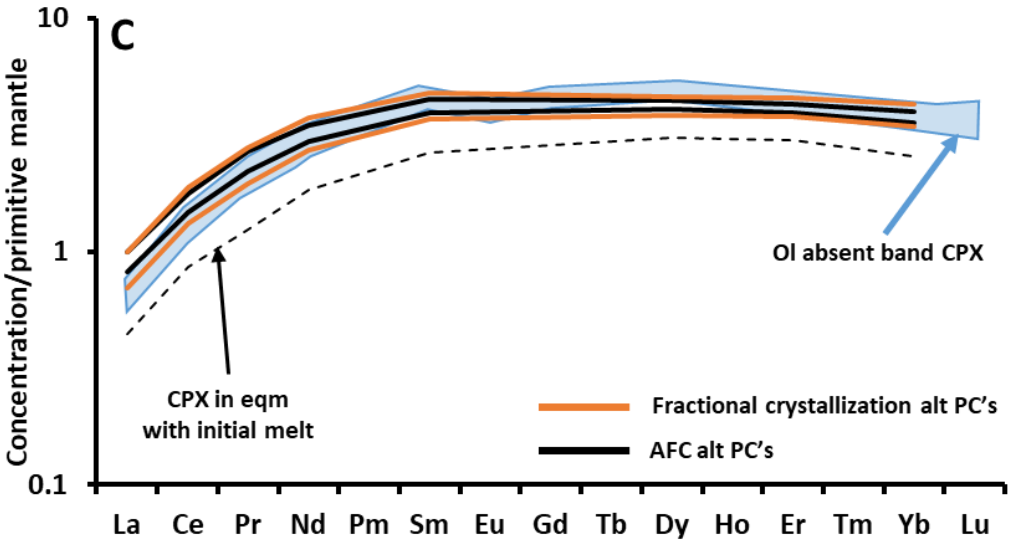
C
Concentration/primitive mantle
Ol absent band CPX
CPX in eqm
with initial melt
Fractional crystallization alt PC's
AFC alt PC's
La Ce Pr Nd Pm Sm Eu Gd Tb Dy Ho Er Tm Yb Lu

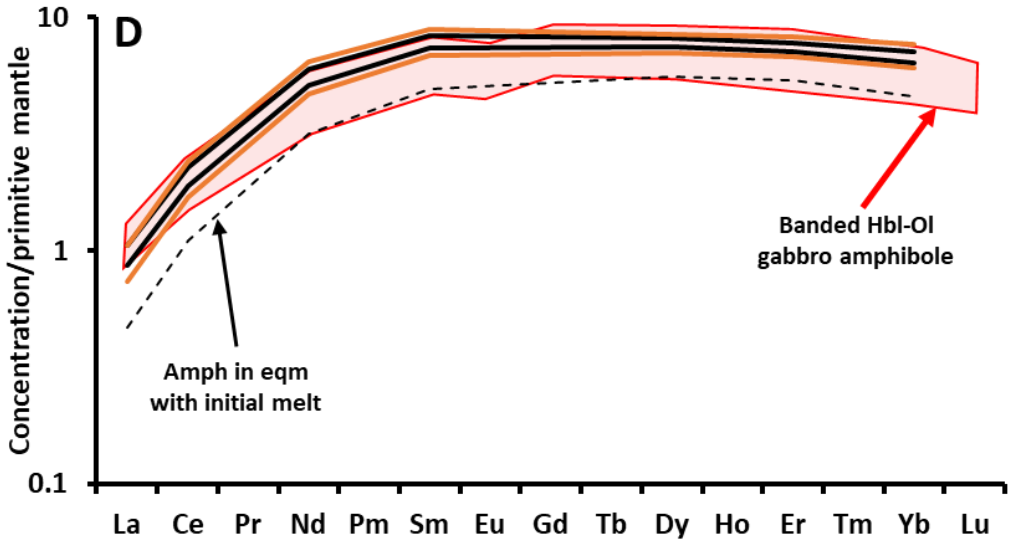
D
Concentration/primitive mantle
Banded Hbl-Ol
gabbro amphibole
Amph in eqm
with initial melt
La Ce Pr Nd Pm Sm Eu Gd Tb Dy Ho Er Tm Yb Lu

Figure 5.34: Ce vs Yb for **A)** olivine absent band clinopyroxene and **B)** amphibole from the banded Hbl-Ol gabbro, compared with modelled trends for FC and AFC ("BANDED GABBRO" model, **Table 5.4, Figure 5.26**). Data symbols are the same as results section plots. Error bars on individual data points show internal 2SE uncertainty. **C)** Primitive mantle normalized REE patterns for olivine absent band clinopyroxene and **D)** primitive mantle normalized REE patterns for amphibole from the banded Hbl-Ol gabbro, shown by the shaded fields. The data are compared to clinopyroxene **C)** and amphibole **D)** compositions in equilibrium with the melt modelled by FC (after 40 and 60 % crystallization) and AFC (after 40 and 50 % crystallization) using the "BANDED GABBRO" model **with alternative partition coefficients for amphibole (**taken from Nandedkar et al., (2016) at 51 wt % SiO_2, see **Appendix 5.2** for D values**)**. The upper lines for each process on **C)** and **D)** represent the higher modelling increment (e.g. 60 % crystallization for the FC model, 50 % crystallization for the AFC model). Primitive mantle normalizing values from Palme and O'Neill (2003).

parameters, it is possible to reproduce the amphibole and olivine absent band clinopyroxene compositions using either FC or AFC models. In other words, geochemical modelling and the trace element compositions of amphibole and clinopyroxene in the banded Hbl-Ol gabbro in isolation cannot clearly distinguish between a FC and reactive melt flow origin for these mineral phase populations. As suggested for the poikilitic Hbl-Ol gabbro, combining the mineral trace element data with textural observations is required to determine the petrogenetic processes recorded by the banded Hbl-Ol gabbro.

Petrogenetic model for banded Hbl-Ol gabbro

A model for the petrogenesis of the banded Hbl-Ol gabbro must account for the olivine gabbro assemblage of the sample matrix, the textural association of amphibole overgrowing clinopyroxene (in the matrix) and the centimetre wide olivine absent band with more evolved plagioclase and clinopyroxene than the matrix. In **section 5.5.1**, we proposed that the sample matrix initially consisted of an olivine gabbro mush similar to the olivine gabbro and Ol-CPX gabbro samples. The range of olivine Fo, plagioclase An and clinopyroxene Mg# in the banded Hbl-Ol gabbro matrix overlaps with these samples and St Vincent olivine gabbros studied by Tollan et al., (2012), supporting this interpretation. Trace element compositions of banded Hbl-Ol gabbro matrix clinopyroxene show a very similar range to the olivine gabbro and Ol-CPX gabbro (**section 5.4.2**) and REE compositions are consistent with a polybaric FC origin (**section 5.5.3.1**). Comparisons of the mineral assemblage and mineral phase molar element ratios with experimental products suggest that the banded Hbl-Ol gabbro is

derived from ~ 12 km depth (**Table 5.2, Appendix 5.1**). Based on these lines of evidence, we conclude that the banded Hbl-Ol gabbro was initially an olivine gabbro mush formed during the mid-crustal stages of polybaric FC from a primitive basaltic magma.

In **section 5.5.1**, we suggested that amphibole-clinopyroxene textural relationships in the banded Hbl-Ol gabbro do not distinguish between a reactive melt flow vs in situ peritectic reaction origin for the amphibole. Cooper et al., (2016) suggested that amphibole with similar textures, referred to as "interstitial amphibole", from Martinique plutonic xenoliths were formed via reactive melt flow. Banded Hbl-Ol gabbro amphibole REE patterns and incompatible trace element contents (Zr, Y, Ba, Nb) overlap the lower end of the range of compositions defined by Martinique interstitial amphiboles (**Figures 5.18 and 5.19)**. However, banded Hbl-Ol gabbro amphibole show limited variation in REE and incompatible trace element contents (e.g. Ce = 2.6-4.3 µg/g, Zr = 14-24 µg/g, Nb = 0.6-1.1 µg/g), in contrast with the wide range observed in Martinique interstitial amphibole (e.g. Ce = 2.7-18.5 µg/g, Zr = 11-58 µg/g, Nb = 0.5-3.7 µg/g**, Figures 5.18 and 5.19**). Compared with poikilitic Hbl-Ol gabbro amphibole, interpreted to have formed via a melt-mush reaction process (**section 5.5.3.2**), banded Hbl-Ol gabbro amphibole have much lower incompatible trace element and REE concentrations (**Figures 5.18 and 5.19**). Therefore, the banded Hbl-Ol gabbro amphibole may not have formed via reactive melt flow.

Cooper et al., (2016) showed that melts in equilibrium with Martinique interstitial amphibole were more trace element enriched than melts in equilibrium with adjacent clinopyroxene, suggesting that an additional source of trace elements (such as an infiltrating reactive melt) was required to produce the interstitial amphibole compositions. Primitive mantle normalized REE compositions of calculated melts in equilibrium with banded Hbl-Ol gabbro matrix clinopyroxene and amphibole are shown in **Figure 5.35**. Three different sets of partition coefficients were used to calculate amphibole equilibrium melts to account for uncertainty over this parameter. In contrast to the results of Cooper et al., (2016), melts in equilibrium with amphibole and matrix clinopyroxene in the banded Hbl-Ol gabbro generally overlap (**Figure 5.35**), except for amphibole equilibrium melts calculated using Brophy (2008) partition coefficients. This result implies that addition of externally derived melt to the initial olivine gabbro mush may not be required to produce the amphibole trace element

compositions. Although this observation does not rule out involvement of an externally derived reactive melt, it favours the interpretation that the banded Hbl-Ol gabbro amphibole formed via a peritectic reaction between clinopyroxene and trapped interstitial melt during crystallization of the initial olivine gabbro mush.

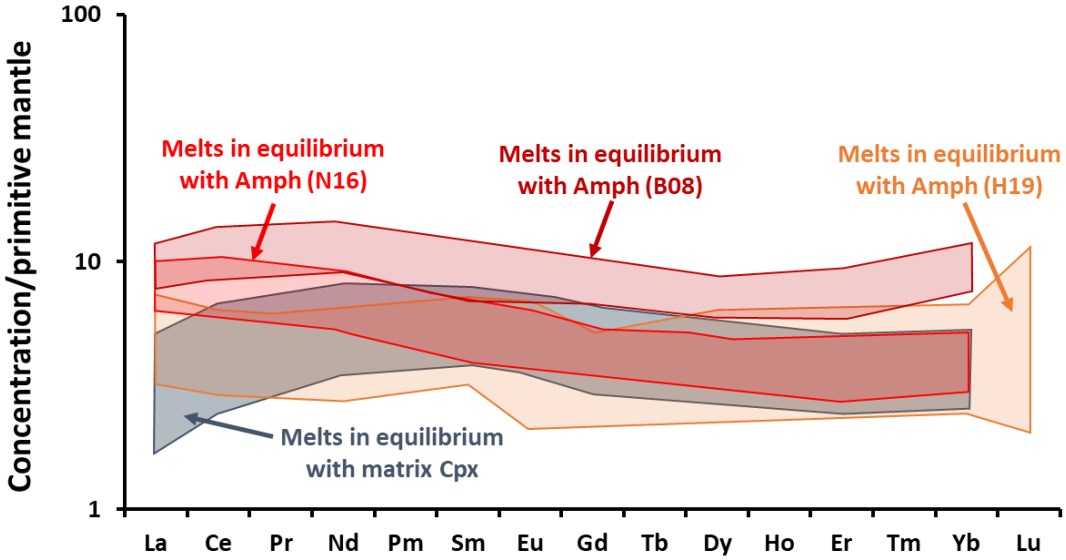

Figure 5.35: Primitive mantle normalized REE compositions of melts in equilibrium with clinopyroxene and amphibole from the banded Hbl-Ol gabbro matrix. Clinopyroxene equilibrium melts were calculated using partition coefficients from Brophy (2008) at 53 wt % SiO_2 (see **Appendix 5.2** for D values). Three sets of partition coefficients were used to calculate amphibole equilibrium melts to account for uncertainty on these values. These include partition coefficients from Brophy (2008) at 53 wt % SiO_2 (B08) and Nandedkar et al., (2016) at 51 wt % SiO_2 (N16) (see **Appendix 5.2** for D values). A third set of partition coefficients calculated using the amphibole trace element partitioning scheme of Humphreys et al., (2019) were also used (H19). Primitive mantle normalizing values from Palme and O'Neill (2003).

We suggest that the olivine absent band, composed of plagioclase + clinopyroxene (+ minor magnetite), formed via reactive melt flow through an initial olivine gabbro mush represented by the sample matrix (**section 5.5.1**). This process is consistent with the reaction: olivine + plagioclase + clinopyroxene + melt -> plagioclase 2 + clinopyroxene 2 + melt 2, by which reactive flow is often proposed to operate in MOR systems (e.g. SanFillipo et al., 2020, Boulanger et al., 2021, Ferrando et al., 2021). Clinopyroxene in the olivine absent band has lower Mg# (**Figure 5.13**), generally slightly higher incompatible trace element contents and lower Ni than clinopyroxene in the sample matrix (**Figure 5.16**), suggesting that the invading reactive melt was slightly more evolved than that which crystallized the initial olivine gabbro mush. A notable feature of the banded Hbl-Ol gabbro is that amphibole is not present within the olivine absent

band. Regardless of the exact mechanism by which the amphibole formed, we infer that it was part of the initial mush assemblage modified during formation of the olivine absent band. In this scenario, it is not possible to determine whether any amphibole was initially present in the region now occupied by the band, but if this was the case it can be assumed that amphibole was also dissolved in the reactive process. We propose two possible scenarios to explain the reactive melt flow process that generated the olivine absent band. Both scenarios assume that the banded Hbl-Ol gabbro thin section represents a small snapshot of a wider region of initial olivine gabbro mush, through which reactive melts migrated.

A possible mechanism for the formation of the olivine absent band is the concept of "reactive infiltration feedback", discussed by Ortoleva et al., (1987b), who mathematically modelled the reactive flow of water through a porous rock. In their model, the flux of reactive water through the rock is greater in regions of initially higher porosity, which causes the rock to dissolve faster in these regions. This process results in a positive feedback and focuses the flux of reactive water into a narrower region as more rock is dissolved. This concept could explain how reactive melt flow became focused into a centimetre wide region to form the olivine absent band and is illustrated (in the context of reactive melt flow through a mush) in **Figure 5.36, a**. The same process was identified by Kelemen et al., (1995) in experiments on fluid flow through porous media and was proposed as a mechanism by which dunite channels can form in mantle peridotites. The thickness of such channels is variable but can be as low as one centimetre (in examples from the Oman ophiolite, Braun and Kelemen, 2002), matching the thickness of the olivine absent band.

Similar texturally/mineralogically distinct bands in MOR plutonic rocks (discussed in **section 5.5.1**), interpreted to have formed via reactive melt flow, are also of approximately one centimetre width (Lissenberg and MacLeod, 2016, SanFillipo et al., 2020). Boulanger et al., 2021, reported similar < two centimetre thickness finer grained bands within MOR gabbros, which were attributed to channelized reactive melt flow. Hepworth et al., (2020) suggested that reactive melt percolation was responsible for the formation of millimetre to centimetre width Cr-spinel seams in cumulates of the Rum layered intrusion. These natural examples support the idea that reactive melt flow through mushes can produce centimetre width band-like features, such as the olivine absent band.

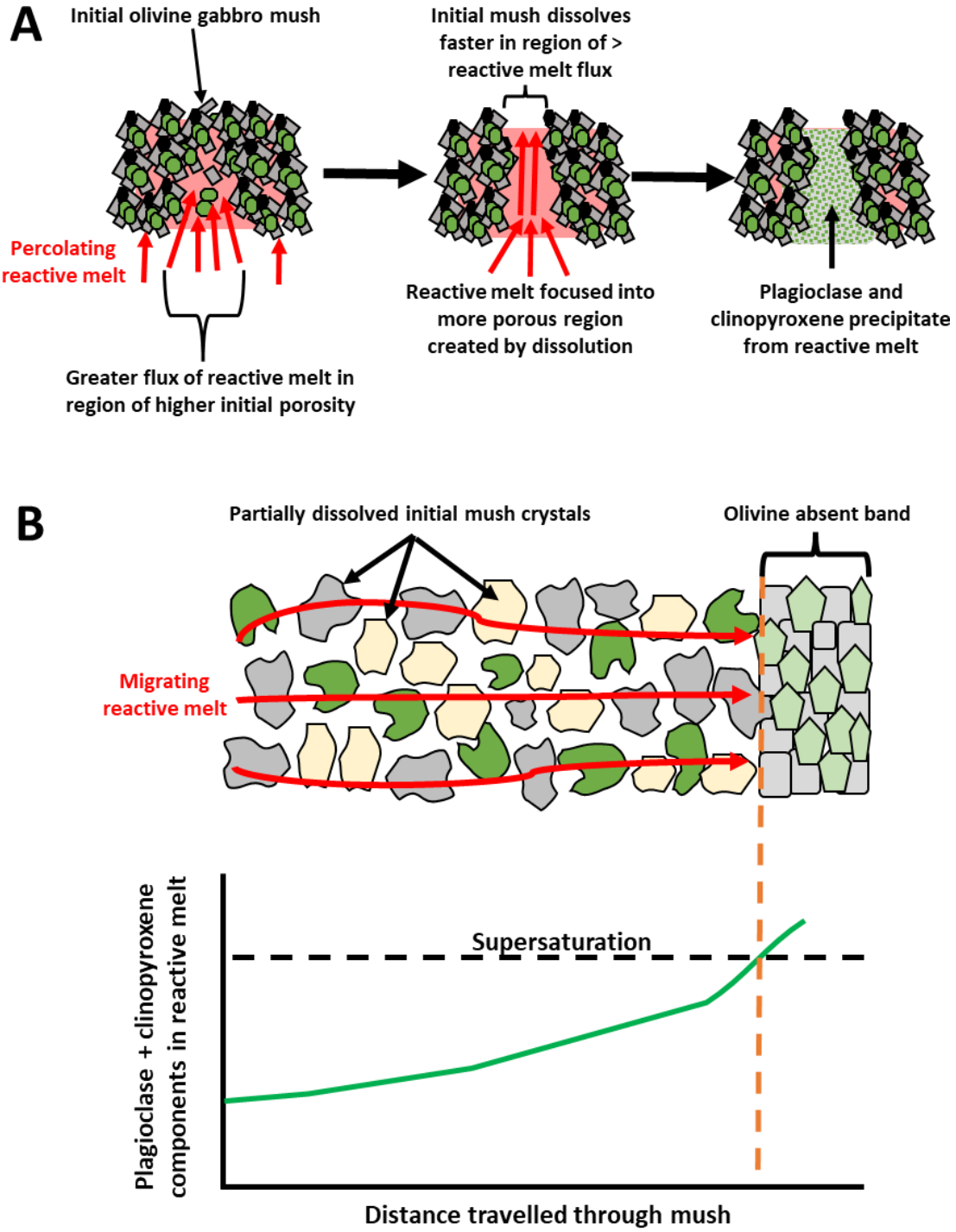

Figure 5.36: Schematics illustrating possible scenarios for formation of the olivine absent band in the banded Hbl-Ol gabbro**.**

A) Details of a potential mechanism by which reactive melts could have been focused into a centimetre wide region to form the olivine absent band. We assume that a small region of higher porosity was present in the initial olivine gabbro mush. The flux of reactive melt through the mush will have been greater in this higher porosity region. The greater flux of reactive melt caused faster dissolution of the mush in this region. The resulting feedback led to focusing of reactive melt flux into the more porous

region created by the enhanced dissolution. New plagioclase and clinopyroxene precipitated from the reactive melt.

B) Alternative mechanism for formation of the olivine absent band via reactive melt flow. Reactive melts percolating through an initial olivine gabbro mush partially dissolve mush crystals, including plagioclase and clinopyroxene. With increasing distance travelled through the mush, the amount of clinopyroxene and plagioclase components in the reactive melt increases due to partial dissolution of these phases. Once a critical threshold is reached, the migrating reactive melt becomes supersaturated in plagioclase and clinopyroxene and these phases are precipitated, forming the band.

An alternative mechanism to explain the olivine absent band is abrupt solidification of a migrating reactive melt due to supersaturation in certain components, in this case plagioclase and clinopyroxene (+ minor magnetite). This process is illustrated in **Figure 5.36, b** and based on the concepts outlined by Ortoleva et al., (1987a) for the formation of spatially periodic structures in rocks, such as bands consisting of a distinct mineral assemblage. In the illustrated scenario, as a reactive melt migrates through an olivine gabbro mush, it reacts with and partially dissolves pre-existing mush crystals, including plagioclase and clinopyroxene. This process enriches the migrating melt in plagioclase and clinopyroxene components (**Figure 5.36, b**), which build up as the melt travels further through the mush. Eventually, the melt becomes supersaturated in plagioclase and clinopyroxene components, causing it to precipitate these mineral phases (**Figure 5.36, b**), forming the olivine absent band. The space into which the band was precipitated may have been a more porous region of initial mush or created via dissolution. In reality, the process is likely to be much more complex, particularly in terms of the number of components involved. Nonetheless, the scenario presented in **Figure 5.36, b**, represents a conceptual model for how the olivine absent band could have formed via reactive melt flow. A similar process was proposed by Namur et al., (2013) to explain the formation of centimetre-decimetre thick bands composed of fine-grained mafic phases (olivine, clinopyroxene, oxides + minor plagioclase) hosted in gabbros of the Skaergaard intrusion. They suggested that infiltration of a primitive reactive melt into gabbroic mush led to partial dissolution of pre-existing mafic phases, resulting in supersaturation of the melt in mafic components and abrupt solidification of the liquid, forming the bands.

5.5.3.4 – Summary

Our geochemical modelling demonstrated that the trace element compositions of clinopyroxene and amphibole in St Vincent plutonic xenoliths, in isolation, cannot distinguish whether these phases were formed via FC or reactive melt flow. This result is most likely due to the significant uncertainty involved in selecting modelling parameters appropriate for a complex mushy magmatic system. Our simple geochemical models, which simulate only the trace element evolution of a melt during FC/AFC, may also not accurately reflect the complexities of magma chemical evolution in mushes. Our findings contrast with studies of mid-ocean ridge systems, where FC and AFC models produce significantly different results and mineral trace element compositions are often only explained via AFC/reactive melt flow (e.g. SanFillipo et al., 2020, Boulanger et al., 2021, Ferrando et al., 2021). Modelling of FC and AFC in mid-ocean ridge systems typically involves only three mineral phases (olivine, clinopyroxene, plagioclase), whereas St Vincent plutonic xenoliths demonstrate that additional phases including amphibole and orthopyroxene are involved in melt-mush reaction processes in an arc system. Therefore, distinguishing the effects of melt-mush reaction and FC on mineral and melt trace element compositions in an arc system may be complicated by the involvement of additional mineral phases.

Combining geochemical and textural constraints, our plutonic xenoliths demonstrate that magma chemical evolution in mushes in the St Vincent magma plumbing system involves both FC and reactions between melts and pre-existing mushes. Such reactions may occur via a "typical" reactive melt flow process of melt migration between crystal boundaries, or via "cannibalization" and disaggregation of mushes into larger intruding bodies of melt.

5.5.4 – Model for St Vincent magma plumbing system

Combining our interpretations for the petrogenesis of the plutonic xenolith samples with constraints from comparisons to experimental studies and previous literature, we propose the following model for the mushy magma plumbing system beneath St Vincent, illustrated in the schematic in **Figure 5.37**. The lower crust beneath St Vincent (at approximately 21-29 km depth, Melekhova et al., 2019) most likely consists of a deep crustal hot zone fed by primitive high Mg basalt magmas, which differentiate producing Ol + Cpx ± Sp cumulates (Tollan et al., 2012, Melekhova et al., 2015, this

study). Within the deep crustal hot zone, melt compositions can be modified by fractional crystallization (e.g. Müntener and Ulmer, 2018, Marxer et al., 2021), reaction with pre-existing cumulates (which may involve the crystallization of amphibole e.g. Bouilhol et al., 2015, Klaver et al., 2017, 2018) and mixing (e.g. Hildreth and Moorbath, 1988, Marxer et al., 2021).

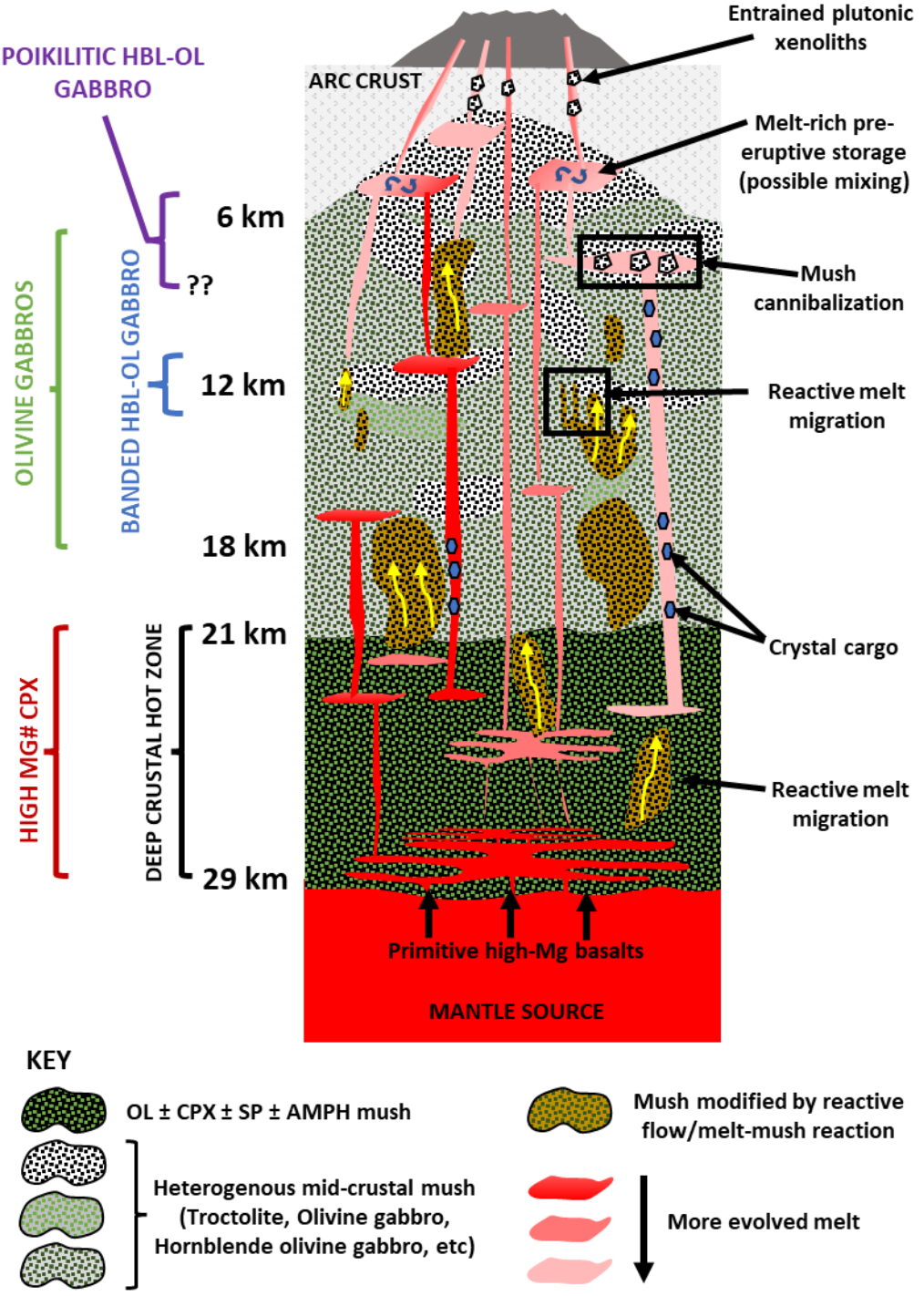

Figure 5.37: Schematic of the envisaged magma plumbing system beneath St Vincent, detailed in the text in **section 5.4.** Depth of base of crust beneath St Vincent (29 km) from Melekhova et al., 2019.

Depth of deep crustal hot zone (21-29 km) inferred from seismic velocity structure of St Vincent crust from Melekhova et al., (2019). The position within the crust at which each plutonic xenolith crystallized, based on constraints from comparison with experimental products (**Table 5.2, Appendix 5.1**), is shown on the left hand side.

A wide variety of melt compositions is generated in and ascends from the deep crustal hot zone into a texturally, mineralogically and chemically heterogenous mid-upper crustal mush zone. The majority of the ascending melts are basaltic and differentiate to basaltic andesite compositions via fractionation of (mainly) troctolite and olivine gabbro (olivine + plagioclase ± clinopyroxene ± magnetite) assemblages, at depths between ~18 and 6 km. Melts departing the deep crustal hot zone may entrain a crystal cargo from lower crustal cumulates and transport these crystals to shallower levels (e.g high Mg# CPX in poikilitic Hbl-Ol gabbro). In some regions of the mush, magma chemical evolution is mainly controlled by FC (e.g. olivine gabbro and Ol-CPX gabbro). Portions of pre-existing mid-crustal mush (formed via FC of earlier batches of melt) may be infiltrated by migrating reactive melts which interact with prior formed crystals. Reactive melt flow leads to localized changes in mineral assemblage, mineral chemistry and textures within the mush (e.g. banded Hbl-Ol gabbro), generating heterogeneity in mineral and melt compositions. Ascending batches of melt may also intrude and disaggregate pre-existing mushes, causing reactions that produce additional textural and mineral and melt chemical heterogeneity within the mid-upper crustal mush (e.g. poikilitic Hbl-Ol gabbro).

Melts are extracted from various regions of the chemically heterogenous mush and may stall in shallow (initially) melt-rich reservoirs prior to eruption, where phenocrysts in equilibrium with the final erupted melts crystallize. Melts extracted from the mush may entrain crystal cargoes (e.g. Fedele et al., 2021) and/or plutonic xenoliths from various levels or regions of the plumbing system. Melts and their crystal cargoes may also mix prior to eruption (e.g. Devine and Sigurdsson, 1983, Heath et al., 1998).

5.5.5 – Limitations of using plutonic xenoliths for interpreting the scales of mush processes

We set out to test to what extent magma chemical evolution in the mushy magma plumbing system beneath St Vincent is controlled by FC vs reactive melt flow. Two of four plutonic xenoliths analysed (the hornblende-olivine gabbros) contain textural and chemical evidence for reactions between melts and pre-existing mushes, in contrast to

the olivine gabbros which appear to record only FC. In this section, we use the term "melt-mush reaction" as opposed to "reactive melt flow" to encompass the varied reaction processes recorded by our plutonic xenoliths. We identified that textural features are an important first-order indicator of melt-mush reaction, which cannot always be distinguished from FC using mineral chemistry alone.

The distinctive textural features indicative of melt-mush reaction in the hornblende-olivine gabbros, including the olivine absent band and poikilitic amphibole and orthopyroxene replacing clinopyroxene/embayed olivine, are unique to these samples among the 17 St Vincent plutonic xenoliths initially considered for this study (**section 5.3.1,** also see **Chapter 3**). These textures are also distinct from those reported in the 17 St Vincent plutonic xenoliths studied petrographically by Tollan et al., (2012). A single St Vincent plutonic xenolith containing amphibole replacing clinopyroxene rims was recently reported, but not studied in detail, by Hu et al., (2022). The apparently rare occurrence of clear melt-mush reaction textures among the plutonic xenoliths raises the question as to how extensive melt-mush reaction processes are within the St Vincent magma plumbing system.

The small size (< 6 cm) of the plutonic xenoliths and lack of spatial context for these samples, which is unavoidable in an active arc system, hinders interpretation of the scales on which melt-mush reaction processes may operate within the St Vincent mush. Insights into scales of melt-mush reaction processes can be obtained from exposed crustal sections of extinct arcs, which provide access to plutonic rocks equivalent to the mushy plumbing systems of active arcs. The Pembroke Granulite in New Zealand represents deformed arc lower crustal gabbros (gabbroic gneiss) through which reactive melts migrated to feed a later phase of magmatism (Stuart et al., 2016, 2018). Reactive melt flow led to replacement of pyroxene in the gabbroic gneiss with amphibole (+ quartz and clinozoisite) along grain boundaries (Stuart et al., 2016, 2018). Relict pyroxene in the Pembroke granulite resembles rounded and embayed olivine in the poikilitic Hbl-Ol gabbro, but the replacement amphibole is often intergrown with quartz and doesn't clearly resemble amphibole in St Vincent plutonic xenoliths studied here. Evidence for reactive melt migration along grain boundaries in the Pembroke Granulite is found at the kilometre scale, though in some regions reactive melts were focused into < 20 m wide channels (Stuart et al., 2018).

In the Kohistan palaeo-arc lower crust, replacement of clinopyroxene with amphibole is observed in olivine-clinopyroxenites intruded by dykes of more evolved (hornblende gabbro and hornblende gabbronorite) composition (Bouilhol et al., 2015). Based on field relationships, the amphibole in the clinopyroxenites is interpreted to have formed due to reaction between invading melts (represented by the dykes) and the clinopyroxenite (Bouilhol et al., 2015). Contacts between amphibole and clinopyroxene resemble the ragged and irregular boundaries observed between these phases in the poikilitic Hbl-Ol gabbro, but poikilitic amphibole are not described. Kohistan clinopyroxenites also contain amphibole and orthopyroxene rims on rounded olivine (Bouilhol et al., 2015), resembling the poikilitic Hbl-Ol gabbro. Kohistan clinopyroxenites with amphibole replacing clinopyroxene and invaded by more evolved dykes are found over > 100 m regions of outcrop (Bouilhol et al., 2015).

In the Skaergaard intrusion, centimetre-decimetre thick bands composed predominantly of mafic phases, interpreted to have formed via melt-mush reaction, are found throughout hundreds of metres of gabbro outcrop (Namur et al., 2013). Similarly, centimetre thick fine-grained bands in mid-ocean ridge gabbros attributed to reactive melt flow are found across > 100 centimetres of core (Boulanger et al., 2021). These outcrop scale constraints suggest that melt-mush reaction processes can operate across broad regions of crystal mush, but that modification of textures and mineral phase assemblages and/or compositions can be highly localized within the affected region.

The presence of textural evidence for melt-mush reaction in a plutonic xenolith of a few centimetres in size is therefore dependent on whether it is derived from a portion of mush where textures and/or mineral assemblages and compositions have been modified by this process. This concept is illustrated in **Figure 5.38**, using the example of the banded Hbl-Ol gabbro. Hence, the low abundance of textures indicative of melt-mush reaction in St Vincent plutonic xenoliths (studied petrographically so far) does not necessarily imply that such processes are rare or of limited importance in the St Vincent plumbing system. Insights from arc crustal sections and other plutonic rocks described above suggest that interactions between migrating reactive melts and pre-existing crystal mushes could occur throughout broad (up to kilometre scale) regions of the St Vincent magma plumbing system.

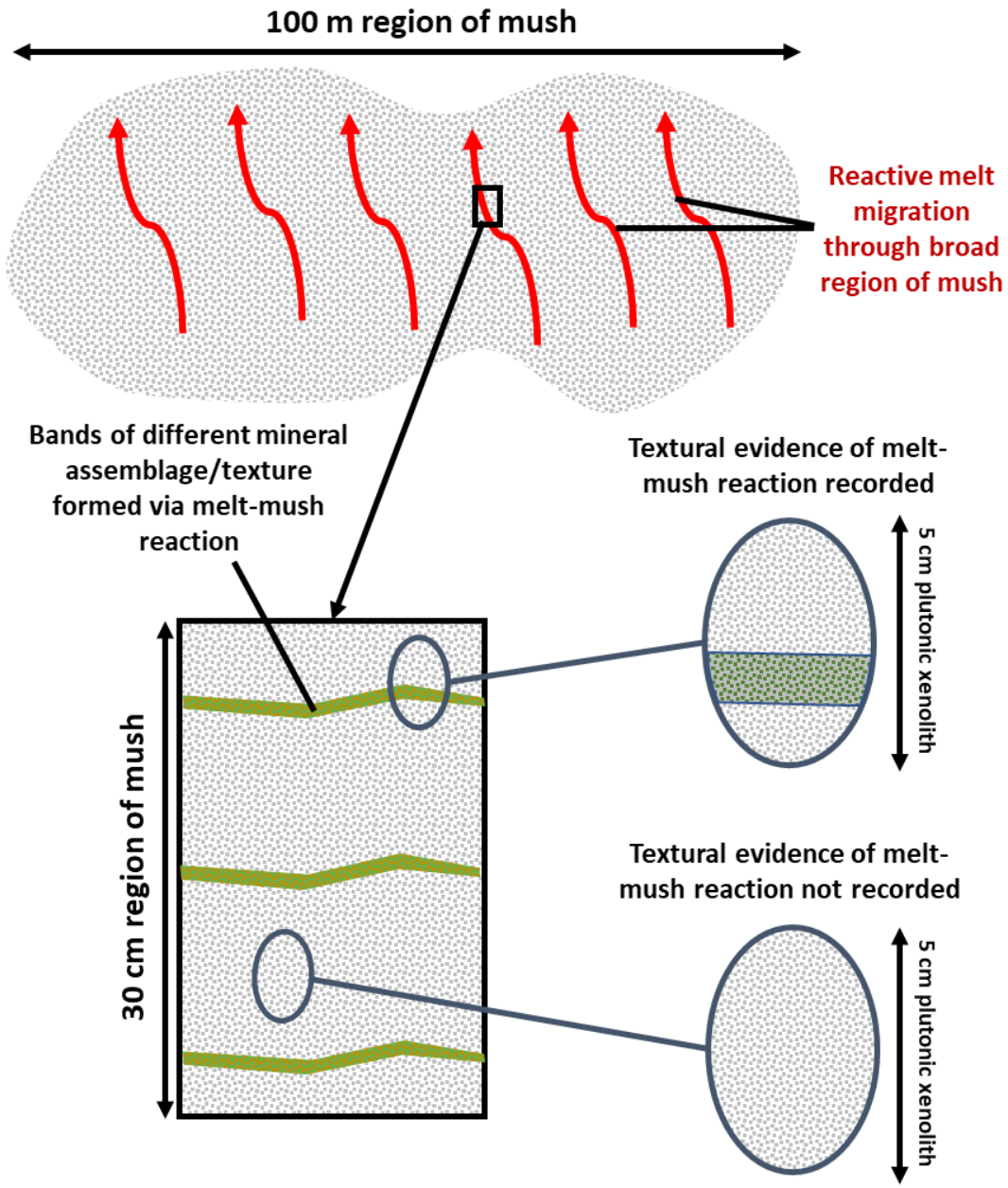

Figure 5.38: Schematic illustrating how the typically small (~ 5 cm) size of plutonic xenoliths affects the likelihood of these samples preserving melt-mush reaction textures.

In examples from arc crustal sections and mid-ocean ridges, precursory mushes such as clinopyroxenites and olivine gabbros are typically interpreted to have formed via (fractional) crystallization of newly emplaced melts, prior to modification via melt-mush reaction (e.g. Bouilhol et al., 2015, SanFillipo et al., 2020, Boulanger et al., 2021, Villares et al., 2022). In our proposed petrogenetic scenarios for the banded and poikilitic Hbl-Ol gabbros, we inferred that initial troctolite and olivine gabbro mushes were products of polybaric FC. These interpretations imply that both FC and melt-mush reaction contribute to magma chemical evolution over time in long-lived magma

plumbing systems. We envisage a scenario for the St Vincent magma plumbing system where, over time, various batches of melt undergo FC at different crustal levels to form new regions of mush, while other melts migrating through the system react with and modify earlier formed mushes (**section 5.5.4, Figure 5.37**). In this scenario, at any given time, magma chemical evolution is controlled by FC in some regions of the mushy magma plumbing system and melt-mush reaction in others. This scenario is broadly similar to the process modelled by Jackson et al., (2018), to simulate magma storage and evolution within crustal reservoirs. In their models, incremental intrusion and incomplete crystallization of sills forms a mush-dominated magma reservoir, within which buoyant melts migrate upwards and react with mushes formed by earlier sill intrusions.

Müntener and Ulmer, (2018) showed that high pressure (≥ 0.7 GPa) FC experiments reproduce major element compositions and assemblages of exposed arc lower crustal cumulates, suggesting that FC represents the dominant magma differentiation process in the lower crust. Furthermore, they suggested that additional FC coupled with reactive melt flow, crustal assimilation and mixing at shallower crustal levels explains the discrepancies between melt compositions produced by high pressure FC and arc lavas. Their proposal suggests that the relative influence of FC and melt-mush reaction processes on magma chemical evolution could vary with depth in the crust. This idea is supported by the banded and poikilitic Hbl-Ol gabbros, which are inferred to be derived from 6-12 km depth, suggesting that melt-mush reaction beneath St Vincent occurs predominantly in the mid-upper crust.

Combining evidence from plutonic xenoliths with insights from arc crustal sections, experimental petrology and numerical modelling, we show that both FC and melt-mush reaction influence magma chemical compositions in the St Vincent plumbing system, and suggest that both processes may be characteristic of arc volcanoes generally.

5.5.6 - Implications for interpreting the trace element compositions of arc lavas

Our observations from plutonic xenoliths suggest that trace element compositions of melts and crystals making up St Vincent lavas can be influenced by both FC and melt-mush reaction processes. In addition, our geochemical modelling highlighted that the effects of FC and melt-mush reaction on the trace element compositions of melts and crystals are not always distinguishable. These findings have major implications for the

interpretation of St Vincent lava trace element compositions. Previous studies have suggested that St Vincent lava whole-rock (WR) trace element compositions are consistent with FC, but our evidence from plutonic xenoliths suggests that contributions from melt-mush reaction also need to be considered.

To assess contributions of FC and melt-mush reaction to the REE compositions of St Vincent lavas, we calculated the REE compositions of melts in equilibrium with plutonic xenolith clinopyroxene and amphibole (using partition coefficients). The equilibrium melts are compared to St Vincent lava whole-rock (WR) compositions in **Figure 5.39**. Data for olivine hosted melt inclusions from St Vincent lapilli deposits (Bouvier et al., 2008, 2010) are also presented and discussed later.

Melts in equilibrium with clinopyroxene and amphibole from plutonic xenoliths recording FC (olivine gabbro and Ol-CPX gabbro) and melt-mush reactions (banded Hbl-Ol gabbro and poikilitic Hbl-Ol gabbro) overlap the lava compositional range (**Figure 5.39**). This result supports the idea that both FC and melt-mush reaction processes can contribute to the bulk trace element compositions of St Vincent lavas. It should be noted that St Vincent lavas are highly porphyritic (Heath et al., 1998, Fedele et al., 2021) and therefore may not represent melt compositions. In addition, some St Vincent eruptions such as the Yellow Tephra and 1979 contain evidence for mixing between basaltic and andesitic to dacitic magmas (Devine and Sigurdsson, 1983, Heath et al., 1998). These factors suggest that St Vincent lava WR compositions reflect the average of their constituent melts and crystals, which may have been influenced by FC and/or melt-mush reaction. In this scenario, the contribution of melt-mush reaction to lava WR trace element compositions is cryptic.

Our findings are consistent with other studies which have identified a role for melt-mush reaction in controlling arc lava and melt inclusion trace element compositions. Basaltic lavas from the Tatara-San Pedro complex, Chilean Andes, show wide ranges in both incompatible and compatible trace elements (Dungan and Davidson, 2004). This unusual geochemical signature was explained via contributions from melting/dissolution of plutonic xenolith mineral phases in addition to entrainment of variable quantities of disaggregated plutonic xenolith minerals as crystal cargoes (Dungan and Davidson, 2004). In another example, Reubi and Blundy (2008) suggested that melt inclusions in lavas from Colima, Mexico with unusually enriched

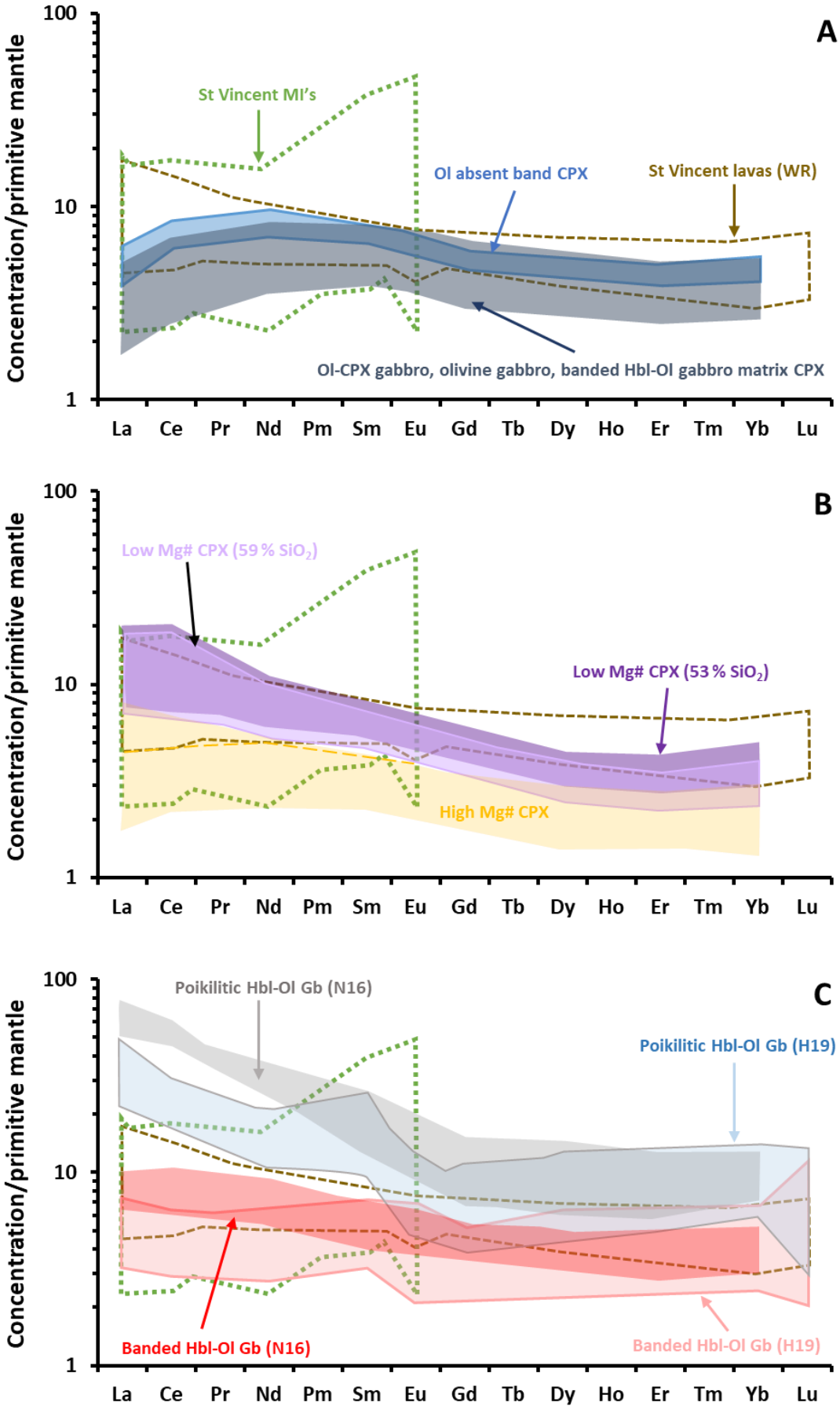
A
Concentration/primitive mantle
100
10
1
St Vincent MI's
Ol absent band CPX
St Vincent lavas (WR)
Ol-CPX gabbro, olivine gabbro, banded Hbl-Ol gabbro matrix CPX
La Ce Pr Nd Pm Sm Eu Gd Tb Dy Ho Er Tm Yb Lu
B
Concentration/primitive mantle
100
10
1
Low Mg# CPX (59 % SiO2)
Low Mg# CPX (53 % SiO2)
High Mg# CPX
La Ce Pr Nd Pm Sm Eu Gd Tb Dy Ho Er Tm Yb Lu
C
Concentration/primitive mantle
100
10
1
Poikilitic Hbl-Ol Gb (N16)
Poikilitic Hbl-Ol Gb (H19)
Banded Hbl-Ol Gb (N16)
Banded Hbl-Ol Gb (H19)
La Ce Pr Nd Pm Sm Eu Gd Tb Dy Ho Er Tm Yb Lu

Figure 5.39: Primitive mantle normalized REE patterns for **calculated melts in equilibrium with A)** banded Hbl-Ol gabbro, olivine gabbro and Ol-CPX gabbro clinopyroxene**, B)** poikilitic Hbl-Ol gabbro clinopyroxene and **C)** amphibole from both the banded Hbl-Ol gabbro and poikilitic Hbl-Ol gabbro. The ranges of calculated equilibrium melt compositions are shown by the coloured fields. The melts in equilibrium with clinopyroxene and amphibole were calculated using partition coefficients from the following sources: banded Hbl-Ol gabbro, olivine gabbro and Ol-CPX gabbro clinopyroxene – Brophy (2008) at 53 wt % SiO_2, poikilitic Hbl-Ol gabbro high Mg# CPX – Brophy (2008) at 49 wt % SiO_2, poikilitic Hbl-Ol gabbro low Mg# CPX – Brophy (2008) at 53 and 59 wt % SiO_2 (see labels in **B**), amphibole – Nandedkar et al., (2016) at 51 wt % SiO_2 (labelled as N16 on plot). See **Appendix 5.2** for partition coefficient values. An additional set of equilibrium melts for amphibole were calculated using the trace element partitioning scheme of Humphreys et al., (2019b), labelled as H19 on plot. The calculated equilibrium melt compositions are compared with primitive mantle normalized REE WR data for St Vincent lavas (Heath et al., 1998, Plank, 2005, DuFrane et al., 2009, Fedele et al., 2021) and LREE data for St Vincent melt inclusions (MI's) (Bouvier et al., 2010). Primitive mantle normalizing values from Palme and O'Neill (2003).

K and large ion lithophile element (LILE) concentrations could be explained by assimilation of gabbroic or amphibole-plagioclase-biotite-magnetite cumulates by a dacitic melt.

Our plutonic xenolith equilibrium melt compositions record much greater trace element chemical heterogeneity in the St Vincent magma plumbing system than is apparent from St Vincent lavas (**Figure 5.39**). This observation is consistent with melt inclusions in plutonic xenoliths from Statia in the northern LAA which record considerably wider compositional diversity than Statia lavas (Cooper et al., 2019). Combined, these observations from LAA plutonic xenoliths suggest that the chemical compositions of arc lavas do not necessarily reflect the compositional diversity of melts in the magma plumbing systems from which they are derived. Hence, attempting to interpret magma plumbing system processes using chemical compositions of arc lavas in isolation is likely to result in a simplified picture which does not truly reflect the complexity of magma chemical evolution in mush-dominated systems.

We interpret the high Mg# CPX population in the poikilitic Hbl-Ol gabbro as having formed during the early stages of magma differentiation beneath St Vincent in the lower crust. Calculated melts in equilibrium with these clinopyroxene therefore provides insights into the compositions of primitive melts in the St Vincent plumbing system. The calculated equilibrium melts extend to lower REE contents than any St Vincent lavas (**Figure 5.39, b**). The WR chemical compositions of primitive, high

MgO lavas in arc settings, including those found on St Vincent, are often inferred to be minimally affected by crustal differentiation processes and have been used to assess arc mantle source compositions (e.g. Plank, 2005, Bezard et al., 2015 a,b). The higher REE contents of St Vincent lavas (including the highest MgO lavas) compared to the high Mg# CPX equilibrium melts (**Figure 5.39**) suggests that high MgO lavas do not represent the most primitive melts in the plumbing system and may have experienced modification within the crust. It is possible that such lavas could be derived from our proposed deep crustal hot zone beneath St Vincent, where melt compositions may be altered by FC, melt-mush reaction or mixing (**section 5.5.4**). St Vincent high MgO lavas may also have entrained crystal cargoes from the hot zone (**section 5.5.4, Figure 5.37**) or shallower regions of mush on ascent, which could influence WR compositions. Hence, it is unlikely that WR trace element compositions of even high MgO St Vincent lavas accurately reflect their mantle source, unless some form of crustal processing can be ruled out, or its impact on WR composition accurately determined. Assuming that St Vincent represents a typical arc magma plumbing system, we suggest that arc lavas generally are unlikely to have avoided some degree of crustal processing and therefore may not retain trace element signatures of their mantle source regions.

Bouvier et al., (2010) used trace element compositions of olivine hosted melt inclusions to study the St Vincent mantle source. These melt inclusions have highly diverse L-MREE compositions that extend beyond the range of the lavas (**Figure 5.39**). Bouvier et al., (2010) suggest that the trace element compositions of these melt inclusions reflect source processes. The melt inclusions are trapped in Fo_{83-90} olivine, which overlaps with olivine compositions from exposed arc lower crustal sections (e.g. Bouilhol et al., 2015) and olivine produced in experiments by Melekhova et al., (2015) and Marxer et al., (2021) at high pressures equivalent to our proposed deep crustal hot zone beneath St Vincent. It is therefore possible that the olivine hosts to the melt inclusions could be derived from a crystal mush, in a deep crustal hot zone (or potentially shallower) and represent an entrained crystal cargo in the lava in which they were erupted. The similar L-MREE compositional ranges of the melt inclusions and equilibrium melts recorded by our plutonic xenoliths (**Figure 5.39**) suggests that the range of REE contents in the melt inclusions could instead reflect melt compositional variations in mushes in which their host crystals were formed. This concept is supported by melt inclusions from Statia (northern LAA) plutonic xenoliths which

show diverse trace element contents (Cooper et al., 2019). If melt inclusion bearing crystals are derived from a mushy plumbing system, potential contributions from crustal differentiation processes, including FC and melt-mush reaction, need to be carefully accounted for to use melt inclusion trace element compositions to study mantle source processes.

5.6 - Conclusions

In this study, we use plutonic xenoliths to assess whether the chemical evolution of magmas in the mushy magma plumbing system beneath St Vincent, Lesser Antilles arc, is controlled by FC or reactive melt flow/melt-mush reaction.

The textures and mineral chemistry of olivine gabbro xenoliths are consistent with crystallization during mid-upper crustal stages (6-18 km depth) of polybaric FC from a primitive basaltic magma. In contrast, hornblende-olivine gabbros from the mid-upper crust (6-12 km depth) display textural and chemical evidence for interaction and reactions between melts and mushes. Using geochemical modelling, we showed that the trace element compositions of plutonic xenolith clinopyroxene and amphibole in isolation cannot clearly distinguish the process (FC or melt-mush reaction) by which they were formed. This finding highlights the importance of textural observations for identifying melt-mush reaction processes in plutonic xenoliths/plutonic rocks. Textures in hornblende-olivine gabbros, supported by mineral molar element ratios and trace element chemistry, suggest that melt-mush reaction may occur via percolation of reactive melts between crystal boundaries in a mush (typical “reactive melt flow”) or by “cannibalization” and disaggregation of mushes into intruding bodies of melt.

Our observations from plutonic xenoliths, combined with insights into equivalent processes from extinct plutonic systems, suggest that over time, both FC and reactive melt flow/melt-mush reactions influence the chemical compositions of magmas in the St Vincent plumbing system. This conclusion is supported by melt compositions in equilibrium with plutonic xenolith clinopyroxene and amphibole which suggest that melts influenced by both FC and melt-mush reaction contribute to trace element compositions of St Vincent lavas. Potential contributions from melt-mush reaction processes are cryptic and only uncovered via (predominantly textural) evidence from our studied plutonic xenoliths.

Using St Vincent as a case study, we suggest that both FC and reactive melt flow/melt-mush reactions influence the trace element compositions of magmas in mushy plumbing systems beneath volcanic arcs generally. This conclusion has important implications for interpreting trace element compositions of arc lavas and melt inclusions, in particular their use in understanding mantle source processes. Even primitive arc lavas may have been influenced by melt-mush reactions or entrainment of crystal cargoes from mushes and hence should not be assumed to represent mantle sources unless these processes can be ruled out. Similarly, if host crystals to melt inclusions are derived from mushes, melt inclusion trace element compositions will reflect magma chemical evolution processes in mushes as opposed to preserving source characteristics.

Chapter 5 Appendices

Appendix 5.1 - Pressure-Temperature-melt H_2O conditions of St Vincent plutonic xenolith crystallization

Understanding the pressures and temperatures at which plutonic xenoliths formed, along with the composition and water content of the melts from which they crystallized, provides valuable information on magma storage conditions in the St Vincent magma plumbing system. A common approach for constraining these intensive variables for plutonic xenoliths is to compare the mineral assemblages and mineral phase compositions to those produced in experiments run at appropriate conditions and using appropriate starting materials (e.g. Stamper et al., 2014, Cooper et al., 2016, 2019, Camejo-Harry et al., 2018, Melekhova et al., 2019). The run conditions (pressure, temperature, melt starting composition and H_2O content) of experiments that produced close matches to the plutonic xenolith assemblages and mineral chemistry can then be used to infer the conditions under which the samples formed.

To estimate the conditions under which the plutonic xenoliths in this study formed, we consider experiments using starting compositions including a high Mg basalt from St Vincent (Melekhova et al., 2015), high Al basalt and andesite from Guadeloupe (Pichavant et al., 2018) and basaltic andesite from Martinique (Pichavant et al., 2002). We refer to basaltic starting compositions as either high Mg basalt (HMB), low Mg basalt (LMB) and high-Al basalt (HMB), using the definitions of Melekhova et al., (2015), where HMB = MgO > 10 wt %, LMB = MgO > 6 wt % and HAB = MgO < 6 wt %, Al_2O_3 > 19 wt %. We also consider fractional crystallization experiments designed to simulate differentiation of hydrous arc magmas within the crust. These include the experiments of Nandedkar et al., (2014) conducted at constant pressure (0.7 GPa) and Marxer et al., (2021) which were conducted over a range of pressures and aim to replicate polybaric fractional crystallization. The starting compositions of these experiments all lie on the liquid line of descent defined by St Vincent lavas and melt inclusions.

The experiments providing the best match to each plutonic xenolith sample and the inferred conditions under which each sample formed are summarized in **Table 5.2** of the main text and discussed in detail below.

A5.1.1 - Olivine gabbro and Ol-CPX gabbro

The best experimental matches to the olivine gabbro and Ol-CPX gabbro samples using LAA starting materials come from experiments on a HAB from Guadeloupe (Pichavant et al., 2018). Experimental runs L2 and L4, with run conditions of 975-1000°C, approximately 0.2 GPa, 5.9-6.3 % H_2O produce plagioclase with An 85-88, olivine with Fo 72.4-74, and clinopyroxene with Mg# 75, which overlap or are close to olivine gabbro and Ol-CPX gabbro mineral phase compositions. A slightly better overlap is achieved by fractional crystallization experiments of Marxer et al., (2021), with experiments FM93 and FM134 using a HAB starting material with 3.73 wt % H_2O, run at 1050°C and 0.6 GPa, crystallizing plagioclase with An 90, olivine with Fo 76-78 and clinopyroxene with Mg# 75-79. Assuming 0.1 GPa equates to approximately 3 km depth, these pressures suggest crystallization at 6-18 km depth within the 29 km deep crust beneath St Vincent (Melekhova et al., 2019). These constraints suggest that the olivine gabbro samples formed from hydrous HAB melts at temperatures between 975-1050 °C in the mid-upper crust.

A5.1.2 - Banded Hbl-Ol gabbro

The compositions of plagioclase, olivine and clinopyroxene in the banded Hbl-Ol gabbro are similar to the olivine gabbro and Ol-CPX gabbro, extending to slightly lower plagioclase An and clinopyroxene Mg# in the olivine absent band. A hornblende-olivine gabbro assemblage (olivine-plagioclase-clinopyroxene-amphibole) was produced by experiment HAB7 from Pichavant et al., (2002), using a Martinique basaltic andesite starting composition with 6.8 wt % H_2O. This experiment was run at 1000°C, 0.4 GPa and crystallized plagioclase with An 84, olivine with Fo 69, CPX with Mg# 72 and amphibole with Mg# 68. These mineral phase compositions are similar to those of the sample, though olivine Fo and plagioclase An are slightly higher in the banded Hbl-Ol gabbro. A hornblende-olivine gabbro assemblage was also

produced by experiment FM129 from Marxer et al., (2021), using a HAB starting composition with 4.6 wt % water, run at 990°C, 0.4 GPa. Mineral compositions produced by the experiment were close to those of the sample, with slightly lower Fo in the experimental olivine**.** These constraints imply that the banded Hbl-Ol gabbro crystallized from a hydrous HAB or basaltic andesite melt at approximately 1000°C and 12 km depth. Alternatively, if the amphibole and olivine absent band formed through melt-mush reaction and therefore are not representative of the primary mineral assemblage, the mineral phase compositions overlap the olivine gabbro and Ol-CPX gabbro implying crystallization under similar conditions.

A5.1.3 - Poikilitic Hbl-Ol Gabbro

The complex mineral assemblage (olivine, plagioclase, clinopyroxene, orthopyroxene, amphibole, apatite) of the poikilitic Hbl-Ol gabbro was not reproduced experimentally in any of the studies discussed above. A lack of experimental counterparts for this assemblage was also noted for a plutonic xenolith containing the same mineral phases and texturally similar poikilitic amphibole from St Kitts (Melekhova et al., 2017). Experiments that reproduced some of the mineral phase associations seen in the sample are discussed below.

The high Mg# CPX population are chemically distinct (higher Mg#, lower incompatible trace element and REE contents) from clinopyroxene in the other plutonic xenolith samples, implying crystallization under different conditions. Clinopyroxene with similar Mg# (85-87) were produced in experiments by Melekhova et al., (2015) using a St Vincent HMB starting material with 2.3-4.5 wt % H_2O, run at 1100-1200°C and 1 GPa. High Mg # (83-85) clinopyroxene were also produced by Marxer et al., (2021) using a LMB starting material with 3-3.5 wt % H_2O, at 1080-1110°C and 0.8 GPa. In these experiments, clinopyroxene co-crystallized with high Fo (typically > 80) olivine and/or spinel. Fractional crystallization experiments from Nandedkar et al., (2014) run at 1070-1150°C, 0.7 GPa, using HMB and LMB starting materials with 3.6-5.1 wt % H_2O also produced clinopyroxene Mg# 84-88 plus high Fo olivine.

These constraints imply that the high Mg# CPX population crystallized at high temperatures and pressures corresponding to lower crustal depths (21-30 km). Plutonic xenoliths with a clinopyroxene-olivine-spinel assemblage and high Mg# clinopyroxene

(Mg# ~88) have been found in Grenada in the LAA (Stamper et al., (2014) and olivine-clinopyroxene (Mg# 81-89) ± amphibole plutonic xenoliths have been reported from the Aleutian arc (Yogodzinski and Kelemen, 2007). Clinopyroxene with similarly high Mg# have also been found in cumulates of exposed lower arc crustal sections (e.g. Bouilhol et al., 2015, Otamendi et al., 2016). The presence of high Mg# clinopyroxene alongside olivine ± spinel in other plutonic xenoliths and in arc lower crust is in good agreement with the experimental constraints and further supports a lower crustal origin for this crystal population.

The Fo contents of the olivine and high An plagioclase cores in the poikilitic Hbl-Ol gabbro overlap with the olivine gabbro and Ol-CPX gabbro, suggesting that these phases could have formed under similar conditions. Experiments on HAB and andesite starting materials from Guadeloupe (Pichavant et al., 2018), with 5.8 and 5.1 wt % H_2O respectively, produced orthopyroxene (Mg# 73)-plagioclase (An 78)-amphibole (Mg# 69) (HAB starter) and orthopyroxene (Mg# 74)-plagioclase (An 64)-clinopyroxene (Mg# 76) (andesite starter) assemblages that closely match the sample mineral phase compositions. In the case of plagioclase, these experimental An compositions lie within the wide range observed in the poikilitic Hbl-Ol gabbro. These experiments were run at 950°C, approximately 0.2 GPa (HAB starter) and 875°C, approximately 0.15 GPa (andesite starter). The presence of orthopyroxene in these lower pressure experiments matches the findings of Marxer et al., (2021) from their fractional crystallization experiments, where orthopyroxene was only produced at 0.2 GPa. Hence, poikilitic Hbl-Ol gabbro plagioclase, low Mg# CPX, orthopyroxene and amphibole compositions are consistent with crystallization from HAB-andesite melts at approximately 6 km depth.

Appendix 5.2 – Table of D Values/partition coefficients

The following table (**Table A5.1**) shows the rare earth element (REE) partition coefficients used for each mineral phase in the FC and AFC models outlined in **section 5.5.2** of the main text. A melt SiO_2 value was assigned to each model/step in each model. The partition coefficients used for each model/step are those listed under the relevant melt SiO_2 value in **Table A5.1**. For example, at step 3 of the "OL GABBRO POLYBARIC FC" model (**Table 5.4** of main text), the partition coefficients used for olivine, clinopyroxene, plagioclase and magnetite are those from Brophy (2008) listed under 53 % SiO_2 in **Table A5.1**.

Mineral phase	Source publication	Element	Melt SiO_2 47	49	51	53	59	62
CPX	Brophy (2008)	**La**	0.102	0.111	0.117	0.122	0.133	0.145
		Ce	0.162	0.172	0.179	0.184	0.203	0.225
		Nd	0.345	0.351	0.357	0.364	0.411	0.465
		Sm	0.577	0.584	0.592	0.605	0.697	0.797
		Dy	0.800	0.867	0.929	0.987	1.184	1.334
		Er	0.663	0.777	0.880	0.971	1.189	1.304
		Yb	0.431	0.563	0.688	0.797	0.996	1.051
Amph	Brophy (2008)	**La**	0.065	0.080	0.094	0.108	0.152	0.180
		Ce	0.080	0.111	0.143	0.176	0.266	0.312
		Nd	0.114	0.190	0.284	0.386	0.658	0.764
		Sm	0.151	0.281	0.457	0.661	1.209	1.390
		Dy	0.218	0.409	0.672	0.983	1.860	2.158
		Er	0.240	0.405	0.615	0.856	1.558	1.839
		Yb	0.244	0.343	0.456	0.580	0.974	1.178
Plag	Brophy (2008)	**La**	0.150	0.139	0.130	0.124	0.121	0.126
		Ce	0.112	0.107	0.105	0.103	0.108	0.115
		Nd	0.066	0.067	0.069	0.072	0.083	0.091
		Sm	0.042	0.044	0.047	0.050	0.062	0.069
		Dy	0.022	0.023	0.023	0.025	0.030	0.035
		Er	0.018	0.018	0.017	0.017	0.020	0.023
		Yb	0.017	0.014	0.013	0.012	0.012	0.014
OPX	Brophy (2008)	**La**	0.001	0.001	0.001	0.002	0.005	0.011

		Ce	0.001	0.001	0.002	0.002	0.008	0.017
		Nd	0.001	0.001	0.002	0.004	0.017	0.035
		Sm	0.001	0.002	0.004	0.007	0.033	0.067
		Dy	0.006	0.010	0.018	0.029	0.109	0.187
		Er	0.019	0.029	0.044	0.065	0.178	0.269
		Yb	0.080	0.100	0.125	0.153	0.272	0.352
Ol	Brophy (2008)	**La**	0.000	0.000	0.000	0.000	0.000	0.000
		Ce	0.000	0.000	0.000	0.000	0.000	0.000
		Nd	0.000	0.000	0.000	0.000	0.000	0.000
		Sm	0.000	0.000	0.000	0.000	0.000	0.000
		Dy	0.004	0.004	0.004	0.004	0.004	0.004
		Er	0.010	0.010	0.010	0.010	0.010	0.010
		Yb	0.022	0.022	0.022	0.022	0.022	0.022
Magnetite	Brophy (2008)	**La**	0.000	0.001	0.002	0.006	0.066	0.159
		Ce	0.000	0.001	0.003	0.007	0.071	0.170
		Nd	0.001	0.001	0.004	0.009	0.082	0.194
		Sm	0.001	0.002	0.005	0.012	0.095	0.218
		Dy	0.002	0.004	0.009	0.019	0.125	0.262
		Er	0.002	0.005	0.012	0.024	0.143	0.282
		Yb	0.003	0.007	0.014	0.030	0.162	0.298
CPX	Bedard (2014)	**La**	0.062	0.073	0.085	0.099	0.157	0.199
		Ce	0.110	0.132	0.157	0.187	0.319	0.416
		Nd	0.245	0.285	0.331	0.385	0.605	0.758
		Sm	0.339	0.394	0.458	0.532	0.835	1.046
		Dy	0.509	0.587	0.677	0.781	1.198	1.484
		Er	0.560	0.633	0.717	0.811	1.173	1.412
		Yb	0.503	0.568	0.641	0.724	1.041	1.248
Amph	Nandedkar et al (2016)	**La**			0.129		0.190	0.279
		Ce			0.237		0.406	0.656
		Nd			0.628		1.121	1.827
		Sm			1.125		2.115	3.312
		Dy			1.796		3.547	5.212
		Er			1.744		3.350	5.396
		Yb			1.418		2.852	4.685
Amph	Nandedkar et al (2016)	**Nb**			0.316		0.492	0.666

Table A5.1: Partition coefficients used in the geochemical models outlined in **section 5.5.2** of the main text**.**

Figure A5.1 shows an example of how the partition coefficients calculated/taken from different sources for clinopyroxene and amphibole vary at a melt SiO_2 content of 59 wt %, corresponding to step 3 of the "POIKILITIC GABBRO POLYBARIC FC" model (**Table 5.5**, main text).

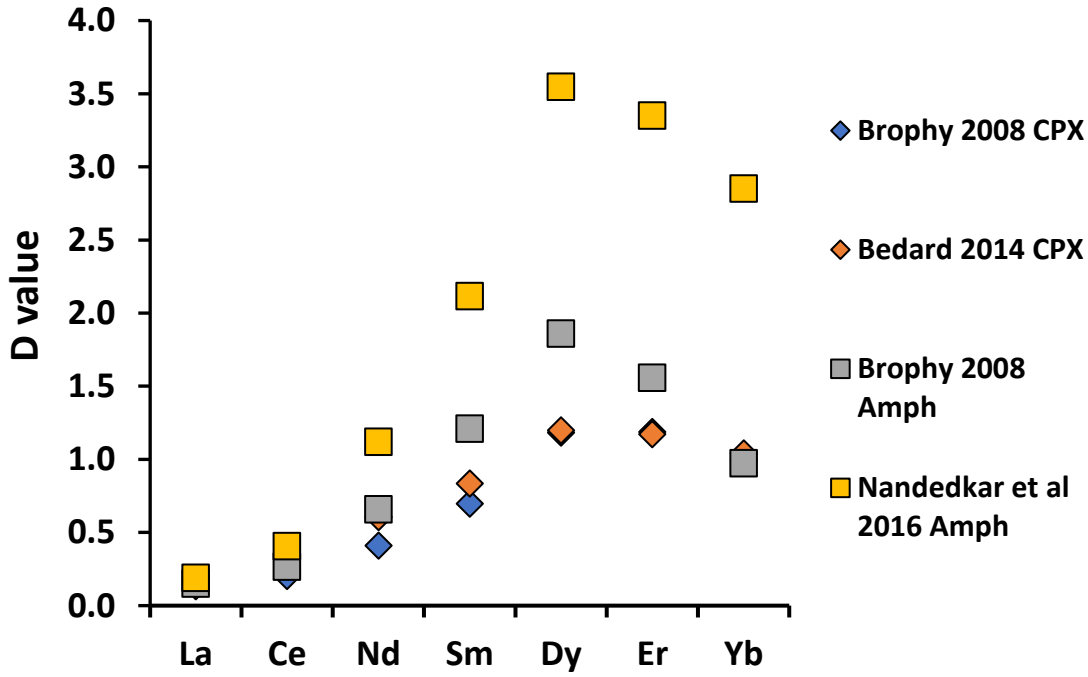

Figure A5.1: Variation in partition coefficients from different source publications (Brophy, 2008, Bedard, 2014 and Nandedkar et al., 2016, see above table and main text) for clinopyroxene and amphibole at a melt SiO_2 content of 59 wt %.

Appendix 5.3 – Alternative FC models

This appendix presents alternative versions of the FC models discussed in the main text in **sections 5.5.2 and 5.5.3**. These alternative FC models demonstrate the effect of changing the initial melt composition parameter. The initial melt compositions used in our alternative models are listed in **Table A5.2**.

	La	Ce	Nd	Sm	Dy	Er	Yb
V37-201	3.55	9.51	7.20	2.18	2.89	1.67	1.50
Adjusted primitive basaltic magma 1	0.75	2.66	2.89	1.04	1.26	0.80	0.84
Adjusted primitive basaltic magma 2	3.46	7.42	4.48	1.24	1.27	0.77	0.96

Table A5.2: Initial melt compositions used in alternative FC models. "V37-201" is a WR basaltic (47 wt % SiO_2) St Vincent lava composition from Plank (2005). "Adjusted primitive basaltic magma 1 and 2" represent theoretical initial melt compositions.

A5.3.1 - Alternative "OL GABBRO POLYBARIC FC" model

This alternative version of the "OL GABBRO POLYBARIC FC" model described in the main text illustrates the effect of changing the initial melt composition at Step 1 on the model outcome – all other parameters were kept identical. The adjusted initial melt composition is shown in **Table A5.2** ("adjusted primitive basaltic magma 1") and has lower La, Ce, and Nd (but identical Sm, Dy, Er, Yb) than the initial melt composition used for the original model (**Table 5.3, main text**). Using this alternative initial melt composition, the LREE (La, Ce, Nd) contents of the most LREE depleted clinopyroxene from the Ol-CPX gabbro and banded Hbl-Ol gabbro matrix are reproduced (**Figure A5.2**), in contrast to the initial version of the model (**Figure 5.28, main text**). Basaltic melts with low LREE contents similar to "adjusted primitive basaltic magma 1" have been reported from other intra-oceanic arc settings (e.g. Kent and Elliot, 2002), which suggests that this theoretical initial melt composition is plausible.

A5.3.2 - Alternative FC model for poikilitic Hbl-Ol gabbro high Mg# CPX

In the main text, the REE compositions of the high Mg# CPX population from the poikilitic Hbl-Ol gabbro were modelled using Step 1 of the "OL GABBRO POLYBARIC FC" model. This alternative model illustrates the effect of changing the initial melt composition on the model outcome – all other parameters were kept

identical. The adjusted initial melt composition is shown in **Table A5.2** ("adjusted primitive basaltic magma 2"). Using this initial melt composition, the most LREE enriched high Mg# CPX compositions were reproduced after 40 % Ol + Cpx + Sp fractionation (**Figure A5.3**). The REE composition of clinopyroxene in equilibrium with this alternative initial melt composition falls within the range of the high Mg# CPX data (**Figure A5.3**). Hence, it can be inferred that this theoretical initial melt composition represents a plausible melt involved in the genesis of the high Mg# CPX.

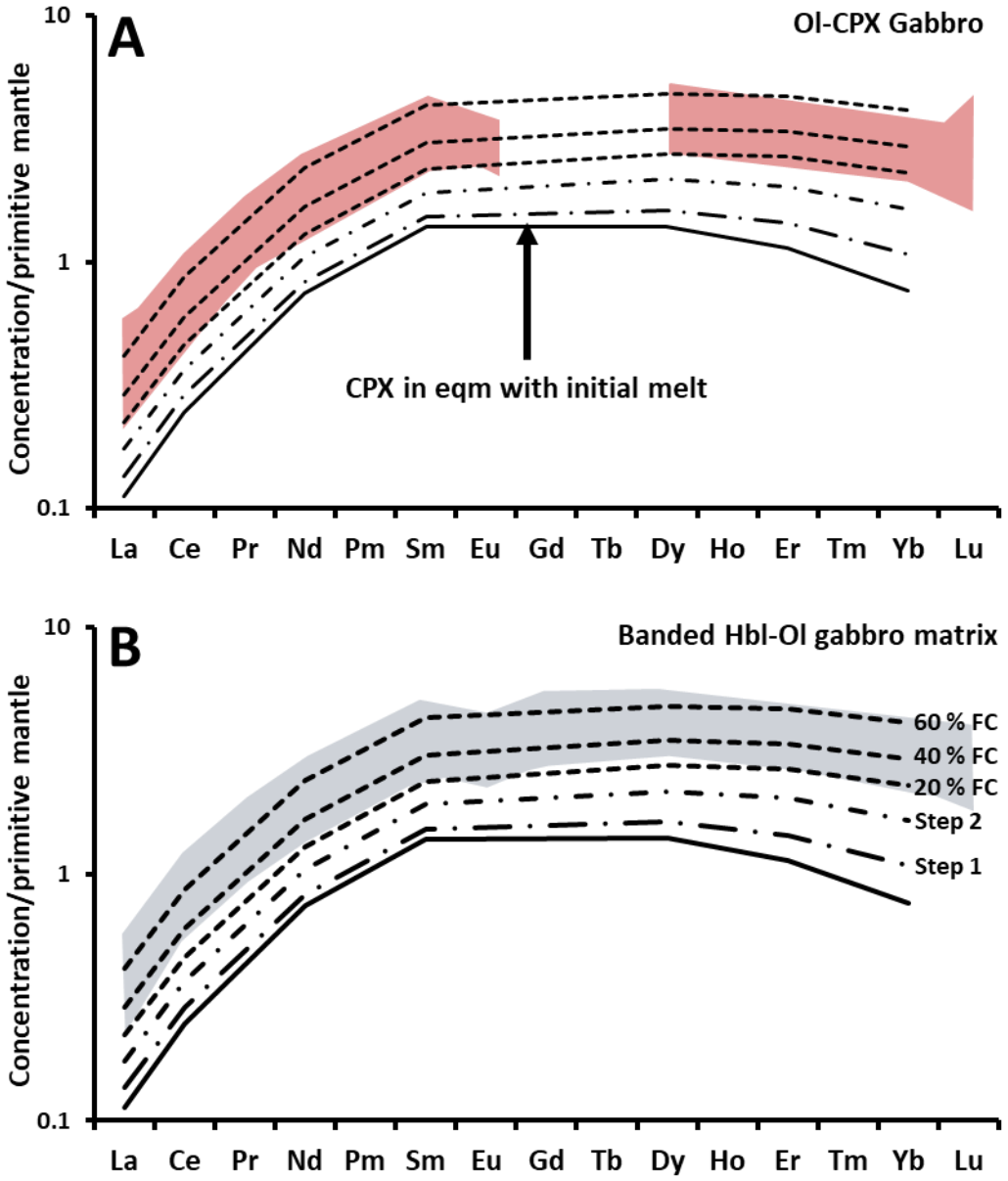

Figure A5.2: Primitive mantle normalized REE patterns of clinopyroxene from **A)** Ol-CPX gabbro and **B)** banded Hbl-Ol gabbro matrix, shown by the shaded fields. The data are compared with the **clinopyroxene compositions in equilibrium with the melt (solid and black dashed lines)** at each step of the "alternative OL GABBRO POLYBARIC FC" model using the "adjusted primitive basaltic

magma 1" initial melt composition. For the third step, the composition of clinopyroxene in equilibrium with the melt after 20, 40 and 60 % fractional crystallization is shown. Primitive mantle normalizing values from Palme and O'Neill (2003).

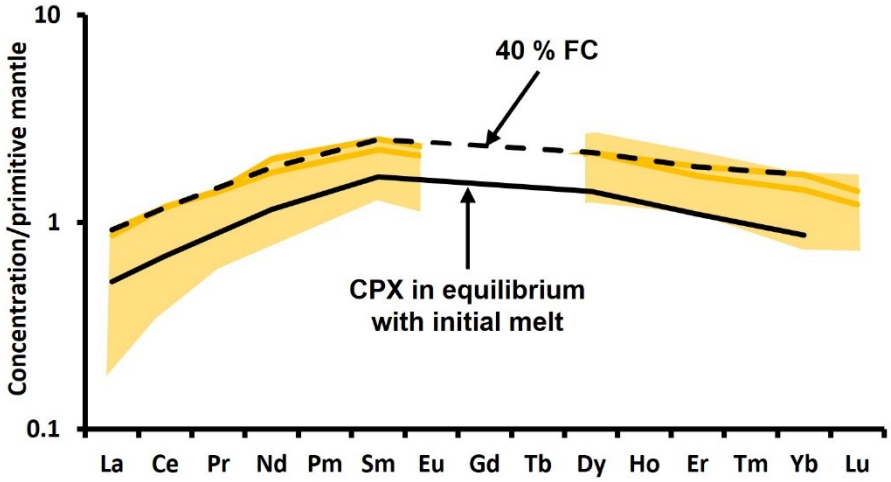

Figure A5.3: Primitive mantle normalized REE patterns of the high Mg# CPX population from the poikilitic Hbl-Ol gabbro (yellow shaded field) compared with modelled clinopyroxene composition (after 40 % crystallization of Ol + Cpx + Sp) when using an alternative initial melt composition for step 1 of the "OLIVINE GABBRO POLYBARIC FC" model. The dark yellow lines show the REE profiles of the most LREE enriched clinopyroxene from the high Mg# CPX population. Primitive mantle normalizing values from Palme and O'Neill (2003). The composition of clinopyroxene in equilibrium with the initial melt was calculated using clinopyroxene-melt partition coefficients from Brophy (2008) at 47 wt % SiO_2.

A5.3.3 - Alternative FC model for poikilitic Hbl-Ol gabbro low Mg# CPX and amphibole

In the main text, the REE compositions of the low Mg# CPX and amphibole from the poikilitic Hbl-Ol gabbro were modelled using the "POIKILITIC GABBRO POLYBARIC FC" model. This alternative model illustrates the effect of changing the initial melt composition on the model outcome – all other parameters were kept identical. The adjusted initial melt composition is shown in **Table A5.2** (V37-201) and was used to represent a considerably more REE enriched initial melt than the composition used for the model in the main text (Inv CPX Bas (Br) from **Table 5.3**). The results, showing the most REE enriched clinopyroxene and amphibole compositions that can be produced by the alternative model (green dashed lines), are compared to the poikilitic Hbl-Ol gabbro low Mg# CPX and amphibole compositions in **Figure A5.4**. A poor fit to the sample data is obtained for the low Mg# CPX, but a

relatively close fit is obtained for amphibole (see main text, **section 5.5.3.2** for discussion of this result).

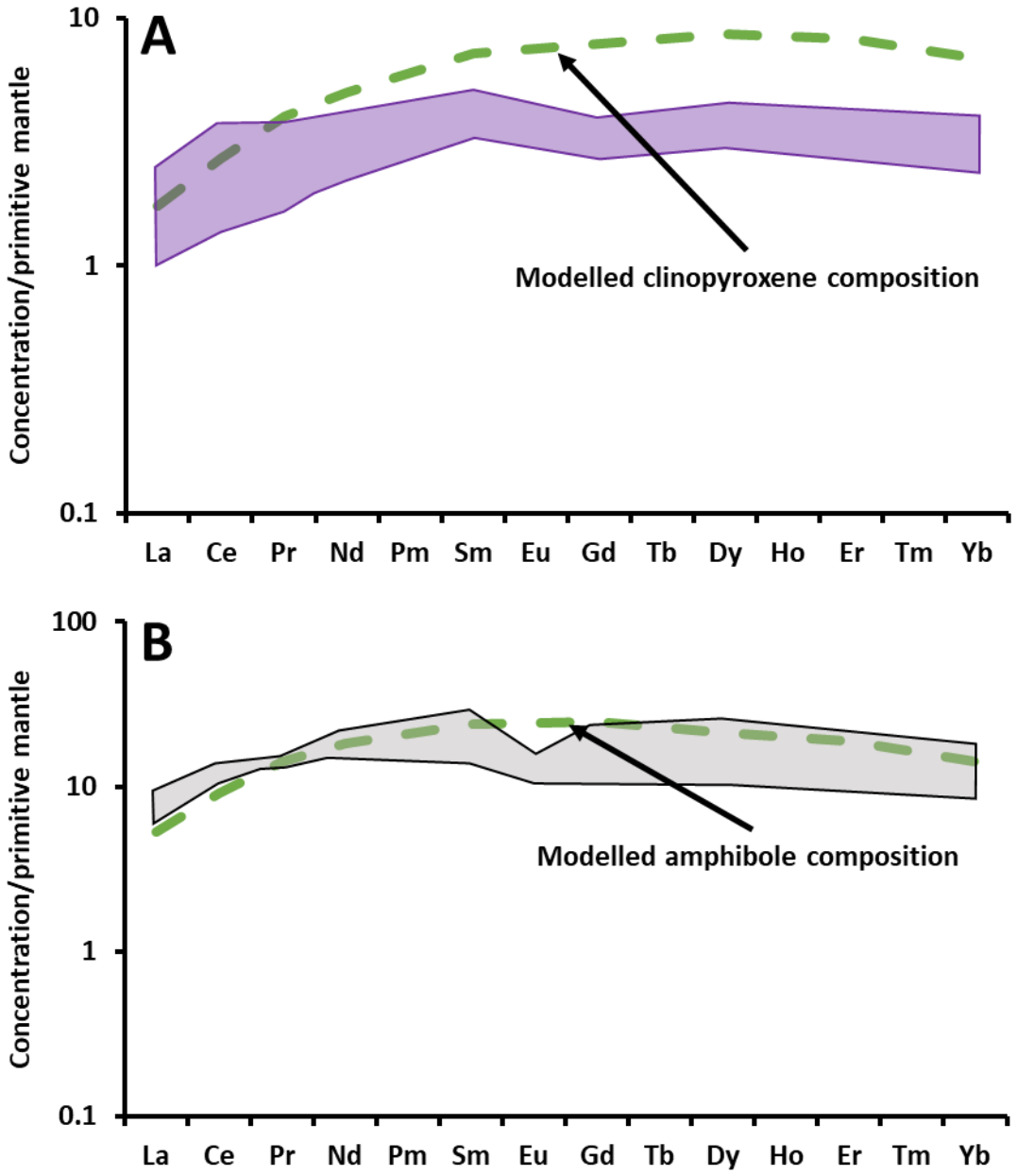

Figure A5.4: A) Primitive mantle normalized REE patterns of poikilitic Hbl-Ol gabbro low Mg# CPX (purple field) compared with the most REE enriched clinopyroxene composition produced by the "POIKILITIC GABBRO POLYBARIC FC" model using the alternative (V37-201) initial melt composition (green dashed line). **B)** Primitive mantle normalized REE patterns of poikilitic Hbl-Ol gabbro amphibole (grey field) compared with the most REE enriched amphibole composition produced by the "POIKILITIC GABBRO POLYBARIC FC" model using the alternative (V37-201) initial melt composition (green dashed line). Primitive mantle normalizing values from Palme and O'Neill (2003). The "most REE enriched clinopyroxene or amphibole compositions produced by the model" are the

clinopyroxene in equilibrium with the melt after Step 3 and the amphibole in equilibrium with the melt after step 4.

A5.3.4 - "POIKILITIC GABBRO POLYBARIC FC" model for Nb

Amphibole in the poikilitic Hbl-Ol gabbro are highly enriched in Nb (8.5-12 μg/g) as well as REE. We tested whether the high Nb of the amphibole could be produced by polybaric fractional crystallization from a primitive basaltic magma, simulated by the "POIKILITIC GABBRO POLYBARIC FC" model. Details of the assumed Nb content in the initial melt and mineral-melt partition coefficients used for Nb are discussed in the main text. The model steps and fractionating assemblages were otherwise identical to the "POIKILITIC GABBRO POLYBARIC FC" model. **Figure A5.5** shows the modelled Nb concentration in amphibole in equilibrium with the melt at each step of the model. The modelled amphibole Nb concentration reaches a maximum of 0.4, considerably lower than the poikilitic Hbl-Ol gabbro amphibole.

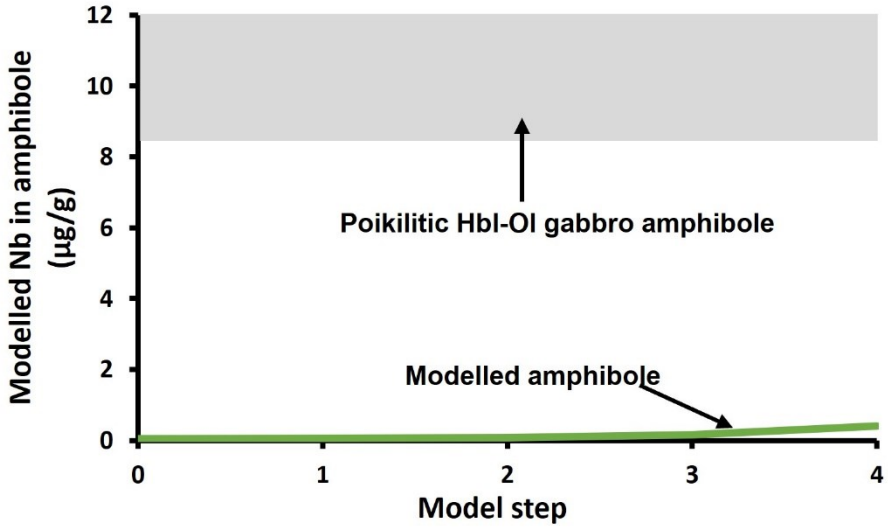

Figure A5.5: Nb concentrations in amphibole in equilibrium with the melt at each step of the "POIKILITIC GABBRO POLYBARIC FC" model (green line). The amphibole Nb concentrations were calculated from modelled melt compositions using the amph-melt partition coefficients for Nb from Nandedkar et al., (2016) at the melt SiO_2 corresponding to each step in the model **(main text, Table 5.5).** Shown for comparison is the range of Nb concentrations in the poikilitic Hbl-Ol gabbro amphibole (grey field).

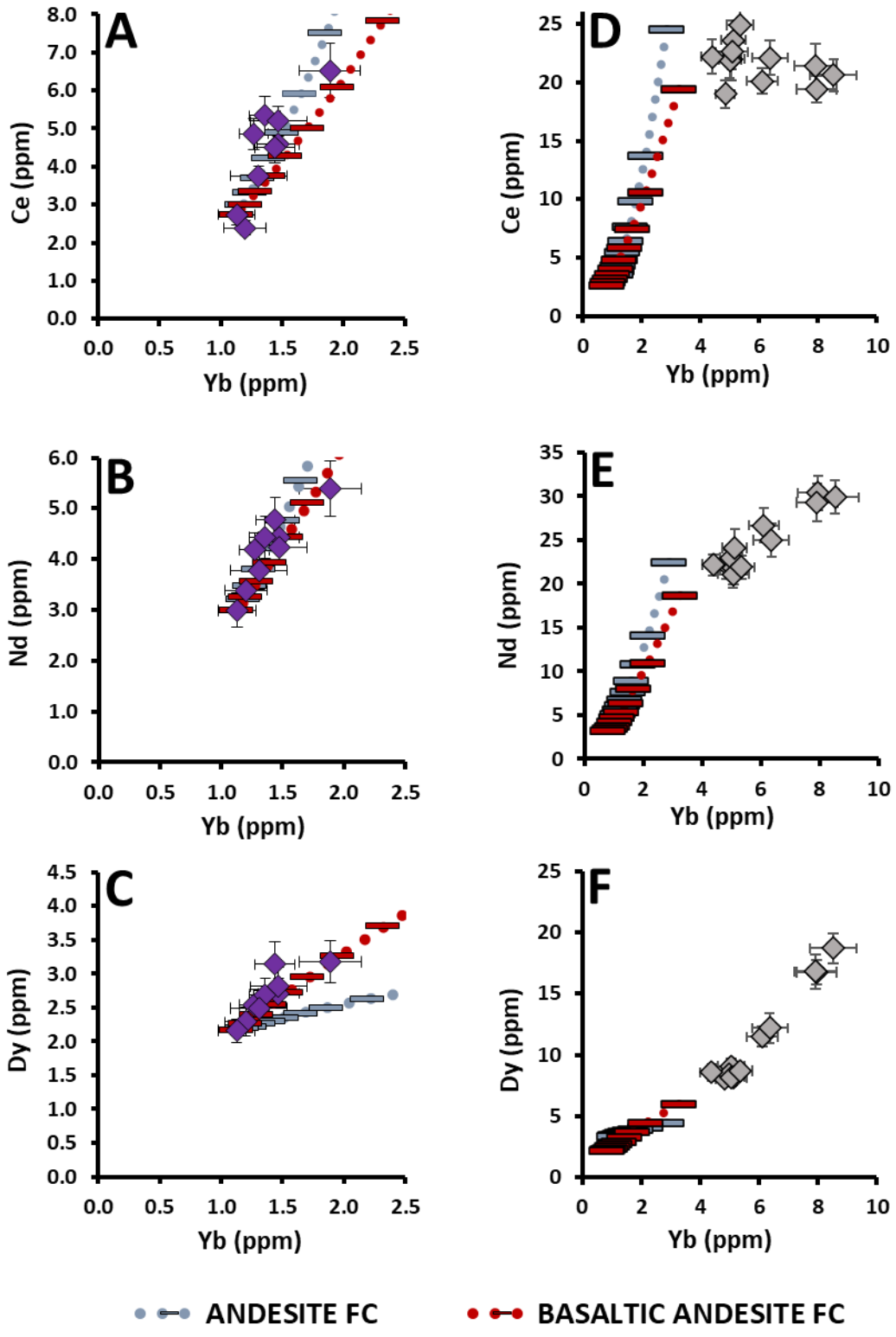

Figure A5.6: A) Ce, **B)** Nd and **C)** Dy vs Yb for poikilitic Hbl-Ol gabbro low Mg# CPX. **D)** Ce, **E)** Nd and **F)** Dy vs Yb for poikilitic Hbl-Ol gabbro amphibole. Clinopyroxene and amphibole data symbols are the same as the main text, in **Figures 5.16 and 5.18**. The data are compared with the "BASALTIC ANDESITE FC" and "ANDESITE FC" fractional crystallization models. Error bars on individual data

points show internal 2SE uncertainty. Each tick mark on fractional crystallization models represents an increment of 10 % fractionation.

A5.3.5 - Single step FC models for poikilitic Hbl-Ol gabbro low Mg# CPX and amphibole using evolved initial melts

In the main text, the REE compositions of the poikilitic Hbl-Ol gabbro low Mg# CPX and amphibole were modelled via AFC, using a basaltic andesite and andesite initial melt composition ("BASALTIC ANDESITE AFC" and "ANDESITE AFC") models, **sections 5.5.2.2 and 5.5.3.2, Table 5.6**). For comparison, FC of the same plagioclase-clinopyroxene-orthopyroxene-amphibole assemblage, without contributions from assimilation, was also modelled here. For these two FC models, the three required parameters of fractionating assemblage, bulk D value and initial melt composition were identical to those used in the "BASALTIC ANDESITE AFC" and "ANDESITE AFC" models listed in **Table 5.6**. The resulting FC models are referred to here as "BASALTIC ANDESITE FC" and ANDESITE FC", shown in **Figure A5.6**. Up to 60 % crystallization of plagioclase-clinopyroxene-orthopyroxene-amphibole from a basaltic andesite or andesite melt can reproduce most of the low Mg# CPX REE compositions (**Figure A5.6**). Neither model comes close to reproducing the amphibole compositions, even after 90 % crystallization.

Appendix 5.4 - St Vincent plutonic xenolith clinopyroxene and amphibole trace element data

Ol-CPX gabbro clinopyroxene

Crystal	CP1 C	CP1 OZ	CP1 OZ 2	CP1 R	C2 C	C2 R	C3 C	C3 R
Sc	118.10	122.80	110.60	102.70	141.50	108.80	138.40	107.50
Ti	3180.00	2580.00	2090.00	3540.00	5220.00	3390.00	3960.00	3490.00
V	328.00	291.00	258.00	361.00	469.00	325.00	420.00	348.00
Cr	97.20	361.00	205.00	379.00	498.00	541.00	461.00	343.00
Ni	23.50	36.90	32.30	37.10	38.60	37.00	36.40	35.90
Rb		0.06	0.05					
Sr	12.40	12.61	12.45	13.70	13.40	12.80	13.80	12.20
Y	11.75	11.25	9.84	12.02	17.80	11.05	11.60	10.82
Zr	10.28	8.99	7.25	10.26	14.57	9.95	10.81	9.99
Nb	0.04	0.05	0.12	0.07	0.02	0.02	0.01	0.01
Ba	0.05	0.08						
La	0.28	0.24	0.23	0.26	0.37	0.20	0.21	0.20
Ce	1.24	1.10	0.94	1.13	1.84	1.14	1.19	1.09
Pr	0.38	0.36	0.30	0.33	0.48	0.28	0.32	0.31
Nd	2.56	2.38	1.87	2.30	3.97	2.13	2.35	2.34
Sm	1.36	1.32	1.08	1.36	1.94	1.27	1.17	1.20
Eu	0.53	0.60	0.49	0.56	0.65	0.48	0.47	0.48
Gd								
Dy	2.70	2.38	2.22	2.54	3.71	2.28	2.75	2.35
Er	1.46	1.30	1.21	1.43	2.08	1.24	1.51	1.44
Yb	1.43	1.22	1.10	1.29	1.74	1.14	1.25	1.13
Lu	0.22	0.23	0.22	0.19	0.25	0.15	0.15	0.16
Pb	0.09	0.05	0.06	0.06	0.02	0.01	0.04	0.01
Th	0.05	0.08	0.08	0.05	0.01	0.01	0.01	0.01
U	0.03	0.12	0.10	0.04	0.00	0.01	0.01	0.01
Mg#	75.3	78.0	78.0	76.3	78.6	77.0	78.2	75.4

Crystal	C4 C	C4 R	C5 C	C5 R	C6 C	C6 R	C8 C	C8 R
Sc	116.30	122.40	127.30	135.60	149.10	133.20	161.80	146.80
Ti	3110.00	3880.00	3480.00	3820.00	4870.00	4860.00	5390.00	5560.00
V	341.00	347.00	344.00	388.00	414.00	364.00	423.00	390.00
Cr	642.00	453.00	278.00	447.00	327.00	216.00	839.00	166.00
Ni	58.60	33.30	37.10	36.60	32.20	33.10	33.80	33.50
Rb			0.14	0.04				
Sr	13.21	12.00	14.20	11.76	12.30	13.10	12.55	13.00

Y	10.46	11.40	12.22	11.61	10.08	10.88	10.20	10.51
Zr	9.23	9.32	10.51	10.99	9.97	9.41	9.82	9.34
Nb	0.01	0.01	0.23	0.05	0.01	0.01	0.01	0.01
Ba			0.30					
La	0.19	0.18	0.40	0.29	0.17	0.17	0.15	0.15
Ce	1.05	1.08	1.34	1.21	0.91	0.99	0.81	0.88
Pr	0.29	0.29	0.50	0.37	0.22	0.25	0.24	0.25
Nd	2.40	2.26	2.51	2.36	1.98	2.00	1.74	2.04
Sm	1.21	1.23	1.52	1.34	1.08	1.16	1.04	1.10
Eu	0.42	0.46	0.67	0.51	0.44	0.46	0.44	0.43
Gd								
Dy	2.23	2.40	2.50	2.54	2.21	2.32	2.07	2.22
Er	1.34	1.38	1.57	1.48	1.17	1.30	1.23	1.31
Yb	1.09	1.09	1.30	1.28	1.03	1.08	1.05	1.05
Lu	0.14	0.14	0.32	0.21	0.12	0.13	0.13	0.13
Pb	0.01	0.01	0.16	0.05	0.01	0.01	0.01	0.02
Th		0.01	0.18	0.05	0.00	0.01		
U			0.19	0.04				
Mg#	74.9	76.0	76.6	76.3	76.4	76.6	75.1	75.1

Crystal	C9 C	C9 R	C10 C	C10 R
Sc	138.90	133.10	156.00	150.70
Ti	5210.00	4000.00	5130.00	4870.00
V	425.00	355.00	411.00	419.00
Cr	212.00	406.00	635.00	361.00
Ni	38.40	35.50	33.10	37.10
Rb		0.11		0.06
Sr	14.00	12.74	12.46	13.20
Y	11.79	10.59	10.71	12.29
Zr	9.83	11.52	9.93	11.27
Nb	0.04	0.19	0.02	0.04
Ba		0.14		0.30
La	0.21	0.37	0.16	0.22
Ce	1.16	1.29	0.94	1.26
Pr	0.31	0.44	0.27	0.32
Nd	2.36	2.34	2.02	2.41
Sm	1.39	1.36	1.17	1.31
Eu	0.58	0.60	0.42	0.48
Gd				
Dy	2.44	2.34	2.37	2.49
Er	1.38	1.43	1.22	1.40
Yb	1.23	1.28	1.05	1.25
Lu	0.19	0.27	0.15	0.17

Pb	0.07	0.15	0.04	0.05
Th	0.04	0.15	0.02	0.03
U	0.06	0.16	0.02	0.02
Mg#	76.5	78.1	77.0	77.8

Table A5.3: Ol-CPX gabbro clinopyroxene trace element compositions, in µg/g. Where no value is listed, the element was below the limit of detection in the measured crystal. No Gd data was obtained for Ol-CPX gabbro clinopyroxene. Mg# values taken from quantitative molar element ratio map.

Poikilitic Hbl-Ol gabbro high Mg# CPX

Crystal	HMGC 1 C	HMGC 1 R	HMGC 2 C	HMGC 2 R	HMGC 3 C	HMGC 3 R	HMGC 4 C	HMGC 4 R
Sc	133.50	114.50	133.00	131.20	123.50	127.90	119.60	131.80
Ti	2210.00	1440.00	2980.00	2370.00	1455.00	2140.00	2280.00	2320.00
V	321.00	169.00	291.00	260.00	163.00	215.00	193.00	238.00
Cr	1406.00	2270.00	1420.00	3550.00	2090.00	3850.00	2200.00	3660.00
Ni	128.60	183.00	135.40	183.00	177.00	179.00	149.00	184.00
Rb							0.26	
Sr	11.25	14.30	8.24	16.50	14.10	15.90	16.50	16.50
Y	8.01	4.56	8.32	6.48	4.40	5.47	8.11	6.32
Zr	5.97	4.69	10.90	8.49	4.25	6.96	11.90	7.59
Nb	0.01	0.01	0.05	0.03		0.01	0.06	0.03
Ba		0.03		0.35		0.04	1.90	0.03
La	0.14	0.20	0.33	0.28	0.14	0.23	0.63	0.32
Ce	0.75	0.84	1.37	1.14	0.71	0.95	2.06	1.39
Pr	0.17	0.17	0.27	0.27	0.16	0.21	0.38	0.27
Nd	1.48	1.33	2.17	1.90	1.26	1.50	2.46	1.92
Sm	0.87	0.64	0.99	0.86	0.60	0.73	1.09	0.73
Eu	0.30	0.23	0.35	0.31	0.21	0.28	0.38	0.31
Gd								
Dy	1.64	1.06	1.84	1.46	1.01	1.18	1.57	1.42
Er	0.96	0.57	0.99	0.83	0.53	0.59	0.87	0.70
Yb	0.79	0.37	0.74	0.63	0.36	0.45	0.81	0.58
Lu	0.10	0.05	0.10	0.07	0.05	0.06	0.10	0.06
Pb	0.02	0.02	0.05	0.03	0.01	0.02	0.10	0.04
Th	0.02	0.02	0.03	0.02	0.01	0.05	0.06	0.05
U		0.01	0.03	0.02		0.02	0.03	0.04
Mg#	84.6	88.7	83.6	87.5	88.9	87.3	88.8	87.1

Crystal	HMGC 5 C	HMGC 5 R	L1C	L1C 2	L1C 3	L1C 4	L1C 5	L1C 6
Sc	108.20	130.80	133.00	143.10	133.80	128.80	124.10	119.80
Ti	1293.00	2530.00	2750.00	2680.00	3030.00	2910.00	2740.00	2510.00
V	154.00	260.00	365.00	344.00	392.00	345.00	327.00	336.00
Cr	2090.00	3640.00	759.00	804.00	350.00	551.00	506.00	658.00
Ni	183.00	185.00	94.10	89.90	92.60	94.70	98.90	112.20
Rb		0.15	0.06	0.05	0.05			0.06
Sr	14.50	17.70	13.40	13.30	13.40	12.80	12.50	16.20
Y	4.13	7.27	8.09	7.21	7.81	7.54	7.39	7.37
Zr	3.63	11.90	8.48	7.65	7.66	7.51	7.19	7.49
Nb	0.01	0.04	0.01	0.01	0.01	0.01	0.02	0.01
Ba		0.84	0.44	0.42	0.52	0.13	0.20	0.29
La	0.18	0.59	0.19	0.20	0.22	0.16	0.17	0.21
Ce	0.67	2.08	1.06	1.05	1.15	0.95	0.96	1.01
Pr	0.16	0.37	0.25	0.22	0.26	0.21	0.24	0.26
Nd	1.12	2.31	1.81	1.66	1.86	1.57	1.83	1.85
Sm	0.58	0.97	0.96	0.86	0.94	0.87	0.92	0.95
Eu	0.19	0.34	0.37	0.35	0.33	0.36	0.34	0.33
Gd								
Dy	0.89	1.57	1.64	1.67	1.79	1.69	1.57	1.53
Er	0.52	0.78	0.92	0.84	0.90	0.96	0.90	0.86
Yb	0.39	0.68	0.81	0.74	0.81	0.72	0.64	0.70
Lu	0.05	0.09	0.12	0.11	0.12	0.10	0.09	0.11
Pb	0.02	0.03	0.08	0.18	0.12	0.10	0.15	0.25
Th	0.02	0.15	0.00	0.00	0.01	0.01	0.00	0.01
U	0.01	0.09	0.01	0.01	0.01	0.01	0.01	0.01
Mg#	88.7	83.3	81.7	81.7	81.7	82.9	82.9	82.9

Crystal	L1C 7	L1R 1	L1R 2	L1R 3
Sc	121.50	152.00	138.10	127.40
Ti	2990.00	2390.00	2480.00	2020.00
V	366.00	235.00	265.00	224.00
Cr	1278.00	3740.00	3890.00	3270.00
Ni	135.00	178.00	178.00	174.00
Rb	0.05	0.05	0.15	0.04
Sr	13.50	17.20	15.80	16.20
Y	7.57	5.00	5.30	4.89
Zr	7.51	6.43	7.71	6.36
Nb	0.02	0.04	0.05	0.01
Ba	0.06	0.34	1.11	0.32
La	0.26	0.22	0.27	0.31
Ce	1.06	1.05	1.43	1.25

Pr	0.23	0.20	0.26	0.23
Nd	1.81	1.62	1.65	1.52
Sm	0.88	0.75	0.78	0.61
Eu	0.37	0.31	0.32	0.26
Gd				
Dy	1.68	1.13	1.25	1.18
Er	0.92	0.57	0.67	0.56
Yb	0.73	0.41	0.52	0.51
Lu	0.09	0.06	0.06	0.07
Pb	0.06	0.11	0.24	0.15
Th	0.01	0.00	0.04	0.07
U	0.01	0.01	0.04	0.05
Mg#	82.9	87.6	87.6	87.6

Table A5.4: Poikilitic Hbl-Ol gabbro high Mg# CPX clinopyroxene trace element compositions, in μg/g. Where no value is listed, the element was below the limit of detection in the measured crystal. No Gd data was obtained for poikilitic Hbl-Ol gabbro high Mg# CPX clinopyroxene. Mg# values taken from quantitative molar element ratio map.

Poikilitic Hbl-Ol gabbro low Mg# CPX

Crystal	C1	C2	C3	C4	C5	C6	C7	C8	C9
Sc	149.10	172.00	142.00	146.10	148.70	141.10	147.90	155.00	143.60
Ti	3370.00	4520.00	2880.00	2900.00	3170.00	2650.00	3340.00	3180.00	3300.00
V	391.00	461.00	351.00	330.00	359.00	307.00	356.00	353.00	359.00
Cr	1480.00	2450.00	1272.00	1455.00	1610.00	1340.00	1476.00	1620.00	1370.00
Ni	122.60	145.00	134.30	142.80	129.00	134.00	117.00	129.00	131.30
Rb	0.07	0.10							0.06
Sr	16.30	18.40	17.10	15.10	15.70	15.80	14.70	17.90	16.80
Y	14.73	15.10	12.96	11.75	13.20	10.61	13.52	13.60	16.90
Zr	22.80	21.90	19.00	12.84	19.10	11.80	18.20	18.50	20.90
Nb	0.06	0.07	0.04	0.02	0.07	0.02	0.04	0.07	0.10
Ba	0.81	1.17	0.51	0.03	0.55	0.07	0.16	0.97	1.44
La	1.30	1.28	1.21	0.65	1.62	0.71	1.14	1.48	1.66
Ce	4.59	4.49	4.86	2.39	5.34	2.74	3.76	5.19	6.52
Pr	0.73	0.77	0.72	0.44	0.81	0.45	0.62	0.72	0.98
Nd	4.43	4.77	4.18	3.39	4.43	2.99	3.78	4.23	5.39
Sm	1.76	1.77	1.66	1.46	1.60	1.43	1.79	1.67	2.16
Eu	0.60	0.65	0.51	0.48	0.58	0.48	0.57	0.62	0.67
Gd	2.07	2.00	1.79	1.60	2.10	1.55	1.87	2.09	2.34
Dy	2.71	3.14	2.54	2.29	2.68	2.16	2.49	2.81	3.18
Er	1.59	1.62	1.53	1.29	1.41	1.27	1.42	1.59	1.92
Yb	1.47	1.44	1.27	1.20	1.36	1.13	1.31	1.47	1.89

Lu	0.18	0.19	0.15	0.16	0.21	0.14	0.17	0.20	0.27
Pb	0.11	0.10	0.07	0.06	0.14	0.06	0.08	0.08	0.10
Th	0.37	0.47	0.28	0.18	0.33	0.16	0.35	0.38	0.25
U	0.20	0.24	0.14	0.09	0.15	0.08	0.20	0.18	0.12
Mg#	77.6	77.3	77.4	79.1	78.1	77.2	77.9	78.0	77.3

Table A5.5: Poikilitic Hbl-Ol gabbro low Mg# CPX clinopyroxene trace element compositions, in µg/g. Where no value is listed, the element was below the limit of detection in the measured crystal. Mg# values taken from quantitative molar element ratio map.

Banded Hbl-Ol gabbro olivine absent band clinopyroxene

Crystal	CP1 R1	CP1 R2	CP2 R	CRB 11	CRB 12	CRB 13	CRB 14	CRB 15
Sc	82.50	86.00	88.10	97.50	95.90	93.30	94.60	87.70
Ti	2390.00	2620.00	2360.00	2970.00	3070.00	3010.00	3140.00	2550.00
V	222.00	236.00	253.00	206.80	213.00	205.00	197.10	180.30
Cr	0.62	0.85		1.82	2.65	2.35	2.44	1.34
Ni	3.87	3.96	2.82	10.38	10.80	9.89	9.20	9.30
Rb			0.09					
Sr	15.70	16.60	14.70	15.90	15.40	15.30	14.90	13.80
Y	17.16	18.00	18.00	15.72	15.89	15.90	16.24	17.81
Zr	10.85	14.06	12.54	14.08	15.80	15.40	15.70	14.81
Nb		0.01			0.02	0.01		0.01
Ba								
La	0.43	0.49	0.44	0.49	0.50	0.44	0.44	0.44
Ce	2.37	2.58	2.34	2.48	2.67	2.39	2.45	2.61
Pr	0.53	0.59	0.56	0.62	0.66	0.60	0.61	0.64
Nd	4.02	4.53	3.93	4.38	4.43	4.32	4.11	4.62
Sm	1.90	2.18	2.04	2.01	1.87	1.97	1.90	2.20
Eu	0.68	0.73	0.69	0.64	0.62	0.66	0.65	0.56
Gd	2.77	2.84	2.82	2.62	2.89	2.69	2.76	2.91
Dy	3.53	3.71	3.48	3.32	3.40	3.38	3.25	3.41
Er	2.08	2.18	2.22	1.91	2.01	1.94	1.85	2.06
Yb	1.87	2.04	1.82	1.72	1.88	1.83	1.81	1.88
Lu	0.25	0.26	0.26	0.26	0.28	0.25	0.26	0.30
Pb	0.03	0.02	0.05	0.03	0.03	0.03	0.03	0.03
Th	0.00		0.01	0.01	0.01	0.00	0.00	0.00
U		0.00	0.00					
Mg#	70.8	72.9	72.8	72.7	72.3	72.2	72.6	73.2

Crystal	CRB 16	CRB 17	CRB1	CRB2	CRB 3	CRB4	CRB 5	CRB6
Sc	80.90	94.80	96.10	95.00	93.20	94.30	95.30	91.90
Ti	1930.00	2930.00	2830.00	3030.00	2900.00	2840.00	3010.00	3180.00
V	192.80	216.00	200.00	197.00	217.00	212.00	215.00	216.00
Cr	1.09	2.57	2.54	2.54	1.76	2.36	2.37	2.66
Ni	1.98	10.60	8.73	9.74	9.50	9.20	10.20	9.38
Rb			0.07					
Sr	13.85	15.80	13.20	15.00	15.80	15.10	15.80	15.54
Y	15.97	15.06	16.10	15.25	16.88	15.99	15.70	16.14
Zr	9.97	14.24	14.67	15.57	13.94	13.37	14.20	15.59
Nb		0.01		0.01	0.01	0.01	0.01	0.01
Ba								
La	0.34	0.48	0.49	0.44	0.47	0.42	0.44	0.46
Ce	2.01	2.51	2.64	2.50	2.51	2.52	2.39	2.64
Pr	0.50	0.59	0.62	0.57	0.63	0.54	0.57	0.61
Nd	3.49	4.25	4.28	3.90	4.46	3.98	4.08	4.19
Sm	1.73	1.87	2.02	1.85	2.12	1.95	1.93	2.04
Eu	0.67	0.61	0.69	0.62	0.68	0.64	0.61	0.65
Gd	2.44	2.61	2.48	2.74	2.88	2.59	2.38	2.62
Dy	3.34	3.15	3.07	3.08	3.58	3.30	3.21	3.35
Er	1.92	1.84	1.90	1.85	2.03	1.94	1.82	2.02
Yb	1.62	1.73	1.67	1.57	1.80	1.65	1.70	1.80
Lu	0.23	0.23	0.24	0.25	0.25	0.24	0.24	0.24
Pb	0.02	0.02	0.03	0.03	0.02	0.02	0.02	0.03
Th		0.01	0.01	0.01	0.00	0.00	0.01	0.00
U								
Mg#	73.5	73	72	73.2	72.8	71.3	72.5	72.4

Crystal	CRB7	CRB8	CRB9	CRB10
Sc	76.10	97.00	94.40	83.30
Ti	2319.00	2880.00	2620.00	2300.00
V	189.00	211.00	196.00	195.20
Cr	0.81	2.08	1.56	1.88
Ni	3.13	9.72	10.00	4.77
Rb				
Sr	14.70	15.10	14.10	14.66
Y	16.08	16.38	18.00	15.91
Zr	11.31	14.06	14.30	11.47
Nb			0.01	
Ba				
La	0.46	0.43	0.47	0.37
Ce	2.31	2.46	2.58	2.22

Pr	0.52	0.59	0.63	0.53
Nd	4.02	4.20	4.44	3.84
Sm	2.02	1.93	1.98	1.89
Eu	0.62	0.64	0.58	0.64
Gd	2.45	2.72	2.87	2.63
Dy	3.21	3.34	3.80	3.29
Er	1.99	1.92	2.18	1.90
Yb	1.69	1.71	1.98	1.68
Lu	0.24	0.23	0.27	0.24
Pb	0.03	0.02	0.03	0.03
Th		0.01		
U				
Mg#	71.5	72.5	72.2	72.8

Table A5.6: Banded Hbl-Ol gabbro olivine absent band clinopyroxene trace element compositions, in µg/g. Where no value is listed, the element was below the limit of detection in the measured crystal. Mg# values taken from quantitative molar element ratio map.

Banded Hbl-Ol gabbro matrix clinopyroxene

Crystal	CP1 C	CP2 C	C1 C	C1 R	C2 C	C2 R	C3 C
Sc	118.80	185.10	175.00	114.60	117.90	114.00	187.00
Ti	2680.00	2750.00	3400.00	2980.00	2920.00	3000.00	4190.00
V	273.00	291.00	324.00	301.00	289.00	299.00	372.00
Cr	19.30	379.00	15.00	1.84	1.40	30.80	22.10
Ni	17.00	25.70	15.70	8.56	10.87	18.60	16.70
Rb							
Sr	12.70	11.40	10.90	12.90	12.60	12.95	12.31
Y	11.50	11.01	10.74	15.00	15.40	14.46	15.23
Zr	11.83	7.46	7.78	9.45	10.17	11.68	12.30
Nb		0.01	0.01			0.01	
Ba							
La	0.34	0.19	0.17	0.28	0.31	0.34	0.32
Ce	1.80	0.98	0.97	1.66	1.72	1.92	1.79
Pr	0.41	0.25	0.26	0.46	0.42	0.45	0.46
Nd	2.89	1.90	1.97	3.04	3.17	3.22	3.41
Sm	1.38	1.13	1.08	1.49	1.71	1.73	1.83
Eu	0.45	0.38	0.44	0.60	0.55	0.61	0.59
Gd	1.75	1.73	1.68	2.49	2.44	2.32	2.44
Dy	2.24	2.15	2.30	3.05	3.26	2.87	3.50
Er	1.32	1.25	1.30	1.74	1.82	1.64	1.87
Yb	1.26	1.05	1.20	1.46	1.47	1.53	1.66
Lu	0.18	0.14	0.15	0.20	0.21	0.21	0.21
Pb	0.02	0.02	0.01	0.01	0.02	0.02	0.01

Th						0.01	0.01	
U								
Mg#	75.0	78.3	76.1	73.9	74.8	73.9	74.7	
Crystal	C3 R	C4 C	C4 R	C5 C	C5 R	C6 C	C6 R	C7 C
Sc	151.50	170.80	120.40	165.50	179.00	193.20	115.30	111.10
Ti	3600.00	3190.00	2960.00	3270.00	3830.00	2660.00	2960.00	3120.00
V	314.00	324.00	305.00	326.00	355.00	294.00	287.00	302.00
Cr	9.60	9.47	0.95	19.50	12.10	237.00	10.71	16.10
Ni	17.80	16.20	7.47	17.80	18.80	21.20	13.60	16.10
Rb								
Sr	13.80	10.70	13.30	11.80	13.30	10.67	13.20	12.80
Y	14.04	12.04	14.90	13.22	13.25	11.31	14.73	14.73
Zr	11.16	9.39	9.23	10.29	9.45	7.57	10.73	11.54
Nb		0.01						0.01
Ba								
La	0.33	0.33	0.27	0.28	0.24	0.22	0.32	0.35
Ce	1.70	1.76	1.52	1.53	1.37	1.03	1.71	1.73
Pr	0.41	0.40	0.39	0.43	0.36	0.26	0.46	0.45
Nd	3.03	2.87	2.98	2.80	2.75	1.83	3.38	3.48
Sm	1.63	1.36	1.68	1.32	1.43	1.13	1.73	1.57
Eu	0.58	0.51	0.57	0.50	0.54	0.44	0.57	0.53
Gd	2.39	1.88	2.40	2.07	2.10	1.90	2.36	2.39
Dy	3.07	2.69	3.19	2.69	2.78	2.41	3.15	3.05
Er	1.70	1.42	1.68	1.56	1.50	1.35	1.73	1.78
Yb	1.46	1.27	1.49	1.46	1.17	1.10	1.50	1.60
Lu	0.21	0.17	0.20	0.19	0.17	0.14	0.22	0.21
Pb	0.02	0.02	0.01	0.01	0.01	0.03	0.02	0.02
Th		0.01		0.01	0.01	0.01	0.01	0.01
U							0.01	0.01
Mg#	74.5	74.0	74.5	75.2	74.6	78.4	74.1	75.8

Crystal	C7 R	C8 C	C8 R	C9 C	C9 R	C10 C	C10 R
Sc	119.80	174.20	179.40	121.90	185.20	206.20	137.70
Ti	3140.00	2920.00	3140.00	2560.00	3540.00	4290.00	4030.00
V	283.00	296.00	302.00	259.00	341.00	373.00	340.00
Cr	4.55	220.00	192.00	14.01	22.30	6.95	5.04
Ni	14.40	22.40	21.70	17.20	18.20	18.00	12.50
Rb							
Sr	13.90	11.75	10.80	13.30	11.71	13.30	14.10
Y	15.23	10.85	10.31	12.73	11.68	14.48	19.40
Zr	10.97	6.79	7.23	11.72	8.06	11.33	15.29

Nb							0.01
Ba							
La	0.32	0.15	0.17	0.36	0.22	0.25	0.39
Ce	1.66	1.01	1.01	1.79	1.12	1.53	2.09
Pr	0.45	0.24	0.26	0.43	0.28	0.40	0.52
Nd	3.26	1.84	1.97	3.08	2.17	2.98	3.94
Sm	1.77	1.13	1.17	1.34	1.27	1.51	2.12
Eu	0.56	0.43	0.43	0.50	0.43	0.62	0.72
Gd	2.32	1.65	1.71	1.88	1.96	2.31	3.13
Dy	3.09	2.28	2.32	2.59	2.50	3.13	3.96
Er	1.76	1.27	1.33	1.58	1.34	1.65	2.24
Yb	1.64	1.04	1.11	1.27	1.18	1.61	1.96
Lu	0.21	0.15	0.15	0.18	0.15	0.19	0.27
Pb	0.02	0.02	0.01	0.01	0.02	0.03	0.02
Th	0.01		0.01	0.02	0.01	0.01	0.01
U	0.01		0.01	0.01			
Mg#	74.4	78.6	77.0	74.7	74.5	76.0	74.6

Table A5.7: Banded Hbl-Ol gabbro matrix clinopyroxene trace element compositions, in µg/g. Where no value is listed, the element was below the limit of detection in the measured crystal. Mg# values taken from quantitative molar element ratio map.

Olivine gabbro clinopyroxene

Crystal	C1 C	C1 R	C2 C	C2 R	C3 C	C3 R	C4 C	C4 R
Sc	113.20	105.00	122.60	169.70	150.80	181.70	159.30	163.70
Ti	2090.00	2710.00	3300.00	4390.00	3180.00	4830.00	4080.00	2620.00
V	277.00	322.00	350.00	381.00	338.00	400.00	378.00	293.00
Cr	43.10	40.70	56.10	61.20	92.10	79.60	160.00	206.00
Ni	23.00	23.90	25.70	24.60	28.20	28.30	26.80	31.90
Rb								
Sr	13.20	14.60	14.40	15.20	15.60	18.10	16.10	14.10
Y	9.68	10.77	13.47	13.99	12.10	15.88	13.68	11.32
Zr	16.90	11.73	11.20	10.51	8.66	12.15	11.49	7.84
Nb	0.01	0.01	0.01			0.01		
Ba								
La	0.39	0.30	0.35	0.28	0.24	0.31	0.31	0.22
Ce	1.95	1.64	1.90	1.53	1.37	1.82	1.71	1.24
Pr	0.40	0.38	0.44	0.38	0.35	0.45	0.37	0.32
Nd	2.69	2.80	3.24	2.91	2.56	3.19	3.26	2.21
Sm	1.14	1.30	1.66	1.53	1.42	1.68	1.49	1.21
Eu	0.34	0.43	0.57	0.59	0.47	0.62	0.59	0.40
Gd	1.51	1.81	2.21	2.36	2.01	2.56	2.13	1.74
Dy	2.01	2.30	2.77	3.01	2.40	3.12	2.85	2.22

Er	1.20	1.37	1.65	1.63	1.40	1.80	1.57	1.27
Yb	1.13	1.16	1.42	1.34	1.31	1.53	1.34	1.23
Lu	0.16	0.17	0.22	0.20	0.16	0.21	0.18	0.14
Pb	0.02	0.02	0.02	0.02	0.01	0.03	0.02	0.01
Th	0.01	0.01	0.01	0.01	0.01	0.01	0.01	0.01
U	0.02							
Mg#	76.4	75.5	76.3	75.8	78	75.9	76.3	75.6

Crystal	C5 C	C5 R	C6 C	C6 R	C7 C	C7 R	C8 C	C8 R
Sc	186.00	147.40	162.10	163.00	161.00	161.80	87.20	184.50
Ti	3750.00	3570.00	4330.00	4500.00	4150.00	3780.00	2250.00	4440.00
V	371.00	356.00	362.00	371.00	359.00	360.00	290.00	352.00
Cr	144.00	118.00	67.10	57.50	49.30	39.10	125.00	61.60
Ni	28.60	25.50	23.70	26.50	24.00	24.50	27.40	24.30
Rb								
Sr	15.20	15.30	13.00	16.50	15.30	14.90	14.00	14.80
Y	13.87	12.64	12.50	14.77	14.10	13.90	10.30	12.24
Zr	10.17	12.80	10.58	11.25	13.28	10.14	13.40	9.37
Nb			0.01		0.02	0.01		0.01
Ba								
La	0.29	0.29	0.24	0.36	0.32	0.26	0.35	0.27
Ce	1.55	1.67	1.32	1.79	1.60	1.46	1.83	1.38
Pr	0.39	0.39	0.36	0.45	0.41	0.35	0.43	0.34
Nd	2.74	3.21	2.61	2.93	2.93	2.70	2.84	2.40
Sm	1.35	1.42	1.39	1.46	1.54	1.58	1.10	1.28
Eu	0.50	0.55	0.47	0.60	0.55	0.52	0.42	0.52
Gd	2.19	2.17	2.14	2.31	2.24	2.26	1.53	2.08
Dy	2.90	2.60	2.65	2.90	2.78	2.85	2.08	2.57
Er	1.67	1.43	1.48	1.72	1.68	1.66	1.25	1.53
Yb	1.32	1.31	1.33	1.43	1.43	1.38	1.22	1.24
Lu	0.17	0.18	0.17	0.22	0.19	0.21	0.16	0.16
Pb	0.02		0.02	0.02	0.02		0.03	
Th	0.00	0.01	0.00	0.01	0.01	0.01	0.01	0.02
U								0.01
Mg#	76.7	76	76.3	76.2	76	76.1	77.2	75.7

Crystal	C9 C	C9 R	C10 C	C10 R
Sc	160.00	181.80	178.70	195.20
Ti	3690.00	4220.00	4290.00	4500.00
V	346.00	364.00	373.00	366.00
Cr	40.90	51.50	49.80	50.40

Ni	26.30	25.80	25.60	26.20
Rb				
Sr	16.00	16.70	15.30	16.30
Y	13.75	15.60	13.33	14.99
Zr	9.18	11.50	9.01	11.14
Nb			0.01	0.02
Ba				
La	0.27	0.31	0.24	0.34
Ce	1.48	1.74	1.24	1.63
Pr	0.38	0.40	0.31	0.39
Nd	2.80	3.20	2.37	2.92
Sm	1.54	1.69	1.27	1.61
Eu	0.57	0.62	0.58	0.58
Gd	2.18	2.52	2.12	2.35
Dy	2.98	3.15	2.81	3.18
Er	1.64	1.93	1.66	1.85
Yb	1.40	1.59	1.37	1.50
Lu	0.19	0.22	0.19	0.21
Pb	0.02	0.02	0.02	0.02
Th	0.01	0.00	0.01	0.02
U			0.01	0.01
Mg#	77.1	75.7	75.8	75.4

Table A5.8: Olivine gabbro clinopyroxene trace element compositions, in µg/g. Where no value is listed, the element was below the limit of detection in the measured crystal. Mg# values taken from quantitative molar element ratio map.

Poikilitic Hbl-Ol gabbro amphibole

Crystal	A1	A2	A3	A4	A5	A6
Sc	85.50	109.90	93.60	91.50	97.30	107.30
Ti	20900.00	20700.00	21400.00	21400.00	19200.00	17240.00
V	781.00	877.00	854.00	852.00	800.00	819.00
Cr	1117.00	1002.00	881.00	1150.00	1070.00	1270.00
Ni	459.00	394.00	435.00	450.00	502.00	464.00
Rb	1.18	1.26	1.01	1.22	1.39	1.54
Sr	93.70	88.40	97.30	95.00	82.70	73.70
Y	45.50	47.70	63.20	48.70	49.70	45.90
Zr	122.10	130.80	123.50	163.30	203.00	200.00
Nb	9.21	9.83	8.96	9.44	10.06	12.08
Ba	73.40	73.50	69.20	77.40	82.10	68.80
La	4.82	5.49	5.00	5.75	6.45	5.82
Ce	19.00	22.00	20.10	21.90	23.60	22.60
Pr	3.68	3.86	4.06	3.96	4.02	3.86

Nd	22.20	21.80	26.70	23.00	24.10	21.10
Sm	6.19	6.90	8.96	6.90	6.87	6.59
Eu	2.02	2.05	2.19	1.95	2.12	1.96
Gd	6.71	7.23	9.10	7.18	6.83	7.14
Dy	8.07	9.07	11.48	8.45	8.17	8.12
Er	4.80	5.18	6.68	5.20	5.48	5.02
Yb	4.85	5.06	6.11	5.00	5.12	5.07
Lu	0.66	0.67	0.80	0.71	0.73	0.64
Pb	0.54	0.71	0.85	0.77	0.84	0.69
Th	0.14	0.22	0.41	0.57	0.84	0.33
U	0.17	0.29	0.29	0.31	0.39	0.29

Crystal	A7	A8	A9	A10	A11	A12
Sc	123.10	132.90	116.00	105.80	111.10	117.40
Ti	21100.00	21900.00	23600.00	18200.00	17440.00	22600.00
V	1066.00	1179.00	1035.00	839.00	822.00	917.00
Cr	957.00	1023.00	956.00	1195.00	1134.00	922.00
Ni	351.00	399.00	426.00	484.00	456.00	465.00
Rb	0.94	1.00	1.03	1.42	1.52	1.22
Sr	94.90	92.60	96.50	77.50	80.90	91.30
Y	88.70	93.70	88.00	50.60	48.40	66.50
Zr	96.50	100.70	135.00	183.00	178.30	173.00
Nb	8.55	8.87	9.57	10.28	8.57	9.19
Ba	71.50	68.00	74.30	75.40	73.60	75.20
La	4.58	5.14	5.05	6.77	6.10	5.88
Ce	19.40	20.60	21.40	24.90	22.20	22.10
Pr	3.91	4.22	4.24	4.18	3.70	3.94
Nd	30.40	29.90	29.30	21.90	22.20	25.00
Sm	11.54	12.60	11.33	6.87	6.85	9.00
Eu	2.76	2.68	2.60	2.09	1.93	2.23
Gd	12.74	14.09	12.70	7.09	6.52	10.08
Dy	16.75	18.70	16.80	8.69	8.58	12.20
Er	9.37	10.09	9.48	5.45	4.91	7.25
Yb	7.96	8.53	7.92	5.35	4.40	6.37
Lu	0.98	1.05	0.93	0.71	0.66	0.79
Pb	0.76	0.79	0.77	0.68	0.73	0.79
Th	0.38	0.40	0.53	0.76	0.54	0.68
U	0.24	0.28	0.33	0.36	0.37	0.32

Table A5.9: Poikilitic Hbl-Ol gabbro amphibole trace element compositions, in µg/g.

Banded Hbl-Ol gabbro amphibole

Crystal	A1	A2	A3	A4	A5	A6
Sc	162.00	173.50	163.50	153.30	161.60	112.70
Ti	13960.00	14690.00	13910.00	14550.00	14070.00	9220.00
V	696.00	713.00	680.00	700.00	697.00	440.00
Cr	19.70	19.90	33.20	17.90	50.80	32.80
Ni	36.50	34.80	37.20	34.30	33.80	23.60
Rb	0.63	0.54	0.66	0.79	0.62	0.48
Sr	101.20	96.40	94.50	97.30	94.70	130.10
Y	31.90	33.40	31.10	31.50	33.30	21.30
Zr	23.50	22.60	20.50	19.80	19.00	14.20
Nb	1.06	1.10	0.97	0.89	0.91	0.63
Ba	27.70	26.00	25.20	26.40	24.10	19.20
La	0.78	0.83	0.72	0.75	0.75	0.59
Ce	3.92	4.29	3.53	3.59	3.87	2.60
Pr	0.97	1.00	0.94	0.89	0.93	0.60
Nd	6.75	7.54	6.53	6.78	6.84	4.65
Sm	3.23	3.34	3.11	2.90	3.50	2.03
Eu	1.10	1.26	1.16	1.19	1.04	0.78
Gd	4.77	5.19	4.76	5.20	5.23	3.36
Dy	5.94	6.34	5.96	6.00	6.45	4.08
Er	3.74	3.97	3.57	3.73	3.81	2.32
Yb	3.07	3.38	3.11	3.11	3.11	2.08
Lu	0.39	0.43	0.39	0.45	0.44	0.29
Pb	0.17	0.18	0.15	0.16	0.17	0.17
Th	0.01	0.02	0.01	0.02	0.01	0.01
U	0.01	0.01	0.01	0.01	0.01	0.01

Crystal	A7	A8	A9	A10
Sc	132.70	144.00	132.60	157.00
Ti	12950.00	12920.00	13260.00	13280.00
V	677.00	646.00	709.00	692.00
Cr	25.90	40.00	22.70	35.80
Ni	36.10	37.40	38.10	37.50
Rb	0.52	0.55	0.63	0.68
Sr	93.60	85.50	97.80	94.30
Y	29.60	32.00	23.40	31.00
Zr	21.90	21.68	23.50	21.70
Nb	0.93	0.93	0.86	0.93
Ba	22.80	20.40	25.70	23.70
La	0.76	0.83	0.87	0.79
Ce	3.78	4.19	4.18	3.98

Pr	0.90	1.01	0.94	0.93
Nd	6.92	7.18	6.34	6.77
Sm	3.11	3.31	2.6	3.21
Eu	1.02	1.05	1.02	1.13
Gd	4.31	4.96	3.67	4.66
Dy	5.50	6.08	4.38	6.25
Er	3.24	3.35	2.69	3.62
Yb	2.92	3.25	2.65	3.28
Lu	0.38	0.42	0.38	0.41
Pb	0.15	0.14	0.17	0.17
Th	0.02	0.02	0.02	0.03
U	0.01	0.02	0.02	0.01

Table A5.10: Banded Hbl-Ol gabbro amphibole trace element compositions, in µg/g.

Chapter 6 - Synthesis and Conclusions

6.1 - Plutonic xenoliths as a tool for investigating crustal magmatic processes

This thesis aimed to determine whether the majority of the trace element and isotopic variation in Lesser Antilles arc (LAA) lavas could be attributed to processes within mush-dominated magma plumbing systems in the arc crust. Plutonic xenoliths, which represent fragments of crystal mushes, were used to investigate three crustal processes by which the chemical compositions of LAA magmas may be modified: crustal sediment assimilation, fractional crystallization and reactive melt flow/melt-mush reaction. This detailed study of plutonic xenoliths has provided novel insights into processes controlling chemical variation in LAA lavas that cannot be obtained from study of the lavas in isolation.

In **Chapter 4**, the sources of radiogenic isotopic variation and extreme "crustal/sedimentary" isotopic compositions in Martinique lavas were investigated. The study aimed to distinguish between competing hypotheses of subducted sediment addition to the mantle source vs assimilation of unsubducted sediments within the arc crust. Strontium isotopic compositions ($^{87}Sr/^{86}Sr$) of plagioclase within mid-crustal (≥ 12 km depth) cumulate and upper crustal (6-12 km depth) non-cumulate gabbro plutonic xenoliths, supplemented by plutonic xenolith whole rock Sr-Nd-Pb isotopic compositions, constrain the location of sediment addition to Martinique magmas. Plagioclase from mid-crustal plutonic xenoliths showed a restricted range of unradiogenic Sr isotopic compositions, whereas plagioclase from upper crustal plutonic xenoliths showed greater intra-sample variation and extend to more radiogenic Sr isotopic compositions. These results suggest that isotopic variation and highly radiogenic "crustal" isotopic compositions in Martinique lavas are produced by upper crustal sediment assimilation. This finding was supported by Assimilation-Fractional Crystallization modelling which showed that majority of the Sr-Nd-Pb isotopic variation in Martinique lavas can be explained by assimilation of chemically and isotopically heterogenous sediments.

Chapter 5 focused on newly acquired plutonic xenoliths from St Vincent. The study aimed to determine whether magma chemical evolution in the mushy magma plumbing

system beneath St Vincent is controlled by fractional crystallization or reactive melt flow/melt-mush reaction. Specifically, the effects of these crustal processes on magma trace element compositions were investigated. Fractional crystallization and melt-mush reaction processes were evaluated by combining textural observations, chemical mapping and clinopyroxene and amphibole trace element chemistry of plutonic xenoliths. Textures and mineral chemistry of olivine gabbro plutonic xenoliths support an origin via polybaric fractional crystallization from a primitive basaltic magma. In contrast, hornblende-olivine gabbros record reactive melt flow/melt-mush reaction processes. Textural evidence, including embayments in olivine resulting from dissolution and replacement of partially dissolved clinopyroxene by amphibole, is a key indicator of melt-mush reaction processes in plutonic xenoliths. The rare earth element compositions of melts in equilibrium with plutonic xenolith clinopyroxene and amphibole suggest that both fractional crystallization and reactive melt flow/melt-mush reaction contribute to trace element compositions of St Vincent lavas. The contribution of melt-mush reaction is cryptic and only identified via study of plutonic xenoliths.

The following discussion begins by considering the implications of the results of **Chapters 4 and 5** for understanding the control exerted by crustal sediment assimilation, fractional crystallization and reactive melt flow/melt-mush reaction on lava chemical compositions throughout the LAA. A typical model for the processes by which magmas ascending through LAA plumbing systems are chemically modified prior to eruption is then proposed. Next, the wider implications of this work for the interpretation of arc lava chemical compositions and their use in studies of subduction zone recycling and mantle source heterogeneity are discussed. Finally, some avenues of future research utilizing plutonic xenoliths collected as part of this study and plutonic xenoliths from other arc systems are proposed.

6.2 - Crustal magmatic processes in the Lesser Antilles arc

In this section, the findings from Martinique and St Vincent are compared with previous studies of plutonic xenoliths and lavas from the LAA. The following subsections discuss whether crustal processes (crustal sediment assimilation, fractional

crystallization, reactive melt flow/melt-mush reaction) can explain majority of the trace element and isotopic variation in LAA lavas.

6.2.1 - Crustal assimilation in the Lesser Antilles arc

The variation in radiogenic isotopic compositions of Martinique lavas encompasses the entire isotopic range seen across the LAA (**Chapter 4, Figures 4.2 and 4.3**). Since crustal sediment assimilation represents the dominant control on radiogenic isotopic variation in Martinique lavas (**Chapter 4**), the possibility that this process may account for isotopic variation in lavas throughout the LAA is explored below.

6.2.1.1 - Crustal assimilation in the northern Lesser Antilles arc?

Lavas in the northern LAA (Saba to Dominica) show a restricted isotopic range compared to the southern islands (Martinique to Grenada) (**Chapter 1**), suggesting that their isotopic compositions have been comparatively little influenced by sediment addition. Carpentier et al., (2008) suggested that the radiogenic isotopic compositions of northern LAA lavas can be explained by < 1% sediment addition to the mantle source. However, based on correlations between Pb isotopes and SiO_2, Toothill et al., (2007) suggested that St Kitts lavas may have assimilated small amounts of biogenic sediment (composed of the tests of marine organisms, such as forams or coccolithophores, and organic matter) within the crust, which has also been suggested for Saba lavas based on trace element ratios (Defant et al., 2001). Davidson and Wilson (2011) proposed that Statia lavas were affected by crustal contamination during differentiation based on correlations between radiogenic isotopes and SiO_2. However, whole rock isotopic compositions of Statia plutonic xenoliths do not display generally more radiogenic Sr and Pb in non-cumulate gabbros (upper crustal) compared with cumulates (mid-crustal) (Cooper and Inglis, 2022) as observed in Martinique plutonic xenoliths (**Chapter 4**). Plutonic xenoliths from other northern LAA islands are yet to be analysed for radiogenic isotopic compositions.

An important factor to consider when assessing potential effects of crustal sediment assimilation in the northern LAA (Saba to Dominica) is the difference in underlying crust composition between the northern and southern parts of the arc (**Chapter 1, Figure 1.2**). Geophysical data suggests that the arc from Saba to Dominica is built on older arc crust of the Caribbean plate, in contrast to sediments (and oceanic crust) in the southern LAA (Allen et al., 2019). Hence, northern LAA magmas may not interact

with sediments when transiting the arc crust. If biogenic sediments are intercalated within the arc crust and assimilated beneath the northern LAA, their isotopic composition may not contrast enough with the magmas to be clearly detected. This scenario could also arise if the amount of biogenic sediment assimilation is very small. Hence, the impact of crustal sediment assimilation on the chemical and isotopic compositions of northern LAA lavas is yet to be well constrained and presents an opportunity for future research (discussed in **Section 6.6**).

6.2.1.2 - Crustal assimilation in the southern Lesser Antilles arc?

According to tectonic reconstructions and geophysical data, Martinique and the southern LAA islands (Martinique through to Grenada) share a common basement of oceanic crust and sediments of the Grenada and Tobago basins (Allen et al., 2019, **Chapter 1, Figures 1.2 and 1.3**). Grenada-Tobago basin sediments have not been sampled or measured for chemical and isotopic compositions. Based on available constraints, Grenada-Tobago basin sediments are inferred to be isotopically heterogenous (**Chapter 4, section 4.4.1.2**). In **Chapter 4**, a variety of sediment end member isotopic compositions were used for Assimilation-Fractional Crystallization (AFC) modelling of Martinique lavas to represent this heterogeneity. Since the southern LAA islands were built through Grenada-Tobago basin sediments, the sediment end member compositions from **Chapter 4** can be assumed to represent viable end members for the entire southern arc. The Îlet à Ramiers basalt from Martinique, used as the parental magma in AFC models in **Chapter 4**, has a similar elemental and isotopic composition to the most mafic lavas from St Lucia, St Vincent and Bequia in the Grenadines (Bezard et al., 2015b). The Îlet à Ramiers basalt could therefore be considered a potential proxy for parental magmas in the southern LAA generally. In **Figure 6.1**, the AFC models from **Chapter 4 (**initially shown in **Figures 4.10 and 4.11)**, which use the Îlet à Ramiers basalt parental magma composition and a variety of sediment end members, are compared with Sr-Nd-Pb isotopic compositions of southern LAA lavas.

Figure 6.1 shows that isotopic variation in a significant proportion of southern LAA lavas can be explained by assimilation of chemically and isotopically heterogenous crustal sediments, represented by the various end members used for the AFC models. The most extreme Martinique lava isotopic composition (most radiogenic Sr and Pb

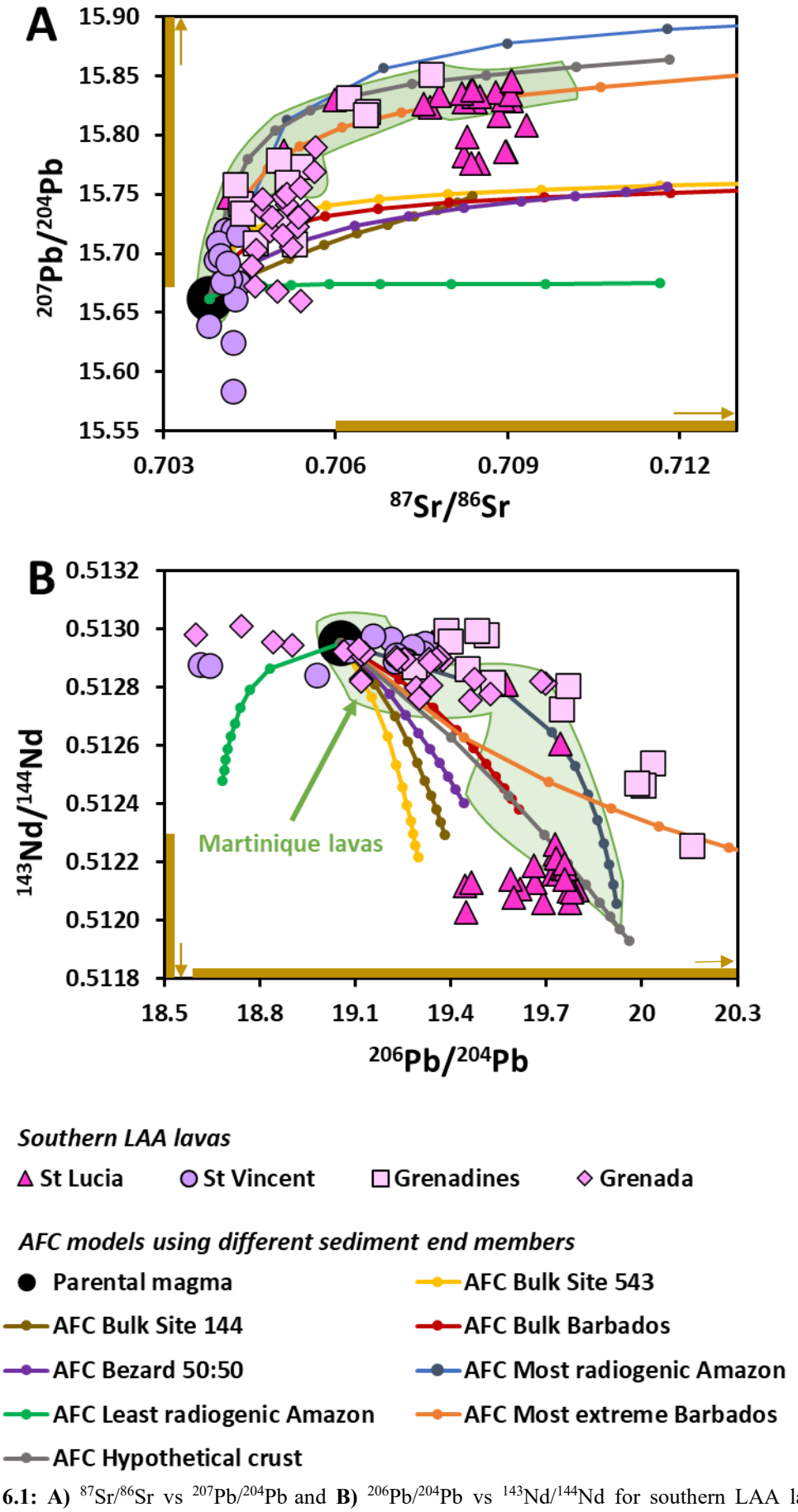

Figure 6.1: A) $^{87}Sr/^{86}Sr$ vs $^{207}Pb/^{204}Pb$ and **B)** $^{206}Pb/^{204}Pb$ vs $^{143}Nd/^{144}Nd$ for southern LAA lavas,

compared with parental magma composition and Assimilation-Fractional Crystallization (AFC) models from **Chapter 4, Figures 4.11 and 4.12**. The green field shows the isotopic range of Martinique lavas. Each coloured curve corresponds to an AFC model using a different crustal sediment end member from **Table 4.3** in **Chapter 4** as the assimilant composition (see legend). The Îlet à Ramiers basalt from Martinique was used as the parental magma composition (**Table 4.3, Chapter 4**). Each point along the AFC curves represents an increment of 10 % crystallization, up to a maximum of 90 %. All data sources as per **Chapter 4**. For all data points, uncertainty (2 SE) is smaller than symbol size. Brown bars along axes show range of isotopic compositions of sediments potentially equivalent to those in the arc crust, as identified in **Chapter 4**.

isotope ratios) can be explained by 23-28 % sediment assimilation (**Chapter 4, section 4.4.4.2**). The most extreme Martinique lava has more radiogenic $^{87}Sr/^{86}Sr$, $^{207}Pb/^{204}Pb$, $^{208}Pb/^{204}Pb$ and more unradiogenic $^{143}Nd/^{144}Nd$ than all southern LAA lavas (**Figure 6.1**). Therefore, it is likely that < 28 % sediment assimilation is required to explain the isotopic compositions of southern LAA lavas reproduced by the AFC models in **Figure 6.1**. The sediment end members used for the AFC models only cover some of the wide range of sediment isotopic compositions that may exist in the arc crust (see **Chapter 4, Figures 4.8** and **4.10,** brown bars on **Figure 6.1**). Theoretically, sediments assimilated by southern LAA magmas could have isotopic compositions anywhere within the inferred possible range identified in **Chapter 4** (**Figures 4.8** and **4.10**). Therefore, where southern LAA lava isotopic compositions are not reproduced by the AFC models in **Figure 6.1**, it is possible that these lavas have assimilated sediments with a different isotopic composition to any of the end members used in the models.

Parental magma elemental and isotopic compositions could also vary between southern LAA islands. Bezard et al., (2015b) showed that the most mafic lavas from Grenada and the southernmost Grenadines are chemically and isotopically different to the most mafic lavas from Martinique, St Vincent, St Lucia and Bequia (northern Grenadines). Hence, the parental magma composition used for the AFC models in **Figure 6.1,** although appropriate for Martinique, may not accurately represent parental magmas of all of the southern LAA islands. Heterogeneity in parental magma/mantle source compositions could explain the less radiogenic Pb isotopic compositions of some St Vincent and Grenada lavas that lie away from any of the AFC model trends (**Figure 6.1**).

6.2.2 – Fractional crystallization in the Lesser Antilles arc

The extensive LAA plutonic xenolith record provides insights into fractional crystallization processes in LAA magma plumbing systems. Plutonic xenoliths containing high An (>80) plagioclase with low Fo (<80) olivine, as observed in St Vincent samples (**Chapter 5**) are found throughout the LAA (Tollan et al., 2012, Cooper et al., 2016, 2019, Melekhova et al., 2015, 2017, 2019, Ziberna et al., 2017, Camejo-Harry et al., 2018). In these studies, high An plagioclase-low Fo olivine plutonic xenoliths are widely interpreted to have crystallized at mid-upper crustal pressures from water-rich parental melts. These parental melts are generally inferred to have been produced by a prior stage of olivine and clinopyroxene dominated crystallization, from primitive basaltic magmas, in the lower crust/at high pressures (Tollan et al., 2012, Cooper et al., 2016, 2019, Melekhova et al., 2015, 2017, 2019, Ziberna et al., 2017, Camejo-Harry et al., 2018). Hence, polybaric fractional crystallization appears to be a common process recorded by plutonic xenoliths throughout the LAA.

Based on thermobarometry, comparisons to experimental products and pressure estimates from melt inclusions, the majority of plutonic xenoliths erupted in the LAA are inferred to have crystallized between 6-21 km depth (Cooper et al., 2016, 2019, Melekhova et al., 2017, 2019, Ziberna et al., 2017, Camejo-Harry et al., 2018). Hence, most LAA plutonic xenoliths could represent products of lower pressure, mid-upper crustal stages of polybaric fractional crystallization. Plutonic xenoliths recording early and/or high-pressure stages of polybaric fractional crystallization, such as wehrlites and clinopyroxenites, have been occasionally reported, for example on Grenada (Stamper et al., 2014, Melekhova et al., 2019). Alternatively, clinopyroxene formed in the lower crust may be present as crystal cargoes in plutonic xenoliths that crystallized at shallower levels (for example, in the poikilitic Hbl-Ol gabbro from **Chapter 5).**

In **Chapter 5,** based on clinopyroxene trace element compositions in St Vincent olivine gabbros, it is inferred that melts modified by FC of mid-upper crustal mush assemblages contribute to the trace element compositions of St Vincent lavas. Lesser Antilles lava trace element compositions often define fractionation trends consistent with crystallization of observed (mid-upper crustal) plutonic xenolith assemblages, such as olivine gabbro (olivine + clinopyroxene + plagioclase ± magnetite), hornblende gabbro (plagioclase + amphibole + magnetite) and gabbronorite/non-cumulate gabbro (plagioclase + clinopyroxene + orthopyroxene + oxides) (e.g. Smith et al., 1996, Heath

et al., 1998, Lindsay et al., 2005, Toothill et al., 2007, Davidson and Wilson, 2011). This observation suggests that FC in mid-upper crustal mushes is an important process controlling the trace element compositions of lavas throughout the LAA.

6.2.3 – Melt-mush reaction in the Lesser Antilles arc

The investigation in **Chapter 5** demonstrates that textural features in plutonic xenoliths are an important indicator of melt-mush reaction processes. The textural association of (sometimes poikilitic) amphibole replacing clinopyroxene has been interpreted as evidence for reactive melt flow/melt-mush reaction in plutonic xenoliths from St Kitts (Melekhova et al., 2017), Guadeloupe (Blundy, 2022), Dominica (Sparks et al., 2021), Martinique (Cooper et al., 2016), Bequia (Camejo-Harry et al., 2018), Grenada (Stamper et al., 2014) and St Vincent (**Chapter 5**). Therefore, the plutonic xenolith record suggests that reactive melt flow/melt-mush reaction is a common process in LAA magma plumbing systems.

The majority of LAA plutonic xenoliths with textural evidence for reactive melt flow are plagioclase bearing and considered to be derived from the mid-upper crust (<18 km) (Cooper et al., 2016, Melekhova et al., 2017, Camejo-Harry et al., 2018, this study). Poikilitic amphibole interpreted to have formed via reactive melt flow is also occasionally found in clinopyroxenites (Stamper et al., 2014), which may have formed in the lower crust (Melekhova et al., 2019). Based on evidence for melt-mush reaction in arc lower crustal sections (e.g. Bouilhol et al., 2015, Villares et al., 2022), it could be expected that this process also occurs in LAA lower crust. Hence, the plutonic xenolith record suggests that reactive melt flow/melt-mush reaction processes operate throughout trans-crustal magma plumbing systems in the LAA.

In **Chapter 5**, it is inferred that melts chemically modified by reactive melt flow/melt-mush reaction may cryptically contribute to the trace element compositions of St Vincent lavas. Melts in equilibrium with amphibole in Martinique plutonic xenoliths interpreted to have formed via reactive melt flow show similar REE patterns and concentrations to Martinique lavas (Cooper et al., 2016), suggesting that this process also influences lava trace element compositions in Martinique. Bezard et al., (2015a) suggested that Os isotopic compositions and correlated La/Sm and Sr/Th ratios of the most mafic lavas from the LAA could be explained by assimilation of a plagioclase-rich cumulate. Such an assimilant could correspond to plagioclase-rich mushes

represented by many LAA plutonic xenoliths. Hence, this chemical signature could be imparted via dissolution of plagioclase-rich mush during melt-mush reaction processes, as recorded by St Vincent plutonic xenoliths (**Chapter 5**). The findings of Bezard et al., (2015a) support the suggestion, based on comparison of St Vincent lavas and plutonic xenolith equilibrium melts, that even primitive LAA lavas are unlikely to have escaped chemical modification within the crust (**Chapter 5**). These lines of evidence, combined with textures indicative of reactive melt flow/melt-mush reaction in plutonic xenoliths from several islands suggests that this process likely contributes to lava trace element compositions throughout the arc.

6.2.4 – Can trace element and isotopic variation in Lesser Antilles arc lavas be generated by crustal processes alone?

Constraints from Martinique plutonic xenoliths combined with AFC modelling (**Figure 6.1**) suggest that assimilation of crustal sediments can explain majority of radiogenic isotopic variation in southern LAA lavas, without the need to invoke significant contribution from subducted sediments or a high degree of mantle heterogeneity. For northern LAA lavas, the potential influence of crustal sediment assimilation is yet to be well constrained. It is possible that melt-mush reaction could also influence isotopic compositions of LAA lavas, though this has yet to be explored and presents an opportunity for future research (see **section 6.6**).

Evidence from plutonic xenoliths suggests that both fractional crystallization and reactive melt flow/melt-mush reaction can influence trace element compositions of LAA lavas. A role for fractional crystallization is often clear based on subaerial lava compositions, but contributions from melts modified by melt-mush reaction are cryptic, since the process is primarily identified through textural features in plutonic xenoliths. Although not specifically investigated here, crustal sediment assimilation may also influence trace element compositions of LAA lavas, as proposed by several previous studies of lavas alone (e.g. Smith et al., 1996, Thirlwall et al., 1996, Davidson and Wilson, 2011, Bezard et al., 2015b).

Chemical compositions of many LAA lavas are also influenced by magma mixing, recorded by both chemical trends and crystal zoning patterns (e.g. Gorgaud et al., 1989, Defant et al., 2001, Boudon et al., 2008, Cassidy et al., 2015, Bezard et al., 2017, White et al., 2017, Pichavant et al., 2018, Solaro et al., 2020). Mixing of melts (and crystal

cargoes) of different chemical composition may homogenize magmas prior to eruption and could explain why LAA lavas do not typically show the chemical diversity recorded in plutonic xenoliths (and melt inclusions) (as observed in St Vincent in **Chapter 5** and Statia, Cooper et al., 2019). Variable crystallization pressures recorded by mineral phases (which may be phenocrysts or antecrysts entrained from mushes) and their melt inclusions in LAA lavas (e.g. Cassidy et al., 2015, Balcone-Boissard et al., 2018, Higgins et al., 2022) suggest that melts and crystals from various regions of magma plumbing systems can be blended to form final erupted products. Hence, LAA lava chemical compositions likely reflect the combined product of multiple crustal processes. Evidence from this study, supported by previous literature, suggests that majority of isotopic and trace element variation in LAA lavas can be attributed to crustal processes.

6.3 - General model for southern Lesser Antilles arc magma plumbing systems

Figure 6.2 shows a general model for how the chemical compositions of LAA magmas are modified during ascent through mushy magma plumbing systems prior to eruption. The schematic is based on the southern LAA (Martinique to Grenada) where the arc crust consists of older oceanic crust and sediments (Aitken et al., 2011, Allen et al., 2019).

Primitive hydrous basaltic magmas are emplaced into a deep crustal hot zone (**Figure 6.2, 1, DCHZ**). Here, primitive magmas differentiate via crystallization of predominantly olivine ± clinopyroxene ± spinel, (this study, Tollan et al., 2012, Melekhova et al., 2015, Cooper et al., 2016, 2019, Camejo-Harry et al., 2018) producing a variety of melt compositions. Reactive melt flow/melt-mush reaction, resulting in replacement of clinopyroxene with amphibole, may also modify mineral and melt chemical compositions in the lower crust.

Batches of H_2O-rich melt with variable chemical composition, potentially carrying entrained crystal cargoes, ascend from the deep crustal hot zone into a heterogenous mid-crustal mush zone (**Figure 6.2, 2, MCMZ**). Here, newly emplaced batches of melt undergo a second stage of fractional crystallization. Variations in chemical composition, H_2O contents and temperature of newly emplaced melts result in

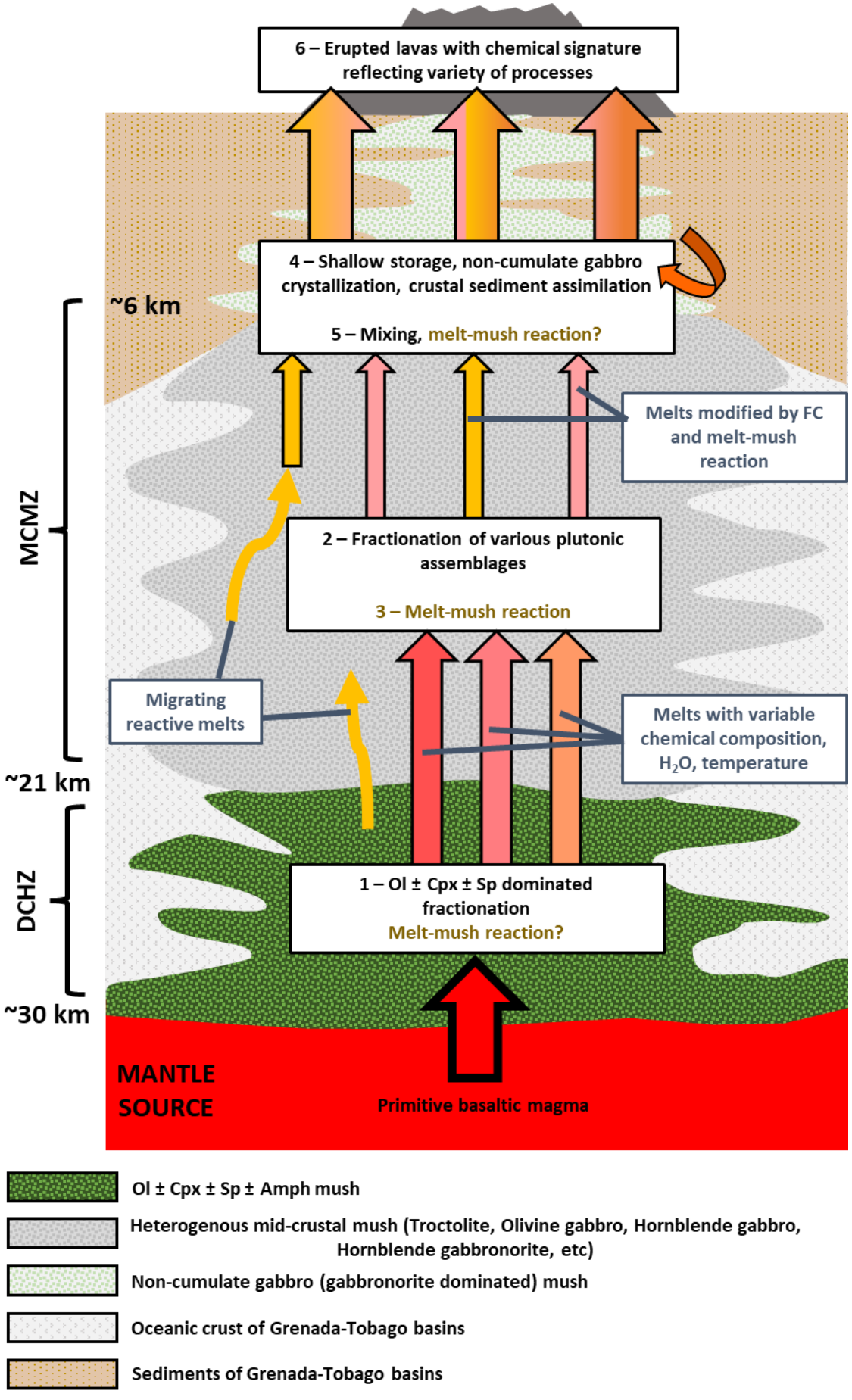
6 – Erupted lavas with chemical signature reflecting variety of processes
4 – Shallow storage, non-cumulate gabbro crystallization, crustal sediment assimilation
5 – Mixing, melt-mush reaction?
~6 km
Melts modified by FC and melt-mush reaction
MCMZ
2 – Fractionation of various plutonic assemblages
3 – Melt-mush reaction
Migrating reactive melts
Melts with variable chemical composition, H_2O, temperature
~21 km
DCHZ
1 – Ol ± Cpx ± Sp dominated fractionation
Melt-mush reaction?
~30 km
MANTLE SOURCE
Primitive basaltic magma
Ol ± Cpx ± Sp ± Amph mush
Heterogenous mid-crustal mush (Troctolite, Olivine gabbro, Hornblende gabbro, Hornblende gabbronorite, etc)
Non-cumulate gabbro (gabbronorite dominated) mush
Oceanic crust of Grenada-Tobago basins
Sediments of Grenada-Tobago basins

Figure 6.2: Schematic illustrating the processes by which the chemical compositions of magmas may be modified during ascent through mushy magma plumbing systems in the southern LAA. DCHZ = deep crustal hot zone. MCMZ = mid-crustal mush zone. Depths to base of crust, top of DCHZ and top of MCMZ are approximate, based on the southern LAA crustal structure defined by seismic properties and plutonic xenolith petrology proposed by Melekhova et al., (2019). Depth to base of sediment layer (shown as ~ 8 km) represents a rough approximation – sediments in the Grenada-Tobago basins reach thicknesses of up to 14 km (Aitken et al., 2011). The variety of colours used to fill the bold arrows with black outlines is designed to reflect variation in magma chemical compositions throughout the plumbing system.

crystallization of a wide variety of plutonic assemblages (Tollan et al., 2012, Cooper et al., 2016, Camejo-Harry et al., 2018, Melekhova et al., 2019). Some melts ascending into and migrating through the mid-crustal mush zone react with pre-existing mushes, modifying textures, mineral assemblages and mineral and melt chemical compositions in portions of the plumbing system (**Figure 6.2, 3**). Hence, magma chemical compositions within the mid-crustal mush zone are modified by fractional crystallization and/or melt-mush reaction.

Melts segregated from the mid-crustal mush zone, plus entrained crystal cargoes (e.g. Stamper et al., 2014, Fedele et al., 2021), ascend to shallow storage regions prior to eruption. Here, further crystallization forms the phenocryst phases in erupted lavas and non-cumulate gabbros (Stamper et al., 2014, Cooper et al., 2016, 2019, Camejo-Harry et al., 2018). Magmas may assimilate significant proportions (up to a maximum of 28 %) of heterogenous upper crustal sediments (**Figure 6.2, 4**), which include turbidites, siltstones, marls, limestones and shales (Aitken et al., 2011), further modifying their chemical and isotopic compositions. Lavas in the LAA arc frequently record evidence for magma mixing (e.g. Gorgaud et al., 1989, Heath et al., 1998, White et al., 2017, Bezard et al., 2017, Pichavant et al., 2018, sample M8321 in **Chapter 4**) which may occur as melts and crystal cargoes interact in shallow reservoirs (**Figure 6.2, 5**) and/or possibly deeper in the mid-crustal mush (Cooper et al., 2019). Chemical compositions of the melts and crystals blended during mixing are likely to have been previously influenced by fractional crystallization and/or melt-mush reaction and/or crustal assimilation.

Eventually, melts and phenocrysts/crystal cargoes ascend from shallow storage regions to erupt as lavas (**Figure 6.2, 6**). It is also possible that magmas from deeper levels of the plumbing system may be directly erupted. Chemical compositions of majority of

lavas reflect one or more processes (fractional crystallization, melt-mush reaction, crustal sediment assimilation, magma mixing) by which magmas can be chemically modified during passage through mushy, trans-crustal LAA magma plumbing systems.

6.4 - Wider implications for understanding subduction zone processes

This study shows that trace element and isotopic compositions of LAA lavas are predominantly controlled by processes within mushy magma plumbing systems in the arc crust. The findings imply that crustal modification of arc magma chemical compositions could explain majority of chemical variation in arc lavas generally. The isotopic, trace element and volatile compositions of arc lavas are commonly used to interpret sediment, chemical element and volatile recycling at subduction zones and arc mantle source heterogeneity (e.g. Plank and Langmuir, 1993, Turner and Hawkesworth, 1997, Turner et al., 1999, Patino et al., 2000, Straub and Layne, 2003, Chauvel et al., 2009, Nebel et al., 2011, Bebout et al., 2014 and references therein). As mentioned in **Chapters 4 and 5**, the findings from this thesis have major implications for whether arc lava chemical compositions can be reliably used in such studies.

The results of **Chapter 4** suggest that the potential influence of crustal sediment assimilation must be considered when interpreting arc lava radiogenic isotopic compositions. In **Chapter 4**, it was noted that the LAA may represent a unique setting, where the presence of a thick layer of sediments inferred to have highly radiogenic isotopic compositions (see discussion in **Chapter 4, section 4.4.1.2**) in the arc crust results in an obvious impact of crustal sediment assimilation on lava isotopic compositions. The thicker crust of the LAA (~25-30 km, Schlaphorst et al., 2021) compared with some other intra-oceanic arcs, such as the South Sandwich, Mariana and Tonga-Kermadec arcs (Melekhova et al., 2019) may also facilitate more extensive crustal assimilation compared with other systems.

In other intra-oceanic arcs where the crustal structure is less well constrained than the LAA, the presence of sediments/older continental material in the arc crust may be less apparent. For example, in the Vanuatu arc, continental material in the arc basement was detected only via inherited zircons in erupted lavas (Buys et al., 2014). Buys et al., (2014) proposed that assimilation of this continental material could explain some of the isotopic variation in Vanuatu arc lavas previously attributed to subducting slab

inputs (Peate et al., 1997). Similar hidden reservoirs of sedimentary/continental material may be intercalated within the crust of other intra-oceanic arcs. Hence, the influence of crustal sediment assimilation must be constrained, for example via isotopic investigation of plutonic xenoliths, if arc lava radiogenic isotopic compositions are to be reliably used to interpret to mantle source heterogeneity and subducting slab inputs to arc mantle sources.

Crustal sediment assimilation may also modify volatile contents of arc magmas. For example, assimilation of crustal carbonate sediments has been shown to significantly affect the CO_2 budget of arc magmas (e.g. Deegan et al., 2010, Troll et al., 2012, Mason et al., 2017) and shale assimilation can affect S budgets (e.g. Deegan et al., 2022). Recently, it has also been suggested that reactive melt flow in crystal mushes may influence magmatic H_2O contents (Gleeson et al., 2022). Hence, constraining the potential influence of crustal processes is vital for interpretation of volatile sources in arc magmas and volatile recycling in subduction zones.

A common approach in studies using arc lava trace element compositions to estimate subduction zone recycling is to use only basaltic/primitive lavas for the calculations, assuming that these lavas have been minimally affected by fractional crystallization and crustal assimilation (e.g. Plank and Langmuir, 1993, Plank, 2005). Even if these processes (and potential influence from variable degrees of mantle partial melting) can be discounted, it is possible that basaltic lava trace element compositions could have been modified by melt-mush reaction processes. The results of **Chapter 5** show that LREE concentrations can be particularly sensitive to melt-mush reaction, as observed in previous studies (e.g. Cooper et al., 2016, Lissenberg and MacLeod, 2016, Boulanger et al., 2021). Hence, melt-mush reaction may influence trace element ratios such as La/Sm and Th/La in arc basalts which are often used to trace subducted sediment additions to arc mantle sources (e.g. Plank, 2005, Labanieh et al., 2012). Basaltic lavas can also be affected by magma mixing (e.g. Reubi et al., 2003) and basaltic whole-rock compositions may be influenced by crystal cargoes entrained from mushes (e.g. Dungan and Davidson, 2004, Cassidy et al., 2015, Fedele et al., 2021). These lines of evidence suggest that even primitive basaltic arc lavas may not preserve trace element compositions and ratios of their mantle source regions.

Plutonic xenoliths and crystal cargoes derived from lower crustal depths, or melt inclusions within these phases, may provide the best available insights into trace element and isotopic compositions of primitive magmas and mantle sources in active arcs. Although it cannot be ruled out that such crystals/samples have not been influenced to some extent by crustal processes, it is more likely that mineral phases and melt inclusions from the deepest and earliest phases of magma differentiation preserve the chemical signature of arc mantle sources than lavas composed of melt(s) and crystals that have been processed in mushy trans-crustal magma plumbing systems.

6.5 – Conclusions

This section summarizes the main findings of this thesis.

6.5.1 – Key conclusions from Chapter 4

-**Chapter 4** uses plutonic xenoliths to investigate whether isotopic variation and highly radiogenic "crustal" isotopic compositions in Martinique lavas are produced by crustal sediment assimilation or addition of subducted sediments to the mantle source.

-Mid-crustal (≥ 12 km depth) plutonic xenoliths show unradiogenic, restricted ranges in plagioclase Sr isotopic compositions. Upper crustal (6-12 km depth) plutonic xenoliths show greater intra-sample variation and extend to more radiogenic plagioclase Sr isotopic compositions.

-These results suggest that isotopic variation and highly radiogenic isotopic compositions in Martinique lavas are acquired via assimilation of upper crustal sediments.

-Assimilation-Fractional Crystallization models demonstrate that Sr-Nd-Pb isotopic variation in Martinique lavas can be explained via < 28% assimilation of chemically and isotopically heterogenous upper crustal sediments.

6.5.2 – Key conclusions from Chapter 5

-**Chapter 5** uses plutonic xenoliths to investigate whether magma chemical evolution in the mushy magma plumbing system beneath St Vincent is controlled by fractional crystallization or reactive melt flow/melt-mush reaction.

-Textures and mineral chemistry of olivine gabbros, which crystallized in the mid-crust (6-18 km depth), are consistent with an origin via polybaric fractional crystallization from a primitive basaltic magma. Hornblende-olivine gabbros from the mid-upper crust (6-12 km depth) display textural and mineral chemical evidence for melt-mush reaction processes.

-Textural features, such as embayed, partially replaced mineral phases, are an important indicator of melt-mush reaction processes in plutonic xenoliths. Trace element compositions of plutonic xenolith clinopyroxene and amphibole in isolation do not distinguish whether these phases formed via fractional crystallization or melt-mush reaction.

-Both fractional crystallization and melt-mush reaction influence magma chemical compositions in the St Vincent plumbing system and contribute to trace element compositions of St Vincent lavas.

6.5.3 – Key conclusions from Chapter 6

-Evidence from Martinique and St Vincent plutonic xenoliths, combined with studies of plutonic xenoliths and lavas from other LAA islands, suggests that majority of the trace element and isotopic variation in LAA lavas can be attributed to crustal processes. These include crustal sediment assimilation, (polybaric) fractional crystallization, melt-mush reaction and magma mixing.

-The influence of crustal processes must be well constrained if arc lava trace element, isotopic and volatile compositions are to be used to robustly interpret recycling processes and mantle source heterogeneity at subduction zones.

6.6 - Future research

This thesis demonstrates that detailed petrographic and geochemical investigation of plutonic xenoliths provides novel insights into the processes by which arc magma chemical compositions are modified in mushy plumbing systems. This section proposes avenues of future research based on plutonic xenoliths for the LAA and other arc systems.

The abundance of plutonic xenoliths in the LAA (e.g. Arculus and Wills, 1980, Melekhova et al., 2019) could be related to high weathering rates in the Caribbean which concentrates them in rivers or gullies from which they are typically collected. Alternatively, it may simply be a result of these samples being targeted on field campaigns, such as this study (**Appendix 1**). Large numbers of plutonic xenoliths (>100) have been obtained from single eruptions, for example in deposits from the explosive VEI 6 Fasnia eruption on Tenerife (Horn et al., 2022). However, most eruptions in the LAA are smaller (VEI typically < 4, Crosweller et al., 2012), hence large explosive eruptions do not appear necessary to mobilize and erupt significant quantities of plutonic xenoliths. Therefore, plutonic xenoliths may also be abundant in other arc systems and searching for these samples could facilitate similar detailed research to that undertaken in the LAA.

6.6.1 - Future studies of plutonic xenoliths in the Lesser Antilles arc

Plutonic xenoliths from St Lucia collected during fieldwork (**Appendix 1**) could provide a potential resource for investigating the chemical and isotopic composition of primitive/parental magmas and mantle source beneath the island. Plutonic xenolith samples were obtained directly from the earliest (Pre-SVC 1) lavas erupted on St Lucia, considered to have been negligibly affected by crustal sediment assimilation (Bezard et al., 2014, 2015b). In this scenario, mineral phases in entrained plutonic xenoliths may record magma compositions unaffected by crustal assimilation and late-stage processes such as mixing which may have affected the lavas. Hence isotopic and trace element analysis (both whole rock and mineral phase) of these samples has potential to reveal the parental magma/mantle source composition beneath St Lucia. Analysis of major element compositions of mineral phases will enable thermobarometry calculations and/or comparison to experimental products to determine approximate crystallization depth of the plutonic xenoliths.

Studies of mineral phase radiogenic isotopic compositions (e.g. plagioclase $^{87}Sr/^{86}Sr$) in plutonic xenoliths from northern LAA islands, using the methods presented in this study for Martinique (**Chapter 4**), may reveal the extent of crustal assimilation in the northern LAA. Such investigations may also confirm the presence of biogenic sediments (composed of the tests of marine organisms and organic matter) inferred to exist within the northern LAA crust (Defant et al., 2001, Toothill et al., 2007).

Variation in mineral phase isotopic compositions within individual plutonic xenoliths would provide evidence for crustal assimilation (**Chapter 4**, Bezard et al., 2014) that is otherwise difficult to detect using lava and plutonic xenolith whole-rock compositions. Constraints on plutonic xenolith crystallization depths via thermobarometry calculations and/or comparison to experimental products could be used to determine the depth of any crustal assimilation and the depth of biogenic sediments in the arc crust.

In addition to $^{87}Sr/^{86}Sr$ in plagioclase, measurement of other radiogenic isotopic systems in plutonic xenolith mineral phases could be used to further investigate crustal assimilation processes throughout the LAA. For example, coupled Pb and Sr isotopic compositions in plagioclase have been used to investigate crustal assimilation in flood basalt lavas (Font et al., 2008). Clinopyroxene have also been analysed for Sr, Nd and Pb isotopic compositions in various studies (e.g. Hepworth et al., 2020, Adams et al., 2021, Geng et al., 2022). On the northern LAA island of St Kitts, evidence for minor sediment assimilation affecting the lavas is based on Pb isotope (and trace element) ratios but is not clearly supported by Sr and Nd isotope ratios (Toothill et al., 2007). Hence, measurement of multiple radiogenic isotope systems in co-existing plagioclase and clinopyroxene in plutonic xenoliths could be used to constrain crustal assimilation processes in the northern LAA.

A detailed petrographic and textural examination of a large suite of plutonic xenoliths, such as the 100 plus samples collected from St Vincent as part of this study (**Appendix 1**) (or even multiple large sample suites), could provide a more representative estimate of how common textures indicative of reactive melt flow/melt-mush reaction are in the LAA plutonic xenolith record. Such a study could have implications for detecting melt-mush reaction as a process in other arc magma plumbing systems. For example, if textural evidence for melt-mush reaction is present, but uncommon in a large suite of plutonic xenoliths, it is possible that evidence for this process may be missed in other arc systems simply due to investigation of too few samples.

Mineral phase isotopic compositions in LAA plutonic xenoliths could be used to investigate melt-mush reaction processes in greater depth. If an infiltrating reactive melt and initial mush have different radiogenic isotopic compositions, crystals formed during the reaction will be isotopically distinguishable from initial mush phases. Thus,

mineral phase isotopic compositions could be used to test interpretations based on textural relationships. For example, in the poikilitic Hbl-Ol gabbro studied in **Chapter 5**, relict high An plagioclase cores interpreted to represent the initial mush may have different radiogenic isotopic compositions (for example different $^{87}Sr/^{86}Sr$) to their rims interpreted to have formed during melt-mush reaction. In an alternative scenario where the infiltrating melt and initial mush have identical radiogenic isotopic compositions, stable Sr ($^{88}Sr/^{86}Sr$) isotopic variation among mineral phases such as plagioclase could be indicative of melt-mush reaction. Plagioclase preferentially incorporates ^{88}Sr (e.g. Charlier et al., 2012) and hence fractionates stable Sr isotope ratios. Thus, melt-mush reaction processes that consume and/or crystallize plagioclase could potentially generate heterogeneity in $^{88}Sr/^{86}Sr$ of plagioclase formed during the reaction.

6.6.2 - Future studies of plutonic xenoliths in other arcs

Chapter 5 shows that reactive melt flow/melt-mush reaction processes in active arc magma plumbing systems can be identified using plutonic xenolith textures and mineral chemistry. Given the prevalence of evidence for reactive melt flow/melt-mush reactions in mid-ocean ridge plutonic rocks, LAA plutonic xenoliths and extinct arc crustal sections, it could be expected that these processes are a typical feature of mush-dominated magma plumbing systems in active arc settings. Detailed textural and mineral chemical study of plutonic xenoliths from other active arcs could be used to test this hypothesis and the suggestions made in this work that melt-mush reaction must be considered when interpreting trace element compositions of arc lavas.

Such investigations could target active arcs where lava trace element compositions have previously been used in subduction recycling studies, for example the Central American Volcanic Arc (Patino et al., 2000) and Izu, Mariana and Tonga-Kermadec arcs (Plank and Langmuir, 1993). The Central American Volcanic Arc could represent a particularly good target location due to the presence of plutonic xenoliths containing textural features indicative of melt-mush reaction, such as poikilitic amphibole enclosing embayed olivine and clinopyroxene (e.g. Beard and Borgia, 1989, Kepezhinskas et al., 2020).

The methodology used in **Chapter 4** could be applied to investigations of crustal assimilation in other intra-oceanic arc systems where sediments are known to exist in

the arc crust, such as the Sunda arc, Indonesia. Handley et al., (2014) suggested along arc isotopic and trace element variations in Sunda arc lavas result from both crustal sediment assimilation and different contributions from the subducting slab in different parts of the arc. Radiogenic isotopic compositions of plutonic xenoliths from multiple volcanic centres along the arc could be used to constrain the impact of crustal sediment assimilation on lavas at each volcano. Plutonic xenoliths from deeper crustal levels could provide insights into the composition of magmas prior to crustal assimilation and therefore may record along arc variation in subducting slab inputs.

Study of radiogenic isotopic compositions of plutonic xenoliths from the intra-oceanic Vanuatu arc could be used to test the proposal of Buys et al., (2014) that Vanuatu arc magmas may be chemically modified by assimilation of hidden continental material in the arc basement. Isotopic compositions of plutonic xenoliths from different crustal levels could potentially be used to locate the depth of the assimilant/continental material. In other intra-oceanic arc systems where sediments/continental material are not known to be present within the arc crust (e.g. the South Sandwich arc, Leat et al., 2013), isotopic investigation of plutonic xenoliths could potentially be used to rule out crustal sediment assimilation as a process. Alternatively, plutonic xenoliths may reveal the presence of sediment layers within the arc crust and an unexpected role for crustal sediment assimilation in such intra-oceanic arc systems.

Plutonic xenoliths could also be used to investigate crustal assimilation and melt-mush reaction processes in continental arc systems. The typically greater crustal thickness in continental arcs compared with intra-oceanic arcs is likely to result in a stronger influence of crustal assimilation on lava chemical and isotopic compositions. In addition, a wide diversity of potential assimilant lithologies may be present in the upper plate crust of continental arcs, as observed in the Northern and Central Andean volcanic zones (e.g. Goss et al., 2011, Ancellin et al., 2017). Hence, plutonic xenoliths from different crustal levels of continental arc systems could be used to constrain the depths of addition of different crustal components to continental arc magmas. A thicker crust leads to more vertically extensive magma plumbing systems in continental arcs, which could increase the likelihood of melt-mush reaction processes as magmas transit the upper plate. Plutonic xenoliths with textures indicative of melt-mush reaction, including poikilitic amphibole replacing partially dissolved clinopyroxene and embayed olivine, have been reported from continental arc settings including the

Chilean Andes (Costa et al., 2002) and Cascades (Grove and Donnelly-Nolan, 1986). Detailed textural and trace element analysis of mineral phases in these and other similar plutonic xenoliths from continental arcs could be used to investigate the impact of melt-mush reaction processes on lava trace element compositions in continental arc settings.

Appendix 1 - St Lucia and St Vincent Fieldwork, March 2019

A1.1 - Fieldwork description and rationale

Fieldwork was conducted between 6-13th March 2019, by Joshua Brown and Dr George Cooper. Two field days were spent in St Lucia, and five in St Vincent. Sampling sites were mostly predetermined localities where samples had previously been collected, though some additional localities observed whilst driving or on the map were added. The age/geological formation of the deposits at each locality were determined from the work of previous visitors or geological maps.

The fieldwork was conducted to supplement the existing sample set of Lesser Antilles plutonic xenoliths from the University of Bristol and Durham University collections. An issue identified with the existing samples is that almost all were collected loose from riverbeds, preventing them from being attributed to specific eruptions. For this reason, the fieldwork focussed on the collection of **in situ** plutonic xenoliths, along with associated juvenile lava clasts, from pyroclastic density current (PDC) deposits of a known age/eruptive cycle. Having such samples facilitates study of the relationship between the plutonic xenoliths and the magmas that erupted them. The second aim of the fieldwork was to obtain samples of high-Mg basaltic lavas, which can represent a potential proxy for primitive magma compositions below the arc. Finally, any unusual material that may represent xenoliths of arc crustal lithologies was also collected to help provide constraints on the composition of potential crustal assimilants.

St Lucia was chosen as a target island due to the suggestions of Bezard, 2014, who recommended searching the Pre-SVC1 lavas (which have experienced little to no crustal assimilation) for plutonic xenoliths. It was proposed that mineral isotope analysis of such samples could help to determine whether assimilation of igneous arc crust is an important process on St Lucia. Bezard, 2014, also suggested that isotopic and trace element analyses of plutonic xenoliths from the SVC lavas could provide insights into conditions deeper in the crust below St Lucia. Hence the Pre-SVC1 and

SVC (specifically the Belfond dacite dome) lavas were examined, with plutonic xenoliths successfully sampled from both.

St Vincent was targeted due to the presence of high-Mg basaltic lavas (previously documented by Heath et al., 1998) and good exposure of recently erupted PDC deposits. The unusually high abundance of plutonic xenoliths on St Vincent indicated that this island would have a good chance of yielding in situ plutonic xenolith samples. Also, the limited isotopic diversity of St Vincent compared to other islands such as Martinique and St Lucia suggested that St Vincent plutonic xenoliths may record contrasting processes. The sampling in St Vincent was a major success, with in situ plutonic xenoliths, juvenile magmas, high-Mg basalts and green lithics (potential crustal xenoliths) all collected.

A1.2 – Sample details

Details of name/sample code, age/formation, sampling location and rock type for all samples collected are listed in **Tables A1.1 (St Lucia)** and **A1.2 (St Vincent).** More detailed descriptions of the samples collected at each locality are provided in the following sections.

Sample Code	Age/Formation	Latitude	Longitude	Locality no.	Rock type
SL100	Pre-SVC1	14˚ 05' 28.2"	60˚ 57' 58.3"	1	Lava
SL101	Pre-SVC1	14˚ 05' 28.2"	60˚ 57' 58.3"	1	Lava
SL102	Pre-SVC1	14˚ 05' 35.6"	60˚ 57' 52.9"	2	Cumulate
SL103	Pre-SVC1	14˚ 05' 35.6"	60˚ 57' 52.9"	2	Cumulate
SL104	Pre-SVC1	14˚ 06' 01.3"	60˚ 57' 00.0"	3	Cumulate
SL105	Pre-SVC1	14˚ 06' 01.3"	60˚ 57' 00.0"	3	Cumulate
SL106	Pre-SVC1	14˚ 06' 01.3"	60˚ 57' 00.0"	3	Cumulate
SL107	Pre-SVC1	14˚ 06' 01.3"	60˚ 57' 00.0"	3	Lava
SL108	Pre-SVC1	14˚ 06' 01.3"	60˚ 57' 00.0"	3	Cumulate
SL109	Pre-SVC1	14˚ 06' 01.3"	60˚ 57' 00.0"	3	Cumulate
SL110	Pre-SVC1	14˚ 06' 01.3"	60˚ 57' 00.0"	3	Cumulate

SL111	Pre-SVC1	14˚ 06' 01.3"	60˚ 57' 00.0"	3	Dyke
SL112	Pre-SVC1	14˚ 04' 21.0"	60˚ 57' 45.7"	4	Lava
SL113	Pre-SVC1	14˚ 04' 21.0"	60˚ 57' 45.7"	4	Cumulate
SL114	Pre-SVC1	14˚ 04' 21.0"	60˚ 57' 45.7"	4	Lava
SL115	Pre-SVC1	14˚ 04' 21.0"	60˚ 57' 45.7"	4	Cumulate
SL116	SVC	13˚ 56' 48.7"	61˚ 02' 12.3"	5	Lava
SL117	SVC	13˚ 56' 48.7"	61˚ 02' 12.3"	5	Lava
SL118	SVC	13˚ 56' 48.7"	61˚ 02' 12.3"	5	Mush/non-cumulate gabbro
SL119	SVC	13° 49' 13.8"	61° 02' 21.7"	6	Crystal clot in host lava
SL120	SVC	13° 49' 13.8"	61° 02' 21.7"	6	Crystal clot in host lava
SL121	SVC	13° 49' 13.8"	61° 02' 21.7"	6	Crystal clot in host lava
SL122	SVC	13° 49' 13.8"	61° 02' 21.7"	6	Mush/non-cumulate gabbro
SL123	SVC	13° 49' 13.8"	61° 02' 21.7"	6	Crystal clot in host lava
SL124	SVC	13° 49' 13.8"	61° 02' 21.7"	6	Cumulate
SL125	SVC	13° 49' 13.8"	61° 02' 21.7"	6	Crystal clot in host lava
SL126	SVC	13° 49' 13.8"	61° 02' 21.7"	6	Mush/non-cumulate gabbro

SL127	SVC	13° 49' 13.8"	61° 02' 21.7"	6	Mush/non-cumulate gabbro

Table A.1: Sample codes, relative ages (where known – samples collected ex situ left blank), sampling location co-ordinates and rock types for St Lucia sample set.

Sample Code	Age/Formation	Latitude	Longitude	Locality no.	Rock type
VS500	Pre Somma	13˚ 15' 41.8"	61˚ 06' 59.6"	7	Lava
VS501	Pre Somma	13˚ 15' 41.8"	61˚ 06' 59.6"	7	Lava
VS502	Pre Somma	13˚ 15' 41.8"	61˚ 06' 59.6"	7	Lava
VS503	Pre Somma	13˚ 15' 41.8"	61˚ 06' 59.6"	7	Lava
VS504	Pre Somma	13˚ 15' 41.8"	61˚ 06' 59.6"	7	Lava
VS505	Pre Somma	13˚ 15' 41.8"	61˚ 06' 59.6"	7	Lava
VS506	Pre Somma	13˚ 15' 41.8"	61˚ 06' 59.6"	7	Cumulate
VS507	Pre Somma	13˚ 15' 41.8"	61˚ 06' 59.6"	7	Cumulate
VS508	Pre Somma	13˚ 15' 41.8"	61˚ 06' 59.6"	7	Cumulate
VS509	Pre Somma	13˚ 15' 41.8"	61˚ 06' 59.6"	7	Cumulate
VS510	Pre Somma	13˚ 15' 41.8"	61˚ 06' 59.6"	7	Pumice
VS511	Pre Somma	13˚ 15' 41.8"	61˚ 06' 59.6"	7	Cumulate
VS512	1902	13˚ 17' 53.4"	61˚ 07' 04.5"	8	Cumulate
VS513		13˚ 17' 53.4"	61˚ 07' 04.5"	8	Cumulate
VS514		13˚ 17' 53.4"	61˚ 07' 04.5"	8	Lava
VS515	1902	13˚ 17' 53.4"	61˚ 07' 04.5"	8	Pumice
VS516	1902	13˚ 17' 53.4"	61˚ 07' 04.5"	8	Pumice
VS517	1902	13˚ 17' 53.4"	61˚ 07' 04.5"	8	Lava
VS518	1902	13˚ 17' 53.4"	61˚ 07' 04.5"	8	Cumulate with host attached

VS519		13˚ 17' 52.7"	61˚ 07' 05.7"	9	Cumulate with host attached
VS520		13˚ 17' 52.7"	61˚ 07' 05.7"	9	Cumulate with host attached
VS521		13˚ 17' 52.7"	61˚ 07' 05.7"	9	Cumulate with host attached
VS522		13˚ 17' 52.7"	61˚ 07' 05.7"	9	Lava
VS523		13˚ 17' 50.0"	61˚ 07' 14.0"	11	Cumulate with host attached
VS524		13˚ 17' 53.4"	61˚ 07' 04.5"	8	Cumulate
VS525	1902	13˚ 17' 54.1"	61˚ 07' 07.8"	10	Lava
VS526		13˚ 17' 52.7"	61˚ 07' 05.7"	9	Cumulate with host attached
VS527		13˚ 17' 52.7"	61˚ 07' 05.7"	9	Cumulate with host attached
VS528		13˚ 17' 52.7"	61˚ 07' 05.7"	9	Cumulate with host attached
VS529	1902	13˚ 17' 54.1"	61˚ 07' 07.8"	10	Crystal
VS530		13˚ 17' 54.1"	61˚ 07' 07.8"	10	Lava with "mushy" enclaves
VS531	1902	13˚ 17' 52.7"	61˚ 07' 05.7"	9	Cumulate with host attached

VS532	1902	13˚ 17' 52.7"	61˚ 07' 05.7"	9	Cumulate with host attached
VS533	1902	13˚ 17' 50.0"	61˚ 07' 14.0"	11	Cumulate
VS534	1902	13˚ 17' 50.0"	61˚ 07' 14.0"	11	Cumulate
VS535	Unknown	13˚ 22' 33.9"	61˚ 08' 24.5"	12	Lava
VS536	Unknown	13˚ 22' 33.9"	61˚ 08' 24.5"	12	Lithic
VS537	Unknown	13˚ 22' 33.9"	61˚ 08' 24.5"	12	Cumulate
VS538	Unknown	13˚ 22' 33.9"	61˚ 08' 24.5"	12	Cumulate
VS539	Unknown	13˚ 22' 33.9"	61˚ 08' 24.5"	12	Cumulate
VS540	Unknown	13˚ 22' 33.9"	61˚ 08' 24.5"	12	Cumulate with host attached
VS541	Unknown	13˚ 22' 33.9"	61˚ 08' 24.5"	12	Cumulate with host attached
VS542	Unknown	13˚ 22' 33.9"	61˚ 08' 24.5"	12	Lava with crystal clots
VS543	Unknown	13˚ 22' 33.9"	61˚ 08' 24.5"	12	Lava with crystal clots
VS544	Unknown	13˚ 22' 33.9"	61˚ 08' 24.5"	12	Lava with crystal clots
VS545	Pre Somma	13˚ 20' 32.6"	61˚ 07' 34.0"	13	Lava
VS546	Pre Somma	13˚ 20' 32.6"	61˚ 07' 34.0"	13	Cumulate
VS547	1902	13˚ 17' 54.1"	61˚ 07' 07.8"	10	Cumulate

VS548		La Soufriere	Windward trail	15	Cumulate with host attached
VS549		La Soufriere	Windward trail	15	Cumulate
VS550	1580	13˚ 19' 37.3"	61˚ 10' 17.6"	16	Lava
VS551	1580	13˚ 19' 37.3"	61˚ 10' 17.6"	16	Cumulate with host attached
VS552	1580	13˚ 19' 37.3"	61˚ 10' 17.6"	16	Cumulate with host attached
VS553	1580	13˚ 19' 37.3"	61˚ 10' 17.6"	16	Cumulate
VS554	1580	13˚ 19' 37.3"	61˚ 10' 17.6"	16	Lava
VS555	1902	13˚ 19' 38.3"	61˚ 10' 21.3"	17	Cumulate
VS556	1902	13˚ 19' 38.3"	61˚ 10' 21.3"	17	Cumulate
VS557	? (1902 or 1979)	13˚ 19' 44.5"	61˚ 10' 26.9"	18	Lava
VS558	1902	13˚ 19' 38.8"	61˚ 10' 21.2"	19	Cumulate
VS559	1902	13˚ 19' 37.4"	61˚ 10' 19.1"	20	Lava
VS560		13˚ 19' 37.4"	61˚ 10' 19.1"	20	Lava
VS561		13˚ 19' 37.4"	61˚ 10' 19.1"	20	Cumulate
VS562		13˚ 19' 37.4"	61˚ 10' 19.1"	20	Cumulate
VS563	1902	13˚ 19' 37.4"	61˚ 10' 19.1"	20	Cumulate with host attached
VS564	1902	13˚ 19' 37.4"	61˚ 10' 19.1"	20	Cumulate with host attached
VS565		13˚ 19' 37.4"	61˚ 10' 19.1"	20	Lithic
VS566	Yellow Tephra	13˚ 15' 11.0"	61˚ 07' 06.1"	14	Cumulate

VS567	Yellow Tephra	13˚ 15' 11.0"	61˚ 07' 06.1"	14	Lava
VS568	Yellow Tephra	13˚ 15' 11.0"	61˚ 07' 06.1"	14	Lava
VS569	Yellow Tephra	13˚ 15' 11.0"	61˚ 07' 06.1"	14	Cumulate with host attached
VS570	Yellow Tephra	13˚ 15' 11.0"	61˚ 07' 06.1"	14	Cumulate with host attached
VS571	Yellow Tephra	13˚ 15' 11.0"	61˚ 07' 06.1"	14	Cumulate with host attached
VS572	Yellow Tephra	13˚ 15' 11.0"	61˚ 07' 06.1"	14	Cumulate with host attached
VS533H	Yellow Tephra	13˚ 17' 54.1"	61˚ 07' 07.8"	10	Lithic

Table A.2: Sample codes, relative ages (where known – samples collected ex situ left blank), sampling location co-ordinates and rock types for St Vincent sample set.

St Lucia

Locality 1: Fort Rodney

Outcrop: Approximately 10 m long exposure of Pre-SVC1 basalts below the man-made structure of Fort Rodney. Basalts have a blocky texture and contain enclaves with paler/darker colouration (enclaves were highly weathered and hence not sampled).

Photo L1.1: Outcrop below Fort Rodney.

Moving upward in the sequence towards Fort Rodney, lavas become more phenocryst rich.

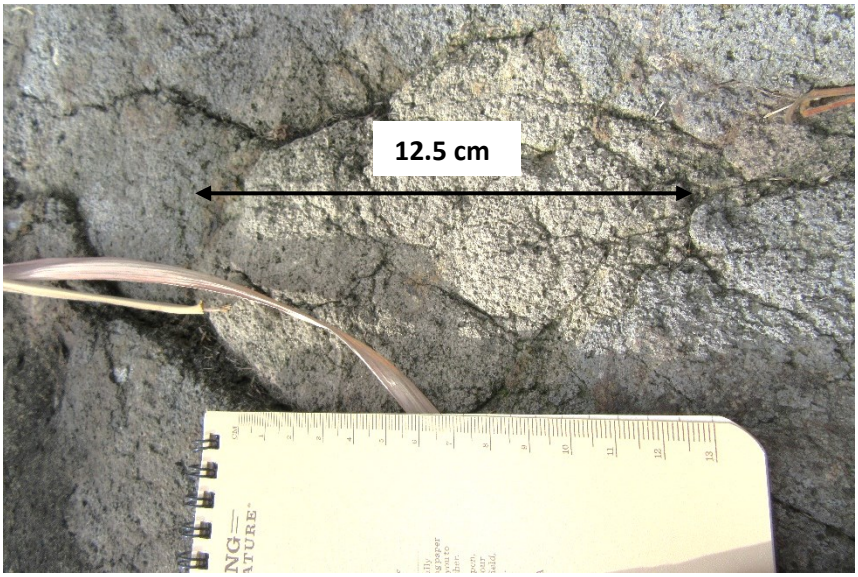

Photo L1.2: Enclave in Pre-SVC 1 basalt, from outcrop in **photo L1.1**.

Samples:

SL100 - From outcrop in **photo L1.1**. Dominantly plagioclase (1-3 mm) phyric basalt, with minor pyroxene (1 mm) and olivine (0.4-0.6 mm).

SL101 - From upward in sequence towards Fort Rodney. Phenocryst rich basalt with plagioclase and amphibole, which mainly occurs as glomerocrysts.

Locality 2: Path west of Fort Rodney

Outcrop: The path heading west away from Fort Rodney contains small, less than 1 m across exposures of apparent reworked volcaniclastic material. This may be interspersed with Pre-SVC1 basalts, but stratigraphic relationship is difficult to determine due to limited exposure on path. Volcaniclastic material may represent reworking of deposits from small explosive eruptions that occurred during the Pre-SVC1 eruptive phase.

Samples:

SL102 - Cumulate from volcaniclastics. Composed of plagioclase and amphibole.

SL103 - Cumulate from volcaniclastics. Composed of plagioclase and amphibole.

Locality 3: Smugglers Cove

Outcrop: Exposure at either end of a small bay on the west coast of St Lucia. Northern end of bay contains a layered volcaniclastic sequence. Southern end consists of poorly sorted conglomerates, cut by a dyke.

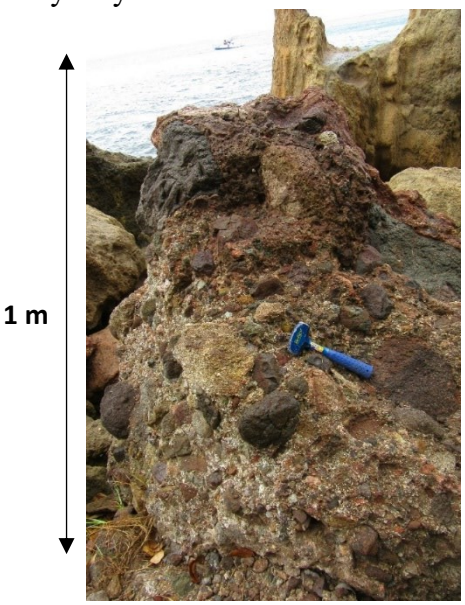

Photo L3.1: Fallen block of conglomerate from the southern side of Smugglers Cove.

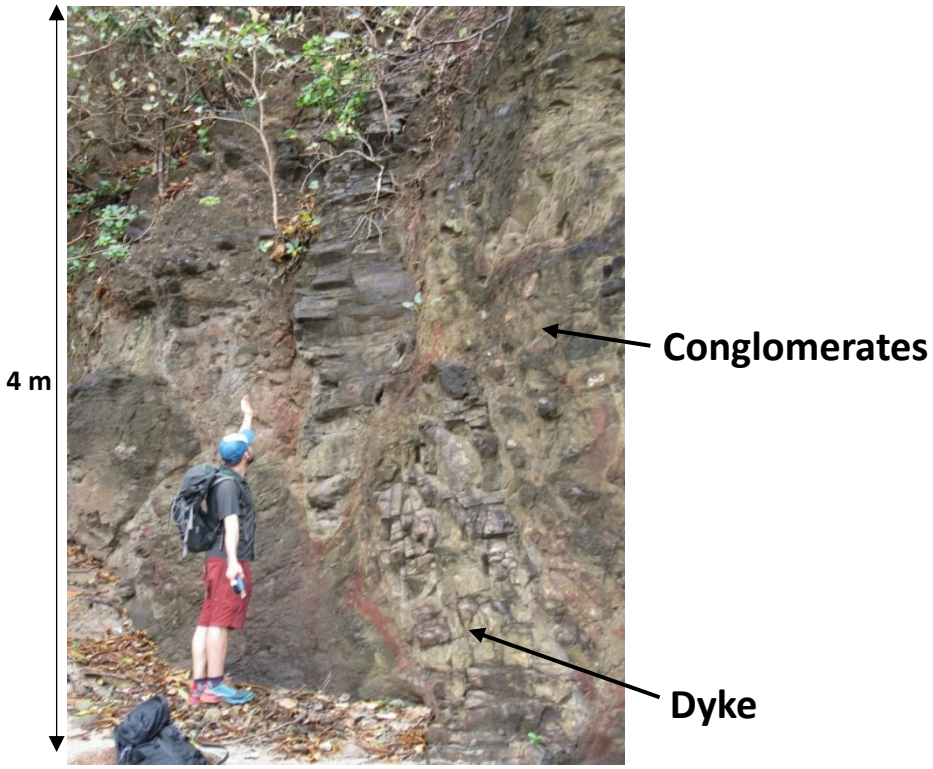

Photo L3.2: Dyke cutting the conglomerates on the southern side of Smugglers Cove.

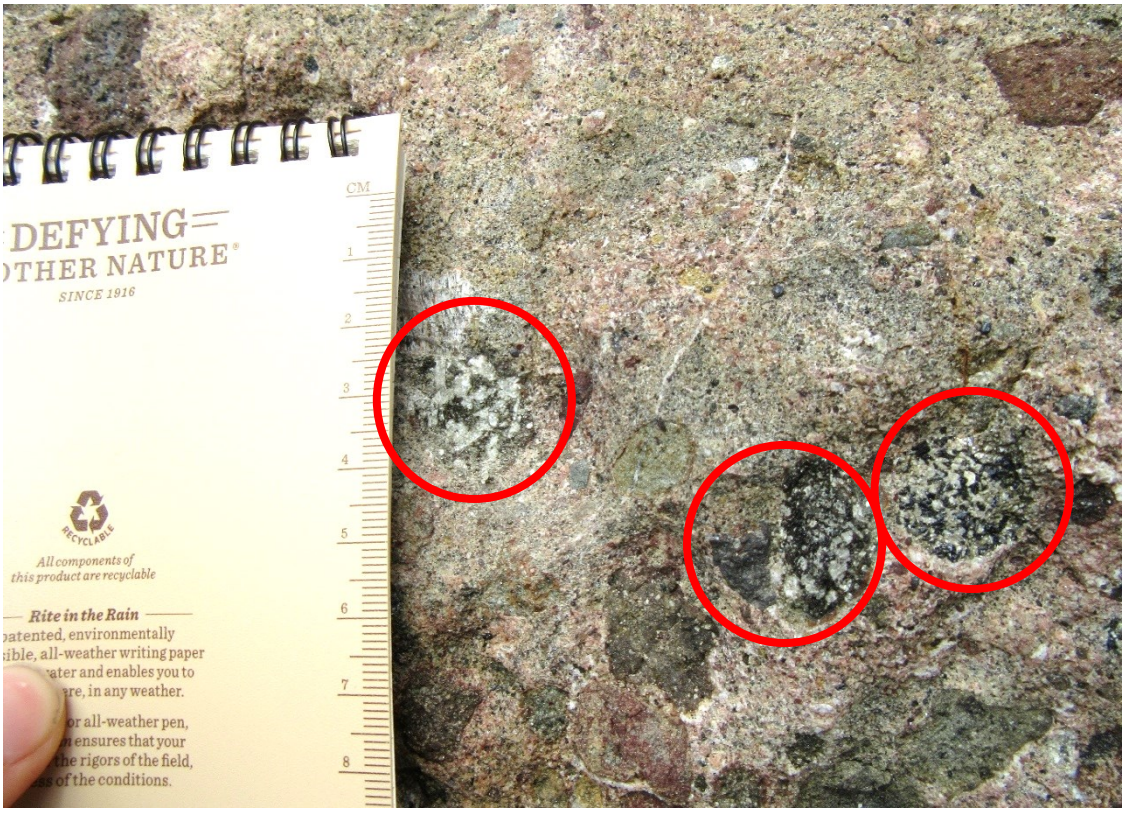

Photo L3.3: Cumulates (circled) in the volcaniclastic deposits on the northern side of Smugglers Cove.

Samples:

SL104 - Cumulate. Amphibole and green weathered plagioclase. Plagioclase contain small black specks which may be oxide inclusions/ melt inclusions.

SL105 - Cumulate. Amphibole and green weathered plagioclase. Interstitial amphibole between plagioclase suggests that amphibole was formed by reactive melt flow.

SL106 - Cumulate/"mush". Equigranular 1mm plagioclase and amphibole - "salt and pepper" texture.

SL107 - Lava in contact with crystal clot. Lava contains abundant plagioclase phenocrysts, in contact with a clot of 3-4 mm amphiboles. Potentially an enclave of an amphibole rich cumulate in its host lava.

SL108 - Cumulate. Amphibole, green weathered plagioclase and red-brown clinopyroxene. 1-2 mm crystals - "salt and pepper" texture.

SL109 - Cumulate. Amphibole, green weathered plagioclase and red-brown clinopyroxene. 1 – 2 mm crystals - "salt and pepper" texture.

SL110 - Cumulate. Amphibole, plagioclase and red weathered olivine.

SL111 - Mafic dyke. Aphyric, dark grey dyke. No vesicles. Two 1 mm across plagioclase are the only crystal phase present.

Locality 4: South Rodney Bay

Outcrop: Continuous exposure of Pre-SVC1 lavas along coastline on the southern side of Rodney Bay. Two cumulates found within 1 m of each other embedded in the lava.

Photo L4.1: Cumulate (circled) in Pre-SVC1 lava flow.

Samples:

SL112 - Pre-SVC1 lava. Pale grey, plagioclase phyric and vesicular. Contains a green enclave.

SL113 - In situ cumulate from Pre-SVC1 lava. Plagioclase, amphibole and minor olivine, 0.3-0.7 mm crystals.

SL114 - Host lava of SL113. Pale grey, plagioclase phyric and vesicular.

SL115 - In situ cumulate from Pre-SVC1 lava. Amphibole dominated with minor plagioclase, 0.2-0.4 mm crystals.

Locality 5: Roseau area

Outcrop: Approximately 60 m long exposure of PDC deposit (SVC age) alongside a road. PDC deposit contains juvenile dacitic (based on appearance) pumice and clasts, along with some more mafic (likely andesitic) clasts. Clast size varies from 2-30 cm. Matrix is heavily weathered.

Following a thorough search, no in situ cumulates were found at this outcrop.

Photo L5.1: Representative section of SVC PDC deposit.

Samples:

SL116 - Juvenile dacitic magma. Pale grey groundmass (60 %) with phenocrysts (40 %) of 1-4 mm plagioclase and amphibole.

SL117 - Andesitic magma (lithic). Dark grey groundmass (50 %), with phenocrysts (50 %) of 1-5 mm plagioclase and amphibole. Possibly represents a dome fragment?

SL118 - Granodiorite/mush fragment? Holocrystalline nodule, dominated by plagioclase with sparse amphibole and pyroxene. 1-5 mm crystals, most 1-2 mm. Nearest to cumulate assemblage found at this locality.

Locality 6: Belfond Quarry dacite dome

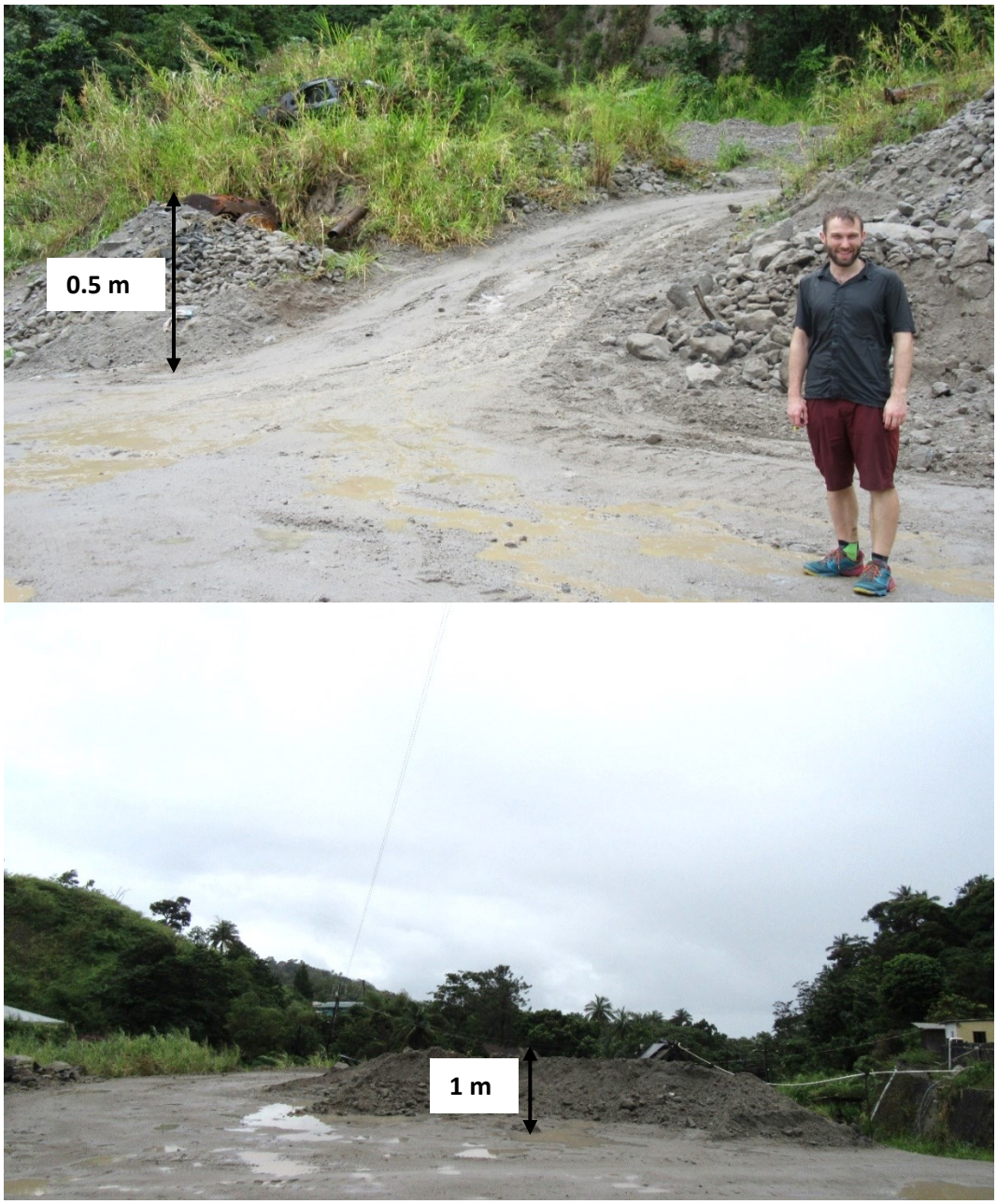

Photo L6.1: Rock piles on the quarry site from which samples were sourced. Scale bar indicates height of rock piles.

Outcrop: Quarry in central St Lucia. The Belfond Dacite dome (SVC age) is the rock quarried. The host lava is a phenocryst rich, plagioclase and amphibole bearing dacite. Abundant cumulate and "mushy" material found in rock piles produced by the quarrying.

Samples:

SL119 - Mafic crystal clot in dacitic host magma. Dacite host has a pale grey groundmass, with 1-9 mm plagioclase, amphibole and quartz phenocrysts. Mafic clot contains 1-5 mm amphibole and minor pyroxene (70%), and plagioclase (30%). Possibly represents a "non-cumulate gabbro".

SL120 - Mafic crystal clot in dacitic host magma. See above, though mineral proportions in mafic clot are 90 % amphibole and minor pyroxene, 10 % plagioclase and crystal sizes are 2-5 mm. The clot has no definable edge and appears to be disaggregating.

SL121 - Mafic enclave in host dacite. See SL119 for dacitic host magma description. Mafic enclave contains 1-2 mm amphibole, minor pyroxene and interstitial glass.

SL122 - "Mush"/non-cumulate gabbro with small felsic enclave. Mush mostly composed of equigranular 1 mm plagioclase and amphibole interspersed with larger 3-6 mm plagioclase. The felsic enclave contains 2-5 mm plagioclase. The larger plagioclase in the mush may have disaggregated from the enclave.

SL123 - Crystal clot in dacite host magma. See SL119 for dacitic host magma description. Clot contains 50 % plagioclase, 50 % amphibole. Crystal size ranges from 2-6 mm and is typically coarser than SL119-120 clots.

SL124 - Potential cumulate? 50 % plagioclase, 50 % amphibole. Crystal sizes range from 1-8 mm, with amphibole typically >2 mm. Elongate amphiboles show strong alignment.

SL125 - "Mushy" material with dacite host attached. See SL119 for dacitic host magma description. Mush contains mostly equigranular 1 mm plagioclase and amphibole, though a few amphiboles measure 2 mm.

SL126 - "Mushy" material with pegmatitic vein. Mushy material contains 85 % amphibole, 15 % plagioclase, with crystal sizes ranging from 1-3 mm. The vein is dominantly composed of 1-2 mm plagioclase surrounding 5-10 mm amphibole and 0.4-1 mm biotite. The mushy material close to the vein also contains a minor biotite component.

SL127 - Mafic enclave in "mushy" material. Mushy material contains 55 % amphibole, 5 % pyroxene, 40 % plagioclase. Crystal sizes range from 1-5 mm, with amphiboles typically > 2 mm. The mafic enclave is fine grained and composition cannot be determined without thin section.

Other localities:

Several localities visited on St Lucia yielded no useful samples. A second SVC PDC deposit and a Pre-SVC1 tuff also contained no cumulates. The mafic Pre-SVC1 basalt at Soufriere Bay contained no cumulates, very few crystals and showed evidence for significant hydrothermal alteration, hence no sample was taken.

St Vincent

Locality 7: Black Point

Outcrop: Approximately 12 m high exposure on coastal side of Black Point tunnel. Three eruptive units are present – the lowermost is a pale brown weathered PDC deposit, followed by an orange-yellow weathered tuff and a basaltic lava. The basaltic lava is that of the STV301 high-Mg basalt of Heath et al, 1998, which is attributed to the Pre-Somma stage of volcanism between 0.6 Ma and 10 ka. This suggests that the underlying pyroclastic deposits are also from this stage of volcanism.

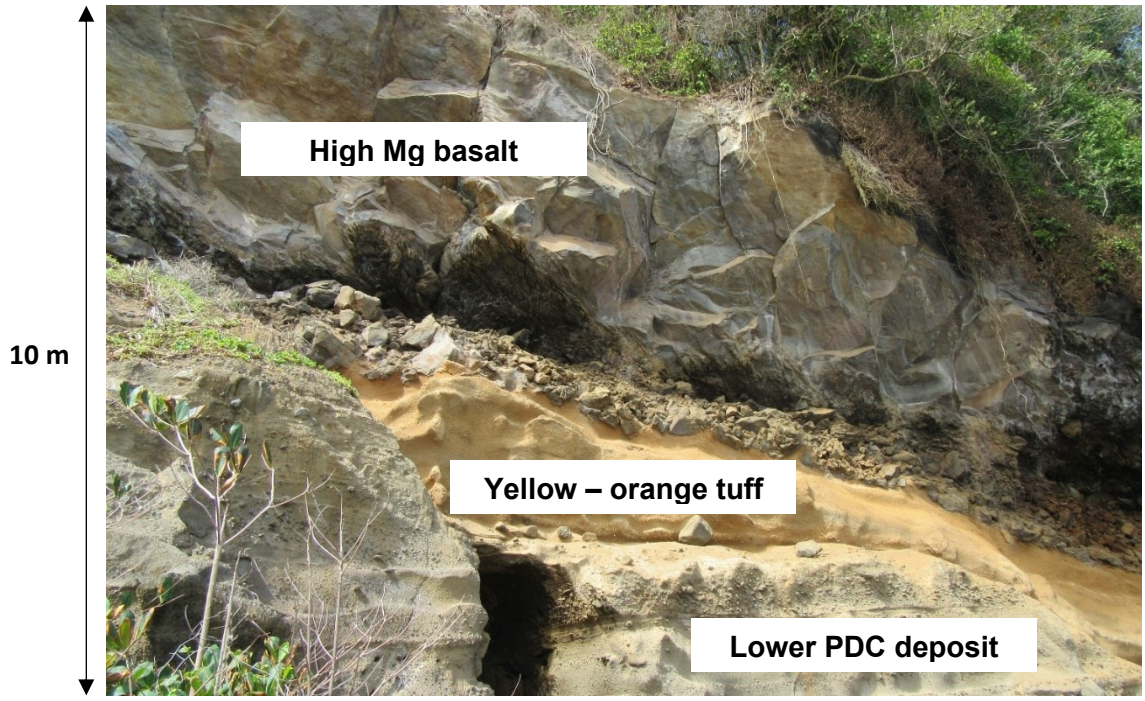

Photo L7.1: Coastal exposure at Black Point.

The lower PDC deposit consists of approximately 60 % weathered matrix, 40 % clasts. The dominant clast component is black/dark grey mafic lava blocks (80 %) with paler coloured lava blocks making up the other 20 %. Clast size varies from 1-28 cm.

The yellow-orange tuff consists of approximately 80 % matrix, 20 % clasts. These are silicic (based on appearance) juvenile pumice (40 %) and lithics (60 %). Clast size varies from 2-6 cm.

The high Mg basalt is blocky with a rubbly, broken up base.

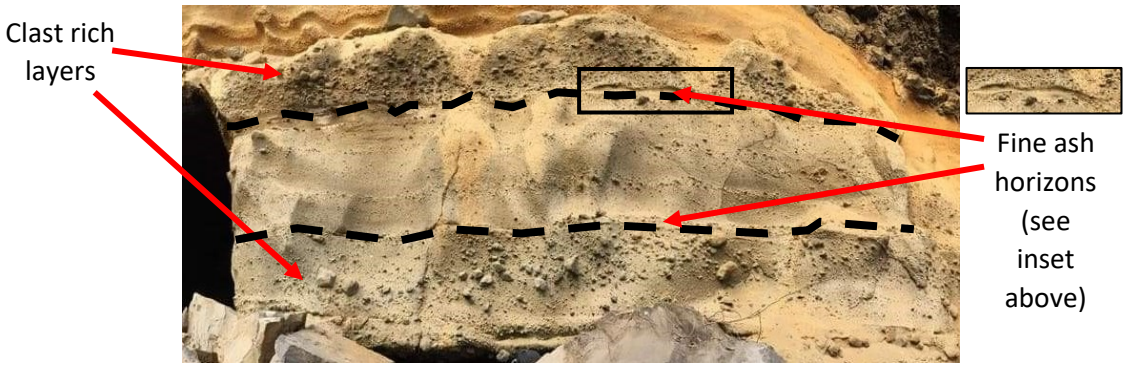

Photo L7.2: Lower PDC deposit. Composed of multiple flow units separated by fine ash horizons of 5 – 10 cm thickness.

Photo L7.3: Yellow-orange tuff.

Photo L7.4: High Mg basalt.

Samples – High Mg basalt:

VS500-VS503 – Basalt with a black groundmass (65 %) and phenocrysts (35 %) of 1 mm plagioclase (85 %) and 1-5 mm olivine (15 %). Plagioclase tend to be aligned and concentrated into elongate clusters.

Samples: Lower PDC deposit

VS504 - Mafic juvenile lava with a dark grey glassy groundmass (70 %), vesicles (5 %) and phenocrysts (25 %) of 1-3 mm olivine (50 %), plagioclase (40 %) and pyroxene (10 %).

VS505 - Paler coloured (intermediate composition?) lava – possible lithic? Pale grey groundmass (70 %) with phenocrysts (30 %) of 1-3 mm plagioclase (70 %) and pyroxene (30 %).

VS506 – Cumulate composed of 2-15 mm plagioclase (60 %), and pyroxene (40 %). Sample consists of three small cumulates grouped together due to their near identical compositions.

VS507 - "Puffed up mush". Cumulate consists of 1-5 mm plagioclase (40 %), 1-2 mm pyroxene (30 %) and vesiculated interstitial glass (30 %).

VS508 - "Salt and pepper" cumulates composed of 1-2 mm plagioclase (40 %), pyroxene (40 %) and olivine (20 %). Sample consists of three small cumulates grouped together.

VS509 - Amphibole dominated cumulate composed of 3-10 mm amphibole (65 %) and heavily weathered minerals (presumably plagioclase) (35 %).

Samples: Yellow – orange tuff

VS510 - Juvenile pumice with a yellow-brown groundmass (85 %), vesicles (5 %) and phenocrysts (10 %) of 1-2 mm pyroxene and plagioclase present in approximately equal proportions. Pumice is crumbly and heavily weathered.

VS511 - "Salt and pepper" cumulates composed of 1-2 mm plagioclase (45 %), pyroxene (45 %) and olivine (10 %). A single 8 mm long pyroxene crystal was measured. The sample consists of seven small cumulates grouped together due to their near identical compositions.

Localities 8-11 – Dry Rabacca

Outcrop: Layered PDC deposits from the 1902 eruption exposed along the flanks of the Dry Rabacca valley. The deposits are approximately 5 m thick along most of the valley walls. Localities include outcrops from the first 500 m of the valley heading inland from the coast. The deposits contain multiple horizons of thicknesses between 30 cm and 1 m. The horizons present and their thicknesses are relatively consistent between localities. The proportions of clasts and matrix show significant variation both between the horizons and laterally. Both rounded and angular clasts are present, ranging in size from 1-40 cm. Clast types include black mafic? vesicular lava, yellow-brown felsic? juvenile pumice, andesitic? lava blocks and various multi-coloured lithics. The proportions of each clast type vary laterally and vertically.

Photo L10.1: 1902 PDC deposit exposure along the walls of the Dry Rabacca valley.

Photo L10.2: Exposure at locality 10.

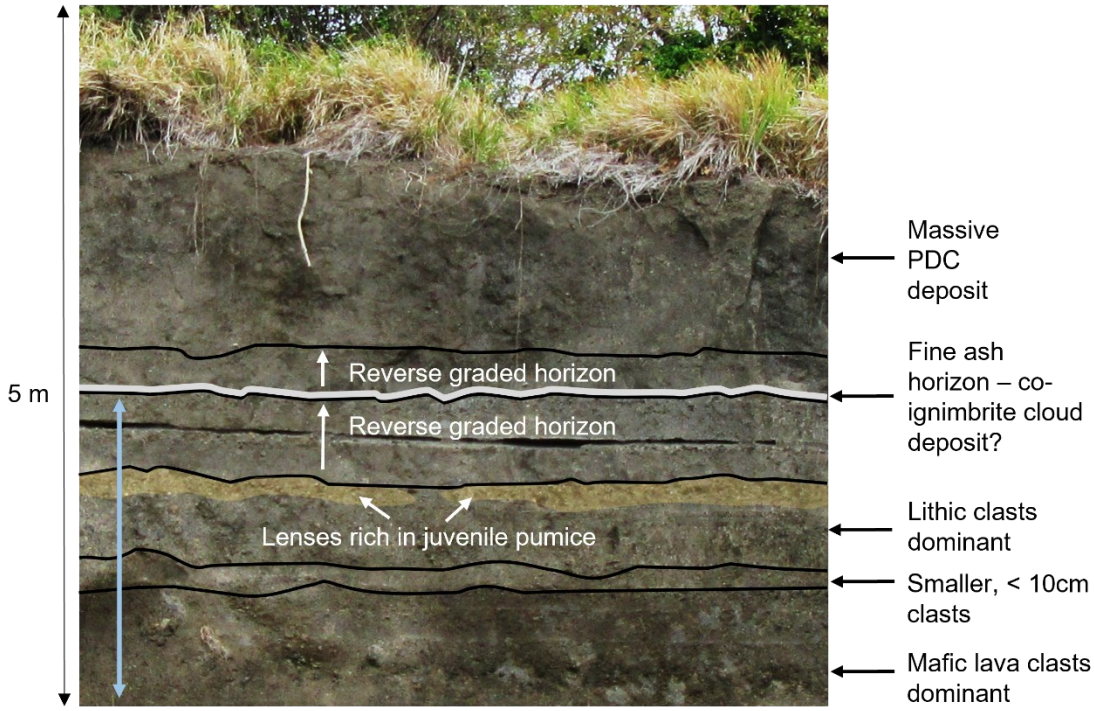

Photo L10.3: Schematic log through exposed 1902 section, indicating the variation in clast type and size throughout. Blue arrow shows horizons from which samples were collected.

Photo L11.1: Exposure at locality 11.

Samples: locality 8

VS512 - Cumulate attached to 1902 mafic lava. Cumulate composed of 1-2 mm plagioclase (70 %), 1-2 mm olivine (15 %) and 1-8 mm amphibole (15 %). 1902 mafic lava contains 1-2 mm plagioclase phenocrysts in a black vesicular groundmass.

VS513 - Cumulate composed of 1-7 mm amphibole (55 %), 1-5 mm plagioclase (40 %) and 1-2 mm olivine (5 %). Sample picked up loose from riverbed.

VS514 - Lava with large plagioclase. Lava contains 1-8 mm plagioclase phenocrysts in black glassy groundmass. Large plagioclase may be from disaggregated cumulates. Sample picked up loose from riverbed.

VS515 - 1902 juvenile pumice with a yellow-brown groundmass (80 %), vesicles (10 %) and phenocrysts (10 %) of 1-9 mm plagioclase (70 %) and 1-8 mm pyroxene (30 %).

VS516 - Banded pumice – showing mixing? Mostly black vesiculated groundmass with a band of yellow-brown (with appearance of VS515). Both bands contain 1-4 mm plagioclase (60 % of total) and 1-2 mm pyroxene (40 % of total) phenocrysts.

VS517 - 1902 mafic lava. Composed of black glassy groundmass (70 %), vesicles (2 %) and phenocrysts (28 %) of 1-4 mm plagioclase (75 %) and 1-2 mm pyroxene (25 %).

VS518 - Cumulate attached to 1902 juvenile pumice (see VS515 for description of pumice). Cumulate composed of 2-11 mm plagioclase (75 %) and 1-3 mm olivine (25 %).

VS524 - Cumulate/"mush" with distinctively smaller crystals than others at this locality. Composed of approximately equal proportions equigranular 1 mm amphibole and plagioclase, showing a "salt and pepper" texture. Sparse larger plagioclase, measuring 2-8 mm are present. Sample picked up loose from riverbed.

Samples: locality 9

VS519 - Cumulate attached to 1902 mafic lava. See VS517 for 1902 mafic lava description. Cumulate composed of 1-3 mm plagioclase (75 %) and 2-7 mm amphibole (35 %). Host magma adjacent to cumulate contains larger plagioclase which may have disaggregated from the cumulate. Sample picked up loose from riverbed.

VS520 - Cumulate attached to 1902 mafic lava. See VS519. Sample also contains a large holocrystalline enclave composed of 1-2 mm plagioclase (70 %) and pyroxene (30 %). Possibly an enclave of "mush"/non-cumulate gabbro.

VS521 - Cumulate attached to 1902 mafic lava. See VS519.

VS522 - Mafic lava with olivine containing plagioclase. See VS517 for mafic lava description. Also contains some >1 cm plagioclase with 1mm olivine present as inclusions. These larger plagioclase are likely from a disaggregated cumulate.

VS526 - Cumulate attached to 1902 mafic lava. See VS517 for mafic lava description. Cumulate composed of 2-5 mm plagioclase (70 %) and 1-2 mm olivine (30 %). Cumulate sized crystals are found in adjacent host suggesting that this sample captures a disaggregating cumulate. Sample picked up loose from riverbed.

VS527 - Cumulate attached to 1902 mafic lava. See VS517 for mafic lava description. Cumulate composed of 1-4 mm plagioclase (65 %), 1-2 mm olivine (20 %) and 1-2 mm pyroxene (15 %). Cumulate sized crystals are found in adjacent host suggesting that this sample captures a disaggregating cumulate. Sample picked up loose from riverbed.

VS528 - Cumulate attached to 1902 mafic lava. See VS517 for mafic lava description. Cumulate composed of 2-4 mm plagioclase (90 %), 1 mm olivine (5 %) and 1-2 mm

amphibole (5 %). Cumulate sized crystals are found in adjacent host suggesting that this sample captures a disaggregating cumulate. Sample picked up loose from riverbed.

VS531 - Cumulate attached to 1902 mafic lava. See VS517 for mafic lava description. Cumulate composed of 1-9 mm plagioclase (60 %), 1-3 mm olivine (20 %) and 1-12 mm pyroxene (20 %).

VS532 - Cumulate attached to 1902 mafic lava. See VS517 for mafic lava description. Cumulate composed of 2-5 mm plagioclase (50 %), 1-4 mm olivine (15 %) and 2-6 mm pyroxene (35 %).

Samples: locality 10

VS525 - Intermediate composition lava. Composed of pale grey groundmass with sparse vesicles (60 %) and phenocrysts (40 %) of 1- 12 mm plagioclase (60 %), 1-5 mm olivine (25 %) and 1-3 mm pyroxene (15 %). Some plagioclase contain olivine inclusions. Likely a lithic/remnant of previously erupted magma due to scarcity in deposit.

VS529 - Plagioclase crystal, 2.5 cm across, found in situ in deposit. Size suggests of cumulate origin.

VS530 - Felsic lava with "mushy" enclaves. Composed of grey-white groundmass (60 %) and phenocrysts (40 %) of 1-2 mm plagioclase (65 %) and 1-3 mm pyroxene (35 %). "Mushy" enclaves composed of 1-2 mm plagioclase (50 %), 1-3 mm pyroxene (40 %) and vesicular interstitial glass (10 %). Sample picked up loose from riverbed.

VS533H - Three in situ green lithics. Pale green and fine grained. Appearance suggests a mafic hornfels composition. Potential crustal material?

VS547 - "King Vincy" – Unusually large, in situ cumulate. Cumulate has many zones with different textures. Most of the cumulate is made up of plagioclase and amphibole in approximately equal proportions, though these vary in the different zones of the sample. Most crystals measure 5-20 mm, though some zones of equigranular 1 or 2 mm crystals (with a "salt and pepper" texture) exist. These may be entrained "non-cumulate gabbros" or just parts of the mush system with a different texture. Small patches of grey interstitial glass exist between some crystals. Some zones contain a minor 1-2 mm olivine component. A distinct zone shows plagioclase rich bands with crystal sizes towards the

lower end of the range interspersed with amphibole rich bands with larger crystals which may represent crude layering.

Samples: locality 11

VS523 - Cumulate with felsic lava attached. See VS530 for description of felsic host. Cumulate composed of 2-11 mm plagioclase and 1-20 mm amphibole (most 5-10 mm). Sample picked up loose from riverbed.

VS533 - Cumulate composed of 1-9 mm plagioclase (50 %) 4-10 mm pyroxene (10 %), 1-2 mm amphibole (30 %), 1-2 mm olivine (7 %) and small pockets of interstitial glass (3 %). One end of the sample displays a zone with "salt and pepper" texture.

VS534 - Troctolite cumulate with interstitial glass composed of 3-13 mm plagioclase (70 %), 1-3 mm olivine (7 %) and black vesicular interstitial glass (23 %). Some parts of the interstitial glass contain no crystals, others contain 1-3 mm plagioclase and olivine. These crystals in the glass may have disaggregated from the cumulate or have formed as a late stage phenocryst phase. Some plagioclase in the cumulate have darker grey cores suggesting that they are zoned. Some of these cores contain several black streaks – possible melt inclusions?

Locality 12 – Owia salt pond

Outcrop: Coastal exposure of dark grey mafic lavas on a headland on the northern coast of St Vincent. No obvious variations in rock type or composition can be observed. Samples taken from across the approximately 30 m wide headland.

Samples:

VS535 - Owia salt pond mafic lava. Dark grey groundmass (65 %) with vesicles (5 %) and phenocrysts (30 %) of 1-6 mm plagioclase (99 %) and 1 mm olivine (1 %).

VS536 - Green lithic within mafic lava. Pale green and fine grained. Appearance suggests a mafic hornfels composition. Potential crustal material?

VS537 - Cumulate from Owia salt pond mafic lava. Cumulate composed of 1-4 mm plagioclase (35 %), 1-3 mm amphibole (45 %) and 1 mm olivine (20 %). One zone of the cumulate contains relatively more amphibole and less plagioclase.

VS538 - Cumulate from Owia salt pond mafic lava. Cumulate composed of 1-3 mm plagioclase (25 %) and pyroxene (75 %).

VS539 - Cumulate from Owia salt pond mafic lava. Cumulate composed of 1-4 mm plagioclase (40 %), 1-2 mm amphibole (45 %) and 1-8 mm pyroxene (15 %). The pyroxenes are green and clumped together in clusters with crystals showing a bladed habit. Possibly some small pockets of interstitial glass.

VS540 - Cumulate with Owia salt pond mafic lava attached. See VS535 for host lava description. Cumulate composed of 1-4 mm plagioclase (50 %) and 1-5 mm pyroxene (50 %).

VS541 - Cumulate with Owia salt pond mafic lava attached. See VS535 for host lava description. Cumulate composed of 1-4 mm plagioclase (60 %) and pyroxene (40 %).

VS542 - Owia salt pond mafic lava with crystal clots/disaggregation. Dark grey groundmass (45 %) with vesicles (10 %) and phenocrysts (45 %) of 1-7 mm plagioclase (95 %), 1 mm olivine (1 %) and 1-2 mm pyroxene (4 %). Crystal clots composed of equigranular 1 mm plagioclase and pyroxene in approximately equal proportions ("salt and pepper" texture).

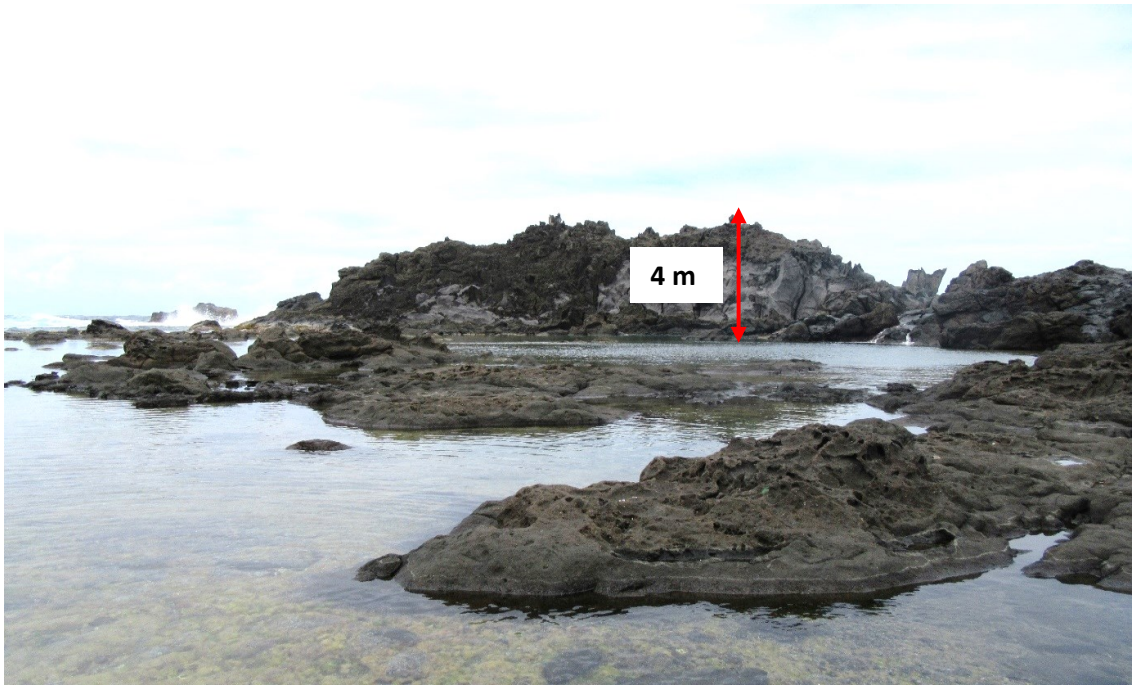

Photo L12.1: Typical exposure at Owia salt pond.

VS543 - Owia salt pond mafic lava with crystal clots/disaggregation. Dark grey groundmass (45 %) with vesicles (10 %) and phenocrysts (45 %) of 1-10 mm plagioclase (95 %), 1 mm olivine (1 %) and 1-2 mm pyroxene (4 %). Crystal clots composed of equigranular 1 mm plagioclase and pyroxene in approximately equal proportions ("salt and pepper" texture). Large plagioclase likely disaggregated from cumulates.

VS544 - Owia salt pond mafic lava with crystal clots/disaggregation. Dark grey groundmass (45 %) with vesicles (10 %) and phenocrysts (45 %) of 1-20 mm plagioclase (95 %), 1 mm olivine (1 %) and 1-2 mm pyroxene (4 %). Crystal clots composed of equigranular 1 mm plagioclase and pyroxene in approximately equal proportions ("salt and pepper" texture). Some plagioclase contain black streaks – possible melt inclusions?

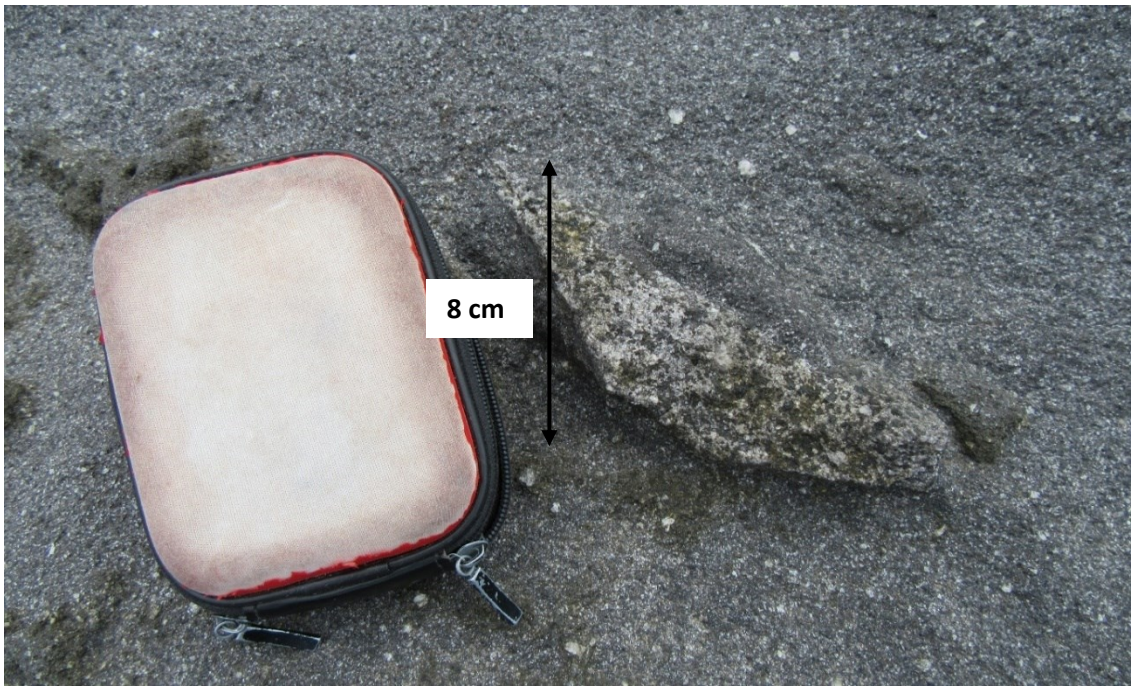

Photo L12.2: In situ cumulate at Owia salt pond (sample VS537).

Locality 13 – Big Sand Bay

Outcrop: Coastal exposure of dark grey lavas previously identified as high-Mg basalts erupted as part of the Pre-Somma stage of volcanism (0.6 Ma to 10 ka) by Heath et al, 1998.

Samples:

VS545 - Big Sand Bay basalt. Dark grey groundmass (80 %) with phenocrysts (20 %) of 1-4 mm plagioclase (85 %), 2-3 mm olivine (5 %) and 1-2 mm pyroxene (10 %).

VS546 - Cumulate from Big Sand Bay basalt composed of 1-3 mm plagioclase (60 %) and 1-4 mm amphibole (40 %).

Photo L13.1: The basalt cliffs at Big Sand Bay.

Locality 14 – Roadcut on Windward side of St Vincent

Outcrop: Approximately 10 m high exposure of the Yellow Tephra formation (indicated by colour of deposit) erupted 3600-4500 years B.P (Heath et al, 1998). Deposit contains abundant lithics, many of which are cumulates. These are particularly concentrated in one of the lower layers with a thickness of around 1 m. The high concentration of lithics and dipping of the layers into an apparent paleo-channel suggests that this exposure represents deposits from localized reworking of the Yellow Tephra. The appearance of the outcrop is shown by the schematic below.

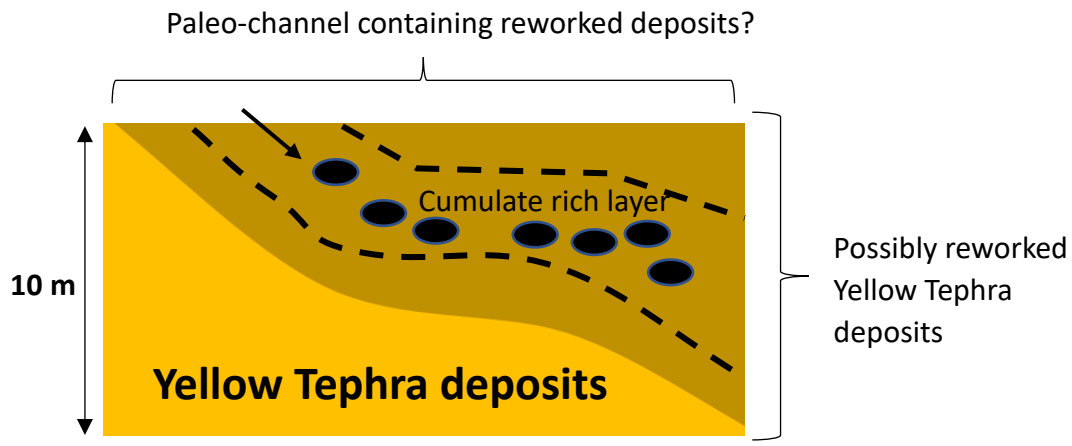

Samples:

VS566 - Layered in situ cumulate composed of 1-3 mm plagioclase (50 %) and 1-5 mm amphibole (50 %). Sample contains bands that are relatively more plagioclase or more amphibole rich.

VS567 - Yellow Tephra juvenile magma. Dark grey groundmass with paler brown bands (70 %) and phenocrysts (30 %) of 1-2 mm plagioclase (60 %) and pyroxene (40 %). Banding of groundmass suggests mixing/mingling before eruption.

VS568 - Yellow Tephra juvenile magma. Dark grey groundmass (60 %) and phenocrysts (40 %) of 1-2 mm plagioclase (50 %) and 1-10 mm pyroxene (50 %). Contains a small amphibole and pyroxene crystal clot.

VS569 - Cumulate with juvenile magma attached. See VS567 and 568 for juvenile magma description. Cumulate composed of 1 mm plagioclase (50 %) and 1-6 mm pyroxene (50 %).

VS570 - Cumulate with juvenile magma attached. Juvenile magma has the colour of the brown band in the groundmass of VS567. Cumulate composed of 1 mm plagioclase (25 %) and 1-4 mm pyroxene (75 %). Very weathered.

VS571 - Cumulate with juvenile magma attached. Juvenile magma has the colour of the brown band in the groundmass of VS567. Cumulate composed of 2 mm plagioclase (25 %) and 2-4 mm pyroxene (75 %). Bands of pyroxene crystals appear to be infiltrating or disaggregating into host magma. Very weathered.

VS572 - Cumulate with juvenile magma attached. Juvenile magma has the colour of the brown band in the groundmass of VS567. Cumulate composed of 2 mm plagioclase (25

%) and 2-4 mm amphibole (75 %). Cumulate has zones where significantly more plagioclase is present relative to amphibole, and vice versa.

Locality 15 – La Soufriere, Windward trail

Outcrop: Path on flank of La Soufriere, Windward side, upper trailhead leading towards crater rim.

Samples:

VS548 - Cumulate with mafic lava attached (lava has appearance of 1902 mafic lava – see VS 517 for description). Cumulate composed of 1-11 mm plagioclase (80 %) and 1-2 mm olivine (20 %). All plagioclase is an unusually dark grey in colour. Sample picked up loose on trail.

VS549 - Cumulate composed of 1-3 mm plagioclase (50 %) and magnetite (50 %). Suggests magnetite may also be a mafic component in some of the other samples.

Locality 16 – La Soufriere, Windward trail, 1580? deposits.

Outcrop: Exposure on path heading down Windward side of La Soufriere. Assumed to be 1580 PDC deposits based on log at this approximate location from Cole et al, 2019. Deposit is highly weathered and consists of a brown groundmass with clasts of black mafic and paler, likely intermediate composition lava.

Samples:

VS550 - Andesitic lava. Pale grey groundmass (60 %) with vesicles (5 %) and phenocrysts (35 %) of 1-11 mm plagioclase (80 %) and 1-3 mm olivine (20 %).

VS551 - Cumulate with 1580 mafic lava attached (see VS554 for mafic lava description). Cumulate composed of 1-3 mm plagioclase (50 %), 1-6 mm amphibole (35 %) and 1-2 mm olivine (15 %).

VS552 - Cumulate with 1580 mafic lava attached (see VS554 for mafic lava description). Cumulate composed of 1-3 mm plagioclase (55 %), 1-6 mm pyroxene (35 %) and 1-2 mm olivine (10 %).

VS553 - Very weathered in situ cumulate composed of 2-9 mm plagioclase (60 %) and 1-5 mm olivine (40 %).

VS554 - 1580 mafic lava. Black groundmass (55 %) with vesicles (5 %) and phenocrysts (40 %) of 1-5 mm plagioclase (90 %) and 2-3 mm olivine (10 %).

Photo L16.1: Exposure of the 1580 deposits on the Windward trail.

Locality 17 – Windward trail ravine with 1902 deposits:

Outcrop: Small ravine just off the trail, with walls made up of exposures of 1902 PDC deposits. Thickness of deposits varies depending on position within ravine.

Photo L17.1: Exposure in the ravine beside the Windward trail.

Samples:

VS555 - In situ cumulate composed almost entirely of 1-8 mm magnetite, with minor amphibole and pyroxene. One zone/vein like feature contains plagioclase and amphibole in equal proportions with sparse olivine. Other small plagioclase and amphibole zones with a "salt and pepper" texture exist within the sample.

VS556 - Layered Cumulate. Lowermost layer composed of 1-10 mm amphibole (70 %) and 2-5 mm plagioclase (30 %). Middle layer composed of 1-5 mm plagioclase (85 %) and 1 mm olivine (15 %), intruded by veins of amphibole crystals. Uppermost layer composed of 1-5 mm plagioclase (45 %), amphibole (45 %) and olivine (10 %). Sample picked up from just below exposure so assumed to have fallen out making it in situ.

Locality 18 – Windward trail

Outcrop: On path of Windward trail.

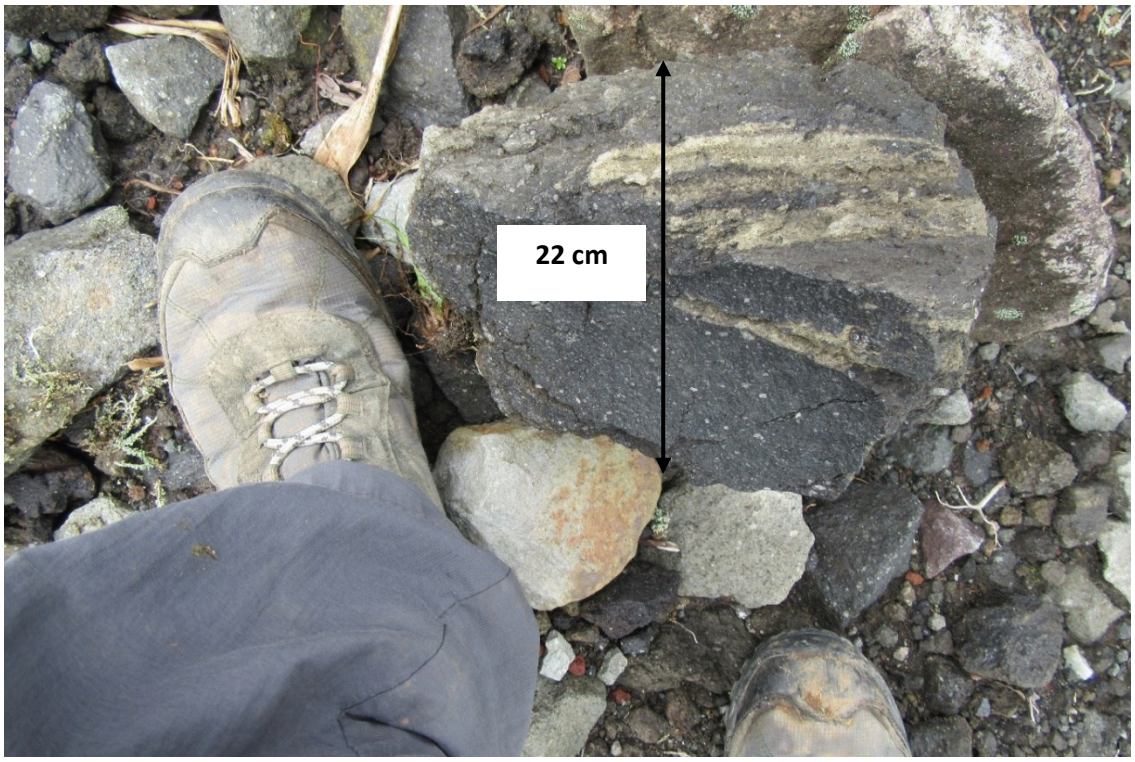

Photo L18.1: Large fresh lava bomb found on trail.

Samples:

VS557 - Fresh lava bomb (either 1902 or 1979). Black glassy groundmass (80 %) with phenocrysts (20 %) of 1-12 mm plagioclase (90 %) and 1-2 mm pyroxene (10 %). Some larger plagioclase display a bladed habit. Bands of the groundmass are pale brown rather than black, yet have the same phenocryst assemblage.

Locality 19 – Further down ravine on Windward trail

Outcrop: See locality 17, also 1902 PDC deposits.

Samples:

VS558 - In situ cumulate. Composed of 2-12 mm plagioclase (60 %), 2-5 mm amphibole (39 %) and 1 mm olivine (1 %). Some zones of the cumulate contain relatively more amphibole or more plagioclase.

Locality 20 – Near end of ravine on Windward trail.

Outcrop: See locality 17, also 1902 PDC deposits.

Samples:

VS559 - Andesitic lava block. Grey groundmass (65 %) with phenocrysts (35 %) of 1-5 mm plagioclase.

VS560 - 1902 mafic lava. Black groundmass (85 %) with vesicles (5 %) and phenocrysts (10 %) of 1-3 mm plagioclase. Sample picked up from ravine bottom.

VS561 - Cumulate with radial amphibole mostly composed of approximately equal proportions equigranular 1 mm plagioclase and amphibole showing a "salt and pepper" texture. Outside the "salt and pepper" core is a layer of elongate, > 1 cm amphiboles aligned radially around the core. A small amount of host lava is attached to one end of the sample, which has the appearance of the 1902 mafic magma. Sample picked up from ravine bottom.

VS562 - Cumulate composed of 1-16 mm plagioclase (75 %) 1 mm olivine (10 %) and 1-5 mm amphibole (15 %). A significantly more amphibole rich lens exists in the sample. Sample picked up from ravine bottom – buried in floor so possibly in situ.

VS563 - Cumulate with host lava attached. See VS517 for host lava description. Cumulate composed of 1-3 mm plagioclase (65 %) and 1-3 mm olivine (35 %).

VS564 - Cumulate with host lava attached. See VS517 for host lava description. Cumulate composed of 1-11 mm plagioclase (50 %), 1-3 mm olivine (20 %) and 2-4 mm pyroxene (30 %).

VS565 - Green lithic picked up on La Soufriere crater rim (exact point unknown). Pale green, fine grained, likely mafic hornfels composition. Possibly representative of arc crustal material. Has a small grey weathered zone attached – possibly felsic/intermediate host magma?

References

Adams, J. V., Jackson, M. G., Spera, F. J., Price, A. A., Byerly, B. L., Seward, G., & Cottle, J. M. (2021). Extreme isotopic heterogeneity in Samoan clinopyroxenes constrains sediment recycling. *Nature Communications*, *12*(1), 1-10.

Aitcheson, S. J., & Forrest, A. H. (1994). Quantification of crustal contamination in open magmatic systems. *Journal of Petrology*, *35*(2), 461-488.

Aiuppa, A., Fischer, T. P., Plank, T., Robidoux, P., & Di Napoli, R. (2017). Along-arc, inter-arc and arc-to-arc variations in volcanic gas CO2/ST ratios reveal dual source of carbon in arc volcanism. *Earth-Science Reviews*, *168*, 24-47.

Aitken, T., Mann, P., Escalona, A., & Christeson, G. L. (2011). Evolution of the Grenada and Tobago basins and implications for arc migration. *Marine and Petroleum Geology*, *28*(1), 235-258.

Allègre, C. J., Dupré, B., Négrel, P., & Gaillardet, J. (1996). Sr-Nd-Pb isotope systematics in Amazon and Congo River systems: constraints about erosion processes. *Chemical Geology*, *131*(1-4), 93-112.

Allen, R. W., Collier, J. S., Stewart, A. G., Henstock, T., Goes, S., Rietbrock, A., & VoiLA Team. (2019). The role of arc migration in the development of the Lesser Antilles: A new tectonic model for the Cenozoic evolution of the eastern Caribbean. *Geology, 47*(9), 891-895.

Amma-Miyasaka, M., & Nakagawa, M. (2002). Origin of anorthite and olivine megacrysts in island-arc tholeiites: petrological study of 1940 and 1962 ejecta from Miyake-jima volcano, Izu-Mariana arc. *Journal of Volcanology and Geothermal Research*, *117*(3-4), 263-283.

Ancellin, M. A., Samaniego, P., Vlastélic, I., Nauret, F., Gannoun, A., & Hidalgo, S. (2017). Across-arc versus along-arc Sr-Nd-Pb isotope variations in the Ecuadorian volcanic arc. *Geochemistry, Geophysics, Geosystems*, *18*(3), 1163-1188.

Annen, C., Blundy, J. D., & Sparks, R. S. J. (2006). The genesis of intermediate and silicic magmas in deep crustal hot zones. *Journal of Petrology*, *47*(3), 505-539.

Antonicelli, M., Tribuzio, R., Liu, T., & Wu, F. Y. (2020). Contaminating melt flow in magmatic peridotites from the lower continental crust (Rocca d'Argimonia sequence, Ivrea–Verbano Zone). *European Journal of Mineralogy*, *32*(6), 587-612.

Arculus, J. R., & Wills, J. A. K. (1980). The petrology of plutonic blocks and inclusions from the Lesser Antilles Island Arc. *Journal of Petrology*, *21*(4), 743–799.

Bachmann, O., & Bergantz, G. W. (2004). On the origin of crystal-poor rhyolites: extracted from batholithic crystal mushes. *Journal of Petrology*, *45*(8), 1565-1582.

Bachmann, O., & Bergantz, G. W. (2006). Gas percolation in upper-crustal silicic crystal mushes as a mechanism for upward heat advection and rejuvenation of near-solidus magma bodies. *Journal of Volcanology and Geothermal Research*, *149*(1-2), 85-102.

Baker, J. A., Macpherson, C. G., Menzies, M. A., Thirlwall, M. F., Al-Kadasi, M., & Mattey, D. P. (2000). Resolving crustal and mantle contributions to continental flood volcanism, Yemen; constraints from mineral oxygen isotope data. *Journal of Petrology*, *41*(12), 1805-1820.

Baker, J., Peate, D., Waight, T., & Meyzen, C. (2004). Pb isotopic analysis of standards and samples using a 207Pb–204Pb double spike and thallium to correct for mass bias with a double-focusing MC-ICP-MS. *Chemical Geology*, *211*(3-4), 275-303.

Balcone-Boissard, H., Boudon, G., Blundy, J. D., Martel, C., Brooker, R. A., Deloule, E., ... & Matjuschkin, V. (2018). Deep pre-eruptive storage of silicic magmas feeding Plinian and dome-forming eruptions of central and northern Dominica (Lesser Antilles) inferred from volatile contents of melt inclusions. *Contributions to Mineralogy and Petrology*, *173*(12), 1-24.

Barker, S. J., Wilson, C. J. N., Baker, J. A., Millet, M. A., Rotella, M. D., Wright, I. C., & Wysoczanski, R. J. (2013). Geochemistry and petrogenesis of silicic magmas in the intra-oceanic Kermadec arc. *Journal of Petrology*, *54*(2), 351-391.

Barker, A. K., Troll, V. R., Carracedo, J. C., & Nicholls, P. A. (2015). The magma plumbing system for the 1971 Teneguía eruption on La Palma, Canary Islands. *Contributions to Mineralogy and Petrology*, *170*(5), 1-21.

Barnes, S. J., Mole, D. R., Le Vaillant, M., Campbell, M. J., Verrall, M. R., Roberts, M. P., & Evans, N. J. (2016). Poikilitic textures, heteradcumulates and zoned orthopyroxenes in the Ntaka Ultramafic Complex, Tanzania: implications for crystallization mechanisms of oikocrysts. *Journal of Petrology*, *57*(6), 1171-1198.

Beard, J. S. (1986). Characteristic mineralogy of arc-related cumulate gabbros: implications for the tectonic setting of gabbroic plutons and for andesite genesis. *Geology*, *14*(10), 848-851.

Beard, J. S., & Borgia, A. (1989). Temporal variation of mineralogy and petrology in cognate gabbroic enclaves at Arenal volcano, Costa Rica. *Contributions to Mineralogy and Petrology*, *103*(1), 110-122.

Beattie, P. (1993). Olivine-melt and orthopyroxene-melt equilibria. *Contributions to Mineralogy and Petrology*, *115*(1), 103-111.

Bebout, G. E. (2014). Chemical and isotopic cycling in subduction zones. *Treatise on Geochemistry*, *4*, 747.

Bédard, J. H. (2014). Parameterizations of calcic clinopyroxene—Melt trace element partition coefficients. *Geochemistry, Geophysics, Geosystems*, *15*(2), 303-336.

Bedini, R. M., & Bodinier, J. L. (1999). Distribution of incompatible trace elements between the constituents of spinel peridotite xenoliths: ICP-MS data from the East African Rift. *Geochimica et Cosmochimica Acta*, *63*(22), 3883-3900.

Bezard, R. C. (2014). Impact of crustal assimilation on the Lesser Antilles arc lava geochemistry. [PhD thesis, Macquarie University] http://hdl.handle.net/1959.14/1138381

Bezard, R., Davidson, J. P., Turner, S., Macpherson, C. G., Lindsay, J. M., & Boyce, A. J. (2014). Assimilation of sediments embedded in the oceanic arc crust: Myth or reality? *Earth and Planetary Science Letters*, *395*, 51–60.

Bezard, R., Schaefer, B. F., Turner, S., Davidson, J. P., & Selby, D. (2015a). Lower crustal assimilation in oceanic arcs: Insights from an osmium isotopic study of the Lesser Antilles. *Geochimica et Cosmochimica Acta*, *150*, 330-344.

Bezard, R., Turner, S., Davidson, J. P., Macpherson, C. G., & Lindsay, J. M. (2015b). Seeing through the effects of crustal assimilation to assess the source composition beneath the southern Lesser Antilles Arc. *Journal of Petrology*, *56*(4), 815-844.

Bezard, R., Turner, S., Davidson, J., Schmitt, A. K., & Lindsay, J. (2017). Origin and evolution of silicic magmas in oceanic arcs; an in situ study from St Lucia, Lesser Antilles. *Journal of Petrology*, *58*(7), 1279-1318.

Bird, D. E., Hall, S. A., Casey, J. F., & Millegan, P. S. (1999). Tectonic evolution of the Grenada Basin. In *Sedimentary basins of the world* (Vol. 4, pp. 389-416). Elsevier.

Blake, S. (1981). Volcanism and the dynamics of open magma chambers. *Nature*, *289*(5800), 783-785.

Blundy, J. (2022). Chemical Differentiation by Mineralogical Buffering in Crustal Hot Zones. *Journal of Petrology*, *63*(7), Art. No. egac054.

Bohrson, W. A., Spera, F. J., Ghiorso, M. S., Brown, G. A., Creamer, J. B., & Mayfield, A. (2014). Thermodynamic model for energy-constrained open-system evolution of crustal magma bodies undergoing simultaneous recharge, assimilation and crystallization: the magma chamber simulator. *Journal of Petrology*, *55*(9), 1685-1717.

Boudon, G., Komorowski, J. C., Villemant, B., & Semet, M. P. (2008). A new scenario for the last magmatic eruption of La Soufrière of Guadeloupe (Lesser Antilles) in 1530 AD Evidence from stratigraphy radiocarbon dating and magmatic evolution of erupted products. *Journal of Volcanology and Geothermal Research*, *178*(3), 474-490.

Bouilhol, P., Schmidt, M. W., & Burg, J. P. (2015). Magma transfer and evolution in channels within the arc crust: the pyroxenitic feeder pipes of Sapat (Kohistan, Pakistan). *Journal of Petrology*, *56*(7), 1309-1342.

Boulanger, M., France, L., Deans, J. R., Ferrando, C., Lissenberg, C. J., & Von Der Handt, A. (2020). Magma reservoir formation and evolution at a slow-spreading center (Atlantis Bank, Southwest Indian Ridge). *Frontiers in Earth Science*, *8*, Art. No. 554598.

Boulanger, M., France, L., Ferrando, C., Ildefonse, B., Ghosh, B., Sanfilippo, A., ... & Bruguier, O. (2021). Magma-Mush Interactions in the Lower Oceanic Crust: Insights From Atlantis Bank Layered Series (Southwest Indian Ridge). *Journal of Geophysical Research: Solid Earth*, *126*(9), Art. No. e2021JB022331.

Bourdier, J. L., Gourgaud, A., & Vincent, P. M. (1985). Magma mixing in a main stage of formation of Montagne Pelée: the Saint Vincent-type scoria flow sequence (Martinique, FWI). *Journal of Volcanology and Geothermal Research*, *25*(3-4), 309-332.

Bouvier, A. S., Métrich, N., & Deloule, E. (2008). Slab-derived fluids in the magma sources of St. Vincent (Lesser Antilles Arc): volatile and light element imprints. *Journal of Petrology*, *49*(8), 1427-1448.

Bouvier, A. S., Deloule, E., & Métrich, N. (2010). Fluid inputs to magma sources of St. Vincent and Grenada (Lesser Antilles): new insights from trace elements in olivine-hosted melt inclusions. *Journal of Petrology*, *51*(8), 1597-1615.

Braszus, B., Goes, S., Allen, R., Rietbrock, A., Collier, J., Harmon, N., ... & Wilson, M. (2021). Subduction history of the Caribbean from upper-mantle seismic imaging and plate reconstruction. *Nature Communications*, *12*(1), 1-14.

Braun, M. G., & Kelemen, P. B. (2002). Dunite distribution in the Oman ophiolite: implications for melt flux through porous dunite conduits. *Geochemistry, Geophysics, Geosystems*, *3*(11), 1-21.

Briden, J. C., Rex, D. C., Faller, A. M., & Tomblin, J. F. (1979). K-Ar geochronology and palaeomagnetism of volcanic rocks in the Lesser Antilles island arc. *Philosophical Transactions of the Royal Society of London. Series A, Mathematical and Physical Sciences*, *291*(1383), 485-528.

Brophy, J. G. (2008). A study of rare earth element (REE)–SiO 2 variations in felsic liquids generated by basalt fractionation and amphibolite melting: a potential test for discriminating between the two different processes. *Contributions to Mineralogy and Petrology*, *156*(3), 337-357.

Buys, J., Spandler, C., Holm, R. J., & Richards, S. W. (2014). Remnants of ancient Australia in Vanuatu: Implications for crustal evolution in island arcs and tectonic development of the southwest Pacific. *Geology*, *42*(11), 939-942.

Camejo-Harry, M., Melekhova, E., Blundy, J., Attridge, W., Robertson, R., & Christopher, T. (2018). Magma evolution beneath Bequia, Lesser Antilles, deduced from petrology of lavas and plutonic xenoliths. *Contributions to Mineralogy and Petrology*, *173*(10), 1-26.

Carpentier, M., Chauvel, C., & Mattielli, N. (2008). Pb-Nd isotopic constraints on sedimentary input into the Lesser Antilles arc system. *Earth and Planetary Science Letters*, *272*(1–2), 199–211.

Carpentier, M., Chauvel, C., Maury, R. C., & Mattielli, N. (2009). The "zircon effect" as recorded by the chemical and Hf isotopic compositions of Lesser Antilles forearc sediments. *Earth and Planetary Science Letters*, *287*(1–2), 86–99.

Cashman, K., & Blundy, J. (2013). Petrological cannibalism: the chemical and textural consequences of incremental magma body growth. *Contributions to Mineralogy and Petrology*, *166*(3), 703-729.

Cashman, K. V., Sparks, R. S. J., & Blundy, J. D. (2017). Vertically extensive and unstable magmatic systems: a unified view of igneous processes. *Science*, *355*(6331), Art. No. eaag3055.

Cashman, K. V., & Edmonds, M. (2019). Mafic glass compositions: a record of magma storage conditions, mixing and ascent. *Philosophical Transactions of the Royal Society A*, *377*(2139), Art. No. 20180004.

Cassidy, M., Edmonds, M., Watt, S. F., Palmer, M. R., & Gernon, T. M. (2015). Origin of basalts by hybridization in andesite-dominated arcs. *Journal of Petrology*, *56*(2), 325-346.

Chadwick, J. P., Troll, V. R., Ginibre, C., Morgan, D., Gertisser, R., Waight, T. E., & Davidson, J. P. (2007). Carbonate assimilation at Merapi Volcano, Java, Indonesia: insights from crystal isotope stratigraphy. *Journal of Petrology*, *48*(9), 1793-1812.

Chadwick, J. P., Troll, V. R., Waight, T. E., van der Zwan, F. M., & Schwarzkopf, L. M. (2013). Petrology and geochemistry of igneous inclusions in recent Merapi deposits: a window into the sub-volcanic plumbing system. *Contributions to Mineralogy and Petrology*, *165*(2), 259-282.

Chang, J., Audétat, A., & Li, J. W. (2021). In situ Reaction-replacement Origin of Hornblendites in the Early Cretaceous Laiyuan Complex, North China Craton, and Implications for its Tectono-magmatic Evolution. *Journal of Petrology*, *62*(5), Art. No. egab030.

Charlier, B. L., Ginibre, C., Morgan, D., Nowell, G. M., Pearson, D. G., Davidson, J. P., & Ottley, C. J. (2006). Methods for the microsampling and high-precision analysis of strontium and rubidium isotopes at single crystal scale for petrological and geochronological applications. *Chemical Geology*, *232*(3-4), 114-133.

Charlier, B. L. A., Nowell, G. M., Parkinson, I. J., Kelley, S. P., Pearson, D. G., & Burton, K. W. (2012). High temperature strontium stable isotope behaviour in the early solar system and planetary bodies. *Earth and Planetary Science Letters*, *329*, 31-40.

Chauvel, C., Marini, J. C., Plank, T., & Ludden, J. N. (2009). Hf-Nd input flux in the Izu-Mariana subduction zone and recycling of subducted material in the mantle. *Geochemistry, Geophysics, Geosystems*, *10*(1).

Cole, P. D., Robertson, R. E. A., Fedele, L., & Scarpati, C. (2019). Explosive activity of the last 1000 years at La Soufrière, St Vincent, Lesser Antilles. *Journal of Volcanology and Geothermal Research*, *371*, 86-100.

Cooper, G. F., & Wilson, C. J. (2014). Development, mobilisation and eruption of a large crystal-rich rhyolite: the Ongatiti ignimbrite, New Zealand. *Lithos*, *198*, 38-57.

Cooper, G. F., Davidson, J. P., & Blundy, J. D. (2016). Plutonic xenoliths from Martinique, Lesser Antilles: evidence for open system processes and reactive melt flow in island arc crust. *Contributions to Mineralogy and Petrology*, *171*(10), 1-21.

Cooper, G. F., Blundy, J. D., Macpherson, C. G., Humphreys, M. C. S., & Davidson, J. P. (2019). Evidence from plutonic xenoliths for magma differentiation, mixing and storage in a volatile-rich crystal mush beneath St. Eustatius, Lesser Antilles. *Contributions to Mineralogy and Petrology*, *174*(5), 1-24.

Cooper, G. F., Macpherson, C. G., Blundy, J. D., Maunder, B., Allen, R. W., Goes, S., ... & Davidson, J. P. (2020). Variable water input controls evolution of the Lesser Antilles volcanic arc. *Nature*, *582*(7813), 525-529.

Cooper, G. F., & Inglis, E. C. (2022). A crustal control on the Fe isotope systematics of volcanic arcs revealed in plutonic xenoliths from the Lesser Antilles. *Frontiers in Earth Science*, *9*. Art. No. 795858.

Cooper, K. M., & Kent, A. J. (2014). Rapid remobilization of magmatic crystals kept in cold storage. *Nature*, *506*(7489), 480-483.

Costa, F., Dungan, M. A., & Singer, B. S. (2002). Hornblende-and phlogopite-bearing gabbroic xenoliths from Volcán San Pedro (36 S), Chilean Andes: evidence for melt and fluid migration and reactions in subduction-related plutons. *Journal of Petrology*, *43*(2), 219-241.

Coulon, C., Clocchiatti, R., Maury, R. C., & Westercamp, D. (1984). Petrology of basaltic xenoliths in andesitic to dacitic host lavas from Martinique (Lesser Antilles): evidence for magma mixing. *Bulletin Volcanologique*, *47*(4), 705-734.

Crosweller, H. S., Arora, B., Brown, S. K., Cottrell, E., Deligne, N. I., Guerrero, N. O., ... & Venzke, E. (2012). Global database on large magnitude explosive volcanic eruptions (LaMEVE). *Journal of Applied Volcanology*, *1*(1), 1-13.

Davidson, J. P. (1985). Mechanisms of contamination in Lesser Antilles island arc magmas from radiogenic and oxygen isotope relationships. *Earth and Planetary Science Letters*, *72*, 163–174.

Davidson, J. P. (1986). Isotopic and trace element constraints on the petrogenesis of subduction-related lavas from Martinique, Lesser Antilles. *Journal of Geophysical Research*, *91*(B6), 5943.

Davidson, J. P. (1987). Crustal contamination versus subduction zone enrichment: examples from the Lesser Antilles and implications for mantle source compositions of island arc volcanic rocks. *Geochimica et Cosmochimica Acta*, *81*, 2185–2198.

Davidson, J. P., & Harmon, R. S. (1989). Oxygen isotope constraints on the petrogenesis of volcanic arc magmas from Martinique, Lesser Antilles. *Earth and Planetary Science Letters*, *95*(3–4), 255–270.

Davidson, J. P., Hora, J. M., Garrison, J. M., & Dungan, M. A. (2005). Crustal forensics in arc magmas. *Journal of Volcanology and Geothermal Research*, *140*(1-3), 157-170.

Davidson, J., Turner, S., Handley, H., Macpherson, C., & Dosseto, A. (2007a). Amphibole “sponge” in arc crust? *Geology*, *35*(9), 787-790.

Davidson, J. P., Morgan, D. J., Charlier, B. L. A., Harlou, R., & Hora, J. M. (2007b). Microsampling and Isotopic Analysis of Igneous Rocks: Implications for the Study of Magmatic Systems. *Annual Review of Earth and Planetary Sciences*, *35*(1), 273–311.

Davidson, J., & Wilson, M. (2011). Differentiation and source processes at Mt Pelée and the Quill; Active volcanoes in the Lesser Antilles arc. *Journal of Petrology*, *52*(7–8), 1493–1531.

Deegan, F. M., Troll, V. R., Freda, C., Misiti, V., Chadwick, J. P., McLeod, C. L., & Davidson, J. P. (2010). Magma–carbonate interaction processes and associated CO2 release at Merapi Volcano, Indonesia: insights from experimental petrology. *Journal of Petrology*, *51*(5), 1027-1051.

Deegan, F. M., Bédard, J. H., Grasby, S. E., Dewing, K., Geiger, H., Misiti, V., ... & Troll, V. R. (2022). Magma–Shale Interaction in Large Igneous Provinces: Implications for Climate Warming and Sulfide Genesis. *Journal of Petrology*, *63*(9), Art. No. egac094.

Defant, M. J., Sherman, S., Maury, R. C., Bellon, H., De Boer, J., Davidson, J., & Kepezhinskas, P. (2001). The geology, petrology, and petrogenesis of Saba Island, Lesser Antilles. *Journal of Volcanology and Geothermal Research*, *107*(1-3), 87-111.

Delph, J. R., Ward, K. M., Zandt, G., Ducea, M. N., & Beck, S. L. (2017). Imaging a magma plumbing system from MASH zone to magma reservoir. *Earth and Planetary Science Letters*, *457*, 313-324.

DePaolo, D. J. (1981). Trace element and isotopic effects of combined wallrock assimilation and fractional crystallization. *Earth and Planetary Science Letters*, *53*(2), 189-202.

Dessimoz, M., Müntener, O., & Ulmer, P. (2012). A case for hornblende dominated fractionation of arc magmas: the Chelan Complex (Washington Cascades). *Contributions to Mineralogy and Petrology*, *163*(4), 567-589.

Devine, J. D., & Sigurdsson, H. (1983). The liquid composition and crystallization history of the 1979 Soufriere magma, St. Vincent, WI. *Journal of Volcanology and Geothermal Research*, *16*(1-2), 1-31.

Dowall, D., Pearson, D., & Nowell, G. (2003). Chemical pre-concentration procedures for high-precision analysis of Hf–Nd–Sr isotopes in geological materials by plasma ionisation multi-collector mass spectrometry (PIMMS) techniques. In: Holland, J. G. & Tanner, S. D. (eds) *Plasma Source Mass Spectrometry: Applications and Emerging Technologies*. Cambridge: Royal Society of Chemistry, pp. 321–337.

Druitt, T. H., Costa, F., Deloule, E., Dungan, M., & Scaillet, B. (2012). Decadal to monthly timescales of magma transfer and reservoir growth at a caldera volcano. *Nature*, *482*(7383), 77-80.

DuFrane, S. A., Turner, S., Dosseto, A., & van Soest, M. (2009). Reappraisal of fluid and sediment contributions to Lesser Antilles magmas. *Chemical Geology*, *265*(3–4), 272–278.

Dungan, M. A., & Davidson, J. (2004). Partial assimilative recycling of the mafic plutonic roots of arc volcanoes: An example from the Chilean Andes. *Geology*, *32*(9), 773-776.

Edmonds, M., Cashman, K. V., Holness, M., & Jackson, M. (2019). Architecture and dynamics of magma reservoirs. *Philosophical Transactions of the Royal Society A*, *377*(2139), Art. No. 20180298.

Escalona, A., & Mann, P. (2011). Tectonics, basin subsidence mechanisms, and paleogeography of the Caribbean-South American plate boundary zone. *Marine and Petroleum Geology*, *28*(1), 8-39.

Fedele, L., Cole, P. D., Scarpati, C., & Robertson, R. E. (2021). Petrological insights on the last 1000 years of explosive activity at La Soufrière volcano, St. Vincent (Lesser Antilles). *Lithos*, *392*, Art. No. 106150.

Ferrando, C., France, L., Basch, V., Sanfilippo, A., Tribuzio, R., & Boulanger, M. (2021). Grain Size Variations Record Segregation of Residual Melts in Slow-Spreading Oceanic Crust (Atlantis Bank, 57° E Southwest Indian Ridge). *Journal of Geophysical Research: Solid Earth*, *126*(4), Art. No. e2020JB020997.

Foden, J. D., & Green, D. H. (1992). Possible role of amphibole in the origin of andesite: some experimental and natural evidence. *Contributions to Mineralogy and Petrology*, *109*(4), 479-493.

Font, L., Davidson, J. P., Pearson, D. G., Nowell, G. M., Jerram, D. A., & Ottley, C. J. (2008). Sr and Pb isotope micro-analysis of plagioclase crystals from Skye lavas: an insight into open-system processes in a flood basalt province. *Journal of Petrology*, *49*(8), 1449-1471.

Forni, F., Bachmann, O., Mollo, S., De Astis, G., Gelman, S. E., & Ellis, B. S. (2016). The origin of a zoned ignimbrite: Insights into the Campanian Ignimbrite magma chamber (Campi Flegrei, Italy). *Earth and Planetary Science Letters*, *449*, 259-271.

Gaetani, G. A., Grove, T. L., & Bryan, W. B. (1993). The influence of water on the petrogenesis of subduction related igneous rocks. *Nature*, *365*(6444), 332-334.

Gasparon, M., & Varne, R. (1998). Crustal assimilation versus subducted sediment input in west Sunda arc volcanics: an evaluation. *Mineralogy and Petrology*, *64*(1), 89-117.

Geng, X., Liang, Z., Zhang, W., Liu, Y., Hu, Z., & Deng, L. (2022). Formation of green-core clinopyroxene in continental basalts through magmatic differentiation and crustal assimilation: Insights from in-situ trace element and Pb isotopic compositions. *Lithos*, *410*, Art. No. 106587.

Germa, A., Quidelleur, X., Labanieh, S., Chauvel, C., & Lahitte, P. (2011). The volcanic evolution of Martinique Island: Insights from K–Ar dating into the Lesser

Antilles arc migration since the Oligocene. *Journal of Volcanology and Geothermal Research*, *208*(3-4), 122-135.

Giacomoni, P. P., Coltorti, M., Bryce, J. G., Fahnestock, M. F., & Guitreau, M. (2016). Mt. Etna plumbing system revealed by combined textural, compositional, and thermobarometric studies in clinopyroxenes. *Contributions to Mineralogy and Petrology*, *171*(4), 1-15.

Giordano, G., & Caricchi, L. (2022). Determining the State of Activity of Transcrustal Magmatic Systems and Their Volcanoes. *Annual Review of Earth and Planetary Sciences*, *50*.

Ginibre, C., & Davidson, J. P. (2014). Sr isotope zoning in plagioclase from Parinacota volcano (Northern Chile): Quantifying magma mixing and crustal contamination. *Journal of Petrology*, *55*(6), 1203–1238.

Gleeson, M. L., Gibson, S. A., & Stock, M. J. (2020). Upper mantle mush zones beneath low melt flux ocean island volcanoes: insights from Isla Floreana, Galápagos. *Journal of Petrology*, *61*(11-12), Art. No. egaa094.

Gleeson, M. L., Gibson, S. A., & Stock, M. J. (2022). Constraints on the behaviour and content of volatiles in Galápagos magmas from melt inclusions and nominally anhydrous minerals. *Geochimica et Cosmochimica Acta*, *319*, 168-190.

Goes, S., Collier, J., Blundy, J., Davidson, J., Harmon, N., Henstock, T., ... & Wilson, M. (2019). Project VoiLA: volatile recycling in the Lesser Antilles.

Goss, A. R., Kay, S. M., & Mpodozis, C. (2011). The geochemistry of a dying continental arc: the Incapillo Caldera and Dome Complex of the southernmost Central Andean Volcanic Zone (~ 28 S). *Contributions to Mineralogy and Petrology*, *161*(1), 101-128.

Gourgaud, A., Fichaut, M., & Joron, J. L. (1989). Magmatology of Mt. Pelée (Martinique, FWI). I: Magma mixing and triggering of the 1902 and 1929 Pelean nuées ardentes. *Journal of Volcanology and Geothermal Research*, *38*(1-2), 143-169.

Grove, T. L., & Donnelly-Nolan, J. M. (1986). The evolution of young silicic lavas at Medicine Lake Volcano, California: Implications for the origin of compositional gaps in calc-alkaline series lavas. *Contributions to Mineralogy and Petrology*, *92*(3), 281-302.

Grove, T. L., Till, C. B., & Krawczynski, M. J. (2012). The role of H_2O in subduction zone magmatism. *Annual Review of Earth and Planetary Sciences*, *40*(413), 2012.

Handley, H. K., Blichert-Toft, J., Gertisser, R., Macpherson, C. G., Turner, S. P., Zaennudin, A., & Abdurrachman, M. (2014). Insights from Pb and O isotopes into along-arc variations in subduction inputs and crustal assimilation for volcanic rocks in Java, Sunda arc, Indonesia. *Geochimica et Cosmochimica Acta*, *139*, 205-226.

Harlou, R., Pearson, D. G., Nowell, G. M., Ottley, C. J., & Davidson, J. P. (2009). Combined Sr isotope and trace element analysis of melt inclusions at sub-ng levels using micro-milling, TIMS and ICPMS. *Chemical Geology*, *260*(3-4), 254-268.

Harris, P. G. (1957). Zone refining and the origin of potassic basalts. *Geochimica et Cosmochimica Acta*, *12*(3), 195-208.

Heath, E., Macdonald, R., Belkin, H., Hawkesworth, C., & Sigurdsson, H. (1998). Magmagenesis at Soufriere volcano St Vincent, Lesser Antilles Arc. *Journal of Petrology*, *39*(10), 1721–1764.

Hepworth, L. N., Daly, J. S., Gertisser, R., Johnson, C. G., Emeleus, C. H., & O'Driscoll, B. (2020). Rapid crystallization of precious-metal-mineralized layers in mafic magmatic systems. *Nature Geoscience*, *13*(5), 375-381.

Higgins, O., Sheldrake, T., & Caricchi, L. (2022). Machine learning thermobarometry and chemometry using amphibole and clinopyroxene: a window into the roots of an arc volcano (Mount Liamuiga, Saint Kitts). *Contributions to Mineralogy and Petrology*, *177*(1), 1-22.

Hildreth, W., & Moorbath, S. (1988). Crustal contributions to arc magmatism in the Andes of central Chile. *Contributions to Mineralogy and Petrology*, *98*(4), 455-489.

Hill, G. J., Caldwell, T. G., Heise, W., Chertkoff, D. G., Bibby, H. M., Burgess, M. K., ... & Cas, R. A. (2009). Distribution of melt beneath Mount St Helens and Mount Adams inferred from magnetotelluric data. *Nature Geoscience*, *2*(11), 785-789.

Holness, M. B., Stock, M. J., & Geist, D. (2019). Magma chambers versus mush zones: constraining the architecture of sub-volcanic plumbing systems from microstructural analysis of crystalline enclaves. *Philosophical Transactions of the Royal Society A*, *377*(2139), Art. No. 20180006.

Horn, E. L., Taylor, R. N., Gernon, T. M., Stock, M. J., & Farley, E. R. (2022). Composition and petrology of a mush-bearing magma reservoir beneath Tenerife. *Journal of Petrology*, *63*(10), Art. No. egac095.

Hu, Y., Teng, F. Z., & Chauvel, C. (2021). Potassium isotopic evidence for sedimentary input to the mantle source of Lesser Antilles lavas. *Geochimica et Cosmochimica Acta*, *295*, 98-111.

Hu, H., Jackson, M. D., & Blundy, J. (2022). Melting, compaction and reactive flow: Controls on melt fraction and composition change in crustal mush reservoirs. *Journal of Petrology*, *63*(11), Art. No. egac097.

Huang, F., Lundstrom, C. C., Sigurdsson, H., & Zhang, Z. (2011). U-series disequilibria in Kick'em Jenny submarine volcano lavas: A new view of time-scales of magmatism in convergent margins. *Geochimica et Cosmochimica Acta*, *75*(1), 195–212.

Huang, H. H., Lin, F. C., Schmandt, B., Farrell, J., Smith, R. B., & Tsai, V. C. (2015). The Yellowstone magmatic system from the mantle plume to the upper crust. *Science*, *348*(6236), 773-776.

Humphreys, M. C. S., Zhang, J., Cooper, G. F., Macpherson, C. G., & Ottley, C. J. (2019a). Identifying the ingredients of hydrous arc magmas: insights from Mt

Lamington, Papua New Guinea. *Philosophical Transactions of the Royal Society A*, *377*(2139), Art. No. 20180018.

Humphreys, M. C., Cooper, G. F., Zhang, J., Loewen, M., Kent, A. J., Macpherson, C. G., & Davidson, J. P. (2019b). Unravelling the complexity of magma plumbing at Mount St. Helens: a new trace element partitioning scheme for amphibole. *Contributions to Mineralogy and Petrology*, *174*(1), 1-15.

Jackson, M. D., Blundy, J., & Sparks, R. S. J. (2018). Chemical differentiation, cold storage and remobilization of magma in the Earth's crust. *Nature*, *564*(7736), 405-409.

Kaufmann, F. E., Vukmanovic, Z., Holness, M. B., & Hecht, L. (2018). Orthopyroxene oikocrysts in the MG1 chromitite layer of the Bushveld Complex: implications for cumulate formation and recrystallisation. *Contributions to Mineralogy and Petrology*, *173*(2), 1-20.

Kelemen, P. B., Whitehead, J. A., Aharonov, E., & Jordahl, K. A. (1995). Experiments on flow focusing in soluble porous media, with applications to melt extraction from the mantle. *Journal of Geophysical Research: Solid Earth*, *100*(B1), 475-496.

Kelemen, P. B., Hanghøj, K., & Greene, A. R. (2003). One view of the geochemistry of subduction-related magmatic arcs, with an emphasis on primitive andesite and lower crust. *Treatise on Geochemistry*, *3*, 659.

Kent, A. J., & Elliott, T. R. (2002). Melt inclusions from Marianas arc lavas: implications for the composition and formation of island arc magmas. *Chemical Geology*, *183*(1-4), 263-286.

Kepezhinskas, N., Kamenov, G. D., Foster, D. A., & Kepezhinskas, P. (2020). Petrology and geochemistry of alkaline basalts and gabbroic xenoliths from Utila Island (Bay Islands, Honduras): Insights into back-arc processes in the Central American volcanic arc. *Lithos*, *352*, Art. No. 105306.

Kiddle, E. J., Edwards, B. R., Loughlin, S. C., Petterson, M., Sparks, R. S. J., & Voight, B. (2010). Crustal structure beneath Montserrat, Lesser Antilles, constrained by xenoliths, seismic velocity structure and petrology. *Geophysical Research Letters*, *37*(19).

Klaver, M., Matveev, S., Berndt, J., Lissenberg, C. J., & Vroon, P. Z. (2017). A mineral and cumulate perspective to magma differentiation at Nisyros volcano, Aegean arc. *Contributions to Mineralogy and Petrology*, *172*(11), 1-23.

Klaver, M., Blundy, J. D., & Vroon, P. Z. (2018). Generation of arc rhyodacites through cumulate-melt reactions in a deep crustal hot zone: evidence from Nisyros volcano. *Earth and Planetary Science Letters*, *497*, 169-180.

Labanieh, S., Chauvel, C., Germa, A., & Quidelleur, X. (2012). Martinique: A clear case for sediment melting and slab dehydration as a function of distance to the trench. *Journal of Petrology*, *53*(12), 2441–2464.

Labanieh, S., Chauvel, C., Germa, A., Quidelleur, X., & Lewin, E. (2010). Isotopic hyperbolas constrain sources and processes under the Lesser Antilles arc. *Earth and Planetary Science Letters*, *298*(1–2), 35–46.

Larocque, J., & Canil, D. (2010). The role of amphibole in the evolution of arc magmas and crust: the case from the Jurassic Bonanza arc section, Vancouver Island, Canada. *Contributions to Mineralogy and Petrology*, *159*(4), 475-492.

Laumonier, M., Gaillard, F., Muir, D., Blundy, J., & Unsworth, M. (2017). Giant magmatic water reservoirs at mid-crustal depth inferred from electrical conductivity and the growth of the continental crust. *Earth and Planetary Science Letters*, *457*, 173-180.

Leat, P. T., Day, S. J., Tate, A. J., Martin, T. J., Owen, M. J., & Tappin, D. R. (2013). Volcanic evolution of the South Sandwich volcanic arc, South Atlantic, from multibeam bathymetry. *Journal of Volcanology and Geothermal Research*, *265*, 60-77.

Lee, C. T. A., & Bachmann, O. (2014). How important is the role of crystal fractionation in making intermediate magmas? Insights from Zr and P systematics. *Earth and Planetary Science Letters*, *393*, 266-274.

Lees, J. M. (2007). Seismic tomography of magmatic systems. *Journal of Volcanology and Geothermal Research*, *167*(1-4), 37-56.

Lindsay, J. M., Trumbull, R. B., & Siebel, W. (2005). Geochemistry and petrogenesis of late Pleistocene to Recent volcanism in Southern Dominica, Lesser Antilles. *Journal of Volcanology and Geothermal Research*, *148*(3-4), 253-294.

Lissenberg, C. J., MacLeod, C. J., Howard, K. A., & Godard, M. (2013). Pervasive reactive melt migration through fast-spreading lower oceanic crust (Hess Deep, equatorial Pacific Ocean). *Earth and Planetary Science Letters*, *361*, 436-447.

Lissenberg, C. J., & MacLeod, C. J. (2016). A reactive porous flow control on mid-ocean ridge magmatic evolution. *Journal of Petrology*, *57*(11-12), 2195-2220.

Lissenberg, C. J., MacLeod, C. J., & Bennett, E. N. (2019). Consequences of a crystal mush-dominated magma plumbing system: a mid-ocean ridge perspective. *Philosophical Transactions of the Royal Society A*, *377*(2139), Art. No. 20180014.

Loocke, M. (2016). *The role of the axial melt lens in crustal accretion at fast-spreading mid-ocean ridges* [PhD thesis, Cardiff University] https://orca.cardiff.ac.uk/id/eprint/97663

Lucci, F., Carrasco-Núñez, G., Rossetti, F., Theye, T., White, J. C., Urbani, S., ... & Giordano, G. (2020). Anatomy of the magmatic plumbing system of Los Humeros Caldera (Mexico): implications for geothermal systems. *Solid Earth*, *11*(1), 125-159.

Macdonald, K. C., & Holcombe, T. L. (1978). Inversion of magnetic anomalies and sea-floor spreading in the Cayman Trough. *Earth and Planetary Science Letters*, *40*(3), 407-414.

Macdonald, R., Hawkesworth, C. J., & Heath, E. (2000). The Lesser Antilles volcanic chain: a study in arc magmatism. *Earth-Science Reviews*, *49*(1-4), 1-76.

Macpherson, C. G., Gamble, J. A., & Mattey, D. P. (1998). Oxygen isotope geochemistry of lavas from an oceanic to continental arc transition, Kermadec–Hikurangi margin, SW Pacific. *Earth and Planetary Science Letters*, *160*(3-4), 609-621.

Magee, C., Stevenson, C. T., Ebmeier, S. K., Keir, D., Hammond, J. O., Gottsmann, J. H., ... & Jackson, M. D. (2018). Magma plumbing systems: a geophysical perspective. *Journal of Petrology*, *59*(6), 1217-1251.

Martel, C., Pichavant, M., Holtz, F., Scaillet, B., Bourdier, J. L., & Traineau, H. (1999). Effects of f O2 and H2O on andesite phase relations between 2 and 4 kbar. *Journal of Geophysical Research: Solid Earth*, *104*(B12), 29453-29470.

Marxer, F., Ulmer, P., & Müntener, O. (2021). Polybaric fractional crystallisation of arc magmas: an experimental study simulating trans-crustal magmatic systems. *Contributions to Mineralogy and Petrology*, *177*(1), 1-36.

Mason, E., Edmonds, M., & Turchyn, A. V. (2017). Remobilization of crustal carbon may dominate volcanic arc emissions. *Science*, *357*(6348), 290-294.

McKenzie, D. P., & O'nions, R. K. (1991). Partial melt distributions from inversion of rare earth element concentrations. *Journal of Petrology*, *32*(5), 1021-1091.

Melekhova, E., Blundy, J., Robertson, R., & Humphreys, M. C. (2015). Experimental evidence for polybaric differentiation of primitive arc basalt beneath St. Vincent, Lesser Antilles. *Journal of Petrology*, *56*(1), 161-192.

Melekhova, E., Blundy, J., Martin, R., Arculus, R., & Pichavant, M. (2017). Petrological and experimental evidence for differentiation of water-rich magmas beneath St. Kitts, Lesser Antilles. *Contributions to Mineralogy and Petrology*, *172*(11), 1-32.

Melekhova, E., Schlaphorst, D., Blundy, J., Kendall, J. M., Connolly, C., McCarthy, A., & Arculus, R. (2019). Lateral variation in crustal structure along the Lesser Antilles arc from petrology of crustal xenoliths and seismic receiver functions. *Earth and Planetary Science Letters*, *516*, 12–24.

Melekhova, E., Camejo-Harry, M., Blundy, J., Wallis, S. R., Annen, C., Kunz, B. E., ... & Thirlwall, M. (2022). Arc crust formation of Lesser Antilles revealed by crustal xenoliths from Petit St. Vincent. *Journal of Petrology*, *63*(5), Art. No. egac033.

Müller, R. D., Zahirovic, S., Williams, S. E., Cannon, J., Seton, M., Bower, D. J., ... & Gurnis, M. (2019). A global plate model including lithospheric deformation along major rifts and orogens since the Triassic. *Tectonics*, *38*(6), 1884-1907.

Müntener, O., & Ulmer, P. (2018). Arc crust formation and differentiation constrained by experimental petrology. *American Journal of Science*, *318*(1), 64-89.

Nagasawa, H., Schreiber, H. D., & Morris, R. V. (1980). Experimental mineral/liquid partition coefficients of the rare earth elements (REE), Sc and Sr for perovskite, spinel and melilite. *Earth and Planetary Science Letters*, *46*(3), 431-437.

Namur, O., Humphreys, M. C., & Holness, M. B. (2013). Lateral reactive infiltration in a vertical gabbroic crystal mush, Skaergaard intrusion, East Greenland. *Journal of Petrology*, *54*(5), 985-1016.

Nandedkar, R. H., Ulmer, P., & Müntener, O. (2014). Fractional crystallization of primitive, hydrous arc magmas: an experimental study at 0.7 GPa. *Contributions to Mineralogy and Petrology*, *167*(6), 1-27.

Nandedkar, R. H., Hürlimann, N., Ulmer, P., & Müntener, O. (2016). Amphibole–melt trace element partitioning of fractionating calc-alkaline magmas in the lower crust: an experimental study. *Contributions to Mineralogy and Petrology*, *171*(8), 1-25.

Nebel, O., Vroon, P. Z., van Westrenen, W., Iizuka, T., & Davies, G. R. (2011). The effect of sediment recycling in subduction zones on the Hf isotope character of new arc crust, Banda arc, Indonesia. *Earth and Planetary Science Letters*, *303*(3-4), 240-250.

Neill, I., Gibbs, J. A., Hastie, A. R., & Kerr, A. C. (2010). Origin of the volcanic complexes of La Désirade, Lesser Antilles: Implications for tectonic reconstruction of the Late Jurassic to Cretaceous Pacific-proto Caribbean margin. *Lithos*, *120*(3-4), 407-420.

Neill, I., Kerr, A. C., Hastie, A. R., Pindell, J. L., & Millar, I. L. (2013). The Albian–Turonian island arc rocks of Tobago, West Indies: geochemistry, petrogenesis, and Caribbean Plate tectonics. *Journal of Petrology*, *54*(8), 1607-1639.

Nowell, G., & Parrish, R. R. (2001). Simultaneous acquisition of isotope compositions and parent/daughter ratios by non-isotope dilution-mode Plasma Ionisation Multi-collector Mass Spectrometry (PIMMS). *Special Publication-Royal Society Of Chemistry*, *267*(1), 298-310.

Nowell, G.M., Luguet, A., Pearson, D.G., Horstwood, M.S.A. (2008). Precise and accurate $^{186}Os/^{188}Os$ and $^{187}Os/^{188}Os$ measurements by multi-collector plasma ionisation mass spectrometry (MC-ICP-MS) part I: Solution analyses. *Chemical Geology*, *248* (3-4), 363-393.

O'Hara, M. J. (1980). Nonlinear nature of the unavoidable long-lived isotopic, trace and major element contamination of a developing magma chamber. *Philosophical Transactions of the Royal Society of London. Series A, Mathematical and Physical Sciences*, *297*(1431), 215-227.

O'Neill, S. C., & Jenner, F. E. (2012). The global pattern of trace-element distributions in ocean floor basalts. *Nature*, *491*(7426), 698-704.

Ortoleva, P., Merino, E., Moore, C., & Chadam, J. (1987a). Geochemical self-organization I; reaction-transport feedbacks and modeling approach. *American Journal of Science*, *287*(10), 979-1007.

Ortoleva, P., Chadam, J., Merino, E., & Sen, A. (1987b). Geochemical self-organization II; the reactive-infiltration instability. *American Journal of Science*, *287*(10), 1008-1040.

Otamendi, J. E., Tiepolo, M., Walker Jr, B. A., Cristofolini, E. A., & Tibaldi, A. M. (2016). Trace elements in minerals from mafic and ultramafic cumulates of the central Sierra de Valle Fértil, Famatinian arc, Argentina. *Lithos*, *240*, 355-370.

Palme, H., & O'Neill, H. S. C. (2003). Cosmochemical estimates of mantle composition. *Treatise on Geochemistry*, *2*, 568.

Parra, M., Faugères, J. C., Grousset, F., & Pujol, C. (1997). Sr-Nd isotopes as tracers of fine-grained detrital sediments: the South-Barbados accretionary prism during the last 150 kyr. *Marine Geology*, *136*(3-4), 225-243.

Patino, L. C., Carr, M. J., & Feigenson, M. D. (2000). Local and regional variations in Central American arc lavas controlled by variations in subducted sediment input. *Contributions to Mineralogy and Petrology*, *138*(3), 265-283.

Paton, C., Hellstrom, J., Paul, B., Woodhead, J., & Hergt, J. (2011). Iolite: Freeware for the visualisation and processing of mass spectrometric data. *Journal of Analytical Atomic Spectrometry*, *26*(12), 2508-2518.

Paulatto, M., Minshull, T. A., Baptie, B., Dean, S., Hammond, J. O., Henstock, T., ... & Voight, B. (2010). Upper crustal structure of an active volcano from refraction/reflection tomography, Montserrat, Lesser Antilles. *Geophysical Journal International*, *180*(2), 685-696.

Paulatto, M., Annen, C., Henstock, T. J., Kiddle, E., Minshull, T. A., Sparks, R. S. J., & Voight, B. (2012). Magma chamber properties from integrated seismic tomography and thermal modeling at Montserrat. *Geochemistry, Geophysics, Geosystems*, *13*(1).

Paulatto M., Hooft, E. E. E., Chrapkiewicz, K., Heath, B., Toomey, D. R., and Morgan J. V. (2022), Advances in seismic imaging of magma and crystal mush. *Frontiers in Earth Science,10*, Art. No. 970131

Peate, D. W., Pearce, J. A., Hawkesworth, C. J., Colley, H., Edwards, C. M., & Hirose, K. (1997). Geochemical variations in Vanuatu arc lavas: the role of subducted material and a variable mantle wedge composition. *Journal of Petrology*, *38*(10), 1331-1358.

Pichavant, M., Martel, C., Bourdier, J. L., & Scaillet, B. (2002). Physical conditions, structure, and dynamics of a zoned magma chamber: Mount Pelée (Martinique, Lesser Antilles Arc). *Journal of Geophysical Research: Solid Earth*, *107*(B5), ECV-1.

Pichavant, M., & Macdonald, R. (2007). Crystallization of primitive basaltic magmas at crustal pressures and genesis of the calc-alkaline igneous suite: experimental evidence from St Vincent, Lesser Antilles arc. *Contributions to Mineralogy and Petrology*, *154*(5), 535-558.

Pichavant, M., Poussineau, S., Lesne, P., Solaro, C., & Bourdier, J. L. (2018). Experimental parametrization of magma mixing: application to the AD 1530 eruption of La Soufrière, Guadeloupe (Lesser Antilles). *Journal of Petrology*, *59*(2), 257-282.

Plank, T. (2005). Constraints from thorium/lanthanum on sediment recycling at subduction zones and the evolution of the continents. *Journal of Petrology*, *46*(5), 921-944.

Plank, T., & Langmuir, C. H. (1993). Tracing trace elements from sediment input to volcanic output at subduction zones. *Nature*, 362(6422), 739-743.

Price, R. C., Gamble, J. A., Smith, I. E., Stewart, R. B., Eggins, S., & Wright, I. C. (2005). An integrated model for the temporal evolution of andesites and rhyolites and crustal development in New Zealand's North Island. *Journal of Volcanology and Geothermal Research*, *140*(1-3), 1-24.

Price, R. C., Smith, I. E., Stewart, R. B., Gamble, J. A., Gruender, K., & Maas, R. (2016). High-K andesite petrogenesis and crustal evolution: Evidence from mafic and ultramafic xenoliths, Egmont Volcano (Mt. Taranaki) and comparisons with Ruapehu Volcano, North Island, New Zealand. *Geochimica et Cosmochimica Acta*, *185*, 328-357.

Putirka, K. D. (2008). Thermometers and barometers for volcanic systems. *Reviews in Mineralogy and Geochemistry*, *69*(1), 61-120.

Reubi, O., & Blundy, J. (2008). Assimilation of plutonic roots, formation of high-K 'exotic' melt inclusions and genesis of andesitic magmas at Volcán de Colima, Mexico. *Journal of Petrology*, *49*(12), 2221-2243.

Reubi, O., Nicholls, I. A., & Kamenetsky, V. S. (2003). Early mixing and mingling in the evolution of basaltic magmas: evidence from phenocryst assemblages, Slamet Volcano, Java, Indonesia. *Journal of Volcanology and Geothermal Research*, *119*(1-4), 255-274.

Ridolfi, F., Renzulli, A., & Puerini, M. (2010). Stability and chemical equilibrium of amphibole in calc-alkaline magmas: an overview, new thermobarometric formulations and application to subduction-related volcanoes. *Contributions to Mineralogy and Petrology*, *160*(1), 45-66.

Robertson, R. (2012). Land Degradation Assessment of St. Vincent, W.I. DOI: 10.13140/RG.2.2.33175.27044.

Rojas-Agramonte, Y., Williams, I. S., Arculus, R., Kröner, A., García-Casco, A., Lázaro, C., ... & Mertz-Kraus, R. (2017). Ancient xenocrystic zircon in young volcanic rocks of the southern Lesser Antilles island arc. *Lithos*, *290*, 228-252.

Rosman, K. K. R., & Taylor, P. D. P. (1998). Isotopic compositions of the elements 1997 (Technical Report). *Pure and Applied Chemistry*, *70*, 217-236.

Rousseau, T. C., Roddaz, M., Moquet, J. S., Delgado, H. H., Calves, G., & Bayon, G. (2019). Controls on the geochemistry of suspended sediments from large tropical South American rivers (Amazon, Orinoco and Maroni). *Chemical Geology*, *522*, 38-54.

Rubin, A. E., Cooper, K. M., Till, C. B., Kent, A. J., Costa, F., Bose, M., ... & Cole, J. (2017). Rapid cooling and cold storage in a silicic magma reservoir recorded in individual crystals. *Science*, *356*(6343), 1154-1156.

Salters, V. J., & Stracke, A. (2004). Composition of the depleted mantle. *Geochemistry, Geophysics, Geosystems*, *5*(5).

Sanfilippo, A., MacLeod, C. J., Tribuzio, R., Lissenberg, C. J., & Zanetti, A. (2020). Early-stage melt-rock reaction in a cooling crystal mush beneath a slow-spreading mid-ocean ridge (IODP Hole U1473A, Atlantis Bank, Southwest Indian Ridge). *Frontiers in Earth Science*, *8*, Art. No. 579138.

Schlaphorst, D., Melekhova, E., Kendall, J. M., Blundy, J., & Latchman, J. L. (2018). Probing layered arc crust in the Lesser Antilles using receiver functions. *Royal Society Open Science*, *5*(11), Art. No. 180764.

Schlaphorst, D., Harmon, N., Kendall, J. M., Rychert, C. A., Collier, J., Rietbrock, A., ... & VoiLA Team. (2021). Variation in upper plate crustal and lithospheric mantle structure in the greater and Lesser Antilles from ambient noise tomography. *Geochemistry, Geophysics, Geosystems*, *22*(7), Art. No. e2021GC009800.

Shamloo, H. I., & Till, C. B. (2019). Decadal transition from quiescence to supereruption: petrologic investigation of the Lava Creek Tuff, Yellowstone Caldera, WY. *Contributions to Mineralogy and Petrology*, *174*(4), 1-18.

Shane, P., Cocker, K., Coote, A., Stirling, C. H., & Reid, M. R. (2019). The prevalence of plagioclase antecrysts and xenocrysts in andesite magma, exemplified by lavas of the Tongariro volcanic complex, New Zealand. *Contributions to Mineralogy and Petrology*, *174*(11), 1-18.

Sisson, T. W., & Grove, T. L. (1993). Experimental investigations of the role of H2O in calc-alkaline differentiation and subduction zone magmatism. *Contributions to Mineralogy and Petrology*, *113*(2), 143-166.

Smith, D. J. (2014). Clinopyroxene precursors to amphibole sponge in arc crust. *Nature Communications*, *5*(1), 1-6.

Smith, T. E., Thirlwall, M. F., & Macpherson, C. (1996). Trace element and isotope geochemistry of the volcanic rocks of Bequia, Grenadine Islands, Lesser Antilles arc: A study of subduction enrichment and intra-crustal contamination. *Journal of Petrology*, *37*(1), 117–143.

Solano, J. M. S., Jackson, M. D., Sparks, R. S. J., Blundy, J. D., & Annen, C. (2012). Melt segregation in deep crustal hot zones: a mechanism for chemical differentiation, crustal assimilation and the formation of evolved magmas. *Journal of Petrology*, *53*(10), 1999-2026.

Solano, J. M. S., Jackson, M. D., Sparks, R. S. J., & Blundy, J. (2014). Evolution of major and trace element composition during melt migration through crystalline mush: implications for chemical differentiation in the crust. *American Journal of Science*, *314*(5), 895-939.

Solaro, C., Balcone-Boissard, H., Morgan, D. J., Boudon, G., Martel, C., & Ostorero, L. (2020). A system dynamics approach to understanding the deep magma plumbing

system beneath Dominica (Lesser Antilles). *Frontiers in Earth Science*, *8*, Art. No. 574032.

Sparks, R. S. J., Huppert, H. E., & Turner, J. S. (1984). The fluid dynamics of evolving magma chambers. *Philosophical Transactions of the Royal Society of London. Series A, Mathematical and Physical Sciences*, *310*(1514), 511-534.

Sparks, R. S. J., & Cashman, K. V. (2017). Dynamic magma systems: Implications for forecasting volcanic activity. *Elements*, *13*(1), 35-40.

Sparks, R. S. J., Annen, C., Blundy, J. D., Cashman, K. V., Rust, A. C., & Jackson, M. D. (2019). Formation and dynamics of magma reservoirs. *Philosophical Transactions of the Royal Society A*, *377*(2139), Art. No. 20180019.

Sparks, R. S. J., Blundy, J. D., Cashman, K. V., Jackson, M., Rust, A., & Wilson, C. J. N. (2022). Large silicic magma bodies and very large magnitude explosive eruptions. *Bulletin of Volcanology*, *84*(1), 1-6.

Speed, R. C., & Walker, J. A. (1991). Oceanic crust of the Grenada Basin in the southern Lesser Antilles arc platform. *Journal of Geophysical Research: Solid Earth*, *96*(B3), 3835-3851.

Speed, R. C., Smith-Horowitz, P. L., Perch-Nielsen, K. V. S., & Sanfilippo, A. B. (1993). Southern Lesser Antilles Arc Platform: pre-late Miocene stratigraphy, structure, and tectonic evolution (Vol. 277). Geological Society of America.

Stamper, C. C., Blundy, J. D., Arculus, R. J., & Melekhova, E. (2014). Petrology of plutonic xenoliths and volcanic rocks from Grenada, Lesser Antilles. *Journal of Petrology*, *55*(7), 1353-1387.

Stepanov, A. S., & Hermann, J. (2013). Fractionation of Nb and Ta by biotite and phengite: Implications for the "missing Nb paradox". *Geology*, *41*(3), 303-306.

Stock, M. J., Geist, D., Neave, D. A., Gleeson, M. L., Bernard, B., Howard, K. A., ... & Maclennan, J. (2020). Cryptic evolved melts beneath monotonous basaltic shield volcanoes in the Galápagos Archipelago. *Nature Communications*, *11*(1), 1-13.

Straub, S. M., & Layne, G. D. (2003). The systematics of chlorine, fluorine, and water in Izu arc front volcanic rocks: implications for volatile recycling in subduction zones. *Geochimica et Cosmochimica Acta*, *67*(21), 4179-4203.

Streckeisen, A. (1976). To each plutonic rock its proper name. *Earth-Science Reviews*, *12*(1), 1-33.

Stuart, C. A., Piazolo, S., & Daczko, N. R. (2016). Mass transfer in the lower crust: Evidence for incipient melt assisted flow along grain boundaries in the deep arc granulites of Fiordland, New Zealand. *Geochemistry, Geophysics, Geosystems*, *17*(9), 3733-3753.

Stuart, C. A., Meek, U., Daczko, N. R., Piazolo, S., & Huang, J. X. (2018). Chemical signatures of melt–rock interaction in the root of a magmatic arc. *Journal of Petrology*, *59*(2), 321-340.

Taylor Jr, H. P. (1980). The effects of assimilation of country rocks by magmas on 18O/16O and 87Sr/86Sr systematics in igneous rocks. *Earth and Planetary Science Letters*, *47*(2), 243-254.

Thirlwall, M. F. (1991). Long-term reproducibility of multicollector Sr and Nd isotope ratio analysis. *Chemical Geology: Isotope Geoscience section*, *94*(2), 85-104.

Thirlwall, M. F., & Graham, A. M. (1984). Evolution of high-Ca, high-Sr C-series basalts from Grenada, Lesser Antilles: the effects of intra-crustal contamination. *Journal of the Geological Society*, *141*(3), 427–445.

Thirlwall, M. F., Graham, A. M., Arculus, R. J., Harmon, R. S., & Macpherson, C. G. (1996). Resolution of the effects of crustal assimilation, sediment subduction, and fluid transport in island arc magmas: Pb-Sr-Nd-O isotope geochemistry of Grenada, Lesser Antilles. *Geochimica et Cosmochimica Acta*, *60*(23), 4785–4810.

Tollan, P. M. E., Bindeman, I., & Blundy, J. D. (2012). Cumulate xenoliths from St. Vincent, Lesser Antilles Island Arc: A window into upper crustal differentiation of mantle-derived basalts. *Contributions to Mineralogy and Petrology*, *163*(2), 189–208.

Toothill, J., Williams, C. A., MacDonald, R., Turner, S. P., Rogers, N. W., Hawkesworth, C. J., ... & Tindle, A.G. (2007). A complex petrogenesis for an arc magmatic suite, St Kitts, Lesser Antilles. *Journal of Petrology*, *48*(1), 3–42.

Troll, V. R., Hilton, D. R., Jolis, E. M., Chadwick, J. P., Blythe, L. S., Deegan, F. M., ... & Zimmer, M. (2012). Crustal CO2 liberation during the 2006 eruption and earthquake events at Merapi volcano, Indonesia. *Geophysical Research Letters*, *39*(11).

Turner, J. S., & Campbell, I. H. (1986). Convection and mixing in magma chambers. *Earth-Science Reviews*, *23*(4), 255-352.

Turner, S., Hawkesworth, C., van Calsteren, P., Heath, E., Macdonald, R., & Black, S. (1996). U-series isotopes and destructive plate margin magma genesis in the Lesser Antilles. *Earth and Planetary Science Letters*, *142*(1–2), 191–207.

Turner, S., & Hawkesworth, C. (1997). Constraints on flux rates and mantle dynamics beneath island arcs from Tonga–Kermadec lava geochemistry. *Nature*, *389*(6651), 568-573.

Turner, S. P., Peate, D. W., Hawkesworth, C. J., Eggins, S. M., & Crawford, A. J. (1999). Two mantle domains and the time scales of fluid transfer beneath the Vanuatu arc. *Geology*, *27*(11), 963-966.

Turner, S. J., & Langmuir, C. H. (2015). The global chemical systematics of arc front stratovolcanoes: Evaluating the role of crustal processes. *Earth and Planetary Science Letters*, *422*, 182-193.

Turner, S. J., & Langmuir, C. H. (2022). An evaluation of five models of arc volcanism. *Journal of Petrology*, *63*(3), Art. No. egac010.

Van Soest, M. C. (2000). Sediment Subduction and Crustal Contamination in the Lesser Antilles Island Arc: The geochemical and isotopic Imprints on Recent Lavas and Geothermal Fluids. PhD thesis. Amsterdam (Netherlands): Vriej Universiteit Amsterdam.

Van Soest, M. C., Hilton, D. R., Macpherson, C. G., & Mattey, D. P. (2002). Resolving sediment subduction and crustal contamination in the Lesser Antilles island Arc: A combined He-O-Sr isotope approach. *Journal of Petrology*, *43*(1), 143–170.

Viers, J., Roddaz, M., Filizola, N., Guyot, J. L., Sondag, F., Brunet, P., ... & Boaventura, G. R. (2008). Seasonal and provenance controls on Nd–Sr isotopic compositions of Amazon rivers suspended sediments and implications for Nd and Sr fluxes exported to the Atlantic Ocean. *Earth and Planetary Science Letters*, *274*(3-4), 511-523.

Villares, F., Blanco-Quintero, I. F., Reyes, P. S., Proenza, J. A., Cartagena, R., Lázaro, C., & Garcia-Casco, A. (2022). Petrogenesis of the Tampanchi Ultramafic–Mafic Complex (Ecuador): Geodynamic implications for the northwestern margin of South America during the late Cretaceous. *Gondwana Research*, *105*, 514-534.

Vroon, P. Z., Van Bergen, M. J., White, W. M., & Varekamp, J. C. (1993). Sr-Nd-Pb isotope systematics of the Banda Arc, Indonesia: Combined subduction and assimilation of continental material. *Journal of Geophysical Research: Solid Earth*, *98*(B12), 22349-22366.

Wager, L. R., Brown, G. M., & Wadsworth, W. J. (1960). Types of igneous cumulates. *Journal of Petrology*, *1*(1), 73-85.

Waight, T. E., & Tørnqvist, J. B. (2018). Sr isotope zoning in plagioclase from andesites at Cabo De Gata, Spain: Evidence for shallow and deep contamination. *Lithos*, *308–309*, 159–167.

Wang, C., Liang, Y., & Xu, W. (2021). Formation of amphibole-bearing peridotite and amphibole-bearing pyroxenite through hydrous melt-peridotite reaction and in situ crystallization: An experimental study. *Journal of Geophysical Research: Solid Earth*, *126*(3), Art. No. e2020JB019382.

Weis, D., Kieffer, B., Maerschalk, C., Barling, J., De Jong, J., Williams, G. A., ... & Mahoney, J. B. (2006). High-precision isotopic characterization of USGS reference materials by TIMS and MC-ICP-MS. *Geochemistry, Geophysics, Geosystems*, *7*(8).

White, W. M., & Patchett, J. (1984). Hf-Nd-Sr isotopes and incompatible element abundances in island arcs: implications for magma origins and crust-mantle evolution. *Earth and Planetary Science Letters*, *67*(2), 167-185.

White, W. M., & Dupré, B. (1986). Sediment subduction and magma genesis in the Lesser Antilles: Isotopic and trace element constraints. *Journal of Geophysical Research*, *91*(B6), 5927.

White, W., Copeland, P., Gravatt, D. R., & Devine, J. D. (2017). Geochemistry and geochronology of Grenada and Union islands, Lesser Antilles: The case for mixing

between two magma series generated from distinct sources. *Geosphere*, *13*(5), 1359-1391.

Wilson, C. J., Cooper, G. F., Chamberlain, K. J., Barker, S. J., Myers, M. L., Illsley-Kemp, F., & Farrell, J. (2021). No single model for supersized eruptions and their magma bodies. *Nature Reviews Earth & Environment*, *2*(9), 610-627.

Witt-Eickschen, G., & O'Neill, H. S. C. (2005). The effect of temperature on the equilibrium distribution of trace elements between clinopyroxene, orthopyroxene, olivine and spinel in upper mantle peridotite. *Chemical Geology*, *221*(1-2), 65-101.

Woodhead, J. D. (1988). The origin of geochemical variations in Mariana lavas: a general model for petrogenesis in intra-oceanic island arcs? *Journal of Petrology*, *29*(4), 805-830.

Xie, X., Mann, P., & Escalona, A. (2010). Regional provenance study of Eocene clastic sedimentary rocks within the South America–Caribbean plate boundary zone using detrital zircon geochronology. *Earth and Planetary Science Letters*, *291*(1-4), 159-171.

Yanagida, Y., Nakamura, M., Yasuda, A., Kuritani, T., Nakagawa, M., & Yoshida, T. (2018). Differentiation of a hydrous arc magma recorded in melt inclusions in deep crustal cumulate xenoliths from Ichinomegata Maar, NE Japan. *Geochemistry, Geophysics, Geosystems*, *19*(3), 838-864.

Yang, A. Y., Wang, C., Liang, Y., & Lissenberg, C. J. (2019). Reaction between mid-ocean ridge basalt and lower oceanic crust: An experimental study. *Geochemistry, Geophysics, Geosystems*, *20*(9), 4390-4407.

Yogodzinski, G. M., & Kelemen, P. B. (2007). Trace elements in clinopyroxenes from Aleutian xenoliths: Implications for primitive subduction magmatism in an island arc. *Earth and Planetary Science Letters*, *256*(3-4), 617-632.

Ysaccis, R. (1997). Tertiary evolution of the northeastern Venezuela offshore. [PhD thesis, Rice University]

Yu, Z., Zhai, S., Guo, K., Zhou, Y., & Zong, T. (2016). Helium isotopes in volcanic rocks from the Okinawa Trough—impact of volatile recycling and crustal contamination. *Geological Journal*, *51*, 376-386.

Zhang, J., Davidson, J. P., Humphreys, M. C. S., Macpherson, C. G., & Neill, I. (2015). Magmatic enclaves and andesitic lavas from Mt. Lamington, Papua New Guinea: implications for recycling of earlier-fractionated minerals through magma recharge. *Journal of Petrology*, *56*(11), 2223-2256.

Zhang, W. Q., Liu, C. Z., & Dick, H. J. (2020). Evidence for multi-stage melt transport in the lower ocean crust: The Atlantis Bank Gabbroic Massif (IODP Hole U1473A, SW Indian Ridge). *Journal of Petrology*, *61*(9), Art. No. egaa082.

Ziberna, L., Green, E. C., & Blundy, J. D. (2017). Multiple-reaction geobarometry for olivine-bearing igneous rocks. *American Mineralogist: Journal of Earth and Planetary Materials*, *102*(12), 2349-2366.